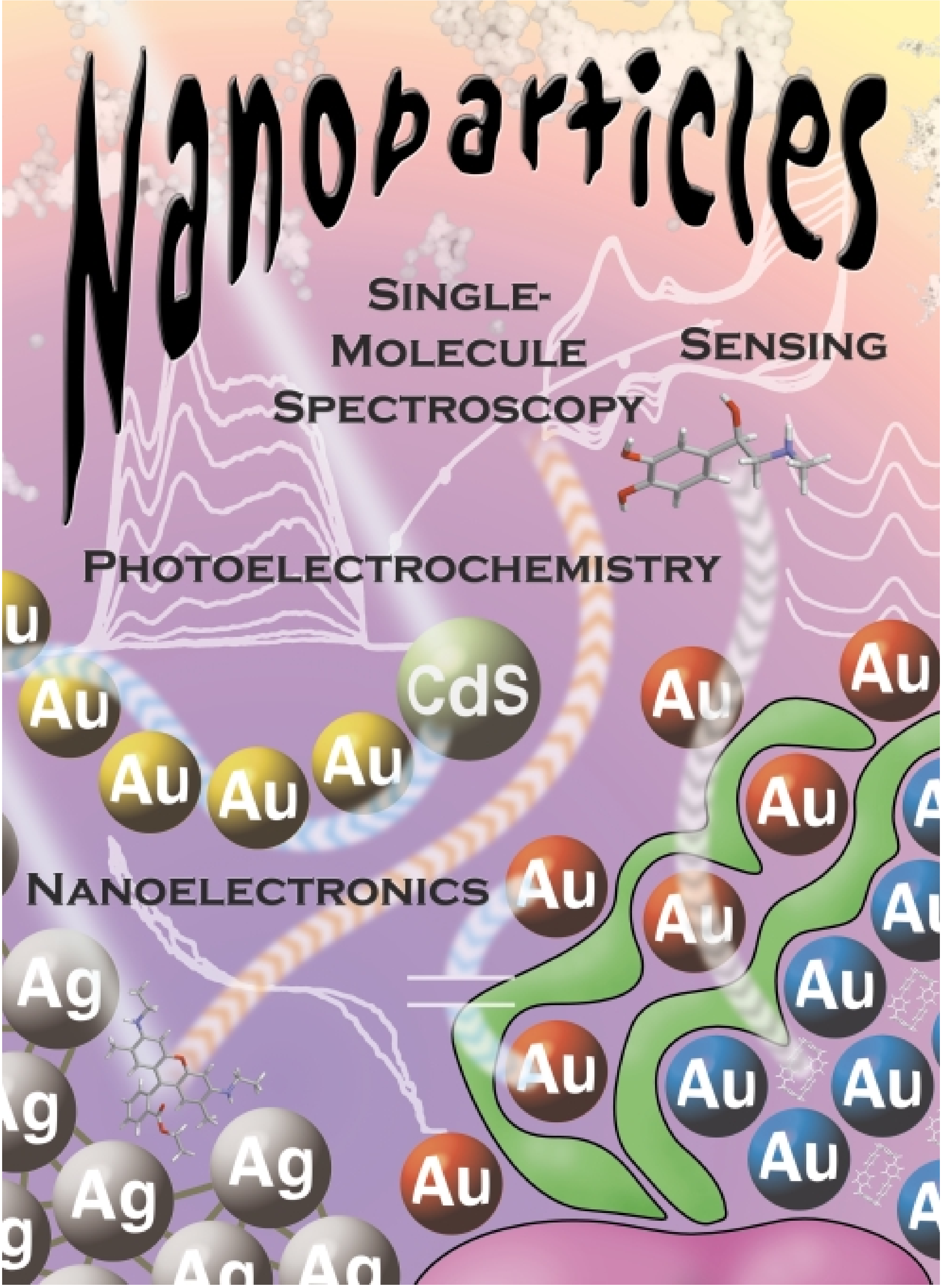
Nanoparticles
Single-Molecule Spectroscopy
Sensing
Photoelectrochemistry
Nanoelectronics
Au
CdS
Ag

Nanoparticle Arrays on Surfaces for Electronic, Optical, and Sensor Applications**

Andrew N. Shipway,[a] Eugenii Katz,[a] and Itamar Willner*[a]

Particles in the nanometer size range are attracting increasing attention with the growth of interest in nanotechnological disciplines. Nanoparticles display fascinating electronic and optical properties as a consequence of their dimensions and they may be easily synthesized from a wide range of materials. The dimensions of these particles makes them ideal candidates for the nanoengineering of surfaces and the fabrication of functional nanostructures. In the last five years, much effort has been expended on their organization on surfaces for the construction of functional interfaces. In this review, we address the research that has led to numerous sensing, electronic, optoelectronic, and photoelectronic interfaces, and also take time to cover the synthesis and characterization of nanoparticles and nanoparticle arrays.

KEYWORDS:

colloids · interfaces · monolayers · nanostructures · sensors

1. Introduction

The emerging disciplines of nanoengineering,[1] nanoelectronics,[2] and nanobioelectronics[3] require suitably sized and functional building blocks with which to construct their architectures and devices. This need has encouraged the development of supramolecular,[4] biomolecular,[5] and dendrimer[6] chemistries for engineering substatnces of Ångström and nanoscale dimensions but, even with lithographic techniques now reaching the 100 nm range, the intermediate scale of 10 – 100 nm remains relatively unexploited (Figure 1). The world of colloid and cluster science[7] has risen to this challenge and is beginning to find ways to organize nanometer-sized particles on the micron and submicron scale. Although many of these particles have been known for a substantial time, it is only now that the tools for their engineering and characterization exist, which open the doors to new disciplines of nanoparticle and nanocrystal devices. Nanoparticles are not just convenient structural elements however, but can also display unique functions. They can be fashioned from many materials and have a wide functional diversity very different from bulk materials, with much of their electronic,[8, 9] optical,[7, 10–13] and catalytic[14] properties originating from their quantum-scale dimensions.[15]

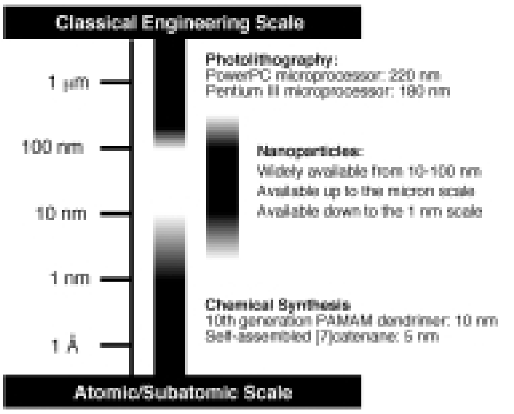

Figure 1. *Bridging the nanometer-size gap between photolithographic and synthetic chemical engineering—colloidal nanoparticles fit the bill.*

In order to tailor the new generation of nanodevices and "smart" materials, ways to organize the nanoparticles into controlled architectures must be found. This conundrum has been addressed to some extent by a large body of recent work describing the construction of colloidal dyads and triads,[16, 17] "strings",[18] clusters,[19] and other architectures[19–22] in solution and at liquid – liquid interfaces. These constructions will not be described in any detail here, since this review is dedicated to surface-bound nanostructures. Likewise, we will not explore the highly active research area of single-nanoparticle electronics in great depth, as excellent reviews already exist.[12, 15, 20] These single-electron devices tap into the quantum properties of nanoparticles for the fabrication of single-electron transistors[23, 24] and similar devices[25–27] from isolated, immobilized nanoparticles. Here, we will focus on efforts to construct organized nanoparticle arrays which perform tangible functions. These superstructures are formed on various solid supports by specific adsorption or self-assembly techniques. Although work on spin-coated, evaporated, or nonspecifically adsorbed nanoparticle films has yielded noteworthy results,[28] these techniques are conceptually macroscopic rather than nanoscopic and so will not be covered here.

The relevance of nanoparticle superstructures to the emerging areas of nanotechnology and nanophotoelectrochemistry, and to the development of nanoelectronics and "smart" materials cannot be underestimated. Colloidal particles offer a

---

[a] *Prof. I. Willner, Dr. A. N. Shipway, Dr. E. Katz*
Institute of Chemistry
The Hebrew University of Jerusalem
Jerusalem 91904 (Israel)
Fax: (+972) 2-6527715
E-mail: willnea@vms.huji.ac.il

[**] *Parts of our studies on nanoparticle arrays are supported by the Israel – U.S. Binational Science Foundation and the German – Israeli program (DIP).*

Itamar Willner
was born in 1947. He completed his Ph.D. studies in chemistry in 1978 at The Hebrew University of Jerusalem. After a postdoctoral stay with M. Calvin at the University of California, Berkeley, from 1978 to 1981 he joined the Institute of Chemistry at the Hebrew University of Jerusalem in 1982. In 1986, he was appointed as Professor at the Hebrew University. He is a fellow of the American Association for the Advancement of Science (AAAS), acts as a member of several editorial boards, and is the recipient of the Kolthoff Award and the Max Planck Research Award. His research interests include light-induced electron transfer processes and artificial photosynthesis, molecular electronics and optoelectronics, bioelectronics and biosensors, optobioelectronics, supramolecular chemistry, nanoscale chemistry, and monolayer and thin-film assemblies.

Eugenii Katz
was born in Moscow in 1952. He completed his Ph.D. in 1983 at the Frumkin Institute of Electrochemistry, Moscow, and acted as senior scientist at the Institute of Photosynthesis, Pushchino, until 1991. In 1991, he undertook postdoctoral research at the Hebrew University of Jerusalem and later (1993), as a recipient of a Humboldt scholarship, he worked at the Technische Universität, Munich. He joined the research group of Itamar Willner at the Hebrew University as Senior Research Associate in 1994. His research interests include electroanalytical chemistry, functionalized monolayers, biosensors and bioelectronics.

Andy Shipway
was born in 1971 in Bristol, UK. He studied for his B.Sc. at the University of Birmingham and stayed on as a Ph.D. student under the supervision of Professor J. Fraser Stoddart with a thesis entitled "Insight into Dendrimers and their Role in Catalysis". He joined the group of Itamar Willner at the Hebrew University in late 1997 as a postdoctoral fellow, coordinating projects inovolving organic synthesis and nanoparticle superstructures.

route to the simple assembly of complex structures and can be used to create a variety of electronic and sensor components. We should note that in this review, we use the terms "nanoparticle" and "colloid" as synonyms for nanosized particles of ambiguous structure, while we consider "nanocrystals" to be necessarily crystalline and "clusters" to have a defined stoichiometry.

2. Synthesis of Nanoparticle Arrays

The construction of nanoparticle arrays on surfaces has only gained significant attention in the last ten years. Nevertheless, the diversity of building blocks, architectures, and construction techniques that have been reported is impressive.[19, 29] This research has also spurred on efforts to synthesize colloids from new materials and with novel surface functionalities. The construction of two-dimensional colloid arrays is well studied. This groundwork has led to methods for the synthesis of much more complex three-dimensional systems and patterned arrays, which may eventually lead to highly functionalized assemblies and composites.

2.1. Synthesis of Colloidal Nanoparticles

Many colloidal nanoparticle syntheses have been known for a considerable amount of time[30, 31] but, more recently, a body of work has grown that is dedicated to nanoparticle syntheses specifically for the construction of devices and nanostructures. These particles may consist of a particular material, be of a particular size, or have specialized surface functionality. It has even become possible to have some degree of control over the nanoparticle shape.[32] Nanoparticles tend to be fairly unstable in solution, so special precautions have to be taken to avoid their aggregation or precipitation. Glassware is cleaned thoroughly, while reagent solutions and solvents are all filtered and of the highest purity. All nanoparticle syntheses also involve the use of a stabilizing agent, which associates with the surface of the particle, provides charge or solubility properties to keep the nanoparticles suspended, and thereby prevents their aggregation.

2.1.1. Reductive Synthesis of Noble Metal Colloids

The simplest and by far the most commonly used preparation for gold nanoparticles is the aqueous reduction of $H[AuCl_4]$ by sodium citrate at reflux.[31, 33] Although sodium citrate is the most common reducing agent, metal nanoparticles can also be synthesized by the use of borohydride and other reducing agents.[31–34] The application of alcohols as reductants for the production of platinum nanoparticles allows control over the size of the particles: Higher alcohols yield larger particles, which indicates that a more rapid reduction rate of the $[PtCl_6]^{2-}$ ions is an important factor for the production of smaller particles.[35]

Particles synthesized by citrate reduction are nearly monodisperse spheres of a size controlled by the initial reagent concentrations (Figure 2 and Table 1).[36] They have a negative surface charge as a consequence of a weakly bound citrate

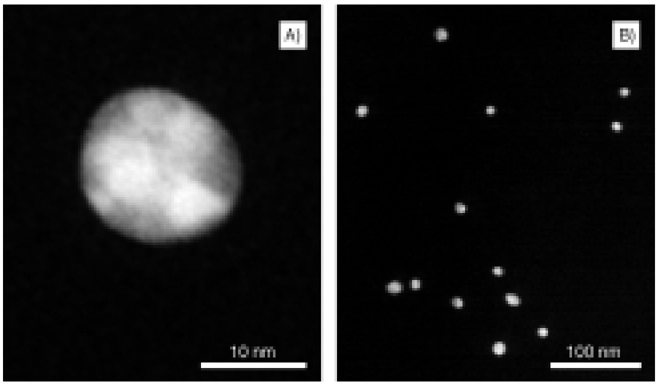

Figure 2. *Gold nanoparticles synthesized by citrate reduction. A) A single particle at high magnification shows its highly spherical shape. B) A region of single nanoparticles at a lower magnification shows the monodispersity of particle sizes.*

Table 1. *The dependence of nanoparticle diameter on citrate concentration in the reductive synthesis of gold nanoparticles.*[a]

Citrate solution added[b] [mL]	Diameter[c] [nm]
1.0	16
0.75	25
0.5	41
0.3	72
0.21	98
0.16	147

[a] Data is taken from reference 34. [b] Trisodium citrate (1% aqueous solution) was added to 50 mL refluxing solution of 0.01% $H[AuCl_4]$. [c] Particle diameters were measured by SEM.

coating and are easily characterized by their plasmon absorbance (at about 520 nm for 15 nm particles; see Section 3.2). Nanoparticles of other noble metals may also be prepared by citrate reduction, such as silver particles from $AgNO_3$, palladium from $H_2[PdCl_4]$, and platinum from $H_2[PtCl_6]$.[37, 38] The similarities in the preparation of these different metal colloids allows the synthesis of mixed-metal particles, which may have functionality different from each individual metal.[30] For example, the reduction of suitable mixtures of noble metal salts can lead to “alloy” or “mixed grain” particles. More interestingly, composite particles can be built up in “shells” by the synthesis of a small colloidal nuclei followed by its enlargement with a different metal: a gold colloid can be covered with silver.[39] Well defined core/shell organosilicon micronetworks with topologically trapped gold particles have also been prepared using a molecular reactor technique.[40] Metallic nanoparticles can be capped with various shells, such as conductive, nonmetallic graphite,[37] or semiconductive CdS.[42] This capping can be done in situ if the reductive formation of nanoparticles is performed in the presence of the shell-forming material[37] or the shell can be organized later through a chemical reaction on the surface of the nanoparticle.[42] The enlargement of a nanoparticle can take place even after the colloidal “seed” particle has been immobilized on a substrate. In such cases, a colloid-functionalized glass substrate is introduced to a gold-[43] or silver-[44] depositing solution, to thereby enlarge the surface-bound nanoparticles and provide a method of control over their size and density. Such “core – shell” particles have been studied extensively because their properties can differ from those of the core or shell materials.[40, 41, 45]

The synthesis of particles that bear surface functionality is desirable for the purpose of nanoparticle handling and the construction of functional architectures. This functionalization of the nanoparticle surface can be accomplished during the nanoparticle synthesis by the addition of a suitable agent to the reaction vessel. As the nanoparticles form, the surface functionalization agent attaches to the nanoparticles, which also imparts an enhanced stability and gives additional control over their size. The borohydride reduction of $H[AuCl_4]$ in the presence of (γ-mercaptopropyl)-trimethoxysilane gives rise to very small (1 – 5 nm) gold nanoparticles which bear a surface silane functionality.[46] Other borohydride reductions in the presence of thiols[47] have produced nanoparticles with a surface functionality from amines to carboxylic acids. Where the surface-functionalization agent is not water soluble, a two-phase synthesis can be used, as in the preparation of long-chain alkanethiol surfaces on gold colloids.[48] The surface-functionalization agent does not even need to bind covalently with the nanoparticle. Nanoparticles have been synthesized in the presence of dendrimeric[49] and polymeric[50–52] stabilizers, and have been formed in the cavities of micelles[53] and silicate sols.[54] Gold and silver nanoparticles functionalized by adsorbed dialkyl disulfides have also been generated in the presence of sodium borohydride.[55] Disulfides offer the advantage that asymmetrical disulfides, that have two distinct functional groups (RSSR′), may be used, which enables the possibility of generating mixed, self-assembled monolayers (SAMs) that possess a homogeneous distribution of functional groups or chain lengths. The use of disulfides also allows the functionalization of nanoparticles with groups such as quinones that are otherwise incompatible with thiols (normally, a thiol would be used rather than a disulfide). The application of different capping materials or the preparation of mixed bimetallic particles allows control of the size and shape of the nanoparticles.[32, 56] For example, platinum nanoparticles with cubic, tetrahedral, polyhedral, or irregular-prismatic shapes could be generated selectively when the initial concentrations of $[PtCl_6]^{2-}$ and polyacrylic acid were varied for the reductive particle formation.[32]

2.1.2. Synthesis of Semiconductor Nanoparticles

The production of semiconductor nanoparticles and their organization on solid supports is of great importance for the fabrication of nanoelectronic devices. The quantum properties of these particles have potential uses in information-processing devices and, in recognition of this, they are often called “Q particles”.[15] By far the most studied of these are cadmium sulfide particles.[57] These and related colloidal particles (for example, PbS,[58] Ag_2S,[59] CdSe,[23] and TiO_2[60, 61]) can be prepared relatively easily by using inverse micelles as nanoscale reaction vessels.[62] Firstly, solutions of inverse micelles are prepared, one containing the metal salt (usually as the chloride) and the other containing Na_2S (or Na_2Se for the production of CdSe, and so forth). These solutions are mixed together and nanoparticles form as the different micelles exchange their contents (Scheme 1). Alternatively, the sulfide can be introduced as H_2S gas. After the particles are formed, they may be stabilized by the addition of a thiol, which bonds to the surface of the nanoparticle and may also contain other functionalities.[63, 64] If a mixture of thiols is used, nanoparticles with a mixture of surface groups are produced.[65] The particles may be isolated after disrupting the micelles (provided that this has not already taken place in the stabilization step). The synthesis of CdS nanoparticles gives a highly monodisperse product but for some other materials, such as PbS, the procedure gives particles with a much wider size distribution. Several metal-sulfide nanoparticles have also been synthesized by a similar route involving a polymer (rather than micellar) stabilizer,[66] and related cadmium compounds have been synthesized from organometallic reagents.[67, 68] Other semiconductor nanoparticles of interest include gallium nitride[68] and titania; nanoparticles of the latter can be synthesized either by precipitation[61, 69] or in micelles.[60]

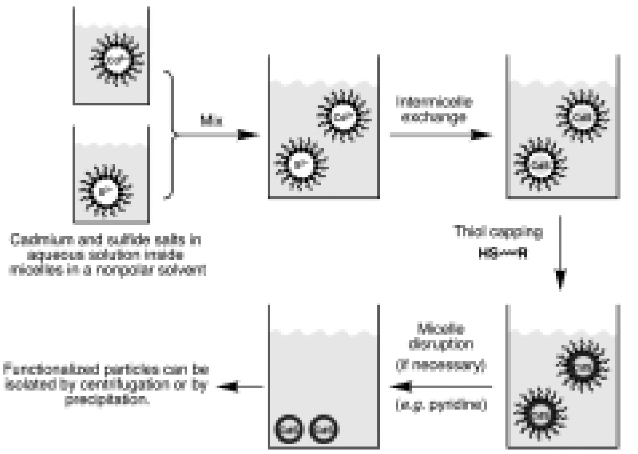

Scheme 1. *The synthesis of CdS particles inside inverse micelles, their capping by thiol molecules, and their recovery from the reaction mixture.*

2.1.3. Other Techniques for Nanoparticle Synthesis

Smaller nanoparticles may be formed in the gas phase,[70] or by ablation using high peak-power laser pulses,[71, 72] while others have been etched,[73, 74] electrodeposited,[75] or synthesized[76, 77, 79–81] directly onto surfaces, or in Langmuir–Blodgett (LB) layers.[82] These techniques cater for the specialized needs of researchers who require colloids of particular sizes, shapes, or materials. For the cheap and easy synthesis of simple nanoparticles, there is no substitute for solution-state synthesis, which can be used to prepare bulk quantities without the need for specialized laboratory apparatus.

2.2. Assembly of Nanoparticle Monolayers

This Section details the first step in the production of colloid interfaces—their ordered immobilization on a solid support. Nanoparticles have been assembled on a wide variety of substrates, sometimes by highly ingenious means, such as the association of a streptavidin-functionalized colloid to a biotin-functionalized surface,[83] but true nanoengineering requires nanoscale control, namely, control over the morphology of nanoparticle packing on the surface. This requirement is finally becoming a reality with new research into the ordering of adsorbed particles, which brings new applications to light, such as the use of nanoparticles as nanoscale "masks" for the lithography of surfaces.[84, 85] It should be noted, that one should expect some nonideality even from networks of nanoparticles with a very narrow size distribution (variation of less than 10%). Theoretical considerations of nanoparticle lattices using a Hamiltonian based on a Hückel-type, tight-binding approximation concludes that they have a configurational disorder and can never be identical.[86]

2.2.1. Assembly by Adsorption on Glass Substrates

Glass substrates may be conductive (such as indium- or fluorine-doped tin oxide—ITO or "K-glass") or nonconductive (such as quartz or soda glass) but are all characterized by their transparency and the availability of surface -OH functionality. Glass substrates allow simple spectroscopic and electron microscopic characterization of thin films and are also advantageous on account of their high rigidity and low cost. The polymerization of a thin film of a trialkoxysilane on the substrate is usually carried out to produce a useful surface functionality (Scheme 2).[71, 83, 87–90] This is a general method, which can be applied to a variety of surfaces, and has been reviewed in detail.[91, 92] The surface must first be scrupulously clean in order to ensure the maximum number of exposed surface OH groups. This is achieved by oxidative cleaning in acidic solution (often "piranha solution", HCl/HNO_3 3/1) and rinses of various solvents. The clean substrate is then immersed in a solution of the siloxane. The conditions for this reaction vary widely and depend upon the desired properties of the film and the nature of the substrate. While quartz and soda glass are relatively easy to functionalize, K-glass substrates normally require much harsher conditions to obtain a similar silane coverage. For characterization by atomic force microscopy (AFM), a very smooth and flat surface is required, so the minimum amount functionalization is used. For electrochemical analysis, an overly thick siloxane film may also be disadvantageous as it insulates and hampers electrical communication between the electrode and the colloid. At the opposite extreme, if a colloid array is to be characterized only by spectroscopy, a very extensive functionalization is advantageous in order to provide the best possible surface for nanoparticle adsorption.

The functionalized glass surface bears chemical groups that are capable of binding a colloid particle either covalently (for example, a thiol to bind gold colloids) or through electrostatic interactions (for example, an quaternary amine to bind anionic particles). The formation of a colloid monolayer is achieved by placing the surface-functionalized substrate in a solution of the nanoparticle, which adsorbs onto the surface and assembles into a saturated monolayer with time. The monolayer density is

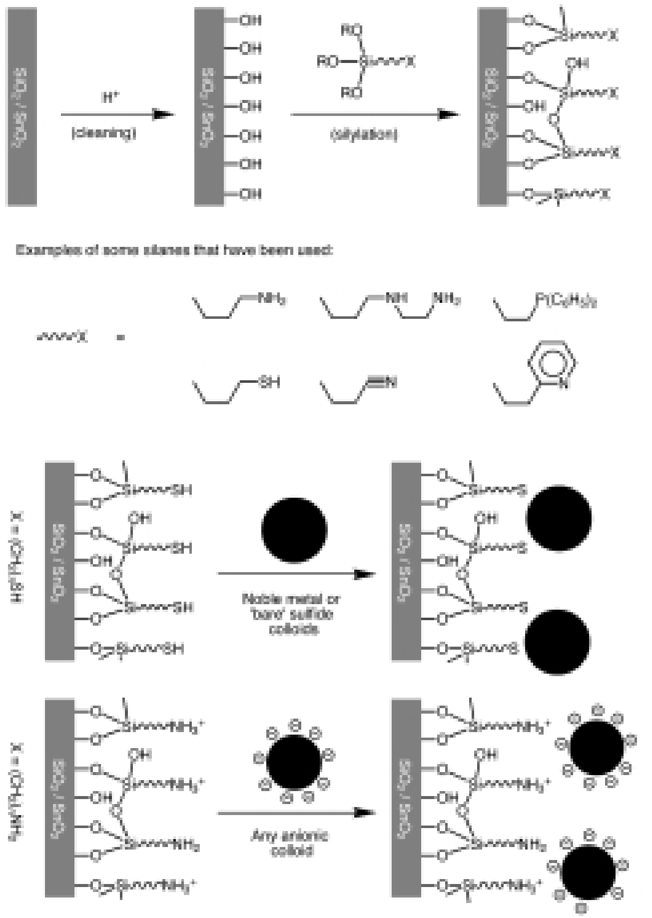

Scheme 2. *The construction of gold-nanoparticle monolayers on glass substrates by adsorption onto a thin film of polymerized siloxane. Top: Modification of the surface of the glass. Middle: A selection of surface-modifying silanes. Bottom: Adsorbtion of the nanoparticles. R = Me, Et.*

dependent on factors such as the size and charge of the particles as well as the attachment method and the substrate.[93] In a study of citrate-stabilized gold nanoparticles assembled on amine- and thiol-functionalized ITO glass surfaces, it was found that 80 nm particles formed layers over 20 times less dense than 15 nm particles (approximately 2×10^9 80 nm particles, as opposed to about 4.5×10^{10} 15 nm particles, per cm^2).[88] This result is supported by an optical reflectometry study of the adsorption of (negatively charged) silica nanoparticles on an aminopropyl silane-functionalized support.[94] The initial rate of nanoparticle adsorption was found to decrease with increasing particle size. Amine-functionalized substrates bind the particles at a slightly higher density than thiol-functionalized substrates. The dynamics of monolayer assembly has been followed directly by quartz-crystal microgravimetry (QCM)[95, 96] and spectroscopy[97] and, for the case of citrate-capped gold particles, occurs over a period of a few hours.

2.2.2. Assembly on Metal Substrates

Assembly of nanoparticles on gold substrates often follows a similar procedure to that for glass substrates, namely, surface modification of the substrate followed by the adsorption of colloidal particles. The modification of the gold surface can be achieved by use of a thiol,[98] which forms a covalent link to the gold surface (Scheme 3). The thiol also bears a group capable of binding to a nanoparticle, for instance, another thiol moiety for CdS or Pt particles,[99] an amine or thiol for Au particles,[100] or a carboxylic acid for TiO_2 particles.[61] Aluminium surfaces are easily functionalized by carboxylic acids (Scheme 3) and thus colloids may be immobilized on them by modification of either the nanoparticles or the surface with a carboxylic acid attached to a colloid-binding group (such as a thiol for gold nanoparticles).[101, 102]

Electrically conductive substrates also allow the possibility of particle adsorption by electrophoretic means.[35, 51, 103] In this procedure, the gold nanoparticle surface is first treated with an alkanethiol in order to lower the surface charge. The particles are then deposited onto the anodic surface under relatively low potentials and are subsequently desorbed if the electrode polarity is reversed. The monolayers formed have extremely regular structures but, since the particles are not truly adsorbed to the substrate, the structures exhibit low stabilities. Real electrocatalyzed adsorption can be accomplished by the use of functionalized nanoparticles. Reduced viologen is known to adsorb strongly to gold electrodes and thus viologen-functionalized gold colloids can be electrochemically activated to form a monolayer on a QCM surface.[104] When the viologen units are subsequently oxidized, the monolayer is released from the electrode surface.

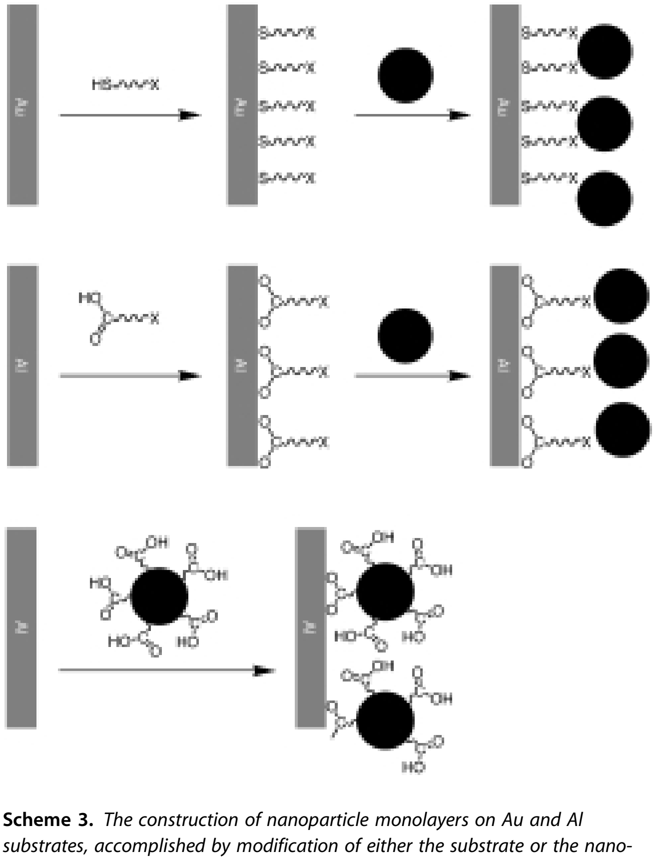

Scheme 3. *The construction of nanoparticle monolayers on Au and Al substrates, accomplished by modification of either the substrate or the nanoparticle.*

2.2.3. Assembly on Carbon Substrates

The electrochemical deposition of metal nanocrystals onto carbon electrodes has been the subject of a large number of investigations,[105, 106] as this type of interface is of great importance to electrocatalysis and as a model system for electroplating. The focus of many of these studies has been on the early stages of electrochemical deposition in order to elucidate the nucleation and growth mechanisms of the metal phase on the substrate (usually a glassy carbon electrode). The mechanisms of electrochemically assisted deposition of metal nanoparticles include the electrochemical reduction of the respective salt (such as $[AuCl_4]^-$ for gold deposition), primary formation of ad-atoms, and the further growth of nanocrystals on the carbon electrode. The overall surface area of gold, as well as the nanocrystal size, density, and surface texture, can be controlled by the variation of deposition conditions (the bulk concentration of the salt and the overpotential applied).[106] A combination of electrochemical and chemical steps allows the formation of sulfur-capped CdS nanocrystals onto a graphite support.[107–109] This procedure includes the electrochemical reduction of Cd^{2+} ions to form metallic Cd^0 precursor particles on the electrode surface. Improved size monodispersity[109] was achieved by the deposition of cadmium precursor particles through a series of 8 – 12 ms deposition voltage pulses separated by 1 – 5 s "mixing" periods during which growth was suspended, instead of a single, long deposition pulse that usually results in a very wide size distribution. After their formation, these metallic particles were electrochemically oxidized to form hydroxylated nanoparticles. Finally, (the chemical step) OH^- anions associated with the nanoparticles were displaced by S^{2-}, to produce CdS capped with a polysulfide shell. These sulfur-capped CdS nanoparticles exhibited photoluminescence emission line widths of 15 – 35 meV at 20 K,[109] which are much narrower than those observed for widely size-distributed CdS particles (125 – 180 meV).[107]

2.2.4. Other Techniques

The assembly of negatively charged nanoparticle layers on adsorbed polycationic polymer films such as poly(ethyleneimine) or poly(diallyldimethylammonium chloride) (PDDA) is of significance. This methodology is very general and yields successful results for metallic,[110, 111] semiconductive,[65, 112] silica,[113] and even mineral[114] nanoparticles. Techniques for the construction of thin polymer films are very well known[115] and allow the construction of nanoparticle arrays almost irrespective of the substrate material. Similarly, nanoparticles have been assembled on polyamidoamine (PAMAM) dendrimer films.[116, 117] Surfaces have also been prepared for nanoparticle organization by the formation of Langmuir – Blodgett films.[118] This method gives very thin and dense sublayers but is not suitable for the large-scale production or shaped substrates. The Langmuir – Blodgett technique and a similar "surface-tension driven" method[119] have also been used for the direct assembly of nanoparticle layers. The nanoparticles can be immobilized at the air – water interface either within a "carrier" monolayer (for instance, negatively charged silver colloids have been immobilized in positively charged fatty amine monolayers)[120] or by virtue of their own properties.[120–122] Langmuir – Blodgett films enable a very high degree of control over the nanoparticle density and ordering, since the monolayer can be manipulated prior to the assembly of the particles on the substrate,[123] but their formation has neither the generality nor the ease of the self-assembly methods.

Other monolayer syntheses are less developed. We have already seen that arrays of nanoparticles can be etched[73, 74] or grown[76, 77, 80] directly on surfaces. It is also possible to synthesize nanoparticles that are prelinked to surface by the immersion of a suitably functionalized substrate in the nanoparticle-generating reaction vessel.[124] If a thiol-functionalized substrate is placed in the reaction vessel during CdS colloid synthesis, then the nanoparticles bind to the surface as they form. This is advantageous, since fully formed CdS particles are usually stabilized by a thiol layer which then inhibits the particle from binding to a substrate. In addition, easy control over the particle size is possible but this method yields only very poor coverage. Finally, there are several examples of nanoparticles that have been assembled on the surface of other, larger nanoparticles.[22, 39, 125–127] The synthetic routes employed are usually analogous to those used for assembly on bulk substrates (such as electrostatic, biotin/avidin,[128] DNA/complementary DNA,[16, 22, 129–131] protein/carbohydrate,[132] or nonbiological host/guest[133] interactions) but the whole process usually proceeds in solution. These solution-state architectures are of great interest to the field of nanoengineering but will not be covered here.

2.2.5. Monolayer Ordering

We have already seen that monolayers formed by electrophoresis can have very regular, close-packed structures. Similar results can be obtained from the evaporation of colloid solutions on substrate surfaces under carefully controlled conditions[134] but other methods of monolayer formation tend to give less organized films with lower coverage. The particle density of electrostatically produced monolayers is dependent on factors such as the particle size[88] and surface charge—the particles in these films are usually well spaced, since their charges prevent close contact with each other. Citrate-stabilized gold nanoparticles normally give around 30 % adsorption coverage for 12 nm particles[89, 97] but closer packing can be achieved by the neutralization of their surface charge (Scheme 4). If a thiol-bound monolayer of citrate-stabilized colloids are exposed to a solution of an alkanethiol, then the alkanethiol displaces the citrate and thereby neutralizes the particle's charge (Scheme 4 A). After this procedure, additional nanoparticles can be adsorbed in the spaces between those in the original layer, as electrostatic repulsion no longer inhibits their approach.[97] Continued cycles of neutralization and nanoparticle adsorption leads to a dense monolayer with interparticle spacings controlled by the choice of the alkanethiol.[110] A similar procedure on an amine-functionalized substrate can even coax the nanoparticles into reorganizing themselves (Scheme 4 B).[87] In this case, when the citrate

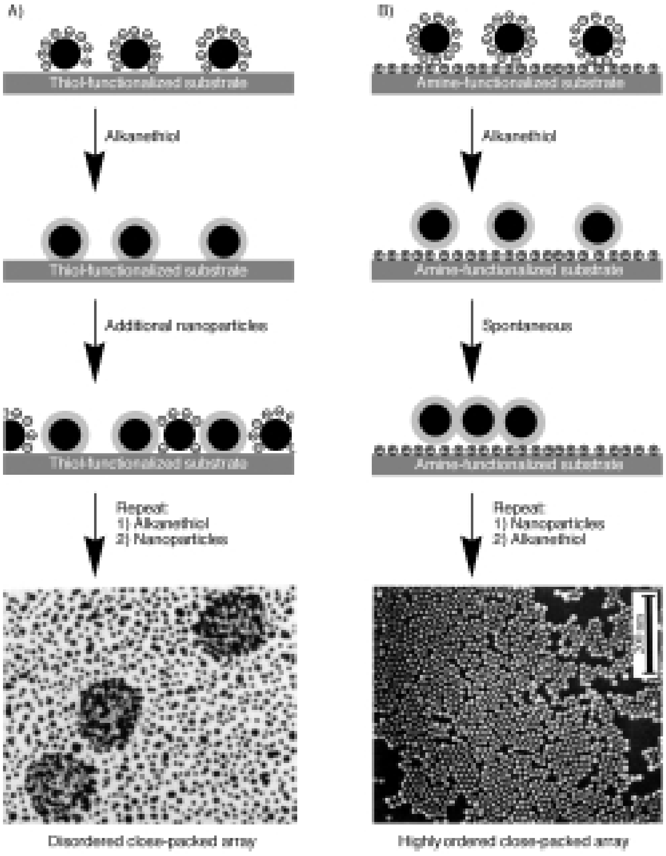

Scheme 4. *Control over interparticle spacing and packing. A) Assembly of a high density monolayer by the neutralization of the nanoparticle surface charge. B) Assembly of a "crystallized" monolayer by loosening the nanoparticle – substrate bond, which allows particle reorganization. Micrographs in (A) and (B) are reproduced from refs. [97] and [87], respectively, with permission.*

layer is removed from the nanoparticles, their electrostatic bond to the substrate is substantially weakened. The freed nanoparticles can then self assemble into highly regular, hexagonally packed structures on the surface, while further neutralization and adsorption cycles give rise to highly ordered surfaces. These monolayers suffer low stabilities, however, as a consequence of the loss of binding between the particles and the surface. Other studies have generated crystallized monolayers through carefully optimized conditions for the colloid deposition[135] or very dense but uneven layers by the aggregation of the colloid solution prior to its deposition.[89] More widely spaced nanoparticle matrices and other superstructures[136] can be constructed with the help of templates. Self-assembled, organized bacterial monolayers have been used as substrates for the adsorption of CdS nanoparticles.[137] The particles only adsorb in the pores between the bacterial subunits, which leads to morphologically controlled wide matrices that are suitable for the construction of addressable device arrays.

2.3. Assembly of Nanoparticle Multilayers

In order to assemble nanoparticle multilayers, a monolayer must be "primed" in some way for the adsorption of the second (and subsequent) particle layers. This priming may be little more than a modification of the surface layer or it may involve its functionalization with another component. The forces used to hold such structures together are either covalent or ionic—although specific interactions, such as DNA duplex formation[16, 22, 129, 130] and biotin/avidin complexation,[128] have been used to form interparticle complexes in solution; such approaches are in their infancy for the construction of a multilayers.[277] Architectures may also be much more complicated than simple alternating layers, and may contain different layers, which consist of different types of nanoparticles[99, 113, 138] or crosslinkers,[131, 139] leading to designed functional materials.

2.3.1. Polymer-Linked Architectures

The polymer-linked nanoparticle multilayer arrays constructed to date have focused on anionic colloidal nanoparticles (usually of gold), although other examples (such as hydroxide-functionalized gold particles crosslinked by titania[141]) do exist. The charge on anionic particles allows them to adsorb onto cationic polymers and vice versa, allowing three-dimensional structures to be built up in a stepwise fashion. Scheme 5 shows how a polymer – colloid multilayer composite can be constructed by the exploitation of electrostatic interactions. The base colloid layer has a net negative charge, so facilitates the assembly of a thin film of a polycationic polymer. In turn, the polymer layer leaves a surface positive charge, on which a second colloid layer is assembled; subsequent layers are built likewise. Polymers that have been used include PDDA,[37, 65, 113, 123, 142] among others,[111, 131, 140] and a wide range of colloidal materials, such as gold,[111, 131] silver,[37] semiconductors,[65] and silica,[113, 142] have been utilized. Although these architectures are only stabilized by ionic interactions, they tend to be highly stable in almost any solvent and require physical scratching or chemical reaction to damage them. Polymer – nanoparticle assemblies hold great promise for the construction of nanoscale electronic devices. Polymer layers can be of controllable thickness, which isolates

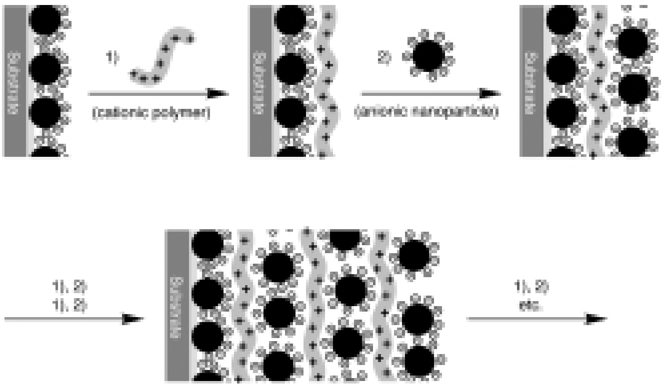

Scheme 5. *The construction of polymer – colloid multilayers by the exploitation of electrostatic interactions between anionic nanoparticles and cationic polymers.*

colloid layers from each other by whatever distance is required, and they may also be conducting, semiconducting, or insulating.

The characteristics of the colloid layers can be controlled by the conditions at which they are adsorbed. A QCM study of PDDA-crosslinked silica colloid (mean 45 nm) grown in layers showed that lower colloid concentrations or the presence of other electrolytes in the colloid solution caused a lower coverage for each layer. These measurements were highly reproducible over many consecutive layers.[113] Careful control over the adsorption time can also prove important. For the same system, sufficient colloid adsorption for a new polymer layer to be laid requires as little as two seconds, even though it requires over ten seconds to achieve colloid saturation.[142]

2.3.2. Other Electrostatically Linked Architectures

The assembly of electrostatically linked nanoparticle arrays is a general method which has been shown to be effective up to micron dimensions.[143] Nanoparticle arrays can be constructed from any charged nanoparticle and an oppositely charged "crosslinker" in an analogous way to the construction of colloid–polymer architectures (Scheme 6). The "crosslinker" may be anything from a small molecule[144] to another nanoparticle[145, 151] but it must bear multiple charges so it can simultaneously interact with the colloid layers both above and below it. Aggregation of gold nanoparticles mediated by C_{60} can be used to construct a C_{60}/Au multilayer with unusual optical and electronic properties.[146] The origin of the interaction between gold particles and fullerene molecules is still unclear but it has been suggested that it involves an electron transfer process between the organic and inorganic components of the array.

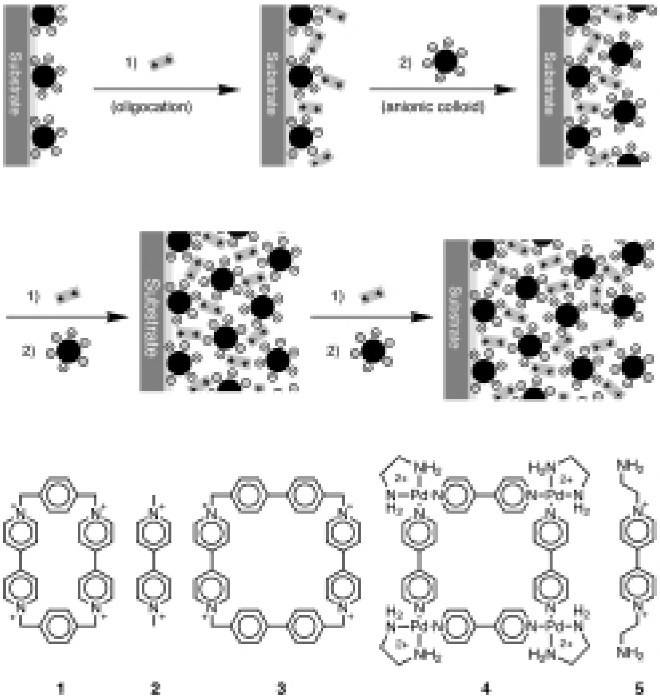

Scheme 6. *The construction of molecular oligocation/anionic colloid multilayers by the exploitation of electrostatic interactions, with examples of some bipyridinium-based oligocations (**1**–**5**).*

Great success has been realized by the use of 4,4′-bipyridinium-based crosslinkers **1**–**5**,[138, 139, 147–150] which also exhibit electrochemical activity as well as other functions (see Section 4). Singly charged species, such as tetrabutylammonium chloride, are able to partially neutralize the colloidal charge, so that greater coverage can be realized, but they cannot be used to assemble true multilayer structures.[151] In fact, not even all oligocations are successful. Those that bind the nanoparticle more strongly than the underlying substrate may destroy the superstructure, while those with a low charge density may not form a superstructure. The oligocationic molecule can be assembled in a variety of solvents but, to achieve efficient coverage, immersion in a fairly concentrated nanoparticle solution (about 10 mM) for at least 30 minutes is usually required. It is very important that the sample is washed very thoroughly before every colloid treatment, as any weakly bound crosslinker can diffuse into the bulk solution and aggregate the colloid.

Like in the construction of polymer-linked structures, treatment of a colloid monolayer with an oppositely charged species results in a surface ready for the assembly of a second colloid layer. In this case, however, the much smaller "crosslinker" means the colloid layers are much closer—even interleaved—such that there can be electrical communication throughout the entire structure.[147] The use of *N*,*N*′-diaminoethyl-4,4′-bipyridine (**5**) as a crosslinker has been used to demonstrate the versatility of the method—gold and silver colloids offer the same assembly characteristics, which allows composite structures to be built.[138]

2.3.3. Covalently Linked Architectures

Covalently linked colloid superstructures can be built analogously to electrostatically linked architectures. This has been accomplished by the use of bisthiol crosslinkers for gold[95, 152–154] and other[99] nanoparticles (Scheme 7) and has been verified by QCM and other techniques. If a gold colloid monolayer is exposed to a solution of a bisthiol, then the crosslinker assembles on the gold surface, which leaves thiol moieties at the nanostructure–solution interface. The assembly of a second colloid layer is thereby possible and the construction can continue in the same way. This method allows some control over

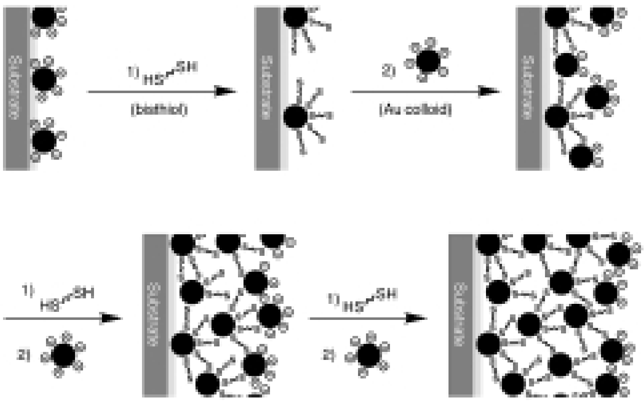

Scheme 7. *The construction of thiol-crosslinked multilayers of gold nanoparticles.*

interparticle spacing by the use of bisthiols with spacers of various lengths[152] and, in turn, the interparticle spacing affects lattice properties such as conductivity (as will be discussed in Section 3.3.2). The conditions required for this assembly are very similar to those for electrostatic assembly but the technique has not yet been extended to include functionally interesting crosslinkers. It should be noted that the reaction of the gold surface with a thiol displaces the negatively charged citrate ions, to leave the thiol – colloid interface uncharged. As is shown in Scheme 7 however, the charge remains at the colloid – solution interface, which leaves a path open for the construction of composite covalent – ionic structures. 2-Mercaptoethylamine has already been used as an interparticle crosslinker.[144]

2.4. Assembly of Patterned Nanoparticle Arrays

The patterning of colloid arrays is of paramount importance if these structures are to be used in nanoelectronic applications or to tailor addressable sensing domains. In recognition of this fact, methods for the patterning of colloid-functionalized surfaces have been developed, which can broadly be categorized into three paradigms: lithography, microcontact printing, and physical engineering. The direct engineering of surfaces by scanning microscopy tools, such as by STM and AFM tips, is intriguing but lies far from a cheap industrial or general laboratory process. Colloid particles have been electrodeposited,[155] "swept",[156] and even etched by CN^-[157] at the touch of a STM tip. Even so, the construction of large devices is unfeasible and even the manipulation of a single particle is currently seen as quite an achievement. Another approach is to adsorb nanoparticles onto a substrate that already bears a pattern. In one such example, a matrix of latex colloids was used as a mask for the evaporation of gold, after which gold colloids were attached to the pattern with a dithiol crosslinker.[127] Engineered colloidal films can also be produced by the exploitation of the monolayer formation reaction (Scheme 8).[158] A silanated substrate was slowly immersed in a solution of gold nanoparticles and was then washed. Since different points on the substrate had been exposed to the colloid for different periods of time, the colloid density varied across the sample. The sample was then rotated 90° and slowly dipped into a solution that deposited silver onto the gold. This procedure resulted in gradients of colloid size and composition across the film and, thus, no two points on the substrate had the same composition. This "combinatorial" surface was used to determine the optimum morphology for surface-enhanced Raman scattering (SERS; Section 4.1.2).

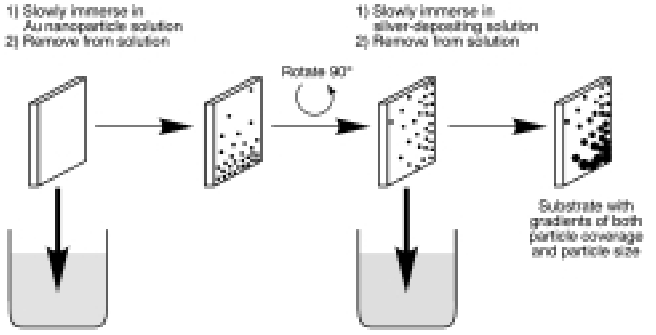

Scheme 8. *The synthesis of a "combinatorial" colloid array by the adsorption of two different colloidal materials in perpendicular concentration gradients across the substrate surface.*

The pattern engineering of the colloid monolayer after its formation has not been studied in any depth. This route would involve the construction of a colloid monolayer and its subsequent patterning by, for instance, scanning nanocapillaries filled with an "etching ink". In one example, a thin film of surfactant-covered palladium nanoparticles was patterned by an electron beam. In the exposed areas, the surfactant coating was removed from the particles, which allowed them to agglomerate into continuous metal. The remaining (unexposed) discrete nanoparticles were then washed away to leave the metal pattern.[78]

2.4.1. Photolithography-Based Patterning

Lithography provides a well known route to patterned substrates and a number of examples concerning colloidal systems are known. The most trivial of these relies on standard lithographic techniques to produce a poly(methylmethacrylate) (PMMA) pattern on a silica substrate.[159] The "windows" in the pattern can then be silanated and a colloid layer assembled by standard procedures (Figure 3 A). In other methods, the substrates have a functionalization which may adsorb colloids, dependent upon their exposure to the lithographic medium. Scheme 9 A shows the photolithographic patterning of a thiol-surfaced substrate.[160] Irradiation at 254 nm under air oxidizes the exposed thiol moieties to sulfonates, which are unable to bind gold colloids. Subsequently, treatment of the photolithographed surface with a gold nanoparticle solution results in the colloids adsorbing only in the areas that have not been irradiated (as seen in Figure 3 B). The system outlined in Scheme 9 B behaves in the converse fashion:[161] An amine monolayer is protected with the photolabile nitroveratryloxycarbonyl (NVOC) group and upon UV irradiation the neutral NVOC amines are photodeprotected, which exposes the positively charged amine.

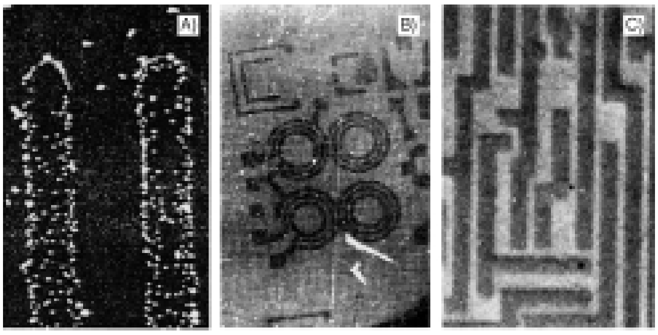

Figure 3. *Images of selectively adsorbed gold nanoparticles. A) Nanoparticles (20 nm) on amine-functionalized regions of a substrate. B) A SEM image of nanoparticles on nonirradiated areas of a thiol-functionalized substrate. C) An optical microscope image of nanoparticles on the photodeprotected regions of a protected amine-functionalized substrate. Images in (A), (B), and (C) are reproduced from refs. [159 – 161], respectively, with permission.*

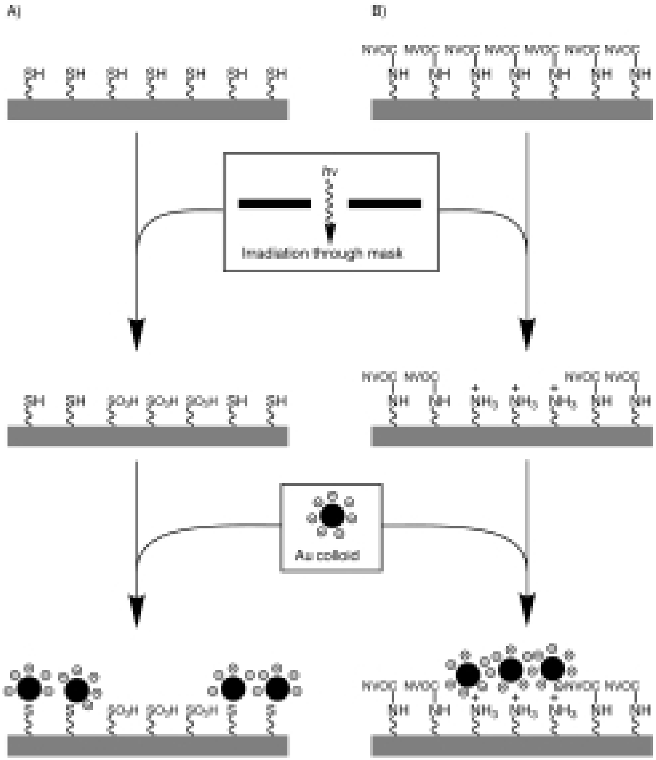

Scheme 9. *The construction of gold nanoparticle patterns by irradiative patterning methods. A) Nanoparticles only assemble on the nonirradiated parts of a thiol-surfaced substrate. B) Nanoparticles only assemble on the irradiated parts of an NVOC-amine-surfaced substrate.*

The colloid pattern is generated by immersing the pattern-irradiated substrate in a solution of negatively charged gold colloids, which adsorbs only to the amine. This pattern of gold colloids can also be intensified by the construction of further layers of colloids crosslinked by bisthiol molecules (the final pattern is shown in Figure 3 C). Other lithographic methods have been used analogously and the final colloid pattern has been used for the deposition of other metals to create continuous metallic patterns.[162]

2.4.2. Printing-Based Patterning

Colloid patterns have also been achieved by the process of microcontact printing, often as a means to construct other architectures.[163, 164] This technique uses a microstructured "stamp" to form the nanoparticle pattern by one of two general routes (Scheme 10). In one of the these routes, the stamp is used to introduce a pattern of functionality onto the substrate, which may be either specifically chosen or of the well known hydrophobic/hydrophilic type (Scheme 10 A). Self assembly of nanoparticles on the functionalized surface yields the colloid pattern. Figure 4 A shows a pattern generated by the evaporation of a colloidal magnetite solution, which had selectively adsorbed to 2-mercaptoethanesulfonic acid functionalized areas, to leave hexadecanethiol-functionalized areas bare.[164] The other, simpler method is to use the stamp to introduce a colloid-containing "ink" directly on the surface (Scheme 10 B). In one such example, a pattern of palladium nanoparticles was deposited on a siloxane-functionalized substrate by means of a poly(dimethylsiloxane) (PDMS) stamp.[163] The colloid domains were used to catalyze the electroless deposition of copper, to form a submicron-scale conductive pattern on the surface, as shown in Figure 4 B.

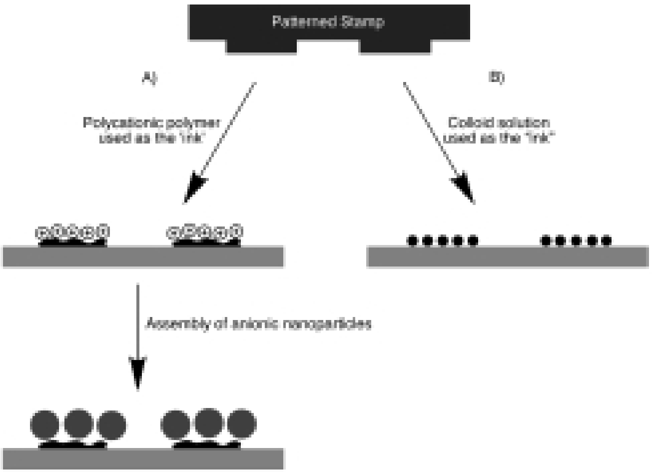

Scheme 10. *The construction of nanoparticle patterns by microcontact printing methods.*

2.4.3. DNA Template-Based Patterning

Recently, the ability to use DNA templates for the organization of nanometer-sized structures has been realized.[130] The possible methods for the preparation of DNA-based inorganic nanostructures can be divided into two categories: 1) The use of duplex DNA as a physical template for growing inorganic wires and organizing nonbiological building blocks into extended hybrid materials, and 2) the use of oligonucleotide (single-stranded DNA)-functionalized nanoparticles and sequence-specific hybridization reactions for organizing such particles into periodic, functional structures. In an early report, DNA was

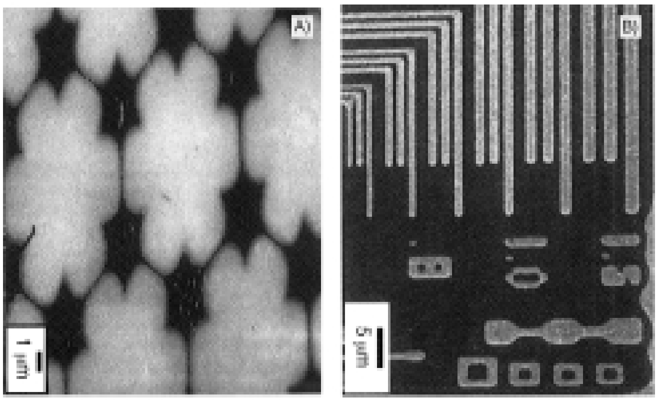

Figure 4. *A) A pattern of magnetite (dark areas) made by selective deposition on hydrophilic areas patterned by microcontact printing. B) Microstructure generated on a glass substrate by microcontact printing with palladium colloids, followed by the electroless deposition of copper. Images in (A) and (B) are reproduced from refs. [164] and [163], respectively, with permission.*

utilized as a stabilizer/template to form both CdS nanoparticles and mesoscopic aggregates from them.[165] These original efforts were based on the use of linear duplexes of DNA in solution as stabilizers for the formation of CdS nanoparticles from Cd^{2+} and S^{2-}. Further studies demonstrated that the DNA base sequence and, more specifically, the adenine content had a significant effect on the size and photophysical properties of the CdS particles thus formed.[166] More interesting for practical applications is a strategy for binding a template DNA strand to a solid substrate,[167] which has been used for the synthesis of a "ring" of CdS nanoparticles by employing the circular plasmid DNA molecule pUCLeu4 (3455 base pairs, 1.17 μm circumference). Initially, Cd^{2+} ions were added to a solution of the plasmid DNA to form a plasmid DNA/Cd^{2+} complex, which was subsequently bound to a polylysine-coated glass surface[168] (Scheme 11 A). Exposure to H_2S led to the formation of 5 nm CdS nanoparticles along the DNA ring backbone. This approach provides many possibilities for the synthesis of mesoscale structures, since the particle character (such as metallic or semiconductive) and the shape, length, and sequence of the DNA template can be controlled. DNA templates have also been used to grow nanometer-scale silver wires.[169] Two gold electrodes, separated by a defined distance (12 – 16 μm), were deposited onto a glass slide using photolithography and were subsequently modified with noncomplementary, hexane disulfide modified oligonucleotides (Scheme 11 B). Phage λ-DNA (16 μm in length) bearing "sticky ends" complementary to the oligonucleotides was introduced to the system and attached to the electrodes. After a single DNA bridge was assembled between the electrodes, silver ions were deposited onto the DNA and reduced with hydroquinone to form small silver aggregates along the DNA backbone. A contiguous silver wire was then formed by hydroquinone-catalyzed Ag^+ reduction onto the previously constructed silver aggregates. A wire 100 nm in diameter and 12 μm long could be synthesized reproducibly by this process. The wires comprised 30 – 50 nm silver grains that were contiguous along the DNA backbone. The nanowires had an extremely high resistance (more than $10^{13}\,\Omega$) and, thus, at low bias (about 10 V), no current was observed in the nanowires. However, at a higher bias the wires become conductive. By the deposition of more silver, the nonconductive threshold was reduced from about 10 V to 0.5 V, which demonstrated a crude control over the electrical properties of these systems. These examples demonstrate a new type of "biochemical lithography" to guide the formation of nanocircuitry for future nanosized electronic devices.[130]

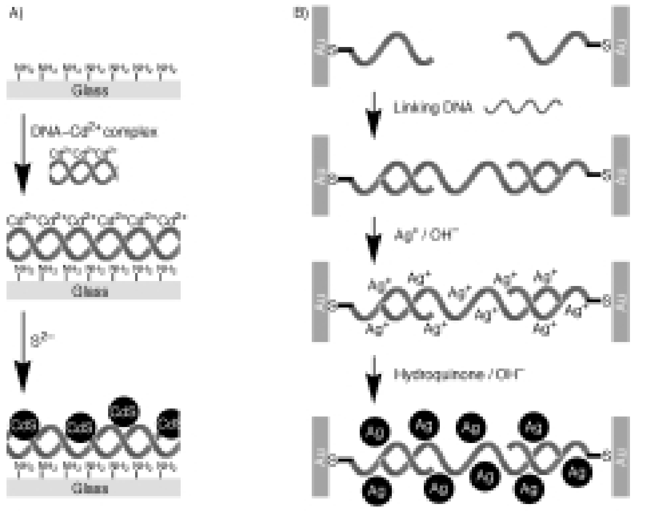

Scheme 11. *The synthesis of DNA-templated silver nanostructures. A) Synthesis of a silver ring immobilized on a glass substrate. B) Synthesis of a silver wire connecting two microelectrodes.*

3. Characterization of Nanoparticle Arrays

The study of functionalized surfaces is a relatively recent discipline and this reflects not only the recent interest in nanotechnology but also the advances in analytical methodology that allow us to characterize such constructions. Bulk and microscopic characterizations of nanoparticle arrays enable us to elucidate structural features, interparticle interactions, and superstructure functionality. Direct imaging on most substrates is now possible by various reliable, high resolution microscopies without prohibitive cost or time requirements. In addition, surface analysis techniques, such as X-ray photoelectron and Fourier-transform infrared spectroscopies (XPS, FTIR), provide tools to probe surface composition as well as to elucidate structural and geometric features at surfaces. These tools, along with others such as surface plasmon spectroscopy (SPS) and quartz crystal microgravimetry (QCM), complement traditional electrochemical and spectroscopic analyses to give us an unprecedented ability to characterize surface structures and functions.

3.1. Microscopic Methods

Microscopy is an invaluable method for the characterization of nanoparticles and their superstructures—only by direct observation can one ascertain an accurate picture of nanoparticle size and shape distributions and film morphologies. These methods do have their drawbacks, however. Sample preparation must conform to stringent requirements, while results can sometimes be difficult to interpret. It is not always certain whether an image is truly representative of the entire sample and whether imaging has affected the sample. Microscopy is used in almost all reports that discuss nanoparticle synthesis or nanoparticle monolayers and sometimes in the study of multilayer assemblies. Here, we will discuss electron and scanning probe techniques separately—a careful comparison has shown that these two methods have complementary features.[170]

3.1.1. Accelerated Electron Techniques

The most popular microscopic analyses of nanoparticles and their monolayers are scanning electron microscopy (SEM) and transmission electron microscopy (TEM). Of these, TEM provides the best images, even allowing the visualization of particle crystallinity and the surface-stabilizing layer (Figure 5 A).[30, 70]

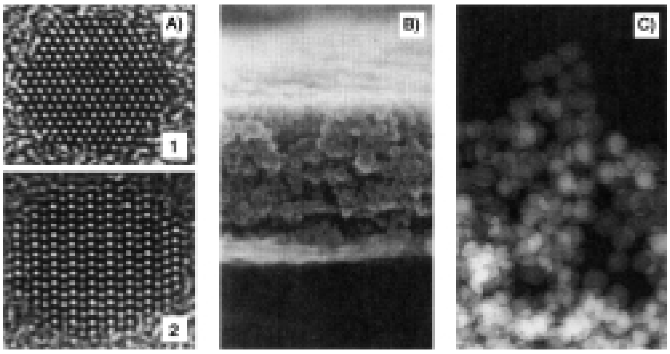

Figure 5. *A) High resolution TEM images of individual nanoparticles, which shows their crystallinity. B) Cross-sectional SEM of a SiO_2/PDDA multilayer. C) TEM of a SiO_2 aggregate, which shows how TEM reveals information through the entire thickness of the sample. Images in (A) and (B) are reproduced from refs. [12] and [113], respectively, with permission.*

Samples must be prepared on a suitable electron-transparent grid however, which makes it impossible to elucidate structural features formed on "everyday" substrates. SEM is capable of imaging layers formed on ordinary substrates but it is sometimes necessary to give the sample a thin conductive coating, which can result in a less defined image. Figure 5 B shows a SEM micrograph of the cross section of a silica-nanoparticle multilayer and Figure 5 C shows a TEM of a silica-nanoparticle aggregate. Consideration of these images reveals another complementary nature of the techniques: Whereas SEM gives an accurate picture of the surface, TEM allows visualization throughout a structure.

3.1.2. Scanning Probe Microscopies

Techniques such as atomic force microscopy (AFM), scanning nearfield optical microscopy (SNOM), and scanning tunneling microscopy (STM)[171, 172] allow visualization of thicker structures and can also provide some chemical information[170] but they suffer several drawbacks. The interpretation of AFM images can be problematic if the the underlying substrate is not completely flat and AFM resolution does not match that of electron microscopy. AFM and SNOM images of the same region of immobilized, 31 nm gold nanoparticles are shown in Figure 6. In gathering AFM data, precautions have to be taken to avoid "sweeping" loosely bound particles across the surface by the imaging tip.[157] Researchers overcome this restriction by various methods, such as the use of "tapping mode" imaging, low tip loads, and imaging under high ionic strengths to minimize electrostatic interactions between particles and the tip. Despite these drawbacks, AFM has great advantages in its ability to image almost any flat surface including multilayered assemblies and problematic substrates such as mica.[171] Scanning probe microscopies are generally not a good indicator of nanoparticle sizes, as the tip shape can cause an apparent particle enlargement. This distortion can be corrected by modeling the experiment with knowledge of the tip dimensions, however, and the particle height measurements remain unaffected.

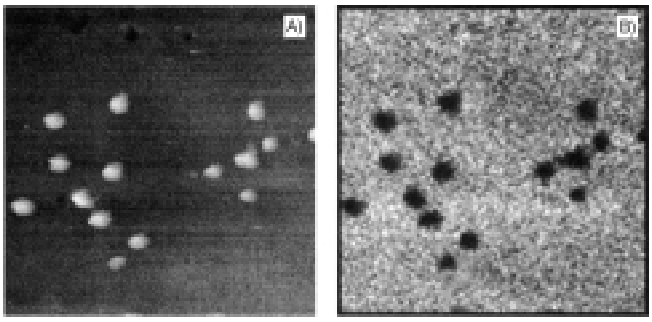

Figure 6. *A) AFM and B) SNOM images of the same region of 31 nm gold nanopaticles adsorbed on aminosilanated glass. Images reproduced from ref. [170] with permission.*

3.2. UV/Vis Spectroscopy

3.2.1. The Plasmon Absorbance

Solutions of colloidal gold particles have a very distinctive red color, which arises from their tiny dimensions.[10, 11, 173, 174] At nanometer dimensions, the electron cloud can oscillate on the particle surface and absorbs electromagnetic radiation at a particular energy. This resonance, known as plasmon absorbance, is a property characteristic of some mesoscale surfaces. Still smaller nanoparticles (quantum dimensions, $<1-2$ nm) do not display this phenomenon, as their electrons exist in discrete energy levels, and bulk gold has a continuous absorbance in the UV/Vis/IR region (which is effectively collapsed into the single plasmon absorbance in the case of the nanoparticle). The plasmon absorbance of gold nanoparticles has been known for some considerable time and has been utilized since Roman times in the production of "ruby" glass. Other metal colloids also display plasmon absorbances in the visible region (for example, silver at about 350 nm for 10 nm particles) and semiconductor colloids display plasmon absorbances in the infrared region because of their lower density of free electrons. The exact wavelength and intensity of the absorbance maximum depends on factors such as surface functionality, temperature,[175] and the solvent (Figure 7), but the effect can be used to give a quick assessment of colloidal concentration and particle size in

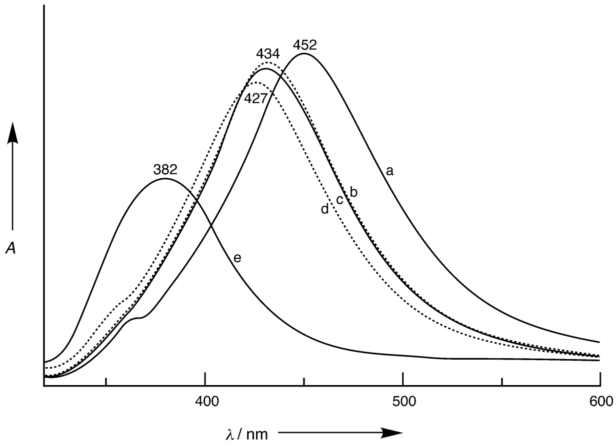

Figure 7. *The extinction spectra and peak wavelengths of a silver nanoparticle monolayer in various solvents: a) benzene, b) hexane, c) 2-propanol, d) water, e) air. Reproduced from ref. [71] with permission.*

solution if these conditions are known.[176] In gold colloid monolayers, the plasmon absorbance can be used as an analytical tool.

3.2.2. *Interparticle Close Contact—Coupled Plasmon Absorbances*

The close contact of optically absorbing nanoparticles leads to the appearance of an absorbance band attributed to the coupled plasmon absorbances of the particles. This property has been predicted theoretically[174] and has been shown with a Langmuir–Blodgett film of gold nanoparticles to emerge together with a loss of electrical resistivity at interparticle separations less than about 5 nm.[177] The more particles that are in contact, the longer the range of the plasmon coupling. Very long range coupling can lead to absorbances that are red-shifted several hundred nanometers from that of the individual particles. Integration of the spectral region containing coupled plasmon absorbances has been used as an empirical assay of the degree of coagulation within collidal gold solutions[178] and as the indicator in DNA sensors.[129] Spectral changes as a consequence of interparticle close contact have also been investigated for silver nanoparticles.[71, 179, 180] It was found that more densely packed films of silver nanoparticles display a much sharper absorbance and are blue shifted by up to 90 nm.

This characteristic absorbance also appears when multilayers of colloidal particles are constructed on surfaces as a consequence of their proximity to each other.[181] Figure 8 A shows the UV/Vis absorbance spectrum of a 13 nm gold nanoparticle superstructure, in which the layers are crosslinked with paraquat (**2**; *N*,*N*′-dimethyl-4,4′-bipyridyl).[151] As the number of layers increases, the plasmon absorbance ($\lambda \approx 520$ nm) of individual particles increases, while simutaneously an absorbance band at $\lambda \approx 650$ nm forms, strengthens, and shifts bathochromatically. This energy is in the region expected for interparticle plasmon absorbances and the gradual increase in wavelength is indicative of increasing particle network size as the assembly grows. A similar feature is also evident in vapor-deposited, semicontinuous gold films but is absent in noncontinuous films.[173] Further evidence that these absorbance changes occur as a result of the close contact of gold particles is obtained by following the UV/Vis spectrum of a citrate-stabilized gold-nanoparticle solution upon the addition of **2**.[151] Figure 8 B shows the spectral changes after the addition of **2** (0.01 mM). Soon after the addition, the intensity of the plasmon absorbance at 520 nm reduces and a band at $\lambda \approx 650$ nm appears. With time, this absorbance intensifies at the expense of the plasmon absorbance from the individual particles and shifts to longer wavelengths and, ultimately, the particles precipitate. TEM micrographs of the aggregating solution over the same periods (Figure 8 C) show that as the absorbance at $\lambda \approx 650$ nm strengthens and shifts bathochromatically, the average size of particle aggregates increases.

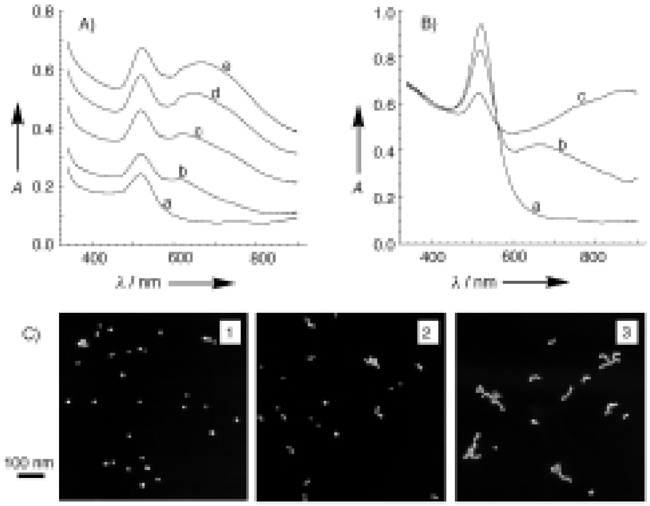

Figure 8. *A) Absorbance spectra of (a–e) 1–5 layers of Au colloid/**2** superstructures on a glass substrate. B) Absorbance spectra of a 12 nm colloidal gold solution a) 15, b) 50, and c) 165 min after the addition of methyl viologen (0.01 mM). C) TEM micrographs of representative aggregates from the same solution after 1) 15, 2) 50, and 3) 165 min.*

3.2.3. *Light Scattering and Reflectance*

Some of the data recorded by UV/Vis spectroscopy of nanoparticle assemblies are artifacts of light scattering and reflectance. In particular, as the particle sizes increase and metallic regions appear (with increasing particle density or layer growth) these components become important. Light scattering contributions of gold-particle aggregates appear in the region of 650–800 nm[182, 183] and reflectance occurs over the entire frequency range. In combination, these effects cause the broadband feature that is observed with the generation of multilayers (Figure 8 A).

3.3. Electrochemistry

3.3.1. *Redox Properties*

When constructed on a suitable substrate, it is possible to estimate the surface coverage of a gold colloid by the assay of its surface area. By applying a cyclic potential (between 0.0 V and 1.5 V versus a saturated calomel electrode (SCE)) to the electrode, modified with colloidal gold in an acidic background electrolyte solution (0.5 M H_2SO_4), oxidation and reduction of the colloidal surface can be achieved.[150] Upon oxidation, a densely packed monolayer of hydroxide species is produced on the gold surface, that is reduced in the course of the cathodic wave of the cyclic voltammogram. The charge density associated with the reductive process on the gold electrode surface is well known (386 $\mu C\,cm^{-2}$ for the [100] plane and similar values for the other planes[184, 185] of a gold crystal). An electrochemical study performed on a glassy carbon electrode covered with gold nanoparticles showed that the charge density associated with the reduction of the oxide layer on the nanoparticles is similar to that of bulk gold electrodes.[186] Thus, the integral surface of the colloidal gold particles involved in the electrochemical process can be determined by measuring the charge associated with the cathodic peak in the cyclic voltammogram. Figure 9 shows cyclic

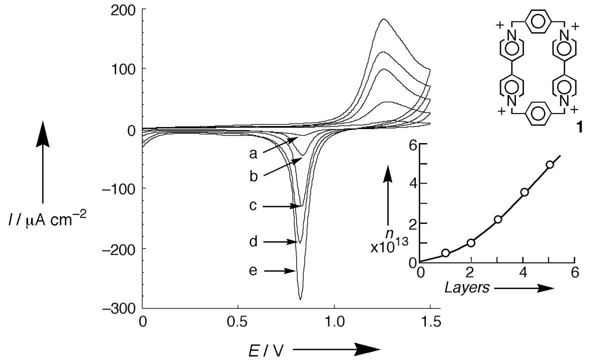

Figure 9. *Cyclic voltammograms of 1 – 5 layers of Au colloid/**1** assemblies corresponding to the electrochemical oxidation and reduction of the particle surface. Experiments were carried out in 1.0 M H_2SO_4 at a scan rate of 50 mV s^{-1}. Inset: Calibration curve corresponding to the surface coverage (measured as the number of of gold nanoparticles per square centimeter,* n*) against the number of layers.*

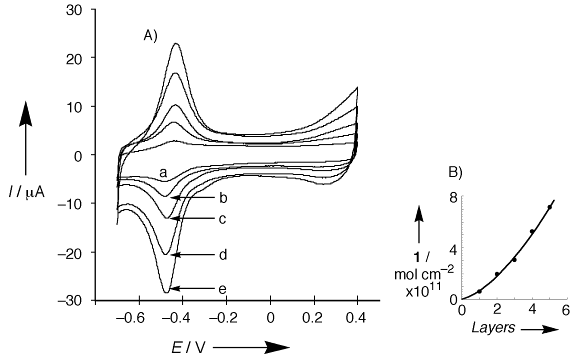

Figure 10. *A) Cyclic voltammograms correspsonding to the redox activity of the crosslinker (**1**) in arrays of 1 – 5 gold layers. Experiments were recorded under argon in 0.1 M buffer solution, at pH 7.2, and a scan rate of 100 mV s^{-1}. B) Calibration curve corresponding to the surface coverage of **1** against the number of layers, as determined by coulometric analysis.*

voltammograms of a gold colloid layered array upon construction of a **1**-crosslinked superstructure.[139] The characteristic cyclic voltammogram of gold is observed, consisting of an anodic wave corresponding to the oxidation of the colloid layer followed by a cathodic peak corresponding to the reductive stripping of the hydroxide layer formed on the gold surface at more positive potentials. The oxidation and reduction waves of the cyclic voltammograms of the gold particle surface increase almost linearly with the number of layers and, by the coulometric assay of the cathodic peak, the total gold surface area per nanoparticle layer can be estimated. Knowing the diameter of the gold particles and assuming that all of the particle surface is exposed to the electrochemical reaction, the surface density of the gold particles in this structure is estimated to have a lower limit of 0.8×10^{11} particles cm^{-2}, similar to the surface coverage of a colloid monolayer as determined by SEM (1.0×10^{11} particles cm^{-2}).[88] Another possiblity to estimate the integral area of the colloidal gold array exposed to an electrolyte solution is based on the capacitance measurements.[187] The double-layer capacitance obtained from the voltammograms is proportional to the integral area of the conductive array, so the area can be calculated if the capacitance per area is known (about 20 µF cm^{-2} for gold electrodes in aqueous solutions). A gold electrode functionalized by a layer of 42 nm gold nanoparticles assembled on a cystamine monolayer revealed an apparent capacitance of approximately 83 µF cm^{-2}, which gives an electrode roughness coefficient of about four.[188] More complex, three-dimensional systems were also characterized using capacitance measurements. For example, nanoporous filtration membranes (30 nm pore diameter, 6×10^8 pores cm^{-2}, 200 nm center-to-center average distance, 0.0042 fractional pore area) were filled with metal (gold) nanowires and the respective nanoelectrode assemblies were characterized by the capacitance measurements.[187] The fractional electrode area, 0.0045, was then derived from this measured capacitance value.

If the crosslinking species is electroactive, then its electrochemical response can reflect the buildup and formation of the particle superstructure. Figure 10 shows cyclic voltammograms of the molecular crosslinking units upon the construction of a **1**-crosslinked gold-colloid array. The cyclic voltammogram of **1** increases with the number of gold layers. This verifies that **1** indeed acts as a "crosslinker" for the particles, such that the formation of each additional gold layer requires its preassembly. By the coulometric analysis of the electrical responses of the crosslinker upon the buildup of the array, the crosslinker content was estimated to be about 1.5×10^{-11} moles cm^{-2} per layer. Knowing the surface coverage of the gold particles, it is estimated that, on average, about 100 crosslinking molecules are associated with each gold particle in the superstructure. Interestingly, this value is in excellent agreement with the number of molecules required to precipitate a gold colloid from solution.[150] The fact that the molecular crosslinker is electrochemically observable upon the buildup of the superstructure implies that the array exhibits three-dimensional conductivity and is porous to the electrolyte solution. A related experiment, in which a large number of layers were constructed, revealed that the response of the electroactive crosslinker reached a maximum, after which further layer growth had little effect.[189] In this case, only the top few layers were accessible to the electrochemical process. Potential-dependent changes of the redox-state of the linker can also result in variation of physicochemical (for example, spectral) properties of the nanoparticle array.[190]

3.3.2. Conductive and Semiconductive Properties

Apart from the vertical conductivity noted from cyclic voltammetry data, the transverse conductivity of colloid assemblies has also been measured. Monolayer films are found to be electrically insulating because individual particles are not in close contact but, when denser arrays are manufactured, electron transport through the matrix becomes possible. Networks consisting of gold nanoparticles connected through dithiols demonstrated a nonmetallic type of conductivity when the temperature was varied.[191] The resistance of gold nanoparticle arrays separated by organic crosslinkers varies with features such as the particle diameter, spacer length, and the number of particle layers. Samples consisting of 38 layers of gold particles separated by alkanedithiols of various chain lengths demonstrated significantly different surface resistances: about 1500, 85, or 6.5 Ω (at room temperature) for structures with 12, 9, or 6 methylene units between the sulfur atoms, respectively.[190] Thus, the addition of three methylene units to the chain can increase the resistance by an order of magnitude. Only one particle array has approached the conductivity of pure gold (resistivity $= 2.4 \times 10^{-6}\,\Omega\,\mathrm{cm}$)[192] but many exceed that of substrates, such as ITO. It has been found that colloidal gold multilayers undergo an insulator–conductor transition at a critical particle density.[144, 152] Samples containing up to 25×10^{11} particles cm^{-2} (11 nm) were found to insulate, with a resistance in excess of $10^7\,\Omega$, but further increases in the number of the gold layers resulted in an enormous decrease in resistance: By the time the gold particle density reached 50×10^{11} particles cm^{-2}, the resistance dropped below 100 Ω—a change of five orders of magnitude upon only doubling the particle content. Highly conductive nanoparticle aggregates can be generated when metallic nanowire connections, produced through electrochemical growth between the particles, are made.[193] Reversible metal–insulator transitions in ordered silver nanocrystal monolayers have been observed when 2D Langmuir–Blodgett films were compressed and decompressed.[194] The admittance of a 35 Å diameter silver nanoparticle film was reversibly modulated between values typical for an insulator and a conductive metal when the interparticle distance was changed from about 10 Å, in case of the uncompressed monolayer, to about 5 Å, when the monolayer is fully compressed. The conductivity change results from the change of the electron transfer mechanism: Quantum tunneling over the long distances between nanoparticles and a delocalized metallic mechanism over the short distances. Reversible optical changes, typical for continuous and discontinuous silver films, were also observed simultaneously with the conductivity changes.[195]

Mono- and multilayered constructions of semiconductor colloids (mainly CdS or TiO_2) have been well characterized by numerous spectral methods (UV/Vis spectroscopy, X-ray diffraction (XRD), resonance Raman scattering, TEM, electron diffraction, Rutherford backscattering, and so forth).[64, 76, 102] The evidence from a variety of characterization techniques indicates that semiconductive nanoparticles can be bound to metal surfaces using self-assembling monolayers. The nanocrystals are deposited intact, without fusion or aggregation, and at relatively high coverage—usually about half a monolayer.[102] The size distribution of nanoparticles on the solid support can be even narrower than the original size distribution of the particles in the solution before deposition. Such homogeneity of the nanoparticles is especially important for study of the electronic properties of the assembly. The samples are durable and may endure for months in air without degradation.

Tunneling spectroscopy (TS) of a single particle whose size was determined from a STM image has allowed the determination of the bandgap energy of the size-quantized particle. For this purpose, a current between a gold support and a TS tip, which passed through a CdS nanoparticle monolayer, was detected upon application of a variable potential difference.[64] The inset in Figure 11 shows the $I-V$ curve obtained for the nanoparticle monolayer (curve a) and that for bulk CdS particles (curve b). The $I-V$ curve obtained for the CdS nanoparticles is nearly symmetric against the potential axis, while that for the bulk CdS particle shows rectification and no appreciable current appears with positive bias. This difference results from the contribution of space charge effects, which are remarkable for the bulk CdS but not for the CdS nanoparticle, which is too small for any remarkable space charge layer to form.[196] The bandgap of the CdS nanoparticle was determined on the basis of a potential region where no appreciable current flow is observed.[64] For example, a bandgap of 2.9 eV was obtained for a 3.1 nm CdS nanoparticle. The TS measurements were carried out for other CdS nanoparticles of different sizes and their bandgap energies decreased with increased particle size (Figure 11). This result is in a good agreement with the theoretical predictions made by tight-binding approximations.[197]

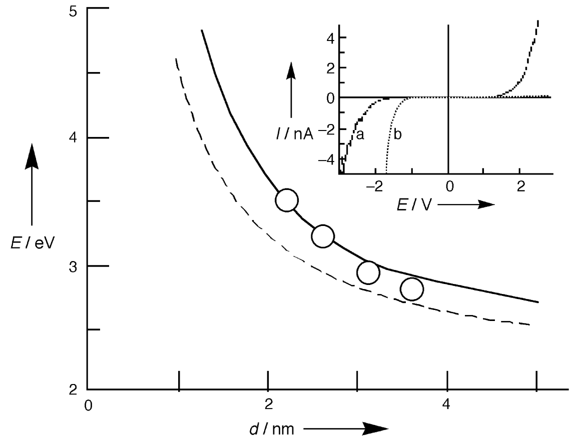

Figure 11. *Bandgap energies of CdS nanoparticles as a function of nanoparticle size. Circles represent experimental data and lines show theoretical calculations based on tight-binding approximations. Inset: the I–V curves obtained by TS measurements of a) a CdS nanoparticle and b) bulk CdS. Reproduced from ref. [64] with permission.*

Assemblies of semiconductive nanoparticles (CdS, CdSe, or TiO_2), upon appropriate illumination, have also been applied to photocurrent generation.[63, 65, 121, 198, 199] These systems demonstrate size-dependent photochemical properties different from those of bulk materials. Figure 12 A shows the photocurrent potential of CdS nanoparticle films consisting of one to three

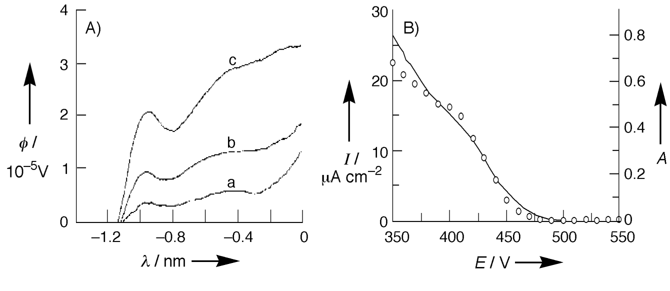

Figure 12. *A) Photocurrent potential of CdS nanoparticle electrodes consisting of a) one, b) two and c) three layers of crosslinked nanoparticles. B) Action spectra of the photocurrent acquired from a CdS nanoparticle film (circles) and the absorbance spectrum of CdS nanoparticles (solid line). Reproduced from ref. [121] with permission.*

monolayers. The photocurrent onset was observed at -1.15 V versus SCE, independent of the number of layers. Anodic photocurrent increases with the increasing anodic polarization, which is typical of n-type semiconductors. The magnitude of the anodic photocurrent increased almost linearly with the number of CdS layers, which indicates that all of the nanoparticles immobilized on the electrodes are photoelectrochemically active.[121] A similar dependence was observed for TiO_2 nanoparticles; however, beyond ten layers, a leveling-off (and even a decrease) of the photocurrent resulted. This phenomenon results from light absorbance by the TiO_2 layers located too far from the conductive support surface to pass electrons to the electrode.[65] Action spectra of the photocurrents (Figure 12B) demonstrate the same spectral shape as that of the absorption spectra, which indicates that all particles are active for the photocurrent generation and there is no significant energy transfer and redistribution.[121] The photocurrent measurements allowed determination of the potentials of the conduction-band edge, E_{CB}, and the valence-band edge, E_{VB}, of the CdS particles with size:[63] Both E_{CB} and E_{VB} are shifted toward negative and positive potentials, respectively, with a decrease of the CdS nanoparticle diameter. The experimental change of the potentials follows the theoretical prediction based on the finite depth potential model.[200] Approximate measurement of the CdSe bandgap was performed using photocurrent spectroscopy, applicable even for very small amounts of the material equivalent to a 2.5 nm thick film (less than a monolayer of the CdSe nanoparticles).[199] Intensity-modulated photoelectrochemical spectroscopy has been applied to determine the kinetics of charge transfer at an electrode modified with a monolayer of CdS nanoparticles.[57] An electrode modified with a CdS-nanoparticle monolayer was irradiated with light chopped at a frequency of about 17 Hz and the modulated current signal was recorded using a lock-in amplifier. The photocurrent response was analyzed in terms of impedance spectroscopy and the charge-transfer kinetics were determined; rate constants for hole and electron transfer were $2.8 \times 10^3\,s^{-1}$ and $5.1 \times 10^3\,s^{-1}$, respectively.

The unique features of the size-quantized semiconductive nanoparticles could result in the development of the novel photovoltaic, light-emitting, and sensory devices that will be discussed in Section 4.4.

3.4. Other Techniques

Of the other techniques used to characterize colloid superstructures, microgravimetric techniques stand out as the most important. With quartz-crystal microgravimetry, the construction of layers can be followed in great detail. Any particle material and crosslinker can be used, although the underlying substrate is usually gold, and construction may be followed for many layers. QCM can monitor the mass change upon the formation of layers, which allows the calculation of layer thicknesses, and can also show the homogeneity of layer thickness in repeating structures.[76, 89, 95, 113, 142, 201] The high mass of metallic colloidal particles means that their adsorption is followed very easily (the frequency decreases upon colloid assembly can be as much as 10000 Hz).[96] For example, colloidal gold particles of about 8 nm in diameter were deposited onto a QCM surface and nonane-1,9-dithiol was used as a linker between the gold layers.[95] Figure 13 shows the mass increase on the QCM surface upon deposition of several layers of the gold colloid. The measurements show clearly that saturated monolayers are obtained, namely, the self-assembly process comes to saturation. The values obtained for the mass of the individual layers are in agreement with expected values. Assuming a particle radius of 4 nm and a maximum coverage of the surface, a mass increase of $9\,\mu g\,cm^{-2}$ can be expected. The measured value of $6\,\mu g\,cm^{-2}$ indicates about 50–60% coverage and is a more reasonable result for the first layer. The larger values, about $8\,\mu g\,cm^{-2}$, for the consecutive layers could be due to an increase in the surface roughness caused by the attachment of the first monolayer. Layer-by-layer deposition of particles formed from different materials (such as Au/CdS/Au[95]) or particles and polymers (such as SiO_2/PDDA/SiO_2[142]) have also been followed using QCM. Alternate layers can show different frequency changes, which translates into a different mass uptake resulting from various sizes and densities of the layer components. For example, the mass uptake in the course of building an Au/CdS/Au multilayer assembly is significantly higher for each gold-layer building step than that for CdS layer, since the CdS particles are lighter.[95]

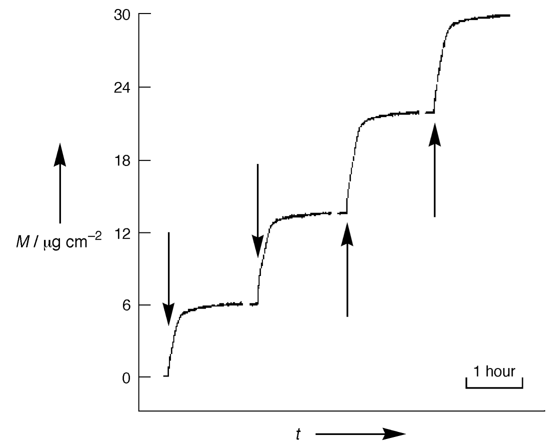

Figure 13. *The deposition of gold nanoparticle layers, as detected by QCM. Arrows show the times at which colloid was added. Reproduced from ref. [95] with permission.*

The only other analyses that can provide related information are the much more troublesome ellipsometry[142, 153, 154, 157] and X-ray diffraction (XRD).[65] Sample preparation is important in these experiments and the interpretation of results can also be problematic. Finally, information about the array surface has also been gleaned from XPS[61, 149] (to verify the presence of certain compounds and their relative abundances), NMR spectroscopy,[202] and surface plasmon spectroscopy (SPS).[10]

4. Functional Nanoparticle Arrays

The ultimate aim of the nanoparticle engineer is the creation of materials and devices that have valuable functions in the real world. The properties of colloidal particles are known to be of use in many disciplines but the challenge is to organize them with complete control. The integration of nanoparticles in composite structures as well as their interface with external inputs and outputs will be necessary to reach their full potential. Assemblies of disorganized nanoparticles have been used successfully to produce rudimentary sensors,[28] ultramicroelectrodes,[203] and unusual materials.[191] While these structures are able to demonstrate concepts, they do not give us access to the direct nanoengineering that is necessary for the development of the next generation of devices. Organized monolayers provide a route towards true nanoengineering. Organized nanoparticle monolayers have been used as masks for the evaporation of gold patterns.[84] If the individual particles in an organized monolayer are "stuck together" (for example, by the evaporation of a thin gold film), then the entire monolayer may be removed from the substrate in one piece.[85] This procedure allows the monolayer mask to be transferred to almost any substrate and provides access to colloid-templated patterning on curved surfaces and unusual materials. Electronic colloid-based devices have been built which take advantage of the precise placement and engineering of colloidal nanoparticles, while sensing matrices have been built which exploit the properties of both the colloidal and the crosslinking materials. As yet, the chemical[204] and catalytic properties of nanoparticles have not been used in functional arrays. Ultimately, it may be possible to integrate different colloid-based components to create highly functional electronic, sensor, and photoelectrochemical devices of nanoscale dimensions.

4.1. Arrays with Optical Functions

The intrinsic optical properties of metallic colloids has led to many applications exploiting their plasmon absorbance (Section 4.1.1) or their ability to enhance the Raman effect (Section 4.1.2). Other research has focused on their use as the components of diffraction gratings. The small size of nanoparticles means that if they are equally spaced in a lattice, the assembly can act as a diffraction grating. Because the properties of a diffraction grating depend on the unit spacing, an event that changes the interparticle spacing in a regular array can be detected optically. Thus, crystalline colloid arrays (CCAs) of polymer particles have been used to detect temperature and binding events.[205] In the latter example, a CCA was polymerized inside a hydrogel containing lead-binding crown ether moieties. The CCA/hydrogel absorbs any Pb^{2+} that is in solution and results in an osmotically driven swelling of the array. The optical consequences of this change are detectable by the naked eye at Pb^{2+} concentrations as low as 40 ppb.

4.1.1. Surface Plasmon Functions

The plasmon absorbance of nanoparticles is a consequence of their small size but it can be influenced by numerous factors. In particular, solvent and surface functionalization are important contributors to the exact frequency and intensity of the band.[10, 182, 183] This dependence on surface effects make the surface plasmon an ideal monitor of adsorption to the particle surface, which allows nanoparticle assemblies to be used as sensing devices. These effects are particularly pronounced for silver colloids and warrant their use in much of the research into SPS.[10]

The specific biochemical binding of biologically complementary pairs (for example, antigen – antibody, biotin – avidin, DNA – complementary DNA) can be performed at an interface and various physical means can be used to detect the corresponding change of the interfacial properties. A general approach includes the modification of a solid support with one component of the recognition pair and then the modified surface is allowed to react with the second complementary component, which produces a complex at the interface. When the applied solid support is electroconductive, electrochemical techniques (such as impedance spectroscopy,[206–208] chronopotentiometry,[207] or cyclic voltammetry[209, 210]) sensitive to an additional barrier against electron-transfer processes at the interface have been applied to detect the formation of these complexes. QCM,[208, 209, 211] ellipsometry,[212, 213] and surface plasmon resonance (SPR)[213, 214] have also been employed for the detection of the corresponding changes at the interface.

If an analyte is coupled to a metal nanoparticle, then the change in the interfacial properties resulting from the formation of the affinity complex at the interface can be greatly enhanced. SPR demonstrates the enhancement of the signal resulting from antigen – antibody complex formation (Figure 14).[215] In this paradigm, either antibody-functionalized nanoparticles bind to an antigen-functionalized surface (Figure 14 A) or antigen-functionalized colloids bind to an antigen-functionalized surface (Figure 14 B), for which a solution-state antibody acts as a linker.

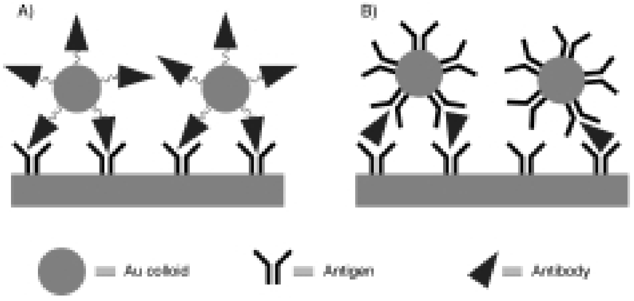

Figure 14. *Schematic representations of particle-enhanced biosensing architectures.*

Exposure of a gold film coated with an antibody (γ-chain-specific monoclonal goat anti-human immunoglobulin G; anti-IgG-γ) to a 1.0 mg mL^{-1} solution of human immunoglobulin G (IgG) results in a 0.1° shift in plasmon angle with no change in curve shape (Figure 15 A). In contrast, a significantly larger shift (1.5°), an approximately 2 % increase in minimum reflectance, and noticeable broadening of the curve is observed (Figure 15 B) upon the exposure of an identically prepared surface to an electrostatically bound conjugate between IgG and 10 nm diameter colloidal gold.[215] Quantitative interpretation of the signal shows an almost linear change with the surface occupation of the

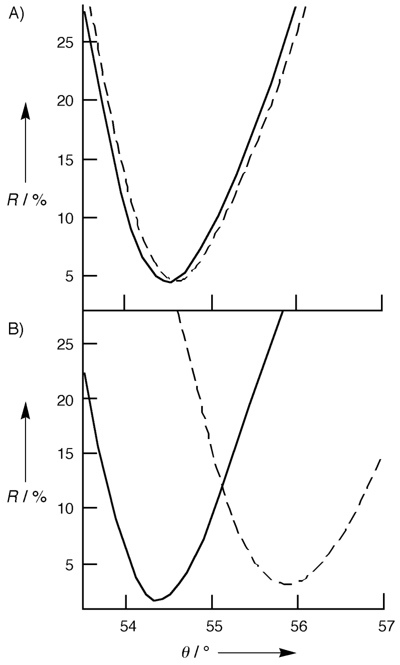

Figure 15. *In situ SPR curves of: A) An evaporated gold film, modified with anti-IgG-γ (——) and exposed to IgG (1.0 mg mL^{-1}; – – –); B) The same experiment, except that the IgG was conjugated with 10 nm gold nanoparticles.* R = *resonance enhancement. Reproduced from ref. [215] with permission.*

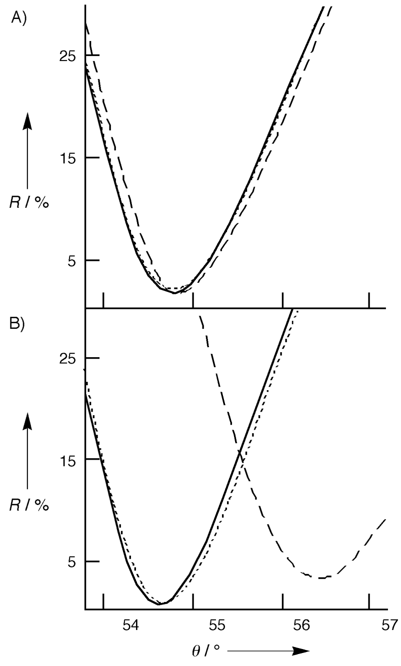

Figure 16. *In situ SPR curves of: A) An evaporated gold film, modified with anti-IgG-γ (——) and sequentially exposed to IgG (0.045 mg mL^{-1}; ····) then anti-IgG-F$_c$ (8.5 mg mL^{-1}; – – –). B) The same experiment, except that the final anti-IgG-F$_c$ was conjugated with 10 nm gold nanoparticles.* R = *resonance enhancement. Reproduced from ref. [215] with permission.*

analyte–gold conjugates. A similar SPR curve was observed using the primary interaction of the sensing interface with IgG followed by interaction with a secondary antibody (F$_c$-specific monoclonal goat anti-human immunoglobulin G; anti-IgG-F$_c$) conjugated with a gold colloid. Whereas little change in the surface plasmon was observed in the absence of gold colloids, (Figure 16 A), the application of the anti-IgG-F$_c$ conjugated with a gold colloid greatly amplified the surface plasmon change (Figure 16 B). The colloidal gold particles introduced to the interface with the anti-IgG-F$_c$ resulted in a 1.7° shift in plasmon angle (rather than 0.06° for pure anti-IgG-F$_c$), a 2% increase in minimum reflectance, and a noticeable broadening of the SPR curve. Both detection schemes clearly demonstrated enhancement of the signal as a result of gold colloids coming to the interface together with the biomaterial. This method can detect IgG to a concentration of about 7 nM.

4.1.2. Surfaced-Enhanced Raman Scattering Functions

When an adsorbate on a rough metal surface is subjected to Raman scattering spectroscopy, very high enhancements (several orders of magnitude) over a flat substrate are observed.[216] This SERS effect is a general analytical method for adsorbates on active metals such as gold, silver, and copper. The enhancement may extend tens of nanometers from the substrate surface and is at its highest for surfaces that are rough on the 10–100 nm scale—exactly the size of gold and silver colloids produced by the simple citrate reduction method. The mechanism of the enhancement is not fully understood but seems to stem from both an enhanced electromagnetic field as a consequence of surface plasmon resonance and the appearance of new electronic states in the adsorbate as a consequence of adsorption.

Solution-state SERS studies of pyridine on gold nanoparticles show that the enhancement occurs when the exciting radiation is coincident with the plasmon absorbance of the nanoparticles.[217] This result is consistent with the theory that the enhancement is caused by an enhanced local electromagnetic field. Later research studied aggregated nanoparticles, which have additional plasmon resonances associated with interparticle plasmon coupling. This work showed that the longer wavelength, interparticle plasmon resonances of nanoparticle aggregates provide an even better excitation frequency for SERS.[182, 183] The production of nanoparticle aggregates in solution can be problematic, however. Not only are the aggregates polydisperse in shape and size, but the process of aggregation is dynamic—the composition of an aggregating solution changes over time—and the particles ultimately precipitate (although there are ways to stabilize colloid aggregates in solution).[218]

Some of the first papers describing the assembly of nanoparticle monolayers were directed towards their use as SERS substrates.[71, 90] Previously, solid SERS substrates had been constructed by etching or deposition, which was both technically demanding and imprecise. The use of nanoparticles, which are easily synthesized to be monodisperse and were known to be excellent SERS substrates in solution, provided an elegant solution to these problems. In addition, immobilized particles are fixed in their morphology, so their aggregation state can be carefully controlled. Monolayers of gold[90] or silver[71] nanoparticles were adsorbed onto silane-functionalized glass slides and were then treated with the analyte adsorbate. As expected, it was found that SERS activity is strongly dependent on the aggregation state of the particles (Figure 17). Enhancements were comparable to those observed from electrochemically roughened electrodes. Even higher enhancements have been obtained by the use of silver-coated gold nanoparticles.[45, 56]

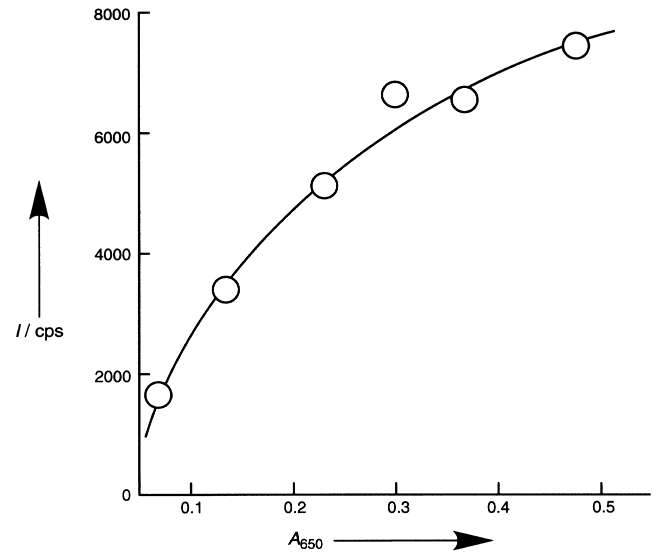

Figure 17. *The SERS intensity of the 1610 cm^{-1} band of* trans-*1,2-bis(4-pyridyl)-ethylene varies with the strength of the interparticle-coupled plasmon absorbance of a gold nanoparticle monolayer on which it is adsorbed (at 632.8 nm excitation).* I = *SERS intensity,* A_{650} = *absorbance at 650 nm. Reproduced from ref. [90] with permission.*

The high SERS enhancements observed on substrates of aggregated colloids are, in fact, an average of the very different enhancements at all the points on the film. Theoretical calculations predict that the variation is very pronounced,[219] which suggests that localized enhancements may be orders of magnitude higher than the (already high) average enhancement. This theory was checked by SERS studies on the tip of an atomic-force microscope.[220] Such a method allows the analysis of single particles and aggregates: If the adsorbate is added in a very low concentration of significantly less than one molecule per particle, then even single molecule analyses can be performed. This study focused on the analysis of rhodamine 6G on silver nanoparticles (of about 35 nm diameter). The dye was first adsorbed onto the surface of the nanoparticles, which were then immobilized on a polylysine-coated glass substrate. About one in 10000 nanoparticles had a very high SERS activity and there seemed little to identify these nanoparticles in terms of size, shape, and aggregation state (Figure 18). The highly active "hot particles" often seemed to be larger or rod-shaped but other particles also displayed this property. Analysis showed that SERS enhancements of up to × 10^{15} were possible, which allows the detailed analysis of single molecules, even to the point of determining their orientation.

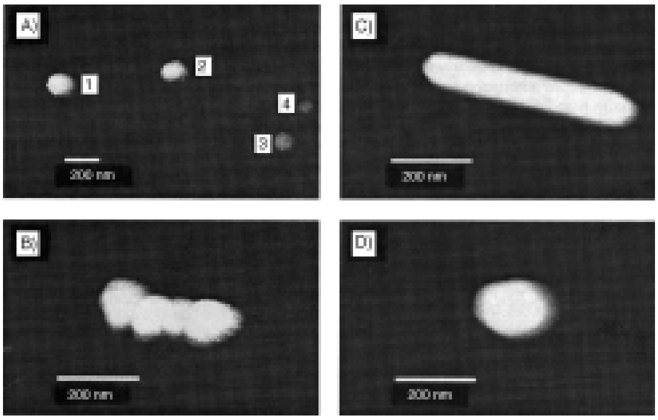

Figure 18. *Tapping mode AFM images of "hot" silver nanoparticles and their aggregates. A) Four particles, of which two show a high Raman enhancement (particles 1 and 2 are "hot") and two do not (particles 3 and 4). B) A "hot" four-particle linear aggregate. C) A "hot" rod-shaped particle. D) A single "hot" particle. Reproduced from ref. [220] with permission.*

4.2. Arrays with Electronic Functions

4.2.1. Colloids as Electrical Contacts

For the construction of colloid-based microelectronics, it is desirable to engineer two- and three-dimensional arrays of colloidal metal particles that can be used as wires and electrodes. The primary requirement for such applications is high electrical conductivity of the assembly, as can be attained by closely-packed colloid multilayers. The cyclic voltammetry of various redox probes (such as $K_3[Fe(CN)_6]$, hydroxymethylferrocene, and hydroquinone) has been studied on glass slides functionalized with different numbers of bisthiol-crosslinked colloidal gold layers.[144] At less than seven layers, the voltammetry is resistive and poorly defined, but at seven layers the voltammetry becomes sigmoid—such as that observed at a microelectrode due to radial diffusion of the redox species to the electrode surface. The electrode can be modeled as many small conductive "islands" with nonoverlapping diffusion layers and thus behaves as a microelectrode array. Cyclic voltammograms of electrodes with higher coverages exhibit the linear diffusion characteristics of planar macroelectrodes. Here, the electrode may be modeled either as a continuous metallic surface or as a microelectrode array, whose component diffusion layers overlap due to the higher density of gold "islands" on the electrode surface. Well defined diffusion-limited voltammograms were recorded, as demonstrated by a classical $t^{-1/2}$ current decay, linear plots of the peak current versus the square root of the potential sweep rate, and peak-to-peak separations (ΔE_{peak}) ranging from 85 mV ($K_3[Fe(CN)_6]$) to 133 mV (hydroquinone), and indicated nearly reversible to quasi-reversible electron-transfer kinetics. The electron-transfer rate constants of $[Fe(CN)_6]^{3-}$, measured at a ten-layer film of colloidal gold, were found to be close to those known for bulk gold electrodes: 7.6×10^{-3} cm s^{-1} and 7.9×10^{-3} cm s^{-1}, respectively.

Reversible and quasi-reversible electrochemical processes have been demonstrated at metal colloid multilayer arrays for many different, soluble redox probes, such as methyl viologen

(**2**),[90] ferrocene derivatives,[187] and $[Fe(CN)_6]^{3-/4-}$.[153, 188, 190] Direct, nonmediated electrochemical activity of cytochrome c was observed at a SnO_2 electrode modified with colloidal gold.[221] This is of particular interest as cytochrome c normally demonstrates reversible electrochemistry only at promoter-modified electrodes, at which favorable orientation of the hemoprotein towards electron transfer is provided.[222] Furthermore, the morphology of the nanoparticle surface is extremely important in the process—aggregated gold particles or particles of an inappropriate size fail to establish efficient electrical contact between the hemoprotein and the electrode.

When a multilayer of colloidal metal particles is organized onto a conductive support, one needs to determine the contributions of the external layer, internal layers, and the conductive support towards the heterogeneous electron-transfer process. A redox probe (*p*-nitrosodimethylaniline) that exhibits different cyclic voltammograms at SnO_2 and Au electrodes has been used to discriminate between the electrochemical responses from a SnO_2 support and the colloidal gold array organized onto it.[89] The recorded cyclic voltammogram clearly demonstrated that the main contribution to the electrochemical process is from the gold particles. Multilayer arrays of gold colloids linked through alkanedithiol bridging molecules were terminated with either the gold colloid or alkanedithiol as the external layer. The colloid-surfaced array demonstrated efficient electrochemical process in the presence of a soluble redox probe, whereas the alkanedithiol-terminated array was highly insulating and nonelectrochemically active.[153] Such electrochemical behavior can be observed if the redox probe does not penetrate inside the array so that the array surface is the only interface responsible for the heterogeneous electron-transfer process. In other cases, however, the array is porous so both the external and internal surfaces can participate in the electrochemical process.[139, 147, 150]

Monolayer (2D) and multilayer (3D) arrays of colloidal metal particles have been used as supports for the immobilization of redox-active molecules. Strong adsorption of $[Fe(CN)_6]^{3-/4-}$ ions onto gold colloids attached to a cystamine-functionalized gold electrode has been demonstrated.[188] Symmetrical anodic–cathodic peaks with very small peak-to-peak separations (3 mV), typical of Laviron-type electrochemistry,[223] were observed in the cyclic voltammograms when the gold colloid-modified electrode was probed in the presence of $[Fe(CN)_6]^{3-/4-}$. Laviron also reported a linear dependence on the potential scan rate, characteristic of adsorbed redox species. These peaks appear in addition to normal diffusional waves of the $[Fe(CN)_6]^{3-/4-}$ and are shifted by +515 mV from the diffusionally controlled redox waves. Such a large shift in potential is evidence of strong adsorption, which results in a significant change of the energetic properties of the redox ions. However, a colloidal gold electrode immersed in an electrolyte solution free of $[Fe(CN)_6]^{3-/4-}$ slowly loses the adsorbed redox-active anions because of their substitution with redox-inactive anions of the electrolyte. Much stronger adsorption of redox species, which results in their permanent immobilization onto conductive (or semiconductive) nanoparticles can be achieved if the adsorbed molecules have special "anchor" groups to provide binding to the solid support. Typical anchor groups used for coupling with gold nanoparticles (which can also be used with silver or platinum particles) are thiol and disulfide groups.[98] Redox-active modifiers (such as ferrocene units[224] or anthraquinones[225]) have been linked to gold colloids by spacers terminated with thiol anchor groups. The redox-functionalized gold nanoparticles can be later assembled on a solid support. Another approach includes the attachment of redox-active modifiers to gold nanoparticles already assembled on a solid support. For example, a ferrocene–thiol monolayer deposited on top of a colloidal gold layer demonstrated the Laviron-type electrochemical behavior typical for monolayers of redox materials on flat, continuous electrodes.[116] The small peak-to-peak separation in the cyclic voltammogram ($\Delta E = 6$ mV at a potential scan rate of $10\,\mathrm{mV\,s^{-1}}$) demonstrates a fairly fast, reversible electrochemical process ($k_{et} = 4\,\mathrm{s^{-1}}$) and a negligible contribution from the resistance between the colloid layer and the conductive support. More complex redox compounds, such as dyads comprising elements with pH-dependent (quinone) and pH-independent (bipyridinium) electrochemistries have been immobilized atop of nanoparticle 2D arrays.[88] For the first case, Equation (1) describes its behavior, where E^0_{pH} and $E^0_{pH\,7}$ are the redox potentials measured at any pH and pH 7; *m* and *n* are numbers of electrons and hydrogen ions involved in the reduction of a quinone molecule; and *R*, *T*, and *F* have their usual meanings of the gas constant, temperature, and Faraday constant, respectively.

$$E^0_{pH} = E^0_{pH\,7} - 2.3\left(\frac{m}{n}\right)\left(\frac{RT}{F}\right)(pH - 7) \tag{1}$$

4.2.2. Colloids in Single-Electron Devices

If metallic particles of a few nanometers in size are arranged within about 1 nm of each other, they build tunnel junctions with electrical capacitances as low as 10^{-19}–10^{-18} F.[20] This allows controlled charge transport between the particles by single-electron tunneling (SET) events at room temperature, which has been recognized to be a fundamental requirement for the development of quantum electronics.[9] Charging energy (E_c) as well as capacitance depends on the size of the metallic nanoparticles and the distances between them. The charging energy (namely, the energy barrier that has to be overcome to transfer a single electron from an initially neutral cluster to a neutral nearest-neighboring cluster) is dependent on the interparticle capacitance *C*, as follows from Equation (2), where *e* is the charge of an electron.

$$E_c = \frac{e^2}{2C} \tag{2}$$

The use of interparticle spacers can be valuable in controlling capacitance. For instance, while the close packing of the $Pd_{561}(phen)_{36}O_{200}$ clusters (phen = 1,10-phenanthroline) produces a capacitance of 4.0×10^{-18} F, the insertion of 4,4′-diamino-1,2-diphenylethane spacers reduces it to 1.6×10^{-18} F.[226] The conductivity and capacitance of nanostructured materials have been studied using direct current (DC) measurements[20, 226] and impedance spectroscopy.[227] Cyclic voltammetry performed on a single gold nanoparticle in contact with an STM tip has also been used to study single-electron transfer processes.[25]

SET devices range from a single conductive nanoparticle located between two microelectrodes[24, 26, 228] or in contact with an STM tip[25, 229] to 2D and 3D arrays that consist of nanoparticles which experience SET between them.[131, 229, 230] Scanning-tip microscopy techniques can be used to observe SET events and even to form the respective devices. For example, scanning tunneling spectroscopy (STS) has been applied to the observation of SET effects on nanoparticle monolayers of $Au_{55}(Ph_2C_6H_4\text{-}SO_3H)Cl_6$ in contact with a tip, to demonstrate "Coulomb staircase" behavior (single electron transfer steps in the current – potential curve) even to room temperature, where the capacitance of the cluster/substrate junction was calculated to be 3.9×10^{-19} F.[231] Similar results were obtained on application of STS to self-assembled gold nanoparticles (1.8 nm) on a dithiol-modified gold surface.[229, 232] A single-particle device was fabricated by AFM-assisted manipulation of a 20 nm gold nanoparticle between two metallic leads.[172] Two-dimensional lattices for SET devices can be prepared by self-assembly techniques.[70, 233] Layer-by-layer assembly has been used for the construction of metal-insulator-nanoparticle-insulator-metal ("MINIM") capacitors, which also demonstrate Coulomb staircase behavior.[131] The MINIM devices were made (Scheme 12) by first priming the surface of a gold substrate with cysteamine (2-aminoethanethiol). Insulating layers of α-$Zr(HPO_4)_2 \cdot H_2O$ (α-ZrP) and polyallylamine hydrochloride (PAH) were sequentially adsorbed, terminating with the cationic substance, until the desired thickness was obtained (typically 3 – 10 nm, as measured by ellipsometry). Subsequently, citrate-stabilized gold particles (about 2.5 nm) were immobilized on top of the insulating layer. The remaining half of the double junction was constructed by simply reversing the adsorption sequence described. For a junction thickness of 80 Å and a particle radius of 1.25 nm, the capacitance of a double-tunnel junction device is 4.5×10^{-19} F, as calculated from Equation (3), where μ_0 is the vacuum permittivity constant, μ_r is the dielectric constant of the insulator, a is the particle radius, and L is the junction thickness.[234] A Coulomb gap of 360 mV ($=e/C$) should be observed at room temperature, since it is substantially higher than values of kT.

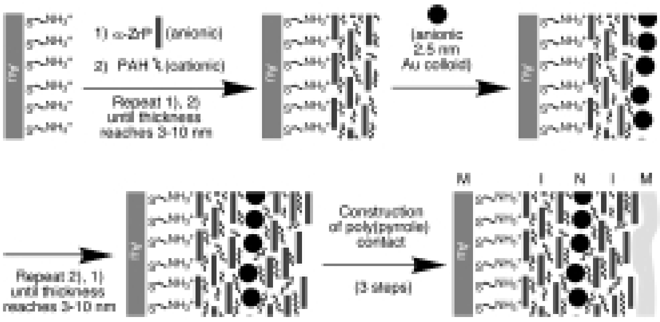

Scheme 12. *The stepwise construction of a MINIM device.*

$$C = 4\mu_0\mu_r[1 + \left(\frac{a}{2L}\right)] \tag{3}$$

A typical current – potential curve for such a MINIM structure is shown in Figure 19 A. The high impedance region is observed on both sides of 0 V and represents the average charging potential ($\pm e/2C$) of each particle at the double junction array by a single electron. When enough energy is supplied to charge a particle, electrons tunnel through the junction, which results in the square-law dependence of the current rise on either side of the gap. Figure 19 B shows similar measurements on a device of similar thickness in the absence of the gold particles. A linear curve, typical for ohmic resistance, is observed.

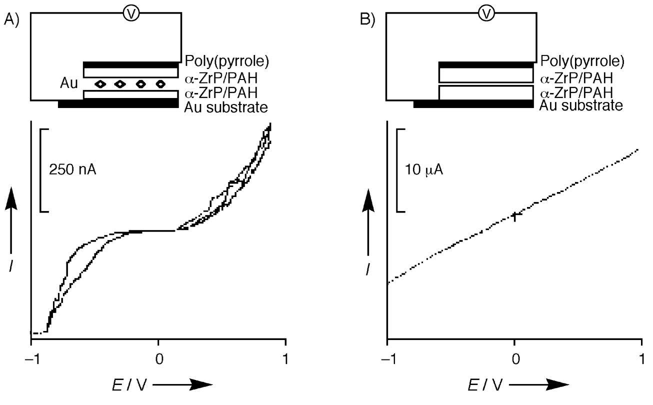

Figure 19. *Current – voltage curves for the MINIM device shown in Scheme 12. A) The properly constructed MINIM device. B) The curve for a device that was built without the nanoparticle layer. Reproduced from ref. [131] with permission.*

In the next generation of single-electron devices,[235] "switchable" quantum dots and quantum channels with correlated electrons will offer components orders of magnitude smaller than classical electronic switches or semiconductor memories. This could result in a new generation of computers,[236] supersensitive electrometers, near-infrared receivers, and very simple miniature lasers.[9, 237] Recently, a single-electron transistor has been constructed using alkanedithiol-stabilized gold nanoparticles as tunnel junctions.[24, 26] Three colloidal gold particles (10 nm) were linked by 1,6-hexanedithiol, to produce a gold colloid chain. The particle chain was formed on a silica substrate with metallic source, drain, and gate electrodes defined by electron-beam lithography (Figure 20). The gold colloid chain bridged a 30 nm gap between the source and drain, which formed a single-electron transistor with a multitunnel junction in the particle chain. Electron conduction through the chain exhibited a clear Coulomb staircase and the periodic conductance oscillated as a function of gate voltage. A similar device was created using a single CdSe nanoparticle (5.5 nm) located between two gold microelectrodes that function as source and drain.[23, 27] Gold nanoparticles capped with dissociating modifier molecules, Au/galvinol, provided pH-dependent resistance to single-electron transfer processes, even if only about ten modifier molecules were present per gold nanoparticle.[238] Single-electron memory devices based on field-effect transistors (FETs), which consist of a single silicon particle[239] (or several particles[240]) embedded in a thin silica insulator, allows the control of current flow (on/off) by the injection of a single

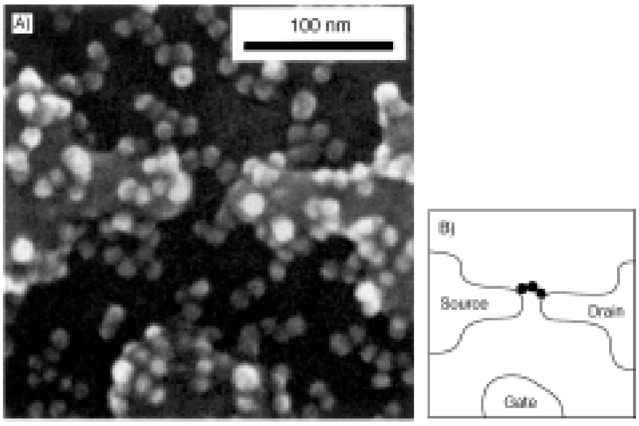

Figure 20. *A) An electron micrograph and B) schematic clarification of a three-nanoparticle bridge constructed between source and drain electodes. The gate electrode is seen in the lower part of the micrograph. Reproduced from ref. [24] with permission.*

electron into the gate. These SET devices displayed read/write times of about 20 ns, lifetimes in excess of 10^9 cycles, and charge retention times of days to weeks.

While single-electron computing continues to be the ultimate goal of SET technology, its most advanced practical application is currently the construction of a super-sensitive electrometer. FET devices with nanoparticles in the gate have provided a charge sensitivity of 600 pA per gate electron.[9] This electrometer could be used as an extremely sensitive tool for detection of the redox-state of a single molecule linked to the nanoparticle, thus allowing the detection of single-molecule chemical reactions.

Combining many SET elements together for the development of computing devices remains challenging. Even if it is not an unreasonable task to make electrical connections to a single nanotransistor, fabricating the 10^{12} transistor network that is required for computing is currently a far-off dream. Two independent approaches to connect many SET units have been suggested recently. The first approach involves the simple combination of SET units with well developed FET devices, in which a multigate FET device is used and each gate is associated with a single SET unit. The second, more novel approach is to forgo the connecting wires altogether.[241] This scheme, named quantum cellular automata (QCA), is based on the electrostatic interactions present between cells of connected clusters. In one possible design, the basic cell is a line of nanoclusters connected by insulating material (Figure 21 A). An electric field polarizes the string to give a "1" or "0" state, depending on the field direction. A similar design is produced from square cells of nanoclusters carrying the polarization states (Figure 21 B). Again, two states are possible, dependent upon the direction of the applied field. In either design, the cells can be connected in various configurations to make more complex logic circuits. Figure 21 C illustrates how the cells can be connected to form a logic gate. The dark and open circles correspond to one-electron rich and one-electron deficient clusters, respectively. The signals in QCA are rapidly transferred between interconnecting cells through electrostatic interactions at the speed of light. Fast intercell interactions and the small size of each cell (as low as about 2.5 nm^2) hold excellent potential for ultrahigh density data storage and processing from this kind of device.

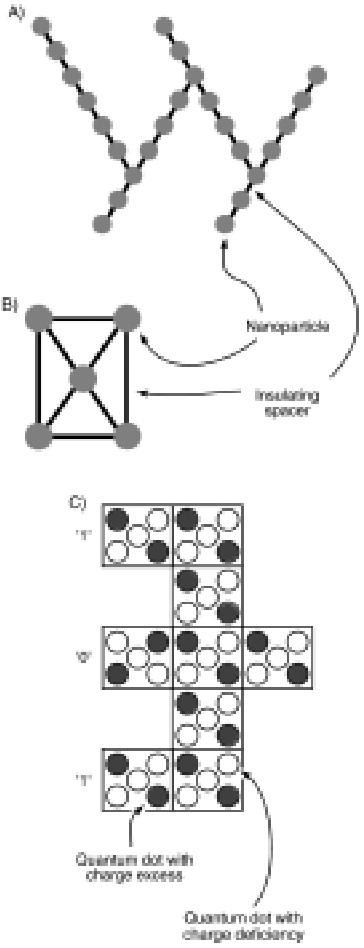

Figure 21. *Schematic representations of proposed "wireless" computation devices based on nanoparticle assemblies.*

4.3. Arrays with Sensor Functions

The use of gold nanoparticle superstructures for the creation of electrochemical sensing devices is an extremely promising prospect. Multilayers of conductive particles give rise to a porous, high surface-area electrode, where the local micro-environment of the gold particles can be controlled by the crosslinking elements and may lead to specific and selective interactions with substrates.

4.3.1. Vapor Sensors

Chemiresistors are simple solid-state devices whose electrical resistance is changed by the presence of chemical species. The resistance of nanoparticle arrays depends on the colloid size, interparticle distance, and dielectric properties of the interparticle material. An array consisting of colloidal gold stabilized with hydrophobic long-chain alkyl thiols is a medium that can accommodate organic materials, such as hydrocarbons or halogenated hydrocarbons, between the particles. Incorporation of the additional material can increase the interparticle distance and lower the relative (dielectric) permittivity of the medium, to result in a decrease of the electrical resistance of the array. This approach was recently applied for the detection of toluene and tetrachloroethylene vapors, which provided a detection threshold of approximately 1 ppm (v/v).[242] The device demonstrated a high sensitivity to these low polarity materials while being almost insensitive to materials with higher polarity (such as 1-propanol and water) at the same vapor pressure. Application of impedance spectroscopy could result in better understanding of the physical mechanisms of the sensing phenomenon, namely, finding which component of the resistance—faradaic or nonfaradaic—is mainly responsible for the resistance change.

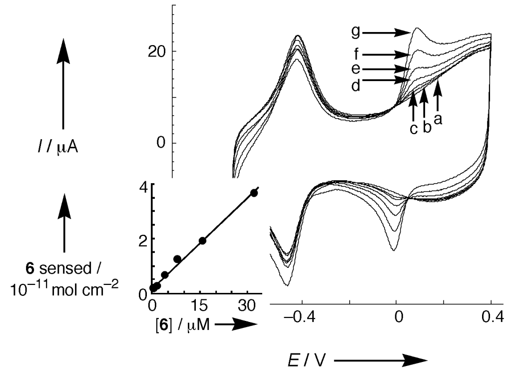

Figure 23. *Cyclic voltammograms of the five-layer electrode in the absence (a) and at various concentrations (b – g) of* ***6****. Inset: Calibration curve for the sensing of* ***6****. Recorded with conditions described in Figure 22.*

4.3.2. Sensing by a Receptor-Crosslinked Array

A series of electrochemical sensors were built by the electrostatic crosslinking of gold nanoparticles with the bipyridinium cyclophanes **1** or **3**, or the square-shaped oligocationic palladium(II)-ethylenediamine-bipyridine complex **4** (Scheme 6).[139, 147, 149, 150] The bipyridinium cyclophanes **1** and **3** act as receptors for the association of π-donor substrates in their cavities and the 3D conductivity of the gold nanoparticle array electrochemically senses π-donor substrates associated with the cyclophane units. The formation of π-donor acceptor complexes between the host receptor and the π-donor analyte enables the preconcentration of the analyte at the conductive surface. Furthermore, control of the number of gold particle layers associated with the ITO electrode allows the sensor sensitivity to be tuned. Figure 22 shows the electrochemical sensing of *p*-hydroquinone (**6**) at a bulk concentration of 1×10^{-5} M by an electrode functionalized with different numbers of **1**-crosslinked gold nanoparticle layers. The electrical responses of both the cyclophane (at $E^0 = -0.450$ V versus SCE) and the analyte increase with the number of layers, which implies that the array must be porous. Figure 23 shows the calibration curve for the electrochemical response of the five-layer electrode to **6**. The response, as indicated by the calibration curve, is approximately linear within the concentration range examined, which demonstrates that the sensor is not easily saturated. The electrochemical sensing of the hydroquinone is possible at concentrations as low as 1×10^{-6} M. In contrast, for a gold nanoparticle array crosslinked by the acyclic molecule *N,N'*-diaminoethyl-4,4'-bipyridinium (**5**), **6** is undetectable electrochemically within the range $10^{-5} - 10^{-6}$ M. These observations clearly reveal that the successful sensing of **6** by the **1**-crosslinked superstructure originates from a specific host – guest interaction rather than from the fabrication of a roughened interface. In addition to the enhanced sensitivity in the analysis of **6** with the number of layers, the electron transfer kinetics of the guest is vastly improved upon the buildup of the layers, as shown by the decrease in its peak-to-peak separation.

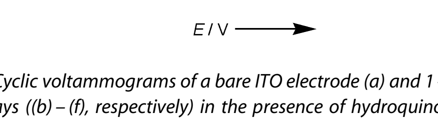

Figure 22. *Cyclic voltammograms of a bare ITO electrode (a) and 1 – 5 layer gold colloid/****1*** *arrays ((b) – (f), respectively) in the presence of hydroquinone (****6****; 1×10^{-5} M). Recorded under argon in 0.1 M phosphate buffer solution, pH 7.2, scan rate 100 mV s^−1, SCE as reference electrode.*

Other π-donor substrates, such as dihydroxyphenyl acetic acid and the neurotransmitters adrenaline (**7**) and dopamine (**8**), can also be sensed by the **1**-crosslinked gold nanoparticle electrode.[150] These substrates contain π-donor *ortho*-hydroquinone units but, in addition, include those with β-aminoalkyl substituents on the aromatic ring. The electrochemistry of these compounds has been examined and discussed for homogeneous aqueous solutions[243] and is summarized in Scheme 13. Oxidation of the *o*-hydroquinone residue to the quinone (**9**) is only partly reversible, since the amine substituent induces a Michael addition accompanied by a ring closure and the formation of **10**, which exhibits reversible or quasireversible electrochemical properties. Figure 24 shows the electrochemical sensing of different concentrations of adrenaline by a **1**-crosslinked gold nanoparticle electrode.[150] In addition to the cyclophane redox wave, an irreversible oxidation wave for adrenaline is observed (at 0.3 V versus SCE), as well as a quasireversible redox wave (at $E^0 = -0.28$ V versus SCE), which corresponds to the electrochemically induced cyclization product **10** (Scheme 13). Coulometric assay of the quasireversible redox wave of the electrogenerated product enables extraction of the calibration curve (Figure 24 inset).

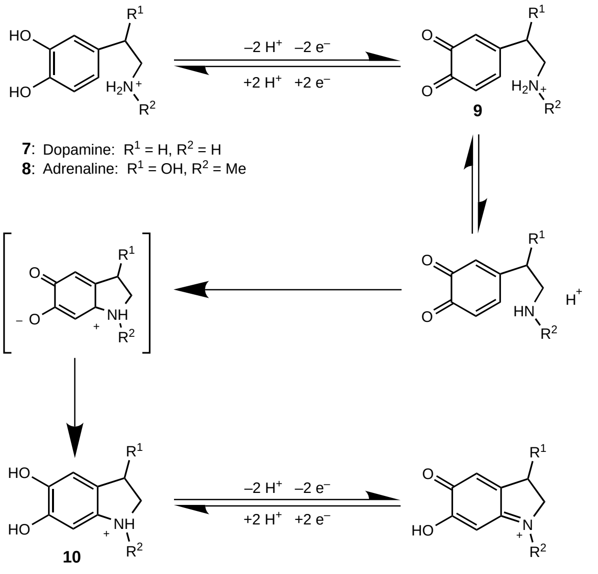

Scheme 13. *The electrochemically promoted intramolecular cyclization of 4-(β-aminoalkyl)1,2-benzohydroquinones.*

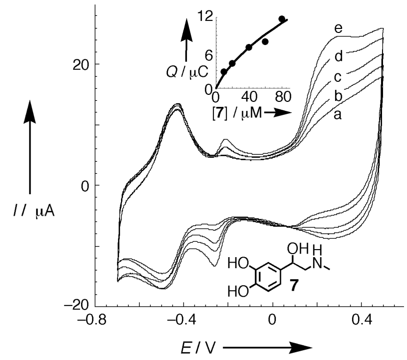

Figure 24. *Cyclic voltammograms of a 5-layer gold colloid/**1** electrode at various concentrations of adrenaline (**7**). Inset: Calibration curve for the signal of **7** from the reduction peak of its electrocatalysed Michael-type cyclization (Scheme 13). Recorded with conditions described in Figure 22.*

4.3.3. Receptor-Induced Selectivity

The selectivity of gold nanoparticle electrodes is controlled by the structure of the crosslinking receptor units. Application of the enlarged cyclophane **3** as a crosslinker for the gold particles enables the electrochemical sensing of *bis*-dihydroxymethylferrocene (**11**; Figure 25 A) but not of **6**, due to its large cavity dimensions.[139] Likewise, the **1**-crosslinked gold nanoparticle superstructure fails to sense **11** because the small receptor dimensions preclude the accommodation of the larger guest (Figure 25 B). The cationic Pd^{II} complex **4** enables the electrochemical sensing of both **6** and **11**, since its cavity is large enough for the former and the latter can associate with it in a diagonal orientation.[149] Lastly, the sensory features of the cyclophane–colloid electrodes are affected by the lattice morphology. A superstructure consisting of three inner layers of **1**-crosslinked gold nanoparticles then by three outer layers of **3**-crosslinked particles enables the electrochemical sensing of both **6** and **11**. Conversely, a gold nanoparticle composite electrode, that consists of **3**-crosslinked gold nanoparticles then **1**-crosslinked gold nanoparticles, enables the electrochemical sensing of **6** only.[139] This phenomenon has been attributed to the porosity control of the gold nanoparticle array by the receptor crosslinking units—the superstructure consisting of **1**-crosslinked gold nanoparticles is porous to **6** but is impervious to the larger molecule **11**.

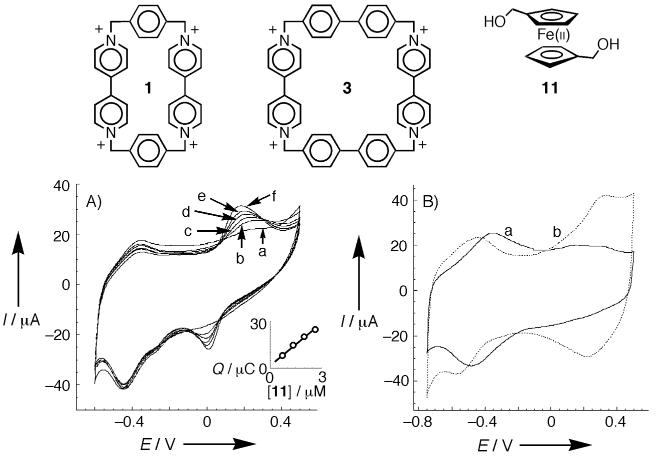

Figure 25. *A) Cyclic voltammograms of a **3**-crosslinked electrode (five layers) in the absence of and in various concentrations of **11**. Inset: Calibration curve for the signal of **11** from the amperometric reponses of the electrode. B) Cyclic voltammograms of five-layer electrodes crosslinked by **1** and **3** in the presence of **11** (1×10^{-6} M). Recorded with conditions described in Figure 22.*

4.3.4. Nanoparticle Arrays as Ion-Sensitive Field-Effect Transistors

The receptor-based sensors described above are efficient in the concentration of the analyte at the substrate surface but, since the sensing is fundamentally electrochemical, the technique is limited to redox-active analytes. The same sensing principle can be used with a different sensing method, however, to allow the analysis of redox-inactive compounds. Ion-sensitive field-effect transistors (ISFETs) provide a means to detect charged species in close proximity to a gate surface. A charged species at the sensing interface (Figure 26 A) of such a device causes a change in the polarization of the underlying SiO_2/Si interface (a thin layer of a nonconductive material on the sensing interface, for example GaAs or Al_2O_3, is often used to ensure insulation). The conductance of electrons from the source electrode to the drain electrode through the semiconductor is highly sensitive to this gate polarization (which has the effect of either attracting or repelling charge carriers). By measuring either 1) the source–drain current at a given gate–source potential (V_{gs}) or 2) the gate–source potential required for a given source–drain voltage (V_{sd}) and source–drain current (I_{sd}), it is possible to determine the polarization of the sensing interface.

An ISFET-based sensor for small π-donors has been made by the fabrication of a **1**/gold nanoparticle surface at the Al_2O_3 sensing interface of an ISFET (Figure 26 B).[244] This assembly was built up by the stepwise deposition of polyethyleneimine, gold

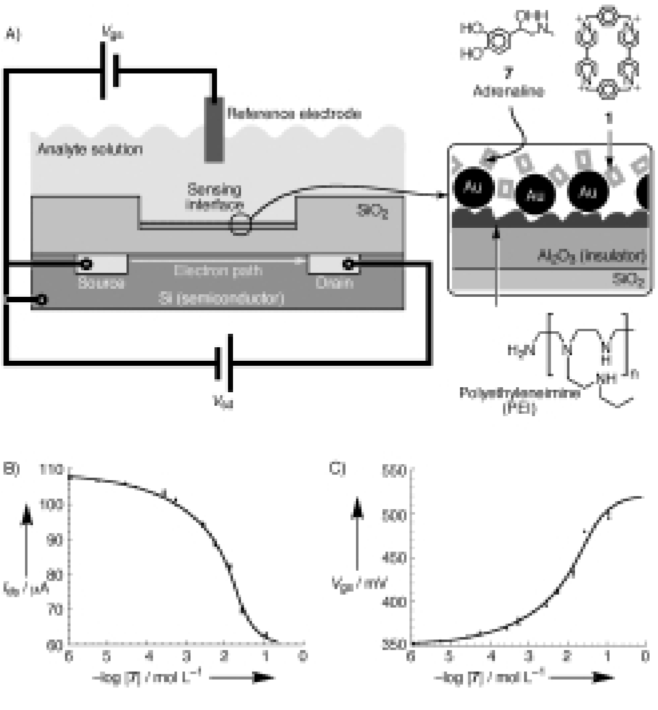

Figure 26. *A) Schematic diagram of a gold colloid/**1**-based ISFET sensor. B) Adrenaline (**7**) sensed by this ISFET by the source–drain current measurement mode. C) **7** sensed by the gate–source potential mode.*

nanoparticles, and **1** on the sensing interface. The resulting sensor is able to detect any charged molecule that complexes with the receptor **1**, including those that are not electrochemically active, such as serotonin. Figure 26C shows the results from a study of adrenaline. Reliable data for the detection of **7** can be obtained over six orders of magnitude of concentration, and Benesi–Hildebrand analysis[245] gave a calculated binding constant between **1** and **7** of $200 \pm 30\,\text{M}^{-1}$.

4.3.5. Nanoparticle–Enzyme Assemblies for Biosensing Applications

The possibility for direct electron transfer between conductive nanoparticles and redox proteins (such as cytochrome c[221]) paves the way for the construction of amperometric biosensors based on redox enzymes as sensing elements and nanoparticle arrays as the conductive matrix onto which the enzyme molecules are implanted. For example, a mixed layer of horseradish peroxidase (HRP) and colloidal gold particles (30 nm) was reported to be electrocatalytically active for hydrogen peroxide reduction without the need for electron-transfer mediators.[246] Although direct, nonmediated electron transfer is well known for some redox proteins and particularly for HRP,[247] it is usually very inefficient and is not generally used for practical biosensory devices. However, the small size of gold nanoparticles allows the conductive material to come into a close proximity of the active center of the enzyme, which facilitates the electron-transfer process and provides bioelectrocatalytic activity that can be utilized in biosensor devices. Another example of a biosensor exploring nonmediated, direct electron transfer is a D-fructose sensitive electrode based on D-fructose dehydrogenase encapsulated into a colloidal gold layer on a glassy carbon conductive support.[28] More attractive, but also more difficult from a nanoengineering point of view, is the organization of spatially ordered assemblies consisting of biocatalytic enzyme molecules and conductive nanoparticles, rather than their nonorganized composites. A thiol-terminated monolayer was prepared in a multistep procedure on a gold support (Scheme 14), to which colloidal gold (diameters of 16, 24, 42, or 51 nm) was added.[248] Finally, HRP was adsorbed onto the immobilized colloidal particles. Such a stepwise procedure provides some spatial organization of the system but the resulting array does not operate in the absence of a diffusional electron-transfer mediator (catechol) because of the long nonconductive spacers used by the system. This problem can be solved by the application of conductive spacers, either with incorporated redox species, which function as intermediate stations for electron shuttling,[249] or with redox mediators tethered to enzyme molecules or nanoparticles.[250] In the case of small semiartificial biocatalyst molecules (for example, microperoxidase-11) that do not require electron-transfer mediators, a multilayer array with 3D-distributed bioelectrocatalysts has been created by a step-by-step deposition of the biomaterial and conductive nanoparticles.[251] The electrocatalytic current exhibited by the system was proportional to the number of biocatalytic layers in the multilayer array, thus all of the electrocatalyst molecules were accessible to the substrate (H_2O_2, in case of the colloidal gold/microperoxidase-11 3D array) and preserved their electrocatalytic activity.

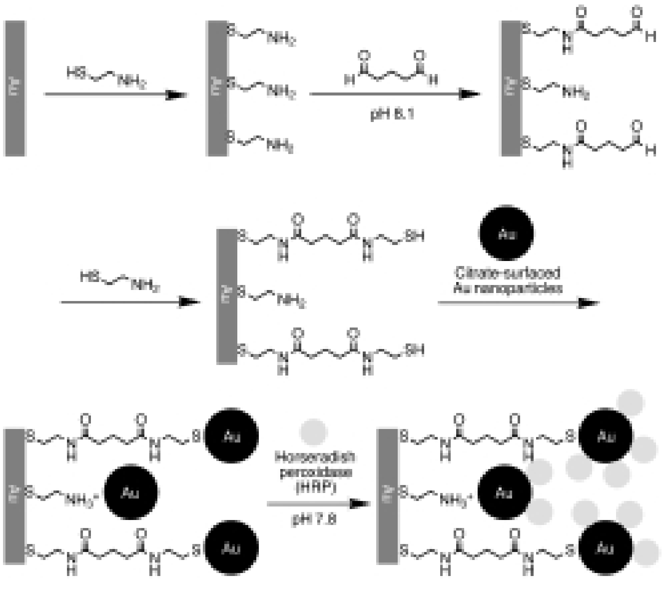

Scheme 14. *The preparation of a gold nanoparticle–horseradish peroxidase H_2O_2 sensor.*

Finally, the conductive properties of gold colloids can be used as an indicator for biosensing applications. A recent study detailed how arrays of individually tailored, addressable biosensors can be built up, where a "positive" signal results in the short circuiting of two microelectrodes by gold nanoparticles (Scheme 15).[252] In the first step, an alternating current between two electrodes causes the collection of polymer-coated magnetic particles between them. These particles, which bear an IgG-binding protein coating, are covalently immobilized before the analyte (IgG) is added. After interaction with the analyte, the assembly is incubated with gold nanoparticles which bear anti-IgG. If IgG is present on the array, these gold colloids bind and provide conductivity between the electrodes (which can be enhanced by a further step of nonelectrochemical deposition of silver on the gold particles). An electron micrograph of two electrodes short circuited in this way is shown in Scheme 15.

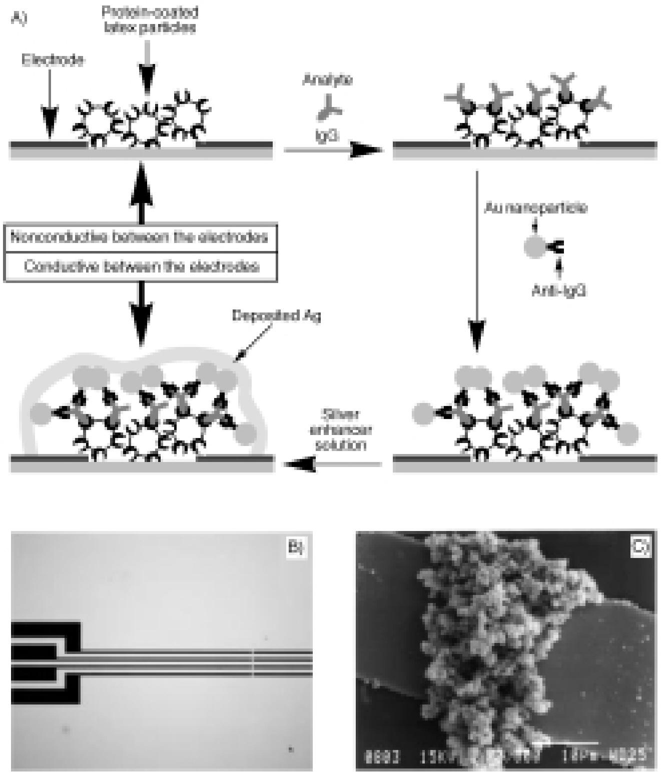

Scheme 15. *A) The assembly of the IgG sensor and its operation. B) An array of four 30 μm wide electrode pairs prior to sensor assembly. C) SEM image of a short-circuited electrode pair after the successful sensing of IgG. Reproduced from ref. [252] with permission.*

4.4. Arrays with Photoelectrochemical Functions

4.4.1. Photoelectrochemical Power To Generate Nanoparticle Superstructures

Photocurrent generation in semiconductor nanoparticle arrays has been used to characterize photoinduced charge separation and electron mobility in and between nanoparticles (see Section 3.3.2). The possibilities for the variation of nanoparticle architecture, for the construction of ordered mixtures of different components, and for the introduction of low-molecular mass additives make semiconductor nanoparticle arrays very attractive for the development of photocurrent generating elements.[253, 254] Lead sulfide based photosensitive nanoparticles capped with hydrophobic long-chain molecules (dioctyl sulfosuccinate) have been assembled onto gold electrode surfaces modified with long-chain thiols.[255] The hydrophobic interaction between the monolayer on the solid gold support and the capping material around the PbS nanoparticles provided immobilization of the particles at the electrode surface. A cathodic or anodic photocurrent was observed when an electron acceptor or donor, respectively, was added to the solution. Photoinduced, interparticle electron transfer between dissimilar semiconductive particles have been used to convert light into electricity. The coupling of two semiconductor particles may offer an opportunity to sensitize a wide bandgap semiconductor material by another with a narrower bandgap. Thus, interparticle conjugates of CdS/TiO_2, CdS/ZnO, CdS/Ag_2S, CdS/AgI, ZnS/AgI, ZnS/Ag_2S, ZnS/Cd_3P_2, ZnS/TiO_2, and ZnS/ZnO have been prepared and their interparticle electron transfer studied.[126, 256] Charge transfer from CdS to TiO_2 particles has been more extensively studied than the other systems. The conduction band of CdS lies above that of TiO_2 and, thus, $CdS \rightarrow TiO_2$ electron transfer is energetically allowed. The possibility of using bifunctional bridging ligands to form rigid and well defined systems that consist of two kind of nanoparticles has been explored to build photosensitive mixed-particle aggregates.[126] Bifunctional linkers that contain both thiol and carboxylic acid groups to couple with CdS and TiO_2 particles, respectively, were applied to build mixed-particle assemblies. Optical and photochemical properties of these assemblies were studied and efficient photoinduced interparticle charge separation was demonstrated. These systems have not yet been used for photocurrent generation, however.

Spectral sensitization of wide bandgap semiconductors in photoelectrochemical cells is an attractive approach for conversion of the visible light from solar energy into electricity. Various organic dyes and metallocomplexes (for example, merocyanine-540[257] or ruthenium(II) polypyridyl species[253]) have been used as sensitizing dye molecules and facilitate an appreciable absorption of incident light. Although substantial effort has been directed towards the optimization of photochemical systems, the observed photocurrent efficiencies have generally been very low. A major factor responsible for the low photoconversion efficiency of an organic dye-sensitized solar cell is the formation of dye aggregates on the semiconductor surface. The photoinduced charge separation can be suppressed significantly because of intermolecular quenching in the dye aggregates. Different possibilities to prevent photosensitizer aggregation have been studied, such as incorporation of dye molecules into β-cyclodextrin cavities[258] and microencapsulation of dye molecules in surfactant systems.[257] Increased molecular spacing between photoexcited dye molecules can significantly diminish interconversion rates, which makes the deactivation pathways less competitive. The incident photon-to-photocurrent generation efficiency exhibited by the encapsulated monomeric dye (around 40%) was reported to be nearly five times larger than the corresponding efficiency of the dye aggregate (about 8%). A prototype solar cell "OTE/TiO_2/MC540/PVP", which consisted of a photoelectrode (photoanode) based on TiO_2 nanoparticles (as a 2–4 μm thick film), merocyanine-

540 dye encapsulated into a surfactant system (aerosol-OT), and a Pt wire gauge (counterelectrode), was studied.[257] Figure 27 shows the photovoltage versus photocurrent dependence (power characteristics) measured under different loading resistances. The maximum photovoltage (open circuit voltage, V_{oc}) and photocurrent (short circuit current, I_{sc}) were 200 mV and 165 μA cm^{-2}, respectively, while the maximum power output (P_{max}) was 19.6 μW cm^{-2} at an incident light intensity (W) of 1.3 mW cm^{-2} (560 nm). The fill factor (f), obtained from Equation (4) and the results of Figure 27, was $f = 0.6$. These parameters yield, from Equation (5), a net power conversion efficiency (Δ) of 1.5 %.

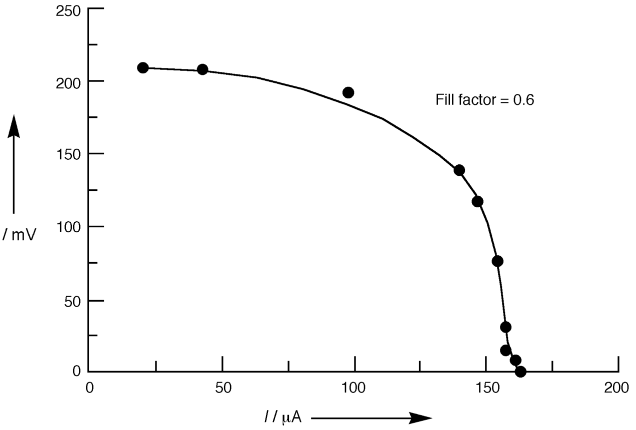

Figure 27. *The power characteristics of a OTE/TiO$_2$/MC540/PVP photosensitive electrode under 1.3 mW cm^{-2} illumination at 550 nm. A Pt counter electrode and 1 M LiI in 0.2 % CF$_3$COOH in CH$_3$CN electrolyte was employed. Reproduced from ref. [257] with permission.*

$$f = \left(\frac{P_{max}}{V_{OC}\, I_{SC}}\right) \tag{4}$$

$$\Delta = 100\left(\frac{P_{max}}{W}\right) \tag{5}$$

The application of semiconductor particles associated with photosensitizing dyes allows the development of low cost, high efficiency solar cells which exhibit commercially realistic energy conversion efficiencies.[259] One such device was based on a 10 mm thick, optically transparent film of TiO$_2$ particles coated with a monolayer of a charge-transfer dye to sensitize the film for light harvesting.[259] Because of the high surface area of the semiconductor film and the ideal spectral characteristics of the dye, the device harvested a high proportion of the incident solar energy flux (46 %) and showed exceptional efficiencies for the conversion of incident photons to electrical current (> 80 %). The large current densities (> 12 mA cm^{-2}) and excellent stability of these constructions, as well as their low cost, make practical applications feasible. Sol – gel techniques[260] and electrophoretic deposition[261] of the colloids have been used successfully to improve the solar cell performance, which were well characterized by numerous methods.[262]

Substantial recent research efforts have been directed to the organization of porous high surface-area electrodes for photoelectrochemical applications and multilayer gold-nanoparticle architectures have been used for the construction of a photoelectrochemical device (Figure 28 A).[148] The multilayer gold-nanoparticle superstructure was assembled by the stepwise crosslinking of citrate-capped gold nanoparticles with the bis(bipyridinium)-Zn(II)/protoporphyrin IX dyad **12** acting as an electrostatic crosslinker. The presence of the photoactive porphyrin was detected in the absorbance spectrum of the array and other features were verified by cyclic voltammetry. Photoirradiation of the porphyrin component leads to electron transfer to the pendant bis(pyridinium) moieties. The gold array enables effective charge transport to the electrode, which generates a photocurrent that is controlled by the number of chromophore/acceptor and gold nanoparticle layers (Figure 28 B).

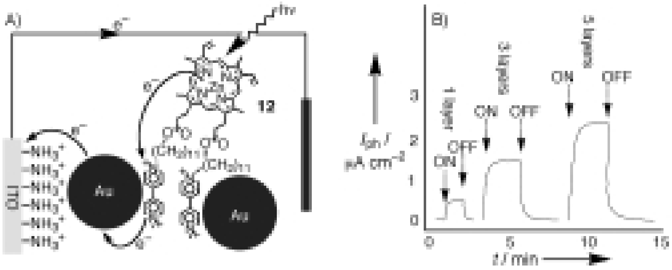

Figure 28. *A) Schematic representation of the functional part of the colloidal gold/**12** photoelectrochemical device showing the mechanism of photocurrent generation. B) The photocurrent generated by the irradiation of one-, three-, and five-layer arrays demonstrating the photocurrent dependence on assembly thickness.*

4.4.2. Electroluminescent Nanoparticle Superstructures

Semiconductor arrays have also been used for the fabrication of electroluminescent devices. In one case, a novel type of light-emitting diode (based on a CdS nanoparticle array) with two distinguishable emissions, that depend on the potential direction, was developed.[263] In another case, a hybrid organic/inorganic electroluminescent device was prepared using semiconductor nanocrystals and a conductive polymer (paraphenylene vinylene, PPV).[264] Five layers of CdSe nanoparticles, with hexanedithiol as a layer crosslinker, were deposited onto ITO/PPV plates. The overall thickness of the nanocrystal multilayer was a few hundred Ångströms and the composite was completed with a layer of magnesium on top of the nanoparticles. The close match between the emitting layer of nanocrystals with the work function of the metal contact lead to an operating voltage of only 4 V. Upon application of bias voltage, with the ITO positively biased with respect to magnesium, holes and excess electrons are created in the PPV and the CdSe nanocrystals, respectively, and the device emits light of approximately 100 cd m^{-2} intensity (visible under normal room light). Adjustment of the applied voltage varies the region (nanoparticles or conductive polymer) where the holes and electrons meet, which provides control over the color of the emitted light. At lower voltages, emission occurs preferentially in the CdSe layer, whereas at higher voltages the green-colored PPV layer dominates (Figure 29). Such a phenomenon has not been observed in bilayer structures of organic polymers, even when similar carrier confinement properties are reported. Additional color control, from red to yellow, can be accomplished by changing the size of the CdSe nanoparticles. The quantum efficiency (emitted photons per passing electron) achieved in this system was in the range 0.001 – 0.01 %. In a similar CdS-nanocrystal system,[265] an overall quantum efficiency of about 1 % was achieved. Further, application of CdS allowed the use of the less active aluminium metal for the electron-injecting electrode while maintaining a very low threshold voltage (3 V). A stable electroluminescence with an intensity of 150 cd m^{-2} was achieved for 1200 hours when 10 V was applied.

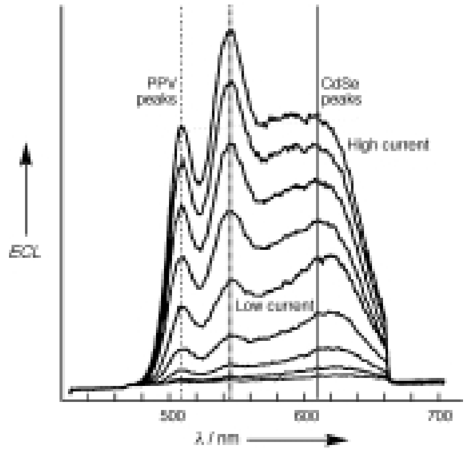

Figure 29. *Electroluminescence spectrum of the CdSe/PPV composite over a range of voltages and demonstrates a color change with the applied potential. ECL = electrochemically generated chemiluminescence intensity. Reproduced from ref. [264] with permission.*

Size-dependent photoemission of a quantum-dot system composed of CdS nanoparticles assembled onto thiol-terminated monolayers on metal surfaces (Au or Al) has been demonstrated.[266] A narrow, electroluminescent emission band was achieved when nearly monodisperse CdSe nanocrystals and a PPV layer were applied to an electroluminescence device.[267] The emission band was tunable with the size of nanoparticles. Conversely, a system composed of a PPV layer and several layers of CdSe particles with a broad size distribution generated a nearly white electroluminescent light (Figure 30) because of the broad fluorescence spectrum of the semiconductor layer.[268] Such a broad emission spectra results from both the deep trap sites at the particle surface and the defects within the particle. The broad particle size distribution also contributes to the inhomogeneous spectral broadening.

Dual properties of photocurrent generation and electroluminescence were found in hybrid devices, which consist of a nanoparticle semiconductor layer and a polymer layer.[269] Polymers such as poly(3-hexylthiophene), poly(2-methoxy-5-(2-ethylhexoxy)-1,4-phenylenevinylene), and poly(6-fluoro-dioxydecyl benzoxazole) covered wide spectral range with absorption edges at 605, 560, and 495 nm, respectively. Monodisperse nanoparticles of CdS (mean size 4.4 and 2.2 nm) capped with 1-thioglycerol were spin coated on the polymer layer. The polymer/nanoparticle bilayer was sandwiched between an ITO plate (polymer side) and vacuum-evaporated aluminium (CdS side). It was observed that the spectral response and efficiency of the photocurrent in these multilayer devices are similar to that of the semiconductor component, whereas the spectral responses of the electroluminescence are closer to that of the polymer layer. Variation of the polymers and the sizes of CdS particles provided tunability of the photocurrent and electroluminescence spectra.

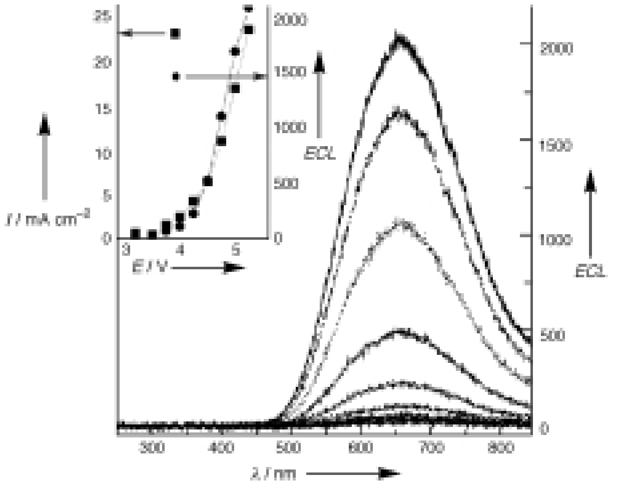

Figure 30. *Electroluminescence spectra of the CdSe/PPV device under ambient conditions and a positive bias on the ITO electrode. Inset: Electroluminescent intensity as a function of voltage. Reproduced from ref. [268] with permission.*

Composite materials consisting of electroluminescent polymers with implanted oxide nanoparticles were applied for the construction of light-emitting diodes. For example, a light-emitting diode based on PPV derivatives with incorporated mixed-oxide nanoparticles gives an enhancement of the current density and radiance by more than an order of magnitude at low voltage.[270] As a result, in these polymer/nanoparticle composite devices, radiances of 10 000 cd m^{-2} have been achieved at a drive voltage of only 5 V. Study of the mechanism responsible for this enhancement revealed that incorporation of nanoparticles into the electroluminescent polymer matrix results in the reduction of the effective layer thickness.[271] Both the magnitude and field dependence of the current are consistent with the assumption that the electrically effective thickness of a composite layer is about half of its physical thickness. Thus, the incorporation of nanoparticles into an electroluminescent polymer opens the possibility to combine the advantages of thick layers for mechanical strength and improved substrate coverage with the favorable electro-optic properties of a thin-layer device.

5. Conclusions, Perspectives, and Future Directions

It is clear that the unique properties of colloidal nanoparticles have much to contribute to the construction of surface-bound nanostructures. Apart from their use as structural components, they have many useful properties which can be tuned by control over the particle size and can be utilized in the fabrication of nanostructured devices (e.g. surface morphology, electrochemical and photoelectrochemical activity, surface plasmon, surface-enhanced Raman scattering). Methods are available for the facile bulk-scale synthesis of monodisperse nanoparticles of many materials and surface functions, and the techniques for their analysis (for example, microscopy, light scattering, and spectroscopy) are now well developed.

The assembly of nanoparticles on solid substrates has been well studied and has given rise to a multitude of techniques for their immobilization on a wide range of conductive, semiconductive, and insulating substrates. Methods to produce patterned arrays of colloids and to organize colloid monolayers into close-packed or well spaced arrays have been found, leading the way towards the construction of addressable arrays of nanoparticle devices. Nanoparticle multilayers have been constructed using many different types of nanoparticle, even with different types in the same architecture. Other materials, such as polymers and molecular species, can also act as a functional part of the architecture, often while acting as a "glue" to hold the structure together. One factor that is missing from the synthesis of three-dimensional nanoparticle superstructures, however, is a high degree of three-dimensional organization. While superstructures may be composed of distinct layers, the exact alignment of each layer with respect to those around it (as well as the two-dimensional ordering within each layer) is an elusive goal. Perhaps this issue may be addressed by the further development of sophisticated fabrication methods that are already proving successful on the millimeter scale.[272]

It is very encouraging to consider the number and diversity of applications that have benefited from research into nanoparticle superstructures. In some cases, colloidal particles may be used in place of a bulk material, providing numerous advantages over the latter. In others, qualities specific to the nanoparticles may be used to create architectures for uses such as SERS or sensory applications. Electrically conducting or semiconducting colloids have been used for the construction of several components of electrical circuits, including wires, contacts, and single-electron components. Ultimately, these devices together with patterning and three-dimensional construction techniques could even lead to nanoparticle-based integrated circuits! Finally, nanoparticle assemblies have found great success in the construction of biosensing devices. With dimensions similar to those of biomaterials, nanoparticles are a natural choice for interfacing units, and have found use in both electrochemically and optically based sensors.

The current state of the art with respect to nanoparticle devices should be put into perspective, however. Nanoparticles are only likely to find commercially viable applications where they are either more convenient than current solutions (in terms of cost, ease of manufacture, performance, and so forth) or offer new opportunities as a consequence of their unique properties. In the construction of electronic nanocircuitry, for instance (see Section 4.2.1), patterned nanoparticle monolayers will face dificulties competing with photolithography, which can now produce feature of sizes approaching 50 nm with extreme-UV irradiation, or features as small as 5 nm by electron-beam lithography. Advantages may be found for the construction of three-dimensional electronic architectures or larger feature sizes, however, as colloid nanostructures may be constructed using very cheap and readily available facilities. In the construction of the next generation of electronic components, nanoparticles are of more interest. They are essential for the construction of single-electron devices (Section 4.2.2) and the self-assembling capabilities of solution-state nanoparticles are very useful in the development of simple fabrication techniques.[20] This field is in its infancy and industrial applications of the devices are unlikely to become apparent for many years.

One area where the outlook for nanoparticle architectures is particularly bright is in the development of SERS substrates (Section 4.1.2).[216] Nanoparticle substrates are cheap, easy, and reproducible to prepare and have even brought Raman spectroscopy into the select club of single-molecule spectroscopies.[220] There are still problems to overcome though—we still need to understand how the enhancement is dependent on factors such as the particular particle and the nature of the analyte.[218] The application of nanoparticle arrays with included receptor molecules for sensory applications has some advantages over other architectures (Sections 4.3.1 and 4.3.2). Immobilized receptor interfaces have the ability to act as selective sensors with an electrochemical[273] or microgravimetric[274] signal. The high surface area, conductive nanoparticle network gives a large surface density of the receptors compared to a single-monolayer array. The highly porous network allows the analyte to penetrate inside the matrix and interact with the receptor sites, although it should be noted that these assemblies do not yet rival the sensitivities of commercial devices. Such three-dimensional recognition matrices can be also organized in polymer layers but polymers rarely provide high porosity and stability. Sensors based on nanoparticle – enzyme assemblies (Section 4.3.5) are of particularly interest, as biosensors based on electrically "wired" enzymes have become very popular over the last two decades. While there are many methods of achieving electical communication with immobilized enzymes,[275] nanoparticles offer a particularly simple route. Nanoparticles can position themselves a short distance from the active sites of enzymes and provide direct, nonmediated electron transfer. Such direct electrical coupling of enzymes with the electrode support has the potential to be more efficient than even the most sophisticated multicomponent enzyme/relay systems, although, at present, few examples exist and the exact tailoring of the assembly is a matter of trial and error.

Photoelectrochemical and electroluminescent devices are becoming increasingly important with the growing need for renewable energy sources and display technologies. Organic and bioorganic light-energy transducers have gained a great deal of attention[276] but they suffer from relatively low stability. Much more stable photocurrent generating systems can be based on nanoparticles, allowing the combination of the very complex architectures of organic materials with the high stability of inorganic compounds (Section 4.4.1). A great deal of progress has been made recently in improving the performance of organic electroluminescence (EL) devices, some of which are now adequate for many applications. The use of nanoparticles to design EL devices has brought novel capabilities to this area (Section 4.4.2). A very narrow or broad emission band, tunable emission band, and high quantum yield emission can become possible when nanoparticles are involved in the process.

The development of this very young field of nanoparticle superstructures has taken off rapidly and will surely continue to expand. While the exploitation of gold, silver, and cadmium sulfide colloids has gained much attention, there are many other functional materials from which nanoparticles can be synthesized. In addition, there is a whole world of materials (molecular and macromolecular) which may be incorporated into nanostructured composites in order to tailor properties to exact specifications. One challenging issue for further research is the ordered organization of nanoparticle arrays on solid supports. The use of biomaterials and specific binding events for the construction of superstructures may address this issue, perhaps along with new nanofabrication techniques such as particle manipulation by scanning microscopy tips. In essence, we should expect the unexpected in the near future. Nanoparticle superstructures are still in their infancy and already provide exciting outlooks for chemists, physicists, biologists, and materials scientists from theoretical, experimental, and practical perspectives.

Received: May 4, 2000 [A 1]

[1] a) *Nanosystems*, *Molecular Machinery*, *Manufacturing and Computation* (Ed.: K. E. Drexler), Wiley, New York, **1992**; b) J.-M. Lehn, *Angew. Chem.* **1990**, *102*, 1347 – 1362; *Angew. Chem. Int. Ed. Engl.* **1990**, *29*, 1304 – 1319; c) F. L. Carter, A. Schultz, D. Duckworth in *Molecular Electronic Devices* (Ed.: F. L. Carter), Marcel Decker, New York, **1987**, pp. 183 – 199; d) P. Ball, *Nature* **1993**, *362*, 123; e) A. C. Benniston, A. Harriman, V. M. Lynch, *J. Am. Chem. Soc.* **1995**, *117*, 5275 – 5291; f) D. Philp, J. F. Stoddart, *Angew. Chem.* **1996**, *108*, 1242 – 286; *Angew. Chem. Int. Ed. Engl.* **1996**, *35*, 1154 – 1196.

[2] a) A. P. DeSilva, H. Q. N. Gunazatne, C. P. McCoy, *Nature* **1993**, *364*, 42 – 44; b) P. Ball, L. Garwin, *Nature* **1992**, *355*, 761 – 766; c) *Molecular Electronics* (Ed.: G. J. Ashwell), Wiley, New York, **1992**; d) B. Tieke, *Adv. Mater.* **1990**, *2*, 222 – 231; e) R. W. Wagner, J. S. Lindsey, J. Seth, V. Palaniappan, D. F. Bocian, *J. Am. Chem. Soc.* **1996**, *118*, 3996 – 3997.

[3] a) W. Göpel, *Biosens. Bioelectron.* **1998**, *13*, 723 – 728; b) I. Willner, E. Katz, B. Willner in *Sensors Update*, *Vol. 5* (Eds.: H. Baltes, W. Göpel, J. Hesse), Wiley-VCH, Weinheim, **1999**, Chap. 2, pp. 45 – 102; c) I. Willner, *Acc. Chem. Res.* **1997**, *30*, 347 – 356; d) E. Katz, V. Heleg-Shabtai, I. Willner, H. K. Rau, W. Haehnel, *Angew. Chem.* **1998**, *110*, 3443 – 3447; *Angew. Chem. Int. Ed.* **1998**, *37*, 3253 – 3256; e) E. F. Bowden, *Interface* **1997**, *6*(4), 40 – 47; f) M. Brunozi, *Biosens. Bioelectron.* **1994**, *9*, 633 – 636; g) C. Ziegler, W. Göpel, H. Hämmezle, H. Hatt, G. Jung, L. Laxhuber, H.-L. Schmidt, S. Schütz, F. Vögtle, A. Zell, *Biosens. Bioelectron.* **1998**, *13*, 539 – 571.

[4] a) J.-M. Lehn, *Supramolecular Chemistry*, VCH, Weinheim, **1995**; b) J.-M. Lehn, *Angew. Chem.* **1988**, *100*, 91 – 116; *Angew. Chem. Int. Ed. Engl.* **1988**, *27*, 89 – 112; c) I. Willner, B. Willner in *Fronties in Supramolecular Organic Chemistry and Photochemistry* (Eds.: H.-J. Schneider, H. Dürr), VCH, Weinheim, **1991**, pp. 337 – 370; d) A. C. Benniston, *Chem. Soc. Rev.* **1996**, 427 – 435; f) M. Fujita, *Acc. Chem. Res.* **1999**, *32*, 53 – 61.

[5] a) C. M. Niemeyer, *Angew. Chem.* **1997**, *109*, 603 – 606; *Angew. Chem. Int. Ed. Engl.* **1997**, *36*, 585 – 587; b) M. Aizawa, T. Hazuyama, G. F. Khan, E. Kolatake, Y. Ikaziyama, *Biosens. Bioelectron.* **1994**, *9*, 601 – 610; c) F. A. Armstrong, H. A. Heezing, J. Hirst, *Chem. Soc. Rev.* **1997**, *26*, 169 – 179; d) H.-L. Schmidt, W. Schuhmann, *Biosens. Bioelectron.* **1996**, *11*, 127 – 135.

[6] a) O. A. Matthews, A. N. Shipway, J. F. Stoddart, *Prog. Polym. Sci.* **1998**, *23*, 1 – 56; b) D. A. Tomalia, A. M. Naylor, W. A. Goddard III, *Angew. Chem.* **1990**, *102*, 119 – 157; *Angew. Chem. Int. Ed. Engl.* **1990**, *29*, 138 – 175; c) G. R. Newkome, C. N. Moorefield, F. Vögtle, *Dendritic Molecules*, VCH, Weinheim, **1996**; d) A. W. Bosman, H. M. Janssen, E. W. Meijer, *Chem. Rev.* **1999**, *99*, 1665 – 1688; e) J.-P. Majoral, A.-M. Caminade, *Chem. Rev.* **1999**, *99*, 845 – 880; f) F. Zeng, S. C. Zimmerman, *Chem. Rev.* **1997**, *97*, 1681 – 1712.

[7] *Clusters and Colloids* (Ed.: G. Schmid), VCH, Weinheim, **1994**.

[8] R. F. Khairutdinov, *Colloid J.* **1997**, *59*, 535 – 548.

[9] "Single Charge Tunneling and Coulomb Blockade Phenomena in Nanostructures": *NATO ASI Ser. Ser. B* **1992**, 294.

[10] P. Mulvaney, *Langmuir* **1996**, *12*, 788 – 800.

[11] M. M. Alvarez, J. T. Khoury, T. G. Schaaff, M. N. Shafigullin, I. Vezmar, R. L. Whetten, *J. Phys. Chem. B* **1997**, *101*, 3706 – 3712.

[12] A. P. Alivisatos, *J. Phys. Chem.* **1996**, *100*, 13 226 – 13 329.

[13] L. E. Brus, *Appl. Phys. A* **1991**, *53*, 465 – 474.

[14] a) L. N. Lewis, *Chem. Rev.* **1993**, *93*, 2693 – 2730; b) V. Kesavan, P. S. Sivanand, S. Chandrasekaran, Y. Koltypin, A. Gedanken, *Angew. Chem.* **1999**, *111*, 3729 – 3730; *Angew. Chem. Int. Ed.* **1999**, *38*, 3521 – 3523; c) Y. Okahata, H.-J. Lim, G.-I. Nakamuza, S. Hachiya, *J. Am. Chem. Soc.* **1983**, *105*, 4855 – 4859; d) Y. Okahata, K. Aziga, T. Seki, *J. Am. Chem. Soc.* **1988**, *110*, 2495 – 2500; e) R. Ahuja, P.-L. Caruso, D. Möbius, W. Paulus, H. Ringsdorf, G. Wildburg, *Angew. Chem.* **1993**, *105*, 1082; *Angew. Chem. Int. Ed. Engl.* **1993**, *32*, 1033 – 1036.

[15] A. P. Alivisatos, *Science* **1996**, *271*, 933 – 937.

[16] A. P. Alivisatos, K. P. Johnsson, X. Peng, T. E. Wilson, C. J. Loweth, M. P. Bruchez, Jr., P. G. Schultz, *Nature* **1996**, *382*, 609 – 611.

[17] a) X. Peng, T. E. Wilson, A. P. Alivisatos, P. G. Schultz, *Angew. Chem.* **1997**, *109*, 113 – 115; *Angew. Chem. Int. Ed. Engl.* **1997**, *36*, 145 – 147; b) L. C. Brousseau III, J. P. Novak, S. M. Marinakos, D. L. Feldheim, *Adv. Mater.* **1999**, *11*, 447 – 449.

[18] a) S. M. Marinakos, L. C. Brousseau III, A. Jones, D. C. Feldheim, *Chem. Mater.* **1998**, *10*, 1214 – 1219; b) G. Hornyak, M. Kröll, R. Pugin, T. Sawitowski, G. Schmid, J.-O. Bovin, G. Karsson, H. Hofmeister, S. Hopfe, *Chem. Eur. J.* **1997**, *3*, 1951 – 1956; c) S.-W. Chung, G. Markovich, J. R. Heath, *J. Phys. Chem. B* **1999**, *102*, 6685 – 6687; M. Sano, A. Kamino, S. Shinkai, *Langmuir* **1999**, *15*, 13 – 15.

[19] M. Antonietti, C. Göltner, *Angew. Chem.* **1997**, *109*, 944 – 964; *Angew. Chem. Int. Ed. Engl.* **1997**, *36*, 910 – 928.

[20] D. L. Feldheim, C. D. Keating, *Chem. Soc. Rev.* **1998**, *27*, 1 – 12.

[21] a) S. L. Westcott, S. J. Oldenburg, T. R. Lee, N. J. Halas, *Langmuir* **1998**, *14*, 5396 – 5401; b) T. Sato, H. Ahmed, *Appl. Phys. Lett.* **1997**, *70*, 2759 – 2761; c) L. Cusack, R. Rizza, A. Gorelov, D. Fitzmaurice, *Angew. Chem.* **1997**, *109*, 887 – 890; *Angew. Chem. Int. Ed. Engl.* **1997**, *36*, 848 – 851; d) R. L. Whetten, J. T. Khoury, M. M. Alvarez, S. Murthy, I. Vezmar, Z. L. Wang, P. W. Stephens, C. L. Cleveland, W. D. Luedke, U. Landman, *Adv. Mater.* **1996**, *8*, 428 – 433; e) A. Chemseddine, H. Jungblut, S. Boulmaaz, *J. Phys. Chem.* **1996**, *100*, 12 546 – 12 551; f) X. M. Lin, C. M. Sorensen, K. J. Klabunde, *Chem. Mater.* **1999**, *11*, 198 – 202; g) W. Shenton, S. A. Davis, S. Mann, *Adv. Mater.* **1999**, *11*, 449 – 452; h) Z. L. Wang, *Adv. Mater.* **1998**, *10*, 13 – 30; i) M. Li, H. Schnablegger, S. Mann, *Nature* **1999**, *402*, 393 – 395.

[22] R. C. Mucic, J. L. Storhoff, C. A. Mirkin, R. L. Letsinger, *J. Am. Chem. Soc.* **1998**, *120*, 12 674 – 12 675.

[23] D. L. Klein, R. Roth, A. K. L. Kim, A. P. Alivisatos, P. L. McEuen, *Nature* **1997**, *389*, 699 – 701.

[24] T. Sato, H. Ahmed, D. Brown, B. F. G. Johnson, *J. Appl. Phys.* **1997**, *82*, 696 – 701.

[25] R. S. Ingram, M. J. Hostetler, R. W. Murray, T. G. Schaaff, J. T. Khoury, R. L. Whetten, T. P. Bigioni, D. K. Guthrie, P. N. First, *J. Am. Chem. Soc.* **1997**, *119*, 9279 – 9280.

[26] T. Sato, H. Ahmed, *Appl. Phys. Lett.* **1997**, *70*, 2759 – 2761.

[27] H. Weller, *Angew. Chem.* **1998**, *110*, 1748 – 1750; *Angew. Chem. Int. Ed.* **1998**, *37*, 1658 – 1659.

[28] S. Yabuki, F. Mitzutani, *Electroanalysis* **1997**, *9*, 23 – 25.

[29] a) M. P. Pileni, *New J. Chem.* **1998**, 693 – 702; b) G. Schmid, L. F. Chi, *Adv. Mater.* **1998**, *10*, 515 – 526; c) C. R. Martin, *Science* **1994**, *266*, 1961 – 1966; d) J. H. Fendler, F. C. Meldrum, *Adv. Mater.* **1995**, *7*, 607 – 632.

[30] a) G. Schmid, *Chem. Rev.* **1992**, *92*, 1709 – 1727; b) N. Toshima, T. Yonezawa *New J. Chem.* **1998**, *11*, 1179 – 1201.

[31] D. A. Handley in *Colloidal Gold. Principles*, *Methods*, *and Applications*, *Vol. 1* (Ed.: M. A. Hayat), Academic Press, New York, **1989**, pp. 13 – 32.

[32] T. S. Ahmadi, Z. L. Wang, T. C. Green, A. Henglein, M. A. El-Sayed, *Science* **1996**, *272*, 1924 – 1925.

[33] J. Turkevich, P. C. Stevenson, J. Hiller, *Discuss. Faraday Soc.* **1951**, *11*, 55 – 75.

[34] C. Yee, M. Scotti, A. Ulman, H. White, M. Rafailovich, J. Sokolov, *Langmuir* **1999**, *15*, 4314 – 4316.

[35] T. Teranishi, M. Hosoe, T. Tanaka, M. Miyake, *J. Phys. Chem*. **1999**, *103*, 3818 – 3827.

[36] a) M. J. Hostetler, J. E. Wingate, C.-J. Zhong, J. E. Harris, R. W. Zashet, M. R. Clark, J. D. Londono, S. J. Green, J. J. Stokes, G. D. Wignall, G. L. Glish, M. D. Porter, N. D. Evans, R. W. Murray, *Langmuir* **1998**, *14*, 17 – 30; b) G. Frens, *Nat. Phys. Sci.* **1973**, *241*, 20 – 22.

[37] T. Cassagneau, J. H. Fendler, *J. Phys. Chem. B* **1999**, *103*, 1789 – 1793.

[38] a) R. M. Bright, M. D. Musick, M. J. Natan, *Langmuir* **1998**, *14*, 5695 – 5701; b) J. Turkevich, G. Kim, *Science* **1970**, *169*, 873 – 879; c) L. D. Rampino, F. F. Nord, *J. Am. Chem. Soc*. **1941**, *63*, 2745 – 2749.

[39] C. D. Keating, K. K. Kovaleski, M. J. Natan, *J. Phys. Chem. B* **1998**, *102*, 9404 – 9413.

[40] C. Roos, M. Schmidt, J. Ebenhoch, F. Baumann, B. Deubzer, J. Weis, *Adv. Mater.* **1999**, *11*, 761 – 766.

[41] R. H. Morriss, L. F. Collins, *J. Chem. Phys*. **1964**, *41*, 3357 – 3363.

[42] P. V. Kamat, B. J. Shanghavi, *J. Phys. Chem. B* **1997**, *101*, 7675 – 7679.

[43] R. M. Bright, D. G. Walter, M. D. Musick, M. A. Jackson, K. J. Allison, M. J. Natan, *Langmuir* **1996**, *12*, 810 – 817.

[44] K. R. Brown, M. J. Natan, *Langmuir* **1998**, *14*, 726 – 728.

[45] R. G. Freeman, M. B. Hommer, K. C. Grabar, M. A. Jackson, M. J. Natan, *J. Phys. Chem*. **1996**, *100*, 718 – 724.

[46] P. A. Buining, B. M. Humbel, A. P. Philipse, A. J. Verkleij, *Langmuir* **1997**, *13*, 3921 – 3926.

[47] a) S. R. Johnson, S. D. Evans, R. Brydson, *Langmuir* **1998**, *14*, 6639 – 6647; b) M. Brust, J. Fink, D. Bethell, D. J. Schiffrin, C. Kiely, *J. Chem. Soc. Chem. Commun*. **1995**, 1655 – 1666.

[48] M. Brust, M. Walker, D. Bethell, D. J. Schiffrin, R. Whyman, *J. Chem. Soc. Chem. Commun*. **1994**, 801 – 802.

[49] a) K. Esumi, A. Suzuki, N. Aihara, K. Usui, K. Torigoe, *Langmuir* **1998**, *14*, 3157 – 3159; b) M. E. Garcia, L. A. Baker, R. M. Crooks, *Anal. Chem.* **1999**, *71*, 256 – 258.

[50] T. Teranishi, I. Kiyokawa, M. Miyake, *Adv. Mater.* **1998**, *10*, 596 – 599.

[51] T. Teranishi, M. Hosoe, M. Miyake, *Adv. Mater.* **1997**, *9*, 65 – 67.

[52] W. P. Wuelfing, S. M. Gross, D. T. Miles, R. W. Murray, *J. Am. Chem. Soc.* **1998**, *120*, 12 696 – 12 697.

[53] J. P. Spatz, A. Roescher, M. Möller, *Adv. Mater.* **1996**, *8*, 337 – 340.

[54] S. Bharathi, O. Lev, *Chem. Commun*. **1997**, 2302 – 2304.

[55] L. A. Porter, Jr., D. Ji, S. L. Westcott, M. Graupe, R. S. Czernuszewicz, N. J. Halas, T. R. Lee, *Langmuir* **1998**, *14*, 7378 – 7386.

[56] N. Félidj, G. Lévi, J. Pantigny, J. Aubard, *New J. Chem*. **1998**, 725 – 732.

[57] S. G. Hickey, D. J. Riley, *J. Phys. Chem*. **1999**, *103*, 4599 – 4602.

[58] F. C. Meldrum, J. Flath, W. Knoll, *Langmuir* **1997**, *13*, 2033 – 2049.

[59] L. Spanhel, H. Weller, A. Fojtik, A. Henglein, *Ber. Bunsen-Ges. Phys. Chem*. **1987**, *91*, 88 – 94.

[60] E. Stathatos, P. Lianos, F. Del Monte, D. Levy, D. Tsiourvas, *Langmuir* **1997**, *13*, 4295 – 4300.

[61] R. Rizza, D. Fitzmaurice, S. Hearne, G. Hughes, G. Spoto, E. Ciliberto, H. Kerp, R. Schropp, *Chem. Mater.* **1997**, *9*, 2969 – 2982.

[62] a) M. L. Steigerwald, A. P. Alivisatos, J. M. Gibson, T. D. Harris, R. Kortan, A. J. Muller, A. M. Thayer, T. M. Duncan, D. C. Douglass, L. E. Brus, *J. Am. Chem. Soc*. **1988**, *110*, 3046 – 3050; b) P. Lianos, J. K. Thomas, *Chem. Phys. Lett*. **1986**, *125*, 299 – 302.

[63] M. Miyake, T. Torimoto, T. Sakata, H. Mori, H. Yoneyama, *Langmuir* **1999**, *15*, 1503 – 1507.

[64] M. Miyake, H. Matsumoto, M. Nishizawa, T. Sakata, H. Mori, S. Kuwabata, H. Yoneyama, *Langmuir* **1997**, *13*, 742 – 746.

[65] N. A. Kotov, I. Dékány, J. H. Fendler, *J. Phys. Chem*. **1995**, *99*, 13 065 – 13 069.

[66] X. Li, J. R. Fryer, D. J. Cole-Hamilton, *J. Chem. Soc. Chem. Commun*. **1994**, 1715 – 1716.

[67] C. B. Murray, D. J. Norris, M. G. Bawendi, *J. Am. Chem. Soc*. **1993**, *115*, 8706 – 8715.

[68] Y. Xie, Y. Qian, W. Wang, S. Zhang, Y. Zhang, *Science* **1996**, *272*, 1926 – 1927.

[69] S. D. Burnside, V. Shklover, C. Barbé, P. Comte, F. Arendse, K. Brooks, M. Grätzel, *Chem. Mater.* **1998**, *10*, 2419 – 2425.

[70] R. P. Andres, J. D. Bielefeld, J. I. Henderson, D. B. Janes, V. R. Kolagunta, C. P. Kubiak, W. J. Mahoney, R. G. Osifchin, *Science* **1996**, *273*, 1690 – 1693.

[71] G. Chumanov, K. Sokolov, B. W. Gregory, T. M. Cotton, *J. Phys. Chem.* **1995**, *99*, 9466 – 9471.

[72] J. Nedderson, G. Chumanov, T. M. Cotton, *Appl. Spectrosc.* **1993**, *47*, 1959 – 1964.

[73] T. R. Jensen, G. C. Schatz, R. P. Van Duyne, *J. Phys. Chem. B* **1999**, *103*, 2394 – 2401.

[74] J. C. Hulteen, D. A. Treichel, M. T. Smith, M. L. Duval, T. R. Jensen, R. P. Van Duyne, *J. Phys. Chem. B* **1999**, *103*, 3854 – 3863.

[75] a) D.-L. Lu, K. Tanaka, *J. Phys. Chem.* **1996**, *100*, 1833 – 1837; b) S. E. Gilbert, O. Cavalleri, K. Kern, *J. Phys. Chem.* **1996**, *100*, 12 123 – 12 130.

[76] R. S. Urquhart, D. N. Furlong, T. Gengenbach, N. J. Geddes, F. Grieser, *Langmuir* **1995**, *11*, 1127 – 1133.

[77] a) G. Sberveglieri, L. E. Depero, M. Ferroni, V. Guidi, G. Martinelli, P. Nelli, C. Perego, L. Sangaletti, *Adv. Mater.* **1996**, *8*, 334 – 337; b) H. Xiong, M. Cheng, Z. Zhou, J. Shen, *Adv. Mater.* **1998**, *10*, 529 – 532.

[78] M. T. Reetz, M. Winter, *J. Am. Chem. Soc.* **1997**, *119*, 4539 – 4540.

[79] M. Nagtegaal, R. Seshadri, W. Tremel, *Chem. Commun*. **1998**, 2139 – 2140.

[80] J. R. Heath, R. S. Williams, J. J. Shiang, S. J. Wind, J. Chu, C. D'Emic, W. Chen, C. L. Stanis, J. J. Bucchignano, *J. Phys. Chem.* **1996**, *100*, 3144 – 3149.

[81] a) H. Yanagi, T. Ohno, *Langmuir* **1999**, *15*, 4773 – 4776; b) Y. Plyuto, J.-M. Berquier, C. Jacqinod, C. Ricolleau, *Chem. Commun.* **1999**, 1653 – 1654; c) H. Kind, A. M. Bittner, O. Cavalleri, K. Kern, *J. Phys. Chem. B* **1998**, *102*, 7582 – 7589.

[82] I. Moriguchi, F. Shibata, Y. Teraoka, S. Kagawa, *Chem. Lett.* **1995**, 761 – 762.

[83] K. C. Grabar, R. G. Freeman, M. B. Hommer, M. J. Natan, *Anal. Chem*. **1995**, *67*, 735 – 743.

[84] a) F. Burmeister, C. Schäfle, B. Keilhofer, C. Bechinger, J. Boneberg, P. Liederer, *Adv. Mater.* **1998**, *10*, 495 – 497; b) F. Burmeister, W. Badowsky, T. Braun, S. Wieprich, J. Boneberg, P. Liederer, *Appl. Surf. Sci.* **1999**, *144 – 145*, 461 – 466.

[85] F. Burmeister, C. Schäfle, T. Matthes, M. Böhmisch, J. Boneberg, P. Leiderer, *Langmuir* **1997**, *13*, 2983 – 2987.

[86] F. Remacle, C. P. Collier, G. Markovich, J. R. Heath, U. Banin, R. D. Levine, *J. Phys. Chem. B* **1998**, *102*, 7727 – 7734.

[87] T. Sato, D. Brown, B. F. G. Johnson, *Chem. Commun*. **1997**, 1007 – 1008.

[88] A. Doron, E. Katz, I. Willner, *Langmuir* **1995**, *11*, 1313 – 1317.

[89] K. C. Grabar, K. J. Allison, B. E. Baker, R. M. Bright, K. R. Brown, R. G. Freeman, A. P. Fox, C. D. Keating, M. D. Musick, M. J. Natan, *Langmuir* **1996**, *12*, 2353 – 2361.

[90] R. G. Freeman, K. C. Grabar, K. J. Allison, R. M. Bright, J. A. Davis, A. P. Guthrie, M. B. Hommer, M. A. Jackson, P. C. Smith, D. G. Walter, M. J. Natan, *Science* **1995**, *267*, 1629 – 1632.

[91] W. J. Albery, A. J. Hillman, *Annu. Rep. Prog. Chem. Sect. C* **1981**, *78*, 377 – 437.

[92] R. W. Murray in *Electroanalytical Chemistry, Vol. 13* (Ed.: A. J. Bard), Marcel Dekker, New York, **1984**, pp. 191 – 368.

[93] J. Schmitt, P. Mächtle, D. Eck, H. Möhwald, C. A. Helm, *Langmuir* **1999**, *15*, 3256 – 3266.

[94] R. A. Hayes, M. R. Böhmer, L. G. J. Fokkink, *Langmuir* **1999**, *15*, 2865 – 2870.

[95] M. Brust, R. Etchenique, E. J. Calvo, G. J. Gordillo, *Chem. Commun*. **1996**, 1949 – 1950.

[96] T. Yonezawa, S. Onoue, T. Kunitake, *Adv. Mater.* **1998**, *10*, 414 – 416.

[97] K. C. Grabar, P. C. Smith, M. D. Musick, J. A. Davis, D. G. Walter, M. A. Jackson, A. P. Guthrie, M. J. Natan, *J. Am. Chem. Soc*. **1996**, *118*, 1148 – 1153.

[98] a) H. O. Finklea in *Electroanalytical Chemistry, Vol. 19* (Eds.: A. J. Bard, I. Rubinstein), Marcel Dekker, New York, **1996**, pp. 109 – 335; b) J. Xu, H.-L. Li, *J. Colloid Interface Sci*. **1995**, *176*, 138 – 149.

[99] K. V. Sarathy, P. J. Thomas, G. U. Kulkarni, C. N. R. Rao, *J. Phys. Chem. B* **1999**, *103*, 399 – 401.

[100] T. Zhu, X. Zhang, J. Wang, X. Fu, Z. Liu, *Thin Solid Films* **1998**, *327 – 329*, 595 – 598.

[101] K. Bandyopadhyay, V. Patil, K. Vijayamohanan, M. Sastry, *Langmuir* **1997**, *13*, 5244 – 5248.

[102] V. L. Colvin, A. N. Goldstein, A. P. Alivisatos, *J. Am. Chem. Soc*. **1992**, *114*, 5221 – 5230.

[103] a) M. Giersig, P. Mulvaney, *Langmuir* **1993**, *9*, 3408 – 3413; b) M. Giersig, P. Mulvaney, *J. Phys. Chem*. **1993**, *97*, 6334 – 6336.

[104] A. C.Templeton, D. E. Cliffel, R. W. Murray, *J. Am. Chem. Soc*. **1999**, *121*, 7081 – 7089.

[105] a) A. Milchev, E. Vassileva, V. Kertov, *J. Electroanal. Chem.* **1980**, *107*, 323 – 336; b) A. Milchev, E. Vassileva, V. Kertov, *J. Electroanal. Chem*. **1980**, *107*, 337 – 352; c) G. Gunawardena, G. Hills, I. Montenegro, B. Scharifker, *J. Electroanal. Chem.* **1982**, *138*, 225 – 239; d) G. Gunawardena, G. Hills, I. Montenegro, *J. Electroanal. Chem*. **1982**, *138*, 241 – 254; e) G. Gunawardena, D. Pletcher, A. Razaq, *J. Electroanal. Chem*. **1984**, *164*, 363 – 367; f) G. Gunawardena, G. Hills, I. Montenegro, *J. Electroanal. Chem*. **1985**, *184*, 357 – 369; g) G. Gunawardena, G. Hills, I. Montenegro, *J. Electroanal. Chem*. **1985**, *184*, 371 – 389; h) K. Shimazu, D. Weisshaar, T. Kuwana, *J. Electroanal. Chem*. **1987**, *223*, 223 – 234; i) K. Shimazu, K. Uosaki, H. Kita, Y. Nodasaka, *J. Electroanal. Chem*. **1988**, *256*, 481 – 487; j) N. Georgolios, D. Jannakoudakis, P. Karabinas, *J. Electroanal. Chem*. **1989**, *264*, 235 – 245; k) J. V. Zoval, P. R. Biernacki, R. M. Penner, *Anal. Chem*. **1996**, *68*, 1585 – 1592; l) J. V. Zoval, R. M. Stiger, P. R. Biernacki, R. M. Penner, *J. Phys. Chem*. **1996**, *100*, 837 – 844; m) J. V. Zoval, J. Lee, S. Gorer, R. M. Penner, *J. Phys. Chem. B* **1998**, *102*, 1166 – 1175; n) Z. Chen, J. Li, E. Wang, *J. Electroanal. Chem*. **1994**, *373*, 83 – 87; o) B. U. Yoon, K. Cho, H. Kim, *Anal. Sci*. **1996**, *12*, 321 – 326.

[106] M. O. Finot, G. D. Braybrook, M. T. McDermott, *J. Electroanal. Chem*. **1999**, *466*, 234 – 241.

[107] a) S. Gorer, G. S. Hsiao, M. G. Anderson, R. M. Stiger, J. Lee, R. M. Penner, *Electrochim. Acta* **1998**, *43*, 2799 – 2809; b) S. Gorer, J. C. Ganske, J. C. Hemminger, R. M. Penner, *J. Am. Chem. Soc*. **1998**, *120*, 9584 – 9593; c) M. A. Anderson, S. Gorer, R. M. Penner, *J. Phys. Chem. B* **1997**, *101*, 5895 – 5899.

[108] a) G. S. Hsiao, M. G. Anderson, S. Gorer, D. Harris, R. M. Penner, *J. Am. Chem. Soc*. **1997**, *119*, 1439 – 1448; b) R. M. Nyffenegger, B. Craft, M. Shaaban, S. Gorer, R. M. Penner, *Chem. Mater*. **1998**, *10*, 1120 – 1129.

[109] S. Gorer, R. M. Penner, *J. Phys. Chem. B* **1999**, *103*, 5750 – 5753.

[110] S. Peschel, G. Schmid, *Angew. Chem.* **1995**, *107*, 1568 – 1569; *Angew. Chem. Int. Ed. Engl*. **1995**, *34*, 1442 – 1443.

[111] J. Schmitt, G. Decher, W. J. Dressick, S. L. Brandow, R. E. Geer, R. Shashidhar, J. M. Calvert, *Adv. Mater.* **1997**, *9*, 61 – 65.

[112] M. A. Correa-Duarte, M. Giersig, N. A. Kotov, L. M. Liz-Marzán, *Langmuir* **1998**, *14*, 6430 – 6435.

[113] K. Ariga, Y. Lvov, M. Onda, I. Ichinose, T. Kunitake, *Chem. Lett*. **1997**, 125 – 126.

[114] a) Y. Hotta, K. Inukai, M. Taniguchi, A. Yamagishi, *Chem. Lett.* **1997**, 83 – 84; b) G. S. Ferguson, E. R. Kleinfeld, *Adv. Mater.* **1995**, *7*, 414 – 416.

[115] A. R. Hillman in *Electrochemical Science and Technology of Polymers, Vol. 1*, (Ed.: R. G. Linford), Elsevier, New York, **1987**, pp. 103 – 239.

[116] S. Rubin, G. Bar, T. N. Taylor, R. W. Cutts, T. A. Zawodzinski, Jr., *J. Vac. Sci. Technol. A* **1996**, *14*, 1870 – 1877.

[117] G. Bar, S. Rubin, R. W. Cutts, T. N. Taylor, T. A. Zawodzinski, *Langmuir* **1996**, *12*, 1172 – 1179.

[118] M. Gao, X. Zhang, B. Yang, J. Shen, *J. Chem. Soc. Chem. Commun*. **1994**, 2229 – 2230.

[119] K. S. Mayya, M. Sastry, *Langmuir* **1999**, *15*, 1902 – 1904.

[120] a) M. Sastry, K. S. Mayya, V. Patil, D. V. Paranjape, S. G. Hegde, *J. Phys. Chem. B* **1997**, *101*, 4954 – 4958; b) V. Patil, M. Sastry, *Langmuir* **1998**, *14*, 2707 – 2711.

[121] T. Torimoto, N. Tsumura, M. Miyake, M. Nishizawa, T. Sakata, H. Mori, H. Yoneyama, *Langmuir* **1999**, *15*, 1853 – 1858.

[122] a) M. Sastry, K. S. Mayya, V. Patil, *Langmuir* **1998**, *14*, 5921 – 5928; b) Y. Tian, J. H. Fendler, *Chem. Mater.* **1996**, *8*, 969 – 974.

[123] J. H. Fendler, *Chem. Mater.* **1996**, *8*, 1616 – 1624.

[124] S. Drouard, S. G. Hickey, D. J. Riley, *Chem. Commun*. **1999**, 67 – 68.

[125] C. D. Keating, K. K. Kovaleski, M. J. Natan, *J. Phys. Chem. B* **1998**, *102*, 9414 – 9425.

[126] D. Lawless, S. Kapoor, D. Meisel, *J. Phys. Chem. B* **1995**, *99*, 10 329 – 10 335.

[127] H. Takei, N. Shimizu, *Langmuir* **1997**, *13*, 1865 – 1868.

[128] a) M. Sastry, N. Lala, V. Patil, S. P. Chavan, A. G. Chittiboyina, *Langmuir* **1998**, *14*, 4138 – 4142; b) M. Li, K. K. W. Wong, S. Mann, *Chem. Mater.* **1999**, *11*, 23 – 26.

[129] a) R. Elghanian, J. J. Storhoff, R. C. Mucic, R. L. Letsinger, C. A. Mirkin, *Science* **1997**, *277*, 1078 – 1081; b) J. J. Storhoff, R. Elghanian, R. C. Mucic, C. A. Mirkin, R. L. Letsinger, *J. Am. Chem. Soc*. **1998**, *120*, 1959 – 1964; c) C. A. Mirkin, R. L. Letsinger, R. C. Mucic, J. J. Storhoff, *Nature* **1996**, *382*, 607 – 609.

[130] a) J. J. Storhoff, C. A. Mirkin, *Chem. Rev.* **1999**, *99*, 1849 – 1862; b) G. P. Mitchell, C. A. Mirkin, R. L. Letsinger, *J. Am. Chem. Soc.* **1999**, *121*, 8122 – 8123.

[131] D. L. Feldheim, K. C. Grabar, M. J. Natan, T. E. Mallouk, *J. Am. Chem. Soc.* **1996**, *118*, 7640 – 7641.

[132] T. Hatakeyama, K. Murakami, Y. Miyamoto, N. Yamasaki, *Anal. Biochem*. **1996**, *237*, 188 – 192.

[133] J. Liu, S. Mendoza, E. Román, M. J. Lynn, R. Xu, A. F. Kaifer, *J. Am. Chem. Soc*. **1999**, *121*, 4304 – 4305.

[134] a) L. Motte, F. Billoudet, E. Lacaze, J. Douin, M. P. Pileni, *J. Phys. Chem. B* **1997**, *101*, 138 – 144; b) M. T. Reetz, M. Winter, B. Tesch, *Chem. Commun*. **1997**, 147 – 148.

[135] a) C. B. Murray, C. R. Kagan, M. G. Bawendi, *Science* **1995**, *270*, 1335 – 1338; b) G. Schmid, M. Bäumle, N. Beyer, *Angew. Chem.* **2000**, *112*, 177 – 179; *Angew. Chem. Int. Ed.* **2000**, *39*, 181 – 183.

[136] P. V. Braun, P. Osenar, S. I. Stupp, *Nature* **1996**, *380*, 325 – 328.

[137] W. Shenton, D. Pum, U. B. Sleytr, *Nature* **1997**, *389*, 585 – 587.

[138] R. Blonder, L. Sheeney, I. Willner, *Chem. Commun.* **1998**, 1393 – 1394.

[139] M. Lahav, A. N. Shipway, I. Willner, M. Nielsen, J. F. Stoddart, *J. Electroanal. Chem.,* **2000**, *482*, 217 – 221.

[140] a) N. I. Kotyukhova, P. J. Ollivier, B. R. Martin, T. E. Mallouk, S. A. Chizhik, E. V. Buzaneva, A. D. Gorchinskiy, *Chem. Mater.* **1999**, *11*, 771 – 778; b) S. Pethkar, R. C. Patil, J. A. Kher, K. Vijayamohanan, *Thin Solid Films* **1999**, *349*, 105 – 109.

[141] T. Yonezawa, H. Matsune, T. Kunitake, *Chem. Mater.* **1999**, *11*, 33 – 35.

[142] Y. M. Lvov, J. F. Rusling, D. T. Thomsen, F. Papadimitrakopoulos, T. Kawakami, T. Kunitake, *Chem. Commun.* **1998**, 1229 – 1230.

[143] J. Tien, A. Terfort, G. M. Whitesides, *Langmuir* **1997**, *13*, 5349 – 5355.

[144] M. D. Musick, D. J. Peña, S. L. Botsko, T. M. McEvoy, J. N. Richardson, M. J. Natan, *Langmuir* **1999**, *15*, 844 – 850.

[145] a) E. Hao, B. Yang, J. Zhang, X. Zhang, J. Sun, J. Shen, *J. Mater. Chem*. **1998**, 1327 – 1328; b) R. Iler, *J. Colloid. Interface Sci*. **1996**, *21*, 569 – 594.

[146] M. Brust, C. J. Kiely, D. Bethell, D. J. Schiffrin, *J. Am. Chem. Soc.* **1998**, *120*, 12 367 – 12 368.

[147] A. N. Shipway, M. Lahav, R. Blonder, I. Willner, *Chem. Mater.* **1999**, *11*, 13 – 15.

[148] M. Lahav, T. Gabriel, A. N. Shipway, I. Willner, *J. Am. Chem. Soc.* **1999**, *121*, 258 – 259.

[149] M. Lahav, R. Gabai, A. N. Shipway, I. Willner, *Chem. Commun.* **1999**, 1937 – 1938.

[150] M. Lahav, A. N. Shipway, I. Willner, *J. Chem. Soc. Perkin Trans. 2* **1999**, 1925 – 1931.

[151] A. N. Shipway, M. Lahav, R. Gabai, I. Willner, *Langmuir*, in press.

[152] M. D. Musick, C. D. Keating, M. H. Keefe, M. J. Natan, *Chem. Mater.* **1997**, *9*, 1499 – 1501.

[153] T. Baum, D. Bethell, M. Brust, D. J. Schiffrin, *Langmuir* **1999**, *15*, 866 – 871.

[154] M. Brust, D. Bethell, C. J. Kiely, D. J. Schiffrin, *Langmuir* **1998**, *14*, 5425 – 5429.

[155] F. P. Zamborini, R. M. Crooks, *J. Am. Chem. Soc.* **1998**, *120*, 9700 – 9701.

[156] a) R. Resch, C. Baur, A. Bugacov, B. E. Koel, A. Madhukar, A. A. G. Requicha, P. Will, *Langmuir* **1998**, *14*, 6613 – 6616; b) S. L. Brandow, W. J. Dressick, C. S. Dulcey, T. S. Koloski, L. M. Shirey, J. Schmidt, J. M. Calvert, *J. Vac. Sci. Technol. B* **1997**, *15*, 1818 – 1824.

[157] A. Doron, E. Joselevich, A. Schlittner, I. Willner, *Thin Solid Films* **1999**, *340*, 183 – 188.

[158] B. E. Baker, N. J. Kline, P. J. Treado, M. J. Natan, *J. Am. Chem. Soc.* **1996**, *118*, 8721 – 8722.

[159] T. Sato, D. G. Hasko, H. Ahmed, *J. Vac. Sci. Technol. B* **1997**, *15*, 45 – 48.

[160] a) J.-F. Liu, L.-G. Zhang, P.-S. Mao, D.-Y. Chen, N. Gu, J.-Y. Ren, Y.-P. Wu, Z.-H. Lu, *Chem. Lett*. **1997**, 1147 – 1148; b) J.-F. Liu, L.-G. Zhang, J.-Y. Ren, Y.-P. Wu, Z.-H. Lu, P.-S. Mao, D.-Y. Chen, *Thin Solid Films* **1998**, *327 – 329*, 176 – 179.

[161] T. Vossmeyer, E. Delonno, J. R. Heath, *Angew. Chem.* **1997**, *109*, 1123 – 1125; *Angew. Chem. Int. Ed. Engl*. **1997**, *36*, 1080 – 1083.

[162] a) W. J. Dressick, C. S. Dulcey, S. L. Brandow, H. Witschi, P. F. Neeley, *J. Vac. Sci. Technol. A* **1999**, *17*, 1432 – 1440; b) S. L. Brandow, M.-S. Chen, R.

Aggarwal, C. S. Dulcey, J. M. Calvert, W. J. Dressick, *Langmuir* **1999**, *15*, 5429 – 5432.

[163] P. C. Hidber, W. Helbig, E. Kim, G. M. Whitesides, *Langmuir* **1996**, *12*, 1375 – 1380.

[164] S. Palacin, P. C. Hildber, J.-P. Bourgoin, C. Miramond, C. Fermon, G. M. Whitesides, *Chem. Mater.* **1996**, *8*, 1316 – 1325.

[165] J. L. Coffer, S. R. Bigham, R. F. Pinizzotto, H. Yang, *Nanotechnology* **1992**, *3*, 69 – 76.

[166] S. R. Bigham, J. L. Coffer, *Colloid Surf. A* **1995**, *95*, 211 – 219.

[167] J. L. Coffer, S. R. Bigham, X. Li, R. F. Pinizzotto, Y. G. Rho, R. M. Pirtle, I. L. Pirtle, *Appl. Phys. Lett.* **1996**, *69*, 3851 – 3853.

[168] J. L. Coffer, *J. Cluster Sci.* **1997**, *8*, 159 – 179.

[169] E. Braun, Y. Eichen, U. Sivan, G. Ben-Yoseph, *Nature* **1998**, *391*, 775 – 778.

[170] K. C. Grabar, K. R. Brown, C. D. Keating, S. J. Stranick, S.-L. Tang, M. J. Natan, *Anal. Chem.* **1997**, *69*, 471 – 477.

[171] G. Schmid, S. Peschel, *New J. Chem.* **1998**, 669 – 675.

[172] G. S. McCarty, P. S. Weiss, *Chem. Rev.* **1999**, *99*, 1983 – 1990.

[173] a) S. Norman, T. Andersson, C. G. Granqvist, O. Hunderi, *Phys. Rev. B* **1978**, *18*, 674 – 695; b) R. H. Dormeus, *J. Appl. Phys.* **1996**, *37*, 2775 – 2781.

[174] M. Quinten, U. Kreibig, *Surf. Sci.* **1986**, *172*, 557 – 577.

[175] S. Link, M. A. El-Sayed, *J. Phys. Chem. B* **1999**, *103*, 4212 – 4217.

[176] N. G. Khlebtsov, V. A. Bogatyrev, L. A. Dyknman, A. G. Melnikov, *J. Colloid Interface Sci.* **1996**, *180*, 436 – 445.

[177] C. P. Collier, R. J. Saykally, J. J. Shiang, S. E. Henrichs, J. R. Heath, *Science* **1997**, *277*, 1978 – 1981.

[178] C. S. Weisbecker, M. V. Merritt, G. M. Whitesides, *Langmuir* **1996**, *12*, 3763 – 3772.

[179] G. Chumanov, K. Sokolov, T. M. Cotton, *J. Phys. Chem.* **1996**, *100*, 5166 – 5168.

[180] J. J. Shiang, J. R. Heath, C. P. Collier, R. J. Saykally, *J. Phys. Chem. B* **1998**, *102*, 3425 – 3430.

[181] K. C. Grabar, K. J. Allison, B. E. Baker, R. M. Bright, K. R. Brown, R. G. Freeman, A. P. Fox, C. D. Keating, M. D. Musick, M. J. Natan, *Langmuir* **1996**, *12*, 2353 – 3261.

[182] C. G. Blatchford, J. R. Campbell, J. A. Creighton, *Surf. Sci.* **1982**, *120*, 435 – 455.

[183] L. A. Lyon, D. J. Peña, M. Natan, *J. Phys. Chem. B* **1999**, *103*, 5826 – 5831.

[184] a) R. Woods in *Electroanalytical Chemistry, Vol. 9* (Ed.: A. J. Bard), Marcel Dekker, New York, **1976**, pp. 1 – 162; b) D. A. J. Rand, R. Woods, *J. Electroanal. Chem.* **1971**, *31*, 29 – 38.

[185] B. E. Conway, *Prog. Surf. Sci.* **1995**, *49*, 331 – 452.

[186] M. O. Finot, G. D. Braybrook, M. T. McDermott, *J. Electroanal. Chem.* **1999**, *466*, 234 – 241.

[187] V. P. Menon, C. R. Martin, *Anal. Chem.* **1995**, *67*, 1920 – 1928.

[188] X.-Y. Hu, Y. Xiao, H.-Y. Chen, *J. Electroanal. Chem.* **1999**, *466*, 26 – 30.

[189] D. L. Gittins, D. Bethell, R. J. Nichols, D. J. Schiffrin, *Adv. Mater.* **1999**, *11*, 737 – 740.

[190] D. Bethell, M. Brust, D. J. Schiffrin, C. Kiely, *J. Electroanal. Chem.* **1996**, *409*, 137 – 143.

[191] M. Brust, D. Bethell, D. J. Schiffrin, C. J. Kiely, *Adv. Mater.* **1995**, *7*, 795 – 797.

[192] Y. J. Liu, Y. X. Wang, R. O. Claus, *Chem. Phys. Lett.* **1998**, *298*, 315 – 319.

[193] J.-C. Bradley, H.-M. Chen, J. Crawford, J. Eckert, K. Ernazarova, T. Kurzeja, M. Lin, M. McGee, W. Nadler, S. G. Stephens, *Nature* **1997**, *389*, 268 – 271.

[194] G. Markovich, C. P. Collier, J. R. Heath, *Phys. Rev. Lett.* **1998**, *80*, 3807 – 3810.

[195] C. P. Collier, R. J. Saykally, J. J. Shiang, S. E. Henrichs, J. R. Heath, *Science* **1997**, *277*, 1978 – 1981.

[196] W. J. Albery, N. Bartlett, *J. Electrochem. Soc.* **1984**, *131*, 315 – 325.

[197] P. E. Lippens, M. Lannoo, *Phys. Rev. B* **1989**, *39*, 10 935 – 10 942.

[198] S. Ogawa, F.-R. F. Fan, A. J. Bard, *J. Phys. Chem.* **1995**, *99*, 11 182 – 11 189.

[199] B. Alperson, H. Demange, I. Rubinstein, G. Hodes, *J. Phys. Chem. B* **1999**, *103*, 4943 – 4948.

[200] Y. Nosaka, *J. Phys. Chem.* **1991**, *95*, 5054 – 5058.

[201] T. Serizawa, H. Takeshita, M. Akashi, *Chem. Lett.* **1998**, 487 – 488.

[202] H. Schmitt, A. Badia, L. Dickinson, L. Reven, R. B. Lennox, *Adv. Mater.* **1998**, *10*, 475 – 479.

[203] C. Demaille, M. Brust, M. Tsionsky, A. J. Bard, *Anal. Chem.* **1997**, *69*, 2323 – 2328.

[204] M. S. Sibbald, G. Chumanov, T. M. Cotton, *J. Electroanal. Chem.* **1997**, *438*, 179 – 185.

[205] a) J. M. Weissman, H. B. Sunkara, A. S. Tse, *Science* **1996**, *274*, 959 – 960; b) J. H. Holtz, S. A. Asher, *Nature* **1997**, *389*, 829 – 832.

[206] a) F. Patolsky, B. Filanovsky, E. Katz, I. Willner, *J. Phys. Chem. B* **1998**, *102*, 10 359 – 10 367; b) A. Bardea, F. Patolsky, A. Dagan, I. Willner, *Chem. Commun.* **1999**, 21 – 22.

[207] L. Alfonta, A. Bardea, O. Khersonsky, E. Katz, I. Willner, *Biosens. Bioelectron.*, in press.

[208] A. Bardea, A. Dagan, I. Willner, *Anal. Chim. Acta* **1999**, *385*, 33 – 43.

[209] R. Blonder, S. Levi, G. Tao, I. Ben-Dov, I. Willner, *J. Am. Chem. Soc.* **1997**, *119*, 10 467 – 10 478.

[210] a) I. Willner, S. Rubin, Y. Cohen, *J. Am. Chem. Soc.* **1993**, *115*, 4937 – 4938; b) P. Skládal, *Electroanalysis* **1997**, *9*, 737 – 745.

[211] a) A. Bardea, A. Dagan, I. Ben-Dov, A. Amit, I. Willner, *Chem. Commun.* **1998**, 839 – 840; b) A. L. Ghindilis, P. Atanasov, M. Wilkins, E. Wilkins, *Biosens. Bioelectron.* **1998**, *13*, 113 – 131.

[212] D. D. Schlereth, *J. Electroanal. Chem.* **1999**, *464*, 198 – 207.

[213] W. Göpel, P. Heiduschka, *Biosens. Bioelectron.* **1995**, *10*, 853 – 883.

[214] a) E. Kaganer, R. Pogreb, D. Davidov, I. Willner, *Langmuir* **1999**, *15*, 3920 – 3923; b) B. Liedberg, C. Nylander, I. Lundström, *Biosens. Bioelectron.* **1995**, *10*, i – ix.

[215] L. A. Lyon, M. D. Musick, M. J. Natan, *Anal. Chem.* **1998**, *70*, 5177 – 5183.

[216] a) A. Campion, P. Kambhampati, *Chem. Soc. Rev.* **1998**, *27*, 241 – 250; b) M. Moskovits, *Rev. Mod. Phys.* **1985**, *57*, 783 – 826.

[217] J. A. Creighton, C. G. Blatchford, M. G. Albrecht, *J. Chem. Soc. Faraday Trans. 2* **1979**, *75*, 790 – 798.

[218] J. C. Jones, C. McLaughlin, D. Littlejohn, D. A. Sadler, D. Graham, W. E. Smith, *Anal. Chem.* **1999**, *71*, 596 – 601.

[219] D. P. Tsai, J. Kovacs, Z. Wang, M. Moskovits, V. M. Shalaev, J. S. Suh, R. Botet, *Phys. Rev. Lett.* **1994**, *72*, 4149 – 4152.

[220] S. Nie, S. R. Emory, *Science* **1997**, *275*, 1102 – 1106.

[221] K. R. Brown, A. P. Fox, M. J. Natan, *J. Am. Chem. Soc.* **1996**, *118*, 1154 – 1157.

[222] a) F. A. Armstrong, H. A. O. Hill, N. J. Walton, *Q. Rev. Biophys.* **1986**, *18*, 261 – 322; b) F. A. Armstrong, H. A. O. Hill, N. J. Walton, *Acc. Chem. Res.* **1988**, *21*, 407 – 413.

[223] E. J. Laviron, *Electroanal. Chem.* **1979**, *101*, 19 – 28.

[224] J. Liu, R. Xu, A. E. Kaifer, *Langmuir* **1998**, *14*, 7337 – 7339.

[225] R. S. Ingram, R. W. Murray, *Langmuir* **1998**, *14*, 4115 – 4121.

[226] U. Simon, R. Flesch, H. Wiggers, G. Schön, G. Schmid, *J. Mater. Chem.* **1998**, *8*, 517 – 518.

[227] a) U. Simon, G. Schön, G. Schmid, *Angew. Chem. Int. Ed. Engl.* **1993**, *32*, 250 – 254; *Angew. Chem.* **1993**, *105*, 264; b) G. Schmid in *Clusters and Colloids. From Theory to Applications*, (Ed.: G. Schmid), VCH, Weinheim, **1994**, pp. 178 – 211.

[228] D. L. Klein, P. L. McEuen, J. E. Bowen Katari, R. Roth, A. P. Alivisatos, *Appl. Phys. Lett.* **1996**, *68*, 2574 – 2576.

[229] R. P. Andres, T. Bein, M. Dorogi, S. Feng, J. I. Henderson, C. P. Kubiak, W. Mahoney, R. G. Osifchin, R. Reifenberger, *Science* **1996**, *272*, 1323 – 1325.

[230] a) S. J. Green, J. J. Stokes, M. J. Hostetler, J. Pietron, R. W. Murray, *J. Phys. Chem. B* **1997**, *101*, 2663 – 2668; b) B. Sweryda-Krawiec, T. Cassagneau, J. H. Fendler, *Adv. Mater.* **1999**, *11*, 659 – 664.

[231] L. F. Chi, M. Hartig, T. Drechsler, T. Schaak, C. Seidel, H. Fuchs, G. Schmid, *Appl. Phys. Lett.* **1998**, *66*, S187-S190.

[232] U. Simon, *Adv. Mater.* **1998**, *10*, 1487 – 1492.

[233] a) J. R. Tucker, *J. Appl. Phys.* **1992**, *71*, 4399 – 4404; b) A. N. Korotkov, R. H. Chen, K. Likharev, *J. Appl. Phys.* **1995**, *78*, 2520 – 2530.

[234] J. B. Barner, S. T. Ruggerio, *Phys. Rev. Lett.* **1987**, *59*, 807 – 810.

[235] K. K. Likharev, T. Claeson, *Sci. Am.* **1992**, *266*(6), 50 – 55.

[236] R. F. Service, *Science* **1997**, *275*, 303 – 304.

[237] E. Corcoran, *Sci. Am.* **1990**, *263*(11), 74 – 83.

[238] L. C. Brousseau III, Q. Zhao, D. A. Shultz, D. L. Feldheim, *J. Am. Chem. Soc.* **1998**, *120*, 7645 – 7646.

[239] L. Guo, G. Lingjie, E. Leobandung, S. Y. Chou, *Science* **1997**, *275*, 649 – 651.

[240] S. Tiwari, F. Rana, H. Hanafi, A. Hartstein, E. F. Crabbe, K. Chan, *Appl. Phys. Lett.* **1996**, *68*, 1377 – 1379.

[241] a) M. S. Montemerlo, J. C. Love, G. J. Opiteck, D. Goldhaber-Gordon, J. C. Ellenbogen, *Technologies and Designs for Electronic Nanocomputers*, Mitre Corp., McLean, VA (USA), **1996**; b) A. O. Orlov, I. Amlani, G. H. Berstein, C. S. Lent, G. L. Snider, *Science* **1997**, *277*, 928 – 930.

[242] H. Wohltjen, A. W. Snow, *Anal. Chem.* **1998**, *70*, 2856 – 2859.

[243] T. E. Young, B. W. Babbit, *J. Org. Chem.* **1983**, *48*, 562 – 566.

[244] a) A. B. Kharitonov, A. N. Shipway, I. Willner, *Anal. Chem.* **1999**, *71*, 5441 – 5443; b) A. B. Kharitonov, A. N. Shipway, E. Katz, I. Willner, *Rev. Anal. Chem.* **1999**, *18*, 255 – 260.

[245] H. Tsukube, H. Furuta, A. Odani, Y. Takeda, Y. Kudo, Y. Inoue, Y. Liu, H. Sakamoto, K. Kimura in *Comprehensive Supramolecular Chemistry, Vol. 8* (Eds.: J.-M. Lehn, J. L. Atwood, J. E. D. Davies, D. D. MacNicol, F. Vögtle), Pergamon Press, Oxford, **1996**, pp. 425 – 482.

[246] J. Zhao, R. W. Henkens, J. Stonehuerner, J. P. O'Daly, A. L. Crumbliss, *J. Electroanal. Chem*. **1992**, *327*, 109 – 119.

[247] a) S. D. Varfolomeev, I. N. Kurochkin, A. I. Yaropolov, *Biosens. Bioelectron*. **1996**, *11*, 863 – 871; b) A. L. Ghindilis, P. Atanasov, E. Wilkins, *Electroanalysis* **1997**, *9*, 661 – 674.

[248] Y. Xiao, H.-X. Ju, H.-Y. Chen, *Anal. Chim. Acta* **1999**, *391*, 73 – 82.

[249] E. Katz, H.-L. Schmidt, *J. Electroanal. Chem*. **1993**, *360*, 337 – 342.

[250] a) Y. Degani, A. Heller, *J. Phys. Chem*. **1987**, *91*, 1285 – 1289; b) W. Schuhmann, T. J. Ohara, H.-L. Schmidt, A. Heller, *J. Am. Chem. Soc*. **1991**, *113*, 1394 – 1397.

[251] F. Patolsky, T. Gabriel, I. Willner, *J. Electroanal Chem.* **1999**, *479*, 69 – 73.

[252] O. D. Velev, E. W. Kaler, *Langmuir* **1999**, *15*, 3693 – 3698.

[253] M. Grätzel, *Nanocrystalline Electronic Junctions*, in *Semiconductor Nanoclusters—Physical*, *Chemical and Catalytic Aspects* (Eds.: P. V. Kamat, D. Meisel), Elsevier, Amsterdam, **1997**, p. 353.

[254] P. V. Kamat in *Nanoparticles and Nanostructural Films* (Ed.: J. Fendler), Wiley-VCH, Weinheim, **1998**, p. 207.

[255] S. Ogawa, K. Hu, F.-R. F. Fan, A. J. Bard, *J. Phys. Chem.* **1997**, *101*, 5707 – 5711.

[256] a) L. Spanhel, H. Weller, A. Henglein, *J. Am. Chem. Soc*. **1987**, *109*, 6632 – 6635; b) K. R. Godipas, M. Bohorquez, P. V. Kamat, *J. Phys. Chem*. **1990**, *94*, 6435 – 6440; c) N. Serpone, E. Borgarello, M. Grätzel, *J. Chem. Soc. Chem. Commun*. **1984**, 342 – 344; d) P. Pichat, E. Borgarello, J. Disdier, J.-M. Herrmann, E. Pelizzetti, N. Serpone, *J. Chem. Soc. Faraday Trans. 1* **1988**, *84*, 261 – 274; e) N. Serpone, E. Borgarello, E. Pelizzetti, *J. Electrochem. Soc.* **1988**, *135*, 2760 – 2766.

[257] A. C. Khazraji, S. Hotchandani, S. Das, P. V. Kamat, *J. Phys. Chem. B* **1999**, *103*, 4693 – 4700.

[258] I. Willner, Y. Eichen, B. Willner, *Res. Chem. Intermed*. **1994**, *20*, 681 – 700.

[259] a) B. O'Regan, M. Grätzel, *Nature* **1991**, *353*, 737 – 740; b) U. Bach, D. Lupo, P. Comte, J. E. Moser, F. Weissortel, J. Salbeck, H. Spreitzer, M. Grätzel, *Nature* **1998**, *395*, 583 – 585.

[260] S. D. Burnside, V. Shklover, C. Barbé, P. Comte, F. Arendse, K. Brooks, M. Grätzel, *Chem. Mater.* **1998**, *10*, 2419 – 2425.

[261] D. Matthews, A. Kay, M. Grätzel, *Aust. J. Chem.* **1994**, *47*, 1869 – 1877.

[262] a) L. Kavan, M. Grätzel, J. Rathousky, A. Zukal, *J. Electrochem. Soc.* **1996**, *143*, 394 – 400; b) V. Shklover, M.-K. Nazeeruddin, S. M. Zakeeruddin, C. Barbé, A. Kay, T. Haibach, W. Steurer, R. Hermann, H.-U. Nissen, M. Grätzel, *Chem. Mater.* **1997**, *9*, 430 – 439.

[263] T. Cassagneau, T. E. Mallouk, J. H. Fendler, *J. Am. Chem. Soc*. **1998**, *120*, 7848 – 7859.

[264] V. L. Colvin, M. C. Schlamp, A. P. Alivisatos, *Nature* **1994**, *370*, 354 – 357.

[265] N. D. Kumar, M. P. Joshi, C. S. Friend, P. N. Prasad, R. Burzynski, *Appl. Phys. Lett*. **1997**, *71*, 1388 – 1390.

[266] a) V. L. Colvin, A. P. Alivisatos, J. G. Tobin, *Phys. Rev. Lett.* **1991**, *66*, 2786 – 2789; b) B. O. Dabbousi, C. B. Murray, M. F. Rubner, M. G. Bawendi, *Chem. Mater*. **1994**, *6*, 216 – 219.

[267] B. O. Dabbousi, M. G. Bawendi, O. Onitsuka, M. F. Rubner, *Appl. Phys. Lett*. **1995**, *66*, 1316 – 1318.

[268] M. Gao, B. Richter, S. Kirstein, *Adv. Mater.* **1997**, *9*, 802 – 805.

[269] K. S. Narayan, A. G. Manoj, J. Nanda, D. D. Sarma, *Appl. Phys. Lett*. **1999**, *74*, 871 – 873.

[270] S. A. Carter, J. C. Scott, P. J. Brock, *Appl. Phys. Lett*. **1997**, *71*, 1145 – 1147.

[271] P. W. M. Blom, H. F. M. Schoo, M. Matters, *Appl. Phys. Lett*. **1998**, *73*, 3914 – 3916.

[272] A. Terfort, N. Bowden, G. M. Whitesides, *Nature* **1997**, *386*, 162 – 164; N. Bowden, A. Terfort, J. Carbeck, G. M. Whitesides, *Science* **1997**, *276*, 233 – 235; W. T. Huck, J. Tien, G. M. Whitesides, *J. Am. Chem. Soc.* **1998**, *120*, 8267 – 8268; J. Tien, T. L. Breen, G. M. Whitesides, *J. Am. Chem. Soc.* **1998**, *120*, 12 670 – 12 671.

[273] a) P. He, J. Ye, Y. Fang, I. Suzuki, T. Osa, *Electroanalysis* **1997**, *9*, 68 – 73; b) M. T. Rojas, R. Königer, J. F. Stoddart, A. E. Kaifer, *J. Am. Chem. Soc.* **1995**, *117*, 336 – 343.

[274] J. Rickert, T. Weiss, W. Kraas, G. Jung, W. Göpel, *Biosens. Bioelectron*. **1996**, *11*, 591 – 598.

[275] I. Willner, E. Katz, *Angew. Chem.* **2000**, *112*, 1230 – 1269; *Angew. Chem. Int. Ed.* **2000**, *39*, 1180 – 1218.

[276] a) J.-P. Collin, A. Harriman, V. Heitz, F. Odobel, J.-P. Sauvage, *J. Am. Chem. Soc.* **1994**, *116*, 5679 – 5690; b) A. C. Benniston, A. Harriman, *J. Am. Chem. Soc.* **1994**, *116*, 11 531 – 11 537; c) H. Imahori, Y. Sakata, *Adv. Mater.* **1997**, *9*, 537 – 546; d) X. Marguerettaz, D. Fitzmaurice, *J. Am. Chem. Soc.* **1994**, *116*, 5017 – 5018; e) K. Uosaki, T. Kondo, X.-Q. Zhang, M. Yanagida, *J. Am. Chem. Soc.* **1997**, *119*, 8367 – 8368; f) S. Yamada, Y. Koide, T. Matsuo, *J. Electroanal. Chem.* **1997**, *426*, 23 – 26; g) H. Imahori, H. Yamada, S. Ozawa, K. Ushida, Y. Sakata, *Chem. Commun.* **1999**, 1165 – 1166; h) E. Katz, *J. Electroanal. Chem.* **1994**, *365*, 157 – 164; i) E. Katz, A. Y. Shkuropatov, O. I. Vagabova, V. A. Shuvalov, *Biochim. Biophys. Acta* **1989**, *976*, 121 – 128; j) A. A. Solov'ev, E. Katz, V. A. Shuvalov, Y. E. Erokhin, *Bioelectrochem. Bioenerg.* **1991**, *26*, 29 – 41.

[277] *Note Added in Proof (July 12, 2000):* The topic of nanoparticle expands rapidly and, in the course of the publication of this review, important advances have been made. In particular, the organization and patterning of nanoparticle arrays has received attention leading to evaporation-driven self-assembly,[278] templated nanoparticle deposition,[279] and increased attention in CCAs[280] and the use of nanoparticle arrays as templates.[281] Patterning by scanning probe microscopy[282] and stamping[283] techniques have been developed further, as has the understanding of the physical properties of nanoparticle arrays.[284] New functions of nanoparticle arrays have been developed, such as ion-gating recognition.[285] Most notable, biomolecule-linked nanoparticle assemblies have gained significant research efforts.[286] Multilayer and dendron-like structures of DNA-linked nanoparticles have been constructed on gold and glass surfaces and the construction procedure has been used for the detection of DNA analytes.[287]

[278] a) S. Maenosono, C. D. Dushkin, S. Saita, Y. Yamaguchi, *Langmuir* **1999**, *15*, 957 – 965; b) C. J. Kiely, J. Fink, G. Zheng, M. Brust, D. Bethell, D. J. Schiffrin, *Adv. Mater.* **2000**, *12*, 640 – 643.

[279] J. P. Spatz, S. Mossmer, C. Hartmann, M. Möller, T. Herzog, M. Krieger, H. G. Boyen, P. Ziemann, B. Kabius, *Langmuir* **2000**, *16*, 407-415.

[280] a) Y. Xia, B. Gates, Y. Yin, Y. Lu, *Adv. Mater.* **2000**, *12*, 693 – 713; b) A. Rogach, A. Sucha, F. Caruso, G. Sukhorokov, A. Kornowski, S. Kershaw, H. Möhwald, A. Eychmüller, H. Weller, *Adv. Mater.* **2000**, *12*, 333 – 337.

[281] a) Z. Zhong, Y. Yin, B. Gates, Y. Xia, *Adv. Mater.* **2000**, *12*, 206 – 209; b) J. E. G. J. Wijnhoven, S. J. M. Zevenhuizen, M. A. Hendriks, D. Vanmaekelbergh, J. J. Kelly, W. L. Vos, *Adv. Mater.* **2000**, *12*, 888 – 890; c) K. M. Kulinowski, P. Jiang, H. Vaswani, V. L. Colvin, *Adv. Mater.* **2000**, *12*, 833 – 837.

[282] a) J. W. Zheng, Z. H. Zhu, H. F. Chen, Z. F. Liu, *Langmuir* **2000**, *16*, 4409 – 4412; b) R. Resch, D. Lewis, S. Meltzer, N. Montoya, B. E. Koel, A. Madhukar, A. A. G. Requicha, P. Will, *Ultramicroscopy* **2000**, *82*, 135 – 139; c) R. Maoz, E. Frydman, S. R. Cohen, J. Sagiv, *Adv. Mater.* **2000**, *12*, 424 – 429.

[283] a) H. X. He, H. Zhang, Q. G. Li, T. Zhu, S. F. Y. Li, Z. F. Liu, *Langmuir* **2000**, *16*, 3846 – 3851.

[284] a) N. Del Fatti, F. Vallee, C. Flytzanis, Y. Hamanaka, A. Nakamura, *Chem. Phys.* **2000**, *251*, 215 – 226; b) J. P. Novak, D. L. Feldheim, *J. Am. Chem. Soc.* **2000**, *122*, 3979 – 3980; c) F. P. Zamborini, J. F. Hicks, R. W. Murray, *J. Am. Chem. Soc.* **2000**, *122*, 4514 – 4515; d) D. M. Kolb, G. E. Engelmann, J. C. Ziegler, *Angew. Chem. Int. Ed.* **2000**, *39*, 1123 – 1125.

[285] W. Zheng, M. M. Maye, F. L. Leibowitz, C.-J. Zhong, *Anal. Chem.* **2000**, *72*, 2190 – 2199.

[286] S. Mann, W. Shenton, M. Li, S. Connolly, D. Fitzmaurice, *Adv. Mater.* **2000**, *12*, 147 – 150.

[287] a) F. Patolsky, K. T. Ranjit, A. Lichtenstein, I. Willner, *Chem. Commun.* **2000**, 1025 – 1026; b) T. A. Taton, R. C. Mucic, C. A. Mirkin, R. L. Letsinger, *J. Am. Chem. Soc.* **2000**, *122*, 6305 – 6306.

Hexamers: From Covalently Bound Organic Structures to Hydrogen Bonded Water Clusters

Ralf Ludwig*[a]

KEYWORDS:

ab initio calculations · clusters · hydrogen bonds · vibrational spectroscopy · water chemistry

Cyclic hexamers are most common in chemistry. This structural motif is found for the saturated hydrocarbon cyclohexane, which exists in two possible nonplanar arrangements, a chair and a boat conformation.[1] Both structural isomers shown in Figure 1 satisfy the need for tetrahedral bond angles and represent constituents of larger organic molecules. Adamantane, twistane, and bicyclo[2.2.2]octane all contain cyclohexane rings (Figure 2). Adamantane includes four chair conformers and bicyclo[2.2.2]octane can be represented by three boat conformers. In twistane, the six-membered ring maintains five twist-boat conformations. Diamond represents another prominent polycyclic structure. This form of elemental carbon, in which each atom is bonded to four other carbon atoms, is an extended three-dimensional network of adamantane units. In common, all of these structures have carbon atoms, each covalently bound in a tetrahedral fashion. These possible tetrahedral structures establish the relationship to the hydrogen bond networks of water. Whereas the carbon atom with four equivalent hybrid orbitals is capable of forming four covalent bonds, the water molecule has also four sites to build hydrogen bonds. In an almost tetrahedral coordination, each water molecule is involved in four hydrogen bonds, the two lone electron pairs as bond acceptors and both hydrogen atoms as bond donors. Hydrogen bonds are about ten times weaker than covalent bonds. Recently, it was shown by Compton scattering experiments on ice[2] and NMR measurements of internucleotide scalar coupling in biomolecules[3] that hydrogen bonds have covalent character and can be regarded as weak covalent bonds. Because of the tetrahedral arrangement and the covalent character of the hydrogen bond, the structural motifs of organic molecules can be found in all known crystalline phases of ice.[4–7] In Figure 3,

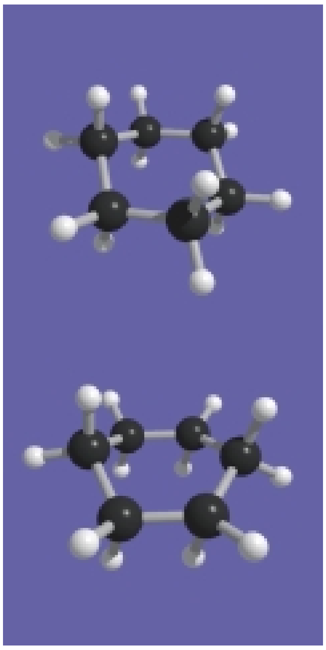

Figure 1. Chair (above) and boat (below) conformations of cyclohexane.

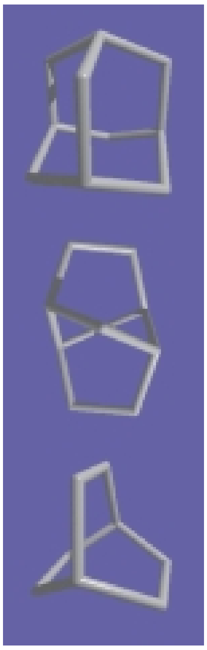

Figure 2. Adamantane (above), twistane (center), and bicyclo[2.2.2]octane (below) are all composed of chair and boat conformations.

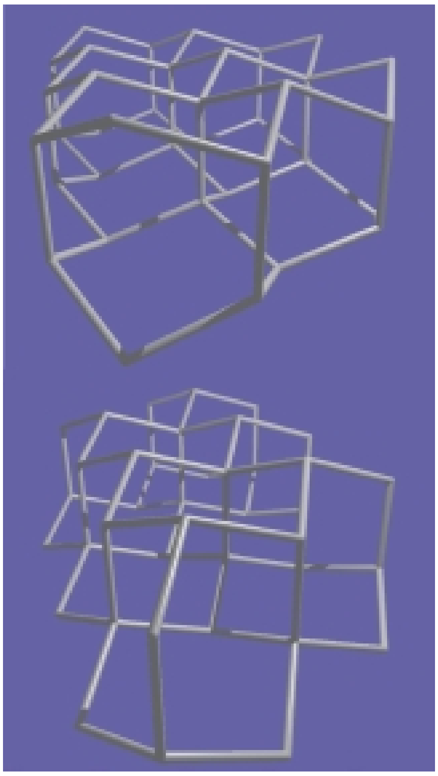

Figure 3. The structure of hexagonal ice I_h (above) and cubic ice I_c (below). Each line represents a hydrogen bond O–H···O and vertices correspond to the oxygen atomic positions.

---

[a] Priv.-Doz. Dr. R. Ludwig
Physikalische Chemie
Fachbereich Chemie der Universität Dortmund
Otto-Hahn-Strasse 6, 44221 Dortmund
(Germany)
Fax: (+49) 231-755-3937
E-mail: ludwig@pc2a.chemie.uni-dortmund.de

the two prominent polymorphs are shown. Hexagonal ice I_h is ordinary ice, gels below the freezing point at normal pressure, and is composed of chair and boat conformers. The metastable cubic ice I_c can be formed by warming vitreous ice at low temperatures or by warming any of the quenched high-pressure ices. From Figure 3 it can be easily seen that the cubic lattice includes adamantane-like structures and is isomorphous with diamond. That the structural motifs of isomeric cyclic hexamers of covalently bonded organic molecules are present in the hydrogen bonded polymorphs of ice has been known for long time.[4–7] On the other hand, the microscopic properties of liquid water remain poorly understood. However, computer simulations[8] and thermodynamic models[9] suggest that the cyclic hexamer is also one of the prominent morphologies in liquid water.

The structural motifs of ice crystals are fairly well understood; those of liquid water can be supposed by theoretical models. But what about pure isolated water clusters in the gas phase or in an inert environment? Do they exist as hexamers at all? And, if so, do they form quasiplanar rings or three-dimensional cage structures? These questions were intensively addressed by a palette of experimental and theoretical methods. In particular, vibration-rotation-tunneling (VRT) spectroscopy, infrared (IR) spectroscopy, and quantum mechanical methods were used to solve the puzzle of small water clusters. Recent research in this field is an excellent example for a fruitful interplay between theory and experiment.

First of all, enormous progress in laser spectroscopy has facilitated new, highly detailed studies of water clusters. Far-infrared (FIR) VRT spectroscopy of clusters has been developed by Saykally and coworkers[10–13] to study the structure and dynamics of isolated water clusters. Low frequency van der Waals vibrations in clusters can be measured with tunable FIR lasers to resolve rotational and tunneling motions. The resulting VRT spectra can be analyzed in terms of permutation-inversion (PI) group theory and scattering theory to yield pair potentials of unprecedented accuracy and detail for important, weakly bound systems. FIR-VRT spectroscopy is also a powerful probe of the tunneling dynamics that occur in hydrogen-bonded clusters. This method allows investigation of the cooperative (nonpairwise) effects in hydrogen bonding through the VRT spectroscopy of water clusters. In a series of beautiful experiments, Saykally et al. characterized the cyclic water trimer,[10] tetramer,[11] and pentamer.[12] The results unambiguously establish that the structures of the water clusters (Figure 4) responsible for the observed spectra were indeed the quasiplanar rings predicted by theory.[14–16] These spectra permitted estimates of the oxygen–oxygen interatomic distances, $R_{O\text{-}O}$, to be extracted for each of the clusters, which yields a quantitative experimental measure of the hydrogen bond cooperativity. In Figure 5, the $R_{O\text{-}O}$ distances obtained from VRT spectroscopy and theoretical studies of water clusters are plotted. Cooperative effects are manifest, as all methods produced an exponential $R_{O\text{-}O}$ contraction with increasing cluster size and convergent to the bulk (ordered ice) value of about 2.759 Å.[5, 6] Experiment and theory strongly suggest that the water trimer, tetramer, and pentamer ($n = 3-5$) have cyclic, quasiplanar minimum energy structures. Larger water clusters were expected to have three-dimensional geometries, with the hexamer ($n = 6$) representing the transition from cyclic to such three-dimensional structures.

Indeed, a cagelike hexamer, bound by eight hydrogen bonds, is in best agreement with the measured rotational constants from VRT measurements by the Saykally group.[18] This three-dimensional water hexamer, shown in Figure 6 , turned out to be the absolute minimum structure in a gas-phase experiment at temperatures about 5 K.

Forced by the surprising experimental results for the water hexamer in the gas phase, Kim and Kim[19] performed extensive ab initio (MP2) and density functional theory (DFT) calculations on the five lowest energy structures of the water hexamers, as shown in Figure 6. The authors demonstrated that the ring, book, bag, cage, and prism structures are nearly isoenergetic, to within 0.7 kcal mol^{-1}. Their high performance MP2 calculations showed that the lowest energy conformer is the cage followed by

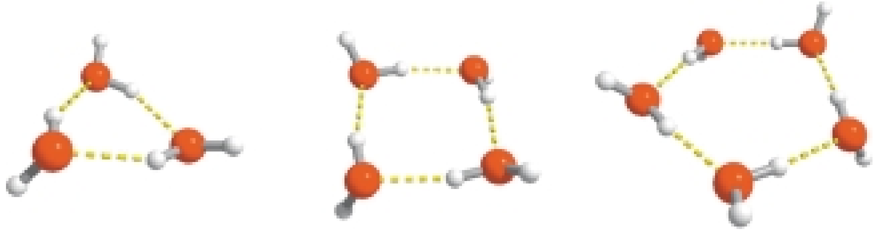

Figure 4. *Ring structures of the water trimer, tetramer, and pentamer. Hydrogen bonds are indictated with a broken line.*

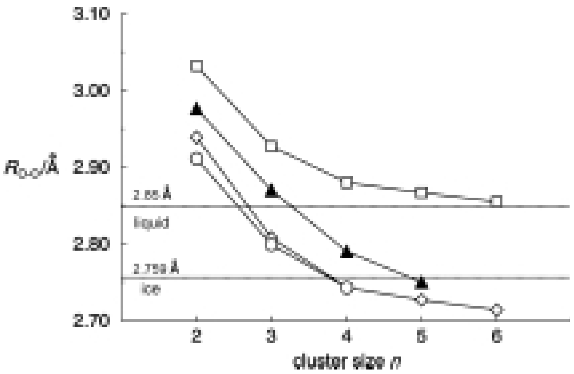

Figure 5. *The $R_{O\text{-}O}$ distances versus cluster size n obtained from VRT spectroscopy[10–13] (▲) and three different levels of theory[14–16]: Hartree–Fock (HF, □), Møller–Plesset second-order perturbation (MP2, ○), and density functional theory (DFT, B-LYP level, ◇). The experimental $R_{O\text{-}O}$ distances in liquid water at 298 K[17] and hexagonal ice at 183 K[5, 6] are shown for comparison, as indicated by dotted lines.*

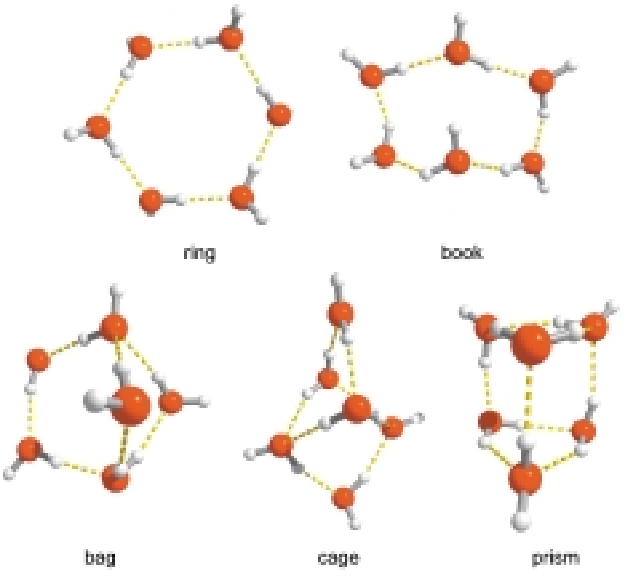

Figure 6. *Five calculated water hexamer isomers showing quasiplanar and cagelike clusters. Hydrogen bonds are indicted with a broken line.*

the book and prism structures lying less than 0.1 and 0.2 kcal mol^{-1} higher in energy. The ring and the bag structures exist only slightly higher (0.5 and 0.7 kcal mol^{-1}) than the cage hexamer. The lowest energy structure of the water hexamer, at low temperatures, is now believed to be a three-dimensional cage from both experimental and theoretical viewpoints. At high temperatures, the populations of the five hexamer isomers would be almost the same. The ab initio calculations clearly showed that zero-point vibrational effects can alter the energy ordering of the low-lying hexamer structures. Thus, there was some hint that other hexamer isomers could be detected experimentally by changing the physical and chemical conditions. This proved to be the case. Nauta and Miller[20] recently reported the experimental observation of the cyclic water hexamer, a higher energy isomer than the cage structure characterized in the gas phase by the Saykally group. The cyclic hexamer was formed in liquid helium droplets and studied with infrared spectroscopy. The infrared spectrum for the OH stretches of water clusters formed in liquid helium were compared with that of the corresponding complexes formed in a free jet expansion.[21] The vibrational frequency shifts resulting from the interaction with the helium were negligible and the bands for the dimer, trimer, tetramer, and pentamer are essentially in coincidence with gas-phase bands. An additional peak in the spectrum shifted further to the red than the pentamer was assigned to the cyclic isomer of the water hexamer. The most compelling support for this assignment comes from comparing the frequency shifts for all of these cyclic complexes with corresponding ab initio and DFT calculations, as shown in Figure 7. In correspondance with the changes in the intra- and intermolecular geometries, the frequency shifts vary smoothly with cluster size *n* and the cyclic hexamer peak is precisely where it is expected theoretically. Better agreement with experimental and theoretical values cannot be expected since the theoretical values are based on harmonic frequency calculations. Theoretical methods were mostly helpful in characterizing the measured species clearly as cyclic hexamers. On the other hand, the experimental frequencies support theory. As shown in Figure 7, the calculated frequency shifts can be scaled to the experimental data. Increasing cluster size obviously does not require different scaling factors. The cage isomer characterized in the gas phase[18] has an intense OH vibrational band, which is shifted further to much lower. It wavenumbers was shown earlier that several calculated local minima[19] lie lower in energy than the cyclic hexamer. Obviously, the path between this hexamer and the three-dimensional cage structure will involve a great deal of hydrogen bond rearrangement, which is expected to be difficult in liquid helium.

So far, a cage and a quasiplanar water hexamer could be detected experimentally. Both structures were characterized by theoretical methods. Distinct chair and boat conformers of water hexamers do not exist as free species and require a crystal host for stability. Recently, cyclic water hexamers with an icelike chair conformer were found included inside the channels of an organic host.[22] The average $R_{O\text{-}O}$ distance is 2.776 Å. For

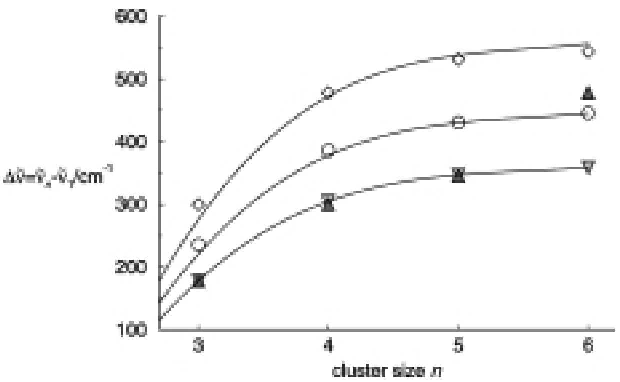

Figure 7. *The red-shifted signals of the vibrational spectra of cyclic water clusters from the trimer to the hexamer, $\tilde{\nu}_n$, compared to that of the water monomer, $\tilde{\nu}_1$, from experimental[20, 21] (in the gas phase, ▲; in liquid helium droplets, ▼) and theoretical[14–16] (DFT at the B-LYP level, ◇; MP2, ○) studies. The shifts are taken in both cases relative to the average of the symmetric and asymmetric O–H stretches of the monomer. The frequency shifts are essentially the same for the data collected in the gas phase and in liquid helium droplets up to the pentamer. The cage hexamer detected in the gas phase is red shifted further than the quasiplanar ring hexamer that exists in liquid helium. The solid curves present a guideline; they are obtained by scaling the fitted experimental curve to the theoretical data.*

comparison, the analogous value in ice I_h is 2.759 Å at 183 K. However, there is a wide variation in the value of the angle ∢(O-O-O): With an average of 116.5° it lies considerably far from the value of 109.3° for hexagonal ice. The hexamers are self-assembled by O–H···O hydrogen bonds into extended tapes along the channels, which consist of fused four- and six-membered water rings. The observed inter-hexamer $R_{\text{O-O}}$ value of 2.854 Å is close to the separation of 2.85 Å found in liquid water.[17] This supramolecular association of water molecules into tapes is presumably enforced by the shape of the host channels, whose relatively narrow openings preclude the formation of more stable, three-dimensional clusters, as found in the gas phase. There are no O–H···N hydrogen bonds between the water tapes and the organic host. Thus, the water clusters can be removed by heating without changing the structure of the host. As opposed to the inclusion complexes of water clusters previously described with strong interactions with the host, the water clusters resemble more closely an environment found in liquid water or ice. IR spectra suggest that the water tapes are more similar to liquid water than with hexagonal ice.[22]

In the future, we can expect that larger water clusters with a variety of isomers will be measured and calculated. Results from these studies are yielding important insights into cooperative effects in hydrogen bonding, aqueous solvation, and hydrogen bond network arrangements. There is some promise that we can enhance our understanding of the bulk phase, in particular, of liquid water.

[1] H. Hart, L. E. Craine, D. J. Hart, *Organic Chemistry*, Houghton Mifflin Company, Boston, **1999**.

[2] E. D. Isaacs, A. Shukla, P. M. Platzman, R. D. Hamann, B. Barbiellini, C. A. Tulk, *Phys. Rev. Lett.* **1999**, *82*, 600 – 603.

[3] A. L. Dingley, A. L. Grzesiek, *J. Am. Chem. Soc.* **1998**, *120*, 8293 – 8297.

[4] *Water—A Comprehensive Treatise, Vol. 1 – 7*, (Ed.: F. Franks), Plenum, New York, **1972**.

[5] D. Eisenberg, W. Kauzmann, *The Structure and Properties of Water*, Oxford University Press, Oxford, **1969**.

[6] N. H. Fletcher, *The Chemical Physics of Ice*, Cambridge University Press, Cambridge, **1970**.

[7] J. M. Ugalde, I. Alkorta, J. Elguero, *Angew. Chem.* **2000**, *112*, 733 – 737; *Angew. Chem. Int. Ed.* **2000**, *39*, 717 – 721.

[8] F. H. Stillinger, *Science* **1980**, *209*, 451 – 457.

[9] R. Ludwig, F. Weinhold, T. C. Farrar, *J. Chem. Phys.* **1995**, *103*, 6941 – 6950.

[10] N. Pugliano, R. J. Saykally, *Science* **1992**, *257*, 1937 – 1940.

[11] J. D. Cruzan, L. B. Braly, K. Liu, M. G. Brown, J. G. Loeser, R. J. Saykally, *Science* **1996**, *271*, 59 – 62.

[12] K. Liu, M. G. Brown, J. D. Cruzan, R. J. Saykally, *Science* **1996**, *271*, 62 – 64.

[13] K. Lui, J. D. Cruzan, R. J. Saykally, *Science* **1996**, *271*, 929 – 933.

[14] S. S. Xantheas, T. H. Dunning, Jr., *J. Chem. Phys.* **1993**, *99*, 8774 – 8792.

[15] S. S. Xantheas, *J. Chem. Phys.* **1994**, *100*, 7523 – 7534.

[16] S. S. Xantheas, *J. Chem. Phys.* **1995**, *102*, 4505 – 4517.

[17] A. H. Narten, W. E. Thiessen, L. Blum, Science **1982**, *217*, 1033 – 1034.

[18] K. Liu, M. G. Brown, C. Carter, R. J. Saykally, J. K. Gregory, D. C. Clary, *Nature* **1996**, *381*, 501 – 503.

[19] J. Kim, K. S. Kim, *J. Chem. Phys.* **1998**, *109*, 5886 – 5895.

[20] K. Nauta, R. E. Miller, *Science* **2000**, *287*, 293 – 295.

[21] F. Huisken, M. Kaloudis, A. Kulcke, *J. Chem. Phys.* **1996**, *104*, 17 – 25.

[22] R. Custelcean, C. Afloroaiei, M. Vlassa, M. Polverejan, *Angew. Chem.* **2000**, *112*, in press; *Angew. Chem. Int. Ed.* **2000**, *39*, in press.

Electroweak Quantum Chemistry of Alanine: Parity Violation in Gas and Condensed Phases**

Robert Berger[a] and Martin Quack*[a]

KEYWORDS:

ab initio calculations · amino acids · chirality

The discovery of parity violation in nuclear physics[1,2] has led to the understanding that left- and right-handed enantiomers of chiral molecules are not energetically equivalent but differ by a "parity-violating energy difference", ΔE_{pv}. It was concluded rather quickly that this inequivalence might even have affected the evolution of biopolymers.[3,4] By virtue of quantitative calculations based on an early theoretical approach by Hegstrom, Rein, and Sandars (single determinant excitation-restricted Hartree–Fock, SDE-RHF),[5] it has repeatedly been claimed that L-enantiomers of amino acids are more stable than their D-counterparts.[6,7] Frequently, the suggestion has been added that this might account for the preferred occurrence of L-amino acids in natural proteins.[8] While this line of reasoning can be questioned on many grounds,[9,10] even the starting point of these computed energy differences was fundamentally challenged recently.[11] Indeed, it was discovered on the basis of new theoretical approaches (configuration interaction singles, CIS) that the parity-violating energy difference is in general much larger (typically up to one to two orders of magnitude) than previously calculated and that, furthermore, ΔE_{pv} can be represented as a trace of a tensor, that is the sum of three terms with different signs. From this result, it was concluded that all earlier SDE-RHF calculations on ΔE_{pv} of chiral molecules must be questioned both with respect to absolute magnitude and sign.[11,12] Recent work using different approaches has confirmed the general trends of these results.[13–17]

Recently, we have greatly improved the systematic approach towards electroweak quantum chemistry, that is, quantum chemical calculations which include the parity-violating weak nuclear forces in the framework of the unified electroweak theory of the standard model,[18–20] by introducing the multi-configuration linear response (MC-LR) approach to parity violation.[21,22] This approach has confirmed the order of magnitude increase and has, at the same time, led to a deeper understanding of the results, to allow for systematic improvements, tests, and estimates of reliability. We use our new approach here in a study of parity-violating effects in alanine.

Alanine (Figure 1) has been repeatedly used as a prototype for parity violation in α-amino acids. Mason and Tranter[6,23] used the SDE-RHF approach to find that the zwitterionic form of L-alanine is stabilized with respect to D-alanine. Kikuchi and Wang[24,25] questioned their results, by arguing that the conformation chosen by Mason and Tranter is according to theoretical studies but not the preferred one in aqueous solutions. However, they also found L-alanine to be more stable than the D-form by calculations using special minimal basis sets. Bakasov et al.,[11,12] on the one hand, provided support for Mason and Tranter's results by an extensive basis set study but, on the other hand, rejected all earlier SDE-RHF results (including those of Mason and Tranter, as well as Kikuchi et al.) and found much larger values for ΔE_{pv} using CIS-RHF methods as discussed above. Somewhat similar results were obtained by Zanasi and Lazzeretti,[14,15] who drew, however, different conclusions. Finally, Laerdahl et al.[16,17] have most recently demonstrated that relativistic corrections on ΔE_{pv} are small for molecules containing only atoms of the first rows of the periodic table (including also neutral alanine in the gas phase).

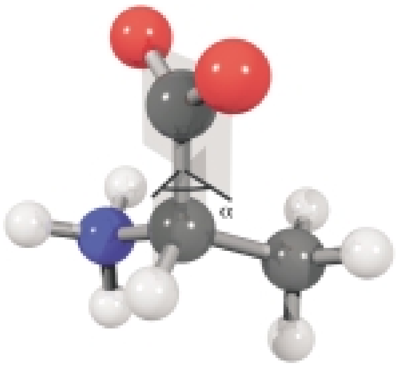

Figure 1. Structure of the zwitterionic form of L-alanine (corresponding to the minimum in Figure 3). The interplane angle α is indicated.

A new study of ΔE_{pv} in alanine seems appropriate for several reasons:

1) Except for reference [24], all previous studies used a conformation of the carboxylato group, which was postulated to be favored in water, but this assumption was neither based on experimental observations nor on theoretical calculations.

2) The calculations have been performed on the zwitterionic forms of the amino acids in vacuo at their presumably "preferred" conformations in water, although it is well known for glycine, the smallest α-amino acid, that the zwitterionic form does not correspond to an equilibrium structure in vacuo if one uses basis sets which are flexible enough for a realistic description of this molecule. Laerdahl et al. studied gaseous, neutral alanine (including complexes with a single H_2O molecule), which presumably is of less relevance to biochemistry.[17]

3) Previous studies aimed at the prediction of the parity-violating potential for L-alanine in water but disregarded any solvent effects except for a modified equilibrium structure. It is well known, for instance, for the calculation of NMR shifts, that an adjusted equilibrium structure is not sufficient to account for

---

[a] Prof. Dr. M. Quack, Dr. R. Berger
Laboratorium für Physikalische Chemie
ETH Zürich (Zentrum)
8092 Zürich (Switzerland)
Fax: (+41) 1-632-10-21
E-mail: quack@ir.phys.chem.ethz.ch

[**] Our work is supported financially by ETH Zürich (including C4 and CSCS) and the Schweizerischer Nationalfonds. Substantial help from and discussions with Jürgen Stohner and Greg Tschumper are gratefully acknowledged.

solvent effects on specific properties without reference to the solute – solvent interactions.

Therefore, all previous studies on the parity-violating potentials of L-alanine are to be considered incapable of answering the question whether either L- or D-alanine is favored in aqueous solutions due to the parity-violating electroweak interactions. This question is thus still open. One should note here, however, that even if L-alanine turns out to be more stable than D-alanine, the relation of this preference to biochemical evolution on earth is by no means obvious (if it exists at all), since in typical kinetic amplification mechanisms, a difference in rate constants for chemical reactions of the enantiomers rather than the relative stability of their equilibrium structure is the driving force for biochemical selection of enantiomers.

We present here the first high level ab initio results for ΔE_{pv}, which compare explicitly gaseous neutral and zwitterionic forms of alanine as well as the effects arising from interactions with water as a solvent. We furthermore present a systematic study on the role of the conformation of the carboxylato group. Table 1 summarizes the main numerical results of our study.

In this Table, we compare calculated potential energies for some main low energy conformers previously established as local minima by Császár[26] at various levels of theory (MP2, RHF, and CAS; see the Computational Methods section and ref. [22]). Besides neutral, gaseous alanine, we also present results for solvated alanine both neutral and in the zwitterionic structure using a multiconfiguration self-consistent reaction field (MCSCRF) linear response approach[27–29] to simulate effects from surrounding solvent molecules (H_2O). Under all conditions, the energies for the three conformers shown are well within thermal (kT) energies at room temperature and thus would have substantial populations under biochemically relevant conditions. The Table also displays values for ΔE_{pv} at the various structures at the RPA (random phase approximation) and CASSCF (complete active space – self-consistent field) level. The sign of ΔE_{pv} varies with the conformer and changes from a neutral to a zwitterionic structure. Again, RPA seems to be a reasonable approximation to the more reliable CASSCF results, a conclusion already reached in our systematic study of ΔE_{pv} for smaller molecules,[22] both as far as the magnitude and sign of ΔE_{pv} are concerned.

Figure 2 displays the ordinary, parity-conserving electronic potential energy $E_{pc}(\alpha)$ (right axis) and the parity-violating potential $E_{pv}(\alpha)$ (left axis) as functions of the conformational angle α of the carboxylato plane with respect to the C_α–CO_2–H_α plane. The other structural parameters were held constant at their equilibrium values (that is, they were not optimized along the reaction path for α). While all values of α in Figure 2 correspond to the L-configuration of alanine, ΔE_{pv} makes large excursions from negative values of E_{pv} (namely, L-alanine is more stable than the D-form) to positive values (that is, D-alanine is stabilized; note also that $\Delta E_{pv}(\alpha) \equiv E_{pv,L}(\alpha) - E_{pv,D}(\alpha) = 2E_{pv,L}(\alpha)$ is the energy difference between enantiomeric structures at a given α). Obviously, there is no correlation between the configuration (D or L) and the sign of E_{pv} (or ΔE_{pv}), a conclusion

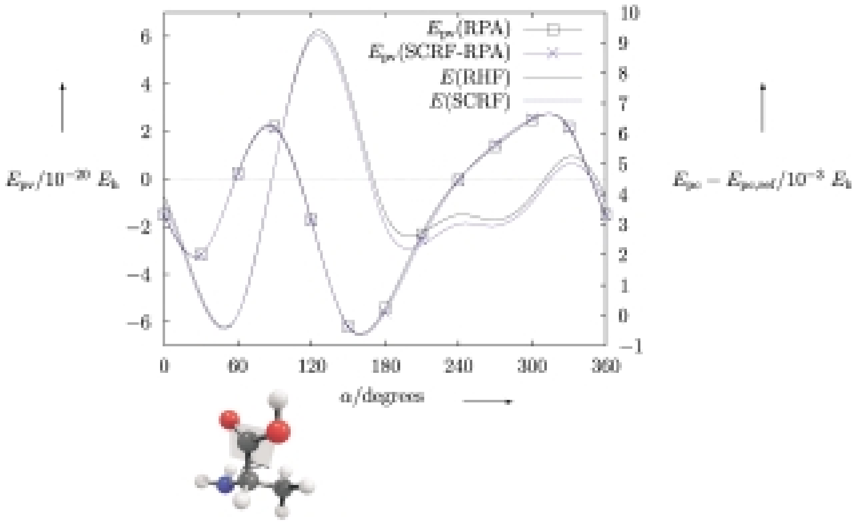

Figure 2. Parity-violating and parity-conserving potentials in the gas phase and solution as a function of the orientation of the carboxylato group of the neutral L-alanine structure I obtained with the 6-31G basis set. The blue lines correspond to results in solution (that is, SCRF calculations), as indicated. The lines with the symbol × and □ represent E_{pv} (left axis in 10^{-20} E_h), whereas the ordinary lines represent the parity-conserving torsional potential (right axis in 10^{-3} E_h).

*Table 1. Parity-violating potentials E_{pv} and relative parity-conserving potentials E for neutral and zwitterionic structures of L-alanine in the gas phase and solution obtained with the 6-31++G** basis set using various methods.*

Structure	Method[a]	Neutral L-alanine			Zwitterionic L-alanine
		I	IIA	IIB	
MP2 optimized	E(MP2)/10^{-6} E_h	0	498	1074	
	E_{pv}(RPA)/10^{-20} E_h	−2.264	1.034	−0.695	
	E(RHF)/10^{-6} E_h	0	4291	4477	
	E_{pv}(CASSCF-LR)/10^{-20} E_h	−2.041	1.147	−0.951	
	E(CASSCF)/10^{-6} E_h	0	−1823	−1366	
RHF optimized	E_{pv}(RPA)/10^{-20} E_h	−1.553	1.181	−1.740	
	E(RHF)/10^{-6} E_h	0	3729	3843	
SCRF optimized	E_{pv}(SCRF-RPA)/10^{-20} E_h	−1.525	1.542	−0.718	2.418
	E(SCRF)/10^{-6} E_h	0	437	756	20271

[a] Hartree energy $E_h = 4.360 \times 10^{-18}$ J.

already drawn earlier on a variety of molecules, including alanine.[11,12,22] Near the minimum of the parity-conserving potential, at $\alpha < 60^\circ$, E_{pv} is actually negative. However, around 60°, at essentially thermal potential energies, E_{pv} changes to positive values (namely, D- is more stable than L-alanine). Figure 2 shows results for both gas phase and solvated, neutral alanine. The differences in $E_{pc}(\alpha)$ and $E_{pv}(\alpha)$ are significant but small and certainly not decisive at the present level of accuracy of the theory.

Figure 3 shows similar results for zwitterionic structures of L-alanine. As expected, the differences between gaseous and solvated (labelled SCRF) alanine are more important. Nonetheless, the qualitative behaviour is fairly similar for the results in the gas phase and in solution. The potential energy function $E_{pc}(\alpha)$ is simpler than for neutral alanine and has its minimum near 60° for both the gaseous and the solvated zwitterionic structures. In this region, $E_{pv,L}(\alpha)$ is small and positive (that is, D- is more stable than L-alanine). However, the change to negative $E_{pv,L}(\alpha)$ occurs at an only slightly smaller α, where the potential energy is within thermal energies from the minimum. Thus, it would be ridiculous to conclude that the present calculations support a significantly and systematically higher stability of D-alanine compared to L-alanine (and even less so for the reverse conclusion). With respect to our previous CIS-RHF calculations, we find that the order of the maximum $E_{pv}(\alpha)$ (about $6 \times 10^{-20}\,E_h$) is about the same as in the present calculation. This is about a factor of six higher than with previous RHF-SDE calculations. The detailed behaviour of $E_{pv}(\alpha)$ in the present calculation differs, however, from the results in ref. [12], which can be attributed to the lack of convergence already noted in that latter work.

The changes of the maximum $E_{pv}(\alpha)$ in Figure 3 when transferring from the gas phase (RPA) to solution (SCRF-RPA) are about 20% and a similar, further change occurs when going to the CASSCF-LR results, which is the highest computational level used in the present study.

Our results, which are the highest level ab initio results on ΔE_{pv} so far reported for the gas phase and solution properties of alanine, provide no support whatsoever for a systematic stabilization of L-alanine compared to D-alanine at thermally accessible conformations. Previous conclusions to this effect, based on lower level calculations should therefore be rejected. Indeed, our calculations indicate that $E_{pv}(\alpha)$ near the minimized geometry is small in absolute value (as compared to the maximum $E_{pv}(\alpha)$ for the geometries investigated here) and changes sign at thermal energies. While considerable improvements upon the present calculation are possible with respect to basis set size and with respect to the treatment of the solvent effects, it appears to be unlikely that such improvements will change our conclusion. Our previous, extensive basis set-size studies indicate that larger and more flexible basis sets lead to somewhat larger $|E_{pv}|$ values but not to fundamental changes.[12,22] Relativistic effects have been shown to be rather unimportant for the calculation of E_{pv} for "light atom" molecules of this kind.[16,17] They are even relatively small for the "heavy atom" system CHBrClF.[30,31]

We conclude, with a comment on speculations, whether the alleged systematic stabilization of L-amino acids by the parity-violating weak nuclear force provides significant evidence for the evolution of L-biomolecular homochirality in amino acids. Since we have shown here the premises of such speculations to be wrong, further discussion may seem unnecessary. However, even if the premises were right, as might be true for other amino acids or for the complementary D-sugars, there is at present no *direct* relation between E_{pv} and the mechanism of selecting a given homochiral form. On the other hand, it would be wrong to conclude that such a relation cannot exist, as has been done recently.[32] As we have discussed elsewhere, the question of the connection between parity-violating forces in nature and biomolecular homochirality is very subtle and a definitive answer in the near future is not to be expected.[9,10,33]

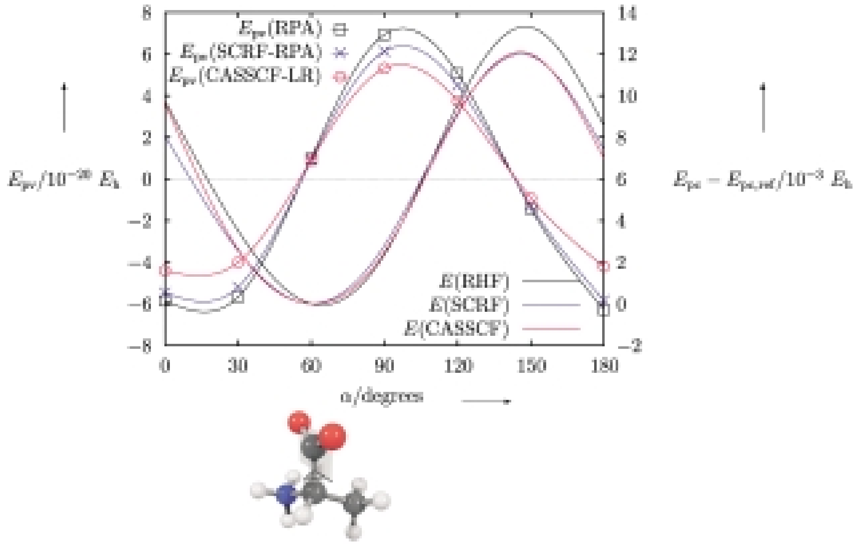

Figure 3. Parity-violating and parity-conserving potentials in the gas phase and solution as a function of the orientation of the carboxylato group of zwitterionic L-alanine obtained with the 6-31G basis set. The blue lines correspond to results in solution. The red lines are from CASSCF-LR calculations. E_{pv} (CASSCF-LR) is represented with the symbol ○. Other symbols and axes are identical to those in Figure 2.

Computational Methods

The calculations of the parity-violating potentials were performed along the lines of the multiconfiguration linear response formulation, as described in ref. [22] for gas-phase computations, whereas the determination of parity-violating potentials in solution will be presented in more detail in ref. [34]. The results were obtained using our modified version[22] of the Dalton program.[35] The Weinberg parameter $\sin^2\theta_w$ employed in this study was set to the experimental value of 0.2319. Solvent effects were represented by the multiconfiguration self-consistent reaction field method,[27–29] in which the solute resides in a spherical cavity enclosed in a linear, homogeneous, and isotropic dielectric medium characterized by the relative permittivity (the dielectric constant). Throughout this work, we used a relative permittivity of water $\varepsilon_r = 78.54$ and applied a common radius of 3.98 Å for the cavity with its center located at the center of mass of the molecule. For geometry optimizations and for parity-violating potentials calculated at those geometries, we used the 6-31 ++ G** basis set. For consistency with earlier studies, we employed the 6-31G basis set when studying the effect of the rotation of the carboxylato groups on the parity-violating potentials. Reference geometrical parameters for these rigid rotations of the carboxylato groups were the crystal structure of the zwitterionic form, as used in previous studies,[11,12] and the L-alanine structure I, from an MP2 optimization employing the 6-31 ++ G** basis set. We adopted the labeling of the neutral forms of L-alanine from ref. [26].

[1] T. Lee, C. Yang, *Phys. Rev.* **1956**, *104*, 254 – 258.

[2] C. Wu, E. Ambler, R. Hayward, D. Hoppes, R. Hudson, *Phys. Rev.* **1957**, *105*, 1413 – 1415.

[3] Y. Yamagata, *J. Theor. Biol.* **1966**, *11*, 495.

[4] D. Rein, *J. Mol. Evol.* **1974**, *4*, 15 – 22.

[5] R. Hegstrom, D. Rein, P. Sandars, *J. Chem. Phys.* **1980**, *73*, 2329 – 2341.

[6] S. Mason, G. Tranter, *Mol. Phys.* **1984**, *53*, 1091 – 1111.

[7] S. Mason, *Nature* **1985**, *314*, 400 – 401.

[8] G. Tranter, A. MacDermott, *Chem. Phys. Lett.* **1986**, *130*, 120 – 122.

[9] M. Quack, *Angew. Chem.* **1989**, *101*, 588 – 604; *Angew. Chem. Int. Ed. Engl.* **1989**, *28*, 571 – 586.

[10] M. Quack, *Nova Acta Leopold. NF* **1999**, *81*, 137 – 173.

[11] A. Bakasov, T.-K. Ha, M. Quack in *Chemical Evolution: Physics of the Origin and Evolution of Life* (Eds.: J. Chela-Flores, F. Raulin), Kluwer Academic, Netherlands, **1996**, pp. 287 – 296.

[12] A. Bakasov, T.-K. Ha, M. Quack, *J. Chem. Phys.* **1998**, *109*, 7263 – 7285.

[13] P. Lazzeretti, R. Zanasi, *Chem. Phys. Lett.* **1997**, *279*, 349 – 354.

[14] R. Zanasi, P. Lazzeretti, *Chem. Phys. Lett.* **1998**, *286*, 240 – 242.

[15] R. Zanasi, P. Lazzaretti, A. Ligabue, A. Soncini in *Advances in BioChirality* (Eds.: G. Pályi, C. Zucchi), Elsevier, Amsterdam, **1999**, pp. 377 – 385.

[16] J. Laerdahl, P. Schwerdtfeger, *Phys. Rev. A* **1999**, *60*, 4439 – 4453.

[17] J. Laerdahl, R. Wesendrup, P. Schwerdtfeger, *ChemPhysChem* **2000**, *1*, 60 – 62.

[18] S. Glashow, *Nucl. Phys.* **1961**, *22*, 579 – 588.

[19] A. Salam in *Proceedings of the Eighth Nobel Symposium* (Ed.: N. Svartholm), Amkvist and Wiksell, Stockholm, **1968**, pp. 367 – 377.

[20] S. Weinberg, *Phys. Rev. Lett.* **1967**, *19*, 1264 – 1266.

[21] R. Berger, M. Quack in *Proc. 37th IUPAC Congress*, *Vol. 2*, GDCh, Berlin, **1999**, p. 518.

[22] R. Berger, M. Quack, *J. Chem. Phys.* **2000**, *112*, 3148 – 3158.

[23] S. Mason, G. Tranter, *Chem. Phys. Lett.* **1983**, *94*, 34 – 37.

[24] O. Kikuchi, H. Wang, *Bull. Chem. Soc. Jpn.* **1990**, *63*, 2751 – 2754.

[25] H. Kiyonaga, T. Yagi, K. Morihashi, O. Kikuchi, *JCPE J.* **1999**, *11*, 165 – 170.

[26] A. Császár, *J. Chem. Phys.* **1996**, *100*, 3541 – 3551.

[27] K. Mikkelsen, E. Dalgaard, P. Swanstrøm, *J. Phys. Chem.* **1987**, *91*, 3081 – 3092.

[28] K. Mikkelsen, H. Ågren, H. Jensen, T. Helgaker, *J. Chem. Phys.* **1988**, *89*, 3086 – 3095.

[29] P.-O. Åstrand, K. Mikkelsen, P. Jørgensen, K. Ruud, T. Helgaker, *J. Chem. Phys.* **1998**, *108*, 2528 – 2537.

[30] M. Quack, J. Stohner, *Phys. Rev. Lett.* **2000**, *84*, 3807 – 3810; M. Quack, J. Stohner, *Z. Phys. Chem.* **2000**, *214*, 679 – 703.

[31] J. Laerdahl, P. Schwerdtfeger, H. Quiney, *Phys. Rev. Lett.* **2000**, *84*, 3811 – 3814.

[32] W. Bonner, *Chirality* **2000**, *12*, 114; but see also the more general discussion and different point of view given by R. N. Zare, W. Bonner, P. Frank in *Chemistry for the 21st Century* (Eds.: E. Keinan, I. Schechter).

[33] M. Quack, *J. Mol. Struct.* **1995**, *347*, 245 – 266.

[34] R. Berger, M. Quack **2000**, unpublished results; R. Berger, M. Quack, G. Tschumper, *Helv. Chim. Acta.* **2000**, in press.

[35] T. Helgaker, H. J. Jensen, P. Jørgensen, J. Olsen, K. Ruud, H. Ågren, T. Andersen, K. L. Bak, V. Bakken, O. Christiansen, P. Dahle, E. K. Dalskov, T. Enevoldsen, B. Fernandez, H. Heiberg, H. Hettema, D. Jonsson, S. Kirpekar, R. Kobayashi, H. Koch, K. V. Mikkelsen, P. Norman, M. J. Packer, T. Saue, P. R. Taylor, O. Vahtras, *Dalton: An Electronic Structure Program*, release 1.0, **1997**.

Received: 20 April, 2000 [Z 38]

D- or L-Alanine: That Is the Question**

Jon K. Laerdahl,[a] Ralf Wesendrup,[a] and
Peter Schwerdtfeger*[a]

KEYWORDS:

ab initio calculations · amino acids · chirality

The chiral purity of biochemical monomers—only L-amino acids are present in proteins and D-sugars in the DNA and RNA of living organisms—is today accepted as an absolute necessity for the existence of life. Since the demonstration of the parity-violating properties of the electroweak interactions of the Standard Model, a link between the asymmetry of biochemistry and of the fundamental forces of nature has been intensively searched for.[1–6] Although observed more than a decade ago in atomic physics,[7] an unambiguous experimental demonstration to link the electroweak, parity-violating neutral currents to a breakdown in mirror symmetry has yet to be found in molecular physics or chemistry. However, a number of theoretical studies on the influence of weak neutral currents (exchange of virtual Z^0 bosons) in chiral molecules[8–20] demonstrate that the energy of the two enantiomers differ by a minute amount. This parity-violating energy difference, ΔE_{PV}, scales to the fifth power of the nuclear charge, Z, of the heaviest atom in the molecule.[8, 20] For the amino acids, these energy differences are of the order of 10^{-16} kJ mol^{-1}, which corresponds to an excess of 10^7 molecules of the more stable enantiomer in a single mole of the nominal racemate. Interestingly, all earlier studies on amino acids reported the naturally occurring L-form to be stabilized by weak neutral currents.[9–13, 18, 19, 21, 22]

It has been argued that this slight energetic preference and the corresponding excess of the more stable L-enantiomer may have been enhanced by an amplification mechanism,[5, 6, 23–25] to give a chiral environment in which life evolved. The choice of the L-form for naturally occurring amino acids would consequently be due to a universal, deterministic, and abiotic scenario as outlined by Bonner.[24] Although the accuracy of the earlier calculations has been questioned, the excellent agreement between the most recent theoretical studies on chiral model compounds[15–17, 20]—based on very different theoretical algorithms—can be taken as a demonstration that theory can currently reproduce the correct order of magnitude of ΔE_{PV} for small chiral molecules. Therefore, we decided to investigate the gas phase parity-violating energy shifts of the L-form of alanine by employing our newly developed, fully relativistic, ab initio method. Although we do not expect scalar relativistic effects to

---

[a] *Prof. Dr. P. Schwerdtfeger, Dr. J. K. Laerdahl, Dr. R. Wesendrup*
Department of Chemistry
University of Auckland
Private Bag 92019, Auckland (New Zealand)
Fax: (+64) 9-373-7422
E-mail: schwerd@ccu1.auckland.ac.nz

[**] *This work was supported by the Marsden Fund Wellington, the Royal Society of New Zealand, the Deutsche Forschungsgemeinschaft, and the Auckland University Research Committee.*

center located at the center of mass of the molecule. For geometry optimizations and for parity-violating potentials calculated at those geometries, we used the 6-31 ++ G** basis set. For consistency with earlier studies, we employed the 6-31G basis set when studying the effect of the rotation of the carboxylato groups on the parity-violating potentials. Reference geometrical parameters for these rigid rotations of the carboxylato groups were the crystal structure of the zwitterionic form, as used in previous studies,[11,12] and the L-alanine structure I, from an MP2 optimization employing the 6-31 ++ G** basis set. We adopted the labeling of the neutral forms of L-alanine from ref. [26].

[1] T. Lee, C. Yang, *Phys. Rev.* **1956**, *104*, 254 – 258.
[2] C. Wu, E. Ambler, R. Hayward, D. Hoppes, R. Hudson, *Phys. Rev.* **1957**, *105*, 1413 – 1415.
[3] Y. Yamagata, *J. Theor. Biol.* **1966**, *11*, 495.
[4] D. Rein, *J. Mol. Evol.* **1974**, *4*, 15 – 22.
[5] R. Hegstrom, D. Rein, P. Sandars, *J. Chem. Phys.* **1980**, *73*, 2329 – 2341.
[6] S. Mason, G. Tranter, *Mol. Phys.* **1984**, *53*, 1091 – 1111.
[7] S. Mason, *Nature* **1985**, *314*, 400 – 401.
[8] G. Tranter, A. MacDermott, *Chem. Phys. Lett.* **1986**, *130*, 120 – 122.
[9] M. Quack, *Angew. Chem.* **1989**, *101*, 588 – 604; *Angew. Chem. Int. Ed. Engl.* **1989**, *28*, 571 – 586.
[10] M. Quack, *Nova Acta Leopold. NF* **1999**, *81*, 137 – 173.
[11] A. Bakasov, T.-K. Ha, M. Quack in *Chemical Evolution: Physics of the Origin and Evolution of Life* (Eds.: J. Chela-Flores, F. Raulin), Kluwer Academic, Netherlands, **1996**, pp. 287 – 296.
[12] A. Bakasov, T.-K. Ha, M. Quack, *J. Chem. Phys.* **1998**, *109*, 7263 – 7285.
[13] P. Lazzeretti, R. Zanasi, *Chem. Phys. Lett.* **1997**, *279*, 349 – 354.
[14] R. Zanasi, P. Lazzeretti, *Chem. Phys. Lett.* **1998**, *286*, 240 – 242.
[15] R. Zanasi, P. Lazzaretti, A. Ligabue, A. Soncini in *Advances in BioChirality* (Eds.: G. Pályi, C. Zucchi), Elsevier, Amsterdam, **1999**, pp. 377 – 385.
[16] J. Laerdahl, P. Schwerdtfeger, *Phys. Rev. A* **1999**, *60*, 4439 – 4453.
[17] J. Laerdahl, R. Wesendrup, P. Schwerdtfeger, *ChemPhysChem* **2000**, *1*, 60 – 62.
[18] S. Glashow, *Nucl. Phys.* **1961**, *22*, 579 – 588.
[19] A. Salam in *Proceedings of the Eighth Nobel Symposium* (Ed.: N. Svartholm), Amkvist and Wiksell, Stockholm, **1968**, pp. 367 – 377.
[20] S. Weinberg, *Phys. Rev. Lett.* **1967**, *19*, 1264 – 1266.
[21] R. Berger, M. Quack in *Proc. 37th IUPAC Congress*, *Vol. 2*, GDCh, Berlin, **1999**, p. 518.
[22] R. Berger, M. Quack, *J. Chem. Phys.* **2000**, *112*, 3148 – 3158.
[23] S. Mason, G. Tranter, *Chem. Phys. Lett.* **1983**, *94*, 34 – 37.
[24] O. Kikuchi, H. Wang, *Bull. Chem. Soc. Jpn.* **1990**, *63*, 2751 – 2754.
[25] H. Kiyonaga, T. Yagi, K. Morihashi, O. Kikuchi, *JCPE J.* **1999**, *11*, 165 – 170.
[26] A. Császár, *J. Chem. Phys.* **1996**, *100*, 3541 – 3551.
[27] K. Mikkelsen, E. Dalgaard, P. Swanstrøm, *J. Phys. Chem.* **1987**, *91*, 3081 – 3092.
[28] K. Mikkelsen, H. Ågren, H. Jensen, T. Helgaker, *J. Chem. Phys.* **1988**, *89*, 3086 – 3095.
[29] P.-O. Åstrand, K. Mikkelsen, P. Jørgensen, K. Ruud, T. Helgaker, *J. Chem. Phys.* **1998**, *108*, 2528 – 2537.
[30] M. Quack, J. Stohner, *Phys. Rev. Lett.* **2000**, *84*, 3807 – 3810; M. Quack, J. Stohner, *Z. Phys. Chem.* **2000**, *214*, 679 – 703.
[31] J. Laerdahl, P. Schwerdtfeger, H. Quiney, *Phys. Rev. Lett.* **2000**, *84*, 3811 – 3814.
[32] W. Bonner, *Chirality* **2000**, *12*, 114; but see also the more general discussion and different point of view given by R. N. Zare, W. Bonner, P. Frank in *Chemistry for the 21st Century* (Eds.: E. Keinan, I. Schechter).
[33] M. Quack, *J. Mol. Struct.* **1995**, *347*, 245 – 266.
[34] R. Berger, M. Quack **2000**, unpublished results; R. Berger, M. Quack, G. Tschumper, *Helv. Chim. Acta.* **2000**, in press.
[35] T. Helgaker, H. J. Jensen, P. Jørgensen, J. Olsen, K. Ruud, H. Ågren, T. Andersen, K. L. Bak, V. Bakken, O. Christiansen, P. Dahle, E. K. Dalskov, T. Enevoldsen, B. Fernandez, H. Heiberg, H. Hettema, D. Jonsson, S. Kirpekar, R. Kobayashi, H. Koch, K. V. Mikkelsen, P. Norman, M. J. Packer, T. Saue, P. R. Taylor, O. Vahtras, *Dalton: An Electronic Structure Program*, release 1.0, **1997**.

Received: 20 April, 2000 [Z 38]

D- or L-Alanine: That Is the Question**

Jon K. Laerdahl,[a] Ralf Wesendrup,[a] and
Peter Schwerdtfeger*[a]

KEYWORDS:

ab initio calculations · amino acids · chirality

The chiral purity of biochemical monomers—only L-amino acids are present in proteins and D-sugars in the DNA and RNA of living organisms—is today accepted as an absolute necessity for the existence of life. Since the demonstration of the parity-violating properties of the electroweak interactions of the Standard Model, a link between the asymmetry of biochemistry and of the fundamental forces of nature has been intensively searched for.[1–6] Although observed more than a decade ago in atomic physics,[7] an unambiguous experimental demonstration to link the electroweak, parity-violating neutral currents to a breakdown in mirror symmetry has yet to be found in molecular physics or chemistry. However, a number of theoretical studies on the influence of weak neutral currents (exchange of virtual Z^0 bosons) in chiral molecules[8–20] demonstrate that the energy of the two enantiomers differ by a minute amount. This parity-violating energy difference, ΔE_{PV}, scales to the fifth power of the nuclear charge, Z, of the heaviest atom in the molecule.[8, 20] For the amino acids, these energy differences are of the order of 10^{-16} kJ mol^{-1}, which corresponds to an excess of 10^7 molecules of the more stable enantiomer in a single mole of the nominal racemate. Interestingly, all earlier studies on amino acids reported the naturally occurring L-form to be stabilized by weak neutral currents.[9–13, 18, 19, 21, 22]

It has been argued that this slight energetic preference and the corresponding excess of the more stable L-enantiomer may have been enhanced by an amplification mechanism,[5, 6, 23–25] to give a chiral environment in which life evolved. The choice of the L-form for naturally occurring amino acids would consequently be due to a universal, deterministic, and abiotic scenario as outlined by Bonner.[24] Although the accuracy of the earlier calculations has been questioned, the excellent agreement between the most recent theoretical studies on chiral model compounds[15–17, 20]—based on very different theoretical algorithms—can be taken as a demonstration that theory can currently reproduce the correct order of magnitude of ΔE_{PV} for small chiral molecules. Therefore, we decided to investigate the gas phase parity-violating energy shifts of the L-form of alanine by employing our newly developed, fully relativistic, ab initio method. Although we do not expect scalar relativistic effects to

---

[a] *Prof. Dr. P. Schwerdtfeger, Dr. J. K. Laerdahl, Dr. R. Wesendrup*
Department of Chemistry
University of Auckland
Private Bag 92019, Auckland (New Zealand)
Fax: (+64) 9-373-7422
E-mail: schwerd@ccu1.auckland.ac.nz

[**] *This work was supported by the Marsden Fund Wellington, the Royal Society of New Zealand, the Deutsche Forschungsgemeinschaft, and the Auckland University Research Committee.*

be important for the molecules studied here, the use of the fully relativistic approach to parity-violating effects is preferable, as the nonrelativistic methods used in earlier studies contain the "picture change" error.[20] Furthermore, the implementation of parity-violating effects into nonrelativistic program packages is far more complicated.

Due to the lack of accurate experimental gas-phase structures available for alanine conformers, we explored the molecular potential energy surface using gradient-corrected density functional theory and searched for the global and all local minima. In agreement with earlier studies,[26] 13 minima were found within an energy range of 26 kJ mol^{-1}. These minima are displayed in Figure 1 together with the calculated parity-violating energy shifts for each conformation. A detailed discussion of the errors and approximations in our procedure has been given earlier,[20] and we expect the calculated E_{PV} values to be of correct sign and order of magnitude.

In distinct contrast to earlier studies but supported by the recent findings of Berger and Quack,[27] a preference for one form of the enantiomeric pair is not evident. A negative E_{PV} indicates that the L-form is lower in energy as compared to the D-form, which means that for seven conformations the L-form is stabilized. Notably, for the global minimum and the remaining five conformers, the D-form is more stable. The parity-violating energy differences are of the order 10^{-16} kJ mol^{-1}, in fair agreement with earlier studies on zwitterionic alanine.[9–11, 15, 18, 19]

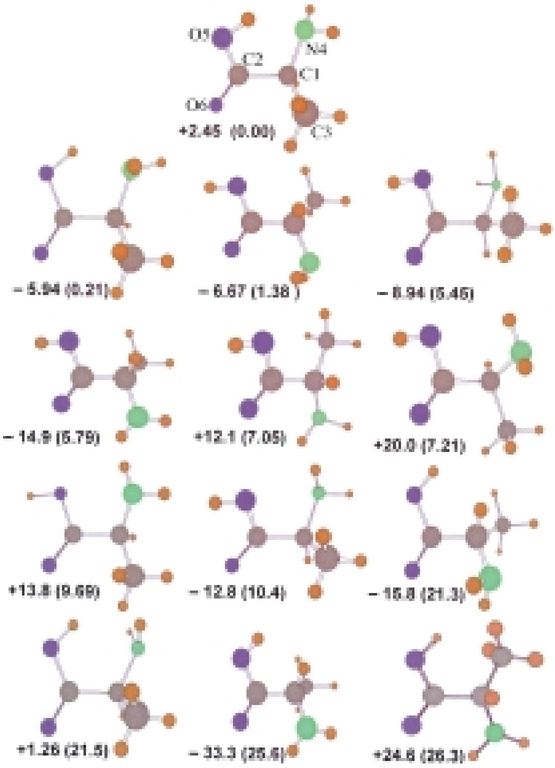

Figure 1. *Parity-violating energy shifts for gas-phase L-alanine. The calculated ab initio parity-violating energy shifts, E_{PV} (in 10^{-17} kJ mol^{-1}), are displayed for the 13 local minima on the molecular potential-energy surface. A negative value for E_{PV} indicates that, at the given conformation, the L-form of alanine is stabilized energetically by the parity-violating energy difference $\Delta E_{PV} = 2 E_{PV}$ relative to the D-form. The calculated density functional energies (in kJ mol^{-1}) relative to the global minimum (top structure) are also given in parentheses.*

We like to point out that all heavy atoms in alanine contribute to the molecular parity-violating energy difference and not, as one naively might assume, the asymmetric carbon atom alone (see Table 1). A related phenomenon was recently observed for the optical rotation of plane-polarized light by chiral molecules.[28]

Table 1. *Atomic contributions E^n_{PV} from nucleus n to the molecular parity-violating energy shift E_{PV} for the four lowest energy conformations of L-alanine, Min 1–4. All energies are given in 10^{-17} kJ mol^{-1}. The positions of the carbon (C1, C2, and C3), nitrogen (N4), and oxygen atoms (O5 and O6) are defined in Figure 1. Contributions from hydrogen atoms are negligible.*

	Min 1	Min 2	Min 3	Min 4
E^{C1}_{PV}	– 2.29	4.25	– 1.62	– 5.12
E^{C2}_{PV}	2.32	– 0.59	1.18	2.49
E^{C3}_{PV}	– 2.76	– 3.70	– 0.70	– 1.53
E^{N4}_{PV}	– 2.80	2.03	– 0.95	– 6.33
E^{O5}_{PV}	10.34	– 7.14	– 3.83	1.11
E^{O6}_{PV}	– 2.36	– 0.79	– 0.75	0.44
E_{PV}	2.45	– 5.94	– 6.67	– 8.94

For most of our calculated alanine structures, the oxygen atoms have the largest absolute value contributions to ΔE_{PV} due to the Z^5 scaling of the parity-violating matrix elements. The parity-violating energy shift is clearly a very complicated function of the molecular geometry. Small geometrical variation result in large and unpredictable changes in the value of E_{PV} and may easily induce a change of sign.

All, or at least most, of the structures in Figure 1 are readily available at the temperatures that are usually assumed to be required for living organisms. A decision on the relative *thermodynamical* stability of the enantiomers would therefore only be possible after a calculation (or at least a sampling of large portions) of the 33-dimensional potential energy surface of alanine and including parity-violating energy shifts. This is a formidable task and is not feasible even with state-of-the-art methods. We must therefore conclude that it currently cannot be determined if the L- or D-form of alanine is thermodynamically more stable in the gas phase. One might argue that the described gas phase results are of minor relevance for the origin of homochirality, since most likely the first amino acids on the prebiotic earth were as zwitterions dissolved in water. Indeed, the zwitterionic form has been addressed in all earlier calculations of parity-violating effects in natural amino acids.

For comparison, we performed calculations on zwitterionic L-alanine within the fully relativistic formalism at the geometries employed in the pioneering study of Tranter.[10] In agreement with Zanasi and Lazzeretti, we find that the results of Tranter were qualitatively correct but approximately an order of magnitude too small.[18, 22] These early results were interpreted as support for the preferred stability of the L-form in water, a conclusion also reached by Kikuchi and Wang.[13] However, we believe that studying only few selected zwitterionic structures is too simple a model to make a reliable estimate of the relative stability of the D- and L-forms. Dissolved alanine will be strongly perturbed by the hydration sphere, which modifies the geometry of the molecule and the electron density significantly.

The preferred geometry of alanine in water appears to be unknown, which might explain why quite different equilibrium structures were applied in the earlier studies.[10, 13] In order to make a simple test of the effects of solvation, we performed calculations with a single water molecule weakly bonded to the polar end of the alanine molecule. We obtain changes of ΔE_{PV} of 15% for alanine and a significant parity-violating energy shift for the water molecule (10% of alanine). Note also, that simply changing the nuclear charge of one oxygen atom by as little as 0.2 elementary charges in hydrogen peroxide (essentially a simple simulation of a small change in polarizability and charge density) changes the E^{n}_{PV} values for both oxygen atoms by approximately 10%. Since the atomic contributions E^{n}_{PV} can be much larger than the total effect, even small changes in the charge density in hydrated alanine could change the sign of E_{PV}. Furthermore, water molecules in the chiral hydration sphere of the alanine molecule will themselves have nonzero parity-violating energy shifts and provide an effect arising from the solvent shell that may be as large as that of the alanine molecule itself. As a consequence, a reliable prediction of the relative thermodynamic stability of the alanine enantiomers in water would have to accurately include the influence of the hydration sphere and of dynamic effects. Unfortunately, this is even more complicated than the gas phase approach and currently not theoretically accessible, although accurate calculations of solution effects in water have recently become possible for some model systems.[29, 30]

We conclude that the role of weak neutral currents for an explanation of biomolecular homochirality has still to be established. Our results suggest that single-point calculations, that include only selected structures of biomolecules, *cannot* solve this problem, irrespective of the level of theoretical accuracy. The main reasons for this are the flexible and highly dynamic structure of the biomolecules and the unknown effects of their environment. We like to point out that this conclusion is not restricted only to amino acids but probably applies to all theories involving chiral biomolecules. Nevertheless, weak neutral currents are now well established as a universal chiral force which, in the near future, may become observable experimentally.[31] It therefore remains possible that these forces are the source of the asymmetry of all living organisms, provided a reliable and reproducible amplification mechanism can be demonstrated. The Z^5 scaling of the parity-violating energy differences also implies that energy differences many orders of magnitude larger than those reported in this study are possible for chiral, biological molecules—provided these molecules contain heavier elements or are adsorbed to surfaces, for example, transition metal containing minerals, as found in hydrothermal vents.[32]

Computational Methods

All gas phase structures of alanine were optimized at the BLYP level and employed the ADF program suite and doubly polarized triple-zeta basis sets.[33] The enantiomeric energy difference due to parity-violating electroweak interactions (virtual Z^0 boson exchange between the electrons and the nuclei) is given in Equation (1), where Ψ_{DHF} is the Dirac-Hartree-Fock wave function, composed of the four component one-electron spinors ψ_i, H_{p} is the nuclear-spin independent parity-violating operator, and E^{n}_{PV} determines the contribution of nucleus n to the parity-violating energy shift E_{PV}.

$$\begin{aligned}\Delta E_{\mathrm{PV}} &= 2E_{\mathrm{PV}} = 2\sum_{n} E^{n}_{\mathrm{PV}} = 2\langle \Psi_{\mathrm{DHF}} | H_{\mathrm{p}} | \Psi_{\mathrm{DHF}} \rangle \\ &= \frac{G_F}{\sqrt{2}} \sum_{n} Q_{\mathrm{w},n} \sum_{i} \langle \psi_i | \gamma^5_i \rho_n(r_i) | \psi_i \rangle \end{aligned} \tag{1}$$

The Fermi electroweak coupling constant is $G_F = 1.166 \times 10^{-11}\,\mathrm{MeV}^{-2}$ ($= 5.835 \times 10^{-11}\,\mathrm{kJ\,mol^{-1}}$), γ^5 is the 4×4 pseudoscalar chirality operator, and the summation is over the electrons i and nuclei n. The normalized nucleon density is $\rho_n(r)$ and, for the weak nuclear charge we have employed $Q_{\mathrm{w},n} = -N_n$ for a nucleus with N_n neutrons. All calculations were performed with uncontracted cc-pVDZ + 3p basis sets[34] and the Dirac program.[35] A more detailed description of the computational methods has previously been given by the authors.[20]

[1] Y. Yamagata, *J. Theoret. Biol.* **1966**, *11*, 495.
[2] D. W. Rein, *J. Mol. Evol.* **1974**, *4*, 15.
[3] V. S. Letokhov, *Phys. Lett. A* **1975**, *53*, 275.
[4] S. F. Mason, *Nature* **1984**, *311*, 19.
[5] D. K. Kondepudi, G. W. Nelson, *Phys. Rev. Lett.* **1983**, *50*, 1023.
[6] D. K. Kondepudi, G. W. Nelson, *Nature* **1985**, *314*, 438.
[7] M.-A. Bouchiat, C. Bouchiat, *Rep. Prog. Phys.* **1997**, *60*, 1351.
[8] R. A. Hegstrom, D. W. Rein, P. G. H. Sandars, *J. Chem. Phys.* **1980**, *73*, 2329.
[9] S. F. Mason, G. E. Tranter, *Proc. R. Soc. London A* **1985**, *397*, 45.
[10] G. E. Tranter, *Mol. Phys.* **1985**, *56*, 825.
[11] G. E. Tranter, *Chem. Phys. Lett.* **1985**, *115*, 286.
[12] A. J. Macdermott, G. E. Tranter, *Croat. Chem. Acta* **1989**, *62*, 165.
[13] O. Kikuchi, H. Wang, *Bull. Chem. Soc. Jpn.* **1990**, *63*, 2751.
[14] H. Kiyonaga, K. Morihashi, O. Kikuchi, *J. Chem. Phys.* **1998**, *108*, 2041.
[15] A. Bakasov, T.-K. Ha, M. Quack, *J. Chem. Phys.* **1998**, *109*, 7263; A. Bakasov, T.-K. Ha, M. Quack, *J. Chem. Phys.* **1999**, *110*, 6081; A. Bakasov, T. K. Ha, M. Quack in *Chemical Evolution: Physics of the Origin and Evolution of Life* (Eds.: J. Chela-Flores, F. Raulin), Kluwer, Dordrecht, **1996**, p. 287.
[16] A. Bakasov, M. Quack, *Chem. Phys. Lett.* **1999**, *303*, 547.
[17] P. Lazzeretti, R. Zanasi, *Chem. Phys. Lett.* **1997**, *279*, 349.
[18] R. Zanasi, P. Lazzeretti, *Chem. Phys. Lett.* **1998**, *286*, 240.
[19] R. Zanasi, P. Lazzeretti, A. Ligabue, A. Soncini, *Phys. Rev. E* **1999**, *59*, 3382.
[20] J. K. Laerdahl, P. Schwerdtfeger, *Phys. Rev. A* **1999**, *60*, 4439.
[21] A. J. Macdermott, *Origins Life Evol. Biosphere* **1995**, *25*, 191.
[22] R. Zanasi, P. Lazzeretti, A. Ligabue, A. Soncini in *Advances in Biochirality* (Eds.: G. Pályi, C. Zucchi, L. Caglioti), Elsevier, Amsterdam, **1999**, p. 377.
[23] B. L. Feringa, R. A. van Delden, *Angew. Chem.* **1999**, *111*, 3624; *Angew. Chem. Int. Ed.* **1999**, *38*, 3418.
[24] W. A. Bonner, *Origins Life Evol. Biosphere* **1991**, *21*, 59.
[25] R. A. Hegstrom, D. K. Kondepudi, *Sci. Am.* **1990**, *262* (1), 98.
[26] A. G. Császár, *J. Phys. Chem.* **1996**, *100*, 3541, and references therein.
[27] R. Berger, M. Quack, *Chem. Phys. Chem.* **2000**, *1*, 57–60.
[28] R. K. Kondru, P. Wipf, D. N. Beratan, *Science* **1998**, *282*, 2247.
[29] D. Marx, M. E. Tuckerman, J. Hutter, M. Parrinello, *Nature* **1999**, *397*, 601.
[30] F. Brugé, M. Bernasconi, M. Parrinello, *J. Am. Chem. Soc.* **1999**, *121*, 10883.
[31] Ch. Daussy, T. Marrel, A. Amy-Klein, C. T. Nguyen, Ch. J. Borde, Ch. Chardonnet, *Phys. Rev. Lett.* **1999**, *83*, 1554.
[32] C. Huber, G. Wächtershäuser, *Science* **1998**, *281*, 670.
[33] *Amsterdam Density Functional* (ADF), Release 99, Vrije Universiteit Amsterdam, The Netherlands, **1999**.
[34] J. K. Laerdahl, P. Schwerdtfeger, H. M. Quiney, *Phys. Rev. Lett.* **2000**, 84, 3811.
[35] T. Saue, T. Enevoldsen, T. Helgaker, H. J. Aa. Jensen, J. K. Laerdahl, K. Ruud, J. Thyssen, L. Visscher, *Dirac: A Relativistic Ab Initio Electronic Structure Program*, Odense, Denmark, **1998**.

Received: March 27, 2000 [Z 39]

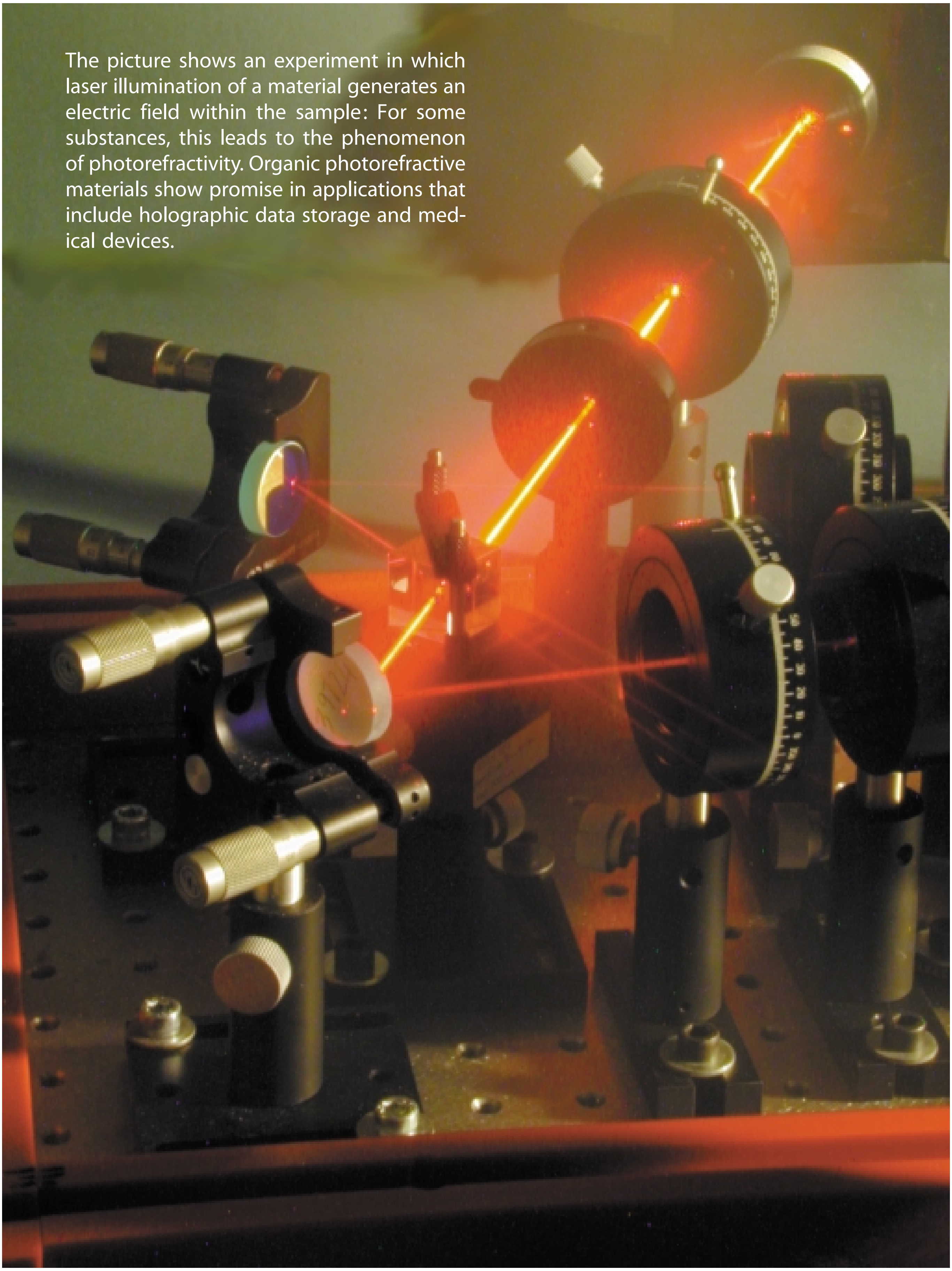

The picture shows an experiment in which laser illumination of a material generates an electric field within the sample: For some substances, this leads to the phenomenon of photorefractivity. Organic photorefractive materials show promise in applications that include holographic data storage and medical devices.

Materials Design and Physics of Organic Photorefractive Systems

Stephan J. Zilker*[a]

Photorefractivity is an intriguing phenomenon which, however, was initially perceived as a nuisance: Laser illumination generates large internal electric fields which, in turn, modify the optical properties of the material. Useful applications in holographic systems were soon recognized and photorefractivity was subsequently demonstrated in many different materials. These materials span from inorganic crystals to semiconductors, from organic liquid crystals to polymers. Nevertheless, nearly 25 years passed from the discovery of inorganic photorefractive materials in 1966 to reports of the first organic systems. This article reviews the rapid progress of organic photorefractive materials in the last decade and focuses on the different chemical concepts and pathways for further optimization. Advanced systems are required to move photorefractivity out of research laboratories into the market.

KEYWORDS:

chromophores · holography · nonlinear optics · photorefractive materials · polymers

1. Introduction

1.1. History of Photorefractivity—Inorganic Materials

Photorefractivity (PR; see Abbreviations and Glossary at the end of this review) was first discovered in 1966 by researchers at Bell Laboratories. The effect led to a strong beam deformation[†] in frequency doubling experiments in the inorganic crystals $LiNbO_3$ and $LiTaO_3$.[1] Potential, useful applications such as digital holographic data storage,[2] image processing,[3] optical pattern recognition,[2] holographic interferometry,[5] wavelength demultiplexing,[6] medical imaging,[7, 8] and other areas soon led to an intensive research effort. Until 1990, the PR effect had been exclusively observed in inorganic crystals[9] and, later, in semiconductor heterostructures.[10] Extensive experimental efforts led to detailed insights into the charge-transport processes in crystals and provided the basis for comprehensive theoretical modeling.[11] Detailed reviews of the methods, crystals, and models were published recently.[12, 13] In spite of this remarkable progress, there are still no commercial devices. This is, on the one hand, due to the difficulties of crystal growth, which mean high production costs, and, on the other hand, due to problems with regard to the reproducibility of the specimens. Semiconductor heterostructures provide fast response times yet their limited thickness (typically 1 μm)[14] allows only for optically thin gratings (Raman–Nath regime)[15] with low angular selectivity, resolution, and diffraction efficiency. Therefore, these structures are mainly suitable for adaptive transient holograms.[10]

1.2. The Development of Organic Materials

Organic photorefractive materials were first reported in 1990, when work on a doped organic crystal was published.[16, 17] However, dopants are often expelled during the growth process (zone refinement), thus specimens of high optical quality are difficult to produce and at least as costly as their inorganic counterparts.

Polymeric photorefractive materials, first reported in 1991,[18] are easy to prepare in high optical quality and, moreover, are comparatively cheap. Polymers are also known for their compositional flexibility, which permits the introduction of a variety of dopants in high concentration. Consequently, charge generation and transport properties as well as the optical characteristics can be tuned individually by incorporating the required functionalities for photorefractivity.

Firstly, a photoconductor (which is, in most cases, the polymer itself) provides the necessary charge transport properties. Secondly, a sensitizer is used in order to obtain charge generation in the wavelength region of interest. This can be either achieved by a charge transfer complex between the sensitizer and photoconductor, or by direct photoinjection into the excited state. Thirdly, the incorporated chromophores react to the internal space-charge field, to generate a refractive index modulation. This can occur due to the Pockels effect or by reorientation of the highly polar chromophores in the space-charge field (the electro-optical Kerr effect). The nonlinear-optical Pockels contribution is zero in isotropic media, thus the

---

[†] *The authors write in their introduction: "The effect, although interesting in its own right, is highly detrimental to the optics of nonlinear devices based on these crystals."*

[a] *Dr. S. J. Zilker[+]
Lehrstuhl Experimentalphysik IV
Universität Bayreuth
95440 Bayreuth (Germany)
E-mail: stephan.zilker@philips.com*

[+] *Current address:
Philips Research Labs
Prof. Holstlaan 4 (WA-14)
5656 AA Eindhoven (The Netherlands)
Fax: (+31) 40-2743352*

chromophores must be oriented in an external electric field, either before the experiment or in situ in the case of materials with low glass-transition temperatures. The Kerr contribution ("orientational enhancement") was discovered by Moerner et al. in 1994;[19] in many systems, more than 80% of the refractive index modulation arises from this linear-optical contribution.

1.3. Differences Between Organic and Inorganic Systems

The two main differences between polymers and inorganic crystals become apparent. Firstly, inorganic materials exhibit less compositional flexibility: Solely the dopant level can be varied, the optical nonlinearity—only present in the rather small class of noncentrosymmetric crystals—is given by the ionic polarizability of the host. Moreover, different sensitizers can be used to tune the writing wavelength over a wide region, that spans from 500 to 900 nm. This range, however, excludes the telecommunications band around 1550 nm, which is accessible to crystals.[20]

Secondly, polymers require an externally applied electric field E to allow for the efficient generation of the space-charge field. This field lowers the electron-hole binding energy and thereby facilitates the generation of free charge carriers. Furthermore, the carrier mobility increases strongly with E. Both effects together yield a field dependence of the photocurrent and, consequently, of the holographic response time.

Finally, a nonzero Pockels contribution can only be present in anisotropic media, realized by an alignment of the chromophores in the external field. The field dependence of nearly all characteristic parameters makes it difficult to apply theoretical descriptions which were developed for inorganic crystals. Thus, our understanding of organic materials is not yet as advanced.

Herein, this article will present recent developments in materials concepts and physics of organic photorefractive systems. A discussion of holographic characterization techniques will be followed by the different materials concepts. Then, two optimization pathways will be presented, based on investigations of the influence of the photoconducting properties and of the chromophores on system performance. The article will close with an overview of potential applications and a summary and outlook. Emphasis will be laid on developments starting in or after 1997. For a detailed description of earlier work, refer to previous review articles.[21–26]

Stephan J. Zilker was born in 1970 and received his Master of Science degree in physics from the University of Delaware, USA, in 1994. In 1997 he earned his PhD in physics with Dietrich Haarer at the University of Bayreuth in Germany. In 1997 became a research scientist at Bayreuth University, heading a group which is working on holographic storage materials. His research interests are orientation and surface gratings in azobenzene copolymers and organic photorefactive materials. Since June 2000, he is a senior research scientist at Philips Natuurkundig Laboratorium in Einhoven, the Netherlands. His current work focuses on polymer electronics.

Figure 1 shows the principle of the photorefractive effect (from top to bottom). Two interfering laser beams create a spatial light intensity modulation $P(x)$.

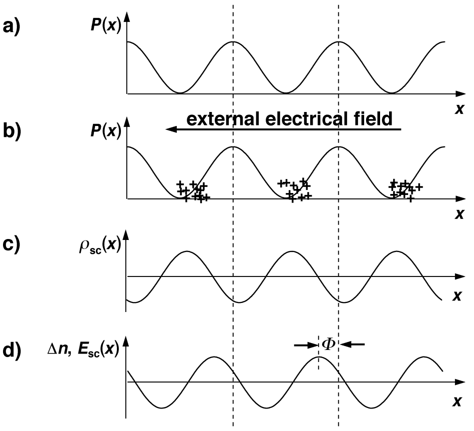

Figure 1. Principle of the photorefractive effect. a) Spatial intensity $P(x)$ *of the two writing beams. b) Generation and drift of the charge carriers. c) The resulting space-charge distribution* $\rho(x)$*. d) The space-charge field* $E_{sc}(x)$ *and refractive index modulation* $\Delta n(x)$*.*

In the bright areas of $P(x)$, free positive charge carriers (holes) are generated by excitation of the sensitizer. Most organic PR materials are hole conductors, therefore the electrons are immobile (however, there have also been reports on electron-conducting systems).[27] Subsequently, the holes drift in the external electric field until they are trapped.[†] A space-charge distribution $\rho(x)$ arises, in which the holes are located predominantly in the minima of $P(x)$. The electrons remain immobile in the bright areas. This space-charge field $E_{sc}(x)$ leads to a refractive index modulation $\Delta n_P(x)$ due to the electro-optical (Pockels) effect, Equation (1). The term r_e is the effective electro-optic coefficient.

$$\Delta n_P(x) = -\frac{1}{2} n^3 r_e E_{sc}(x) \tag{1}$$

Furthermore, the chromophores may reorient under the influence of the space-charge field, to lead to a linear-optical contribution to $\Delta n_K(x)$ due to the electro-optical Kerr effect, Equation (2). The term r_K is the effective Kerr susceptibility.

$$\Delta n_K(x) = \frac{3}{2n} r_K E^2 \tag{2}$$

Due to the hole transport, there is a phase shift ϕ between the light intensity grating and the resulting refractive index modulation. This nonlocal nature of the index grating is a unique feature of the photorefractive effect and distinguishes it from other local grating mechanisms such as, for example, photochromism[28] and thermochromism.[29] The shift gives rise to an energy transfer between the two writing beams, called asymmetric two-beam coupling. The presence of the latter is a commonly accepted proof of photorefractivity for a given material.[30]

[†] *In contrast, charge diffusion is the dominant mechanism in inorganic crystals and organic liquid crystals where the applied electric fields are small.*

2. Experimental and Chemical Approaches

2.1. Holographic Techniques

The two most common holographic techniques are degenerate four-wave mixing (DFWM) and two-beam coupling (2BC). Both experiments can be performed in a common set-up, as depicted in Figure 2.

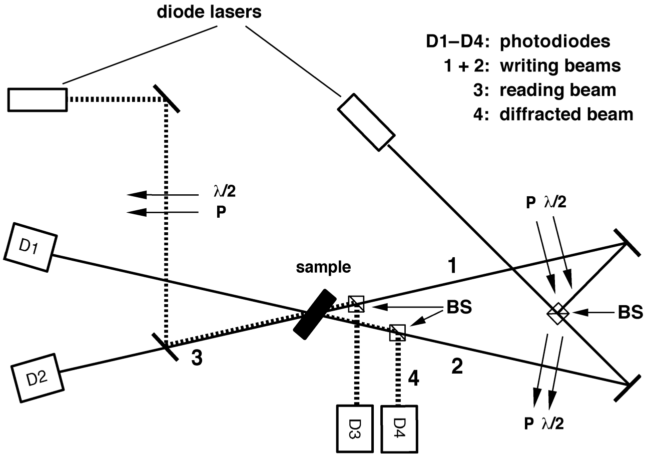

Figure 2. Holographic experiment used for DFWM and 2BC studies. The reading beam (3) counterpropagates one of the writing beams. Its transmitted and diffracted components (4) are detected by photodiodes (D3, D4). P denotes a polarizer, BS a beam splitter, and λ/2 represents a half-wave plate.

Two coherent laser beams intersect at an angle θ in the sample. The latter is tilted by an angle Ψ with respect to the symmetry axis of the writing beams, in order to yield an electric-field component E_p parallel to the grating vector and to break the centrosymmetry. The typical sample geometry is depicted in Figure 3.

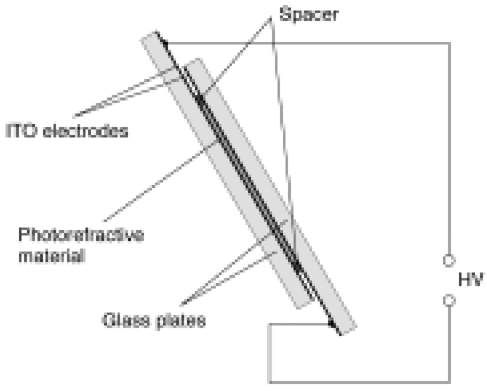

Figure 3. Typical sample geometry for an organic photorefractive material. HV is a high voltage supply.

The material is usually sandwiched between two glass plates which are coated with transparent indium-tin oxide (ITO) electrodes so that an electric field can be applied. Typical sample thicknesses vary between 25 and 100 μm and the electric field strengths are between 40 and 100 $\mathrm{V\,\mu m^{-1}}$ in amorphous organic materials and about 1 $\mathrm{V\,\mu m^{-1}}$ in liquid crystalline materials.

In a degenerate DFWM experiment, a grating is written by the two writing beams and is simultaneously probed by a weak counterpropagating reading beam of the same wavelength, which is diffracted off the grating. The diffraction efficiency η, the ratio between the power of the incident and diffracted light, is then given by Equation (3), in which λ is the wavelength in the material, and L the effective interaction length given by $d/(\cos\Theta\cos\Theta)^{1/2}$. Here, d denotes the sample thickness. $\hat{e}_1$, $\hat{e}_2$ are the unit vectors along the electric field strength of the incident and the diffracted beams, and Θ_1, Θ_2 are their internal angles.

$$\eta = \sin^2\left(\frac{\pi \Delta n L}{\lambda}\hat{e}_1\hat{e}_2\right) \qquad (3)$$

Usually, the writing beams are s-polarized (to yield lower coupling between them), whereas the reading beam is p-polarized in order to probe the maximum Δn value, obtained parallel to the poling field.

DFWM is mainly used to evaluate the rise time τ of the hologram formation and the achievable refractive index modulation Δn. Rise time determination has some ambiguity, since different recording schemes and evaluation methods may be used. Meerholz and co-workers have shown that there is a remarkable difference in its speed, depending on whether both writing beams are switched on simultaneously or consecutively (see Figure 4).[31]

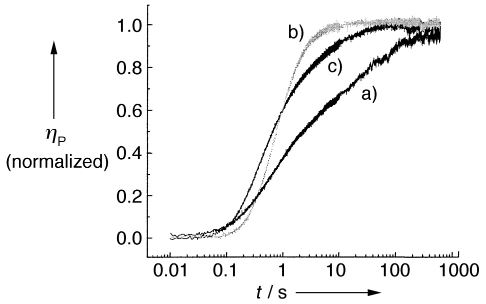

Figure 4. Holographic growth curve of a polyvinylcarbazole-based composite for three experimental conditions. a) Both writing beams are incident on the sample and the field is switched on. b) The field was on and the device was illuminated by one writing beam. The second beam is switched on 30 min later. c) The electric field was on and both writing beams are switched on. All curves are normalized to their value at 600 s. The figure is adapted from Mecher et al.[31]

Most research groups choose the second option because it is faster; the electric field is thereby applied before writing. The usual incident writing intensity for speed determination is 1 $\mathrm{W\,cm^2}$. This still leaves some ambiguity, since the light intensity absorbed by the sensitzer is the real characteristic parameter. Furthermore, there is a debate about how to correctly evaluate the rise time. In most materials, the dynamics of grating formation is rather complex.[31, 32] Moreover, only tentative theoretical descriptions are available.[33, 34] Thus, different analytical functions are used, ranging from single-[35] and double-exponential,[31, 32, 36] and to stretched exponential[37] fits. This is often motivated by assuming that the first time constant τ_1 describes the build-up of the space-charge field, whereas at later times chromophore reorientation and other effects dominate. In many cases, one must also introduce a cut-off at longer time scales, on which the fits deviate significantly from the experimental results.[31, 32] Recent work[32] uses an inverse Laplace transform which does not require any a priori assumptions about the number of processes (such as exponential fits) involved in the grating formation, since the algorithm performs the fit with the smallest possible number of free parameters. Therefore, the inverse Laplace transform analysis might yield new insight into the dynamics of grating formation.

In a two-beam coupling experiment,[30] a separate probe beam is not required. Instead, two photodiodes monitor the intensities P_1 and P_2 of the transmitted writing beams. When the electric field is switched on, there is an energy transfer between both beams. When a steady state has been reached, the grating is quickly shifted with respect to the intensity pattern by moving the sample with a piezo transducer (see Figure 5).

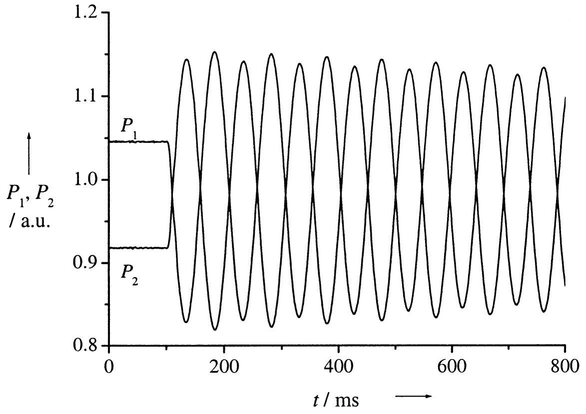

Figure 5. Two-beam coupling curve depicting the transmitted writing beam intensities P$_1$ *and* P$_2$ *(given in arbitary units). In the beginning, there is a steady-state energy transfer between the two beams. The grating is then translated by moving the sample with a piezo transducer. One observes oscillations of the energy transfer, which depend on the momentary phase shift between light intensity pattern and refractive index grating.*

During the shift, one observes oscillations of the direction of energy transfer between the two beams—depending on the momentary phase shift ϕ between the light and refractive index grating. Apart from ϕ, one can also determine the contributions of the phase and of an eventual absorption grating to the refractive index modulation. From the steady state behavior, the optical gain coefficient Γ can be evaluated, see Equation (4), which is a quantitative measure for the energy transfer. The parameter Θ is the angle between the writing beams and β_P the power ratio of the two writing beams in front of the sample, while γ_0 represents the ratio of the beam intensities behind the sample.

$$\Gamma = \frac{1}{d/\cos\Theta}[\ln(\gamma_0\beta_P) - \ln(\beta_P + 1 - \gamma_0)] \tag{4}$$

Each beam is measured while the other beam is blocked. In amorphous organic materials, Γ (as usually measured for p-polarized beams) reaches values up to 200–300 cm^{-1},[37–39] nearly ten times larger than in inorganic crystals (10–40 cm^{-1}).[9] In liquid crystals, even gains of up to 600 cm^{-1} have been reported.[40, 41] However, the transferred total power is proportional to $\exp(\Gamma d)$. The sample thickness d is limited by the required voltages to around 200 μm in organic materials, whereas in inorganic crystals it can reach 1 cm. Consequently, image amplification by factors of up to 10^5 has been demonstrated in crystals.[42, 43] In organic systems, Moerner et al.[44] used a moving grating technique, by which the space-charge field is resonantly enhanced when the interference pattern is moved over the sample at its eigenfrequency.[45] The result is a net amplification of a weak signal beam by a factor of 500 in intensity, through the use of a stack of three samples, as compared to about fourfold amplification with a steady-state grating.

In some references, 2BC dynamics was used to evaluate the response time of the material,[37, 46] since it is a characteristic measure for applications based on 2BC. This procedure, however, is not suited for a comparison with other materials, because 2BC dynamics are governed by both the evolution of the phase and of the refractive index modulation Δn, whereas fast DFWM dynamics are only sensitive to the latter, which allows for an easier interpretation of the underlying physical processes.

2.2. Chemical Approaches

Starting from organic crystals, a variety of different materials concepts have been developed. They can be either classified according to their chemical composition (host–guest polymers, liquid crystals, organic glasses, and so forth) or by the underlying concept: Low T_g materials aim at high orientational enhancement or high T_g systems optimized for a fast, purely electronic, Pockels contribution. The present Section focuses on a comprehensive overview, to include characteristic examples, and on a comparison of the performance in terms of response time, gain, and shelf lifetime.

2.2.1. Host–Guest Polymers

Photorefractive host–guest polymers were first reported in 1991 and still represent the most active area of organic photorefractive research. This is due to the compositional flexibility and the ease of fabrication. In the first study,[18] a nonlinear-optical polymer was doped with a charge transport agent, a sensitizer, and a chromophore, to provide the necessary functionalities for photorefractivity. Most of the recently introduced systems use photoconductive polymers as hosts, which are readily available owing to intense work on photoreceptors and light-emitting diodes. Thus, the amount of inert material which does not participate in charge transport can be reduced. Typical photoconductors are depicted in Scheme 1 and their hole mobilities are given in Table 1.

Polyvinylcarbazole (PVK) is the most common material; a review on carbazole-containing systems has been published recently.[47] The first high performance PR material with high gain and refractive index modulation was a PVK system doped with the chromophore DMNPAA (Scheme 4), the plasticizer ECZ, and a small amount of sensitizer (TNF).[48] The disadvantages of PVK are the relatively poor photoconductivity[49] and the high glass transition temperature ($T_g = 200\,°C$). Therefore, a plasticizing

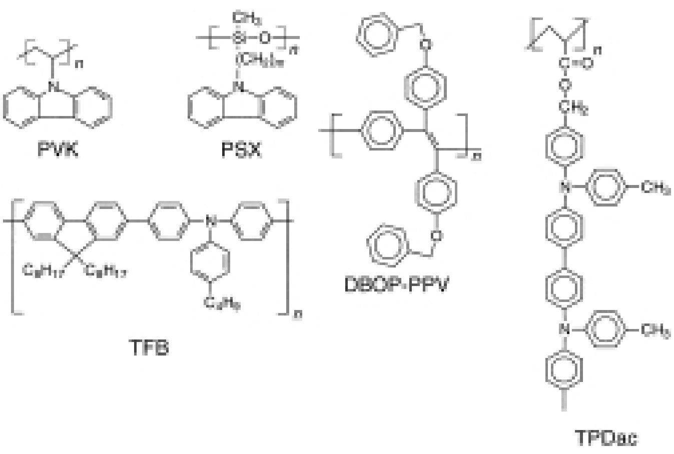

Scheme 1. Five typical photoconducting polymers used as host material for photorefractive systems: PVK, PSX, DBOP-PPV,[50] TPDac polymer,[49] and TFB.[32]

Table 1. Mobilities of organic photoconductors μ in their pure state and in a typical photorefractive composite (n.a.: not applicable).

Material	μ in pure state $[\mathrm{cm^2V^{-1}s^{-}}]$	μ in PR system $[\mathrm{cm^2V^{-1}s^{-}}]$
PVK	10^{-6}[109]	unknown
PSX	10^{-6}[157]	10^{-8}[a][158]
DBOP-PPV	10^{-5}[159]	unknown
TFB	10^{-3}[160]	10^{-5}[32]
TPDac[49]	10^{-4}	10^{-5}
DR1-DCTA[64]	n.a.	10^{-6}
LC[78]	n.a.	10^{-7}

[a] Determined by holographic time-of-flight.

agent such as the PVK-monomer ECZ was required to lower the T_g to room temperature. This allows for both orientational enhancement of the refractive index modulation and in situ poling of the chromophores by the applied electric field. Depending on the chromophore, its content, and the choice of plasticizer, most PVK systems yield response times between 4 and 100 ms (see Figure 6).

Polysiloxanes with pendant carbazolyl groups (PSX; Scheme 1) allow T_g to be tuned by varying the spacer length, thus eliminating the need of a separate plasticizer. However, the PSX materials thus far reported have a relatively slow holographic response (500 ms).[38]

High performance hole-conducting polymers—as usually employed in organic light-emitting diodes—provide higher photoconductivity. Among them are poly(phenylenevinylene) (PPV) derivatives such as DBOP-PPV,[50] acrylates with tetraphenyldiaminobiphenyl[49] units in the monomer (TPDac), and polyfluorenes, of which TFB is an example,[32] is shown in Scheme 1. A TFB-based host–guest system is also currently the fastest organic PR material (see Figure 6);[32] yet it is remarkable that the large difference in mobility of more than two orders of magnitude between PVK and TFB composites only corresponds to a holographic response of TFB that is four times faster (1[32] versus 4 ms[36]).

Host–guest systems demonstrate the best photorefractive performance, which reaches refractive index modulations of up to $\Delta n = 10^{-2}$[38, 51] and response times down to 1 ms (see also Figure 6).[32, 36, 46] A significant disadvantage, however, is their lack of compositional stability: The highly polar chromophores, which are mobile in low T_g systems, tend to crystallize over a time span between hours and a couple of months in the apolar photoconductive host material.[52, 53] Therefore, the issue of limited shelf lifetime has to be addressed, for example by using eutectic[53] and isomeric[54] dye mixtures or by improving the compatibility of the components.[55, 56] By these methods, shelf lifetimes on the order of several years have been achieved.[57] However, each new host–guest system requires the elaboration of a suitable composition which might involve the time-consuming synthesis of corresponding isomers. This is the motivation for alternative chemical concepts, such as monolithic materials.

2.2.2. Fully Functionalized Polymers

A synthetic method to increase phase stability is the use of functionalized systems: The polar chromophore is covalently attached to the polymer backbone, which is itself either a photoconductor[58] or is functionalized with photoconducting moieties.[59–61] Typical examples for both classes are depicted in Scheme 2.

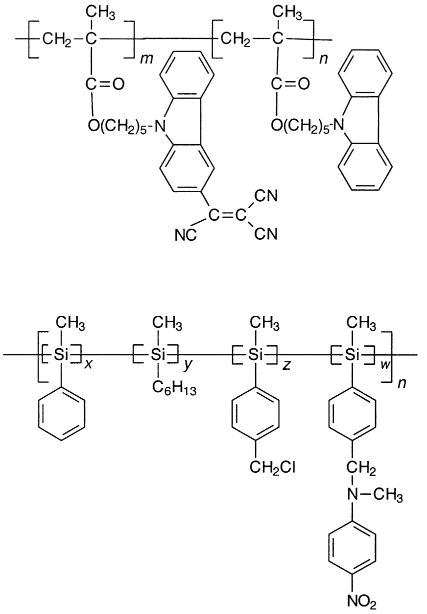

Scheme 2. Fully functionalized photorefractive materials. The upper system is a carbazole-tricyanovinylcarbazole polymer[60] (an inert methacrylate chain functionalized with photoconductive and electro-optic side groups) whereas the lower structure shows a polysilane system in which the main chain serves as the photoconductor.[58]

Most fully functionalized polymers (FFPs) have glass transition temperatures which are higher than room temperature (up to 50 °C), so that orientational enhancement plays only a reduced role. Furthermore, the material is isotropic after its preparation and would yield no electro-optic response—and thereby no PR effect at all. Therefore, electrical poling above its T_g has to be performed first. The smaller contribution of orientational enhancement was initially viewed as an advantage of FFPs, since chromophore reorientation was considered to be slow. Therefore, it was thought to limit the holographic response of host–guest materials. High T_g materials, based purely on the electronic Pockels effect, were consequently considered to be faster. However, two important new results have to be considered: Kippelen and co-workers reported on the orientational mobility of molecular-doped chromophores in a host–guest polymer ($T_g = 39\,^{\circ}C$) and obtained a time constant of about 500 µs.[36] Thus, orientational enhancement in host–guest systems can indeed occur on rapid time scales. Secondly, FFPs demonstrate slow grating dynamics, on the order of 200 ms or longer, and are limited by the slow build-up of the space-charge field.[61] Furthermore, the refractive index modulations and the two-beam coupling gains were low. The slow response arises from the poor photoconductivity. This is due to the direct covalent attachment of polar chromophores to the photoconductor (or to the backbone) but only poor hole conductors have been incorporated. Consequently, fully functionalized polymers have not yet fulfilled the high expectations which were connected with their development.

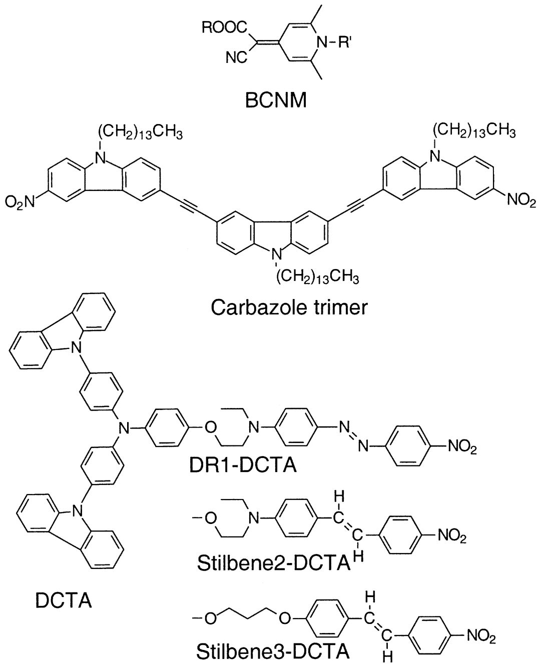

Scheme 3. *Amorphous low molecular weight glasses. From top to bottom: BCNM (R, R' = methyl or ethyl(hexyl) groups), carbazole trimer, and DCTA glasses with three different chromophores.*

2.2.3. Low Molecular Mass Glasses

A low molecular mass material, in which the chromophore forms a stable amorphous phase (with T_g around room temperature), yields high compositional stability but still exhibits sufficiently low viscosity to allow chromophore reorientation. Such a system was first introduced by Lundquist et al.[62] in 1996. It is based on the bifunctional chromophore BCNM (depicted in Scheme 3) which also exhibits photoconductivity.

BCNM was doped with 10% poly(methyl methacrylate) and 0.3% of TNF was added as a sensitizer. The result was a high Δn, 10^{-2}, and an extraordinarily low scattering efficiency of about 10^{-4}. The poor photoconductivity still limited the response time to about 80 s. Wang et al. introduced a second concept, in which the glass-forming component is a bifunctional carbazole oligomer to provide both photoconductivity and nonlinear-optical response (Scheme 3).[63] Response times below 1 s were first obtained for DR1-DCTA, composed of a high performance photoconductor covalently attached to a chromophore (see Scheme 3).[64] However, 28 wt% of plasticizer is required in order to achieve a T_g close to room temperature. The response time, initially 30 ms,[64] can be pushed down to 2.5 ms with the use of an optimized plasticizer and a high Δn of 6×10^{-3} was obtained.[65, 66] Furthermore, shelf lifetimes of nearly two years have been reported.[65]

Thus, low molecular weight glasses show promise for further development; nevertheless, systematic variations of the chromophore and the photoconductor require extensive synthetic efforts.

2.2.4. Liquid Crystals

One of the limitations of organic photorefractive materials is the need for relatively high external electric fields, on the order of about 50 V µm. Nematic liquid crystals (LCs) with low molecular masses, in contrast, can be easily switched with field strengths of about a volt per micrometer,[67] for example, in LC displays. Thus, LCs can be used as low voltage photorefractive materials, provided that a sufficient photoconductivity can be obtained. The first materials, reported in 1994,[68, 69] consisted of a low molecular mass liquid crystal (LLC), pentylcyanobiphenyl (5CB), which was doped with a photoionizable dye, such as, among others, rhodamine 6G. The photocurrent arises mainly from diffusion of the low molecular mass cations and anions, both having different, but low, mobilities. Drift lengths of ions are too small to generate a sizable contribution to the photocurrent.[70] In spite of the diffusion mechanism, a weak external electric field E must still be applied for two reasons: Firstly, the reorientation in nematic LLCs is dominated by a strong quadratic effect ($\delta\varepsilon \sim E^2$, in which $\delta\varepsilon$ is the modulation of the dielectric constant), that would form a grating with twice the frequency of the incident intensity pattern. Secondly, an external field also enhances the obtained degree of orientation [Eq. (5)], with E_{sc} being the magnitude of the space-charge field and Λ the grating period.[71]

$$\delta\varepsilon \propto E E_{sc} \cos(\Lambda x) \qquad (5)$$

Due to the low photoconductivity, the response times were initially on the order of seconds (see ref. [72], and references therein). Moreover, the systems provided only poor spatial resolution, since the elastic energy associated with distortions of the optical axis (namely, the director) increases strongly with fringe spacings smaller than approximately 10 µm. In order to improve the resolution, the continuity of the LC phase must be broken.

Polymer-stabilized LCs exhibit an anisotropic gel-like phase, in which the liquid crystal can be oriented.[73] Photorefractive polymer-dispersed liquid crystals (PDLCs) have small LC domains embedded in a polymer host.[74, 75] Therefore, the elastic energy problem can be avoided, since the LC islands are randomly oriented. Furthermore, photoconducting polymers can be used as host materials, thus increasing the photoelectric and, consequently, the holographic speed.[74] However, domain sizes on the order of the writing wavelength lead to strong scattering and, hence, to poor optical quality. The isolated LC domains also require higher switching voltages (several volts per micrometer). An alternative way is to dope high molecular mass LCs (HLCs), for example liquid-crystalline side-chain polymers,[76] into the LLC. Only the LLC ions are mobile and can contribute to the charge transport. However, the high viscosity of the HLC decreases the orientational mobility and, thus, limits the response time. Recently, Ono et al.[77] showed that HLCs with a lower molecular weight (and therefore lower viscosity) lead to a strong decrease of the holographic response time, to reach values down to 15 ms at field strengths of only 0.2 V µm^{-1}. At the same time, the two-beam coupling gain still exceeded 200 cm^{-1}, so that this material is among the fastest organic systems available (see Figure 6). Further speed enhancement is clearly possible because the ion mobilities are still rather low (10^{-7} cm^{2}V^{-1}s^{-1} or less) and the difference between anion and cation mobility is also small.[24, 78] Consequently, the space-charge field is about two orders of magnitude smaller than in amorphous systems,[79] so that refractive index modulations as high as those in electrically switched LCs have not yet been achieved (see Table 2).

Table 2. *Comparison of mechanisms and performance of three types of photorefractive materials. The values given reflect the highest performance achieved and, thus, all of the listed properties may not be realized in one given material.*

	Inorganic crystalline	Organic amorphous	Organic liquid crystalline
Mechanism	Pockels	Kerr + Pockels	Kerr
Δn	10^{-4} [9]	10^{-2} [38, 62]	10^{-2} [79]
τ [ms]	10^{3} [9]	1[32]	15[77]
Γ [cm^{-1}]	40[9]	280[39]	600[40]
d [cm]	1	0.02	0.005
E [V µm]	0	10 – 100	0.1 – 1

2.2.5. Other Concepts

There are many more materials concepts which have been realized. Sol – gel systems[80, 81] are motivated by phase stability arguments similar to those for FFPs. Furthermore, they provide higher poling stabilities of the nonlinear-optical chromophores. This was confirmed by a recent publication.[82] The gains exceed 200 cm^{-1} but the poor photoconductivity of the carbazole-doped silica host leads to holographic response times on the order of tens of seconds.[82]

Organic – inorganic nanocomposites make use of the efficient photosensitizing properties of inorganic nanoparticles which are employed, for example in organic solar cells. They reach internal quantum efficiencies for charge-carrier generation on the order of 90 %,[83] about ten times higher than typical C_{60}:photoconductor charge transfer complexes.[64, 84] Furthermore, their optical band-gap is blue shifted with decreasing particle size (the quantum size effect)[85] which allows tuning of the spectral sensitivity.

However, the nanoparticle clusters of solar cells exhibit high optical scattering. This must be prevented in PR materials while maintaining a high solubility of the individual particles in the polymer. Prasad and co-workers[86] used CdS particles which were covered with an organic coating and then embedded in a PVK host. While higher photocurrents even than in PVK:C_{60} composites were achieved,[87] the holographic response times were slow ($\tau = 7$ s).[86] The authors argue that this may be due to the higher dielectric constant of the material—which diminishes the space-charge field—and to a lower trap density. Moerner and co-workers showed that C_{60}^{-} ions strongly increase the number of active traps in PVK:C_{60}, which leads to an increased space-charge field.[88] This effect may be absent in the PVK:CdS systems.

2.3. Qualitative Comparisons

Table 2 summarizes the main mechanisms and the performance of three types of photorefractive systems, inorganic crystals, organic amorphous systems, and organic liquid crystals, which are the three basic types in use.

The organic amorphous systems exhibit the best dynamics due to their high photoconductivity. Their refractive index modulations and gains are comparable to, or slightly lower than, those of LC systems. Inorganic crystals have high sample thicknesses, which allow for efficient beam amplification and high Bragg selectivity in holographic storage or wavelength demultiplexing. Table 2 shows the highest values which have been reached for each parameter—which has not necessarily been achieved in the same material. Therefore, Figure 6 shows the actual performance of selected organic systems from 1997—

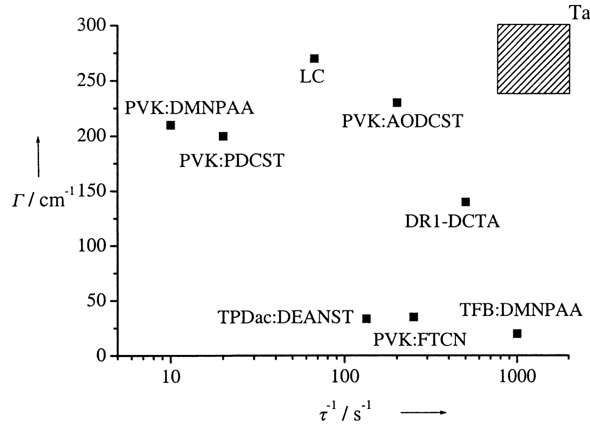

Figure 6. *Performance characteristics of organic photorefractive materials in terms of holographic speed τ^{-1} and optical gain Γ at a power density of 1 W cm^{-2}. The systems are the amorphous glass DR1-DCTA[65] and the fastest liquid crystal reported so far.[77] The host – guest systems depicted are PVK composites with the chromophores AODCST,[55] DMNPAA,[48] FTCN,[36] and PDCST,[37] a polyfluorene (TFB),[32] and TPDac.[49]*

which exhibited the best performance at the time of their publication—in terms of optical gain Γ (unfortunately, refractive index modulations were not published for all materials) and holographic speed τ^{-1} at a fixed light intensity. As a reference, the first high performance polymer, PVK:DMNPAA, is also given.[48]

Video rates have been accessible since 1998, which opens up new perspectives for organic PR systems. However, there is a trend that faster materials tend to exhibit lower gains (and also lower refractive index modulations). This may be due to the use of low-performance chromophores, such as DMNPAA, in these fast materials. Further experiments are needed to clarify this point.

3. Recent Trends in Materials Physics

Figure 6 reflects the recent research activities towards faster materials. In many cases, distinct improvements in the response time were achieved by varying the chromophore (compare the different PVK materials). It is obvious that a change of the chromophore will affect the maximum value of Δn because the electronic properties (polarizability anisotropy, electro-optic coefficient) and the reorientational mobilities are different. The first part of this Section will concentrate on this effect. It is much more intriguing, however, that the choice of the chromophore also strongly affects the holographic response time τ_1 of the material. Investigations of the charge transport properties will therefore conclude the discussion.

3.1. Optimizing the Refractive Index Modulation

Apart from the nonlinear-optical Pockels effect, there is an electro-optical Kerr contribution to Δn, which arises from the reorientation of the chromophores (orientational enhancement) in the internal space-charge field and which accounts in some cases for more than 80 % of Δn.[48] Thus, a suitable figure-of-merit F, which characterizes the efficiency of the chromophore dopants with respect to the maximum Δn, must include both effects. F is given by Equation (6), in which μ_D is the dipole moment, $\Delta\alpha_p$ the difference of the first-order polarizability α parallel and perpendicular to the molecular axis (polarizability anisotropy), β represents the second-order polarizability along the axis of the dipole moment, and M the molar mass.[89]

$$F = \frac{9\mu_D\beta + 2\mu_D^2\Delta\alpha_p/(kT)}{M} \tag{6}$$

The first part of the numerator of [Eq. (6)] corresponds to the electro-optic (EO) contribution, whereas the second part is related to birefringence.

Structure–property relationships for α_p and β have already been developed.[89, 90] It is not possible to maximize both contributions simultaneously,[89] since, in the framework of an electronic two-level model, $\Delta\alpha_p$ reaches a maximum when β vanishes.[91] The magnitudes of the maximum contributions of both effects, however, differ by nearly two orders of magnitude,[89, 92] with the EO effect being the minor one. Consequently, chromophores optimized for orientational enhancement (maximum $\mu_D^2\Delta\alpha_p$) have the best figure-of-merit F[93–95]—which represents a change in the direction of research initially aiming at efficient EO chromophores.

The new molecules are close to the "cyanine limit" (present in symmetrical cyanines) where the neutral and the zwitterionic wave functions contribute equally to the ground and excited state. Hence, the change of the static dipole moment on excitation will be zero, whereas the transition dipole moment is at its maximum. Geometry changes upon excitation are small, leading to short Franck–Condon progressions and sharp optical absorption spectra. The standard azo-chromophore DMNPAA and four optimized chromophores are presented in Scheme 4.

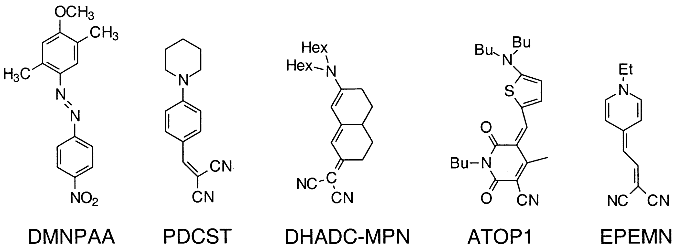

Scheme 4. *Chromophores for photorefractive applications. DMNPAA is a standard system with a low figure-of-merit (F = 0.2), whereas PDCST (F = 0.5), DHADC-MPN (F = 0.6), ATOP1 (F = 1.4), and EPEMN (F = 3.1) are more optimal dyes. The unit of F is $10^{-74}\,C^2V^{-2}m^4kg^{-1}mol$; the values are taken from Wortmann et al.[93]*

It was shown that increasing F significantly lowers the external electric field necessary to reach a certain diffraction efficiency (for the same polymer host material).[57, 96] It is interesting to note that chromophores with high F do not warrant large Δn, as they do not yet surpass the best, low F, DMNPAA composite in this respect.[38] The figure-of-merit values do not consider the actual degree of orientation achieved in a composite, which depends both on the orientational mobility of the chromophore (which can be increased by lowering T_g) and on the magnitude of the space-charge field. The latter can be influenced by the dipole moment and the orbital energy of the chromophore (see below). The requirement of a large dipole moment μ_D leads to problems with regard to solubility, compatibility, and aggregation, which leads to phase separation and a reduced shelf lifetime.[39, 97] Furthermore, high F composites exhibit slow optical response times[39] as the highly polar chromophores may lower the photoconductivity.[115] Consequently, the figure-of-merit is an important, but not the only, guideline for chromophore design.

3.2. Optimizing the Response Time—The Role of Photoconductivity

Charge transport is one of the most important parameters in the optimization of photorefractive materials. This has been recognized at an early stage[98–100] but only very recently the number of related studies has dramatically increased. They reflect the shift from initial development issues, such as compatibility and high diffraction efficiency, towards obtaining a faster response. The second trend at present is the search for a theory for the grating growth rate, for which—in contrast to crystals—only first attempts have been made.[34, 101, 102]

3.2.1. Charge Transport

In the standard model for photorefractive crystals,[11, 103, 104] the response time τ of the holographic grating is proportional to the photoinduced dielectric relaxation time, as shown by Equation (7), where ε is the dielectric constant and σ is the photoconductivity.

$$\tau = \frac{\varepsilon}{\sigma} \tag{7}$$

This means that τ is inversely proportional to σ, which is given in turn by Equation (8).

$$\sigma = ne\mu = \Phi_{cg}\frac{\alpha_{abs} P \tau_{life}}{h\nu} e\mu. \tag{8}$$

Here, n is the charge-carrier density, τ_{life} the lifetime of the carriers, e the elementary charge, and α_{abs} the absorption coefficient at the laser frequency ν. Measurements on organic systems showed an identical dependence of τ^{-1} and σ on the electric field, which was considered as a proof of the applicability of Equation (7).[37, 46] Consequently, the important parameters to be optimized would be the internal quantum efficiency for charge-carrier generation Φ_{cg} and the hole mobility μ. The number of available sensitizers is rather limited, hence, there have been only few attempts to optimize Φ_{cg}.[105] The hole mobility μ can be tuned by both the choice of the photoconductor and of the chromophore, which may itself act as a trap.

However, charge transport in amorphous organic systems differs strongly from that in ordered materials such as crystals. This is clearly observed in the standard experiment for the determination of μ, the time-of-flight (TOF) technique.[106, 107] A short laser pulse, whose penetration depth is on the order of 100 nm, generates a thin sheet of charge carriers on the surface of the material. Using a suitable bias, the electrons are collected by the adjacent semi-transparent anode, whereas the mobile holes wander through the material under the influence of an applied electric field E (electron mobility can be measured by reversing the applied voltage). In ordered materials, transport occurs in well defined conduction bands and the carrier packet is only broadened by thermal diffusion (Figure 7, left). This is called Gaussian transport.

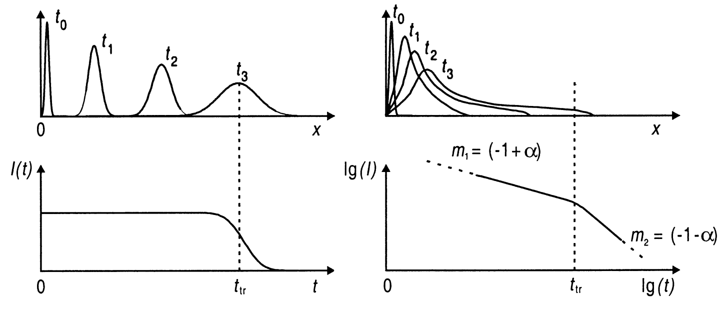

Figure 7. Charge transport processes in semiconductors and organic materials. Left: Gaussian transport; right: dispersive transport. The upper graphs depict the movement of the charge-carrier packet with increasing time t_i ($i = 0, 1, \ldots$). The lower graphs show the external displacement current I as a function of time, such as that detected in a TOF experiment. m_1 and m_2 are the slopes of the curves in the pre- and post-transit regime, respectively.

The average mobility μ is determined by the mean arrival time at the counterelectrode (the transit time t_{tr}); after this time the displacement current quickly drops to zero. Equation (9) gives μ for a sample of thickness d.

$$\mu = \frac{d}{E t_{tr}} \tag{9}$$

In organic PR systems, the transport is based on charge drift (diffusion becomes negligible as drift is enhanced through application of an external electric field) and is limited by intrinsic traps which arise from the energetic and/or positional disorder of the amorphous host—in only a few cases from deliberately added impurities.[108] There are no conduction bands and the charges move by hopping or tunneling from one localized trap state to the next (Figure 8).

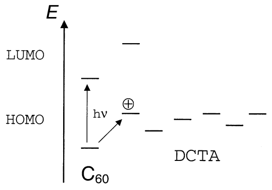

Figure 8. Charge generation and transport in an organic photorefractive material (DCTA system, see Scheme 3). Laser excitation of the sensitizer C_{60} generates a hole on a DCTA molecule. The hole can hop to the next DCTA site—this constitutes the elementary charge transport step.

As a consequence of the disorder, the mobility depends strongly on the electric field, as given in Equation (10), which helps the carriers to overcome the energy barriers between the trap states.[109]

$$\mu(E) = \mu_0 \exp\left[\frac{\Delta_0 - \beta_B\sqrt{E}}{k_B T_{eff}}\right] \tag{10}$$

The term Δ_0 represents the effective trap depth, μ_0 the mobility in the conduction band, and T_{eff} is an effective temperature, which is itself a function of temperature. The term proportional to $\sqrt{E}$ accounts for a field-assisted lowering of the trap depth in the direction of E and β_B is a proportionality constant. Organic PR materials exhibit strongly trap-dominated transport ("dispersive transport")[110, 111] in which the peak of the charge packet barely moves, whereas the wing broadens with time (Figure 7, right). The strong dispersion of the arrival times of the carriers at the counterelectrode makes it difficult to determine the average mobility. Experimentally, it is usually defined by the kink in the current transient, at which roughly the fastest 20% of the charge carriers have arrived.[110] It is evident that the mobility under the conditions of dispersive transport is not well defined. In this case, TOF measures a distribution of mobilities for a given sample thickness d but not an average mobility, which is independent of the length scale. Dispersive transport means that the charge carriers are never in equilibrium with the trap distribution—they continue to relax down to lower energies. Thus, they will move faster at the beginning due to their excess energy, whereas their speed will decrease with increasing time (equivalent to increasing travel distance).[110] The apparent mobility determined by TOF consequently becomes a function of the sample thickness d, according to [Eq. (11)], where α is the so-called dispersivity parameter, which varies between 0 (fully dispersive) and 1 (Gaussian transport).

$$\mu(d) \propto d^{1-1/\alpha} \tag{11}$$

The applicability of the concept of dispersive transport to organic PR systems was recently demonstrated by Zilker and co-workers for the case of the glass Stilbene3-DCTA (Scheme 3).[112] Length-scale dependent charge transport is a core result of the Scher–Montroll model. Thus, it provides a more intuitive description of PR materials than the Gaussian disorder model (GDM) by Bässler and co-workers,[113] which can also describe energetic relaxation.

3.2.2. Influence of the Chromophore

It is well known that polar dopants increase the energetic disorder and, thus, the effective trap depth Δ_0.[112, 114] As a consequence, the mobility decreases (see [Eq. (10)]). This was demonstrated by Ducharme and co-workers by TOF measurements in PR polymers doped with different concentrations of various chromophores.[115, 116] The holographic response time of the composites was not determined, however.

Furthermore, depending on the energetic position of the HOMO (highest occupied molecular orbital) level, the chromophore might also directly act as a trap. This has recently been investigated independently by Moerner and co-workers[46] and by Kippelen and co-workers.[117] Using different substituents, they were able to tune the HOMO level of their chromophores with respect to that of the PVK host. A clear correlation between the HOMO and the photoconductivity was obtained. Figure 9 shows the photoconductivity σ and the speed τ^{-1} for PVK composites as a function of the energy gap between the chromophore HOMO and the HOMO of the PVK monomer ethylcarbazole (ECZ).[46] The values of σ and τ are normalized by the absorption coefficient α_{abs} in order to account for a variation of the concentration of the C_{60} sensitizer.

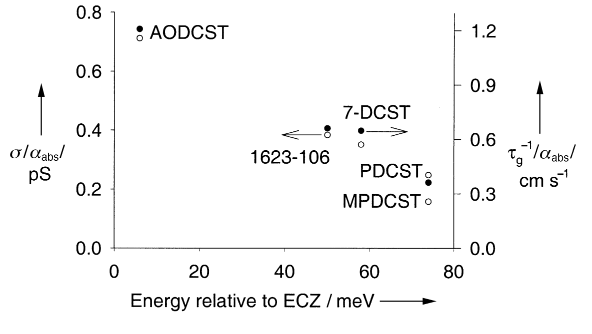

Figure 9. *Normalized photorefractive speed τ^{-1}/α_{abs} (right axis, filled circles) and normalized photoconductivity σ/α_{abs} (left axis, open circles) versus energy position of the HOMO of the chromophore relative to that of ECZ. Reprinted from ref. [46], with permission.*

The chromophore clearly acts as a trap when its HOMO lies at a higher energy than that of PVK. This leads to a lower photoconductivity and to longer response times. These results are in agreement with earlier studies, in which a second photoconductor (with a higher HOMO level) was introduced as a dopant.[118–120]

3.2.3. Traps and Photorefractive Response

The previous Section may have indicated that it is crucial to remove any additional traps from a photorefractive composite. However, one has to take into account that trapping effects were mostly studied in low mobility systems, such as PVK, which already has a large amount of intrinsic traps. Equation (7) fails when the carriers encounter only a small amount of traps, which are not sufficient to generate a strong space-charge field E_{sc}. Its fast build-up requires both fast transport and rapid immobilization of the carriers. Without traps, they would eventually leave the material at the counterelectrode. Therefore, the mean drift length w of the charge carriers (being the distance which they travel before being trapped on the time scale of the experiment) should be on the order of the grating spacing, given by Equation (12).

$$w = \mu \tau_{life} E \tag{12}$$

In $LiNbO_3$, w is on the order of a few nanometers,[121] so that insufficient trapping is not a problem. A carrier has to be re-excited about 100 times until it reaches the dark areas of the light intensity pattern. In a high mobility organic system (such as Stilbene3-DCTA; see Scheme 3) on the other hand, Leopold et al.[122] determined $w = 2.4\,\mu m$ by using a combination of conventional[106] and holographic TOF[123, 124] experiments. Thus, the situation in organic, high mobility materials differs strongly from that in crystals and in organic systems with a low μ such as PVK ($w < 1\,\mu m$ was recently obtained by Däubler et al.[125]): It is important to have just the right number of traps in order to warrant both rapid transport and quick immobilization of the carriers, that is, a mean drift length which is close to the grating spacing. This was recently demonstrated[112] in the bifunctional amorphous systems DR1-DCTA, Stilbene2-DCTA, and Stilbene3-DCTA (Scheme 3). These materials differ only in the chromophore, which is covalently attached to the photoconductor. Whereas the mobilities in the materials are very similar, there is a strong difference in the holographic rise times τ_1 (see Table 3). It was shown that a short time τ_1 correlates with a large effective trap depth Δ_0.

Table 3 presents these two parameters together with theoretical values of the dipole moment μ_D of the individual

Table 3. *Trap depth Δ_0, holographic speed τ_1^{-1}, and dipole moment μ_D of the chromophore for the three bifunctional DCTA glasses.*

	Δ_0 [eV]	τ_1^{-1} [ms]	μ_D [D]
DR1-DCTA	0.73	30	8.2
Stilbene2-DCTA	0.67	80	7.6
Stilbene3-DCTA	0.47	150	5.8

chromophores, as determined by semi-empirical calculations (MOPAC-AM1). Obviously, deeper traps (larger $\varDelta_0$) lead to rapid immobilization and thus enhance the build-up of the space-charge field, as long as sufficiently fast transport still takes place. Hofmann et al. demonstrated this in the case of DR1-DCTA using two different plasticizers, diisooctyl phthalate (DOP) and *N*-(2-ethyhexyl)-*N*-(3-methylphenyl)-aniline (EHMPA).[65] Whereas the mobility barely changed, the plasticizer EHMPA strongly increased the degree of dispersivity, meaning that it increased $\varDelta_0$. Remarkably, the EHMPA-doped material is faster by an order of magnitude (2.5 ms) than the compound doped with DOP—a result of faster immobilization.

In the Scher–Montroll theory, there is no contradiction between strongly dispersive transport and high mobility. Even in a broad distribution of trap levels, the carriers have sufficient initial excess energy to be transported rapidly until they either reach the electrode or encounter a deep trap which immobilizes them over the time scale of the experiment.

The dipole moment μ_D of the chromophore yields insight into the origin of the different trap states in the DCTA materials. Table 3 shows a direct correlation between the dipole moment μ_D and the trap depth, which is in accordance with studies of Ducharme and co-workers on PR polymers doped with chromophores with varying dipole moments.[115, 116] This interplay between the speed of transport and trapping is a distinct feature of organic photorefractive materials. Consequently, an important goal of future research will be the direct determination of the energy distribution of the trap states.

4. Applications of Organic Photorefractive Materials

In recent years, a number of applicability studies have been performed with photorefractive polymers, clearly moving away from the initial work which was mainly focused on data storage. This Section discusses the reasons for this change and shows selected examples of proposed applications.

4.1. Data Storage in Photorefractive Polymers

Our "information society" has an increasing demand for large-scale data storage and processing technology. Holography allows for massively parallel operations, which leads to high data-transfer rates. Furthermore, such memories can store several thousand data pages in the same volume element by changing the incidence angle of the reference beam (angular multiplexing).[126] A high storage density requires firstly a large dynamic range (large Δn) and secondly a high angular Bragg selectivity (namely, a small value of $\Delta\theta$). This parameter $\Delta\theta$ is the angular range over which an incident reading beam can reconstruct the stored image. Small $\Delta\theta$ values require samples several millimeters thick.

This thickness can easily be achieved in photorefractive crystals[127] which, therefore, have been extensively studied for this type of application.[128] An important breakthrough was the storage of more than 10^3 holograms in a single crystal and the development of fixing[129–131] mechanisms for the space-charge field, which yield permanent holograms with a long dark lifetime and, even more importantly, nondestructive readout (see Buse et al.,[132] and references therein). However, these holograms have writing times on the order of several seconds.[132] Recent work of Buse and co-workers with a pulsed-laser system shows promise for a much faster response.[133]

Organic materials provide a larger dynamic range of Δn in combination with faster recording and lower material costs.[48, 62, 134, 135] However, sample thickness and volatility issues have to be addressed. Up to now, no applicable fixing mechanism for the space-charge field is known. Prasad and co-workers[136] have realized a different approach in a high T_g (69 °C) system. The PR grating is written above the glass transition temperature and the sample is subsequently cooled down to room temperature, thereby freezing the modulated orientational distribution of the chromophores (but not the space-charge field). However, the gain was only 3 cm^{-1} and the technical realization of the method is complicated.

The longest dark lifetimes reported are on the order of hours.[134] However, dark lifetime and grating growth rate are inversely proportional to each other, since systems with higher mobilities tend also to exhibit larger dark currents. The sample thickness of a photorefractive polymer is mainly limited by the need of external fields on the order of 50 $\mathrm{V\,\mu m^{-1}}$. Therefore, one-layer samples thicker than 200 μm have not yet been fabricated. On the other hand, a layered structure of films 100 μm thick separated by buffers with transparent electrodes (a so-called stratified volume holographic element) has been successfully demonstrated to overcome this limitation.[137] Consequently, fixing the space-charge field is the main issue.

4.2. Image Processing and Optical Correlation

In 1996, Volodin et al. proposed a pattern-recognition system for security verification, for example of credit cards, based on a PR polymer.[4] The document carries a virtually invisible phase mask which is difficult to forge. In the 4f-correlator, a beam reflected off the test object is combined in a photorefractive polymer with a second beam from the master mask.[138] The hologram then acts as a filter for the reading beam: The diffracted beam will be the cross-correlation of the two patterns. If they agree, then a diffraction signal will be detected by a photodiode. In contrast to inorganic crystals, an organic material will have lower manufacturing and processing costs. Semiconductor heterostructures exhibit a faster response, their resolution, however, is limited to grating periods above 10 μm.[139, 140] The higher resolution of an organic material allows the use of short focal length lenses to yield compact devices. This advantage of combining high spatial resolution with a fast response has also been put forward to image processing based on phase conjugation.[141, 142]

4.3. Medical Applications

As our expected lifespan increases, cancer has already become the second leading cause of death in the USA. At the same time, the survival chances decrease dramatically when the tumor is not discovered at an early stage.[†] Conventional techniques, such as X-ray and ultrasound imaging, provide resolution only on the order of a millimeter.[143] Furthermore, ionizing radiation raises widespread concerns about possible side-effects.

Human tissue has a region of maximum optical transparency between 700 and 900 nm in which the absorption is small, for example, less than 0.1 cm^{-1} in breast tissue.[144] In contrast to this, the attenuation coefficient due to scattering events during passage is about 10 cm^{-1}.[144] Therefore, one has to extract the ballistic light (which has not experienced any scattering events during passage) from the scattering noise floor by a suitable time-gating scheme. There is a variety of pulsed[145–149] and continous-wave (cw)[150] methods which are based on the temporal stretching of short laser pulses upon their passage through a scattering medium. However, many of them require expensive equipment, such as pico- or femtosecond lasers[147] and streak cameras,[149] or involve time-consuming point-to-point scanning for the acquisition of 2D images.[148]

Holographic time-gating with an incoherent cw laser takes advantage of the coherence properties of the hologram formation.[150] Only the ballistic light can interfere with a suitably delayed reference beam when both are superimposed in a photorefractive material (see Figure 10). The scattered light has a path-length difference longer than the coherence length of the laser source and, thus, does not contribute to the signal. The result is a 2D image which carries detailed information about absorption centers in the medium. This has been demonstrated in inorganic crystals[7, 15] and semiconductor heterostructures.[140]

Kippelen and co-workers reported the first realization in an organic system in 1998.[8, 57] Imaging of a transmission mask (see Figure 10) was achieved through a scattering medium with an effective optical density of 4. An organic system combines its high resolution and sensitivity with a holographic rise time an order of magnitude below the response times of inorganic crystals in the same type of application.[151] The technique also allows for rapid acquisition without extensive processing and computational efforts. In a reflection geometry, depth (3D) resolution can be achieved with a suitable delay of the reference beam.[7] Therefore, the technique could become a useful complement to existing diagnostic tools.

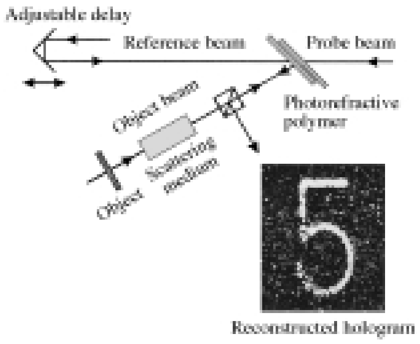

Figure 10. Holographic time-gating apparatus with the reconstructed hologram. The wavelength of the laser light was 800 nm and the mask was immersed in a suspension of polystyrene microspheres in water. Reprinted from ref. [57], with permission.

4.4. Vibration Analysis

Contact-free detection of ultrasonic surface displacements by two-wave mixing in a PR polymer is the most recently proposed application.[152] The hologram acts as an adaptive beam splitter with exact wavefront matching: A plane-wave reference beam is diffracted into the speckled signal beam which is reflected from the test surface. This allows for efficient homodyne detection of the optical sidebands of the signal beam which are produced by the ultrasound. The hologram compensates slow perturbations due to the apparatus, which removes the need for expensive path-length stabilization, such as in conventional interferometric receivers.[153, 154] The polymeric material exhibits a detection threshold which is only a factor of three from the theoretical limit. This is comparable to values achieved in semiconductor heterostructures[155] and a factor of ten better than in inorganic crystals.[156]

Applications of vibrational analysis are remote sensing, manufacturing diagnostics, and in-service inspection, especially in problematic environments such as high-temperature or hazardous areas. One could also think of medical diagnostics without direct, sometimes unpleasant, skin contact.

5. Conclusions and Outlook

Photorefractive organic materials have experienced a rapid progress since the first demonstration in 1991. Large refractive index modulations and optical gains, high speed, and significant improvements in shelf lifetimes have been achieved. However, further optimization of the materials is required until the first devices may appear on the market: Primary concerns are to lower the presently required strong electric fields and the realization of practical fixing schemes to yield nondestructive readout and long dark lifetimes. Apart from being a materials science challenge, this requires progress in theoretical modeling, which has thus far been lacking behind the experiment progress. More insight into charge-carrier dynamics and trapping may help to improve device performance significantly. As far as the different materials concepts are concerned, liquid-crystalline materials may offer the best opportunities, if their photoconductivity can be further enhanced. An ideal organic system would have the charge generation efficiency of a solar cell, the transport characteristics of a high performance polymeric hole conductor, and the reorientational speed and switching voltages of a liquid crystal. This calls for sophisticated hybrid concepts.

Abbreviations

ATOP1	1-butyl-5-[2-(5-dibutylaminothienyl)methylene]-4-methyl-[2,6-dioxo-1,2,5,6-tetrahydropyridine]-3-carbonitrile
cw	continuous wave

[†] *Source: American Cancer Society, www.cancer.org*

BCNM	*N*-2-butyl-2,6-dimethyl-4*H*-pyridone-4-ylidene-cyanomethylacetate
DBOP-PPV	poly[1,4-phenylene-1,2-di(4-benzyloxyphenyl)-vinylene]
DCTA	4,4′-di(n-carbazolyl)-4″-(2-*N*-ethyl-4-[2-{4-nitro-phenyl}-1-azo]anilinoethoxy)-triphenylamine
DHADC-MPN	*N*,*N*-dihexylamino-7-dicyanomethylidenyl-3,4,5,10-pentahydronaphthalene
DMNPAA	2,5-dimethyl-4-*p*-nitrophenylazoanisole
DOP	diisooctyl phthalate
DR1	disperse red 1
DWFM	degenerate four-wave mixing
ECZ	9-ethylcarbazole
EHMPA	*N*-(2-ethyhexyl)-*N*-(3-methylphenyl)-aniline
EO	electro-optic
EPEMN	2-(1-ethyl-1*H*-(4)pyridyliden)-ethylidenemalonitrile
FFP	fully functionalized polymer
FTCN	fluorinated cyano-toluene chromophore
GDM	Gaussian disorder model
HLC	high molecular mass LC
HOMO	highest occupied molecular orbital
ITO	indium-tin oxide
LC	liquid crystal, liquid crystalline
LLC	low molecular mass LC
PDCST	4-piperidinobenzylidenemalonitrile
PDLC	polymer-dispersed LC
PPV	poly(phenylenevinylene)
PR	photorefractivity
PSX	polysiloxane
PVK	polyvinylcarbazole; (poly[9(9H)-carbazolyl-1,2-ethanediyl]
TOF	time-of-flight
TFB	poly-(9,9′-dioctylfluorene-*co*-*N*-(4-butylphenyl)-diphenylamine)
TNF	2,4,7-trinitro-9-fluorenone
TPDac	tetraphenyldiaminobiphenyl; *N*-(4-acryloyloxyme-thylphenyl)-*N*′-phenyl-*N*,*N*′-bis(4-methylphenyl)-[1,1′-biphenyl]-4,4′-diamine
2BC	two-beam coupling
5CB	pentylcyanobiphenyl

Glossary of Symbols

d	sample thickness
E	externally applied electric field
E_p	electric field component parallel to the grating vector
E_{sc}	space-charge field
e	elementary charge
$\hat{e}$	unit vector of the electric field
F	figure-of-merit
I	displacement current
k	Boltzmann's constant
L	effective interaction length
M	molecular mass
m	curve slope
n	refractive index; n_K, n_P due to the Kerr or Pockels effect
P	laser beam intensity
r_e	effective electro-optic coefficient
r_K	effective Kerr susceptibility
T	temperature
T_{eff}	effective temperature
T_g	glass transition temperature
t_{tr}	transit time
w	mean drift length
x	position
α	dispersivity parameter
α_{abs}	laser absorption coefficient
α_p	first order polarizability, polarization anisotropy
β	second-order polarizability along the axis of μ_D
β_B	proportionality constant
β_P	power ratio
Γ	optical gain coefficient
γ_0	beam intensity ratio behind the sample
Δ_0	effective trap depth
ε	dielectric constant
η	diffraction efficiency
θ	intersection angle
Θ	internal angle of ê; angle between the writing beams
Λ	grating period
λ	wavelength
μ	hole mobility
μ_0	mobility in the conduction band
μ_D	dipole moment
ν	laser frequency
ρ	space-charge distribution
σ	photoconductivity
τ	holographic rise (response) time
τ^{-1}	holographic speed
τ_{life}	charge-carrier lifetime
Φ, Φ_{cg}	quantum efficiency; cg = charge generation
ϕ	phase shift between light intensity grating and refractive index modulation
Ψ	tilt angle

The research activities of the author were supported by the Bayerische Forschungsstiftung and the Deutsche Forschungsgemeinschaft (SFB 481, B2). I am very grateful to K. Meerholz and M. Thelakkat for careful proofreading and important comments. Thanks go to U. Hofmann, A. Leopold, and M. Grasruck for their comments and their experimental help, and to D. Haarer for his continuous support. T. Breiner was helpful in many chemical questions, C. Hohle, P. Strohriegl, M. Thelakkat, and H.-W. Schmidt provided most of our materials. I would also like to acknowledge stimulating discussions with many colleagues who gave important comments on this manuscript.

Received: July 20, 2000 [A 77]

[1] A. Ashkin, G. D. Boyd, J. M. Dziedzic, R. G. Smith, A. A. Ballman, J. J. Levinstein, K. Nassau, *Appl. Phys. Lett.* **1966**, *9*, 72.

[2] I. McMichael, W. Christian, D. Pletcher, T. Y. Chang, J. H. Hong, *Appl. Opt.* **1996**, *35*, 2375.

[3] C. Denz, T. Dellwig, J. Lembcke, T. Tschudi, *Opt. Lett.* **1996**, *21*, 278.

[4] B. L. Volodin, B. Kippelen, K. Meerholz, B. Javidi, N. Peyghambarian, *Nature* **1996**, *383*, 58.

[5] B. L. Volodin, Sandalphon, K. Meerholz, B. Kippelen, N. V. Kukhtarev, N. Peyghambarian, *Opt. Engin.* **1994**, *34*, 2213.

[6] D. D. Breer, K. Buse, *Appl. Phys. B* **1998**, *66*, 339.

[7] S. C. W. Hyde, N. P. Barry, R. Jones, J. C. Dainty, P. M. W. French, M. B. Klein, B. A. Wechsler, *Opt. Lett.* **1995**, *20*, 1331.

[8] D. D. Steele, B. L. Volodin, O. Savina, B. Kippelen, N. Peyghambarian, H. Röckel, S. R. Marder, *Opt. Lett.* **1998**, *23*, 153.

[9] "Photorefractive Materials and Their Applications I": *Topics in Applied Physics Vol. 62* (Eds.: P. Günter, J.-P. Huignard), Springer, Berlin, **1988**.

[10] D. D. Nolte, *J. Appl. Phys.* **1999**, *85*, 6259.

[11] N. V. Kukhtarev, *Sov. Tech. Phys. Lett.* **1976**, *2*, 438.

[12] K. Buse, *Appl. Phys. B* **1997**, *64*, 273.

[13] K. Buse, *Appl. Phys. B* **1997**, *64*, 391.

[14] D. D. Nolte, D. H. Olson, G. E. Doran, W. H. Knox, A. M. Glass, *J. Opt. Soc. Am. B* **1990**, *7*, 2217.

[15] C. V. Raman, N. S. N. Nath, *Proc. Indian Acad. Sci.* **1935**, *2*, 406.

[16] K. Sutter, J. Hullinger, P. Günter, *Solid State Commun.* **1990**, *74*, 867.

[17] K. Sutter, P. Günter, *J. Opt. Soc. Am. B* **1990**, *7*, 2274.

[18] S. Ducharme, J. C. Scott, R. J. Twieg, W. E. Moerner, *Phys. Rev. Lett.* **1991**, *66*, 1846.

[19] W. E. Moerner, S. M. Silence, F. Hache, G. C. Bjorklund, *J. Opt. Soc. Am. B* **1994**, *11*, 320.

[20] S. Breer, K. Buse, *Appl. Phys. B* **1998**, *66*, 339.

[21] W. E. Moerner, S. M. Silence, *Chem. Rev.* **1994**, *94*, 127.

[22] W. E. Moerner, A. Grunnet-Jepsen, C. L. Thompson, *Annu. Rev. Mater. Sci.* **1997**, *27*, 585.

[23] Y. Zhang, R. Burzynski, S. Ghosal, M. K. Casstevens, *Adv. Mater.* **1996**, *8*, 111.

[24] G. P. Wiederrecht, B. A. Yoon, M. R. Wasielewski, *Adv. Mater.* **1996**, *8*, 535.

[25] B. Kippelen, K. Meerholz, N. Peyghambarian in *Nonlinear Optics of Organic Molecules and Polymers* (Eds.: H. S. Nalwa, S. Miyata), CRC, Boca Raton, **1997**, pp. 465 – 513.

[26] K. Meerholz, B. Kippelen, N. Peyghambarian in *Photonic Polymer Systems* (Eds.: D. Wise, G. Wnek, D. Trantalo, T. Cooper, J. Gresser), Marcel Dekker, New York, **1998**, pp. 571 – 631.

[27] K. Okamoto, T. Momura, S.-H. Park, K. Ogino, H. Sato, *Chem. Mater.* **1999**, *11*, 3279.

[28] *Photochromism, Molecules and Systems* (Eds.: H. Dürr, H. Bouas-Laurent), Elsevier, Amsterdam, **1990**.

[29] M. Levitus, P. F. Aramendía, *J. Phys. Chem. B* **1999**, *103*, 1864.

[30] C. A. Walsh, W. E. Moerner, *J. Opt. Soc. Am. B* **1992**, *9*, 1642.

[31] E. Mecher, R. Bittner, C. Bräuchle, K. Meerholz, *Synth. Met.* **1999**, *102*, 993.

[32] U. Hofmann, A. Schreiber, D. Haarer, S. J. Zilker, A. Bacher, D. D. C. Bradley, M. Redecker, M. Inbasekaran, W. W. Wu, E. P. Woo, *Chem. Phys. Lett.* **1999**, *311*, 41.

[33] J. S. Schildkraut, A. V. Buettner, *J. Appl. Phys.* **1992**, *72*, 1888.

[34] Y. Cui, B. Swedeck, N. Cheng, J. Zieba, P. N. Prasad, *J. Appl. Phys.* **1999**, *85*, 38.

[35] K. Ogino, S.-H. Park, H. Sato, *Appl. Phys. Lett.* **1999**, *74*, 3936.

[36] J. A. Herlocker, K. B. Ferrio, E. Hendrickx, B. D. Guenther, S. Mery, B. Kippelen, N. Peyghambarian, *Appl. Phys. Lett.* **1999**, *74*, 2253.

[37] D. Wright, M. A. Díaz-García, J. D. Casperson, M. DeClue, W. E. Moerner, R. J. Twieg, *Appl. Phys. Lett.* **1998**, *73*, 1490.

[38] S. Schloter, U. Hofmann, P. Strohriegl, H.-W. Schmidt, D. Haarer, *J. Opt. Soc. Am. B* **1998**, *15*, 2473.

[39] F. Würthner, R. Wortmann, R. Matschiner, K. Lakaszuk, K. Meerholz, Y. DeNardin, R. Bittner, C. Bräuchle, R. Sens, *Angew. Chem.* **1997**, *109*, 2933; *Angew. Chem. Int. Ed. Engl.* **1997**, *36*, 2765.

[40] H. Ono, N. Kawatsuki, *Opt. Lett.* **1999**, *24*, 130.

[41] H. Ono, N. Kawatsuki, *J. Appl. Phys.* **1999**, 85, 2482.

[42] F. Laeri, T. Tschudi, J. Albers, *Opt. Commun.* **1983**, *47*, 387.

[43] A. Brignon, S. Breugnot, J.-P. Huignard, *Opt. Lett.* **1995**, *20*, 1689.

[44] A. Grunnet-Jepsen, C. L. Thompson, W. E. Moerner, *Opt. Commun.* **1998**, *145*, 145.

[45] Ph. Refregier, L. Solymar, H. Rajbenbach, J. P. Huignard, *J. Appl. Phys.* **1985**, *58*, 45.

[46] M. A. Díaz-García, D. Wright, J. D. Casperson, B. Smith, E. Glazer, W. E. Moerner, L. I. Sukhomlinova, R. J. Twieg, *Chem. Mater.* **1999**, *11*, 1784.

[47] Y. Zhang, T. Wada, H. Sasabe, *J. Mater. Chem.* **1998**, *8*, 809.

[48] K. Meerholz, B. L. Volodin, Sandalphon, B. Kippelen, N. Peyghambarian, *Nature* **1994**, *371*, 497.

[49] K. Ogino, T. Nomura, T. Shichi, S. Park, H. Sato, T. Aoyama, T. Wada, *Chem. Mater.* **1997**, *9*, 2768.

[50] E. Mecher, C. Bräuchle, H. H. Hörhold, J. C. Hummelen, K. Meerholz, *PCCP* **1999**, *1*, 1749.

[51] E. Hendrickx, J. Herlocker, J. L. Maldonaldo, S. R. Marder, B. Kippelen, A. Persoons, N. Peyghambarian, *Appl. Phys. Lett.* **1998**, *72*, 1679.

[52] E. Hendrickx, B. L. Volodin, D. D. Steele, J. L. Maldonaldo, G. Guillemet, B. Kippelen, N. Peyghambarian, *Appl. Phys. Lett.* **1997**, *71*, 1159.

[53] K. Meerholz, R. Bittner, Y. De Nardin, C. Bräuchle, E. Hendrickx, B. L. Volodin, B. Kippelen, N. Peyghambarian, *Adv. Mater.* **1997**, *9*, 1043.

[54] E. Hendrickx, B. L. Volodin, D. D. Steele, J. L. Maldonaldo, J. F. Wang, B. Kippelen, N. Peyghambarian, *Appl. Phys. Lett.* **1997**, *71*, 1159.

[55] A. Grunnet-Jepsen, C. L. Thompson, R. J. Twieg, W. E. Moerner, *Appl. Phys. Lett.* **1997**, *70*, 1515.

[56] A. M. Cox, R. D. Blackburn, D. P. West, T. A. King, F. A. Wade, D. A. Leigh, *Appl. Phys. Lett.* **1996**, *68*, 2801.

[57] B. Kippelen, S. R. Marder, E. Hendrickx, J. L. Maldonaldo, G. Guillemet, B. L. Volodin, D. D. Steele, Y. Enami, Sandalphon, Y. J. Yao, J. F. Wang, H. Röckel, L. Erskine, N. Peyghambarian, *Science* **1998**, *279*, 54.

[58] E. Hendrickx, D. Van Steenwinckel, A. Persoons, A. Watanabe, *Macromolecules* **1999**, *32*, 2232.

[59] K. Tamura, A. B. Padias, H. K. Hall, Jr., N. Peyghambarian, *Appl. Phys. Lett.* **1992**, *60*, 1803.

[60] B. Kippelen, K. Tamura, N. Peyghambarian, A. B. Padias, J. K. Hall, Jr., *Phys. Rev. B* **1993**, *48*, 10710.

[61] S. Schloter, U. Hofmann, K. Hoechstetter, G. Bäuml, D. Haarer, K. Ewert, C.-D. Eisenbach, *J. Opt. Soc. Am. B* **1998**, *15*, 2560.

[62] P. M. Lundquist, R. Wortmann, C. Geletneky, R. J. Twieg, M. Jurich, V. Y. Lee, C. R. Moylan, D. M. Burland, *Science* **1996**, *274*, 1182.

[63] a) L. Wang, Y. Zhang, T. Wada, H. Sasabe, *Appl. Phys. Lett.* **1996**, *69*, 728; b) Y. Zhang, L. Wang, T. Wada, H. Sasabe, *Appl. Phys. Lett.* **1997**, *70*, 2949.

[64] a) S. Schloter, A. Schreiber, M. Grasruck, A. Leopold, M. A. Kol'chenko, J. Pan, C. Hohle, P. Strohriegl, S. J. Zilker, D. Haarer, *Appl. Phys. B* **1999**, *68*, 899; b) C. Hohle, U. Hofmann, S. Schloter, M. Thelakkat, P. Strohriegl, D. Haarer, S. J. Zilker, *J. Mater. Chem.* **1999**, *9*, 2205.

[65] U. Hofmann, M. Grasruck, A. Leopold, A. Schreiber, S. Schloter, C. Hohle, P. Strohriegl, D. Haarer, S. J. Zilker, *J. Phys. Chem. B* **2000**, *104*, 3887.

[66] U. Hofmann, M. Grasruck, A. Leopold, A. Schreiber, S. Schloter, S. J. Zilker, D. Haarer, M. Thelakkat, C. Hohle, H.-W. Schmidt, P. Strohriegl, *Proc. SPIE Int. Soc. Opt. Eng.* **1999**, *3799*, 32.

[67] P. G. de Gennes, *The Physics of Liquid Crystals*, Clarendon Press, Oxford, **1974**.

[68] E. V. Rudenko, A. V. Sukhov, *JETP Lett.* **1994**, *59*, 142.

[69] I. C. Khoo, H. Li, Y. Liang, *Opt. Lett.* **1994**, *19*, 1723.

[70] G. P. Wiederrecht, M. P. Niemczyk, W. A. Svec, M. R. Wasielewski, *Chem. Mater.* **1999**, *11*, 1409.

[71] E. V. Rudenko, A. V. Sukhov, *JETP* **1994**, *78*, 875.

[72] I. C. Khoo, *IEEE J. Quantum Electron.* **1996**, *32*, 525.

[73] G. P. Wiederrecht, M. R. Wasielewski, *J. Am. Chem. Soc.* **1998**, *120*, 3231.

[74] H. Ono, N. Kawatsuki, *Opt. Lett.* **1997**, *22*, 1144.

[75] A. Golemme, B. Kippelen, N. Peyghambarian, *Appl. Phys. Lett.* **1998**, *73*, 2408.

[76] H. Ono, I. Saito, N. Kawatsuki, *Appl. Phys. Lett.* **1998**, *72*, 1942.

[77] H. Ono, A. Hanazawa, T. Kawamura, H. Norisada, N. Kawatsuki, *J. Appl. Phys.* **1999**, *86*, 1785.

[78] H. Ono, N. Kawatsuki, *Appl. Phys. B* **1999**, *69*, 51.

[79] H. Ono, private communication.

[80] F. Chaput, D. Riehl, J. P. Boilot, K. Cargnelli, M. Canva, Y. Lévy, A. Brun, *Chem. Mater.* **1996**, *8*, 312.

[81] B. Darracq, F. Chaput, K. Lahlil, J.-P. Biolot, Y. Lévy, V. Alain, L. Ventelon, M. Blanchard-Desce, *Opt. Mater.* **1998**, *9*, 265.

[82] B. Darracq, M. Canva, F. Chaput, J.-P. Boilot, D. Riehl, Y. Lévy, A. Brun, *Appl. Phys. Lett.* **1997**, *70*, 292.

[83] B. O'Regan, M. Grätzel, *Nature* **1991**, *353*, 737.

[84] T. K. Däubler, V. Cimrová, S. Pfeiffer, H.-H. Hörhold, D. Neher, *Adv. Mater.* **1999**, *11*, 1274.

[85] M. L. Steigerwald, L. E. Brus, *Acc. Chem. Res.* **1990**, *23*, 183.

[86] J. G. Winiarz, L. Zhang, M. Lai, C. S. Friend, P. N. Prasad, *J. Am. Chem. Soc.* **1999**, *121*, 3287.

[87] J. G. Winniarz, L. Zhang, M. Lai, C. S. Friend, P. N. Prasad, *Chem. Phys.* **1999**, *245*, 417.

[88] A. Grunnet-Jepsen, D. Wright, B. Smith, M. S. Bratcher, M. S. DeClue, J. S. Siegel, W. E. Moerner, *Chem. Phys. Lett.* **1998**, *291*, 553.

[89] a) R. Wortmann, C. Poga, R. J. Twieg, C. Geletneky, C. R. Moylan, P. M. Lundquist, R. G. DeVoe, P. M. Cotts, H. Horn, J. E. Rice, D. M. Burland, *J.

Chem. Phys. **1996**, *105*, 10637; b) B. Kippelen, F. Meyers, N. Peyghambarian, S. R. Marder, *J. Am. Chem. Soc.* **1997**, *119*, 4559; c) C. R. Moylan, R. Wortmann, R. J. Twieg, I.-H. McComb, *J. Opt. Soc. Am. B* **1998**, *15*, 929.

[90] a) S. R. Marder, C. B. Gorman, F. Meyers, J. W. Perry, G. Bourhill, J.-L. Brédas, B. M. Pierce, *Science* **1994**, *265*, 632; b) C. B. Gorman, S. R. Marder, *Chem. Mater.* **1995**, *7*, 215.

[91] R. Wortmann, P. Krämer, C. Glania, S. Lebus, N. Detzer, *Chem. Phys.* **1993**, *173*, 99.

[92] S. Beckmann, K.-H. Etzbach, P. Krämer, K. Lukaszuk, R. Matschiner, A. J. Schmidt, P. Schuhmacher, R. Sens, G. Seybold, R. Wortmann, F. Würthner, *Adv. Mater.* **1999**, *11*, 536.

[93] R. Wortmann, C. Glania, P. Krämer, K. Lukaszuk, R. Matschiner, R. J. Twieg, F. You, *Chem. Phys.* **1999**, *245*, 107.

[94] E. Hendrickx, B. D. Guenther, Y. Zhang, J. F. Wang, K. Staub, Q. Zhang, S. R. Marder, B. Kippelen, N. Peyghambarian, *Chem. Phys.* **1999**, *245*, 407.

[95] A. Fort, J. Muller, O. Cregut, L. Mager, J. P. Vola, M. Barzoukas, *J. Appl. Phys.* **1998**, *83*, 2888.

[96] K. Meerholz, Y. De Nardin, R. Bittner, R. Wortmann, F. Würthner, *Appl. Phys. Lett.* **1998**, *73*, 4.

[97] F. Würthner, A. Sautter, C. Legrand, E. Mecher, K. Meerholz, R. Wortmann, *Proc. Am. Chem. Soc., Div. Polym. Mat. Sci. Eng.* **1999**, *80*, 252.

[98] J. C. Scott, L. Th. Pautmeier, W. E. Moerner, *Synth. Met.* **1993**, *54*, 9.

[99] J. C. Scott, L. Th. Pautmeier, W. E. Moerner, *J. Opt. Soc. Am. B* **1992**, *9*, 2059.

[100] B. E. Jones, S. Ducharme, M. Liphardt, A. Goonesekera, J. M. Takacs, L. Zhang, R. Athalye, *J. Opt. Soc. Am. B* **1994**, *11*, 1064.

[101] J. S. Schildkraut, A. V. Buettner, *J. Appl. Phys.* **1992**, *72*, 1888.

[102] J. S. Schildkraut, Y. Cui, *J. Appl. Phys.* **1992**, *72*, 5055.

[103] N. V. Kukhtarev, V. Markov, S. Odulev, *Opt. Commun.* **1977**, *23*, 338.

[104] G. C. Valley, *J. Appl. Phys.* **1986**, *59*, 3363.

[105] Z. Peng, A. R. Gharavi, L. Yu, *Appl. Phys. Lett.* **1996**, *69*, 4002.

[106] A. Szymanski, M. M. Labes, *J. Chem. Phys.* **1969**, *50*, 3568.

[107] D. Adam, P. Schumacher, J. Simmerer, L. Häusling, K. Siemensmeyer, K. H. Etzbach, H. Ringsdorf, D. Haarer, *Nature* **1994**, *371*, 141.

[108] G. G. Malliaras, V. V. Krasnikov, H. J. Bolink, G. Hadziioannou, *Appl. Phys. Lett.* **1995**, *66*, 1038.

[109] W. D. Gill, *J. Appl. Phys.* **1972**, *43*, 5033.

[110] H. Scher, E. W. Montroll, *Phys. Rev. B* **1975**, *12*, 2455.

[111] H. Scher, M. F. Shlesinger, J. T. Bendler, *Phys. Today* **1991**, *46*, 26.

[112] M. Grasruck, A. Schreiber, U. Hofmann, S. J. Zilker, A. Leopold, S. Schloter, C. Hohle, P. Strohriegl, D. Haarer, *Phys. Rev. B* **1999**, *60*, 16543.

[113] H. Bässler, *Phys. Status Solidi B* **1993**, *175*, 15.

[114] P. M. Borsenberger, D. S. Weiss, *Organic Photoreceptors for Xerography*, Marcel Dekker, New York, **1998**.

[115] A. Goonesekera, S. Ducharme, J. M. Takacs, L. Zhang, *J. Chem. Phys.* **1997**, *107*, 8709.

[116] A. Goonesekera, S. Ducharme, *J. Appl. Phys.* **1999**, *85*, 6506.

[117] E. Hendrickx, Y. Zhang, K. B. Ferrio, J. A. Herlocker, J. Anderson, N. R. Armstrong, E. A. Mash, A. P. Persoons, N. Peyghambarian, B. Kippelen, *J. Mater. Chem.* **1999**, *9*, 2251.

[118] D. M. Pai, J. F. Yanus, M. Stolka, *J. Phys. Chem.* **1994**, *88*, 4714.

[119] a) G. G. Malliaras, V. V. Krasnikov, H. J. Bolink, G. Hadziioannou, *Proc. SPIE* **1995**, *2526*, 94; b) G. G. Malliaras, V. V. Krasnikov, H. J. Bolink, G. Hadziioannou, *Appl. Phys. Lett.* **1995**, *67*, 455.

[120] Y. Zhang, S. Ghosal, M. K. Casstevens, R. Burzynski, *Polymer Prepr.* **1994**, *35*, 233.

[121] H. Veenhuis, K. Buse, E. Krätzig, N. Korneev, D. Mayorga, *J. Appl. Phys.* **1999**, *86*, 2389.

[122] A. Leopold, M. Grasruck, U. Hofmann, M. A. Kol'chenko, S. J. Zilker, *Appl. Phys. Lett.* **2000**, *76*, 1644.

[123] G. G. Malliaras, V. V. Krasnikov, H. J. Bolink, G. Hadziioannou, *Phys. Rev. B* **1995**, *52*, 14324.

[124] S. J. Zilker, M. Grasruck, J. Wolff, S. Schloter, A. Leopold, M. A. Kol'chenko, U. Hofmann, A. Schreiber, P. Strohriegl, C. Hohle, D. Haarer, *Chem. Phys. Lett.* **1999**, *306*, 285.

[125] T. K. Däubler, R. Bittner, K. Meerholz, V. Cimrova, D. Neher, *Phys. Rev. B* **2000**, *61*, 13515.

[126] J. J. Amodei, D. L. Staebler, *Appl. Phys. Lett.* **1971**, *18*, 540.

[127] F. H. Mok, *Opt. Lett.* **1993**, *18*, 915.

[128] D. Psaltis, F. Mok, *Sci. Am.* **1995**, *273*, 52.

[129] J. J. Amodei, D. L. Staebler, *Appl. Phys. Lett.* **1971**, *18*, 540.

[130] F. Micheron, G. Bismuth, *Appl. Phys. Lett.* **1972**, *20*, 79.

[131] G. Montemezzani, P. Günter, *J. Opt. Soc. Am. B* **1990**, *7*, 2323.

[132] K. Buse, A. Adibi, D. Psaltis, *Nature* **1998**, *393*, 665.

[133] J. Imbrock, S. Wevering, K. Buse, E. Krätzig, *J. Opt. Soc. Am. B* **1999**, *16*, 1392.

[134] P. M. Lundquist, R. J. Twieg, R. Wortmann, R. M. Shelby, C. Geletneky, M. Jurich, D. M. Burland, *Proc. SPIE* **1996**, *2850*, 78.

[135] C. Poga, P. M. Lundquist, V. Lee, R. M. Shelby, R. J. Twieg, D. M. Burland, *Appl. Phys. Lett.* **1996**, *69*, 1047.

[136] N. Cheng, B. Swedek, P. N. Prasad, *Appl. Phys. Lett.* **1999**, *71*, 1828.

[137] J. J. Stankus, S. M. Silence, W. E. Moerner, G. C. Bjorklund, *Opt. Lett.* **1994**, *19*, 1480.

[138] C. Halvorson, B. Kraabel, A. J. Heeger, B. L. Volodin, K. Meerholz, Sandalphon, N. Peyghambarian, *Opt. Lett.* **1994**, *20*, 76.

[139] Q. Wang, R. M. Brubaker, D. D. Nolte, M. R. Melloch, *J. Opt. Soc. Am. B* **1992**, *9*, 1626.

[140] R. Jones, S. C. W. Hyde, M. J. Lynn, N. P. Barry, J. C. Dainty, P. M. W. French, K. M. Kwolek, D. D. Nolte, M. R. Melloch, *Appl. Phys. Lett.* **1996**, *69*, 1837.

[141] T. Wada, L. Wang, Y. Zhang, M. Tian, H. Sasabe, *Nonlinear Opt.* **1996**, *15*, 103.

[142] A. Grunnet-Jepsen, C. L. Thompson, W. E. Moerner, *Science* **1997**, *277*, 549.

[143] Z.-H. Cho, J. P. Jones, M. Singh, *Foundations of Medical Imaging*, Wiley, New York, **1993**.

[144] R. Cubbedu, A. Pifferi, P. Taroni, A. Torricelli, G. Valentini, *Appl. Phys. Lett.* **1999**, *74*, 874.

[145] N. H. Abramson, K. G. Spears, *Appl. Opt.* **1989**, *28*, 1834.

[146] A. Rebane, J. Feinberg, *Nature* **1991**, *351*, 379.

[147] J. A. Moon, R. Mahon, M. D. Duncan, J. Reintjes, *Opt. Lett.* **1994**, *19*, 1234.

[148] M. R. Hee, J. A. Izatt, J. M. Jacobson, J. G. Fujimoto, E. A. Swanson, *Opt. Lett.* **1993**, *18*, 950.

[149] B. B. Das, K. M. Yoo, R. R. Alfano, *Opt. Lett.* **1993**, *18*, 1092.

[150] N. Abramson, *Opt. Lett.* **1978**, *3*, 121.

[151] S. C. W. Hyde, N. P. Barry, R. Jones, J. C. Dainty, P. M. W. French, *Opt. Lett.* **1995**, *20*, 2330.

[152] M. B. Klein, G. D. Bacher, A. Grunnet-Jepsen, D. Wright, W. E. Moerner, *Opt. Commun.* **1999**, *162*, 79.

[153] J.-P. Monchalin, R. Heon, P. Bouchard, C. Padioleau, *Appl. Phys. Lett.* **1989**, *55*, 1612.

[154] R. J. Dewhurst, Q. Shan, *Meas. Sci. Technol.* **1999**, *10*, R139.

[155] I. Lahiri, L. J. Pyrak-Nolte, D. D. Nolte, M. R. Melloch, R. A. Kruger, G. D. Bacher, M. B. Klein, *Appl. Phys. Lett.* **1998**, *73*, 1041.

[156] a) A. Blouin, J.-P. Monchalin, *Appl. Phys. Lett.* **1994**, *65*, 932. b) L.-A. de Montmorillon, I. Biaggio, P. Delaye, J.-C. Launay, G. Roosen, *Opt. Commun.* **1996**, *129*, 293.

[157] H. Domes, R. Fischer, D. Haarer, P. Strohriegl, *Makromol. Chem.* **1989**, *190*, 165.

[158] Wolff, S. Schloter, U. Hofmann, D. Haarer, S. J. Zilker, *J. Opt. Soc. Am. B* **1999**, *16*, 1080.

[159] E. Lebedev, Th. Dittrich, V. Petrova-Koch, S. Karg, W. Brütting, *Appl. Phys. Lett.* **1997**, *71*, 2686.

[160] M. Redecker, D. D. C. Bradley, M. Inbasekaran, W. W. Wu, E. P. Woo, *Adv. Mater.* **1999**, *11*, 241.

Artificial Noses Sniff DNA

Hauke Clausen-Schaumann,[a] Matthias Rief[a], and Markus Seitz*[a]

KEYWORDS:

atomic force microscopy · DNA recognition · oligonucleotides · sensors

The development of experimental tools that allow the precise application and measurement of minute forces has opened new perspectives in the material and life sciences. One of the most prominent tools, the atomic force microscope (AFM), was originally introduced by Binnig et al.[1] as a high-resolution microscope. The underlying principle is the detection of the bending of a microfabricated cantilever as a response to external forces. Since this detection method operates even under physiological conditions, the AFM has found widespread applications in the life sciences. Next to the imaging of surfaces at molecular resolution, the high force sensitivity of the technique can be utilized to measure the strength of intermolecular forces, such as individual ligand – receptor bonds as well as the elasticity of single polymer molecules.[2, 3]

Moreover, researchers have used single microfabricated cantilevers as highly sensitive, miniature sensors with rapid responses to monitor processes at the sensor surface itself. In particular, changes in surface stress cause a microfabricated cantilever with two different faces to bend. The sensitivity of this technique is so high that tiny changes resulting from silanization, changes in pH or salt concentration, as well as adsorption of proteins or thiol monolayers can be detected.[4, 5]

So far, such measurements have been limited by the residual drift of the cantilever deflection. Recently, scientists at the IBM laboratories in Rüschlikon (Switzerland) and at the University of Basel have overcome this problem using an array of microfabricated silicon cantilevers for differential measurements of surface stress changes. Calibration offsets and drift can be thereby compensated, which made possible the identification and quantification of analyte vapors in gas mixtures. In short, an artificial nose was created.[6] Based on this technological advancement, Fritz et al. have now taken the next step: The observation of specific biomolecular binding events, particularly the hybridization of complementary oligonucleotides, with surprisingly high precision and even so far as the detection of single base-pair mismatches (Figure 1).[7]

The gold-coated faces of two cantilevers were covered with monolayers of thiol-functionalized 12-mer oligonucleotides differing in only one base at the central positions of their sequences (Figure 1 a). This allows for specific binding of a complementary oligonucleotide to the cantilever which carries the matching DNA sequence while the other cantilever surface remains essentially unaffected. Thus, in the experiment, the hybridization of matching DNA strands resulted in a relative deflection of the corresponding cantilever (Figure 1 b). Injection of the second oligonucleotide complementary to the sequence on the reference cantilever eliminated the differential signal (Figure 1 c).

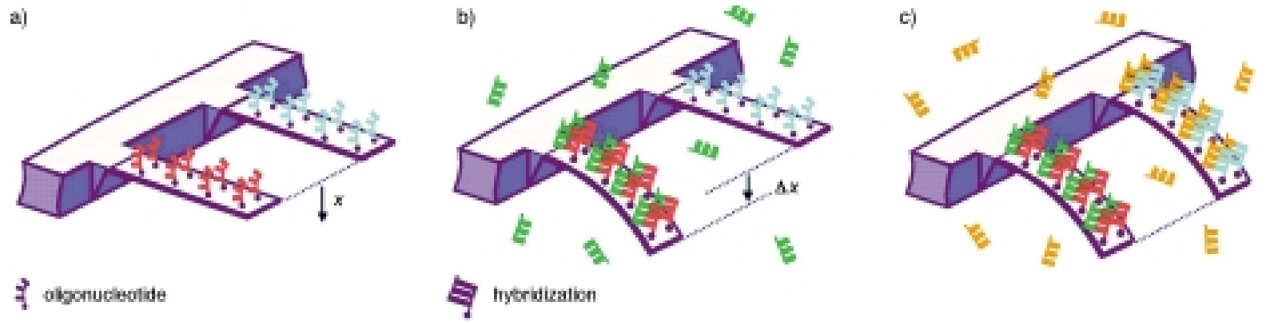

Figure 1. Detection method for single base-pair mismatches in oligonucleotide-functionalized cantilevers (adapted from ref. [7]). The surface-bound oligonucleotides are represented in red and blue, those in solution are green and orange.

The work by Fritz et al. has demonstrated that molecular recognition events can be selectively detected by the "nanomechanical" response of parallel cantilevers, that is, without the need of fluorescent or radioactive labels, optical excitation, or other external probes. After the experiment, the analyte DNA strands can be removed by rinsing with denaturation and unbinding agents, which allows for the repeated recycling of the cantilever arrays. Currently, the cantilevers provide a surface area to carry approximately the same number of oligonucleotides as on a typical DNA chip ($\sim 10^{10}$) but it is expect-

---

[a] Dr. M. Seitz, Dr. H. Clausen-Schaumann,
Dr. M. Rief
Lehrstuhl für Angewandte Physik
and Center for NanoScience
Ludwig-Maximilians-Universität
Amalienstrasse 54, 80799 München (Germany)
Fax: (+49) 89-2180-2050
E-mail: markus.seitz@physik.uni-muenchen.de

ed that this number can be further reduced by a factor of 10^3. In addition, the parallel integration of more than one thousand cantilevers has been realized,[8] such that the technique is envisioned to enable development of a new generation of DNA chips with potential for the detection of single nucleotide polymorphisms (SNP). Moreover, it provides a general scheme for highly sensitive binding assays based on nanomechanics, which can be used to specifically detect minute amounts of analyte. The specific transduction of (bio-)chemical stimuli into nanomechanical work opens new perspectives for the development of "smart" devices.

[1] G. Binnig, C. F. Quate, C. Gerber, *Phys. Rev. Lett.* **1986**, *56*, 930 – 933.
[2] E.-L. Florin, V. T. Moy, H. E. Gaub, *Science* **1994**, *264*, 415 – 417.
[3] M. Rief, F. Oesterhelt, B. Heymann, H. E. Gaub, *Science* **1997**, *275*, 1295 – 1298.
[4] H. J. Butt, *J. Colloid Interface Sci.* **1996**, *180*, 251 – 260.
[5] R. Berger, E. Delamarche, H. P. Lang, C. Gerber, J. K. Gimzewski, E. Meyer, H. J. Güntherodt, *Science* **1997**, *276*, 2021 – 2024.
[6] M. K. Baller, H. P. Lang, J. Fritz, C. Gerber, J. K. Gimzewksi, U. Drechsler, H. Rothuizen, M. Despont, P. Vettiger, F. M. Battiston, J. P. Ramseyer, P. Fornaro, E. Meyer, H. J. Güntherodt, *Ultramicroscopy* **2000**, *82*, 1 – 9.
[7] J. Fritz, M. K. Baller, H. P. Lang, H. Rothuizen, P. Vettiger, E. Meyer, H. J. Güntherodt, C. Gerber, J. K. Gimzewski, *Science* **2000**, *288*, 316 – 318.
[8] P. Vettiger, J. Brugger, M. Despont, U. Drechsler, U. Durig, W. Haberle, M. Lutwyche, H. Rothuizen, R. Stutz, R. Widmer, G. Binnig, *Microelectron. Eng.* **1999**, *46*, 11 – 17.

Ordered Mesostructured Materials with Optical Functionality**

Gernot Wirnsberger[a] and Galen D. Stucky*[a]

KEYWORDS:

mesoporosity · nanostructures · photochemistry · polymers · surfactants

Nearly ten years have passed since the first reports on ordered mesoporous materials appeared. Research on these materials has mainly focused on either synthetic routes to new compounds within this class or on their potential uses as sorbents, catalysts, and for separation. On the other hand, until very recently, there has been only a limited number of publications dealing with mesostructured and mesoporous materials that have an optical functionality. One reason may be the ordering length scale of mesostructures itself: Whereas small molecules can be well aligned by microporous hosts (pore sizes ~3 – 15 Å), this is not easily feasible without external stimuli (like electrical fields) in mesostructured materials since the channels/pores have diameters of at least about 20 Å. At the other end of the length scale are macroporous solids, ordered structures with repeat motifs or modulations of several hundred nanometers. They are thought to be very promising candidates for photonic crystals which can, for example, route light or provide laser cavities if the emission of a photo-active species falls within the band-gap of the photonic crystal.[1] Is there also room on the mesoscale to synthesize new, useful composites which have optical functionalities? Indeed, a deeper look at mesostructured compounds reveals a rich chemistry which can be used to generate composites that have desirable optical properties. Here, we briefly summarize very recent reports in this field showing how one can make use of the porous structure, the silica – surfactant interface, direct dye – surfactant co-assembly, and several other routes to create exciting new composite materials (Figure 1).

One obvious way of generating optical mesostructured materials is to utilize organized pores as host media after removal of the surfactant, either by calcination or milder solvent extraction. These accessible pores can then be used for *intrapore* guest alignment. As mentioned, this alignment is generally difficult for small molecules without the application of external stimuli. However, larger species like polymers can be oriented in monolithic MCM-41 type materials.[2] An important point is that the surface properties (hydrophobicity, polarity) of the silica host need to be matched with those of the polymer in order to successfully incorporate a polymer. This can be achieved by treating monolithic pieces with silylating agents, such as chlorotrimethylsilane or chlorodimethylphenylsilane. Additionally, this treatment reduces the effective free pore diameter and, hence,

---

[a] *G. D. Stucky, G. Wirnsberger*
Department of Chemistry and Biochemistry
University of California
Santa Barbara, CA 93106 (USA)
Fax: (+1) 805-893-4120
E-mail: stucky@chem.ucsb.edu

[**] *G.W. is on leave from the Karl-Franzens-University (Graz, Austria) and would like to acknowledge the Fonds zur Förderung wissenschaftlicher Forschung (Austria) for an Erwin Schrödinger fellowship (J1643-CHE). This work was supported in part by the US Army Research Office MURI program, by the US National Science Foundation (grant DMR 96-34396), and by the US National Science Foundation IGERT program.*

ed that this number can be further reduced by a factor of 10^3. In addition, the parallel integration of more than one thousand cantilevers has been realized,[8] such that the technique is envisioned to enable development of a new generation of DNA chips with potential for the detection of single nucleotide polymorphisms (SNP). Moreover, it provides a general scheme for highly sensitive binding assays based on nanomechanics, which can be used to specifically detect minute amounts of analyte. The specific transduction of (bio-)chemical stimuli into nanomechanical work opens new perspectives for the development of "smart" devices.

[1] G. Binnig, C. F. Quate, C. Gerber, *Phys. Rev. Lett.* **1986**, *56*, 930 – 933.
[2] E.-L. Florin, V. T. Moy, H. E. Gaub, *Science* **1994**, *264*, 415 – 417.
[3] M. Rief, F. Oesterhelt, B. Heymann, H. E. Gaub, *Science* **1997**, *275*, 1295 – 1298.
[4] H. J. Butt, *J. Colloid Interface Sci.* **1996**, *180*, 251 – 260.
[5] R. Berger, E. Delamarche, H. P. Lang, C. Gerber, J. K. Gimzewski, E. Meyer, H. J. Güntherodt, *Science* **1997**, *276*, 2021 – 2024.
[6] M. K. Baller, H. P. Lang, J. Fritz, C. Gerber, J. K. Gimzewksi, U. Drechsler, H. Rothuizen, M. Despont, P. Vettiger, F. M. Battiston, J. P. Ramseyer, P. Fornaro, E. Meyer, H. J. Güntherodt, *Ultramicroscopy* **2000**, *82*, 1 – 9.
[7] J. Fritz, M. K. Baller, H. P. Lang, H. Rothuizen, P. Vettiger, E. Meyer, H. J. Güntherodt, C. Gerber, J. K. Gimzewski, *Science* **2000**, *288*, 316 – 318.
[8] P. Vettiger, J. Brugger, M. Despont, U. Drechsler, U. Durig, W. Haberle, M. Lutwyche, H. Rothuizen, R. Stutz, R. Widmer, G. Binnig, *Microelectron. Eng.* **1999**, *46*, 11 – 17.

Ordered Mesostructured Materials with Optical Functionality[**]

Gernot Wirnsberger[a] and Galen D. Stucky*[a]

KEYWORDS:

mesoporosity · nanostructures · photochemistry · polymers · surfactants

Nearly ten years have passed since the first reports on ordered mesoporous materials appeared. Research on these materials has mainly focused on either synthetic routes to new compounds within this class or on their potential uses as sorbents, catalysts, and for separation. On the other hand, until very recently, there has been only a limited number of publications dealing with mesostructured and mesoporous materials that have an optical functionality. One reason may be the ordering length scale of mesostructures itself: Whereas small molecules can be well aligned by microporous hosts (pore sizes ~3 – 15 Å), this is not easily feasible without external stimuli (like electrical fields) in mesostructured materials since the channels/pores have diameters of at least about 20 Å. At the other end of the length scale are macroporous solids, ordered structures with repeat motifs or modulations of several hundred nanometers. They are thought to be very promising candidates for photonic crystals which can, for example, route light or provide laser cavities if the emission of a photo-active species falls within the band-gap of the photonic crystal.[1] Is there also room on the mesoscale to synthesize new, useful composites which have optical functionalities? Indeed, a deeper look at mesostructured compounds reveals a rich chemistry which can be used to generate composites that have desirable optical properties. Here, we briefly summarize very recent reports in this field showing how one can make use of the porous structure, the silica – surfactant interface, direct dye – surfactant co-assembly, and several other routes to create exciting new composite materials (Figure 1).

One obvious way of generating optical mesostructured materials is to utilize organized pores as host media after removal of the surfactant, either by calcination or milder solvent extraction. These accessible pores can then be used for *intrapore* guest alignment. As mentioned, this alignment is generally difficult for small molecules without the application of external stimuli. However, larger species like polymers can be oriented in monolithic MCM-41 type materials.[2] An important point is that the surface properties (hydrophobicity, polarity) of the silica host need to be matched with those of the polymer in order to successfully incorporate a polymer. This can be achieved by treating monolithic pieces with silylating agents, such as chlorotrimethylsilane or chlorodimethylphenylsilane. Additionally, this treatment reduces the effective free pore diameter and, hence,

---

[a] *G. D. Stucky, G. Wirnsberger*
Department of Chemistry and Biochemistry
University of California
Santa Barbara, CA 93106 (USA)
Fax: (+1) 805-893-4120
E-mail: stucky@chem.ucsb.edu

[**] *G.W. is on leave from the Karl-Franzens-University (Graz, Austria) and would like to acknowledge the Fonds zur Förderung wissenschaftlicher Forschung (Austria) for an Erwin Schrödinger fellowship (J1643-CHE). This work was supported in part by the US Army Research Office MURI program, by the US National Science Foundation (grant DMR 96-34396), and by the US National Science Foundation IGERT program.*

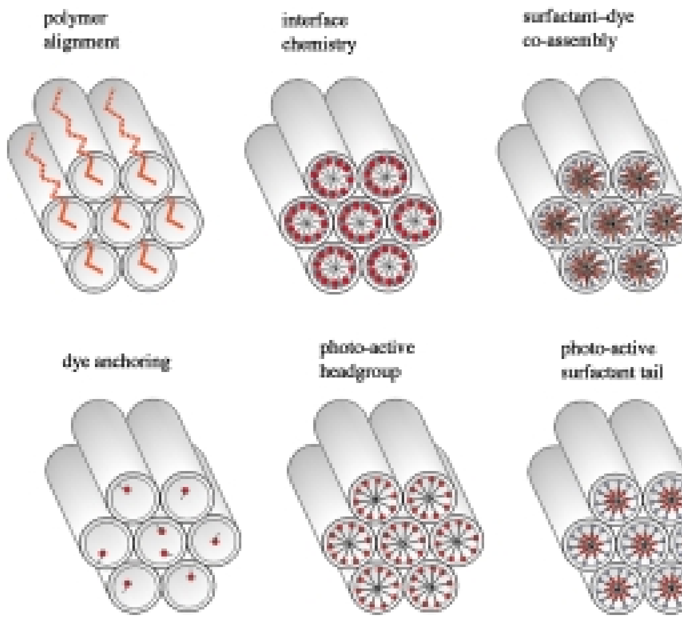

Figure 1. *Schematic illustration of some possibilities to derive photo-active mesostructured/mesoporous materials. The photo-active units are highlighted in red.*

helps in aligning the polymer effectively. The optical properties of the composite in the visible to near UV range are determined by the polymer and the anisotropy of its alignment. The silica host only functions as a rigid template for the polymer alignment. It also does not significantly emit or absorb light in the important visible range and is, therefore, an ideally suited host for polymers. A relatively small pore size (of about 17 Å) induces a highly orientated ordering for the polymers when they are embedded, as shown by polarization-dependent fluorescence measurements.[2] This example nicely demonstrates how nanopore architecture can be combined with pore chemistry to engineer new nanocomposites with strongly anisotropic optical properties.

Another approach is to use the highly reactive walls of as-synthesized materials as attachment sites for optically active species,[3] a procedure which has been elegantly adopted by the group of G. A. Ozin. Instead of using empty pore spaces, this group directly uses as-synthesized mesostructures as hosts for the synthesis of size-confined silicon clusters.[4] Although the composites in their as-synthesized form are relatively dense materials, hydrophobic precursor molecules can enter the pores via the vapor phase, since the hydrophobic part of the surfactant enables the reactive precursor uptake. The very large inner inorganic/organic surface provides a highly reactive area for subsequent attachment of the molecules. Once sorbed into the mesostructured film, surface silanols are especially responsible for the anchoring of the Si_2H_6 precursor and the nucleation of silicon clusters. This process is performed at comparably low temperatures (100 – 140 °C). The size of the resulting silicon clusters is then limited by the rigid silica structure (and, probably, by the space available between the surfactants). In a manner similar to porous silicon, these clusters, with a size of about 1 nm, exhibit a yellow-orange photoluminescence. Although the incorporation of these materials into straightforward devices like light-emitting diodes seems currently to be limited by the fact that the photoluminescence is strongly reduced at room temperature, this very mild chemical vapor deposition (CVD) method to form size-limited silicon clusters represents an important way for low-temperature routes towards optical composites for devices.

Besides polymers and clusters, mesostructured and mesoporous materials can also host dyes. Dye-doping into organic matrices and inorganic sol – gel glasses has now a long tradition and, above all, the latter class finds wide application as host materials. Most reports have focused on the incorporation of laser dyes in silica sol – gel glasses[5] (pure oxides and organically modified silicates, the ORMOSILs) and these matrices were shown to combine rigidity with high photostability of the dyes. All these advantages are also offered by ordered mesostructured materials. Additionally, the well defined nanoseparation of hydrophilic/hydrophobic regions also makes possible a more sophisticated tuning of the dye microenvironment. The dyes can be easily incorporated during synthesis, which is the simplest way of generating such multicomponent materials. In the case of mesostructured materials employing cetyltrimethylammonium surfactants (pore sizes up to around 60 Å), dyes have been occluded during synthesis to give mainly dye-doped powders. Copper phthalocyanine doped materials were derived by the simultaneous use of specially designed surfactants which solubilize the phthalocyanine through hydrophopic interactions.[6] From the optical properties of the embedded phthalocyanines, it was concluded that they are in a rather isolated state and that the formation of copper phthalocyanine aggregates was prevented. Similar results were obtained for zinc phthalocyanines.[7] Here, however, very high dye concentrations were used, which resulted in small distances between the dyes of about 3 nm in the solid. Despite this, the photophysical behavior of the dyes is indicative of isolated units, thus confirming the high dispersion achieved by a proposed surfactant – dye co-assembly process.[7] It was also demonstrated that positively and negatively charged phthalocyanines, as well as neutral ones, can be highly dispersed, to thus reveal a very general concept.

Dyes can also be incorporated in fibers grown from two-phase systems.[8] This is an important task, as materials with well defined macroscopic shape are needed for most optical applications. In these fibers, which were doped with the laser dye rhodamine 6G, the distribution of the dye is homogeneous along the macroscopic dimensions of the fiber (several millimeters), as shown by the only small variation in the absorption. The usefulness of these composite fibers was demonstrated by the fact that they exhibit amplified spontaneous emission (ASE) under optical pumping, an effect which leads to a laser-like, narrow spectral width emission (full width at half-height maximum (FWHM) of 7 – 8 nm) at the end of the fibers. A further easy and rapid approach to bring dye-doped mesostructures into a desired shape is to use soft lithographic methods, such as micromolding in capillaries.[9] For example, high fidelity waveguide patterns composed of silica and block copolymers can be generated within hours.[10] When doped with rhodamine 6G, these waveguides exhibit ASE at thresholds as low as around 5 $kW\,cm^{-2}$. Recently, the threshold could be further improved to $\sim 1.4\ kW\,cm^{-2}$ by employing a microring laser geometry on an optical fiber which yields very narrow (multi)line output (FWHM of ~ 1.5 Å).[11] This value compares very well with the better, purely organic systems (for example, semiconducting polymers). The fact that the threshold can be reduced by employing relatively high dye concentrations suggests that the again block copolymers help to highly disperse the dye molecules and hence to prevent unwanted dimerization (which reduces quantum efficiency). However, for all the studies employing direct dye-doping during synthesis, further spectroscopic studies are clearly necessary in order to elucidate whether the dye molecules are completely co-assembled with the surfactants or whether the dyes are also partially incorporated within the silica walls.

A direct anchoring of dye molecules during synthesis is a further extension and the first steps towards this have been made. For example, 3-(2,4-dinitrophenylamino)propyltriethoxysilane was incorporated in transparent monoliths during synthesis.[12] Anchoring is achieved by the hydrolysis of the triethoxysilane unit of the dye and condensation reactions with the proper silica source (in most cases tetraethoxysilane or tetramethoxysilane). Similarly, azo and laser dyes have been incorporated into MCM-41 powders by microwave synthesis.[13] This covalent dye linking should allow one to remove the surfactant by a low temperature hydro- or solvothermal post-process, to leave behind a porous matrix where the anchored dye (or complex) is easily accessed by vapors or liquids—an especially important task in sensing applications, in which fast response times are required. Covalent dye incorporation as part of the extended mesostructure framework through the use of $(R'O)_3Si\text{-}R\text{-}Si(OR')_3$ siloxane precursors[14–16] is a possible alternative approach.

Another method of anchoring dyes involves the use of functional silanes (such as 3-aminopropyltrimethoxysilane) to create mesoporous compounds with reactive sites. This approach has been successfully combined with rapid printing procedures like inkjet printing, micropen lithography, and dip coating on surface-aligned monolayers.[17] The latter procedures allow a very fast processing of photonic and microfluidic mesoporous systems of designed macroscopic shape on arbitrary surfaces. After surfactant removal, the dyes can be attached to the inner surface of the mesoporous structures by using the reactive amino group which does not degrade during calcination. In this way, pH-sensing microfluidic systems have been created, in which the fluorescence in the center of a fluidic system is dependent on the acidity of the solution introduced into the system at one end.

To summarize, the very young field of photo-active mesostructured materials is an exciting area that opens the path to useful composite materials. New concepts such as polymer alignment with mesopores, the use of reactive interfaces, surfactant – dye co-assembly, anchoring of dyes, and the incorporation of complexes and clusters, as well as tuning the inorganic component (frameworks of different oxides and sulfides are available) provide a broad basis for photo-active compounds to be structured on a length scale between 2 and 15 nm. Some of these compounds have already been shown to have improved properties when compared with conventional sol – gel glasses.[10] The use of modified surfactants, which themselves may carry a subunit located either on the headgroup[18] or the hydrophobic tail, is a further promising route. Figure 1 depicts, in a schematic fashion, these different approaches. Further, new synergetic effects in silica – dye – surfactant co-assembled systems can be expected, as has been recently shown for sol – gel glasses housing both dyes and surfactants (in low concentrations).[19]

[1] For an introduction, see: J. D. Joannopoulos, R. D. Meade, J. N. Winn, *Photonic Crystals*, Princeton University Press, Princeton, **1995**.

[2] J. Wu, A. F. Gross, S. H. Tolbert, *J. Phys. Chem. B* **1999**, *103*, 2374 – 2384.

[3] J. C. Vartuli, K. D. Schmitt, C. T. Kresge, W. J. Roth, M. E. Leonowicz, S. B. McCullen, S. D. Hellring, J. S. Beck, J. L. Schlenker, D. H. Olson, E. W. Sheppard, *Chem. Mater.* **1994**, *6*, 2317 – 2326.

[4] Ö. Dag, G. A. Ozin, H. Yang, C. Reber, G. Bussière, *Adv. Mater.* **1999**, *11*, 474 – 480.

[5] For review articles, see, among others: S. Sakka, *Struct. Bond.* **1996**, *85*, 1 – 50; R. Reisfeld, *Struct. Bond.* **1996**, *85*, 215 – 234.

[6] H. S. Zhou, H. Sasabe, I. Honma, *J. Mater. Chem.* **1998**, *8*, 515 – 516.

[7] M. Ganschow, D. Wöhrle, G. Schulz-Ekloff, *J. Porphyrins Phthalocyanins* **1999**, *3*, 299 – 303.

[8] F. Marlow, M. D. McGehee, D. Zhao, B. F. Chmelka, G. D. Stucky, *Adv. Mater.* **1999**, *11*, 632 – 636.

[9] Y. Xia, J. A. Rogers, K. E. Paul, G. M. Whitesides, *Chem. Rev.* **1999**, *99*, 1823 – 1848.

[10] P. Yang, G. Wirnsberger, H. Huang, S. R. Cordero, B. Scott, M. D. McGehee, T. Deng, G. M. Whitesides, B. F. Chmelka, S. K. Buratto, G. D. Stucky, *Science* **2000**, *287*, 465 – 467.

[11] G. Wirnsberger, G. D. Stucky, *Chem. Mater.* **2000**, in press.

[12] B. Lebeau, C. F. Fowler, S. R. Hall, S. Mann, *J. Mater. Chem.* **1999**, *9*, 2279 – 2281.

[13] M. Ganschow, M. Wark, D. Wöhrle, G. Schulz-Ekloff, *Angew. Chem.* **2000**, *112*, 167 – 170; *Angew. Chem. Int. Ed.* **2000**, *39*, 161 – 163.

[14] S. Inagaki, S. Guan, Y. Fukushima, T. Ohsuna, O. Terasaki, *J. Am. Chem. Soc.* **1999**, *121*, 9611 – 9614.

[15] B. J. Melde, B. T. Holland, C. F. Blanford, A. Stein, *Chem. Mater.* **1999**, *11*, 3302 – 3308.

[16] T. Asefa, M. J. MacLachlan, N. Coombs, G. A. Ozin, *Nature* **1999**, *402*, 867 – 871.

[17] H. Fan, Y. Lu, A. Stump, S. T. Reed, T. Baer, R. Schunk, V. Perez-Luna, G. P. López, C. J. Brinker, *Nature* **2000**, *405*, 56 – 60.

[18] H. B. Jervis, M. E. Raimondi, R. Raja, T. Maschmeyer, J. M. Seddon, D. W. Bruce, *Chem. Commun.* **1999**, 2031 – 2032.

[19] C. Rottman, G. Grader, Y. D. Hazan, S. Melchior, D. Avnir, *J. Am. Chem. Soc.* **1999**, *121*, 8533 – 8543.

Photoluminescence of Titanosilsesquioxanes in Solution and Its Relevance for the Understanding of the Emission of Titanosilicates**

Avelino Corma,*[a, †] Mark Crocker,[b]
Hermenegildo García,*[a] and Emilio Palomares[a]

KEYWORDS:

heterogeneous catalysis · luminescence · titanium · zeolite analogues

Titanium-containing (alumino)silicates are important industrial catalysts for aromatic hydroxylation and alkene epoxidation reactions.[1–8] It is widely accepted that the catalytic sites are four-coordinate titanium atoms that are bipodally or tripodally bound to the framework of the (alumino)silicate. The improvement of the efficiency and activity of these materials is a continuous task, which would be facilitated by a deeper understanding of the active site structure and the characteristics of the corresponding transition states. For this reason, the development of more powerful, routine characterization techniques that specifically enable the minor proportion of the active titanium atoms to be monitored is required. The resulting structural information and novel experimental techniques should allow the design, preparation, and characterization of titanium-containing solids having the optimum activity and selectivity as heterogeneous catalysts.

A significant contribution in this area have been the recent reports showing that photoluminescence can be applied in titano(alumino)silicates, particularly Ti/MCM-41 and TS-1 to the determination of titanium atom distribution among different populations that have distinctive coordination spheres.[8–11] Depending on the sample preparation and post-synthetic treatments, two different weakly emitting titanium atoms were reported ($\lambda_{em} = 430$, 490 nm), that were assigned to tripodally bound titanol groups and to tetrapodally bound titanium atoms, respectively.

These initial reports have been more recently challenged by the observation that as-synthesized and silylated samples of mesoporous titanosilicates obtained by direct incorporation of titanium during the hydrothermal crystallization of the solid exhibits a remarkably more intense photoluminescence and have emission maxima at much shorter wavelengths ($\lambda_{em} = 390$ nm).[12] The intensity of the emission drops dramatically and λ_{em} shifts to longer wavelengths upon calcination and template decomposition of the original, as-synthesized Ti/MCM-41.

A fruitful strategy to understand the architecture and the catalytic activity of the active titanium sites in titanosilicates has been to synthesize simple model molecules, wherein the titanium atoms have precise coordination spheres to emulate those thought to exist in titanosilicates.[13–16] In recent papers, several groups have used homogeneous soluble titanosilsesquioxanes as model compounds.[17] They have proposed, based on the results obtained by extended X-ray absorption fine structure (EXAFS) spectroscopy, X-ray absorption near-edge structure (XANES) measurements, and molecular dynamics calculations, that the most active sites of Ti/MCM-41 are four-coordinate titanium atoms tripodally anchored to the silicate framework.[17]

Owing to the controversy surrounding the assignment of emission maxima, we have studied the photoluminescence of a series of titanosilsesquioxanes in solution. In principle they can serve as soluble model molecules to facilitate assignment of the photoluminescence observed in Ti/MCM-41 samples to specific coordination environments, thereby providing firm evidence to support or challenge previously reported assignments. In addition, photoluminescence measurements in solution have allowed us to obtain, for the first time, a whole set of quantum yields and quenching rate constants that cannot be measured for opaque solids. This quantitative measurement of photophysical parameters associated with titanium atoms is important in order to achieve a full understanding the photoluminescence of titanosilicates.

The structure and characteristics of the series of titanosilsesquioxanes under scrutiny are contained in Table 1. A full account of the synthesis and characterization of these compounds has been previously reported by one of us.[15, 16] The set has been selected to encompass a range of possible titanium coordination forms that are thought to be present in solid titanosilicates. With the exception of **4**, the titanosilsesquioxanes contains a single four-coordinate Ti atom. In this series, Ti atoms can be bonded to the polycyclic silsesquioxane skeleton by three bonds ("tripodal", as in **1** – **3**) or it can be connected to the cyclic framework by only two bonds ("bipodal", as in **5**). In the case of tripodal Ti, the fourth coordination site is saturated either by a trimethylsilyloxy group (as in [$Ti(OSi)_4$]) or by a simple alkoxy group. Compound **4** purposely contains a certain amount of the titanosilsesquioxane dimer that should allow one to address the influence of pentacoordinate, bridged "Ti–(μ-OR)$_2$–Ti" atoms on the photoluminescence. A comparison between **3** and **4** should additionally allow one to assess the sensitivity of this technique in determing the distribution of Ti atoms among different families of sites.

All the titanosilsesquioxanes studied are highly soluble in dichloromethane and cyclohexane. Studying the photolumines-

---

[a] A. Corma, H. García,[+] E. Palomares
Instituto de Tecnología Química CSIC-UPV
Universidad Politécnica de Valencia
46022 Valencia (Spain)
Fax: (+34) 96-387-78-09
E-mail: acorma@itq.upv.es

[b] M. Crocker
Shell International Chemicals, B.V.
Shell Research and Technology Centre Amsterdam
Postbus 38000, 1030 BN Amsterdam (The Netherlands)

[+] Present address:
dmc² Degussa Metals Catalysts Cerdec Corporation
Auburn Hills, MI 48326 (USA)

[†] Avelino Corma is a member of the Editorial Advisory Board of ChemPhysChem.

[**] Financial support by the Spanish CICYT (grant no. MAT97-1016-CO2) is gratefully acknowledged.

Table 1. *Structure and relevant structural parameters of the series of titanosilsesquioxanes studied in this work.*

Compound	Structure[a]	Ti coordination
1	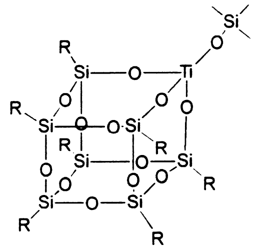	tripodal
2	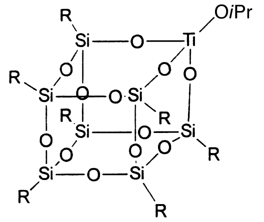	tripodal
3	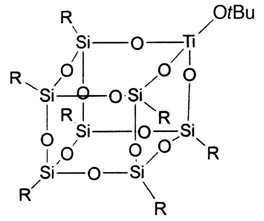	tripodal
4	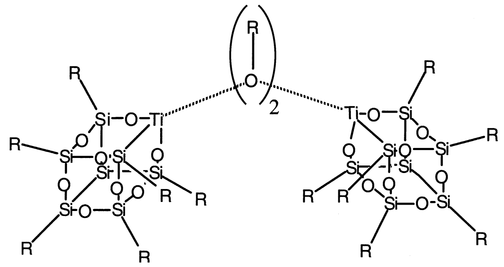	as **3** + pentacoordinate Ti dimer
5	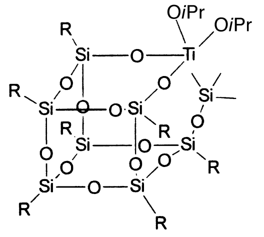	bipodal

[a] R = *cyclo*-C_6H_{11}.

cence of these compounds in different solvents permits one to obtain a set of absolute photoluminescence quantum yields and quenching rate constants, and also to determine the influence of polarity on the emission intensity and photoluminescence spectra. As far as we know, none of these data have ever been reported for titanosilsesquioxanes. These important photophysical parameters cannot be measured for opaque solids, such as titanosilicate powders, since the number of photons actually adsorbed from the incident radiation cannot be accurately determined.

The absorption spectrum of titanosilsesquioxanes in dichloromethane shows an intense band at $\lambda_{max} \approx 215$ nm, with a tail up to 300 nm. The broadness of this absorption band suggests that the 0,0-transition is at a longer wavelength than λ_{max} (see below). In cyclohexane, the absorption band shows a bathochromic shift ($\lambda_{max} \approx 225$ nm) but the onset of the absorption band also starts at 300 nm. These values for λ_{max} are typical for isolated titanium atoms and the relatively minor but significant shift in λ_{max} reflects the influence of solvent polarity on the electronic transition. The corresponding extinction coefficients are presented in Table 2. Even though sample **4** contains some dimeric "Ti–(μ-OR)$_2$–Ti" units, they are not apparent in its transmission UV spectrum.

Table 2. *Molar extinction coefficients ε, quantum yields ϕ, and luminescence lifetimes τ obtained for titanosilsesquioxanes **1**–**5** in solution.*

	Dichloromethane			Cyclohexane			
Compound	ε [M^{-1} cm^{-1}]	$\phi(N_2)$ × 10^4	$\tau(N_2)$[a,b] [ns]	ε [M^{-1} cm^{-1}]	$\phi(N_2)$ × 10^2	$\tau(N_2)$ [ns]	$\tau(O_2)$[a] [ns]
1	3595	4.8	3.5	34460	2.9	34.4	16.38
2	5170	6.0	2.8	10750	3.0	30.4	16.8
3	6130	10.0	6.2	9880	2.8	30.1	17.7
4	6470	7.9	4.2(72) 1.2(28)	9540	2.4	42.6(65) 3.5(35)	15(78) 3.3(22)
5	7915	5.3		7540	1.3	35	13.6

[a] From the best fit to first-order decays. Compound **4** has two monoexponential lifetimes, whose relative contributions are indicated within brackets. [b] Lifetimes under oxygen are too short to be measured with our apparatus.

Upon UV excitation, all titanosilsesquioxanes **1**–**5** emit and the emission spectra are independent on the excitation wavelength over the range 220–280 nm. This is expected for pure compounds which have a single fluorophore. Figure 1 shows the absorption, emission, and excitation spectra of **1** in dichloromethane. The emission spectra of the rest of the series upon 250 nm excitation are compiled in Figure 2. From the crossing point of the absorption and emission spectra and assuming that both spectra involve the same electronic states, the 0,0-

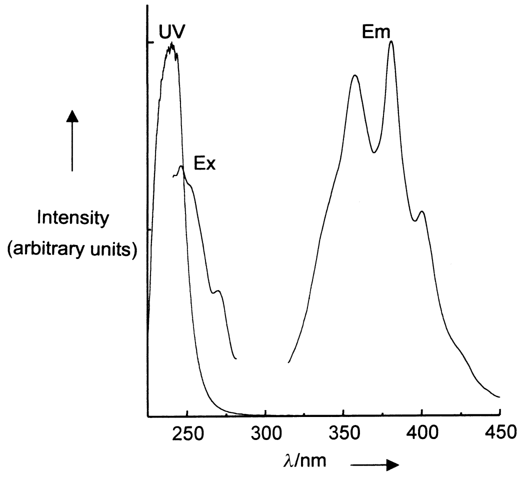

Figure 1. *UV/Vis absorption (UV), emission (Ex; λ_{ex} = 250 nm), and excitation (Ex; λ_{em} = 360 nm) spectra of **1** in CH_2Cl_2 recorded at room temperature after a nitrogen purge.*

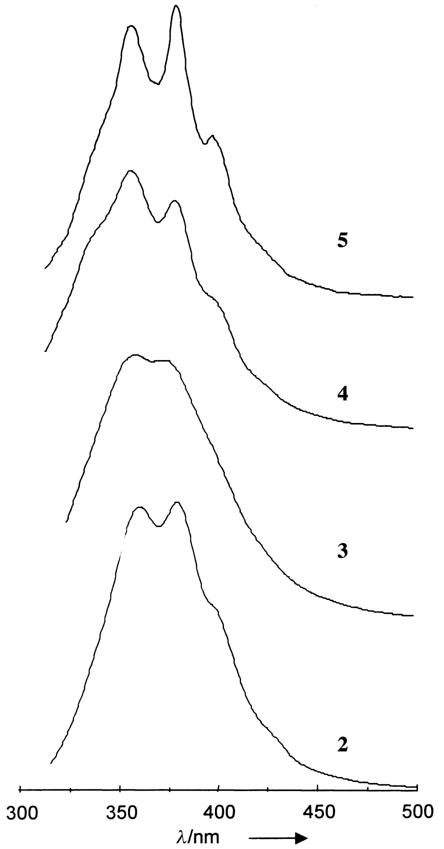

Figure 2. *Emission ($\lambda_{ex} = 250$ nm) spectra of* ***2–5*** *in CH_2Cl_2 recorded at room temperature after a nitrogen purge.*

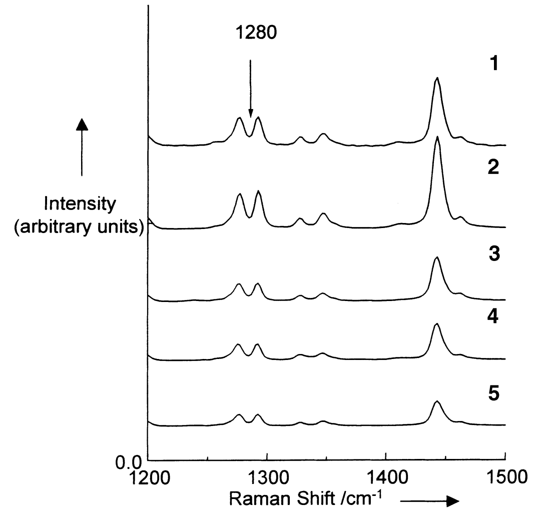

Figure 3. *FT-Raman spectra of* ***1–5*** *in CH_2Cl_2. The vibration corresponding to the fine structure observed in Figures 1 and 2 is indicated with an arrow.*

transition could be experimentally measured, to provide a value of about 306 nm.

Interestingly, the emission spectra of compounds **1–4** at room temperature all exhibit vibrational fine structure. The vibration energy was very similar in all these samples ($E_{vib} \sim 1300$ cm^{-1}). These values correspond to the wavenumbers of the Ti–O bond observed in Raman or IR spectroscopy. Thus, this vibrational structure can be taken as an evidence to show that Ti atoms participate in the emitting moiety that is observed by photoluminescence spectroscopy. As an example, Figure 3 presents the Raman spectra of titanosilsesquioxanes **1–5** in dichloromethane, in which the position of the Ti–O vibration observed in the emission spectra has been indicated.

The most significant feature of the emission spectra of **1–5** with respect to some earlier reports concerning the photoluminescence of solid titanosilicate samples is the wavelength of the maximum emission intensity. As can be seen in Figures 1 and 2, the whole series **1–5** emit in the range between 350 and 390 nm, well below the $\lambda_{em} = 490$ nm reported earlier for four-coordinate, tetrapodally bound titanium atoms[8–11] and coincident with that previously reported by us for silylated Ti/MCM-41 samples.[13] Thus, the present spectra lend strong support to our assignment of the 390 nm emission to four-coordinate titanium present in titanosilicates. Furthermore, no significant variations in the wavelength of the emission maxima are observed for titanosilsesquioxanes having tripodal or bipodal titanium atoms or "Ti–(μ-OR)$_2$–Ti" dimers. Given the fact that emissions for solid samples are characterized by much broader emission bands as compared to solution spectra, it can be concluded that it is not possible to distinguish between tripodal and bipodal titanium atoms in titanosilicates exclusively on the photoluminescence spectra. However, it still remains to be seen whether titanol groups emit in a different region. Since titanosilsesquioxanes having a ≡Ti–OH group are not stable compounds, it is not possible to address this point using titanosilsesquioxanes as model compounds and this question remains open. The possibility that the titanol groups emit at a different wavelength would reconcile our photoluminescence spectra with those reported by other groups.

It has been stated that titanosilicates exhibit an intense photoluminescence but no quantum yields have been reported. In this study, we have measured absolute emission quantum yields at room temperature in dichloromethane and cyclohexane, that clearly prove that Ti–O groups are, in reality, very weakly photoluminescent fluorophores. The values of quantum yields after nitrogen purging are included in Table 2. No large variation in the emission quantum yield values was found for the five titanosilsesquioxanes, both for the data measured under nitrogen or oxygen. Oxygen reduces the emission quantum yield by a factor of about two in every case but does not totally quench the photoluminescence. We also noted that the presence of oxygen results in the disappearance the vibrational fine structure of the emission and a blue shift of λ_{em}. In cyclohexane, the emission quantum yields for all the titanosilsesquioxane are similar and are about two orders of magnitude higher than the values measured in dichloromethane. This can be rationalized on the basis that dichloromethane is somehow quenching the emission of Ti–O groups. Related precedents, that report dichloromethane can interact with weakly emitting azo compounds through an aborted hydrogen transfer mechanism to decrease the photoluminescence intensity, can be found in the literature.[18] By applying the Stern–Volmer equation[19] and given that the lifetime of fluorescence lifetime in the absence of quencher is 3.5 ns (see below), the quenching rate constant of the photoluminescence by oxygen in dichloromethane can be calculated. The value obtained ($2.4 \times 10^{10}\,\mathrm{M\,s^{-1}}$) indicates that the quenching is predominantly a diffusion-controlled process.

Analysis of the photoluminescence kinetics is a powerful tool to gain information about site distribution and relative population as well as the influence of the environment on the emitting fluorophores. However, in spite the importance of time-resolved studies in emission spectroscopy, there is a paucity of emission lifetime measurements in titanosilicates. We measured emission time profile for the series of titanosilsesquioxanes, both in dichloromethane and in cyclohexane (Table 2). In the absence of oxygen, all the emission decays occur on the nanosecond timescale and one order of magnitude longer in cyclohexane than in dichloromethane. This observation is in agreement with our previous measurements of much higher emission quantum yields in cyclohexane than in dichloromethane, which suggests a special photoluminescence quenching mechanism in dichloromethane.[18] All the kinetic results, except that for **4**, can be fitted to single exponential decays, to indicate that there is only a single family of light-emitting titanium atoms. The corresponding lifetimes can be, then, obtained from the best fit to the experimental decay. A list of the values are summarized in Table 2. As expected, oxygen purging not only reduces the emission intensity but shortens the lifetime of the emission. A selection of representative emission decays under different conditions together with the corresponding fit from which lifetimes have been obtained are shown in Figure 4.

In the case of **4**, in which a mixture of monomeric and dimeric titanosilsesquioxane exists, a single first-order decay does not fit. An adequate fit is obtained by considering two superimposed monoexponential decays. Taking into account that the lifetime of the pure titanosilsesquioxane monomer **3** (see Table 2), it seems reasonable to conclude that the short and long components of **4** correspond to the decay of the dimer and monomer, respectively. The relative contribution of the shorter lifetime component to the total emission is around 30% (see Table 2), which is in reasonable agreement with the amount of dimer present in **4**. It is worth noting that while photoluminescence spectrum do not report the presence of two types of titanium atoms in **4** (monomer plus dimer), the kinetic analysis of the emission decay is much more informative in this respect. Precedents which use the fit of the emission decay to determine the relative population of different families of a fluorophore abound in the literature.

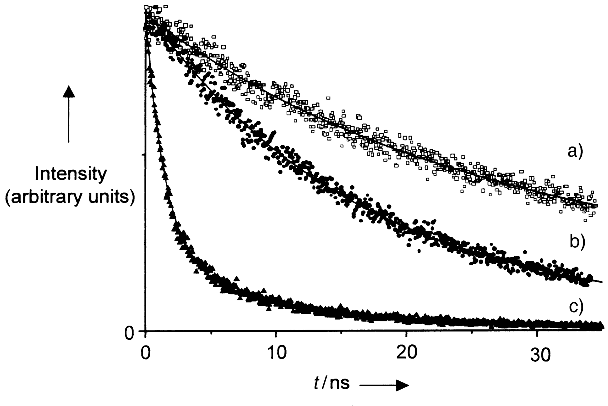

*Figure 4. Photoluminescence decays of **1** ($\lambda_{ex} = 250$ nm) monitored at 375 nm in cyclohexane under nitrogen (a) or oxygen (b), or in dichloromethane under nitrogen (c).*

The photoluminescence time profile of the titanosilicates has been studied.[12] Thus, it is of interest to compare the decay of titanosilicates with that measured here for titanosilsesquioxane in solution since this can give a good indication of how valid soluble titanosilsesquioxanes are as model compounds for solid titanosilicates. Figure 5 provides a comparison of the emission decay of silylated Ti-MCM-41 with that of titanosilsesquioxane **1** in dichloromethane. The similarity between these two decays is remarkable and experimentally supports the validity of using titanosilsesquioxane to investigate the photophysical properties of solid titanosilicates.

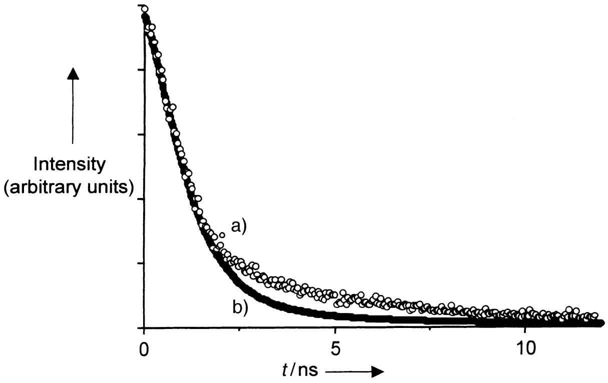

*Figure 5. Comparison of the photoluminescence decay of **1** in dichloromethane under nitrogen (a) with that of silylated Ti-MCM-41 (b).*

From the results presented on the photoluminescence of titanosilsesquioxanes in solution, it can be concluded that Ti–O is, in general, a weakly emitting group. The emission quantum yields are, however, strongly influenced by the experimental conditions of the measurements and particularly by the nature of the solvent. The wavelength recorded for the emission maxima is well below 400 nm and is apparently rather insensitive to the solvent and to the bipodal, tripodal, or dimeric structure of the titanosilsesquioxane. This observation lends strong support to our previous assignment of an emission at $\lambda = 390$ nm observed for titanosilicates as characteristic of four-coordinate titanium atoms lacking bonded OH groups.

Experimental Section

Compounds **1**–**5** correspond to the same samples as those prepared and characterized in refs. [15, 16]. The solvents used were of spectrophotometric grade and used as received. Except for oxygen-purged measurements, titanosilsesquioxanes were handled under a nitrogen atmosphere in a glove box and weighed amounts of them transferred to Suprasil quartz tubes. In most of the experiments, the tubes sealed under vacuum (10^{-4} Torr) or, alternatively, capped with septa for quenching experiments. In the latter case, the photoluminescence measurements were measured shortly after preparation. UV/Vis spectra of compounds **1**–**5** in solution (10^{-3}–10^{-4} M) were collected on Cary 5-G Varian spectrophotometer. Emission and excitation spectra were recorded in a Edinburgh FS-900 spectrophotometer. Quantum yields were obtained using a solution of naphthalene in cyclohexane as reference, whose optical density matched that of the samples at the excitation wavelength. For oxygen quenching, the solutions were purged with an oxygen stream for at least 10 min before photoluminescence measurements. Lifetimes were measured with a FL-900 single-photon counting photometer using a nanosecond hydrogen flash lamp.

[1] B. Notari, *Adv. Catal.* **1996**, *41*, 253–334.
[2] J. Reddy, R. Kumar, P. Ratnasamy, *Appl. Catal.* **1990**, *58*, 1.
[3] J. S. Reddy, U. K. Khire, P. Ratnasamy, R. B. Mitra, *J. Chem. Soc. Chem. Commun.* **1992**, 1234–1235.
[4] D. Scarano, A. Zecchina, S. Bordiga, F. Geobaldo, G. Spoto, G. Petrini, G. Leofanti, M. Padovan, G. Tozzola, *J. Chem. Soc. Faraday Trans.* **1993**, *89*, 4123.
[5] A. Corma, M. A. Camblor, P. Esteve, A. Martínez, J. Pérez-Pariente, *J. Catal.* **1994**, *145*, 151–158.
[6] A. Corma, P. Esteve, A. Martínez, S. Valencia, *J. Catal.* **1995**, *152*, 18–24.
[7] M. Alvaro, A. Corma, H. García, S. Valencia, *Appl. Catal. A* **1995**, *128*, L7–L11.
[8] M. E. Raimondi, L. Marchese, E. Gianotti, T. Maschmeyer, J. M. Seddon, S. Collucia, *Chem. Comm.* **1999**, 87–88.
[9] C. Lamberti, S. Bordiga, D. Arduino, A. Zecchina, F. Geobaldo, G. Spanó, F. Genoni, G. Petrini, F. Villain, G. Vlaic, *J. Phys. Chem. B* **1998**, *102*, 6382–6390.
[10] L. Marchese, T. Maschmeyer, E. Gianotti, S. Coluccia, J. M. Thomas, *J. Phys. Chem. B* **1997**, *101*, 8836–8838.
[11] L. Marchese, E. Gianotti, T. Maschmeyer, G. Martra, S. Coluccia, J. M. Thomas, *Nuov. Cimento Soc. Ital. Fis. D* **1997**, *19*, 1707–1718.
[12] A. Corma, H. García, M. T. Navarro, E. Palomares, F. Rey, *Chem. Mater.*, in press.
[13] H. C. L. Abbenhuis, S. Krijnen, R. A. van Santen, *Chem. Commun.* **1997**, 331–332.
[14] T. Maschmeyer, M. C. Klunduk, C. M. Martin, D. S. Shepard, J. M. Thomas, B. F. G. Johnson, *Chem. Commun.* **1997**, 1847–1848.
[15] M. Crocker, R. H. M. Herold, A. G. Orpen, *Chem. Commun.* **1997**, 2411–2412.
[16] M. Crocker, R. H. M. Herold, A. G. Orpen, M. T. A. Overgaag, *J. Chem. Soc. Dalton Trans.* **1999**, 3791–3804.
[17] J. M. Thomas, G. Sankar, M. C. Klunduk, M. P. Attfield, T. Maschmeyer, B. F. G. Johnson, R. G. Bell, *J. Phys. Chem. B* **1999**, *103*, 8809–8813.
[18] W. M. Nau, G. Greiner, H. Rau, J. Wall, M. Olivucci, J. C. Scaiano, *J. Phys. Chem. A* **1999**, *103*, 1579–1584.
[19] A. Gilbert, J. Baggott, *Essentials of Organic Photochemistry*, Blackwell, Oxford, **1990**.

Received: June 2, 2000 [Z 45]

Physical Consequences of a Mechanically Interlocked Architecture: Benzylic Amide Catenane NH Stretching Vibrations as Sensitive Probes for Weakly Hydrogen-Bonding Environments**

Charles-Andre Fustin,[a] David A. Leigh,*[b]
Petra Rudolf,*[a] Dirk Timpel,[c] and
Francesco Zerbetto*[c]

KEYWORDS:

catenanes · hydrogen bonds · macrocycles · molecular dynamics · vibrational spectroscopy

One of the issues still to be fully explored in the interlocking of molecular-level components to form catenanes and rotaxanes is the nature of the physical and chemical effects that can be induced or influenced through such architectures.[1] The weak intercomponent forces generally used to promote the assembly of such structures, combined with the restricted degrees of freedom imposed on the components by interlocking, provide a situation unlike either supramolecular systems (in which the weakly bound components are normally exchangeable between assemblies) or conventional molecular architectures (where the rules of covalent bonding tend to impose rigorous requirements on every bond distance and angle). The benzylic isophthalamide macrocycle **1** is remarkable in that it can be studied under all three situations (Scheme 1); as a simple macrocycle, a supramolecular complex with (and sensor for) CO_2[2] or as an interlocked dimer in the form of the [2]catenane **2**.[3] Differences,

---

[a] *Dr. P. Rudolf, Dr. C.-A. Fustin*
Laboratoire Interdisciplinaire de Spectroscopie Electronique
Facultes Universitaires Notre-Dame de la Paix
Rue de Bruxelles, 5000 Namur (Belgium)
Fax: (+32) 81-72-45-95
E-mail: Petra.Rudolf@fundp.ac.be

[b] *Prof. D. A. Leigh*
Centre for Supramolecular and Macromolecular Chemistry
Department of Chemistry
University of Warwick
Coventry CV4 7AL (UK)
Fax: (+44) 2476-523258
E-mail: David.Leigh@warwick.ac.uk

[c] *Dr. F. Zerbetto, Dr. D. Timpel*
Dipartimento di Chimica "G. Ciamician"
Università degli Studi di Bologna
V. F. Selmi 2, 40126 Bologna (Italy)
Fax: (+39) 051-209-94-73
E-mail: gatto@ciam.unibo.it

[**] *This work has been supported by the European Community (TMR contract FMRX-CT97-0097) and by the Belgian National Program of Interuniversity Research (Project "Science of Interfaces and Mesoscopic Structures"). C.-A.F. acknowledges the FRIA for financial support. F.Z. received partial financial support from MURST project "Supramolecular Devices". D.A.L. is an EPSRC Advanced Research Fellow (AF/98/2324).*

septa for quenching experiments. In the latter case, the photoluminescence measurements were measured shortly after preparation. UV/Vis spectra of compounds **1**–**5** in solution (10^{-3}–10^{-4} M) were collected on Cary 5-G Varian spectrophotometer. Emission and excitation spectra were recorded in a Edinburgh FS-900 spectrophotometer. Quantum yields were obtained using a solution of naphthalene in cyclohexane as reference, whose optical density matched that of the samples at the excitation wavelength. For oxygen quenching, the solutions were purged with an oxygen stream for at least 10 min before photoluminescence measurements. Lifetimes were measured with a FL-900 single-photon counting photometer using a nanosecond hydrogen flash lamp.

[1] B. Notari, *Adv. Catal.* **1996**, *41*, 253–334.

[2] J. Reddy, R. Kumar, P. Ratnasamy, *Appl. Catal.* **1990**, *58*, 1.

[3] J. S. Reddy, U. K. Khire, P. Ratnasamy, R. B. Mitra, *J. Chem. Soc. Chem. Commun.* **1992**, 1234–1235.

[4] D. Scarano, A. Zecchina, S. Bordiga, F. Geobaldo, G. Spoto, G. Petrini, G. Leofanti, M. Padovan, G. Tozzola, *J. Chem. Soc. Faraday Trans.* **1993**, *89*, 4123.

[5] A. Corma, M. A. Camblor, P. Esteve, A. Martínez, J. Pérez-Pariente, *J. Catal.* **1994**, *145*, 151–158.

[6] A. Corma, P. Esteve, A. Martínez, S. Valencia, *J. Catal.* **1995**, *152*, 18–24.

[7] M. Alvaro, A. Corma, H. García, S. Valencia, *Appl. Catal. A* **1995**, *128*, L7–L11.

[8] M. E. Raimondi, L. Marchese, E. Gianotti, T. Maschmeyer, J. M. Seddon, S. Collucia, *Chem. Comm.* **1999**, 87–88.

[9] C. Lamberti, S. Bordiga, D. Arduino, A. Zecchina, F. Geobaldo, G. Spanó, F. Genoni, G. Petrini, F. Villain, G. Vlaic, *J. Phys. Chem. B* **1998**, *102*, 6382–6390.

[10] L. Marchese, T. Maschmeyer, E. Gianotti, S. Coluccia, J. M. Thomas, *J. Phys. Chem. B* **1997**, *101*, 8836–8838.

[11] L. Marchese, E. Gianotti, T. Maschmeyer, G. Martra, S. Coluccia, J. M. Thomas, *Nuov. Cimento Soc. Ital. Fis. D* **1997**, *19*, 1707–1718.

[12] A. Corma, H. García, M. T. Navarro, E. Palomares, F. Rey, *Chem. Mater.*, in press.

[13] H. C. L. Abbenhuis, S. Krijnen, R. A. van Santen, *Chem. Commun.* **1997**, 331–332.

[14] T. Maschmeyer, M. C. Klunduk, C. M. Martin, D. S. Shepard, J. M. Thomas, B. F. G. Johnson, *Chem. Commun.* **1997**, 1847–1848.

[15] M. Crocker, R. H. M. Herold, A. G. Orpen, *Chem. Commun.* **1997**, 2411–2412.

[16] M. Crocker, R. H. M. Herold, A. G. Orpen, M. T. A. Overgaag, *J. Chem. Soc. Dalton Trans.* **1999**, 3791–3804.

[17] J. M. Thomas, G. Sankar, M. C. Klunduk, M. P. Attfield, T. Maschmeyer, B. F. G. Johnson, R. G. Bell, *J. Phys. Chem. B* **1999**, *103*, 8809–8813.

[18] W. M. Nau, G. Greiner, H. Rau, J. Wall, M. Olivucci, J. C. Scaiano, *J. Phys. Chem. A* **1999**, *103*, 1579–1584.

[19] A. Gilbert, J. Baggott, *Essentials of Organic Photochemistry*, Blackwell, Oxford, **1990**.

Received: June 2, 2000 [Z 45]

Physical Consequences of a Mechanically Interlocked Architecture: Benzylic Amide Catenane NH Stretching Vibrations as Sensitive Probes for Weakly Hydrogen-Bonding Environments[**]

Charles-Andre Fustin,[a] David A. Leigh,*[b]
Petra Rudolf,*[a] Dirk Timpel,[c] and
Francesco Zerbetto*[c]

KEYWORDS:

catenanes · hydrogen bonds · macrocycles · molecular dynamics · vibrational spectroscopy

One of the issues still to be fully explored in the interlocking of molecular-level components to form catenanes and rotaxanes is the nature of the physical and chemical effects that can be induced or influenced through such architectures.[1] The weak intercomponent forces generally used to promote the assembly of such structures, combined with the restricted degrees of freedom imposed on the components by interlocking, provide a situation unlike either supramolecular systems (in which the weakly bound components are normally exchangeable between assemblies) or conventional molecular architectures (where the rules of covalent bonding tend to impose rigorous requirements on every bond distance and angle). The benzylic isophthalamide macrocycle **1** is remarkable in that it can be studied under all three situations (Scheme 1); as a simple macrocycle, a supramolecular complex with (and sensor for) CO_2[2] or as an interlocked dimer in the form of the [2]catenane **2**.[3] Differences,

---

[a] *Dr. P. Rudolf, Dr. C.-A. Fustin*
Laboratoire Interdisciplinaire de Spectroscopie Electronique
Facultes Universitaires Notre-Dame de la Paix
Rue de Bruxelles, 5000 Namur (Belgium)
Fax: (+32) 81-72-45-95
E-mail: Petra.Rudolf@fundp.ac.be

[b] *Prof. D. A. Leigh*
Centre for Supramolecular and Macromolecular Chemistry
Department of Chemistry
University of Warwick
Coventry CV4 7AL (UK)
Fax: (+44) 2476-523258
E-mail: David.Leigh@warwick.ac.uk

[c] *Dr. F. Zerbetto, Dr. D. Timpel*
Dipartimento di Chimica "G. Ciamician"
Università degli Studi di Bologna
V. F. Selmi 2, 40126 Bologna (Italy)
Fax: (+39) 051-209-94-73
E-mail: gatto@ciam.unibo.it

[**] *This work has been supported by the European Community (TMR contract FMRX-CT97-0097) and by the Belgian National Program of Interuniversity Research (Project "Science of Interfaces and Mesoscopic Structures"). C.-A.F. acknowledges the FRIA for financial support. F.Z. received partial financial support from MURST project "Supramolecular Devices". D.A.L. is an EPSRC Advanced Research Fellow (AF/98/2324).*

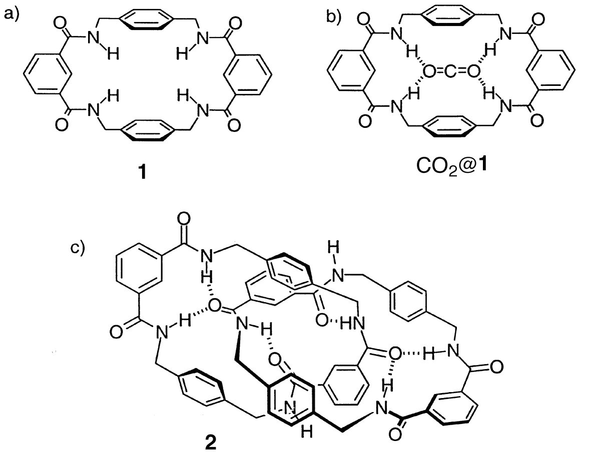

*Scheme 1. Benzylic amide macrocycle **1** as a) a discrete molecule, b) an idealised supramolecular complex with CO_2 and c) an interlocked dimer, the [2]catenane **2**.*

*Table 1. Experimental position[a] of the centres of the peaks for the NH stretching vibrations of the benzylic amide macrocycle **1** and [2]catenane **2** in various salt matrices. Linewidths are given in parentheses.*

	1	2
CsI	3331 (58)	3332 (162)
CsBr	3330 (62)	3319 (135)
KI	3329 (58)	3323 (170)
KBr	3328 (66)	3304 (154)
NaCl	3327 (70)	3294 (146)

[a] In wavenumbers [cm^{-1}].

and to some extent similarities, between the properties of the macrocycle and the [2]catenane—which differ solely by a mechanical bond[4]—are of particular importance if one is to bridge the gap between the synthesis of interlocked molecules, which is beginning to become almost routine,[1] and the actual exploitation of effects intrinsic only to mechanically interlocked architectures.

Recently, a full and detailed characterisation of the structure and properties of benzylic amide [2]catenanes has begun.[5] Somewhat surprisingly, in the solid state vibrational spectrum of **2** it was found a change in the salt matrix from KBr to CsI shifted the peak of the NH stretching band by several wavenumbers. The shift was neglible in the spectra of the parent macrocycle (large matrix-dependent shifts are extremely rare for the great majority—including hydrogen-bonded examples—of organic compounds). Because of the contrast between the free and interlocked systems, the unusual behaviour could, in this case, be unambiguously ascribed to the topologically nontrivial nature of **2** but a quantitative and detailed explanation of the phenomenon remained elusive. In principle, this unusual sensitivity to the matrix could be used to generate a novel family of sensors for weakly hydrogen bonding environments based on their infrared activity. Knowledge of the general trend and the mechanism are, however, necessary to take advantage of the effect which demonstrates, for the first time, that mechanical interlocking can have major consequences on the vibrational properties of a chemical system.

Herein, the effect of the salt matrix on the NH vibrational frequencies of the simplest isophthaloyl benzylic amide [2]catenane, **2**, is examined in detail and qualitatively simulated. The infrared spectra of both **1** and **2** in CsI, CsBr, KI, KBr and NaCl were recorded and substantial differences—up to 40 cm^{-1}—in the NH stretching region of **2** were found.[6] Molecular dynamics simulations were performed, which included the salt ions, and the infrared spectra were calculated from the dynamics.[7] The approach includes both anharmonic and temperature effects. The agreement with experiment, and the further analysis in terms of the dynamically averaged distance of the inter-macrocycle hydrogen bonds, that is, the (N)H$\cdots$O distances, explains the origin of the effect.

Table 1 shows the wavenumbers of the vibrations of the catenane **2** and the parent macrocycle **1** in the five salt matrices. The linewidth nearly doubles going from the macrocycle to the catenane, whereas only the catenane has large variations in the NH stretch region. Minor (<8 cm^{-1}) modifications are present in the CO stretch region, while the other vibrational regions are hardly affected. Despite, or perhaps because of, the simplicity of the experiments, a fundamental issue arises that concerns the different spectral behavior of the macrocycle and the catenane. Simply put, despite being identical in terms of covalent bonding patterns, the macrocycle does not do something that the catenane does! No simple phenomenological correlation between the NH shifts and the type of anion or the cation of the matrix was found, the implication being that both types of ions determine the degree of the signal shift.

Molecular dynamics simulations were carried out with the intent of providing a qualitative understanding of the phenomenon. As a model, a single molecule was embedded in the salt.[7] This is a necessary exaggeration—aggregates are probably the most numerous species dispersed in the medium—that likely enhances the effects that exist when the experimental sample is prepared. The use of Fourier transform techniques to calculate the infrared bands is preferable to the traditional quantum-chemical approach, which involves the use of the normal modes obtained from diagonalization of the mass-weighed Hessian and their overlap with the dipole-moment derivative. The appeal of the procedure lies in the inclusion of the anharmonicities and in the possibility of dynamically sampling over the co-conformations that the system can take.

Preliminary insight into the model can be obtained by comparing the experimental and calculated spectra in the region that begins above 1000 cm^{-1}. While failure of the procedure in such a broad range would not diminish its chances of describing accurately a single type of vibrational motion, its success increases our understanding of these complicated molecules. Figure 1 shows a very reasonable agreement between calculation and experiment. Below 1000 cm^{-1}, the comparison was not attempted because this region is dominated by the pure carbon (CCC) bending modes, which do not carry a dipole moment in the present computational model and therefore cannot contribute to the spectrum.

Table 2 compares calculated and experimental shifts of the centers of the NH stretching bands. The agreement is satisfactory and, in a sense, it exceeds what is required for the present purposes. It proves that the higher sensitivity of the NH stretch

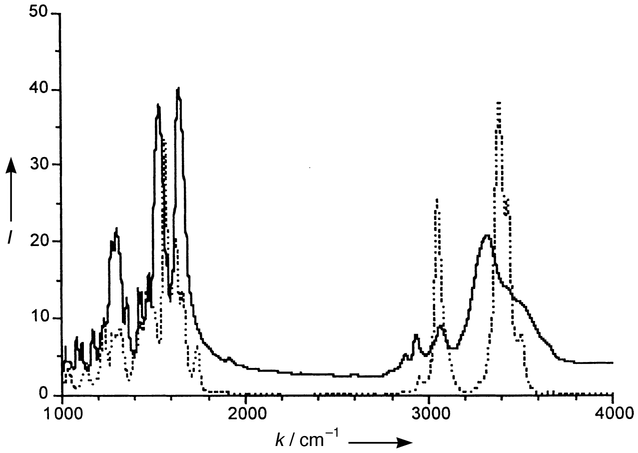

Figure 1. *Comparison of calculated and experimental spectra of **2** in KI for the region above 1000 cm^{-1}. —— = experimental, •••• = calculated.*

Table 2. *Calculated and experimental shifts[a] with respect to the spectrum recorded in NaCl of the centre of the NH stretch band of the benzylic amide macrocycle **1** and [2]catenane **2** in various salt matrices.*

	1		**2**	
	Calculated	Experimental	Calculated	Experimental
CsI	1	4	40	38
CsBr	9	2	27	25
KI	8	2	32	29
KBr	9	1	18	10
NaCl	0	0	0	0

[a] In wavenumbers [cm^{-1}].

band of the catenane to the salt ions can be accounted for by a simple model in which the salt–molecule interactions are described as the combination of a coulombic term plus an exponential repulsion term.[7] Furthermore, the simulated spectra of the macrocycle show some shifts that are less than one third of those calculated for the interlocked system. Careful (re-)parameterisation of the salt–molecule potential and/or addition of the dispersion forces could well make the agreement quantitative. However, while it would probably be remarkable, it would not add to our understanding of the phenomenon that can be simulated through simple potential energy functions.

Analysis of the molecular dynamics experiments can further unravel the nature of the effect. Qualitatively, one can estimate visually the number of inter-ring hydrogen bonds during the simulations; quantitatively, the same analysis can be perfomed by calculating the pair-distribution function of the (N)H$\cdots$O distances. Inspection of these shows that the number of normal and bifurcated hydrogen bonds varies with the nature of the matrix. When embedded in CsI, snapshots of the catenane show that there are either zero or one "normal" (that is, containing two heteroatoms) hydrogen bonds along with three or two bifurcated ones. In CsBr, one bifurcated hydrogen bond is accompanied by two normal ones. The remaining salt matrices display three bifurcated and no regular hydrogen bonds. These numbers can be compared with the two normal and two bifurcated intercomponent hydrogen bonds present in the X-ray crystal structure[3] (the X-ray crystal structure of the macrocycle has only intermolecular, normal hydrogen bonds) and with the one normal and three bifurcated bonds found by the same computational procedure for the isolated molecule.[5] The salt matrix therefore modifies the hydrogen bonding pattern of the catenane which, in turn, affects the frequencies of the NH stretching vibrations. It has been reported that various halogen anions possess different degrees of hydrogen bond strength.[13] The data reported here require the joint action of both types of ions. Although it is not possible to determine the contribution of the individual ions, further and more quantitative understanding can be obtained by calculating the inter-macrocycle (N)H$\cdots$O pair-distribution function (see Figure 2). The structure located around and above 2 Å is of interest. At longer lengths, intra-ring and other inter-ring distances contribute. The peaks can be fitted by the linear combination of two Gaussian functions (see Table 3) with a peak separation of roughly 0.2 Å. The presence of two components supports the intuitive notion that the vibrational inter-macrocycle (N)H$\cdots$O dynamics is governed by the competition between regular (that is, shorter) and bifurcated (that is, longer) hydrogen bonds. Interestingly, for CsBr, which in the qualitative assessment most affects the hydrogen bonding pattern of the catenane, displays a very different pair distribution function to the others.

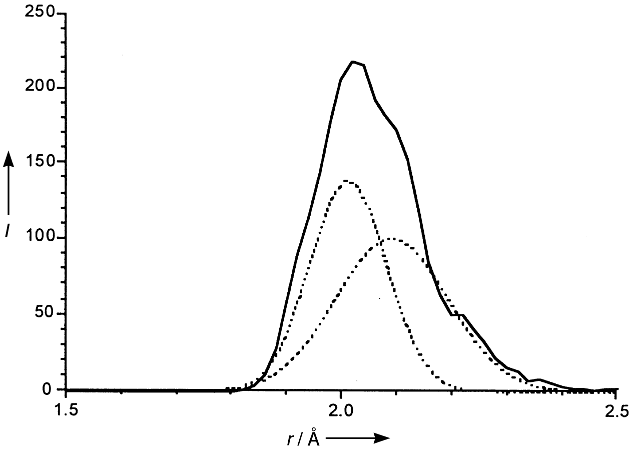

Figure 2. *Typical inter-macrocycle (N)H$\cdots$O pair-distribution function obtained from the molecular dynamics simulations of **2** in KI.*

Table 3. *Fitting the pair-distribution function of the (N)H$\cdots$O inter-ring distance in the catenane by the sum of two Gaussian functions.[a]*

	Gaussian 1		Gaussian 2	
	Centre	Width	Centre	Width
CsI	1.9658	0.1276	2.1325	0.2829
CsBr	2.1868	0.2190	2.3782	0.1828
KI	2.0218	0.1721	2.1773	0.2804
KBr	2.0049	0.1231	2.1249	0.2147
NaCl	1.9701	0.1065	2.0784	0.1945

[a] All curve characteristics are given in Ångström units.

In conclusion, the center of the NH stretching peak in the spectrum of **2** in different salt matrices can shift by as much as 40 cm^{-1}. The matrix-dependent behavior is, however, virtually absent in the spectra of its non-interlocked component, **1**. The wavenumber variation can be simulated using molecular dynamics. Analysis of the results proves that the shifts are entirely due to the interlocked molecular architecture which provides a geometry suitable for the formation of the intramolecular, inter-component hydrogen bonds. Two major issues will have to be addressed in the near future: 1) the identification of the benzylic amide catenane structure which provides the highest "tunability" of the hydrogen bond system to the environment; and 2) an investigation of the pressure dependence of the infrared spectrum which could ultimately exploit the mechanically bonded systems as "molecular manometers".

[1] a) G. Schill, *Catenanes, Rotaxanes and Knots*, Academic Press, New York, **1971**; b) J.-P. Sauvage, *Acc. Chem. Res.* **1990**, *23*, 319 – 327; c) D. B. Amabilino, J. F. Stoddart, *Chem. Rev.* **1995**, *95*, 2725 – 2828; d) H. W. Gibson, M. C. Bheda, P. T. Engen, *Prog. Polym. Sci.* **1994**, *19*, 843 – 945; e) C. A. Hunter, *J. Am. Chem. Soc.* **1992**, *114*, 5303 – 5311; f) F. Vögtle, T. Dunnwald, T. Schmidt, *Acc. Chem. Res.* **1996**, *29*, 451 – 460; g) J. G. M. Gruter, F. J. J. de Kanter, P. R. Markies, T. Nomoto, O. S. Akkerman, F. Bickelhaupt, *J. Am. Chem. Soc.* **1992**, *115*, 12179 – 12180; h) M. Fujita, F. Ibukuro, H. Hagihara, K. Ogura, *Nature* **1994**, *367*, 720 – 723; i) D. G. Hamilton, J. K. M. Sanders, J. E. Davies, W. Clegg, S. J. Teat, *Chem. Commun.* **1997**, 897 – 898; j) *Molecular Catenanes, Rotaxanes and Knots* (Eds.: J.-P. Sauvage, C. O. Dietrich-Buchecker), VCH-Wiley, Weinheim, **1999**.

[2] A. G. Johnston, D. A. Leigh, A. Murphy, J. P. Smart, M. D. Deegan, *J. Am. Chem. Soc.* **1996**, *118*, 10662 – 10663.

[3] a) A. G. Johnston, D. A. Leigh, R. J. Pritchard, M. D. Deegan, *Angew. Chem.* **1995**, *107*, 1324 – 1327; *Angew. Chem. Int. Ed. Engl.* **1995**, *34*, 1209 – 1212; b) A. G. Johnston, D. A. Leigh, L. Nehzat, J. P. Smart, M. D. Deegan, *Angew. Chem.* **1995**, *107*, 1327 – 1331; *Angew. Chem. Int. Ed. Engl.* **1995**, *34*, 1212 – 1216.

[4] A "mechanical" bond is the term used to describe the relationship between two or more molecular components which, although not joined at any point by covalent bonds, cannot in fact be separated from each other without breaking a covalent bond. Examples include two rings which are interlinked (a "catenane") or a ring locked onto a thread by bulky end groups (a "rotaxane"). It is sometimes (technically incorrect for a rotaxane) called a "topological bond". A similar meaning, describing the relative positions of noncovalently linked submolecular fragments, is given to the term "mechanically interlocked architecture". For examples see ref. [1j]; V. Balzani, M. Gómez-López, J. F. Stoddart, *Acc. Chem. Res.* **1998**, *31*, 405 – 414; J.-P. Sauvage, *Acc. Chem. Res.* **1998**, *31*, 611 – 619.

[5] a) M. Fanti, C.-A. Fustin, D. A. Leigh, A. Murphy, P. Rudolf, R. Caudano, R. Zamboni, F. Zerbetto, *J. Phys. Chem. A*, **1998**, *102*, 5782 – 5788; b) D. A. Leigh, A. Murphy, J. P. Smart, M. S. Deleuze, F. Zerbetto, *J. Am. Chem. Soc.*, **1998**, *120*, 6458 – 6467; c) A. M. Brouwer, W. J. Buma, R. Caudano, M. Fanti, C.-A. Fustin, D. A. Leigh, A. Murphy, P. Rudolf, F. Zerbetto, J. M. Zwier, *Chem. Phys.* **1998**, *238*, 421 – 428; d) R. Caciuffo, A. Degli Esposti, M. S. Deleuze, D. A. Leigh, A. Murphy, B. Paci, S. Parker, F. Zerbetto, *J. Chem. Phys.* **1998**, *109*, 11094 – 11100; e) M. S. Deleuze, D. A. Leigh, F. Zerbetto, *J. Am. Chem. Soc.* **1999**, *121*, 2364 – 2379.

[6] The infrared spectrum experiments were carried out using a highly standardised approach that ensured the reproducibility of spectra for both the catenane and macrocycle. The catenane/macrocycle concentration used in the CsI, CsBr, KI, KBr and NaCl matrices was 1.25% by weight. The pellets were prepared using ten tonnes of compression exerted for five minutes. The spectra were insensitive to different grinding procedures and did not show appreciable differences when the compression in the preparation was decreased to two tonnes, a limit under which the pellet is too brittle to use. The standard infrared spectra were recorded with a Fourier transform spectrometer FT 60A (Bio-Rad, Cambridge, MA, USA) equipped with a KBr beamsplitter and a deuterated triglycine sulfate (DTGS) detector. The inferometer was of the Michelson type and the resolution was set to 2 cm^{-1}.

[7] Molecular dynamics calculations were performed using the MM3 potential-energy model.[8] The approach is the same as that was used previously to study the potential-energy surfaces and dynamics of several benzylic amide [2]catenanes.[5] The salt ions were simulated with a rigid ion potential, $U(r_{ij})$, that, in its complete form, combines electrostatic Coulombic forces with a repulsive Born – Mayer term and attraction dispersion forces [Eq. (1)], A and ρ with q_i the charge on atom i, and r_{ij} the interatomic distance.

$$U(r_{ij}) = \frac{q_i q_j}{r_{ij}} + A_{ij} \exp\left(-\frac{r_{ij}}{\rho_{ij}}\right) \quad (1)$$

This potential was first suggested by Tosi[9] and has successfully been applied to a variety of ionic structures.[10] The other parameters were obtained using the relation in [Eq. (2)],[9] where $b = 15.23\ \text{kJ mol}^{-1}$, $\rho = 0.296$ Å, $c_{++} = 1.25$, $c_{+-} = 1.00$, $c_{--} = 0.75$, and σ is the ionic radius.

$$A_{ij} = \left(1 + \frac{Z_i}{k_i} + \frac{Z_j}{k_j}\right) b \exp\left(\frac{\sigma_i + \sigma_j}{\rho}\right) = c_{ij} b \exp\left(\frac{\sigma_i + \sigma_j}{\rho}\right) \quad (2)$$

The same model was adopted for the interactions between the catenane atoms and the salt ions because the simple Lennard-Jones treatment gave inaccurate results. Embedding the catenane in the salt was achieved using both a random and a nonrandom approach. The former entailed the generation of a randomised salt matrix around the molecule with subsequent annealing of the system for 90000 steps (18 ps, from $T_{\max} = 1200$ K). The latter used a molecule sandwiched between two relaxed salt surfaces which were then equilibrated for 10 ps (50000 steps) at constant temperature. The two approaches resulted in similar infrared spectra. For convenience, the systematic investigation used the nonrandom structure generation that avoids the high temperature treatment and is probably more meaningful in terms of the experimental process. The smallest size of the supercell was set to $27 \times 27 \times 20$ Å^3, which, in turn, resulted in systems of 400 to 800 atoms. At this supercell size, equilibration of the salt gave a stable, chemically reasonable structure. In practice, to sandwich the catenane, the shorter edge of the box was increased to ~35 Å and, after deposition of the catenane on the surface, the periodic boundary conditions effectively sandwiched it between two surfaces. After preparation of the sample and its equilibration, the simulation run consisted of 84000 steps, saved every tenth step. The dynamics of the salt matrices only, were calculated using 1 fs integration steps, while the vibrations of the embedded catenane required 0.2 fs steps. This allowed calculation of the vibrational properties up to ~8000 cm^{-1}. The infrared spectra can be calculated as the Fourier transform of the autocorrelation function of the dipole moment or of the dipole-moment derivative with respect to time.[11] For the NH stretch, the use of the dipole-moment time derivative was preferred. To analyse the salt-induced variations, radial pair distribution functions—of particular interest is the N–H···O one—were calculated as an average over the entire simulation run. All the calculations were performed using a canonical ensemble with the TINKER program[12] that had been modified to handle the trajectory files for the subsequent calculations of the correlation functions and to implement the Born – Mayer potential terms. Periodic boundary conditions were applied and the different crystal structure of the salts were taken into account (CsI and CsBr are simple cubic; KI, KBr and NaCl are face-centred cubic).

[8] a) N. L. Allinger, Y. H. Yuh, J.-H. Lii, *J. Am. Chem. Soc.* **1989**, *111*, 8551 – 8566; b) J.-H. Lii, N. L. Allinger, *J. Am. Chem. Soc.* **1989**, *111*, 8566 – 8575; c) J.-H. Lii, N. L. Allinger, *J. Am. Chem. Soc.* **1989**, *111*, 8576 – 8582; d) N. L. Allinger, K. Chen, J.-H. Lii, *J. Comput. Chem.* **1996**, *17*, 642 – 668.

[9] M. P. Tosi, *Solid State Phys.* **1964**, *16*, 1.

[10] a) Z. X. Gong, G. K. Horton, E. R. Cowley, *Phys. Rev. B* **1988**, *38*, 10820 – 10829; b) Z. X. Gong, G. K. Horton, E. R. Cowley, *Phys. Rev. B* **1989**, *40*, 3294 – 3300; c) P. Zielinski, C. Marzluf, *J. Chem. Phys.* **1992**, *96*, 1735 – 1740.

[11] a) S. Brawer, *J. Chem. Phys.* **1983**, *79*, 4539 – 4544; b) S. Goncalves, H. Bonadeo, *Phys. Rev. B* **1992**, *46*, 10738 – 10742; c) B. Boulard, J. Kieffer, C. C. Phifer, C. A. Angell, *J. Non-Cryst. Solids* **1992**, *140*, 350 – 358.

[12] a) J. Ponder, F. Richards, *J. Comput. Chem.* **1987**, *8*, 1016 – 1024; b) C. Kundrot, J. Ponder, F. Richards, *J. Comput. Chem.* **1991**, *12*, 402 – 409; c) M. Dudek, J. Ponder, *J. Comput. Chem.* **1995**, *16*, 791 – 816.

[13] a) G. Aullón, D. Bellamy, L. Brammer, E. A Bruton, A. G. Orpen, *Chem. Commun.* **1998**, 653 – 654; b) M. Mascal, *J. Chem. Soc. Perkin 2* **1997**, 1997 – 2001.

Received: April 25, 2000 [Z 10]

Hydrophilic/Hydrophobic Nanostripes in Lipopolymer Monolayers**

Heiko Ahrens,[a] Thomas Rosleff Bækmark,[b]
Rudolf Merkel,[b] Johannes Schmitt,[a]
Karlheinz Graf,[a, c, e] Roberto Raiteri,[a, d] and
Christiane A. Helm*[a, c, e]

KEYWORDS:

amphiphiles · lipophilicity · monolayer · nanostructures · thin films

Lipopolymers with covalently bound poly(ethylene oxide) (EO_N) head groups have been introduced to stabilize bilayer membranes[1] and thus to prepare stealth liposomes and drug carriers.[2] Tremendous interest was stimulated by the fact that, under certain conditions, an EO_N chain can passivate against protein binding.[3–5] Furthermore, EO_N is water soluble, yet it adsorbs to hydrophobic surfaces. The function of the ethylene oxide (EO) groups is not well understood. Obviously, the interaction with water is too complex to be described with just one interaction parameter, as is traditional in polymer physics.[6–8]

Furthermore, molecules combining lipid and polymer groups may both show new features,[9] as well as improve our understanding of molecular self-association. Monolayers of such insoluble lipopolymers at the air/water interface are well suited as model systems[10] because of the defined variability of parameters, especially the grafting density, and because lateral mobility ensures equilibrium. In this work, we demonstrate the existence of a laterally nanostructured phase within the monolayer, which is characterized by weakly ordered aliphatic tails immersed in solubilized polymer.

The isotherms of $DSPE\text{-}EO_N$ (L-α-distearoylphosphatidyl-ethanolamine with covalently attached polyethylene oxide chains, $N = 44$, 112; see Scheme 1) show two pronounced phase transitions, which can be controlled externally and reversibly by temperature and surface coverage. As expected for the longer polymer, all phase transitions are shifted to larger molecular areas. At very low surface coverage at a lateral pressure π_c (see inset in Figure 2), the EO_N undergoes a pancake-to-brush transition that has been reported earlier.[11]

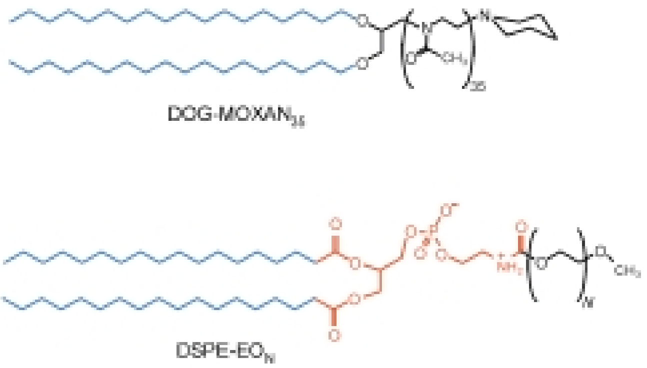

Scheme 1. Structural formula of $DSPE\text{-}EO_N$. Blue denotes the hydrophobic region, red the hydrophillic phosphate group, and black the hydrophillic polymer.

In this paper, we shall focus on the compressed phase, which occurs at pressures above π_t. The compressed phase was studied previously at the air/water interface by in situ infrared spectroscopy.[11–13] In those experiments, strong evidence for an all-*trans* conformation of the lipid alkyl tails was found. The stretched conformation, together with the first-order phase transition in the isotherm, suggests chain ordering. These features are reminiscent of the chain-ordering transition of phospholipid monolayers.[10] However, for all double-tailed lipopolymers studied so far, the mean molecular area in the compressed phase exceeds that of two stretched alkyl chains (≤ 46 Å^2) by at least a factor of two, to suggest a more complex structure. In principle, this phase should be determined by two competing interactions, the short-range van der Waals attraction of the aliphatic alkyl chains (a typical lipid phenomenon) and the entropic long-range repulsion of a polymer brush.

Complementary experiments were reported[11–13] with lipopolymers with two alkyl chains containing very different water-soluble polymer moieties, namely, di-octadecyloxy-glycerol-poly(2-methyl-2-oxazoline)$_{35}$ (DOG-MOXAN$_{35}$) and di-octadecyloxy-glycerol-poly(2-ethyl-2-oxazoline)$_{31}$ (DOG-EOXAN$_{31}$).[12] Water is a good solvent for EO_N and MOXAN$_N$, whereas it is a marginal solvent for EOXAN$_N$. This condensed phase was not found for shorter lipid tails ($< C_{14}$) or unsaturated alkyl chains. It appears that all lipopolymers that contain long, saturated alkyl chains display a similar high density phase. Thus we are

---

[a] C. A. Helm, H. Ahrens, J. Schmitt, K. Graf, R. Raiteri
Institut für Physikalische Chemie
Johannes-Gutenberg-Universität
Jakob-Welder Weg 11, 55099 Mainz (Germany)
Fax: (+49) 6131-392-3768
E-mail: helm@physik.uni-greifswald.de

[b] T. R. Bækmark, R. Merkel
Physik Department E22 (Biophysics Laboratory)
Technische Universität München
85748 Garching (Germany)

[c] C. A. Helm, K. Graf
Universität des Saarlandes
Fachbereich Physik: Strukturforschung
Postfach 151150, 66041 Saarbrücken (Germany)

[d] R. Raiteri
Department of Biophysical and Electronic Engineering
University of Genova
Via Opera Pia11 a, 16415 Genova (Italy)

[e] C. A. Helm, K. Graf
Ernst-Moritz-Arndt-Universtität Greifswald
Angewandte Physik
Friedrich-Ludwig-Jahnstrasse 16, 17487 Greifswald (Germany)

[**] We gratefully acknowledge generous support of Hans-Jürgen Butt and Erich Sackmann. Discussions with Helmuth Möhwald were enjoyable. We appreciate that Thomas Wiesenthal joined us with some of the GID experiments. The financial support of the DFG (He 1616-9/1,2 and SFB 266, D13) was helpful. T.R.B. was supported by the Danish Research Academy. R.R. thanks the TMR program.

Supporting information for this article is available on the WWW under http://www.wiley-vch.de/home/angewandte/ or from the author.

convinced that this study on EO and MOXAN lipopolymers bears relevance for other lipopolymers as well.

Lipopolymers DSPE-EO$_N$ (N = 44 and N = 112), when floating on the water surface, were characterized by grazing incidence X-ray diffraction (GID; cf. Figure 1) along the isotherm (see the inset of Figure 2).[14] On compressing the monolayer beyond the tail-ordering transition π_t, a pronounced diffraction peak suddenly appeared (Figure 1). A similar Bragg peak was observed with MOXAN as the water-soluble polymer moiety. Unfortunately, radiation damage was a serious problem for this compound and prohibited quantitative peak analysis.

Peak-shape analysis of DSPE-EO$_N$ reveals tails that are ordered in an orthorhombic lattice and tilted with respect to the surface normal. However, compared to the pure lipid, the tail lattice is more expanded and distorted.[15, 16] The peak width perpendicular to the water surface measures the thickness of the two-dimensional Bragg scattering moieties. We obtained 17 ± 1 Å, somewhat less than 22.5 Å expected for stretched C_{18}-alkane chains. This shortening is already observed if the pure lipid DSPE is mixed with up to 9% DSPE-EO$_{44}$.[15, 16] The peak width parallel to the water surface measures the in-plane correlation length. For the pure lipopolymers, it amounts to 19 ± 2 Å (four to five lattice constants). This is much less than observed with the above mentioned mixtures, where the coherence length of the pure lipid (130 Å) decreases only slightly (83 Å) on addition of 9% DSPE-EO$_{44}$. Thus, while only a few percent lipopolymer in the lipid caused thickness reduction of the Bragg-scattering moieties, the additional packing stresses due to more bound polymer are relaxed by in-plane lattice distortions.

Peak analysis along the isotherm[17] shows that both tail tilt ($19 \rightarrow 14^\circ$) and lattice constants decrease on compression. Assuming the molecular area to be the sum of two tail areas, the molecular area diminishes from about 44 Å^2 to 41.6 Å^2. These molecular areas are a factor two to four smaller than those found in the isotherm, which are obtained from the average over the macroscopic areas. We have to conclude that the monolayer is laterally heterogeneous, which could correspond to 2D micelles. Comparing the molecular areas as derived from GID and the isotherm, one finds that the area fraction α covered with ordered lipid tails increases on compression from 20% to 30% and 25% to 50% for the long and short lipopolymer, respectively.

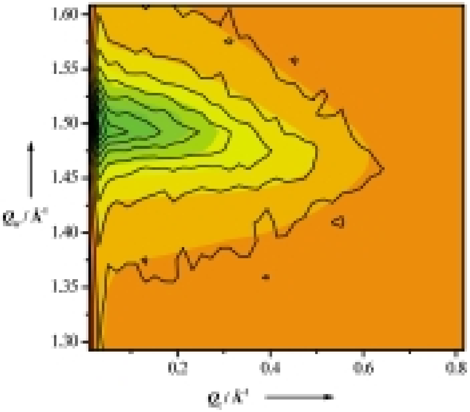

Figure 1. GID diffraction peak of DSPE-EO$_{44}$, which can be only found in the condensed phase, $\pi > \pi_t$ (here: $\pi = 30$ mN m^{-1}, T = 20 °C). The equipotential lines of the fit are separated by different colors.

To locate the ordered tails within the lipopolymer monolayer, specular X-ray reflectivity experiments were performed.[18, 19] Specular reflection provides information on the electron-density variation (scattering length density variation) perpendicular to the surface with Ångström-level resolution. Due to the loss of the phase information in conventional X-ray reflectivity experiments, the data analysis is generally based on finding proper electron-density functions, whose reflectivity properties retrospectively best match the observed reflectivity data. To obtain structural parameters within one phase of the polymer film, the layer is subdivided into homogeneous slabs with a roughness between the layers ("box model").[20] To additionally cross-check this approach, the electron-density profile is determined by a model-independent method[21, 22] (see the Supporting Information). We used the simplest slab model with which all reflectivity curves measured within one phase—independent of polymer length—could be fitted satisfactorily.

Reflectivity curves of DSPE-EO$_{44}$ are shown in Figure 2. The major difference in the reflectivity below (a, b) and above (c, d) the phase transition π_t is the maximum at large Q_z values (~0.3 Å^{-1}) in the compressed state. On compression, the maximum at low Q_z (~0.05 Å^{-1}) is continuously increasing in intensity and shifting towards lower Q_z values, to indicate film thickening. The longer DSPE-EO$_{112}$ shows a similar additional maximum on passing the phase transition (e). The maximum at large Q_z values occurs for both compressed lipopolymers at the same position, which indicates the same size of the corresponding structure. However, in the case of the longer lipopolymer, the contrast is decreased due to the larger mean molecular area. The maxima at low Q_z are also strongly shifted toward lower values, to indicate an pronounced increase of monolayer thickness with increased polymer length.

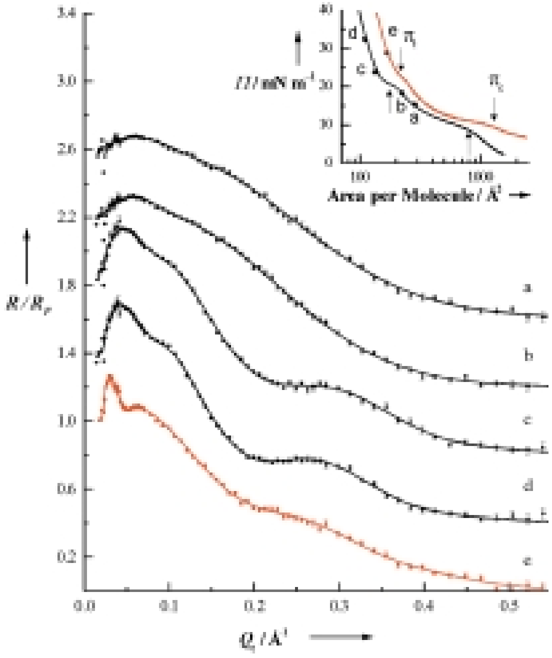

Figure 2. a) X-ray reflectivity curves of DSPE-EO$_{44}$ (black line) and DSPE-EO$_{112}$ (red line) together with fits taken along the isotherm as indicated in the inset. Inset: The monolayer phase transitions are indicated by arrows.

Typical electron-density profiles are shown in Figure 3. The expanded phase of DSPE-EO$_N$ could be described with a two-slab model. This results in six free parameters for DSPE-EO$_N$ (one thickness and one electron density for each slab, and one roughness for all interfaces except the polymer/water interface, which exhibits an additional structural roughness; Table 1). As expected for a roughness attributed to capillary waves, it increases with the lateral pressure.[20]

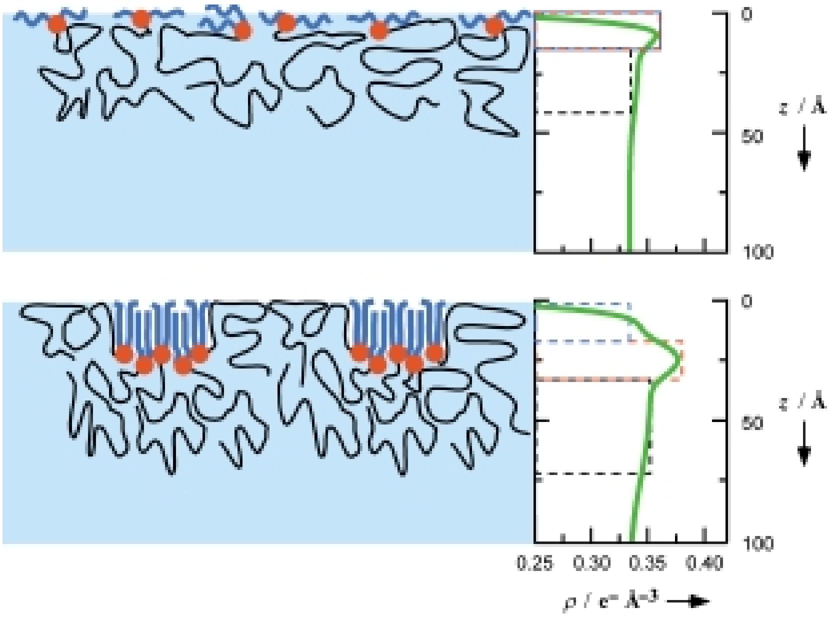

Figure 3. *Electron density profiles together with schematic molecular arrangement. Full lines represent the electron density profile, whereas broken lines give the slab model without roughness.*

In the compressed phase, the additional extrema at large Q_z indicate more complex density profiles (Figure 2). Indeed, a three-slab model is necessary, with eight free parameters. The functional groups of the DSPE-EO$_N$ can be recognized by their different electron densities. The alkyl chains ($0.32\,e^-\,Å^{-3}$) exhibit a slightly lower electron density than the water subphase ($0.334\,e^-\,Å^{-3}$), whereas the hydrated PEO has a slightly higher one than water (the exact value depends on the degree of hydration, namely $0.358\,e^-\,Å^{-3}$ for three water molecules per monomer). However, the good contrast in the reflectivity curves is provided by the phosphate group with its extremely high electron density ($0.46\,e^-\,Å^{-3}$ in a phospholipid monolayer).[18] Therefore, the phosphate groups serve as a marker of the alkyl chains/polymer interface.

In the expanded phase, the highest electron density, which indicates the phosphate group, is found at the surface. The air-adjacent slab describes therefore a mixture of phosphate groups and alkyl chains. The polymer brush is accounted for by the second slab. On compression, it increases in thickness and density, due to stretching and dehydration. Qualitatively, these results agree with theoretical expectations.

In the condensed phase, the slab with the highest electron density (the phosphate groups) is found within the monolayer. The hydrophobic alkyl chains are situated above the phosphate groups, in the air-adjacent slab. Its thickness (17.1 ± 0.5 Å) is

Table 1. *The parameters describing the electron density profile within the slab model. The first slab is the air-adjacent one, if necessary, it is counted down. l_{tot} gives the total monolayer thickness.*

Area [Å^2]	σ_{sub} [Å]	l_1 [Å]	ρ_1 [e$^-$ Å^{-3}]	σ_{air} [Å]	l_2 [Å]	ρ_2 [e$^-$ Å^{-3}]	l_3 [Å]	ρ_3 [e$^-$ Å^{-3}]	l_{tot} [Å]
DSPE-EO$_{44}$									
364	34(61)	10.0(12.3)	0.374(12)	3.6(3)	22.8(17.2)	0.346(5)			32.8
286	13(45)	11.9(11.0)	0.365(42)	3.7(8)	23.8(17.3)	0.343(6)			35.7
240	15(31)	12.0(52.1)	0.374(24)	4.0(4.1)	25.8(22.8)	0.348(19)			37.8
225	18(25)	13.0(8.6)	0.369(29)	4.0(6)	27.4(9.2)	0.347(5)			40.4
224	18(41)	11.6(18.1)	0.377(99)	4.2(1.5)	28.1(14.2)	0.347(7)			39.7
134	21(17)	17.0(5.4)	0.346(19)	3.7(3)	11.0(10.2)	0.377(18)	35.3(8.1)	0.353(4)	63.3
111	18(16)	17.4(4.9)	0.341(13)	3.9(4)	12.8(9.8)	0.380(16)	35.9(9.7)	0.354(5)	66.0
109	19(12)	18.4(5.2)	0.343(11)	4.0(3)	11.4(10.4)	0.382(21)	38.9(7.6)	0.355(5)	68.7
DSPE-EO$_{112}$									
450	24.7(32.4)	12.0(7.5)	0.354(15)	3.3(3)	62.8(19.3)	0.342(3)			74.8
307	29.6(43.8)	11.8(11.0)	0.367(47)	3.8(8)	63.9(25.1)	0.344(5)			75.7
248	27.3(21.9)	11.5(28.7)	0.357(46)	3.8(8)	17.8(24.3)	0.349(4)	72.9(17.6)	0.345(3)	102.3
204	35.8(21.0)	17.5(7.2)	0.349(6)	3.8(2)	14.4(10.9)	0.359(5)	77.4(16.2)	0.348(3)	109.3
167	32.9(12.1)	16.9(2.2)	0.338(5)	3.7(1)	16.8(5.0)	0.360(3)	88.2(10.1)	0.350(2)	121.9
DOG-MOXAN$_{35}$									
205	16.1(9.9)	51.0(9.8)	0.357(8)	3.6(0.1)					51.0
178	15.4(10.5)	57.5(7.0)	0.355(6)	4.0(0.2					57.6
171	15.1(8.3)	58.6(5.9)	0.360(5)	4.1(0.2)					58.6
166	14.2(10.9)	61.0(4.6)	0.354(7)	4.2(0.2)					61.0
160	14.8(9.0)	61.4(6.3)	0.356(5)	4.3(0.2)					61.4
134	18.3(5.0)	14.4(10.2)	0.353(17)	4.4(0.4)	52.9(12.9)	0.363(3)			67.3
107	20.6(6.0)	17.8(4.6)	0.348(8)	4.5(0.3)	56.9(7.2)	0.363(3)			74.7

consistent with the length of the Bragg-scattering moieties but less than the length of stretched alkyl chains. Again, the subphase-adjacent slab describes the polymer.

Since the mean molecular areas exceed by far the molecular area of two condensed alkyl chains, the first two air-adjacent slabs have to consist of lipid molecules and something else. Indeed, the electron density of the phosphate group slab is to low for a homogeneous phosphate group layer. Interestingly, the alkyl chain slab exhibits an electron density exceeding that of an homogeneous alkane layer and even exceeding that of water. Note that for laterally inhomogeneous layers with structures smaller than the coherence length (1 µm in our set-up), the electron densities obtained by X-ray reflectivity are averages. Therefore we propose that the monolayer is composed of two different parts, *A* and *B*, with area fractions α and 1-α, respectively. Part *A* consists of alkyl chains at the surface with their attached phosphate groups and the polymer underneath, and is described by the three-slab model already introduced for the entire condensed phase. Since the first slab is assumed to consist only of alkyl chains, its number of electrons is fixed to 274, corresponding to two C_{17} alkyl chains. With this constraint, the alkyl chain electron density is no longer a free parameter. Instead, the area fraction α of *A* is introduced as new independent variable. Part *B* consists of one slab of hydrated polymer and, with the total thickness equivalent to that of *A*, the polymer electron density is identical to the polymer component of *A*. Therefore, we need the same number of parameters for this model as for the simple slab model, gaining additional information about the area fraction α. The area fractions obtained by X-ray reflectivity agree with those obtained by GID.

The apparent shortening of the lipid tails observed both with GID and reflectivity is accompanied by an apparent thickness increase (a factor of two) and electron-density decrease of the phosphate group. These features suggest a roughening of the inner hydrophobic/hydrophilic interface or a staggered arrangement of the lipids. However, the roughness of the tail/air interface is unchanged, indicating kinks at the tail/air interface. Such a structure was already found on addition of 9% DSPE-EO_{44} to pure DSPE.[15]

The reflectivity curves obtained from DOG-$MOXAN_N$ monolayers support the conclusions obtained for DSPE-EO_N, yet they are less structured and interpretation is thus more ambiguous.[23] In principle, the DOG-$MOXAN_{35}$ reflectivity curves in the expanded phase can be fitted with one slab (namely, four free parameters: one for thickness, one for electron density, and two for roughnesses). A second slab (another thickness and density) does improve the fit, yet the overall monolayer thickness and the polymer density remain the only well defined parameters. In the condensed phase, a two-slab model is sufficient. Similar to DSPE-EO_N, the electron density of the 17 Å thick air-adjacent slab is higher than the one of the subphase (and all theoretical values for alkyl chains) but lower than the one of the hydrated polymer.

Both grafted polymer brushes (EO_N and $MOXAN_{35}$) behave very reasonably on compression: they thicken and water is expelled. Within the experimental range, the water content in the swollen polymer is reduced from eight to three water molecules per EO monomer unit. The mean polymer layer thickness is roughly proportional $NA^{-0.62}$ and $NA^{-0.54}$ for EO and MOXAN polymers, respectively (where *N* is the degree of polymerization and *A* the molecular area; Figure 4). Note that the normalized $MOXAN_{35}$ brush is thicker than the EO_N brush, even though the monomer length is comparable. The increased $MOXAN_{35}$ length may be attributed to two effects: a) EO_N forms helical structures in water, thus reducing the length of the repeat unit,[4, 5] and b) EO_N adsorbs much more strongly to the air/water interface, which effectively reduces the brush thickness. Because at least 90% of the monolayer volume can be attributed to hydrated polymer, it is reasonable that no influence from the lipid tail nanodomains on the scaling behavior can be discerned. Indeed, the experimentally determined scaling exponents are larger than the predictions for a polymer brush in a θ solvent ($NA^{-0.5}$) and much larger than those for brushes in a good solvent ($NA^{-0.67}$).[8]

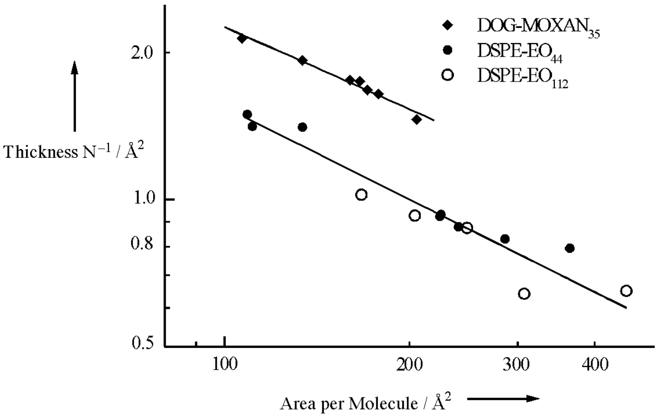

Figure 4. The average normalized polymer thickness obtained by the solubilized polymer volume divided by the average molecular area as function of grafting density, together with scaling laws as described in the text.

The well known scaling theories[6–8] to describe the mushroom and brush phases were recently modified to describe the phase diagram of surface-attached adsorbent polymers by introducing a short-range attraction between the EO_N and the anchoring surface.[24, 25] A large deviation from the predicted scaling law ($NA^{-0.33}$) was found for short polymers ($N < 400$), in agreement with our results.

In order to detect the in-plane structure in the condensed phase, the compressed DSPE-EO_N monolayers (pressures around π_t, 8 °C) were transferred onto mica and imaged by an AFM in the tapping mode. On mica, 10 to 100 µm-sized islands were detected, about 5 – 7 and 10 – 12 nm high, respectively, Figure 5.

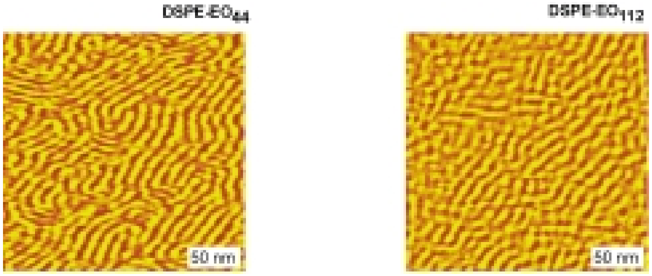

Figure 5. The condensed phase of DSPE-EO_{44} (as obtained) and DSPE-EO_{112} (low-pass filter and back-ground corrected) transferred onto mica imaged by AFM in air.

For both DSPE-EO_{44} and DSPE-EO_{112}, a stripe pattern with a 12 nm periodicity was observed. The surface pattern is independent of the polymer chain length and the area fraction of each phase is about 50 %. On water, such a high area fraction was only observed for the shorter lipopolymer at its most compressed state. For the longer lipopolymer on water, the highest area fraction of the lipid part was 30 %. Obviously, water molecules are removed from the polymer layer during the transfer onto mica, which leads to a lateral compression and, eventually, fission of the monolayer into the large islands. Within these islands, a new equilibrium structure is apparently established, which is a function of the surface energy of the solid support.

To further probe the influence of water incorporation, the monolayer was stored and imaged at various relative humidities (r.h.). At ambient conditions (40 % r.h.), the monolayer was unstable; over 24 hours the stripe pattern disappeared, while the islands grew in height. However, at 100 % r.h. the monolayer remained stable for days. To demonstrate that the stripe pattern is due to ordered alkyl chains, the DSPE-EO_{44} monolayer was heated to 60°C (r.h. = 100 %). At this temperature, $(C_{18})_2$-lipids are disordered, independent of the hydrophilic head group.[26] Indeed, at 60 °C no stripe pattern is detected and the monolayer is extremely soft. The stripe pattern reappears on cooling to room temperature. The same monolayer was subject to numerous heating/cooling cycles over a one-week period and the phase transition remained reversible. Preliminary results indicate that on slow cooling, the stripes are longer, while on fast cooling more defects occur and the stripes seem to be shorter. However, the stripe periodicity is independent of the cooling speed, always 12 nm, just as was found directly after transfer from the water surface. Considering the low transfer temperature, we may assume that the alkyl chains remain frozen during transfer and maintain their morphology. However, the polymer water content changes on transfer and may even influence the nanostructure.

Obviously, when the monolayer is compressed or cooled down, the alkyl tails order. According to the accepted picture, an ordered domain is stable as soon as its size exceeds that of the critical nucleus, a value which is determined by the balance of alkyl-chain condensation energy and domain line tension.[27, 28] The stripe width can be seen as an upper limit of the diameter of the circular critical nucleus. This assumption yields a 6 nm diameter or 140 alkyl chains. This is the same order of magnitude as found for phospholipids: 400 alkyl chains or 10 nm diameters were deduced by thermodynamic arguments.[27, 28]

However, phospholipid monolayer nuclei grow to the one- to ten-micrometer range. Obviously, the growth of the lipopolymer nuclei is constrained by the attached polymers. The maximum separation of alkyl chain domains would occur if the EO_N is adsorbed flat on the water surface. Considering the EO monomer length (0.24 nm),[4, 5] maximum domain separations of 21.4 and 53.7 nm, respectively, are obtained. The stripe width (6 nm) we find is less than the contour length of EO_N. These estimates show that any lipopolymer monolayer with weakly ordered lipid domains has to exhibit a lateral nanostructure, although we cannot say more about its details at this stage.

The most unexpected feature of our experiments is that alkyl chain ordering occurs at all. Energy considerations show that tail ordering is indeed feasible. Even though the EO and MOXAN adsorption energies are very different, the sublimation energy of the alkyl tails (44 kJ mol^{-1} ± 100 %)[24] obviously exceeds the loss in polymer conformational energy. One of the few quantitative calculations in the literature on PEO brushes[24, 25] gave the compression energy for EO_{44} from "infinity" to a molecular area of 130 Å^2 as 83 kJ mol^{-1}. This estimates show that the energies are comparable. Since the ordered nanodomains contribute at most 10 % to the monolayer volume, one may yet assume that disturbance in polymer conformation is local and limits the loss in conformation energy. This hypothesis is supported by the facts that, for DSPE-EO_N, both the transition pressure π_t and the size of the critical nuclei (namely, the width of the nanostripes) are independent of the polymer length.

Another likely monolayer structure would be hydrophobic nanodomains immersed in air instead in hydrated polymer. This structure, however, appears to be less favorable. One possible reason is the line tension, the product of the interfacial energy of the domain wall and the thickness of ordered alkyl chains. Apparently, polymer adsorption occurs and decreases the interfacial energy of a hydrophobic surface in water (50 mJ m^{-2}) to a value smaller than the one of a hydrophobic surface in air (23 mJ m^{-2}). This is reasonable for EO_N.[29] That the same embedded structure is observed with DSPE-$MOXAN_N$ is more surprising, as this lipopolymer does not adsorb onto hydrophobic surfaces. Apparently the immersion of the nanodomains into the polymer phase is favored for entropic reasons, to yield an increase in the conformational space of the grafted polymers.

The lipopolymer nanodomains differ in several aspects from the structures of diblock copolymers. Lipopolymer patterning occurs on a scale an order of magnitude smaller (10 nm scale instead of 100 nm) than reported for surface micelles of amphiphilic diblock copolymer monolayers.[30] Furthermore, each surface micelle protrudes from the water surface, to result in a corrugated surface. In contrast, the lipopolymers exhibit a constant height, even though the chemical composition varies laterally. Conceptually, the reversible formation of diblock copolymer surface micelles is akin to a wetting phenomenon, whereas the alkyl tails undergo an ordering transition within the monolayer.

The tail lattice does not constitute a nanocrystal but is only weakly ordered. The width of the nanodomains exceeds the positional order found with GID by a factor of five. Furthermore, the shape of a macroscopic crystal reflects the angles of its lattice, whereas the nanodomain morphology is reminiscent of images of block copolymers. These features suggest that the tails are ordered in a hexatic glass or a mesophase[31] or even form cylindrical surface micelles.[32, 33] The polymer bound to the lipid head group leads to an interpenetration of the phosphate groups into the hydrophobic tails and to a rough internal interface or a staggered conformation. The details of the tail lattice do not determine the domain shape nor its size. Obviously, the growth of the nanodomain nuclei is limited by the loss in polymer entropy.

In conclusion, we demonstrated for the first time the existence of weakly ordered lipid nanostripes in lipopolymer monolayers.

This was shown for EO_N lipopolymers immobilized on mica; EO_N and $MOXAN_{35}$ lipopolymers floating on the water surface are nanostructured, with domains of weakly ordered alkyl chains embedded in the polymer. The lipid tail "crystal" is frustrated by the rough internal interface, which shortens the ordered part of the alkyl chains.

Experimental Section

DSPE-EO_{44} and DSPE-EO_{112} were purchased from Avanti Polar Lipids (Birmingham, AL (USA)). The DSPE-$MOXAN_N$ and DSPE-$EOXAN_N$ samples were a generous gift from Peter Kuhn and Oskar Nuyken.

GID measurements were performed at the Wiggler beamline BW1 at the HASYLAB synchrotron source (Hamburg, Germany) at the pressures indicated at the isotherm. For DSPE-$MOXAN_N$, which was subject to severe radiation damage, a peak was only observed when the monolayer was moved laterally beneath the X-ray beam and simultaneously recompressed. For specular X-ray reflectivity, a home-built device was used.[34]

For AFM images, the monolayers were transferred at $\pi_t + 3$ mN m^{-1} and 8°C onto mica. The AFM was a PicoSPM and, including the heating stage, a generous loan from Molecular Imaging (Phoenix, AZ (USA)). We obtained the same images independent of the transfer speed (varied by a factor of 50) or the compression speed on the water surface (varied by a factor of 16). The transfer ratio from water to substrate was always 1 (within 10%). While DSPE-EO_{44} monolayers are relatively homogeneous, DSPE-EO_{112} is very soft and extremely difficult to image; both a low-pass filter and a background correction were necessary to remove medium and large scale height fluctuations. Initial experiments suggest that no nanopattern can be obtained if the DSPE-EO_N is transferred in the expanded phase or at very high pressures, nor did we succeed to observe a pattern within the domains of a DOG-$MOXAN_{35}$ monolayer.

[1] E. Sackmann, *Science* **1996**, *271*, 43.
[2] D. D. Lasic, *Science* **1995**, *267*, 1275.
[3] J. N. Israelachvili, *PNAS* **1997**, *94*, 8378.
[4] F. Oesterhelt, M. Rief, H. E. Gaub, *New J. Phys.* **1999**, *1*, 6.1.
[5] H. J. Kreuzer, R. L. C. Wang, M. Grunze, *New J. Phys.* **1999**, *1*, 21.1.
[6] S. Alexander, *J. Phys.* **1977**, *38*, 983.
[7] P.-G. de Gennes, *Macromolecules* **1980**, *13*, 1069.
[8] S. T. Milner, *Science* **1991**, *251*, 905.
[9] B. W. Discher, Y. Y. Won, D. S. Ege, J. C. Lee, F. S. Bates, D. E. Discher, D. A. Hammer, *Science* **1999**, *284*, 1143.
[10] H. Möhwald, *Rep. Prog. Phys.* **1993**, *56*, 653.
[11] T. R. Baekmark, T. Wiesenthal, P. Kuhn, T. M. Bayerl, O. Nuyken, R. Merkel, *Langmuir* **1997**, *13*, 5521.
[12] T. R. Baekmark, T. Wiesenthal, P. Kuhn, A. Albersdorfer, O. Nuyken, R. Merkel, *Langmuir* **1999**, *15*, 3616.
[13] T. Wiesenthal, T. R. Baekmark, R. Merkel, *Langmuir* **1999**, *15*, 6837.
[14] K. Kjaer, J. Als-Nielsen, C. A. Helm, L. A. Laxhuber, H. Möhwald, *Phys. Rev. Lett.* **1987**, *58*, 2224.
[15] T. L. Kuhl, D. E. Leckband, D. D. Lasic, J. N. Israelachvili, *Biophys. J.* **1994**, *66*, 1479.
[16] J. Majewski, T. L. Kuhl, K. Kjaer, M. C. Gerstenberg, J. Als-Nielsen, J. N. Israelachvili, G. S. Smith, *J. Am. Chem. Soc.* **1998**, *120*, 1469.
[17] J. Als-Nielsen, K. Kjaer in *Phase Transitions of Soft Condensed Matter*, *Vol. 211* (Eds.: T. Riste, T. Sherrington), Plenum, New York, **1989**, p. 113.
[18] C. A. Helm, H. Möhwald, K. Kjaer, J. Als-Nielsen, *Europhys. Lett.* **1987**, *4*, 697.
[19] L. Bosio, J. J. Benattar, F. Rieutord, *Rev. Phys. Appl.* **1987**, *22*, 775.
[20] J. Als-Nielsen in *Structure and Dynamics of Surfaces* (Ed.: W. S. a. W. Blanckenhagen), Springer, New York, **1986**.
[21] J. S. Pederson, *J. Appl. Crystallogr.* **1992**, *25*, 129.
[22] J. S. Pederson, I. W. Hamley, *J. Appl. Crystallogr.* **1994**, *27*, 36.
[23] T. Gutberlet, A. Wurlitzer, U. Dietrich, E. Politsch, G. Cevc, R. Steitz, M. Lösche, *Physica B* **2000**, *283*, 37.
[24] M. C. Faure, P. Basserau, M. A. Carignano, I. Szleifer, Y. Gallot, D. Andelman, *Eur. Phys. J. B* **1998**, *3*, 365.
[25] E. P. K. Currie, F. A. M. Leermakers, M. Cohen-Stuart, G. J. Fleer, *Macromolecules* **1999**, *32*, 487.
[26] G. Cevc, D. Marsh, *Phospholipid Bilayers: Physical Principles and Models*, *Vol. 5*, Wiley, New York, **1987**.
[27] D. J. Benvegnu, H. M. McConnell, *J. Phys. Chem.* **1993**, *97*, 6686.
[28] C. A. Helm, H. Möhwald, *J. Phys. Chem.* **1988**, *92*, 1262.
[29] B. Cao, M. W. Kim, *Faraday Discuss. Chem. Soc.* **1994**, *98*, 245.
[30] Z. Li, M. W. Zhao, J. Quinn, M. H. Rafailovich, J. Sokolov, R. B. Lennox, A. Eisenberg, X. Z. Wu, M. W. Kim, S. K. Sinha, M. Tolan, *Langmuir* **1995**, *11*, 4785.
[31] D. R. Nelson, B. I. Halperin, *Phys. Rev. B* **1979**, *19*, 2457.
[32] L. Chi, S. Jacobi, B. Anczykowski, M. Overs, H.-J. Schäfer, H. Fuchs, *Adv. Mater.* **2000**, *12*, 25.
[33] S. A. Safran, M. O. Robbins, S. Garoff, *Phys. Rev. A* **1986**, *33*, 2186.
[34] H. Baltes, M. Schwendler, C. A. Helm, H. Möhwald, *J. Colloid Interface Sci.* **1996**, *178*, 135.

Received: May 4, 2000 [Z 18]

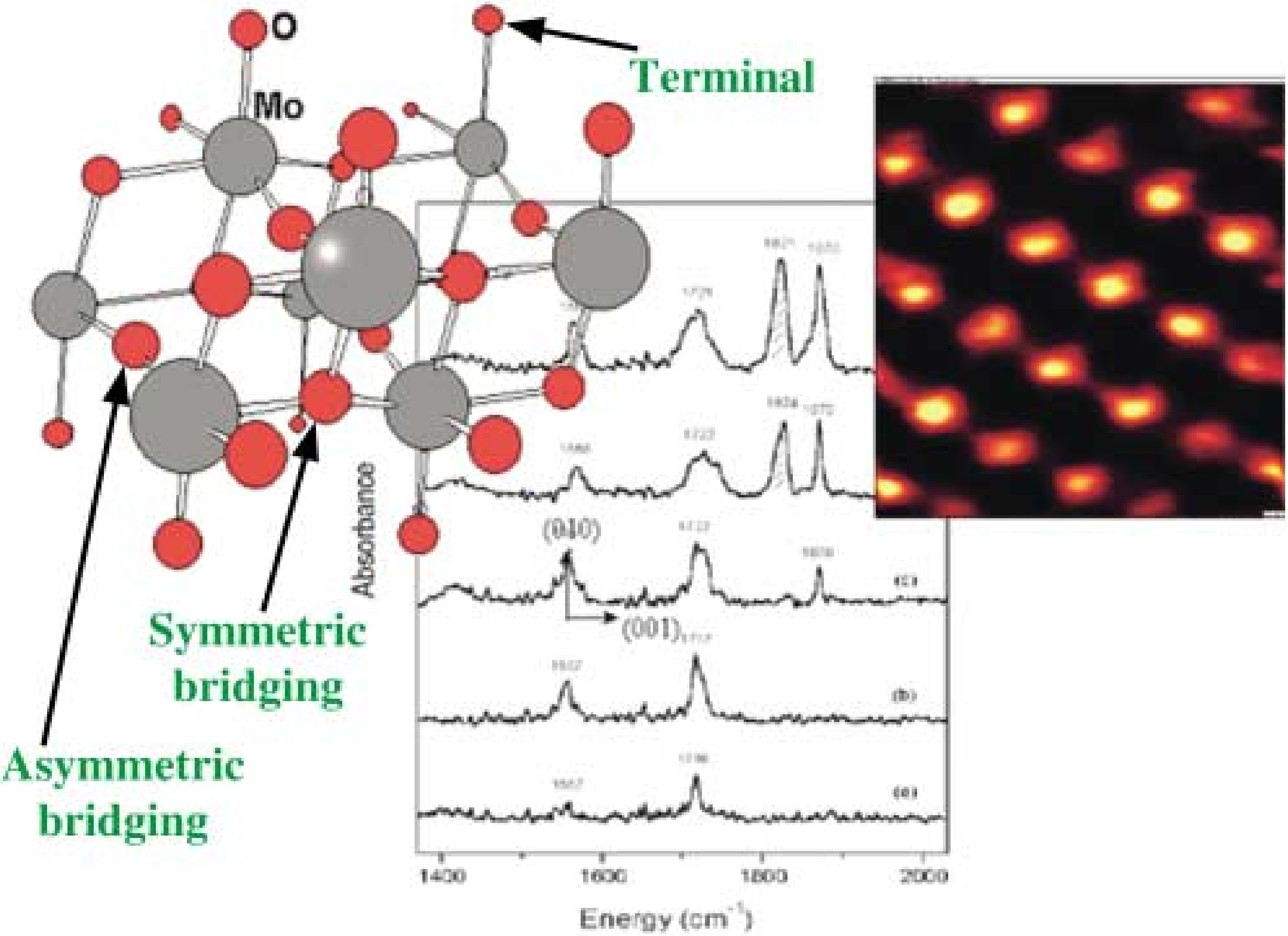

Molybdenum trioxide is a potential catalyst for the reduction of NO_x species that arise from combustion. Surface reactions contribute to elementary steps in the overall reduction, however, due to the complex nature of the catalyst, it is not possible to study specific elementary steps. By forming a thin film on a single crystal of the Mo(110) substrate to model one type of MoO_3 surface, reaction intermediates can be identified by, among other techniques, vibrational spectroscopy.

1439-4235/00/01/03 $ 17.50+.50/0

Site-Selective Surface Reactions: Nitric Oxide Reduction on Mo(110)

Katherine Queeney[a] and Cynthia M. Friend*[a]

The catalytic reduction of NO_x compounds formed in combustion processes is a critical factor in maintaining a clean environment. The introduction of the "catalytic converter" has been extremely effective in reducing these pollutants in automobile exhaust over the last two decades. Nevertheless, new environmental regulations have necessitated the development of processes that operate over a wider range of conditions and that are more efficient, so that NO_x emissions can be reduced further. The need for new catalysts and processes has motivated a considerable number of studies of NO reduction using metal oxides as catalysts. In order to better understand the mechanisms for NO reduction on oxides, we have systematically studied the reactions of NO on thin-film oxides grown on Mo(110). By using a thin-film oxide, we are able to change the type of coordination sites that are available for NO binding and to use surface-sensitive spectroscopies to identify intermediates on the surface. We specifically explore the role of low-temperature NO coupling to a dinitrosyl species in our work and contrast this reaction to the higher temperature process, NO dissociation followed by nitrogen atom coupling.

KEYWORDS:

nitrogen oxides · heterogeneous catalysis · surface chemistry · vibrational spectroscopy

1. Introduction

The increasing emphasis on emissions control, spurred by concern for the global environment, has rendered certain catalytic processes among the most important global technologies. Of paramount importance in reaching the goals for improved emissions standards is improvement in heterogeneous catalysts for NO reduction in automotive exhausts and power plants. Such an improvement would take the form of catalysts that operate efficiently both at lower temperatures and over a wider range of reaction conditions than existing catalysts (for example, in fuel/air mixtures in the case of automobile exhaust). Recent work has focused on the use of metal-oxide based catalysts for NO reduction,[1–6] since some of these materials have shown promise for satisfying the above requirements at a relatively low cost.

The three-way catalyst currently used in catalytic converters for automobile exhaust contains rhodium, platinum, and palladium, in which rhodium the essential component for NO_x reduction. This system is less than optimal because of both the high cost of rhodium and the narrow window of operating conditions under which efficient NO reduction takes place.[7]

Several studies have shown that, upon addition of even small amounts of MoO_3 to Rh-,[8] Pt-,[9] and Pd-based catalysts,[10–12] the activity of those catalysts for NO reduction is improved. Specifically, the addition of MoO_3 reduced the proportion of NO detectable in the product stream relative to that achieved in the absence of MoO_3. Since NO is known to form dinitrosyl species (Figure 1) on MoO_3 and MoO_3-containing catalysts,[9, 13–16] the coupling of two intact NO molecules on a single catalytic site has been proposed[9] to favor N–N bond formation and NO reduction. While this model makes intuitive sense, it is important to note that there is no *direct* evidence from the aforementioned catalytic studies to link dinitrosyl formation to improved efficiency in NO reduction.

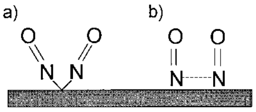

Figure 1. Schematic representation of NO coupling in a) surface dinitrosyl species and b) condensed-phase type NO dimers.

The possibility that direct N–N coupling leads to NO reduction frames a rather general question in NO surface reactions: Is it more favorable to form N–N bonds via a dissociative pathway—such as the reaction of adsorbed nitrogen atoms either with itself or with NO—or via the reaction of two intact NO molecules? In this Review, we illustrate how ultrahigh vacuum, single-crystal studies can be used to elucidate fundamental details about site selectivity in surface reactions. Specifically, we examine possible mechanisms for the low temperature reduction of NO on oxidized molybdenum to see how the presence of MoO_3 might enhance the NO-reduction activity of noble-metal catalysts.

---

[a] Prof. C. M. Friend, Prof. K. Queeney[+]
Harvard University
Department of Chemistry
Cambridge, MA 02138 (USA)
Fax: (+1) 617-496-8410
E-mail: friend@chemistry.harvard.edu

[+] Present address:
Smith College
Department of Chemistry
Northampton, MA 01063 (USA)

The reduction of NO induced by MoO_3 is an example of a complex system that is difficult to understand on a molecular level. Molybdenum trioxide is a layered material with a distorted perovskite lattice, which has three types of oxygen atom coordination: a twofold-coordinated asymmetric bridging oxygen, a threefold-coordinated symmetric bridging oxygen, and the singly coordinated terminal oxygen, Mo=O. Furthermore, oxygen vacancies, generally thought to be required for catalytic processes on oxides, are also typically present in catalysts that contain MoO_3. In addition to the structural complexity of MoO_3, the high pressures and temperatures used for actual catalytic reactions result in a complex mixture of gas-phase and adsorbed species, which make it virtually impossible to investigate individual elementary steps.

The approach we have taken to studying the elementary steps important in processes on metal oxide surfaces, for example NO reduction, is to synthesize model systems using controlled oxidation of a metal surface. This approach, used by us and others,[17, 18] offers the additional advantage that electron-based surface spectroscopies can be applied to the investigation of these processes. By varying the conditions for Mo(110) oxidation, we are able to control not only the extent of Mo oxidation but also the structure of the surface oxide, since oxygen atoms occupy different coordination sites depending on the exact oxidation protocol followed.[19]

While the surface chemistry of a bulk oxide material, such as MoO_3, is, naturally, distinct from that of its component metal, our model system provides insight into how the geometric and electronic properties of different coordination sites affect specific elementary steps. Furthermore, the use of an oxidized single crystal allows us to regenerate the surface for a series of comparative studies. A link between the behavior of our model oxides and that of MoO_3 itself is provided by companion theoretical studies that probe the effect of specific oxygen vacancies in MoO_3 both on oxide electronic structure and on the resultant NO reduction chemistry. This information can then be used to guide thinking about the analogous steps in the related catalytic process.

Our work shows that dinitrosyl species do, in fact, form on both clean and oxidized Mo(110) under ultrahigh vacuum conditions. Furthermore, these intermediates lead to N–N bond formation and to the evolution of gas-phase reduction products. Surface vibrational spectroscopy not only demonstrates the existence of dinitrosyl species but also sheds light on the role of surface oxygen in the formation and reaction of these potential intermediates in selective catalytic reduction of NO. Our theoretical studies of dinitrosyl binding to MoO_3 provide a picture of the bonding interactions that are important in N–N coupling, as well as insight into the mechanism for their formation.

We have subsequently made use of our detailed understanding of NO chemistry on oxidized Mo(110) to investigate the reduction of adsorbed NO by alkyl species. Methane (CH_4) has shown promise as a reducing agent for NO over a variety of metal oxide catalysts,[1, 2, 4–6] to potentially offer a cheaper, safer, and more effective route than current technologies used for NO reduction in both automobile and stationary sources of NO_x emissions. Since the active alkyl species in these reactions are thought to be gas-phase methyl radicals ($^{\bullet}CH_3$), our studies focus on the elementary step of the $^{\bullet}CH_3$ reaction with adsorbed NO on a range of oxidized Mo(110) surfaces. We find that $^{\bullet}CH_3$ reacts preferentially with molecular NO species on oxidized Mo(110). At low temperature, there is a loss of NO_x species, which suggests that coupled NO species are also potentially important in the reduction of NO in the presence of hydrocarbons.

Cynthia Friend is recognized for her research studying complex reactions occurring on solid surfaces. She joined the Harvard faculty in 1982 after receiving her Ph.D. in Physical Chemistry from the University of California, Berkeley, and doing postdoctoral research at Stanford University. She was promoted to Full Professor at Harvard University in 1989 and is now the Theodore William Richards Professor of Chemistry. In her current research, she studies the mechanisms of reactions important in semiconductor device fabrication and heterogeneous catalysis. Prof. Friend has received several honors recognizing her research, which include the 1991 Garvan Medal of the American Chemical Society, the 1991 Iota Sigma Pi Agnes Fay Morgan Research Award in Chemistry, the 1990 Distinguished Young Alumna Award, University of California, Davis, and a Union Carbide Innovation Recognition Award in 1988 – 89. She is also featured as a "host scientist" in the "Science in American Life" exhibit at the Smithsonian Institution.

Kate Queeney received her B.A. in Chemistry from Williams College in 1992 and her Ph.D. from Harvard University in 1998. Her thesis work with Prof. Friend, including the studies described in this article, focused on the role of surface oxygen in a variety of catalytically-relevant reactions on Mo(110). After a postdoctoral period at Bell Labs, using surface infrared spectroscopy to investigate silicon passivation, she joined the chemistry department at Smith College as an assistant professor. Her current research centers on studies of surface chemistry at solid/liquid interfaces under ambient conditions.

2. NO Reduction: Dissociation versus Dinitrosyl Formation

Pathways to selective catalytic reduction of NO can be divided into two general classes: dissociative and molecular. In the first class, the catalyst dissociates NO into its constituent N and O atoms, with surface-bound atomic N subsequently undergoing N–N bond formation; in the second case, NO binds as a molecular species and the catalyst induces N–N bond formation directly from this molecular precursor. Our studies of NO reduction on oxidized Mo(110) demonstrate that both pathways operate and that their relative importance depends on the number of vacant coordination sites that can accept the dissociation products, O_a and N_a. Molecular pathways can lead to the evolution of both N_2 and N_2O from the surface; in fact, both of these products are observed for a range of surface oxidation conditions on Mo(110). As with NO dissociation, the branching ratio for N_2 versus N_2O production also depends on the availability of vacant oxygen coordination sites. Taken together, our results indicate that molecular pathways may be more important for efficient NO reduction over oxide catalysts and that the electronic structure of the oxide catalyst is instrumental in accessing the molecular reduction pathway. These conclusions are based on a combination of experimental and theoretical studies, which are discussed below.

2.1. NO Reaction on Mo(110): The Dissociative Pathway

Dissociation of NO is known to occur on a variety of transition metal surfaces and ultimately leads to NO reduction to N_2 via recombination of nitrogen atoms. However, nitrogen atom recombination is often a very thermally active process on surfaces that are capable of NO dissociation, since the strong metal-nitrogen bond that promotes the production of N_a from NO_a leads to a high energy barrier for nitrogen atom diffusion. For example, N_2 is formed from the coupling of nitrogen atoms above 1000 K on Mo(110), at 805 K on Pd(100),[20] and at 770 K on Rh(100).[21] Another limitation of the dissociative pathway for N_2 formation is its requirement for open coordination sites to accommodate nitrogen and oxygen atoms—four sites for a completely dissociative pathway versus two sites for reaction of two intact NO molecules.

The reaction of NO on Mo(110) allows direct comparison of dissociative versus nondissociative NO reduction, since both reaction pathways are accessable on this surface. Nitric oxide dissociates even at 100 K on clean Mo(110), which subsequently leads to nitrogen atom recombination and N_2 evolution at $\approx$1200 K. The amount of NO dissociation on clean Mo(110) is self-limiting and is at least in part related to the availability of open coordination sites for the dissociation products, N_a and O_a, as discussed below. It is also possible that the dissociation products change the electronic properties of the surface, which thereby helps inhibit dissociation by altering the extent of intramolecular bond weakening in adsorbed NO. The existence of such an indirect electronic effect is supported by the fact that molecular NO adsorption *is* observed after some NO dissociation has taken place but while there are still open surface sites for further dissociation to occur. Notably, however, molecular NO is only stable with respect to dissociation after the surface has been at least partially oxidized, whether that oxidation takes place via NO dissociation or via deliberate preoxidation of the surface, such as through a reaction with O_2.

Dissociation of NO produces surface atomic oxygen species in both high coordination and terminal (Mo=O) configurations,[22] identified by characteristic Mo–O vibrational modes detected with high resolution electron energy loss spectroscopy (EELS; modes below 1000 cm^{-1} in Figure 2). The presence of N_a produced during NO dissociation seems to promote the formation of doubly bound Mo=O species, so-called "terminal oxygen", even at 100 K. This is particularly remarkable, since terminal oxygen species are only created under higher temperature and flux conditions when O_2 is used as the oxidant. Isotopic labeling studies reveal no vibrational modes which can be readily ascribed to surface atomic nitrogen species because of the limited resolution of EELS. Since nitrogen is clearly present on the surface, nitridation as well as oxidation of the Mo(110) surface no doubt contribute to the stabilization of molecular NO and to its subsequent reactive chemistry.

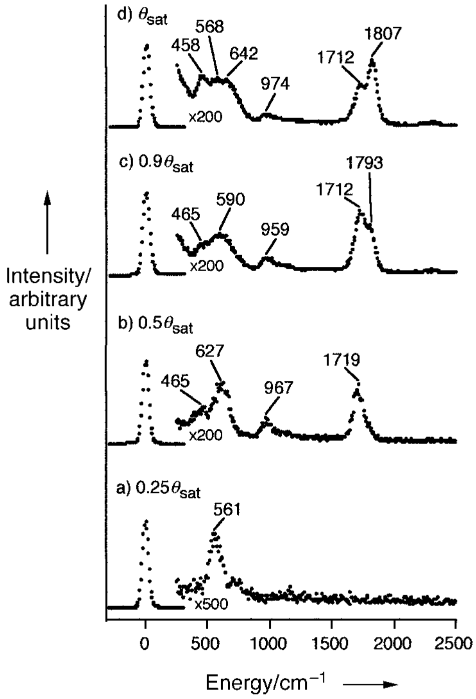

Figure 2. Electron energy loss spectra acquired after NO adsorption at 100 K on Mo(110), with coverages corresponding to a) $0.2\theta_{sat}$, b) $0.35\theta_{sat}$, c) $0.65\theta_{sat}$ and d) θ_{sat}. Reprinted with permission from ref. [22].

Preoxidation of the Mo(110) surface with O_2 inhibits NO dissociation, as demonstrated by a marked decrease in the amount of recombinant N_2 formation as θ_0 is increased prior to NO exposure (Figure 3). Some evidence for a simple site-blocking mechanism is given by NO reaction on an oxygen overlayer with $\theta_0 = 0.4$ ML (θ_0 = surface coverage, ML = monolayer; Figure 3 a). On this well-defined surface, oxygen atoms

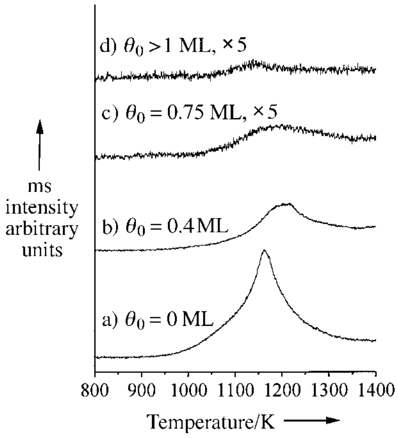

Figure 3. Temperature-programmed reaction of recombinant N_2 formation following reaction of a saturated NO overlayer on a) clean Mo(110), b) an oxygen overlayer with $\theta_0 = 0.4$ ML (see Figure 2a), c) the 0.75-ML oxygen overlayer (Figure 2b), and d) a thin-film oxide with Mo=O species (Figure 2c). Mass-spectrometric detection at m/z = 28. Reprinted with permission from ref. [23].

reside in long-bridge sites; EELS measurements of NO dissociation products on clean Mo(110) shows that these same bridge sites are the first ones populated by oxygen atoms from the NO dissociation.[22] The passivation of these preferred dissociation sites by atomic oxygen is consistent with the approximately 60% decrease in N–O dissociation observed on this surface. However, EELS studies that used isotopically labeled NO[23] also demonstrated that oxygen formed via NO dissociation can displace predeposited atomic oxygen from its initial binding sites, which suggests that electronic modification of the surface by O_a may also play a role in determining NO chemistry on oxygen-modified surfaces.

2.2 Molecular Pathways for NO Reduction

The potentially advantageous characteristics of direct coupling of NO *without* dissociation to nitrogen and oxygen atoms have prompted many researchers to look for evidence of such reaction pathways. There have been several studies that provide evidence of NO dimers, such as those formed in the condensed phase (Figure 1b) on transition metal surfaces above the temperature required for NO condensation. Infrared spectroscopy was used to identify NO dimers on Ag(111) at temperatures as high as 90 K, and N–N bond formation to evolve gaseous N_2O was observed from these dimer precursors.[24, 25] The same type of NO dimers on Cu(111) were subsequently observed using infrared spectroscopy.[26] The fact that the condensed-phase type dimers observed on these surfaces have ν(NO) vibrational frequencies virtually unperturbed from those of true condensed-phase dimers suggests that their interaction with silver and copper is minimal. The metal surface in this case acts more as a physical support to allow the NO molecules to assume a condensed-phase configuration at gas-phase concentrations, than as a chemical participant in the reaction. Such a weak surface/adsorbate interaction is confirmed by the low temperatures at which these species react and/or desorb, which suggests that there would be a low steady-state concentration of such species at the higher temperatures typically used for NO reduction catalysis. Therefore, this type of NO coupling is probably not an efficient route to N–N bond formation.

Dinitrosyl species, such as those identified on MoO_3, should involve stronger binding of NO to the surface, since both NO molecules are bound to a metal atom. This picture is supported by the fact that the intramolecular vibrational features of dinitrosyl species are more strongly perturbed, relative to the condensed phase, than the dimers discussed above. It is important to note, though, that while such intermediates apparently form readily under some catalytic conditions, the sterically crowded nature of dinitrosyl species does not favor their formation under conditions of extremely low pressure. Studying such species under an ultrahigh vacuum is thus intrinsically difficult; however, ultrahigh vacuum (UHV) studies provide a unique opportunity to directly correlate the presence of dinitrosyls with specific NO reaction pathways.

Although NO dissociation accounts for the majority of NO reactions on clean Mo(110) as outlined above, intact NO species are also detected with vibrational spectroscopy (Figure 2b, c). The intramolecular ν(N–O) vibration is extremely sensitive to the degree of metal–NO interaction and ν(N–O) can therefore be used to distinguish between different NO binding sites and/or orientations on the same surface. One of the intact NO species formed on Mo(110) is, indeed, the same dinitrosyl species identified previously on MoO_3 and implicated in the catalytic activity of this material. In fact, dinitrosyl species are formed on *all* Mo(110) surfaces studied, namely over a range of surface oxidation conditions, and provide a low temperature pathway to NO reduction.

While high resolution EELS spectra, such as those shown in Figure 2, allow resolution of distinct NO_a binding environments like those giving rise to $\tilde{\nu}(NO) = 1712$ and $1807\,cm^{-1}$ (Figure 2d), a more exact understanding of the nature of those binding environments can often be derived from surface infrared spectroscopy. In particular, dinitrosyl species (or any other discrete, coupled species) can be definitively identified on the basis of infrared spectra of isotopically mixed overlayers. The infrared spectrum of a saturated overlayer formed from a ≈1:1 mixture of ^{15}NO and ^{14}NO is shown in Figure 4a iii, with spectra of both isotopically pure overlayers (Figure 4a i, ii) for comparison. As demonstrated by comparison of the experimental spectrum with a simulated spectrum and the assumption of only isolated nitrosyl species (Figure 4b), the $\tilde{\nu}(^{14}NO)$ peak at $1820\,cm^{-1}$ arises from coupled nitrosyl species; the maximum of this peak in the mixed overlayer, at $1807\,cm^{-1}$, corresponds to a $^{15}NO/^{14}NO$ pair. This general behavior of the isotopically mixed overlayer identifies the $1820\,cm^{-1}$ species as a coupled one; from the nearly exact correspondence of the vibrational peaks in Figure 5a to those in spectra of dinitrosyl species on MoO_3,[13] this peak is assigned specifically to the dinitrosyl species ($(NO)_2Mo$) on Mo(110).

The spectroscopic signature of the dinitrosyl species is identical on all Mo(110)-based oxygen-modified surfaces studied[23] and even on MoO_3. This apparent insensitivity of adsorbate intramolecular bond potentials to oxidation state is

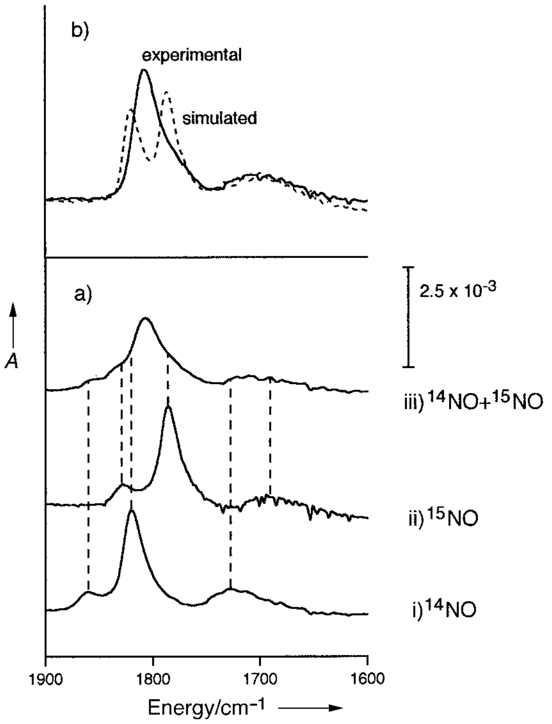

Figure 4. *Identification of surface dinitrosyl species by infrared spectroscopy. Infrared spectra of saturated NO overlayers are shown in a) after adsorption of i) pure ^{14}NO, ii) pure ^{15}NO, and iii) a 1:1 mixture of ^{14}NO + ^{15}NO. Comparison of the experimental spectrum acquired after heating the surface in (iii) to 200 K with a simulated spectrum with assumed uncoupled NO species is presented in (b). Reprinted with permission from ref. [22].*

consistent with results for methoxy (CH_3O) species formed via the reaction of methanol (CH_3OH) on these same oxygen-modified surfaces:[27] namely, that perturbation of these bond potentials is highly sensitive to local electronic structure at the bonding site but not to the overall extent of surface oxidation. What is different in the NO case, as compared to CH_3O, is that the dinitrosyl structure is apparently virtually *identical* on the clean and oxygen-modified Mo(110) surfaces, whereas there is a distinct difference between the bonding of CH_3O on clean Mo(110)[28] and on Mo(110) with even a small amount (0.5 ML) of preadsorbed oxygen. This is almost certainly due to the fact that dinitrosyl species on "clean" Mo(110) form only after approximately 0.5 ML of atomic oxygen is deposited through NO dissociation, so that the "clean" surface is in fact an oxygen-modified one. Methanol on clean Mo(110) also undergoes a significant amount of dissociation[28] but the surface oxygen created either is insufficiently high in concentration or does not populate the correct sites to influence the intramolecular potential of the methoxy adsorbent in the same manner as preadsorbed O atoms from the O_2 reaction. The significance of the apparent insensitivity of dinitrosyl formation to overall surface oxidation is that this effect suggests than even partially oxidized Mo(110) surfaces may approximate the bonding sites available on MoO_3 well enough to describe accurately the NO reduction chemistry that takes place in real catalytic systems.

Identifying dinitrosyl species on Mo(110) is the first step in understanding the role of these species in NO reduction; the well controlled conditions of UHV now allow us to correlate the formation of surface dinitrosyl species with specific reaction pathways. Indeed, dinitrosyl species which are formed on *all* Mo(110) surfaces react via N–N bond formation at relatively low temperatures, as shown by temperature-programmed reaction of isotopically mixed overlayers. For example on clean Mo(110), in addition to the high temperature recombinant N_2 formation discussed above, at high NO coverages both N_2 and N_2O evolve below 400 K along with some NO desorption (Figure 5). By predissociation of a small amount of ^{15}NO on the surface prior to the ^{14}NO reaction, we showed that N_2O production results only from the reaction of two intact NO molecules, since only $^{14}N_2O$ was evolved from the surface. Both infrared and EELS studies show a correlation between the appearance of the vibrational signature of dinitrosyl and N_2O production, which confirms that the dinitrosyl is an intermediate for N–N bond formation on Mo(110).[29] Nitrogen evolution at low temperature is shown to arise partly from reaction of NO_a with N_a but also in part from a dinitrosyl reaction.[22]

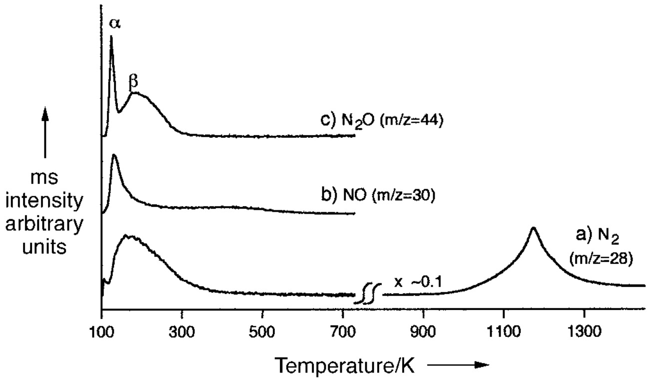

Figure 5. *Temperature-programmed reaction which shows low and high temperature reaction pathways for NO adsorbed on clean Mo(110). Reprinted with permission from ref. [22].*

While predissociation of NO or preoxidation of the surface with O_2 is required for dinitrosyl formation on Mo(110), the presence of atomic oxygen and/or nitrogen species ultimately inhibits the reaction of these NO reduction intermediates. On both the clean and oxygen-modified surfaces, the spectroscopic signature of dinitrosyl species can be detected as high as 500 K, well past the cessation of intermolecular N–N bond formation. This can be understood by recognizing that the formation of NO reduction products via any pathway involves N–O bond scission, which in turn requires empty surface sites for atomic oxygen deposition. The inability of dinitrosyl species to react at high temperatures may again be due to surface-site blocking, electronic effects, or to a combination of the two phenomena. We postulate that the unreacted dinitrosyl species contribute to the long tail of NO desorption observed at temperatures beyond N_2 and N_2O evolution (Figure 5 b).

In fact, although surface oxidation is required for dinitrosyl formation, studies of NO reaction on the various oxygen overlayers reveal that surface oxidation also favors desorption of intact NO rather than NO reduction (Table 1). The increasing

Table 1. *Relative yields of products from NO reaction on clean and oxygen-modified Mo(110) surfaces.*[a, b]

θ_O	N_2O	N_2[c]	NO	N_2[d]	Total reaction[e]
0 ML	0.13	0.11	0.03	0.73	1.00
0.75 ML	0.35	0.28	0.23	0.14	0.23
>1 ML	0.29	0.25	0.46	0.00	0.36

[a] Table adapted with permission from ref. 23. [b] Yields of individual products are expressed as percentages of the total reaction for that surface. [c] At low temperatures. [d] From recombination. [e] The amount of total reaction on each surface is normalized to unity on clean Mo(110).

dominance of NO desorption with increasing θ_0 is largely due to the stabilization of new mononitrosyl species on the oxygen-modified surfaces. The temperature-dependent infrared spectra of saturated NO overlayers on an oxygen overlayer with $\theta_0 =$ 0.75 ML oxygen overlayer and on a thin-film oxide formed by higher-temperature O_2 exposure ($\theta_0 > 1$ ML) are shown in Figure 6; note the appearance of manifold ν(NO) signatures that are not detected after NO adsorption on clean Mo(110) (Figure 4a i).

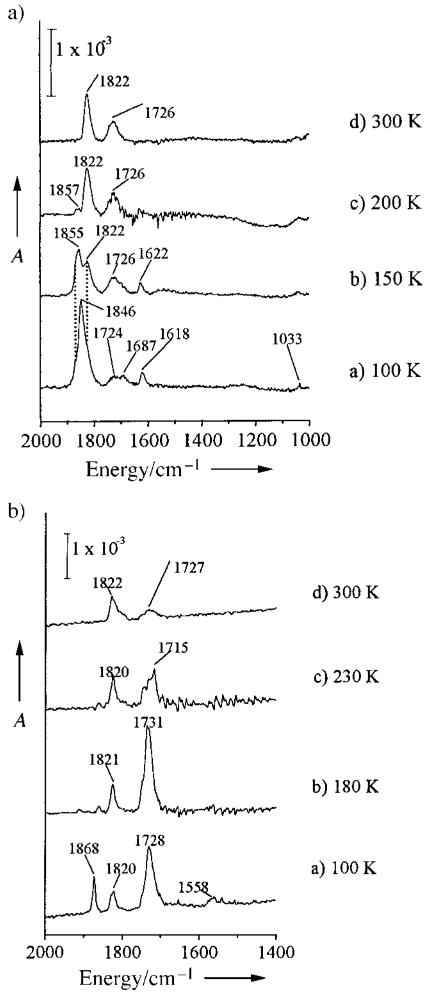

Figure 6. *Infrared spectra of saturated NO overlayers adsorbed on a) a 0.75-ML oxygen overlayer and b) a thin-film oxide with Mo=O species. NO was adsorbed at ~100 K and heated to the temperature shown prior to data acquisition at ~100 K. Reprinted with permission from ref. [23].*

The reactivities of nitrosyl species formed upon NO adsorption on oxygen-modified Mo(110) surfaces are discussed in detail elsewhere[23] but, in general, the strength of the metal–NO interaction, as judged by the resultant perturbation of the intramolecular N–O vibrational frequency, does *not* correlate with the desorption temperature of these species. As outlined in earlier studies of NO on oxygen-modified Ni(111),[30] the simplest interpretation of ν(NO) frequency shifts with surface oxidation is that electronegative surface oxygen species withdraw electron density from the surface and thereby decrease the amount of charge donated to the 2π* antibonding orbital of adsorbed nitrosyl species. Such an effect would tend to increase $\tilde{\nu}$(NO) with increasing oxygen coverage. However, on Mo(110), the presence of surface oxygen stabilizes new nitrosyl binding environments, to lead to both lower *and* higher ν(NO) frequencies relative to the clean surface and therefore such a simplified argument cannot explain the effect of surface oxidation on NO adsorption on these surfaces. Furthermore, since the strength of Mo–NO bonding, as judged by the amount of intramolecular bond perturbation, does *not* scale with NO desorption temperature, it appears that entropic effects are important in determining the stability of surface nitrosyls, whose formation is favored by surface preoxidation. These studies therefore illustrate the complexity of even a model system in describing the effect of surface oxidation state on NO reduction chemistry and highlight the need for companion theoretical studies to link observed behavior (electronic structure as judged by vibrational frequencies, desorption temperature, reaction pathways) with specific catalytic binding sites.

3. The Role of Metal-Mediated Coupling in N–N Bond Formation

Our studies have clearly shown the importance of dinitrosyl species formation in low temperature pathways to NO reduction on molybdenum-based surfaces. In order to understand the general implications of this finding—namely, whether such reaction pathways are a universal template for efficient routes to selective catalytic reduction of NO—we must understand exactly how such intermediates form and what influences their propensity to react in the desired manner. In the following Section, we briefly describe how a combination of experimental and theoretical studies have elucidated these issues.

3.1 Comparison of Dimer versus Dinitrosyl Stability and Reactivity

The relative robustness of dinitrosyl species relative to condensed-phase NO dimers suggests that metal-mediated coupling of two intact NO molecules, where both nitrosyl groups form a metal–NO bond, is the more effective mechanism for N–N bond formation. However, differences in the electronic structures of Mo, which forms dintrosyl species, and metals such as Ag and Cu, which favor dimer formation, introduce other complicating factors into the comparison. Fortuitously, though, both dinitrosyl ($Mo(NO)_2$) *and* dimeric (ON–NO) species can be formed on Mo(110) under certain ultrahigh vacuum conditions.

Specifically, oxidation of Mo(110) at ≈ 1200 K under about 1×10^{-9} Torr O_2 creates a thin-film oxide that stabilizes both types of coupled nitrosyl species, which allows for a direct comparison of the relative reactivities of these two coupling mechanisms.[31]

Dinitrosyl species on the thin-film oxide are identified by the same infrared experiment described above for the clean surface. The presence of another dimeric species is revealed by the same experiment,[31] as shown in Figure 7. Weak coupling of two nitrosyl groups gives rise to an 8 cm^{-1} splitting of each of the two different, isotopically mixed dimers. The geometry proposed for these species is weak N–N coupling of NO in a second, physisorbed layer to NO directly adsorbed on the surface through interactions similar to those in the condensed phase dimers. Such a picture is supported by an experiment in which the physisorbed species of an isotopically pure NO overlayer were desorbed from the surface and preferentially replaced with isotopically labeled ^{15}NO, to give rise solely to dimers with chemisorbed ^{14}NO and physisorbed ^{15}NO (Figure 7 b).

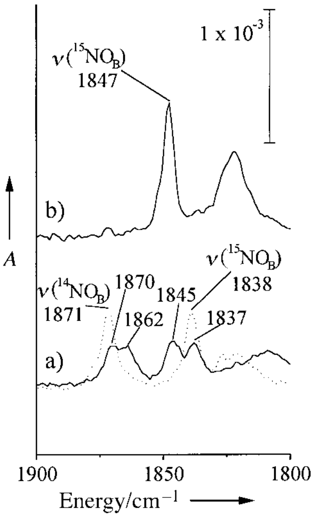

Figure 7. Infrared spectra of ν(NO) of weakly bound NO dimers on oxidized Mo(110). The solid trace in (a) corresponds to the spectrum of a 1/1 mixture of ^{14}NO/^{15}NO at 100 K; the dotted line represents the simple addition of the isotopically pure spectra to represent the uncoupled case. The spectrum in (b) was acquired after postadsorption of ^{15}NO at 100 K on a saturated overlayer of ^{14}NO that had been heated to 180 K to desorb the weakly bound species. Reprinted with permission from ref. [31].

In contrast to the chemistry observed for these dimers on Ag(111), where N_2O production is observed at low temperature,[24] the weak N–N bond on oxidized Mo(110) is cleaved to yield NO desorption below 150 K. This difference can be ascribed to the stronger Mo–NO bonding interaction relative to Ag–NO, which anchors one NO of the dimer pair to the metal surface, where it may undergo subsequent reactions. On this same oxidized Mo(110) surface, of course, dinitrosyl species, which are simultaneously present, persist to evolve N_2O and N_2. Therefore, on a metal surface capable of stronger metal–NO interactions, N–N bond formation is favored by metal-mediated bonding in a dinitrosyl over unmediated coupling of intact molecules.

3.2 The Role of Metal Atoms in Dinitrosyl Formation and Reactions

The above experiments demonstrate unequivocally that the specific choice of transition metal has profound implications for the viability of molecular routes to NO reduction. Electronic structure calculations have the unique potential to lend insight into these bonding mechanisms that lead to N–N bond formation and NO reduction. Advances in electronic structure theory and in computational power have now made it possible to study systems of this level of complexity using full, band-structure calculations coupled with a frontier orbital analysis of the bonding.

In our work, we have applied density functional theory to the investigation of monomeric NO and dinitrosyl bound to a MoO_3(010) slab containing a (2×2) array of vacancies at terminal oxygen positions.[32] When dinitrosyl species are adsorbed on the Mo centers, which are in turn exposed by creating the terminal oxygen vacancies, electron density is donated from the Mo d orbitals (primarily the d_{z^2}) to the π^* orbitals of the dinitrosyl moiety. This interaction contributes to the binding to the surface and facilitates the necessary N–O dissociation. In addition, the Mo center mediates a bonding interaction between the N(2p) orbitals of the individual NO molecules in the dinitrosyl; that is, there is N–N coupling in the dinitrosyl group itself.

The density functional calculations also show that the degree of electron donation to the π^* orbitals of NO is higher for a single NO bound to the Mo site at the vacancy, which would indicate that dissociation would be more facile than for the dinitrosyl species. Furthermore, the binding energies of the NO and $(NO)_2$ also indicate that the dinitrosyl will only form by adding gaseous NO to bound NO on the surface. The formation of dinitrosyl from two equilibrated, adsorbed NO molecules is energetically unfavorable by 3.52 eV; the reaction of an adsorbed mononitrosyl with an incoming gas-phase NO molecule is energetically *favorable* by 0.24 eV. This conclusion agrees remarkably well with our experimental results, which show that surface-bound mononitrosyl on a oxygen-modified Mo(110) surface react with incoming NO to convert to dinitrosyl species.[33]

4. Reaction of Methyl Radicals with Adsorbed NO

Methane potentially offers a more effective route for NO reduction. We therefore made use of our detailed understanding of NO chemistry and methyl radical reactions on oxidized Mo(110) to investigate the reduction of adsorbed NO by alkyl species. Since the active species are thought to be gas-phase methyl radicals ($^{\bullet}CH_3$), our studies focus on the elementary step of $^{\bullet}CH_3$ reaction with adsorbed NO on a range of oxidized Mo(110) surfaces.

Our previous studies of $^{\bullet}CH_3$ reaction with oxidized Mo(110) were important in understanding the reactions of methyl radicals with NO. In previous work, we demonstrated that methyl radicals preferentially react with oxygen in high coordination (namely quasi-threefold) sites on Mo(110).[19] These studies were possible because of our ability to selectively populate different types of coordination sites by controlled oxidation of Mo(110), as determined using EELS.[34]

Evidence of methyl addition to oxygen in high coordination sites is obtained from infrared experiments, which consisted of observing the spectrum characteristics of methoxy groups. The same spectrum is obtained following exposure of $^{\bullet}CH_3$ to oxygen in quasi-threefold sites. Importantly, only oxygen in the threefold sites reacted with $^{\bullet}CH_3$. We found no evidence for addition to Mo=O or oxygen in twofold coordination sites, which indicates a kinetic preference for reaction with the oxygen in threefold sites.[19]

In our more recent studies, we found that $^{\bullet}CH_3$ reacts preferentially with *molecular* NO on oxidized Mo(110) at low surface temperatures (100 K).[35] The fact that the methyl radical abstracts oxygen from NO is demonstrated in experiments where gaseous $^{\bullet}CH_3$ is dosed onto a surface containing ^{18}O bound in high coordination sites and $N^{16}O$, present as both mono- and dinitrosyl species. The appearance of a $\tilde{\nu}(^{16}O\text{-}CH_3)$ peak at 1005 cm^{-1} in the infrared spectrum is evidence for reaction with the $N^{16}O$ (Figure 8). There is also a $\tilde{\nu}(^{18}O\text{-}CH_3)$ peak at 935 cm^{-1} due to the reaction of methyl radicals with $^{18}O_a$ surface oxygen, detected after dosing with methyl radicals (Figure 8). Notably, the intensity of the peak derived from the reaction with NO is about three times greater than the peak signifying reaction with surface-bound oxygen. Furthermore, there is a loss of nitrogen-containing species from the surface during methyl radical dosing. Specifically, the amount of NO desorption from the surface measured in temperature-programmed desorption experiments is reduced to 40% of that for a pure NO layer on the same surface by the exposure to methyl radicals. In addition, there is less NO dissociation after radical dosing. These data suggest that there is low temperature coupling, which leads to the evolution of gaseous reduction products (specificially N_2 and/or N_2O). We are in the process of performing isothermal experiments that will enable us to detect gas-phase species produced during dosing.

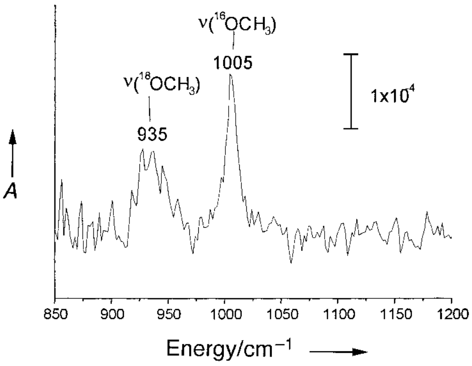

Figure 8. *Infrared spectrum obtained after reaction of methyl radicals with a saturation coverage of $N^{16}O$ on an ^{18}O-labelled surface Mo(110) surface ($^{18}\theta_0 =$ 0.75 ML) at 100 K. The $\tilde{\nu}(^{16}O\text{-}CH_3)$ peak indicates that there is direct reaction with molecular $N^{16}O$ since there is no dissociation under these conditions.*

The results of our studies of methyl reactions with NO indicate that there is a molecular pathway for this process. Accordingly, we are now investigating the reactions of several possible intermediates in the methyl-plus-NO reaction—CH_3ONO and CH_3NO_2—on oxidized Mo(110). Both of these molecules have been suggested as possible intermediates in this reaction on oxide catalysts.[6, 36, 37] By studying the microscopic pathways by which these molecules react, we will be able to gain insight into whether they are plausible intermediates in the reaction of methyl radicals with NO. Our experimental approach is similar to that taken in our previous work. By combining spectroscopic studies with reactivity measurements, we will develop an understanding of the elementary steps by which these possible intermediates react.

5. Conclusions

Our investigations of NO reduction on oxidized Mo(110) demonstrate that reactions through a dinitrosyl intermediate is a viable pathway. Furthermore, our work provides an example of how detailed mechanistic information is obtained in surface reactions by separating complex problems into elementary reaction steps on well defined materials. This methodology is particularly powerful for the study of fundamental structure–reactivity relationships, which includes issues of site specificity.

In comparing the results of such fundamental studies with the macroscopic trends observed in real catalytic systems, it is important to have experimental checkpoints to evaluate the strength of the correlation between real and model systems. For example, the exact correspondence between the infrared spectra of surface dinitrosyl species on Mo(110) in UHV and the same species on MoO_3 under catalytic conditions demonstrates that the model system, in this case, accurately represents adsorption of NO in the real system. This example also highlights one of the advantages of using infrared spectroscopy in UHV studies, since this technique is also used at higher pressures and therefore allows direct comparison across the pressure gap.

This same example, however, points out the need for using these checkpoints to recognize where the model system diverges from the real one. In the case of NO reduction through dinitrosyl species on Mo(110), the deposition of surface oxygen and nitrogen ultimately limits N–N bond formation on the single crystal surface. This poisoning effect may not be as significant a factor in the real catalyst, where higher operating temperatures and a constant stream of feed gases may remove such poisons from the surface of the catalyst during the course of the reaction. Nevertheless, the self-inhibition of NO dissociation illustrates the importance of oxygen vacancies in the NO reduction process.

Although the model systems employed in these studies are chosen for their simplicity relative to mixed, supported catalysts, it is apparent that even these "simple" systems are often governed by a complex set of interactions. While careful experimental design often allows us to separate the effects of these interactions, it is clear that coupling these experimental studies with state-of-the-art electronic structure calculations vastly improves our understanding of the chemical and physical principles behind the observed chemistry.

We gratefully acknowledge the support of this work by the U.S. Department of Energy, Basic Energy Sciences under grant no. DE-FG02-84-ER13289. We also thank Dr. Joshua Levinson for his careful proof reading of the manuscript and assistance with preparing the final figures.

[1] T. Yamashita, A. Vannice, *J. Catal.* **1996**, *163*, 158.
[2] M. A. Vannice, A. B. Walters, X. Zhang, *J. Catal.* **1996**, *159*, 119.
[3] T. Yamashita, A. Vannice, *Appl. Catal. B* **1997**, *13*, 141.
[4] X. Zhang, A. B. Walters, M. A. Vannice, *J. Catal.* **1994**, *146*, 568.
[5] X. Zhang, A. B. Walters, M. A. Vannice, *J. Catal.* **1995**, *155*, 290.
[6] V. I. Parvulescu, P. Grange, B. Delmon, *Catal. Today* **1998**, *46*, 233.
[7] M. Shelef, G. W. Graham, *Catal. Rev. Sci. Eng.* **1994**, *36*, 433.
[8] W. C. Hecker, M. D. Wardinsky, P. G. Clemmer, P. B. Rasband in *Progress in Catalysis* (Eds.: K. J. Smith, E. C. Sanford), Elsevier, Amsterdam, **1992**, p. 211.
[9] H. C. Yao, W. G. Rothschild, H. S. Gandhi, *Stud. Surf. Sci. Catal. Catal.* **1984**, *19*, 71.
[10] I. Halasz, A. Brenner, M. Shelef, *Catal. Lett.* **1992**, *16*, 311.
[11] I. Halasz, A. Brenner, M. Shelef, *Catal. Lett.* **1993**, *18*, 289.
[12] I. Halasz, A. Brenner, M. Shelef, *Catal. Lett.* **1993**, *22*, 147.
[13] W. S. Millman, W. K. Hall, *J. Phys. Chem.* **1979**, *83*, 427.
[14] A. Kazusaka, R. F. Howe, *J. Catal.* **1980**, *63*, 447.
[15] "Surface Interaction in the MoO_3/γ-Al_2O_3 System. II. Effect of Surface Structure on NO Chemisorption": H. C. Yao, W. G. Rothschild, *4th Int. Conf. on the Chemistry and Uses of Molybdenum*, Climax Molybdenum Co., Ann Arbor, MI, **1982**, p. 31.
[16] T. E. Hoost, G. W. Graham, M. Shelef, O. Alexeev, B. C. Gates, *Catal. Lett.* **1996**, *38*, 57.
[17] H.-J. Freund, *Angew. Chem.* **1997**, *109*, 444; *Angew. Chem. Int. Ed. Engl.* **1997**, *36*, 452.
[18] D. W. Goodman, *J. Phys. Chem.* **1996**, *100*, 13090.
[19] K. T. Queeney, C. M. Friend, *J. Chem. Phys.* **1999**, *104*, 409.
[20] S. W. Jorgensen, N. D. S. Canning, R. J. Madix, *Surf. Sci.* **1987**, *179*, 322.
[21] J. S. Villarubia, W. Ho, *J. Chem. Phys.* **1987**, *87*, 750.
[22] K. T. Queeney, C. M. Friend, *J. Chem. Phys.* **1997**, *107*, 6432.
[23] K. T. Queeney, C. M. Friend, *J. Phys. Chem. B* **1998**, *102*, 9251.
[24] W. A. Brown, P. Gardner, D. A. King, *J. Phys. Chem.* **1995**, *99*, 7065.
[25] W. A. Brown, P. Gardner, M. P. Jigato, D. A. King, *J. Chem. Phys.* **1995**, *102*, 7277.
[26] P. Dumas, M. Suhren, Y. J. Chabal, C. J. Hirschmugl, G. P. Williams, *Surf. Sci.* **1997**, *371*, 200.
[27] K. T. Queeney, C. M. Friend, *J. Chem. Phys.* **1998**, *109*, 6067.
[28] M. K. Weldon, P. Uvdal, C. M. Friend, J. G. Serafin, *J. Chem. Phys.* **1995**, *103*, 5075.
[29] F. P. Nart, C. M. Friend, unpublished results.
[30] J. G. Chen, W. Erley, H. Ibach, *Surf. Sci.* **1989**, *224*, 215.
[31] K. T. Queeney, S. Pang, C. M. Friend, *J. Chem. Phys.* **1998**, *109*, 8058.
[32] M. Chen, C. M. Friend, E. Kaxiras, unpublished results.
[33] K. T. Queeney, C. M. Friend, *Surf. Sci.* **1998**, *414*, L957.
[34] M. L. Colaianni, J. G. Chen, W. H. Weinberg, J. T. Yates, *Surf. Sci.* **1992**, *279*, 211.
[35] K. T. Queeney, F. P. Nart, C. M. Friend, unpublished results.
[36] Y. Li, T. L. Slager, J. N. Armor, *J. Catal.* **1994**, *150*, 388.
[37] D. B. Lukyanov, J. L. d'Itri, G. Sill, W. K. Hall, *Stud. Surf. Sci. Catal.* **1996**, *101*, 651.

Received: July 10, 2000 [A 64]

CHEMPHYSCHEM

An Experimental Charge Density Study of the Effect of the Noncentric Crystal Field on the Molecular Properties of Organic NLO Materials**

R. Srinivasa Gopalan,[a] Giridhar U. Kulkarni,[a] and C. N. R. Rao*[a]

The structure, packing, and charge distribution in molecules of nonlinear optical materials have been analysed with reference to their counterparts in centrosymmetric structures based on low temperature X-ray measurements. The systems studied are the centric and noncentric polymorphs of 5-nitrouracil as well as the diamino, dithio, and thioamino derivatives of 1,1-ethylenedicarbonitrile; the latter possesses a noncentric structure. The molecular structure of 5-nitrouracil is invariant between the two forms, while the crystal packing is considerably different, leading to dimeric N–H···O rings in the centric polymorph and linear chains in noncentric one. There is an additional C–H···O contact in the centric form with a significant overlap of the electrostatic potentials between the alkenyl hydrogen atom and an oxygen atom of the nitro group. The dipole moment of 5-nitrouracil in the noncentric form is much higher ($\mu = 9$ D) than in the centric form (≈ 6 D). Among the 1,1-ethylenedicarbonitriles, there is an increased charge separation in the noncentric thioamino derivative, leading to an enhanced dipole of 15 D compared to the centric diamino (5 D) and dithio (6 D) derivatives. The effect of the crystal field is borne out by semiempirical AM1 calculations on the two systems. Dipole moments calculated for the molecules in the frozen geometries match closely with those obtained for centric crystals from the experimental charge densities. The calculated values of the dipole moment in the frozen or optimized geometries in the noncentric structures are, however, considerably lower than the observed value. Furthermore, the conformation of the S–CH_3 group in the noncentric crystal is anti *with respect to the central C=C bond while the* syn *conformation is predicted for the free molecule in the optimized geometry.*

KEYWORDS:

charge density · dipole moment · materials science · nonlinear optics · semiempirical calculations

Several organic materials with nonlinear optical (NLO) properties have been described in the recent literature.[1–5] Nitroaniline and push–pull ethylenes are typical examples of NLO materials involving intramolecular charge transfer. Besides having a polarizable π-cloud with electron-donating and -accepting groups, an essential feature of such compounds is that they crystallize in noncentrosymmetric space groups. Espinosa et al.[6] have reported a charge density study of L-arginine phosphate. Puig-Molina et al.[7] have compared the topological properties of charge density of 2-amino-5-nitropyridinium dihydrogen phosphate from experiment and theory. Charge density studies of 2-methyl-4-nitroaniline[8] and urea[9] show that there is a considerable enhancement of the molecular dipole moment in the solid state. Based on a charge density study on *N*-(4-nitrophenyl)-L-prolinol, Fkyerat et al.[10, 11] extracted hyperpolarizability from the octapole moments. Such a possibility has been discussed in connection with inorganic NLO materials as well.[12, 13] While there is some speculation as to whether charge densities can provide hyperpolarizability,[14] it is generally accepted that reliable molecular dipole moments can be extracted from charge densities.[15] Thus, Hamazaoui et al.[16] obtained the dipole moment of 3-methyl-4-nitropyridine-*N*-oxide from its charge density, which agrees well with that from semiempirical calculations. Recently, Madsen et al.[17] have evaluated the dipole moment of phosphangulene from its charge density to be 42% higher than that measured in a chloroform solution. They also obtained the pyroelectric coefficient by combining the derived dipole moment with temperature-dependent measurements of the unit cell volume.

We have carried out an experimental charge density investigation of organic NLO systems in order to understand the manner in which the noncentric nature of the crystal field affects the molecular dipole moment and other properties in the solid. For this purpose, we have examined two systems—one where the center of symmetry is destroyed by crystallizing the molecule in a related polymorphic structure and the other where the noncentric nature is introduced by changing the pattern of substitution. For the first system, we have chosen the two polymorphic forms of 5-nitrouracil, **1**, which crystallizes in orthorhombic $P2_12_12_1$ and *Pbca* space groups, the former being noncentrosymmetric. The NLO activity of the noncentric form at 1.06 μm is ~160 times that of potassium dihydrogen phos-

---

[a] Prof. Dr. C. N. R. Rao, R. S. Gopalan, Dr. G. U. Kulkarni
Chemistry and Physics of Materials Unit
Jawaharlal Nehru Centre for Advanced Scientific Research
Jakkur P.O., Bangalore, 560064 (India)
E-mail: cnrrao@jncasr.ac.in

[**] The authors thank Dr. S. N. Ghanshyam Acharya for the synthesis of dicarbonitrile derivatives **2–4**.

phate.[18] In order to explore the effect of substitution, we have studied 1,1-ethylenedicarbonitriles (EDCN), in which the positions of the dimethylamino and methylthio substituents have been varied to give the symmetric and unsymmetric molecules bis(*N*,*N*-dimethylamino)-EDCN (**2**), 2,2-bis(methylthio)-EDCN (**3**), and 2-(*N*,*N*-dimethylamino)-2-methylthio-EDCN (**4**). The diamino and the dithio derivatives, **2** and **3**, crystallize in centric structures whereas the thioamino, **4**, occurs in a noncentrosymmetric structure exhibiting NLO properties. In both the systems, we have examined the intramolecular bonding using the Laplacian of the total electron density. Where necessary, we have analyzed the intermolecular interactions in terms of the electrostatic potential. We have computed the dipole moments from the experimental charge densities and compared the results with those from semiempirical AM1 calculations.

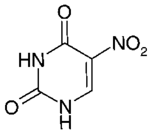

1

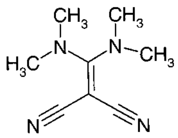

2

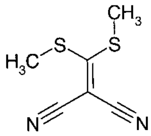

3

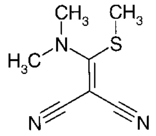

4

Editorial Advisory Board Member:* **C. N. R. Rao** received his M.Sc. in Chemistry from Banaras Hindu University (1953), Ph.D. in Chemistry from Purdue University (1958), and D.Sc. from the University of Mysore (1961). Following postdoctoral study in Berkeley, he worked as a faculty member at the Indian Institute of Technology, Kanpur, and the Indian Institute of Science, Bangalore. His main research interests are in the chemistry of materials and chemical spectroscopy. He is at present the Linus Pauling Research Professor at the JNCASR. He has been a Visiting Professor at the Universities of Cardiff, Cambridge, and California at Santa Barbara. He is a member of the Royal Society, US National Academy of Sciences, Pontifical Academy of Sciences, French Academy of Sciences, Japan Academy, and several others. He is a recipient of the Marlow Medal of the Faraday Society, Einstein Medal of UNESCO, Centenary Medal of the Royal Society of Chemistry, and the Hughes Medal of the Royal Society.

5-Nitrouracil

The centric polymorph of **1** crystallizes with eight molecules per unit cell (*Pbca*; $a = 8.308(3)$, $b = 10.426(3)$, $c = 13.363(4)$ Å) while the unit cell of the noncentric form contains four molecules ($P2_12_12_1$; $a = 5.4342(1)$, $b = 9.8406(1)$, $c = 10.3659(1)$ Å). The densities of both forms are similar (Table 1). The space groups *Pbca* and $P2_12_12_1$ contain the same set of symmetry elements but for the inversion center, which makes the problem interesting. In both polymorphs, the asymmetric unit comprises a whole molecule. The intramolecular geometry is essentially the same in both cases and the molecule is nearly planar (Table 2): The nitro group forms an angle of 1.5° with the plane of the uracil ring in the centric form and 2.0° in the noncentric polymorph.

In Figure 1, the packing diagram along with the atom labels are shown. In the centric form, the molecule is held by the dimeric N–H···O contacts of $R_2^2(8)$ type[19] with the two neighboring coplanar molecules (Figure 1 a). The N–H···O contacts in the noncentric form are of D(2) type arising from four different molecules (Figure 1 b). In both the cases, the N–H···O bonds are ~1.8 Å long, with $\sphericalangle$N–H···O angles of 155–174°. The centric polymorph, in addition, exhibits an intermolecular C–H···O interaction with the nitro group at a relatively short distance of 2.15 Å. The nitro group of the noncentric polymorph is in an unfavorable geometry to establish such a contact (Figure 1 b).

The results of the multipolar refinement (see Experimental Section) are described using the Laplacian of the total charge density. The topology of the Laplacian field allows one to obtain a chemical model of the bonded and nonbonded pairs and to characterize the local concentration ($\nabla^2\rho < 0$) and depletion ($\nabla^2\rho > 0$) of the molecular charge distribution.[20, 21] Figure 2 shows the contour maps of the negative Laplacian obtained for the two polymorphs. The lone electron pairs on the oxygen

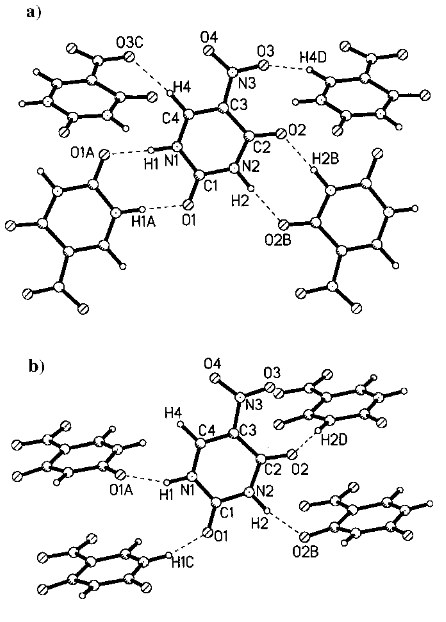

*Figure 1. Molecular packing in a) centric and b) noncentric **1** showing the intermolecular hydrogen bonds. Atom labels are also shown.*

---

[*] *Members of the Editorial Advisory Board will be introduced to the readers with their first manuscript.*

Table 1. *Crystal data for 5-nitrouracil (**1**) and the 1,1-ethylenedicarbonitriles (**2**–**4**).*[a]

Crystal	1		2	3	4
	centric	noncentric			
Chemical formula (g mol^{-1})	$C_4H_3N_3O_4$ (157.09)		$C_8H_{12}N_4$ (164.22)	$C_6H_6N_2S_2$ (170.25)	$C_7H_9N_3S$ (167.23)
Crystal system	orthorhombic	orthorhombic	orthorhombic	monoclinic	orthorhombic
Space group	*Pbca* (No. 61)	$P2_12_12_1$ (No. 19)	*Pcab* (No. 6)	$P2_1/n$ (No. 14)	$Pna2_1$ (No. 33)
a [Å]	8.308(3)	5.4342(1)	7.6280(1)	4.0261(1)	7.904(2)
b [Å]	10.426(3)	9.8406(1)	14.455	13.227	8.630(2)
c [Å]	13.363(4)	10.3659(1)	16.3489(2)	14.3906(1)	12.856(3)
β [°]	90	90	90	95.445(1)	90
V [cm^3]	1157.5(6)	554.32(1)	1802.70(3)	762.89(2)	876.9(3)
Z	8	4	8	4	4
F_{000}	640	320	704	352	352
ρ [g cm^{-3}]	1.803	1.882	1.210	1.482	1.267
No. of reflections for cell parameters	45	37	60	60	60
μ [mm^{-1}]	0.16	0.17	0.079	0.617	0.309
Crystal form	cuboidal	hexagonal	cuboidal	cuboidal	cuboidal
Crystal size [mm]	0.3 × 0.2 × 0.2	0.15 × 0.15 × 0.1	0.2 × 0.1 × 0.1	0.2 × 0.15 × 0.1	0.2 × 0.1 × 0.1
Crystal color	colorless	colorless	colorless	yellow	colorless
No. of measured reflections	16262	16515	29153	12914	24387
No. of independent reflections	5026	8371	8589	6451	8576
No. of observed reflections	3879	3239	4894	4863	2874
R_{merge}	0.0644	0.0434			
R_{int}	0.0763	0.0454	0.0361	0.0301	0.0692
θ_{min} [°]	3.0	2.8	2.49	2.10	2.84
θ_{max} [°]	49.4	49.4	49.48	49.47	49.89
Range of *h*, *k*, *l*	$-12 \leq h \leq 16$ $-22 \leq k \leq 11$ $-28 \leq l \leq 27$	$-10 \leq h \leq 11$ $-19 \leq k \leq 20$ $-21 \leq l \leq 21$	$-15 \leq h \leq 15$ $-15 \leq k \leq 30$ $-34 \leq l \leq 34$	$-8 \leq h \leq 7$ $-21 \leq k \leq 27$ $-29 \leq l \leq 28$	$-16 \leq h \leq 15$ $-18 \leq k \leq 18$ $-27 \leq l \leq 27$
After multipole refinement					
Weighting scheme	0.02, 0.3	0.02, 0.1	0.05, 0.5	0.03, 0.3	0.04, 0.3
*R*1	0.0345	0.0391	0.0501	0.0397	0.0332
*wR*2	0.0416	0.0454	0.0775	0.0475	0.0513
S	1.05	1.00	0.94	1.06	1.27
No. of variables	399	404	161	178	197
N_{ref}/N_v	20.5	17.2	30.4	27.3	14.6
Cambridge Crystallographic Database	145990	145991	145987	145988	145989

[a] Experimental details: Siemens CCD diffractometer, crystal–detector distance 5.0 cm, $Mo_{K\alpha}$ radiation ($\lambda = 0.71073$ Å, 50 kV, 40 mA), 130 ± 1 K

atoms occur as (3, −3) critical points. There are some differences in the Laplacian maps of the two polymorphs. The atomic basins are generally linked in the centrosymmetric form but they appear to be disjoint in the noncentric case. The N3–O3 bond region in the centrosymmetric form contains nonoverlapping atomic lobes, which indicate a closed shell interaction. This is reflected in the properties of the bond critical points, listed in Table 3. This bond carries a much smaller Laplacian (-3.0 e Å^{-5}) compared to the other N–O bond of the molecule as well as the N–O bonds of the noncentric form, though the electron density itself is quite comparable. We also notice from Table 3 that the densities and the associated Laplacians of the non-hydrogen bonds are somewhat higher in the noncentric form while those of the N–H bonds are higher in the centric form. Moreover, the pseudo-atomic charges are generally higher in the noncentric polymorph. This implies that there is an increased charge separation in the noncentric case. The nitro group charge is -0.19 and -0.38 e respectively, in the centric and the noncentric forms, which compare well with -0.25 e obtained for 3-methyl-4-nitropyridine-*N*-oxide.[16] We also observe that the properties of the various bonds of the uracil moiety match closely with those reported in the case of 1-methyluracil.[22]

The nature of the intermolecular bonding is described in terms of the electrostatic potential. In Figure 3, contour maps of the electrostatic potential maps in the N–H⋯O and the C–H⋯O bond regions are shown. The contours originating from the N–H region overlap with those from the oxygen atom (Figures 3 a, b). The penetration is significant and indicates that these are strong contacts.[23] They are associated with (3, −1) critical points in ρ as well as in electrostatic potential. The Laplacian at the CPs are small and positive (Table 4), as generally found in hydrogen bonds.[24] The C–H⋯O contact of the centric form also exhibits a noticeable overlap of the potentials ($\rho = 0.08(2)$ e Å^{-3}, $V = 0.28(1)$ e Å^{-1}), while in the noncentric form a zero potential surface passes between the proton and the oxygen atom to indicate no interaction between them (Figure 3 c). This is understandable, since in the presence of a carbonyl group, a nitro group acts as a secondary hydrogen bond acceptor.[25] The C–H⋯O contact of the centric form is special in that the oxygen O3, which participates in intermolecular bonding, tends to have nearly ionic interaction with the nitro group (Figure 2). Such bonding would be favored by the centrosymmetric packing of the molecules. For the same reason, this contact is absent in the noncentric form.

Table 2. *Bond lengths and angles of **1**.*

Bond length [Å]	centric **1**	noncentric **1**
O1-C1	1.2284(13)	1.2310(13)
O2-C2	1.2252(13)	1.2290(12)
O4-N3	1.2364(12)	1.235(2)
O3-N3	1.2294(12)	1.2306(14)
N2-C1	1.3667(13)	1.3663(12)
N2-C2	1.3945(13)	1.3900(14)
N2-H2	1.01	1.01
N1-C4	1.3427(14)	1.341(2)
N1-C1	1.3807(13)	1.3786(14)
N1-H1	1.01	1.01
N3-C3	1.4432(13)	1.4412(14)
C2-C3	1.4568(14)	1.454(2)
C3-C4	1.3575(14)	1.3621(14)
C4-H4	1.08	1.08
Bond angle [°]	**centric 1**	**noncentric 1**
C1-N2-C2	127.18(9)	127.47(9)
C1-N2-H2	116.41(6)	116.27(6)
C2-N2-H2	116.41(6)	116.27(6)
C4-N1-C1	122.51(9)	122.90(8)
C4-N1-H1	118.74(6)	118.55(6)
C1-N1-H1	118.74(6)	118.55(5)
O3-N3-O4	123.09(9)	123.46(11)
O3-N3-C3	119.36(9)	119.20(11)
O4-N3-C3	117.56(9)	117.33(10)
O1-C1-N2	123.08(9)	122.60(10)
O1-C1-N1	121.61(9)	122.54(9)
N2-C1-N1	115.31(9)	114.85(9)
O2-C2-N2	119.86(9)	118.82(10)
O2-C2-C3	127.55(10)	128.32(10)
N2-C2-C3	112.59(8)	112.85(8)
C4-C3-N3	116.49(9)	116.94(10)
C4-C3-C2	120.79(9)	120.32(10)
N3-C3-C2	122.62(8)	122.73(9)
N1-C4-C3	121.39(9)	121.40(10)
N1-C4-H4	119.30(6)	119.30(6)
C3-C4-H4	119.30(6)	119.30(7)

In situ dipole moments of molecules in crystals can be obtained from charge densities by using Equation (1).

$$\boldsymbol{p}_i = \sum_i z_i \boldsymbol{R}_i + \int \boldsymbol{r}\rho_i(\boldsymbol{r}_i)\,\mathrm{d}\boldsymbol{r} \qquad (1)$$

The XDPROP routine (the XD program) was used to calculate dipole moments and the dipole moment vectors are shown in Figure 4. The vectors lie close to the N(1)–H(1) bond direction in the plane of the molecule, with magnitudes of $\mu = 5.5(6)$ and 9(1) D in the centric and the noncentric polymorphs, respectively.[26] As the intramolecular geometry remains the same in the two cases (Table 2), the enhancement of the dipole moment in the noncentric structure is likely to arise mainly due to packing. The effect of crystal packing can be understood by calculating the dipole moment of the molecule ex situ in the frozen geometry. For this purpose, we carried out AM1, PRECISE calculations by freezing the molecular geometries obtained from X-ray diffraction. The calculated dipole moments are very similar in the two polymorphs ($\mu = 5.5$ and 5.6 D for centric and noncentric cases, respectively) and point in the same direction (Figure 4). Interestingly, the vectors obtained from the calculation lie close (in magnitude as well as in direction) to that from

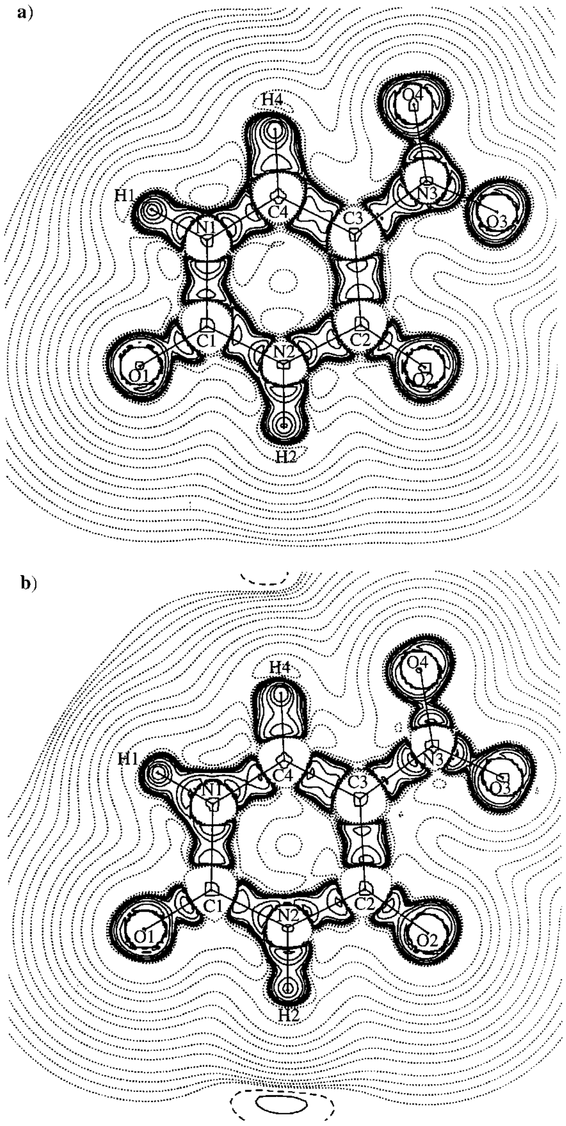

Figure 2. *Contour maps of the total density Laplacian in the C1-C2-C4 plane for a) centric and b) noncentric **1**.*

Table 3. *Analysis of the bond critical points in **1**.*

	centric			noncentric		
Bond	ρ[a]	$\nabla^2\rho$[b]	ε[c]	ρ[a]	$\nabla^2\rho$[b]	ε[c]
O1-C1	2.91(5)	– 38.2(3)	0.21	3.31(9)	– 51.9(5)	0.27
O2-C2	2.77(6)	– 26.8(4)	0.18	3.21(97)	– 51.3(4)	0.17
N1-C1	2.16(5)	– 26.8(2)	0.06	2.36(8)	– 27.9(3)	0.29
N1-C4	2.29(5)	– 27.3(2)	0.25	2.50(9)	– 31.5(4)	0.28
N1-H1	1.98(6)	– 28.8(4)	0.06	1.9(1)	– 30.1(8)	0.00
N2-C1	2.12(4)	– 23.9(2)	0.21	2.34(8)	– 30.1(3)	0.38
N2-C2	2.09(4)	– 23.5(2)	0.12	2.22(7)	– 23.7(3)	0.24
N2-H2	1.92(6)	– 29.8(4)	0.04	1.8(1)	– 36(1)	0.04
N3-C3	1.87(4)	– 15.4(2)	0.37	1.96(8)	– 17.1(4)	0.39
C2-C3	1.93(3)	– 16.0(1)	0.27	1.98(7)	– 7.0(2)	0.46
C3-C4	2.21(3)	– 22.1(1)	0.34	2.31(7)	– 24.7(2)	0.43
C4-H4	1.79(5)	– 20.1(2)	0.05	1.9(1)	– 29.5(7)	0.07
O3-N3	3.19(5)	– 3.0(2)	0.09	3.48(9)	– 14.5(3)	0.05
O4-N3	3.28(5)	– 11.9(2)	0.08	3.61(9)	– 18.6(4)	0.08

[a] electron density, in e Å^{-3}. [b] Laplacian, in e Å^{-5}. [c] Ellipticity.

Table 4. *Hydrogen bond critical points in* **1**.

Polymorph	D-H ··· A	ρ [e Å^{-3}]	$\nabla^2\rho$ [e Å^{-5}]	V [e Å^{-1}]
centric	N(1)-H(1) ··· O(1)[a]	0.18(3)	3.32(2)	0.55(2)
	N(2)-H(2) ··· O(2)[a]	0.17(3)	2.88(2)	0.47(2)
	C(4)-H(4) ··· O(3)[b]	0.08(2)	1.39(1)	0.28(1)
noncentric	N(1)-H(1) ··· O(1)[c]	0.16(5)	2.99(4)	0.52(3)
	N(2)-H(2) ··· O(2)[d]	0.15(6)	3.05(5)	0.61(4)
	O(1) ··· H(1)-N(1)[e]	0.14(5)	2.64(5)	0.53(3)
	O(2) ··· H(2)-N(2)[f]	0.13(5)	2.69(5)	0.60(3)

Symmetries: [a] $-x, -y, 1-z$. [b] $\frac{1}{2}-x, \frac{1}{2}+y, z$. [c] $\frac{1}{2}+x, \frac{1}{2}-y, 1-z$. [d] $-\frac{1}{2}+x, \frac{1}{2}-y, -z$; [e] $-\frac{1}{2}+x, \frac{1}{2}-y, 1-z$. [f] $\frac{1}{2}+x, \frac{1}{2}-y, -z$.

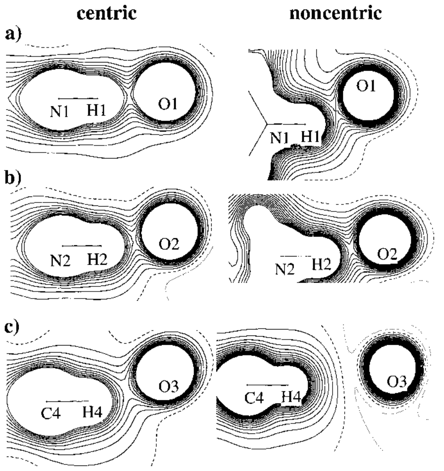

Figure 3. *Contour maps of the electrostatic potential in the intermolecular regions (contour level at 0.05 e Å^{-1}): a) N1–H1 ··· O1, b) N2–H2 ··· O2, c) C4–H4 ··· O3. The centric and noncentric forms are given on the left and right sides, respectively.*

experiment for the centric polymorph. This seems to suggest that the packing in the centric form of **1** has a minimal effect on the intramolecular charge distribution. This observation also

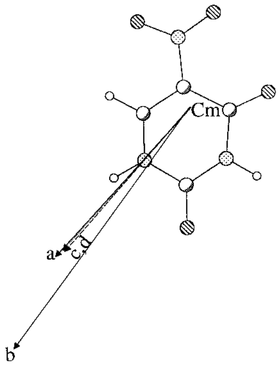

Figure 4. *Orientation of the molecular dipole moment of* **1**: *a) centric, multipole; b) noncentric, multipole; c) centric, AM1; d) noncentric, AM1. Cm refers to the center of mass of the molecule.*

demonstrates that an asymmetric crystal field in a noncentric structure can significantly enhance the dipole moment of a molecule. To our knowledge, this is the first instance of charge density study of a compound crystallizing in closely related space groups exhibiting differing molecular properties.

1,1-Ethylenedicarbonitriles

The two nitriles, **2** and **3**, crystallize in the centrosymmetric *Pcab* and $P2_1/n$ space groups, respectively, whereas **4** crystallizes in the noncentric $Pna2_1$ space group (Table 1). We show the molecular diagrams along with the thermal ellipsoids in Figure 5, where the bond lengths and angles associated with the non-hydrogen atoms are also indicated. Diamine **2** possesses a pseudo two-fold symmetry along C3–C4 while the dithio **3** exhibits a *syn–anti* methylthio conformation. Thioamine **4** has methylthio group in the *anti* conformation. The 1,1-ethylenedicarbonitrile moiety, which contains a formal C3=C4 bond and two single C1–C3 and C2–C3 bonds, along with the cyano group, is essentially planar in all three molecules. The C≡N bond lengths are also similar (1.14(3) Å) and close to those reported in the literature. There are however, some differences between the formal C–C single and double bonds. In **2**, the single and the

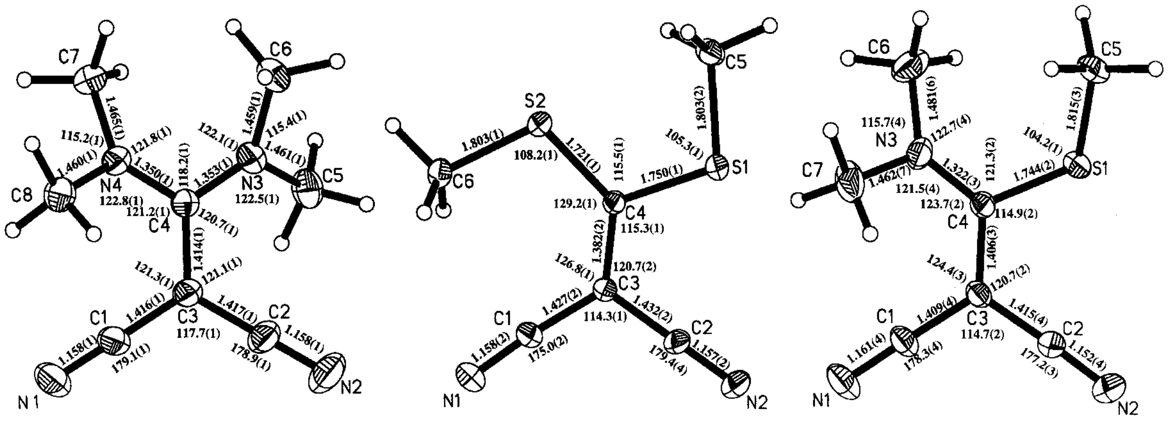

2 **3** **4**

Figure 5. *Molecular diagrams of the diamino* **2**, *dithio* **3**, *and thioamino* **4** *EDCN derivatives, showing thermal ellipsoids. The bond lengths and angles of the non-hydrogen bonds are shown.*

double bonds are of equal length (~1.416 Å), while they differ in **3** (1.432(2) and 1.427(2), versus 1.382(2) Å). In **4**, the differences are moderate (see Figure 5). A survey of formally uncharged molecules containing the ethylenedicarbonitrile moiety (466 compounds with $r < 10\%$) listed in the Cambridge Crystallographic Database have mean C–C and C=C bond lengths of 1.43(2) and 1.37(3) Å, respectively. The shortening of the C–C single bonds in this moiety is noteworthy. The C_{sp^2}–N (or C_{sp^2}–S) bonds are shorter than C_{sp^3}–N (or C_{sp^3}–S). In **3**, there exist considerable differences between the bond lengths and the angles associated with the *syn* and *anti* conformations of the methylthio groups. The C–C≡N bond angle associated with the *syn*-methythio group is 175° instead of ~180°. An earlier structural report on this molecule suggested steric interaction to be responsible for the discrepancy.[27] However, 3,3-bis(methylthio)-2-nitro-2-propene-1-nitrile does not show significant differences in the bond lengths and angles between the *syn*- and the *anti*-configurations of the methylthio groups.[28]

Figure 6 shows the contour maps of the negative Laplacian of the total density in the plane defined by the N1-N2-C3 atoms. The lone pairs on the nitrogen and sulfur atoms exhibit (3, −3) as critical points. The lobes near sulfur are similar to those seen previously by Mallinson and co-workers in the case of 3,3,6,6-tetramethyl-*S*-tetrathiane.[29] In the diamine **2**, the contours associated with the amino groups are small, since this group is out of plane with the rest of the molecule. The C–S bonds of both **3** and **4** exhibit disjoint lobes.

Figure 7 depicts the critical points in the total density for the various bonds in the molecules. The values of total electron density, the Laplacian, and the ellipticity at the critical points are also shown. The C≡N group exhibits similar densities (~3.2 e Å^{-3}) in the three molecules although the Laplacian values are somewhat different, −36, −20, and −16 e Å^{-5} in **1**, **2**, and **3**, respectively. Interestingly, the densities of the C–C single and double bonds are not significantly different in the three compounds. The Laplacian values are also similar, the differences are less than ~5 e Å^{-5}. This result is in contrast with what is expected of normal single and double bonds. The electron densities associated with the isolated single and double bonds are generally 1.71 and 2.5 e Å^{-3} respectively.[30] In the present

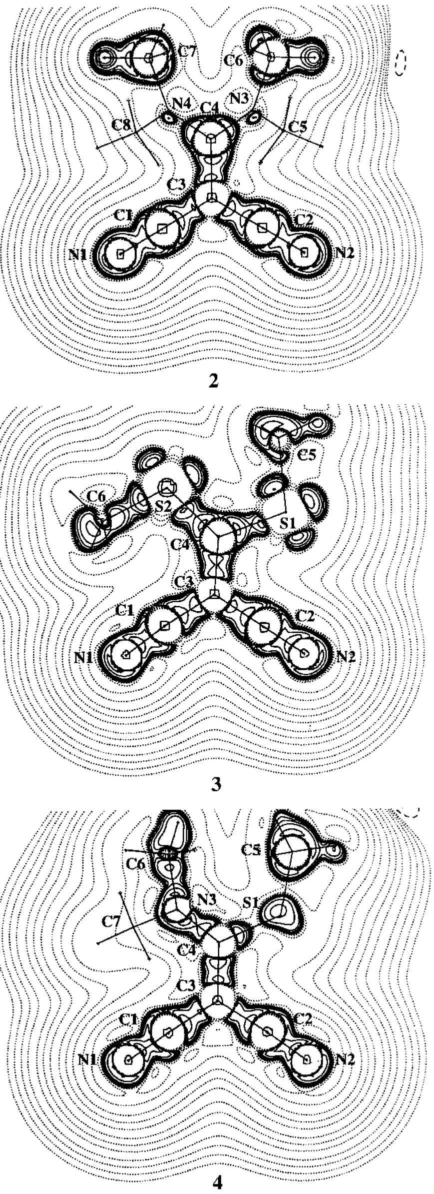

2

3

4

*Figure 6. Contour maps of the Laplacian of the total electron density of the diamino **2**, dithio **3**, and thioamino **4** EDCN derivatives in the N1-C3-C4 plane.*

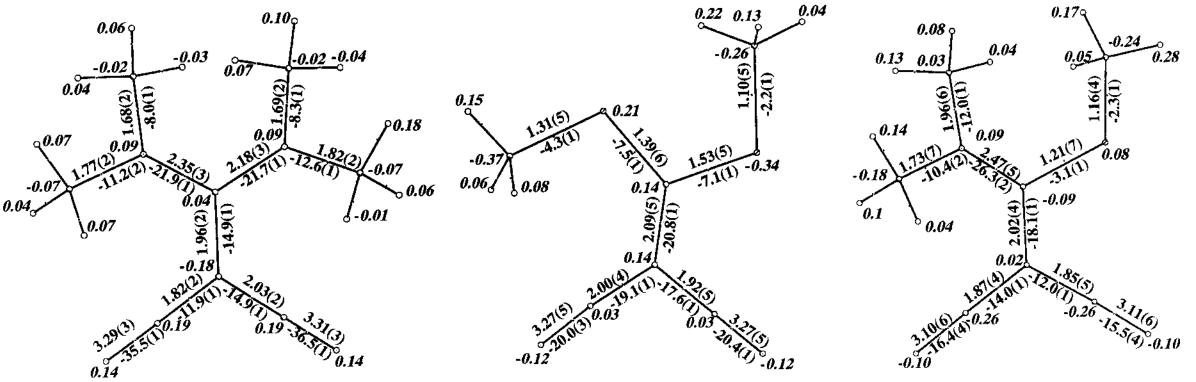

2 3 4

*Figure 7. Stick diagrams showing the critical points for the various bonds of the diamino **2**, dithio **3**, and thioamino **4** EDCN derivatives. The electron density and the Laplacians associated with each bond are shown nearby. The pseudo-atomic charges are also indicated in italics. The atoms are labeled as in Figure 5.*

case, there is probably some delocalization of electrons in the bonding region. A similar observation was made earlier by Espinosa et al.[31] in the case of the BTDMTTF-TCNQ complex. The low values of the densities and the Laplacians in the C—S bonds are characteristic of hypervalent species.[29] A recent study on tetrasulfurtetranitride[32] has reported low values of densities and Laplacians in the N—S bonds. The charge density analysis reflects the differences between the C_{sp^2} and C_{sp^3} bonding regions, as expected from the structural features discussed above. Accordingly, the C_{sp^2} bonding regions carry higher densities and Laplacians. Based on the pseudoatomic charges shown in Figure 7, there appears to be an increased charge separation in the noncentric thioamine **4**.

The intermolecular contacts of the structures **2**–**4** are listed in Table 5. Both **2** and (**3**) exhibit five C—H···N contacts while the thioamine (**4**) makes only three such contacts. These are typical C—H···N contacts in terms of both the geometry and the charge density. In addition, there are intermolecular S···S and S···N contacts in the dithio compound and S···N contacts in the thioamine (Table 5). The distances as well as the charge densities associated with these contacts are similar to the contacts found in other molecules.[29, 32]

The in situ dipole moments of the molecules in the three crystals are projected in Figure 8. The dipole moment vectors lie close to the mean planes of the molecules. An important observation from Figure 8 is that the dipole moment of the thioamine **4**, in the noncentric structure, is much higher ($\mu = 15(2)$ D) than the values of the diamino (**2**) and the dithio (**3**) derivatives in the centric structures ($\mu = 5(2)$ and 6(2) D).[26] The enhancement of the dipole moment in the thioamine could arise from the asymmetric substitution of the electron donating groups or due to the noncentric crystal field. In order to shed more light, we have computed dipole moments of the three molecules in the free state in both the frozen and the optimized (AM1, PRECISE) geometries using MOPAC. In Figure 9, we depict the frozen and the optimized dipole moments projected along with the molecule. The calculated dipole moment remains essentially unchanged between the frozen and the optimized geometries in the case of **2** and **3**. Compared to the in-crystal dipole moment, these values are slightly higher in the diamino and are comparable in the case of the dithio compound (see Figures 8 and 9). The noncentric thioamine **4**, on the other hand, exhibits much smaller dipole moments outside the lattice. Both the optimized ($\mu = 5.9$ D) and the frozen ($\mu = 8.1$ D) moments are considerably lower than the in-crystal dipole moment of $\mu = 15$ D. It is interesting that in the optimized geometry, the

Table 5. Intermolecular contacts in **2**–**4**.

Hydrogen contacts between donor (D) and acceptor (A)

D—H···A	H···A [Å]	D···A [Å]	∢D-H···A [°]	ρ [e Å^{-3}]	$\nabla^2\rho$ [e Å^{-5}]
2					
C5-H5A···N1[a]	2.745	3.531	130.9	0.061(3)	0.601(2)
C7-H7A···N1[b]	2.510	3.467	149.6	0.103(5)	0.967(2)
C8-H8C···N1[c]	2.872	3.649	130.4	0.041(2)	0.41(1)
C8-H8B···N2[d]	2.720	3.353	137.2	0.059(3)	0.616(1)
C7-H7B···N2[e]	2.493	3.504	136.8	0.103(5)	0.951(2)
3					
C6-H6C···N1[f]	2.564	3.541	152.8	0.035(6)	0.653(5)
C6-H6A···N1[g]	2.840	3.500	120.6	0.042(5)	0.523(3)
C5-H5B···N1[h]	2.586	3.631	168.6	0.04(2)	0.619(5)
C5-H5A···N2[i]	2.560	3.603	167.8	0.040(2)	0.522(2)
C6-H6A···N2[j]	2.886	3.554	121.3	0.048(4)	0.566(3)
4					
C5-H5B···N1[k]	2.594	3.617	162.0	0.032(8)	0.572(9)
C6-H6B···N1[k]	2.780	3.633	137.5	0.025(8)	0.420(4)
C5-H5A···N2[l]	2.443	3.463	161.2	0.05(1)	0.691(4)

Sulfur contacts	Distance [Å]	ρ [e Å^{-3}]	$\nabla^2\rho$ [e Å^{-5}]
3			
S1···S1[m]	3.515	0.067(1)	0.654(2)
S1···S1[n]	3.952	0.030(1)	0.305(1)
N2···S2[o]	3.307	0.055(1)	0.603(1)
N2···S2[p]	3.549	0.055(1)	0.603(1)
4			
N1···S1[q]	3.194	0.055(2)	0.586(3)

Symmetries: [a] $x, -\frac{1}{2}+y, \frac{1}{2}+z$. [b] $\frac{3}{2}-x, -\frac{1}{2}+y, -z$. [c] $\frac{1}{2}+x, \frac{3}{2}-y, z$. [d] $2-x, \frac{3}{2}-y, -\frac{1}{2}+z$. [e] $\frac{3}{2}-x, y, -\frac{1}{2}+z$. [f] $1+x, y, z$. [g] $-x, 1-y, -z$. [h] $-\frac{1}{2}-x, \frac{1}{2}+y, \frac{1}{2}-z$. [i] $1-x, 1-y, 1-z$. [j] $\frac{1}{2}-x, \frac{1}{2}+y, \frac{1}{2}-z$. [k] $2-x, -y, \frac{1}{2}+z$. [l] $2-x, 1-y, \frac{1}{2}+z$. [m] $1-x, 1-y, 1-z$. [n] $-x, 1-y, 1-z$. [o] $\frac{1}{2}-x, -\frac{1}{2}+y, \frac{1}{2}-z$. [p] $-\frac{1}{2}-x, -\frac{1}{2}+y, \frac{1}{2}-z$. [q] $\frac{3}{2}-x, -\frac{1}{2}+y, -\frac{1}{2}+z$.

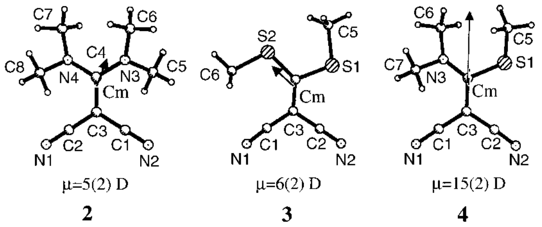

Figure 8. Molecular diagrams showing the dipole moment vectors computed from charge density in **2**–**4**. Cm refers to the center of mass of the molecule.

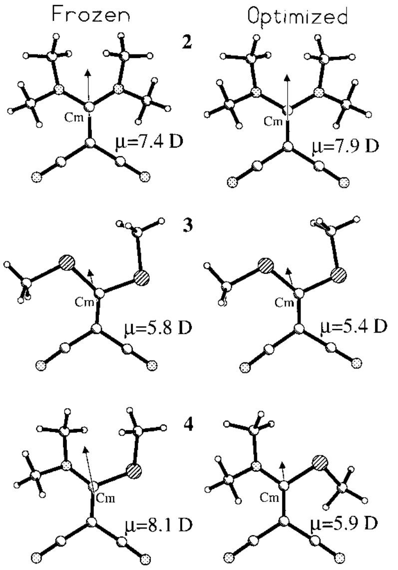

Figure 9. Molecular dipole moments calculated using AM1 (MOPAC) in the frozen (left) and the optimized (right) geometries of the diamino **2**, dithio **3**, and thioamino **4** EDCN derivatives. Cm refers to the center of mass of the molecule. Atomic labeling is given in Figure 8.

thioamine exhibits a *syn*-methylthio conformation with a smaller dipole moment compared to the *anti*-methylthio conformation found in the frozen geometry of the crystal. It appears that the noncentric structure induces significant distortions in the molecule and enhances the dipole moment.

In conclusion, the present charge density study on the centric and noncentric molecular systems has provided valuable insight into the effect of the crystal field on molecular properties. In the case of 5-nitrouracil, the dipole moment is 5.5(6) D in the centric structure and increases to 9(1) D in the noncentric lattice, while the molecular geometry essentially remains the same; the difference in the dipole moments clearly arises from the crystal packing. In the centric structure, there are N—H···O hydrogen bonded dimers, whereas in the noncentric the molecules form N—H···O linear chains. The centric crystal exhibits an additional contact, C—H···O_{nitro}, absent in the noncentric structure. The molecular dipole moment in the noncentric crystal is considerably greater than the value calculated for a free molecule of outside the crystal (frozen geometry). In centric polymorph, the dipole moment is close to that obtained from the free molecule.

In the ethylenedicarbonitriles, the crystal is centrosymmetric when the two substituents are the same, as in the diamino (**2**) and dithio (**3**) derivatives, and they have low dipole moments ($\mu \sim 6$ D). The dipole moment values are close to those obtained by AM1 calculations on the frozen molecular geometries. In contrast, the thioamine (**4**), with the *anti*-methylthio conformation of the S—CH_3 group, occurs in a noncentric structure where there is an increased charge separation within the molecule and, hence, a considerably higher dipole moment ($\mu = 15(2)$ D) than that calculated for the molecule of frozen geometry. When the molecule is subjected to optimization, it adopts a *syn*-methylthio conformation and the dipole moment falls to below $\mu = 5.9$ D. The enhancement of the dipole moment in the thioamino system is partly due to the *anti*-conformation forced on the molecule by the noncentric crystal field and partly due to the field itself.

Experimental Section

On cooling an aqueous solution of 5-nitrouracil from 70 °C, crystals of the centrosymmetric polymorph were obtained. The noncentric crystals were obtained from an acetonitrile solution at room temperature. The dinitriles **2**–**4** were synthesized by employing reported procedures[33–35] and the crystals were grown from toluene, ethyl acetate, and benzene solutions, respectively. High quality crystals were chosen after examination under an optical microscope. X-ray diffraction intensities were measured by ω scans using a Siemens three-circle diffractometer.

The unit cell parameters and the orientation matrix of the crystal were initially determined using ~45 reflections from 25 frames collected over a small ω scan of 7.5° sliced at 0.3° intervals. A hemisphere of reciprocal space was then collected in two shells using the SMART software[36] with 2θ at 28° and 70°. Data reduction was performed using the SAINT program[36] and the orientation matrix along with the detector and the cell parameters were refined for every 40 frames. Further experimental details are listed in Table 1. The crystal structures were first determined with the low-resolution data up to $(\sin\theta)/\lambda = 0.56$ Å^{-1}. The phase problem was solved by direct methods and the non-hydrogen atoms were refined anisotropically, by means of the full-matrix least-squares procedures using the SHELXTL program.[37] All the hydrogen atoms were located using the difference Fourier method and the temperature factors of these atoms were refined isotropically. The crystal structures agreed well with those reported previously.[27, 38, 39] The structure of the centrosymmetric 5-nitrouracil polymorph (*Pbca*) is reported for the first time and deposited in the Cambridge Crystallographic Database.

Charge density analysis was carried out based on multipole expansion of the electron density centered at the nucleus of the atom.[40] Accordingly, the aspherical atomic density can be described in terms of spherical harmonics [Eq. (2)]. Thus, for each atom, in which the origin at the atomic nucleus, [Eq. (3)] holds. The population coefficients, P_{lmp}, are to be refined along with the$\kappa$and κ' parameters which control the radial dependence of the valence shell density. The analysis was carried out in several steps.

$$\rho_{atom}(r) = \rho_{core}(r) + \rho_{valence}(r) + \rho_{def}(r) \tag{2}$$

$$\rho_{atom}(r) = \rho_{core}(r) + P_v \kappa^3 \rho_{valence}(\kappa r) + \sum_{l=0} \kappa'^3 R_l(\kappa' \zeta r) \sum_{m=0} \sum_{p=\pm l} P_{lmp} Y_{lmp}(\theta,\varphi) \tag{3}$$

The hydrogen atomic positions were found using the difference Fourier method and were adjusted to average neutron values,[41] as is usually done during the multipole refinement (C_{sp^3}—H 1.06, C_{sp^2}—H 1.083, N—H 1.01 Å). A high order refinement of the data was performed using reflections with $(\sin\theta)/\lambda \geq 0.6$ Å^{-1} and $F_0 \geq 4\sigma$. All the hydrogen atoms were held constant throughout the refinement along with their isotropic temperature factors. Multipolar refinement for the charge density analysis was carried out using the XDLSM routine of the XD package;[42] details are given in Table 1. The atomic coordinates and the thermal parameters obtained from the high order refinement were used as input to XD refinement. Sulphur atoms were refined up to hexadecapole moments, carbon, nitrogen, and oxygen atoms up to octapole moments, while hydrogen atoms were restricted to dipole moments. During the refinement, the charge neutrality constraint was applied in all the cases. Kappa refinement was carried out on both the spherical and deformation valence shells of the non-hydrogen atoms, while those for the hydrogen atoms were restricted to the spherical valence. The multipolar refinement strategy was the following: a) scale factor, b) P_v, c) P_{lm}, d) repeat (b, c) until convergence, e) κ, f) repeat (b, c) until convergence, g) κ', h) repeat (b, c) until convergence, i) positional and thermal parameters of all nonhydrogen atoms, and finally j) P_v and P_{lm} together. The quality of the refinement was monitored using the residual density; the magnitude of the highest residual peak in the final refinement was 0.19, 0.2, 0.2, 0.2, 0.15 e Å^{-3} for the centric **1**, noncentric **1**, **2**, **3**, and **4**, respectively. Difference mean-square displacement amplitudes for the various bonds obtained from XD were found to follow closely the Hirshfeld criterion.[43]

The XDPROP routine was used to calculate the total electron density $\rho(r)$, the Laplacian $\nabla^2\rho$, and the ellipticity ε, at the bond critical points (CPs). Electrostatic potential (*V*) and dipole moments were also obtained using this routine. The Laplacian maps have been plotted using the XDGRAPH routine. The MOPAC program[44] was used for the calculation of the dipole moments at the frozen and optimized molecular geometries. This calculation, although semiempirical, is known to provide reliable estimates of molecular dipole moments.[16]

[1] P. N. Prasad, J. D. Williams, *Introduction to Nonlinear Optical Effects in Molecules and Polymers*, Wiley, New York, **1990**.

[2] J. Zyss, *Molecular Nonlinear Optics: Materials, Physics, Devices*, Academic Press, Boston, **1994**.

[3] C. Bosshard, K. Sutter, P. Pretre, J. Hullinger, M. Flörsheimer, P. Kaatz, P. Gunter, *Organic Nonlinear Optical Materials*, Gordon & Breach, Amsterdam, **1995**.

[4] D. S. Chemla, J. Zyss, *Nonlinear Optical Properties of Organic Molecules and Crystals*, Academic Press, Orlando, FL, **1987**.

[5] D. R. Kanis, M. A. Ratner, T. J. Marks, *Chem. Rev.* **1994**, *94*, 195.

[6] E. Espinosa, C. Lecomte, E. Molins, S. Veintemillas, A. Cousson, W. Paulus, *Acta Crystallogr. Sect. B* **1996**, *52*, 519.

[7] A. Puig-Molina, A. Alvarez-Larena, J. F. Piniella, S. T. Howard, F. Baert, *Struct. Chem.* **1998**, *9*, 395.

[8] S. T. Howard, M. B. Hursthouse, C. W. Lehmann, P. R. Mallinson, C. S. Frampton, *J. Chem. Phys.* **1992**, *97*, 5616.

[9] C. Gatti, V. R. Saunders, C. Roetti, *J. Chem. Phys.* **1994**, *101*, 10686.

[10] A. Fkyerat, A. Guelzim, F. Baert, W. Paulus, G. Heger, J. Zyss, A. Perigaud, *Acta Crystallogr. Sect. B* **1995**, *51*, 197.

[11] A. Fkyerat, A. Guelzim, F. Baert, J. Zyss, A. Perigaud, *Phys. Rev. B* **1996**, *53*, 16236.

[12] N. K. Hansen, J. Protas, G. Marnier, *C. R. Acad. Sci. Ser. B* **1988**, *307*, 475.

[13] N. K. Hansen, J. Protas, G. Marnier, *Acta Crystallogr. Sect. B*, **1991**, *47*, 660.

[14] M. A. Spackman, *Annu. Rep. Prog. Chem. Sect. C* **1998**, *94*, 177.

[15] P. Coppens in *X-ray Charge Densities and Chemical Bonding*, Oxford University Press, **1997**.

[16] F. Hamazaoui, F. Baert, J. Zyss, *J. Mater. Chem.* **1996**, *6*, 1123.

[17] G. K. H. Madsen, F. C. Krebs, B. Lebech, F. K. Larsen, *Chem. Eur. J.* **2000**, *6*, 1797.

[18] H. Youping, S. Genbo, W. Bochang, J. Rihong, *J. Cryst. Growth* **1992**, *119*, 393.

[19] M. C. Etter, *Acc. Chem. Res.* **1990**, *23*, 120.

[20] P. R. Mallinson, K. Wozniak, T. Garry, K. L. McCormak, *J. Am. Chem. Soc.* **1997**, *119*, 11502.

[21] P. R. Mallinson, K. Wozniak, C. C. Wilson, K. L. McCormak, D. M. Yufit, *J. Am. Chem. Soc.* **1999**, *121*, 4640.

[22] W. T. Klooster, S. Swaminathan, R. Nanni, B. M. Craven, *Acta Crystallogr. Sect. B* **1992**, *48*, 217.

[23] R. F. Stewart in *The Application of Charge Density Research to Chemistry and Drug Design* (Eds.: G. A. Jeffrey, J. F. Piniella), Plenum, New York, **1991**.

[24] R. F. W. Bader, *Atoms in Molecules—A Quantum Theory*, Clarendon Press, Oxford, **1990**.

[25] R. Srinivasa Gopalan, G. U. Kulkarni, S. Renganayaki, E. Subramanian, *J. Mol. Struct.* **2000**, *524*, 169.

[26] Following referee comments, R_{int} for centric **1** and **4** were improved to ~ 0.04 by eliminating reflections above 0.9 Å^{-1}. The dipole moments did not vary significantly.

[27] H. U. Hummel, H. Procher, *Acta Crystallogr. Sect. C* **1986**, *42*, 1602.

[28] N. U. Kamath, K. Venkatesan, *Acta Crystallogr. Sect. C* **1984**, *40*, 1211.

[29] K. L. McCormack, P. R. Mallinson, B. C. Webster, D. S. Yufit, *J. Chem. Soc. Faraday Trans*. **1996**, *92*, 1709.

[30] D. Cremer, E. Kraka, *Croat. Chem. Acta.* **1984**, *57*, 1259.

[31] E. Espinosa, E. Molins, C. Lecomte, *Phys. Rev. B* **1997**, *57*, 1820.

[32] W. Scherer, M. Spiegler, B. Pedersen, M. Tafipolsky, W. Hieringer, B. Reinhard, A. J. Downs, G. S. McGrady, *Chem. Commun.* **2000**, 635.

[33] E. Ericsson, J. Sandström, I. Wennerbeck, *Acta Chem. Scand.* **1970**, *24*, 3102.

[34] L. Dalgaard, H.-K. Andersen, S.-O. Lawesson, *Tetrahedron* **1973**, *29*, 2077.

[35] N. H. Nilsson, *Synthesis* **1974**, 433.

[36] Siemens Analytical X-ray Instruments, **1995**, Madison, WI, USA.

[37] SHELXTL (SGI version), Siemens Analytical X-ray Instruments, **1995**, Madison, WI, USA.

[38] J. G. Bergman, G. R. Crane, B. F. Levine, C. G. Bethea, *Appl. Phys. Lett.* **1972**, *20*, 21.

[39] D. Adhikesavulu, K. Venkatesan, *Acta Crystallogr. Sect. C* **1983**, *39*, 589.

[40] N. K. Hansen, P. Coppens, *Acta Crystallogr. Sect. A* **1978**, *34*, 909.

[41] F. H. Allen, O. Kennard, D. G. Watson, L. Brammer, A. G. Orpen, R. Taylor, *J. Chem. Soc. Perkin Trans. 2* **1987**, S1.

[42] T. Koritsansky, S. T. Howard, T. Richter, P. R. Mallinson, Z. Su, N. K. Hansen, *XD, A Computer Program Package for Multipole Refinement and Analysis of Charge Densities from Diffraction Data*, Cardiff University (UK), **1995**.

[43] H. L. Hirshfeld, *Acta Crystallogr. Sect. A* **1976**, *32*, 239.

[44] J. J. P. Stewart, *J. Comput. Aided Mol. Des.* **1990**, *4*, 1.

Received: June 26, 2000 [Z 57]

Nanometer – Nanosecond Oscillatory Expansion and Contraction Behavior of Polymer Films Induced by 248 nm Excimer Laser Excitation**

Tomokazu Masubuchi,[a] Hiroshi Furutani,[a]
Hiroshi Fukumura,[a] and Hiroshi Masuhara*[a]

KEYWORDS:

interferometry · laser chemistry · oscillatory dynamics · photochemistry · polymers

Intense excitation of organic materials with ultraviolet excimer laser pulses has received much attention, as it induces unique physicochemical processes in addition to normal photophysics and photochemistry. A representative example is laser ablation, which is indeed a nonlinear process with respect to laser fluence, and etching of material surfaces is induced only when the fluence exceeds a certain threshold value.[1–4] Generation of high-density excited states[5–9] and explosive ejection behavior of ablated plumes and fragments[4–6, 10–12] are characteristic of laser ablation. It was considered, in general, that no appreciable morphological change occurs below the ablation threshold, whereas repetitive excitation with a low-intensity pulse leads to some etching. Indeed, elucidation of the underlying mechanism in laser ablation is an essential research subject of laser – material interactions.

A few years ago, we developed nanosecond time-resolved interferometry, which made measurements on nanosecond surface displacement of doped polymer films possible.[13, 14] The intense laser excitation of dopant molecules results in rapid photothermal heating of the polymer films via cyclic multiphotonic absorption,[15, 16] so that the subsequent morphological change above and below the ablation threshold can be measured directly in the nano- to millisecond domain.[17–20] Above the ablation threshold, transient expansion in the effectively excited surface layer commenced during the excitation laser pulse and the ablated polymer was then explosively ejected. On the other hand, below the ablation threshold, expansion of the polymer film was also observed even during the excitation laser pulse and a succeeding contraction then recovers the original, flat surface. Nanosecond surface displacement of photodecomposable polymer films and amorphous solids were also investigated by the interferometry, to reveal novel dynamics.[17–20]

For neat poly(methyl methacrylate) (PMMA) films, some theoretical models have been proposed for describing laser ablation phenomena observed from various kinds of experiments.[4, 11] However, morphological changes of neat PMMA films at the fluence, where no permanent etching of the polymer film occurs, have not been well elucidated. As absorbance of the neat PMMA film is very weak at the excitation wavelengths and the film homogeneously and rapidly warms, new morphological changes are expected to be brought about. In the present work, we have applied the nanosecond time-resolved interferometry to a neat PMMA film and measured precisely its nanosecond transient surface displacement induced by the excimer laser irradiation below the ablation threshold.

A schematic diagram of the nanosecond time-resolved interferometric measurement system is shown in Figure 1. A KrF excimer laser was used as an excitation light source and its fluence was adjusted with partially transmitting laser mirror. A probe light pulse was the second harmonic of a Q-switched Nd^{3+}:YAG laser. Time-resolved measurements were carried out by controlling the delay time (Δt) between the excitation and probe laser pulses with a digital delay/pulse generator, while nanosecond interference patterns were acquired by a CCD camera. The origin of the time axis, $\Delta t = 0$, is defined as the time when both laser pulse peaks coincide and the delay time was monitored shot-by-shot by a digital oscilloscope. In the experiment, a shift of one fringe spacing to the left or right corresponds to an expansion or etching of 266 nm, a half-wavelength of the probe laser.[13] The system can interrogate expansion and contraction of a few nanometers with a time resolution of 10 ns. All measurements were carried out at room temperature in air. All data were obtained by one-shot measurements in order to avoid effects brought about by exciting photoproducts formed by previous irradiation.

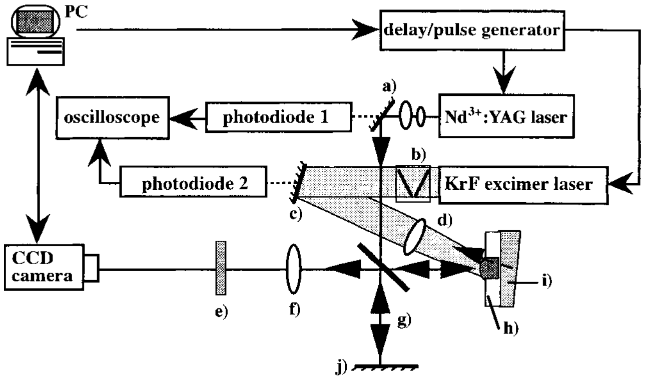

Figure 1. *A schematic diagram of the nanosecond time-resolved interferometry. Optical components are a) beam expander, b) attenuator, c) mirror, d) lens (f = 250 mm), e) bandpass filter, f) lens (f = 200 mm), g) beam splitter, h) sample film, i) substrate, and j) reference mirror.*

In Figure 2 a, expansion and contraction dynamics are given at a laser fluence of 1100 and 870 mJ cm^{-2}, below the ablation threshold of 1400 mJ cm^{-2}. Transient expansion starts during the excimer laser pulse and reaches the maximum value at the end of the pulse; the film then undergoes contraction. Clear fringe patterns of interference images of the area irradiated by the

---

[a] *Prof. Dr. H. Masuhara, T. Masubuchi, Dr. H. Furutani, Prof. Dr. H. Fukumura*
Department of Applied Physics
Osaka University
Suita, Osaka 565-0871 (Japan)
Fax: (+81) 6-6876-8580
E-mail: masuhara@ap.eng.osaka-u.ac.jp

[**] *The present work was partially supported by the Grant-in-Aid for Scientific Research on Priority Area (B) "Laser Chemistry of Single Nanometer Organic Particles" from the Ministry of Education, Science, Sports, and Culture of Japan (No. 10207204).*

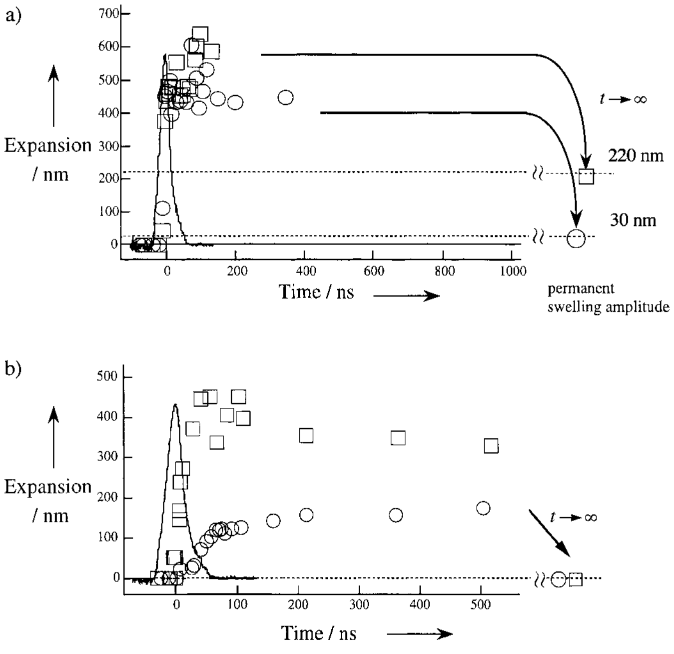

Figure 2. a) Expansion and contraction dynamics of the PMMA film at 1100 (□) and 870 mJ cm^{-2} (○) fluence. The dashed line represents the permanent swelling amplitude. Arrows represent the time domain in which the fringe pattern of the interference images in the irradiated area could not be observed by the darkening. b) As (a), but at 700 (□) and 540 mJ cm^{-2} (○) fluence. The solid curve represents the time profile of the excimer laser pulse.

Editorial Advisory Board Member:[*]
Hiroshi Masuhara

is a Professor of Applied Physics at Osaka University and currently the President of the Japanese Photochemistry Association (2000–2001). He received his B.S. degree in Chemistry from Tohoku University in 1966 and obtained his Ph.D. degree in Physical Chemistry from Osaka University under the supervision of Professor Noboru Mataga in 1971. He worked as a professor of the Kyoto University of Technology and as a director of Masuhara Microphotoconversion ERATO Project, JST, and has joined the present faculty in 1991. He has developed various time- and space-resolved spectroscopic and laser manipulation methods, utilizing confocal and scanning near-field microscopes as well as lasers, and has conducted studies on spectroscopy and chemistry in small domains. Recently, he has become interested in femtosecond excitation–nanometer morphological dynamics (fs–nm) of organic solids. By developing fs regular and diffuse reflectance spectroscopy, fs light scattering imaging, fs polarization microscopy, and ns–nm intoferometry, he studies the dynamics of cooperative isomerization, melting, expansion/contraction, and ablation in organic mesoscopic systems.

excimer laser could not be observed because of the darkening after 130 and 350 ns for 1100 and 870 mJ cm^{-2} fluence, respectively. This may be due to the fact that the film surface is no longer sufficiently flat for this measurement after several hundred nanoseconds. It is worth noting that the original surface position was not recovered and a permanent swelling to 220 and 30 nm was induced at 1100 and 870 mJ cm^{-2} fluence, respectively. These values are, of course, in agreement with the etch depth measured by a depth profiler (Sloan Dektak3).

In the case of 700 and 540 mJ cm^{-2} fluence (Figure 2 b), the irradiated film begins to expand at the late stage of the excimer laser pulse, maintains the expansion, and returns to its original state: The expansion disappeared completely after a delay time and the original surface was recovered. Comparing the present transient expansion and contraction dynamics with that of a biphenyl-doped PMMA film,[13, 14] we find the expansion overshoots at a delay of around 100 ns and 700 mJ cm^{-2} fluence.

In Figure 3, expansion and contraction dynamics are given at fluences of 400, 300, and 250 mJ cm^{-2}. It is very interesting to note that at these fluences, the film surface showed repetitive expansion and contraction of several tens of nanometers before recovering the original flat surface. This novel behavior has never been observed for other polymer films, such as doped PMMA, neat and doped polystyrene, triazenopolymers, and nitrocellulose.[17–19] The oscillatory behavior is clearly observed only in the low fluence range, which is a key for understanding its correlation with physical properties of polymer films.

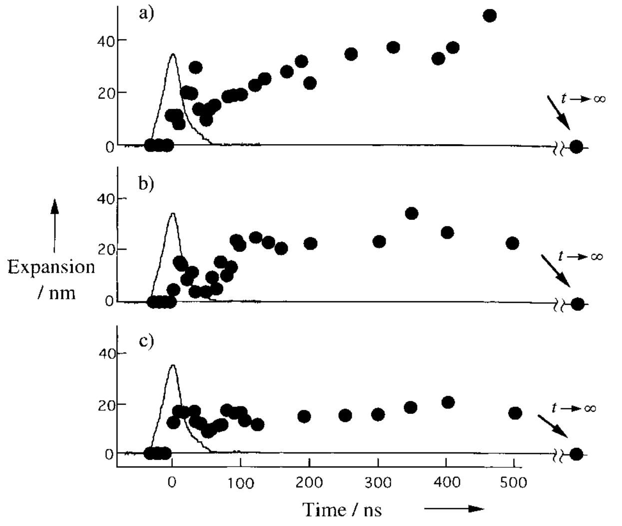

Figure 3. Expansion and contraction dynamics of the PMMA film at fluences of a) 400, b) 300, and c) 250 mJ cm^{-2}. The solid curve represents an excimer laser pulse.

In Figure 4, the fluence dependence of the expansion of PMMA film at 1 µs after the excimer laser irradiation is plotted below and near the ablation threshold. At this delay time, the bump at 700 mJ cm^{-2} and oscillatory behavior below 400 mJ cm^{-2} disappears, so that expansion may be considered in relation to the state of polymer films. It is worth noting that the expansion of the PMMA film shows a discontinuous fluence dependence. An inflection point was observed around 450 mJ cm^{-2} fluence, above which the curve gradient increased

---

[*] *Members of the Editorial Advisory Board will be introduced to the readers with their first manuscript.*

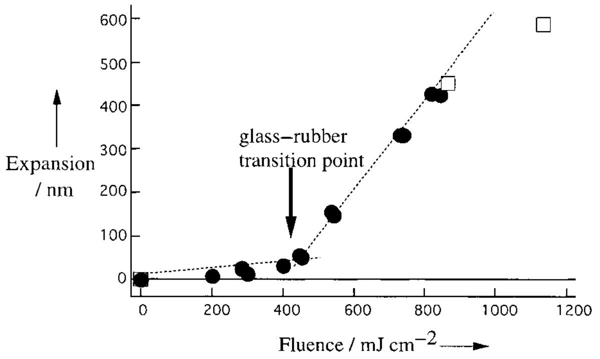

Figure 4. *Fluence dependence of the PMMA film expansion at + 1 μs after the 248 nm irradiation at the fluence below (●) and near (□) the ablation threshold.*

by a factor of about 8.6. A rough estimation of temperature at this fluence, assuming the Lambert – Beer equation and unitary quantum yield of photothermal conversion, suggests that the inflection corresponds to a glass – rubber transition (T_g). Below this point, the film is always glassy, while a transition to a rubbery state occurs above ~450 mJ cm^{-2}. A similar laser induced glass – rubber transition of doped PMMA films was already reported by us.[14] By comparing the expansion rate above and below this transition, it was estimated that the transition requires 10 – 20 ns.

As the expansion, as a function of the fluence, changes around T_g, the thermal expansion coefficients above and below T_g for PMMA are also different; $\alpha_{\text{rubber}} = (5.6 - 5.8) \times 10^{-4}$ and $\alpha_{\text{glass}} = (2.5 - 2.7) \times 10^{-4}$ K^{-1}.[21] It is interesting to see that $(\alpha_{\text{rubber}}/\alpha_{\text{glass}})^3$ almost matches the difference in the gradient below and above the bending point. It suggests that the one-dimensional expansion was induced in a direction perpendicular to the film, since the polymers outside the irradiated area are, of course, very rigid. In other words, the area irradiated by the excimer laser was excited as a whole, on which we can also estimate the surface temperature of the PMMA film at the critical 450 mJ cm^{-2} fluence by using the expansion amplitude at α_{glass}. A surface temperature obtained was about 410 K, which is a little higher than the T_g of PMMA (378 K) but supports our interpretation well.

Thermal expansion dynamics of the PMMA film changed remarkably at the glass – rubber transition point. This is because the properties of polymeric solids, thermal expansion coefficients, specific heats, elastic moduli, permittivities, and so on, are strongly influenced at T_g.[22–27] All properties are ascribed to the differences in polymer chains entanglement and, consequently, the temporal response against the pulse excitation should also changed. In the glassy region below 378 K, the film behaves like rigid solid and quick heating results in a rapid expansion; its overshooting may result in the oscillatory behavior. Above 378 K, the film undergoes the transition and the expansion involves a large polymer-chain slippage, which quenches overshooting, and the oscillatory behavior vanishes.

In conclusion, nanosecond transient expansion and contraction dynamics of PMMA films induced by excimer laser irradiation depends on the laser fluence. In the fluence range where the glass – rubber transition is not induced, we have found, for the first time, a novel phenomenon that the film surface shows repetitive expansion and contraction of several tens of nanometers and then the original flat surface is recovered. Elucidation of the morphological dynamics is indispensable to understand polymer conformation relaxation in films and to develop polymeric, micromechanical systems.

Experimental Section

PMMA (Kuraray, weight-averaged $M_W = 10 \times 10^4$) was dissolved in chlorobenzene and a solution (15 wt%) was spin-coated on a wedged quartz substrate. The film was baked to remove the residual solvent (2 min, 80 °C). The film thickness was about 2 μm and its absorbance at $\lambda = 248$ nm was 0.015.

The KrF excimer laser (Lextra 200, Lambda Physik) operated at $\lambda = 248$ nm and 30 ns full-width at half maximum (fwhm), while the Nd^{3+}:YAG laser (Surelite I, Continuum) operated at $\lambda = 532$ nm and 10 ns fwhm. Both lasers were controlled by a digital delay/pulse generator (DG 535, Stanford Research Systems).

[1] R. Srinivasan, *Science* **1986**, *234*, 559 – 565.
[2] R. Srinivasan, B. Baren, *Chem. Rev.* **1989**, *89*, 1303 – 1316.
[3] J. C. Miller, *Laser Ablation—Principles and Applications*, Springer, Berlin, **1994**.
[4] R. Srinivasan, B. Braren, K. G. Cassey, M. Yeh, *Appl. Phys.* **1989**, *55*, 2790 – 2791.
[5] Y. Tsuboi, K. Hatanaka, H. Fukumura, H. Masuhara, *J. Phys. Chem.* **1994**, *98*, 11 237 – 11 241.
[6] H. Fukumura, E. Takahashi, H. Masuhara, *J. Phys. Chem.* **1995**, *99*, 750 – 757.
[7] Y. Tsuboi, H. Fukumura, H. Masuhara, *J. Phys. Chem.* **1995**, *99*, 10 305 – 10 312.
[8] H. Fujiwara, H. Fukumura, H. Masuhara, *J. Phys. Chem.* **1995**, *99*, 11 844 – 11 853.
[9] H. Fujiwara, H. Fukumura, H. Masuhara, *J. Phys. Chem.* **1995**, *99*, 11 481 – 11 488.
[10] R. Srinivasan, B. Braren, K. G. Cassey, M. Yeh, *J. Appl. Phys.* **1990**, *67*, 1604 – 1606.
[11] R. Srinivasan, *J. Appl. Phys.* **1993**, *73*, 2743 – 2750.
[12] Y. Tsuboi, K. Hatanaka, H. Masuhara, *Appl. Phys. Lett.* **1994**, *64*, 2745 – 2747.
[13] H. Furutani, H. Fukumura, H. Masuhara, *Appl. Phys. Lett.* **1994**, *65*, 3413 – 3415.
[14] H. Furutani, H. Fukumura, H. Masuhara, *J. Phys Chem.* **1996**, *100*, 6871 – 6875.
[15] H. Fukumura, H. Masuhara, *Chem. Phys. Lett.* **1994**, *221*, 373 – 378.
[16] D. E. Hare, J. F. Franken, D. D. Dlott, *J. Appl. Phys.* **1995**, *77*, 5950 – 5960.
[17] H. Furutani, H. Fukumura, H. Masuhara, T. Lippert, A. Yabe, *J. Phys. Chem. B* **1997**, *101*, 5742 – 5747.
[18] H. Furutani, H. Fukumura, H. Masuhara, S. Kambara, T. Kitaguchi, H. Tsukada, T. Ozawa, *J. Phys. Chem. B* **1998**, *102*, 3395 – 3401.
[19] T. Lippert, L. S. Bennet, T. Kunz, C. Hahn, A. Wokaun, H. Furutani, H. Fukumura, H. Masuhara, T. Nakamura, A. Yabe, *Proc. SPIE J.* **1997**, *2992*, 135 – 143.
[20] M. Hosoda, H. Furutani, H. Fukumura, H. Masuhara, M. Nishii, N. Ichinose, S. Kawanishi, *Rev. Laser Eng.* **1997**, *25*, 306 – 311.
[21] J. Brandrup, E. H. Immergut, *Polymer Handbook*, 3rd. ed., Wiley, New York, **1989**.
[22] G. Schwarz, *Cryogenics* **1988**, *28*, 248 – 254.
[23] J. L. Viovy, L. Monnerie, F. Merola, *Macromolecules* **1985**, *18*, 1130 – 1137.
[24] P. D. Hyde, M. D. Ediger, T. Kitano, K. Ito, *Macromolecules* **1989**, *22*, 2253 – 2259.
[25] J. Colmenero, A. Alegria, J. M. Alberdi, F. Alvarez, B. Frick, *Phys. Rev. B* **1991**, *44*, 7321 – 7329.
[26] A. K. Rizos, G. Fytas, J. E. L. Roovers, *J. Chem. Phys.* **1992**, *97*, 6925 – 6932.
[27] L. H. Sperling, *Introduction to Physical Polymer Science*, Wiley, New York, **1986**, chap. 6.

Received: May 29, 2000 [Z 43]

Growth of Rodlike Silver Nanoparticles by Vapor Deposition of Small Clusters**

Sergej A. Nepijko,[a] Dmitrij N. Ievlev,[a] Wilfried Schulze,[a] Joachim Urban,[a] and Gerhard Ertl*[a]

KEYWORDS:

chemical vapor deposition · crystal growth · electron microscopy · silver

The growth of crystallites from the gas phase is affected by a series of parameters, such as the nature and temperature of the substrate as well as characteristics of the cluster beam flux. In the case of weak interactions between the substrate and the deposit, for example, very small Ag particles may exhibit a decahedral or icosahedral structure and, if the growth conditions are close to thermodynamic equilibrium, the size ranges for predominantly icosahedral, decahedral, or single-crystal cubic structures may be determined.[1] Thus, multiply twinned particles,[2] including polyparticles, may be formed. Examples for the latter are combinations of icosahedral and decahedral structures[3] or two icosahedral particles connected by a single crystal bridge.[4] In all these cases, the dimensions of the resulting particles in the three directions are not appreciably different from each other. By contrast, in the present study, Ag particles with pronounced prolate shape were grown (with the majority being of spherical shape) by deposition of small Ag clusters onto the (100) plane of air-cleaved NaCl. Similar observations were, to our knowledge, only made before with metal particles formed from solution.[5, 6] For that case, Cu needles resulted from the reduction of copper(II) bis(2-ethylhexyl)sulfosuccinate, [Cu(AOT)$_2$], in isooctane/NaCl/water colloidal self-assemblies, where the ligands stabilised large truncated decahedra.

Silver clusters generated by the gas aggregation technique[7] of a mean size of about 2 – 3 nm were deposited on the (100) plane of freshly cleaved NaCl at 300 K, where they subsequently agglomerate to larger particles. Afterwards, an amorphous carbon film was evaporated onto it, the NaCl substrate was removed by dissolution in distilled water, and the carbon film was supported by a copper grid. The structures of the Ag particles were then investigated by transmission electron microscopy (TEM; Philips CM 200 FEG operating at 200 kV with an information limit better than 0.18 nm). For improvement of the image quality, image processing was performed in the usual way by evaluating the Fourier transforms and filtering the resulting data before backtransformation.[8, 9] This procedure also provides information on the symmetry of the particles and allows direct calculation of lattice spacings and angles. Tilting of the sample was achieved by a rotable tilt-sample holder (GATAN).

Silver particles produced by the noble gas aggregation generally exhibit cuboctahedral or Wulff polyhedral (cubic) structures if their diameters exceed about 5 nm and are icosahedra or decahedra (fivefold symmetry) with spherical shape below this size.[10] Figure 1 illustrates the kind of particles in the cluster beam used in present study. This beam was directed onto an amorphous carbon film for 2 sec. The resulting TEM image (Figure 1) reveals only spherical particles, which are frequently multiply twinned, and the inset shows a decahedron in the fivefold orientation. If the exposure to the beam was reduced, only the mean mutual distance of the particles changed but not their size. Therefore, we conclude that coalescence can be ruled out and the particles shown on Figure 1 indeed represent the clusters in the beam. The dependence of the cluster size distribution in the beam and its dependence on the parameters of the gas-phase aggregation source has been discussed previously.[7, 11, 12]

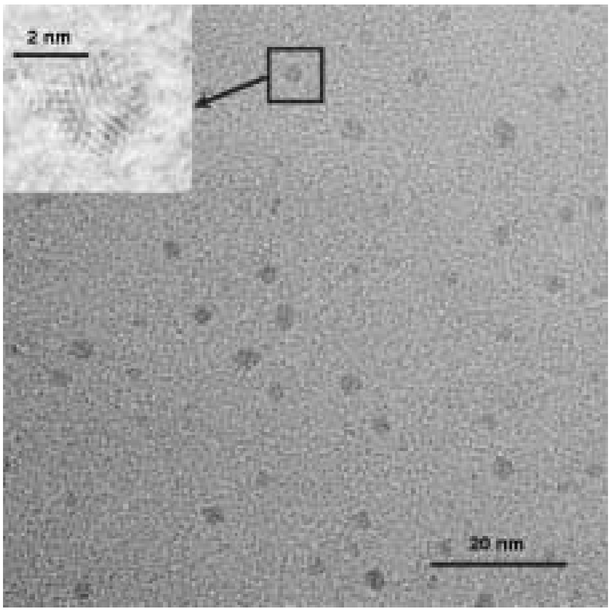

Figure 1. TEM image from Ag clusters deposited onto an amorphous carbon film. The inset shows a spherical decahedral particle of about 3 nm diameter.

Prolonged exposure of the carbon film to the cluster beam eventually causes the appearance of larger spherical particles due to coalescence, concomitant with a broadening of the particle size distribution. If an NaCl crystal is cleaved in air and its (001) plane is used as a substrate, a small fraction (typically a few percent) of the particles are no longer spherical but exhibit cylindrical shape of up to 70 nm length and a length-to-width ratio of up to 10:1, as shown in Figure 2. The fraction of these rodlike particles increases with increasing concentration of steps on the NaCl (001) surface, so that these steps presumably serve as nucleation centers for the formation of the nanorods.

---

[a] G. Ertl, S. A. Nepijko, D. N. Ievlev, W. Schulze, J. Urban
Fritz-Haber-Institut der Max-Planck-Gesellschaft
Faradayweg 4-6, 14195 Berlin (Germany)
Fax: (+49) 30-8413-5106

[*] G. Ertl is a member of the Editorial Advisory Board for ChemPhysChem.

[**] Technical assistance by K. Weiss and H. Sack-Kongehl is gratefully acknowledged.

© WILEY-VCH-Verlag GmbH, D-69451 Weinheim, 2000 1439-4235/00/01/03 $ 17.50+.50/0

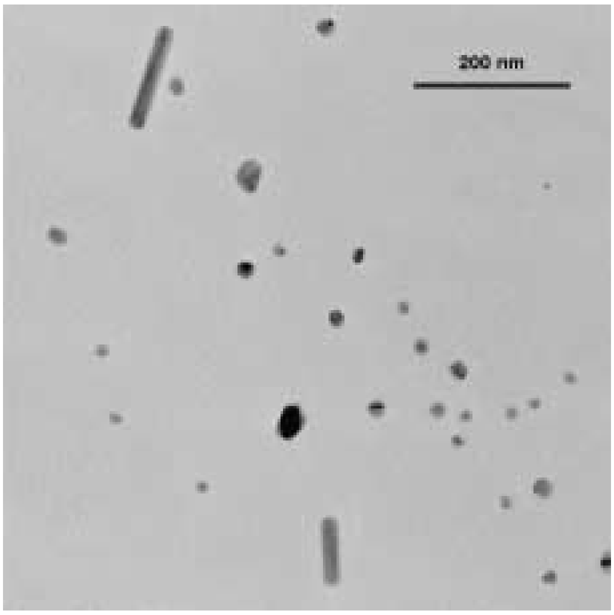

Figure 2. TEM overview image from Ag clusters formed on a NaCl (100) substrate, which exhibits the formation of two rodlike nanoparticles.

A high resolution image of such a particle is shown in Figure 3 a, together with a cut from the central section (Figure 3 b) and the associated power spectrum (PS; Figure 3 c). Inspection of Figure 3 b suggests the existence of stacking faults of (111)-type planes of a face-centered cubic lattice. In bulk silver, the probability for the occurrence of stacking faults is of the order of about 1 %[13, 14] but increases markedly for smaller particles.

The reflections in the power spectrum (Figure 3 c) are grouped into three equitorial pairs 1 – 3 and pairs 4 – 8 and 9 outside the equator lines. The resulting lattice parameters are $d_1 = 0.243$, $d_2 = 0.380$, $d_3 = 0.631$, $d_4 = 0.209$, $d_5 = 0.286$, $d_6 = 0.286$, $d_7 = 0.254$, $d_8 = 0.211$, and $d_9 = 0.147$ nm, within $\pm 2\%$ error. The data of reflections 1, 4, 8, and 9 are very close to the Ag (111), (200), (020), and (220) plane spacings with bulk values of 0.2359, 0.2043, 0.2043, and 0.1445 nm, respectively. The angle between planes (200) and (020) is 88° instead of 90° for bulk silver. The coexistence of these two reflections, together with the (111) reflection, demonstrates that the cylinder contains more than one subunit, namely, it is twinned. The splitting of the reflections, in particular 2, 5, 6, 7, and 9, suggests the existence of some lattice distortion, a conclusion which is supported by the deviation of the angle between (200) and (020) from 90°. The elongation of the reflections, on the other hand, mirrors the shape function of the particle.

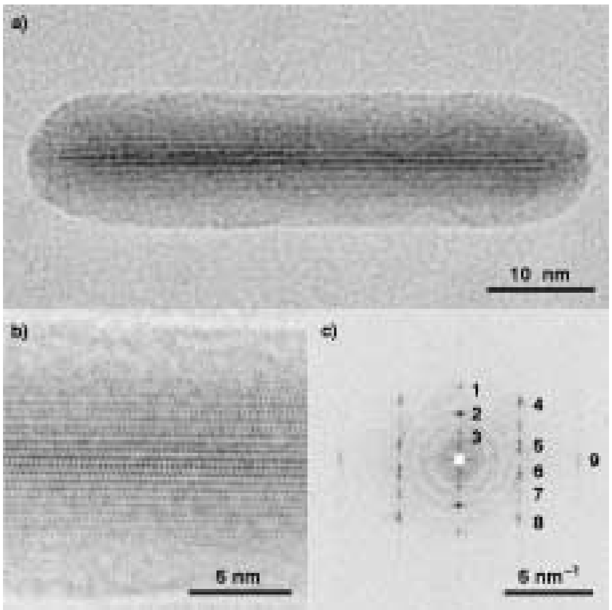

Figure 3. High resolution images from a particle showing a) a truncated decahedron structure, b) the central section of the rod, and c) its power spectrum.

Figure 4 shows a series of images, together with their PS, taken at various tilt angles around the axis of the cylinder. The images and their PS for tilt angles of 0° and ±36° are identical. Images recorded at ±18°, on the other side, showed predominantly lattice planes on the right-hand side for the positive tilt and on the left-hand side for the negative tilt, while the associated PS were identical. Such features cannot be attributed to stacking faults. They were similarly observed with the quoted

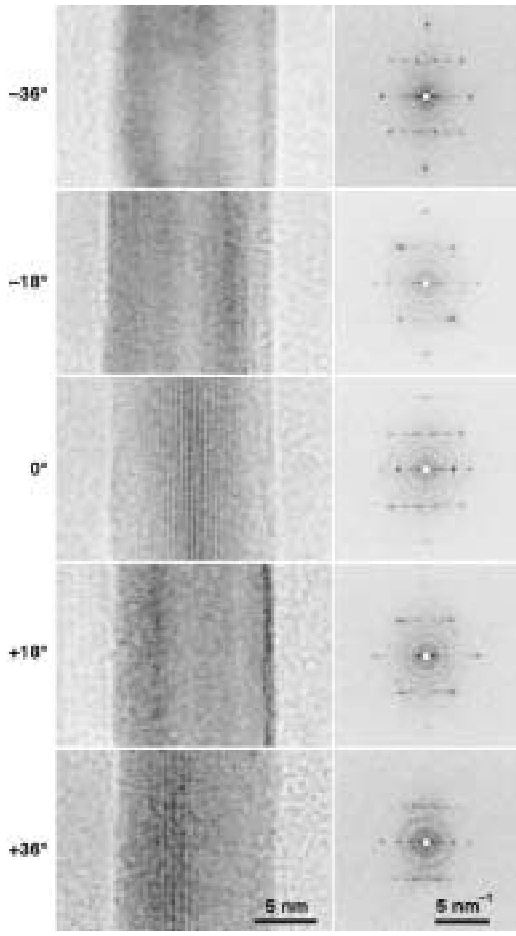

Figure 4. Series of images at different tilt angles (left) together with the associated power spectra (right). Tilt angles (from top to bottom): −36°, −18°, 0°, +18°, +36°.

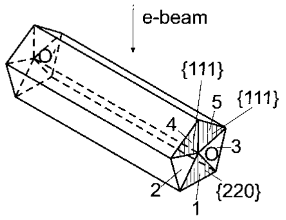

Figure 5. Model of a truncated decahedron.

copper needles formed from colloidal solution[5, 6] and are identified with the formation of a truncated decahedron as depicted in Figure 5. Here, the fivefold cylinder axis runs along the (110) orientation, which is parallel to the substrate, and the truncation is formed by the (100) planes of the five deformed tetrahedral subunits.

The properties of such structures have been discussed in detail before[14] and will be used here for further interpretation of the electron microscopy data. All reflections are created from different subunits and are partly due to multiple scattering events. Inspection of Figure 5 reveals that if the electron beam is parallel to the (111) planes of subunits 4 and 5, it will also be parallel to the (110) planes of subunit 1. This defines the 0° orientation. The (111) reflection is then labeled 1 and the (220) reflection 9. Reflections 4 and 8 are the (020) and (200) reflections, respectively, from subunit 1. The other reflections are the results of multiple scattering events. As can also be derived from Figure 5, tilts at $\pm 36^\circ$ will yield the same pattern as 0° tilt, while $\pm 18^\circ$ tilts will lead to patterns different from the 0° tilt, in which the (111) planes will appear on opposite sides of the particles for positive or negative tilts, in agreement with the data of Figure 4.

For the formation mechanism of these particles with quite unusual structural properties the following picture emerges: Figure 1 suggests that the Ag clusters deposited from the gas aggregation cell may exhibit fivefold symmetry and an average size of about 3 nm, in good agreement with previous extended X-ray absorption fine-structure (EXAFS) studies.[15] Under the chosen conditions, their mean mutual distance is in the range of 4 – 8 nm. If these clusters are deposited onto the cleaved NaCl (100) surfaces, presumably steps act as efficient "traps" for the migrating clusters and, thereby, growth of prolate particles of truncated decahedra may take place besides the formation of large spherical particles resulting from isotropic agglomeration. Formation of the prolate particles along step edges had also been reported for other systems, for example, Au on NaCl (100)[16] and Au on CaF_2 (111).[17] It has to be emphasized, however, that the structure of the resulting rodlike particles is affected by their mode of preparation. In the case of thermal evaporation of atoms, they consist of stacked icosahedra.[16] Their formation is, on the other hand, not restricted to the presence of steps on the substrate surface found with the growth of needlelike CdS crystals with fivefold symmetry and lenghts of up to several micrometers.[18]

It is tempting to speculate on possibilities for increasing the fraction of the anisotropic nanoparticles which might exhibit novel physical properties.

[1] S. Ino, *J. Phys. Soc. Jpn.* **1969**, *27*, 941.
[2] K. Yagi, K. Takayanagi, K. Kobayashi, G. Honjo, *J. Cryst. Growth* **1975**, *28*, 117.
[3] D. J. Smith, L. D. Marks, *Philos. Mag. A* **1981**, *44*, 735.
[4] D. J. Smith, L. D. Marks, *J. Cryst. Growth* **1981**, *54*, 433.
[5] I. Lisiecki, A. Filankembo, H. Sack-Kongehl, K. Weiss, M.-P. Pileni, J. Urban, *Phys. Rev. B* **2000**, *61*, 4968.
[6] I. Lisiecki, H. Sack-Kongehl, K. Weiss, J. Urban, M.-P. Pileni, *Langmuir*, submitted.
[7] F. Frank, W. Schulze, B. Tesche, J. Urban, B. Winter, *Surf. Sci.* **1985**, *156*, 90.
[8] G. Nihoul, *Microsc. Microanal. Microstruct.* **1991**, *2*, 637.
[9] S. Giorgio, G. Nihoul, J. Urban, H. Sack-Kongehl, *Z. Phys. D* **1992**, *24*, 395.
[10] S. Giorgio, J. Urban, W. Kunath, *Philos. Mag. A* **1989**, *60*, 553.
[11] H. Abe, W. Schulze, B. Tesche, *Chem. Phys.* **1980**, *47*, 95.
[12] W. Schulze, F. Frank, K.-P. Charlé, B. Tesche, *Ber. Bunsenges. Phys. Chem.* **1984**, *88*, 263.
[13] A. Taylor, *X-Ray Metallography*, Wiley, New York, **1961**.
[14] C. N. J. Wagner, *Acta Metall.* **1957**, *5*, 477.
[15] P. A. Montano, J. Zhao, M. Ramanathan, G. K. Shenoy, W. Schulze, J. Urban, *Chem. Phys. Lett.* **1989**, *164*, 126.
[16] S. A. Nepijko, H. Hofmeister, H. Sack-Kongehl, R. Schlögl, *J. Cryst. Growth* **2000**, *213*, 129.
[17] J. Viereck, W. Hoheisel, F. Träger, *Surf. Sci.* **1995**, *340*, L988.
[18] A. E. Romanov, I. A. Polonsky, V. G. Gryaznov, S. A. Nepijko, T. Junghanns, N. I. Vitrykhovski, *J. Cryst. Growth* **1993**, *129*, 691.

Received: June 23, 2000 [Z 60]

Polarized Photoluminescence and Spectral Narrowing in an Oriented Polyfluorene Thin Film**

Christian Bauer,*[a] Gunter Urbasch,[a] Harald Giessen,[a]
Andreas Meisel,[b] Heinz-Georg Nothofer,[b]
Dieter Neher,[c] Ullrich Scherf,[b] and Rainer F. Mahrt[a, b]

KEYWORDS:

luminescence · oriented materials · polymers · optical properties · thin films

Since the early work of Burroughes et al. on polymeric light-emitting diodes (LED)[1] the emissive properties of conjugated polymers have received growing interest. Intense research not

---

[a] *C. Bauer, G. Urbasch, Dr. H. Giessen, Dr. R. F. Mahrt*
Fachbereich Physik
Institut für Physikalische Chemie
and Wissenschaftliches Zentrum für Materialwissenschaften
Philipps-Universität Marburg
Renthof 5, 35032 Marburg (Germany)
Fax: (+49)6421-2827036
E-mail: bauerc@mailer.uni-marburg.de

[b] *A. Meisel, H.-G. Nothofer, Dr. U. Scherf, Dr. R. F. Mahrt*
Max-Planck-Institut für Polymerforschung
Ackermannweg 10, 55128 Mainz (Germany)

[c] *Prof. Dr. D. Neher*
Institut für Physik
Universität Potsdam
Am Neuen Palais 10, 14469 Potsdam (Germany)

[**] *We thank G. Wegner, K. Müllen, W. Knoll, H. Bässler, and W. W. Rühle for stimulating discussions. The cooperation with Sony International (Europe) is gratefully acknowledged. The work was supported by the Deutsche Forschungsgemeinschaft (Sonderforschungsbereich 383) and the Volkswagen-Stiftung.*

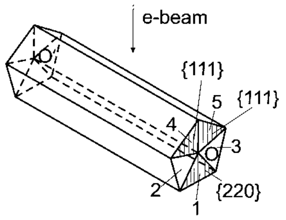

Figure 5. *Model of a truncated decahedron.*

copper needles formed from colloidal solution[5, 6] and are identified with the formation of a truncated decahedron as depicted in Figure 5. Here, the fivefold cylinder axis runs along the (110) orientation, which is parallel to the substrate, and the truncation is formed by the (100) planes of the five deformed tetrahedral subunits.

The properties of such structures have been discussed in detail before[14] and will be used here for further interpretation of the electron microscopy data. All reflections are created from different subunits and are partly due to multiple scattering events. Inspection of Figure 5 reveals that if the electron beam is parallel to the (111) planes of subunits 4 and 5, it will also be parallel to the (110) planes of subunit 1. This defines the 0° orientation. The (111) reflection is then labeled 1 and the (220) reflection 9. Reflections 4 and 8 are the (020) and (200) reflections, respectively, from subunit 1. The other reflections are the results of multiple scattering events. As can also be derived from Figure 5, tilts at ± 36° will yield the same pattern as 0° tilt, while ± 18° tilts will lead to patterns different from the 0° tilt, in which the (111) planes will appear on opposite sides of the particles for positive or negative tilts, in agreement with the data of Figure 4.

For the formation mechanism of these particles with quite unusual structural properties the following picture emerges: Figure 1 suggests that the Ag clusters deposited from the gas aggregation cell may exhibit fivefold symmetry and an average size of about 3 nm, in good agreement with previous extended X-ray absorption fine-structure (EXAFS) studies.[15] Under the chosen conditions, their mean mutual distance is in the range of 4 – 8 nm. If these clusters are deposited onto the cleaved NaCl (100) surfaces, presumably steps act as efficient "traps" for the migrating clusters and, thereby, growth of prolate particles of truncated decahedra may take place besides the formation of large spherical particles resulting from isotropic agglomeration. Formation of the prolate particles along step edges had also been reported for other systems, for example, Au on NaCl (100)[16] and Au on CaF_2 (111).[17] It has to be emphasized, however, that the structure of the resulting rodlike particles is affected by their mode of preparation. In the case of thermal evaporation of atoms, they consist of stacked icosahedra.[16] Their formation is, on the other hand, not restricted to the presence of steps on the substrate surface found with the growth of needlelike CdS crystals with fivefold symmetry and lenghts of up to several micrometers.[18]

It is tempting to speculate on possibilities for increasing the fraction of the anisotropic nanoparticles which might exhibit novel physical properties.

[1] S. Ino, *J. Phys. Soc. Jpn.* **1969**, *27*, 941.
[2] K. Yagi, K. Takayanagi, K. Kobayashi, G. Honjo, *J. Cryst. Growth* **1975**, *28*, 117.
[3] D. J. Smith, L. D. Marks, *Philos. Mag. A* **1981**, *44*, 735.
[4] D. J. Smith, L. D. Marks, *J. Cryst. Growth* **1981**, *54*, 433.
[5] I. Lisiecki, A. Filankembo, H. Sack-Kongehl, K. Weiss, M.-P. Pileni, J. Urban, *Phys. Rev. B* **2000**, *61*, 4968.
[6] I. Lisiecki, H. Sack-Kongehl, K. Weiss, J. Urban, M.-P. Pileni, *Langmuir*, submitted.
[7] F. Frank, W. Schulze, B. Tesche, J. Urban, B. Winter, *Surf. Sci.* **1985**, *156*, 90.
[8] G. Nihoul, *Microsc. Microanal. Microstruct.* **1991**, *2*, 637.
[9] S. Giorgio, G. Nihoul, J. Urban, H. Sack-Kongehl, *Z. Phys. D* **1992**, *24*, 395.
[10] S. Giorgio, J. Urban, W. Kunath, *Philos. Mag. A* **1989**, *60*, 553.
[11] H. Abe, W. Schulze, B. Tesche, *Chem. Phys.* **1980**, *47*, 95.
[12] W. Schulze, F. Frank, K.-P. Charlé, B. Tesche, *Ber. Bunsenges. Phys. Chem.* **1984**, *88*, 263.
[13] A. Taylor, *X-Ray Metallography*, Wiley, New York, **1961**.
[14] C. N. J. Wagner, *Acta Metall.* **1957**, *5*, 477.
[15] P. A. Montano, J. Zhao, M. Ramanathan, G. K. Shenoy, W. Schulze, J. Urban, *Chem. Phys. Lett.* **1989**, *164*, 126.
[16] S. A. Nepijko, H. Hofmeister, H. Sack-Kongehl, R. Schlögl, *J. Cryst. Growth* **2000**, *213*, 129.
[17] J. Viereck, W. Hoheisel, F. Träger, *Surf. Sci.* **1995**, *340*, L988.
[18] A. E. Romanov, I. A. Polonsky, V. G. Gryaznov, S. A. Nepijko, T. Junghanns, N. I. Vitrykhovski, *J. Cryst. Growth* **1993**, *129*, 691.

Received: June 23, 2000 [Z 60]

Polarized Photoluminescence and Spectral Narrowing in an Oriented Polyfluorene Thin Film**

Christian Bauer,*[a] Gunter Urbasch,[a] Harald Giessen,[a]
Andreas Meisel,[b] Heinz-Georg Nothofer,[b]
Dieter Neher,[c] Ullrich Scherf,[b] and Rainer F. Mahrt[a, b]

KEYWORDS:

luminescence · oriented materials · polymers · optical properties · thin films

Since the early work of Burroughes et al. on polymeric light-emitting diodes (LED)[1] the emissive properties of conjugated polymers have received growing interest. Intense research not

---

[a] *C. Bauer, G. Urbasch, Dr. H. Giessen, Dr. R. F. Mahrt*
Fachbereich Physik
Institut für Physikalische Chemie
and Wissenschaftliches Zentrum für Materialwissenschaften
Philipps-Universität Marburg
Renthof 5, 35032 Marburg (Germany)
Fax: (+49)6421-2827036
E-mail: bauerc@mailer.uni-marburg.de

[b] *A. Meisel, H.-G. Nothofer, Dr. U. Scherf, Dr. R. F. Mahrt*
Max-Planck-Institut für Polymerforschung
Ackermannweg 10, 55128 Mainz (Germany)

[c] *Prof. Dr. D. Neher*
Institut für Physik
Universität Potsdam
Am Neuen Palais 10, 14469 Potsdam (Germany)

[**] *We thank G. Wegner, K. Müllen, W. Knoll, H. Bässler, and W. W. Rühle for stimulating discussions. The cooperation with Sony International (Europe) is gratefully acknowledged. The work was supported by the Deutsche Forschungsgemeinschaft (Sonderforschungsbereich 383) and the Volkswagen-Stiftung.*

only lead to improved LEDs with high efficiencies, long stability times, and spectral variety[2–4] but also to the observation of stimulated emission and even real lasing in these materials.[5–9] A challenging topic will be the future realization of an electrically pumped laser diode. In order to achieve high current densities and low driving voltages, the active layer in such devices will have a thickness of approximately 100 nm. Such thin polymer layers are most commonly prepared by spin coating. Due to the intrinsic disorder present in these polymer films, the transition dipole moments of the molecules exhibit no optimal configuration with regard to the absorption and emission of light. One way to overcome this restriction is the use of oriented materials, in which the transition dipole moments lie, preferably, parallel to each other; absorption of light polarized parallel to this direction is enhanced significantly. At the same time, polarized emission is observed. Today, the polarized emission of conjugated polymers is under close investigation.[10] Potential applications are polarized backlights in liquid crystal displays (LCDs),[11] light sources for integrated optics, and polarizing emissive filters.[12]

A promising class of materials for these applications are alkyl-substituted blue-emitting polyfluorenes.[13, 14] These polymers show thermotropic liquid crystallinity with the phase transition at 100 – 170 °C, dependent upon the chosen substituents. The polyfluorenes can be aligned using rubbed polyimide (PI) alignment layers. High orientational order leads to a strong anisotropy in both absorption and emission characteristics.[15, 16]

In this paper, we report on a combined study of femtosecond (fs) and steady-state spectroscopy of poly[9,9-di(ethylhexyl)-fluorene] **1**, a material with excellent alignment properties and pronounced dichroism.[17, 18] We present wavelength-dependent measurements of polarized photoluminescence (PL), where depolarization effects can be monitored. Additionally, the behavior at high excitation densities is examined. Spectral narrowing, which is clearly dependent on the polarization of the incident light is observed. Employing fs pump – probe measurements, positive differential transmission was found, which can be attributed to optical gain in this spectral regime.

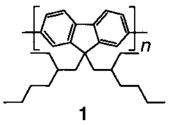

1

Figure 1 shows polarized absorption and photoluminescence (PL) spectra with respect to the alignment direction of the film. The absorption shows a broad, featureless band with its maximum centered at 3.25 eV. The sample exhibits a strong dichroism ($D \sim 12$) because the dipole transition moments are preferably oriented parallel to the alignment direction. The PL spectra were recorded using depolarized light (Hanle depolarizer) for excitation and with an analyzing polarizer in the detection light path. For both polarization directions, the PL spectra show a distinct structure with peaks at 2.93, 2.76, 2.56, and 2.39 eV caused by the vibronic coupling in the polymer. For the measured intensities, a maximum polarization ratio of $I_\mathrm{p}/I_\mathrm{s} \sim 14$ is found. Subscripts p (parallel) and s (perpendicular) refer to the detection polarization with respect to the alignment direction of the sample. This ratio is of similar magnitude as the value found for polarized electroluminescence (EL)[17] and the absorption dichroism of **1**.

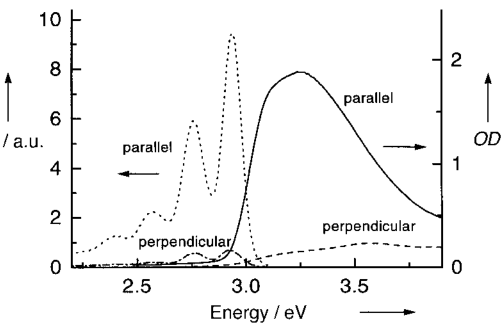

Figure 1. Absorption spectra at room temperature and photoluminescence (PL) spectra at 80 K with respect to the film alignment direction: parallel absorption (——), perpendicular absorption (- - - -), parallel PL (••••) and perpendicular PL (•–•–) (E_exc (PL) = 3.20 eV).

PL intensities have been measured for four different polarization configurations I_pp, I_ps, I_sp, and I_ss, where the subscripts denote polarization, the first of the excitation beam with respect to the film orientation and the second of the emitted light. The energy per laser pulse was 0.7 µJ. The detection energy was chosen to be 2.76 eV, which coincides with the peak of the $S_1 \rightarrow S_0$ (0-1) transition. This spectral position was selected to maximize the signal-to-noise ratio and to avoid the influence of reabsorption. Figure 2 shows the excitation-energy dependent polarization ratios after either parallel or perpendicular excitation with respect to the film orientation. The ratio $I_\mathrm{pp}/I_\mathrm{ps}$ remains fairly constant at a value of 12 over the whole range examined. If the excitation polarization is changed from parallel to perpendicular, the situation is different. Here, $I_\mathrm{sp}/I_\mathrm{ss}$ starts with a value of 6 at high energies and decreases significantly below an energy of about 3 eV. Results below 2.95 eV are not presented because of their low reliability caused by the poor absorption in this region.

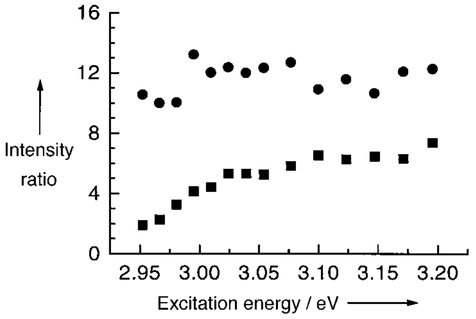

Figure 2. Dependence of the luminescence intensity ratios I_{pp}/I_{ps} (●) and I_{sp}/I_{ss} (■) on the excitation energy. The first subscript denotes the polarization of the incident beam, the second of the emitted light, with respect to the film alignment direction. The ratios were taken at a spectral position of 2.76 eV.

Adopting the concept of spectral relaxation in a Gaussian-like density of states (DOS),[19] the energy dependence of the polarization ratio indicates excitation localization below a certain localization threshold. Excitations located above this threshold move to energetically favorable sites, whereas below it, excitation decay from the primarily excited segments is more likely than further relaxation (see Figure 3 a). In this context, the

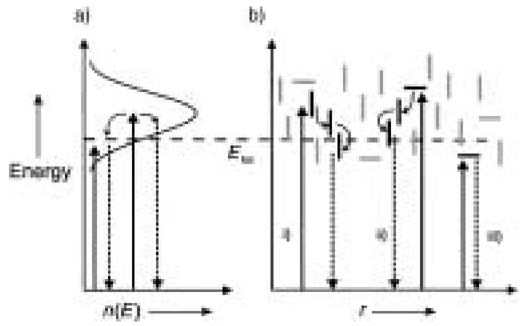

Figure 3. Schematic view of the energetic distribution of polymer segments. Vertical and horizontal lines represent aligned and unaligned molecules, respectively. n(E) *denotes the energy density,* r *is a generalized spatial coordinate, and* E_{loc} *represents the localization energy.*

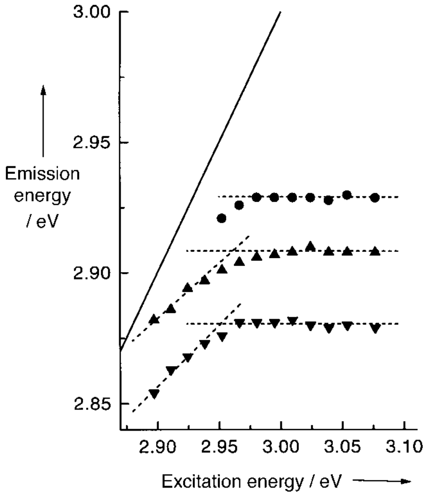

Figure 4. Energy of the $S_1 \rightarrow S_0$ *(0-0) (●; 2.93 eV), (0-1) (▲; 2.76 eV), and (0-2) (▼; 2.56 eV) transitions as a function of the excitation energy. The solid line represents the resonance line. Data for the emission peaks at 2.76 eV and 2.56 eV are shifted vertically for clarity. Dashed lines are guides to the eye.*

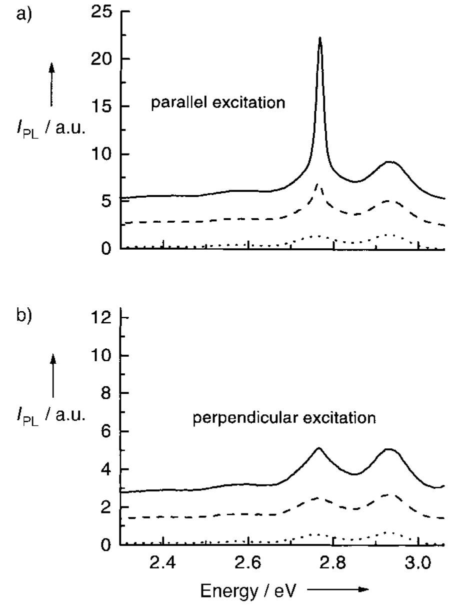

Figure 5. PL spectra at different excitation intensities. Excitation is (a) parallel and (b) perpendicular to the film alignment. The spectra are shifted vertically for clarity. The excitation energy was 3.1 eV. Energies per pump pulse are 0.5 (••••), 1.5 (- - -), and 5 μJ (——).

decrease in the value of I_{sp}/I_{ss} in Figure 2 while approaching the absorption edge can be explained. Above the threshold, perpendicular excited sites tend to relax to parallel oriented sites (see Figure 3 b ii). In their vicinity, they merely find sites with transition moments parallel to the film alignment direction and therefore lose their initial polarization. Thus at higher energies, the emitted light is mainly polarized parallel, rather than perpendicularly, to the film orientation. If, on the other hand, the polymer is excited below the localization energy, absorption and emission will take place at the same molecular segment (see Figure 3 b iii). The ratio I_{sp}/I_{ss} decreases significantly because perpendicular excited segments will emit light with the same polarization. This implies the existence of fluorescence depolarization after perpendicular excitation. In contrast to this, the relatively constant value of I_{pp}/I_{ps} over a wide range of excitation energies indicates that any fluorescence depolarization is weak for parallel excitation. The excitations keep their initial polarization during the relaxation process. Due to the high order within the film, they preferably jump to sites with the same orientation[20] (here parallel, see Figure 3 b i).

To check the validity of our explanation, we employed site-selective fluorescence spectroscopy (SSFS) on **1** in order to determine the localization energy, independent of polarization effects.[21, 22] Since there is no spectral relaxation at excitation energies below that threshold, the peak maximum of any optical transition shifts linearly with the excitation energy while it remains constant for higher excitation energies. In Figure 4, the emission energies of the dominant transitions are shown. It can be seen that at approximately 2.97 eV the spectral position of the emission follows the resonance line indicating the existence of a localization energy. This energetic value agrees well with the one observed from polarized PL measurements. The slight discrepancy of the shift with respect to the resonance line is probably due to the finite temperature or to interchain interaction in the dense polymer film.

Considering the high PL quantum efficiency of the polyfluorenes, these materials are promising candidates for lasing applications.[16, 23–25] Figure 5 shows the effect of increasing the intensity of the exciting laser beam on the PL spectra of **1**. During this measurement, the emitted light was collected independently of its polarization. At pulse energies larger than 1 μJ, a spectral narrowing of the $S_1 \rightarrow S_0$ (0-1) transition is observed in combination with a simultaneous superlinear increase of that peak. This is a clear indication of amplified spontaneous emission (ASE) which has been reported for several other conjugated polymers.[26–29] Spontaneously emitted photons are waveguided within the polymer film and cause stimulated emission of other segments. In the case of poly(9,9-dioctylfluorene) (PFO), Long et al.[23] also discussed the influence of superfluorescence but, for a detailed distinction, time-dependent PL measurements are necessary. In our case, we want to emphasize the difference between parallel and perpendicular excitation of the sample. As already mentioned, the parallel excitation leads to a clear spectral narrowing, whereas the situation for perpendicular excitation is different, as shown in Figure 5 b. At identical excitation conditions (same pump intensity) only a small change in peak shape is visible. This difference might be governed by the difference in excitation density due to the large dichroism of the sample. The results demonstrate that the high orientation of the polymer, which already has been shown by absorption and low intensity luminescence measurements, strongly affects the threshold for stimulated emission. Increasing the excitation energy over 15 µJ per pulse, the effect of spectral narrowing decreases (not shown here). This is probably caused by structural damage of the film due to excessive energy input.

To further investigate the subject of gain narrowing, we performed time-resolved pump – probe measurements. Figure 6 shows the transient differential transmission (DT) at different times after the excitation pulse. The excitation energy was 5 nJ per pump pulse. Both pulses were polarized parallel to the alignment direction of the polymer film. The large positive signal for energies higher than 2.9 eV is due to bleaching of the ground state. The positive signal between 2.5 eV and 2.9 eV, however, can be attributed to stimulated emission because there is no significant absorption in this spectral region (see Figure 1). The spacing of the two peaks corresponds to the vibronic progression of about 200 meV as found in the PL measurements. The appearance of line narrowing, as shown in Figure 5, depends critically on the actual absorption at this spectral position. Only at spectral positions where the positive differential transmission signal, $-\Delta\alpha L$, exceeds that of the linear absorption (αL) is optical gain present.[30] Thus at the maximum of the optical gain, line narrowing in the emission is observed. The energetic difference between the occurrence of line narrowing in Figure 5 and the maximum of differential transmission in Figure 6 can therefore be explained. The red shift of the $S_1 \rightarrow S_0$ (0-1) transition with time towards the value of steady-state PL is due to the spectral relaxation within the DOS already mentioned.

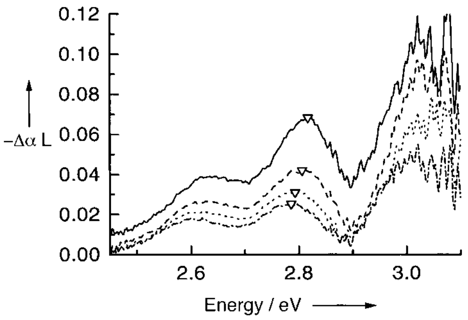

Figure 6. Temporal evolution of the differential transmission spectrum after an excitation at 3.1 eV with a pump power of 5 µW. The triangles ▽ indicate the maximum of the $S_1 \rightarrow S_0$ (0-1) stimulated emission band. Pump and probe pulses are both polarized parallel to the sample orientation. The time delays between the pump and probe pulses are 0.1 (——), 0.5 (– – –), 1 (••••), and 2 ps (•–•–). $-\Delta\alpha$ denotes the photoinduced change of the absorption coefficient α and L is the film thickness.

In conclusion, the photophysical behavior of aligned layers of the alkyl-substituted polyfluorene **1** can be fully explained in terms of spectral relaxation: Due to the high order of the oriented films, fluorescence depolarization for parallel excitation is effectively suppressed, however, excitation-dependent loss of polarization memory is observed for perpendicular excitation. Site-selective fluorescence spectroscopy confirmed the existence of a localization energy, in accordance with a value determined from the polarization measurements. At high excitation densities, spectral narrowing was observed exclusively when the sample was illuminated with light polarized parallel to the film alignment direction, while fs pump – probe measurements showed positive differential transmission due to optical gain at this spectral position. The use of oriented polymers as emitting materials can be helpful in reducing the threshold for an optically pumped polymer laser.

Experimental Section

Polymer **1** was synthesized using a polycondensation procedure, as described previously.[17] The polystyrene-equivalent molecular masses were $M_n = 127\,000$ and $M_w = 210\,000$. These molecular weights seem to be slightly overestimated due to the rigid structure of the polyfluorene backbone.[15] The PI precursor (ZLI 2650 kit from Merck, Darmstadt) for the orientation layers was first spin-coated onto a glass substrate, then thermally converted to the final PI layer at 300 °C (thickness 50 nm), which was subsequently rubbed unidirectionally. Films of **1** were then spun onto the PI layer from a toluene solution (10 g L^{-1}) at 2000 rpm to obtain a polyfluorene film about 80 nm thick. Monodomain alignment was achieved by annealing the samples in a CO$_2$ atmosphere (0.1 bar) for two hours at 180 °C. The samples were rapidly cooled to transfer the orientation into a glassy state.

Absorption spectra were recorded using a Lambda 9 UV/VIS spectrometer (Perkin – Elmer), equipped with additional polarizers. The PL spectroscopy was carried out with an excimer pumped dye-laser system (10 Hz repetition rate, 20 ns pulse width). The pulse energies could be tuned between 0.5 – 50 µJ, dependent on the dye. The emitted light was detected in backscattering geometry by an optical multichannel analyzer (OMA), which consisted of a 0.27 m monochromator in conjunction with a liquid-nitrogen cooled CCD camera (resolution 10 meV). The measurements were performed in a cryostat (10^{-4} mbar pressure) at approximately 80 K. Site-selective fluorescence spectra were recorded at approximately 30 K. Glan – Thomson polarizers were placed in the excitation and the emission light paths. In front of the OMA, a broad range quarter-wave plate was inserted to minimize polarization effects due to the monochromator grating.

Differential transmission spectra were recorded using a pump – probe setup. The second harmonic of the output of a Ti:sapphire amplifier system (photon energy 3.1 eV) was used as the pump source. The pulse width was 200 fs at 1 kHz repetition rate with a pulse energy of 5 nJ. The pump focus diameter was approximately 80 µm. A fraction of the second harmonic beam was focused onto a sapphire crystal to generate a white light continuum between 2.4 – 3.1 eV. This was used as probe light to detect the photoinduced absorption change of the film. The sample was kept under vacuum at 20 K. The differential transmission spectra were corrected for the chirp of the white-light continuum.

[1] J. H. Burroughes, D. D. C. Bradley, A. R. Brown, R. N. Marks, K. Mackay, R. H. Friend, P. L. Burns, A. B. Holmes, *Science* **1990**, *347*, 539.
[2] D. Braun, A. J. Heeger, *Appl. Phys. Lett.* **1991**, *58*, 1982.
[3] J. R. Sheats, H. Antoniadis, M. Hueschen, W. Leonhard, J. Miller, R. Moon, D. Roitmann, A. Stocking, *Science* **1996**, *273*, 884.
[4] R. H. Friend, R. W. Gymer, A. B. Holmes, J. H. Burroughes, R. N. Marks, C. Taliani, D. D. C. Bradley, D. A. Dos Santos, J. L. Brédas, M. L. Löglund, W. R. Salaneck, *Nature* **1999**, *297*, 121.
[5] N. Tessler, G. J. Denton, R. H. Friend, *Nature* **1996**, *382*, 695.
[6] G. Wegmann, H. Giessen, D. Hertel, R. F. Mahrt, *Solid State Commun.* **1997**, *104*, 759.
[7] A. Schülzgen, C. Spiegelberg, M. M. Morell, S. B. Mendes, B. Kippelen, N. Peyghambarian, M. F. Nabor, E. A. Mash, P. M. Allemand, *Appl. Phys. Lett.* **1997**, *72*, 269.
[8] M. Berggren, A. Dodabalapur, R. E. Slusher, A. Timko, O. Nalamasu, *Appl. Phys. Lett.* **1997**, *72*, 410.
[9] S. V. Frolov, Z. V. Shkunov, Z. V. Vardeny, K. Yoshino, *Phys. Rev. B* **1997**, *56*, R4363.
[10] M. Grell, D. D. C. Bradley, *Adv. Mater.* **1999**, *11*, 895.
[11] P. Dyreklev, M. Berggren, O. Inganäs, M. R. Andersson, O. Wennerström, T. Hjertberg, *Adv. Mater.* **1995**, *7*, 43.
[12] A. Montali, C. Bastiaansen, P. Smith, C. Weder, *Nature* **1998**, *392*, 261.
[13] M. Grell, D. D. C. Bradley, M. Inbasekaran, E. P. Woo, *Adv. Mater.* **1997**, *9*, 798.
[14] J. Teetsov, M. A. Fox, *J. Mater. Chem.* **1999**, *9*, 2117.
[15] M. Grell, D. D. C. Bradley, X. Long, T. Chamberlain, M. Inbasekaran, E. P. Woo, M. Soliman, *Acta Polym.* **1998**, *49*, 439.
[16] X. Long, M. Grell, A. Malinowski, D. D. C. Bradley, *Opt. Mater.* **1998**, *9*, 70.
[17] M. Grell, W. Knoll, D. Lupo, A. Meisel, T. Miteva, D. Neher, H.-G. Nothofer, U. Scherf, A. Yasuda, *Adv. Mater.* **1999**, *11*, 671.
[18] T. Miteva, A. Meisel, M. Grell, H.-G. Nothofer, D. Lupo, A. Yasuda, W. Knoll, L. Kloppenburg, U. H. F. Bunz, U. Scherf, D. Neher, *Synth. Met.* **2000**, *111 – 112*, 173.
[19] U. Rauscher, H. Bässler, D. D. C. Bradley, M. Hennecke, *Phys. Rev. B* **1990**, *42*, 9830.
[20] B. Schartel, V. Wachtendorf, M. Grell, D. D. C. Bradley, M. Hennecke, *Phys. Rev. B* **1999**, *60*, 277.
[21] H. Bässler in *Optical Techniques To Characterize Polymer Systems* (Ed.: H. Bässler), Elsevier, Amsterdam, **1989**, p. 181.
[22] S. Heun, R. F. Mahrt, A. Greiner, U. Lemmer, H. Bässler, *J. Phys. C* **1993**, *5*, 247.
[23] X. Long, A. Malinowski, D. D. C. Bradley, M. Inbasekaran, E. P. Woo, *Chem. Phys. Lett.* **1997**, *272*, 6.
[24] M. N. Shkunov, R. Österbacka, A. Fujii, K. Yoshino, Z. V. Vardeny, *Appl. Phys. Lett.* **1999**, *74*, 1648.
[25] T. Virgili, D. G. Lidzey, D. D. C. Bradley, G. Cerullo, S. Stagira, S. De Silvestri, *Appl. Phys. Lett.* **1999**, *74*, 2767.
[26] F. Hide, M. A. Díaz-García, B. J. Schwartz, M. R. Andersson, Q. Pei, A. J. Heeger, *Science* **1996**, *273*, 1833.
[27] G. H. Gelinck, J. M. Warman, M. Remmers, D. Neher, *Chem. Phys. Lett.* **1997**, *265*, 320.
[28] G. J. Denton, N. Tessler, M. A. Stevens, R. H. Friend, *Adv. Mater.* **1997**, *9*, 547.
[29] B. Schweitzer, G. Wegmann, H. Giessen, H. Bässler, R. F. Mahrt, *Appl. Phys. Lett.* **1998**, *72*, 2933.
[30] G. Wegmann, B. Schweitzer, D. Hertel, M. Oestreich, U. Scherf, K. Müllen, R. F. Mahrt, *Chem. Phys. Lett.* **1999**, *312*, 376.

Received: May 18, 2000 [Z 32]

Chiral J-Aggregates Formed by Achiral Cyanine Dyes[**]

Stefan Kirstein,*[a] Hans von Berlepsch,[a]
Christoph Böttcher,[b] Christian Burger,[a] Andre Ouart,[c]
Günter Reck,[d] and Siegfried Dähne[d]

KEYWORDS:

chirality · dyes · helical structures · J-aggregates

Self-organization of molecular species into chiral supramolecular structures is a fundamental building principle in living materials and found in various systems ranging from double-stranded DNA to complex structures like the tobacco mosaic virus. In all natural systems, only one type of the two possible enantiomers is found, namely they are enantiomerically pure. Although this observation has attracted much research interest during the last decades, two basic questions are still open: How is the chiral structure of the molecular building block transmitted into a chiral superstructure of large, sometimes micrometer sized, molecular assemblies, and what was the reason for the spontaneous break in symmetry between the two possible enantiomeric structures, which in ancient times must have happened in nature? Both questions are currently addressed by investigating various artificial systems; for example, the spontaneous break in symmetry was mostly studied on crystals formed by nonchiral molecules.[1, 2] Recently, for liquid crystals, a spontaneous formation of macroscopic chiral domains from achiral molecules was reported.[3] Many other systems are known where macroscopic chirality is induced by chirality of the molecules, such as helicenes,[4, 5] helical metal complexes,[6] block copolymers,[7] gemini surfactants,[8] or the coiled aggregates of (crown ether

---

[a] *S. Kirstein,[+] H. von Berlepsch, C. Burger*
Max-Planck-Institute for Colloids and Interfaces
Am Mühlenberg 2, 14476 Golm/Potsdam (Germany)
Fax: (+49) 30-2093-7832
E-mail: kirstein@physik.hu-berlin.de

[b] *C. Böttcher*
Freie Universität Berlin
Takustrasse 3, 14195 Berlin (Germany)

[c] *A. Ouart*
Federal Institute for Materials Research and Testing
Rudower Chaussee 5, 12489 Berlin (Germany)

[d] *G. Reck, S. Dähne*
Institute of Chemistry
Humboldt-Universität zu Berlin
Hessische Strasse 1 – 2, 10115 Berlin (Germany)

[+] *Current address:*
Institute of Physics
Humboldt-Universität zu Berlin
Invalidenstr. 110, 10115 Berlin (Germany)

[**] *This work was supported by the Deutsche Forschungsgemeinschaft (Ki 544/3-1, Da 268/6-2, and Ab 74/5-2) and the Max Planck Society, which we gratefully acknowledge. We thank Professors H. Möhwald, H.-W. Abraham, and J.-H. Fuhrhop for generous support and encouraging discussions. We are also obliged to Christian Spitz for his constructive criticism and contributions.*

[1] J. H. Burroughes, D. D. C. Bradley, A. R. Brown, R. N. Marks, K. Mackay, R. H. Friend, P. L. Burns, A. B. Holmes, *Science* **1990**, *347*, 539.
[2] D. Braun, A. J. Heeger, *Appl. Phys. Lett.* **1991**, *58*, 1982.
[3] J. R. Sheats, H. Antoniadis, M. Hueschen, W. Leonhard, J. Miller, R. Moon, D. Roitmann, A. Stocking, *Science* **1996**, *273*, 884.
[4] R. H. Friend, R. W. Gymer, A. B. Holmes, J. H. Burroughes, R. N. Marks, C. Taliani, D. D. C. Bradley, D. A. Dos Santos, J. L. Brédas, M. L. Löglund, W. R. Salaneck, *Nature* **1999**, *297*, 121.
[5] N. Tessler, G. J. Denton, R. H. Friend, *Nature* **1996**, *382*, 695.
[6] G. Wegmann, H. Giessen, D. Hertel, R. F. Mahrt, *Solid State Commun.* **1997**, *104*, 759.
[7] A. Schülzgen, C. Spiegelberg, M. M. Morell, S. B. Mendes, B. Kippelen, N. Peyghambarian, M. F. Nabor, E. A. Mash, P. M. Allemand, *Appl. Phys. Lett.* **1997**, *72*, 269.
[8] M. Berggren, A. Dodabalapur, R. E. Slusher, A. Timko, O. Nalamasu, *Appl. Phys. Lett.* **1997**, *72*, 410.
[9] S. V. Frolov, Z. V. Shkunov, Z. V. Vardeny, K. Yoshino, *Phys. Rev. B* **1997**, *56*, R4363.
[10] M. Grell, D. D. C. Bradley, *Adv. Mater.* **1999**, *11*, 895.
[11] P. Dyreklev, M. Berggren, O. Inganäs, M. R. Andersson, O. Wennerström, T. Hjertberg, *Adv. Mater.* **1995**, *7*, 43.
[12] A. Montali, C. Bastiaansen, P. Smith, C. Weder, *Nature* **1998**, *392*, 261.
[13] M. Grell, D. D. C. Bradley, M. Inbasekaran, E. P. Woo, *Adv. Mater.* **1997**, *9*, 798.
[14] J. Teetsov, M. A. Fox, *J. Mater. Chem.* **1999**, *9*, 2117.
[15] M. Grell, D. D. C. Bradley, X. Long, T. Chamberlain, M. Inbasekaran, E. P. Woo, M. Soliman, *Acta Polym.* **1998**, *49*, 439.
[16] X. Long, M. Grell, A. Malinowski, D. D. C. Bradley, *Opt. Mater.* **1998**, *9*, 70.
[17] M. Grell, W. Knoll, D. Lupo, A. Meisel, T. Miteva, D. Neher, H.-G. Nothofer, U. Scherf, A. Yasuda, *Adv. Mater.* **1999**, *11*, 671.
[18] T. Miteva, A. Meisel, M. Grell, H.-G. Nothofer, D. Lupo, A. Yasuda, W. Knoll, L. Kloppenburg, U. H. F. Bunz, U. Scherf, D. Neher, *Synth. Met.* **2000**, *111 – 112*, 173.
[19] U. Rauscher, H. Bässler, D. D. C. Bradley, M. Hennecke, *Phys. Rev. B* **1990**, *42*, 9830.
[20] B. Schartel, V. Wachtendorf, M. Grell, D. D. C. Bradley, M. Hennecke, *Phys. Rev. B* **1999**, *60*, 277.
[21] H. Bässler in *Optical Techniques To Characterize Polymer Systems* (Ed.: H. Bässler), Elsevier, Amsterdam, **1989**, p. 181.
[22] S. Heun, R. F. Mahrt, A. Greiner, U. Lemmer, H. Bässler, *J. Phys. C* **1993**, *5*, 247.
[23] X. Long, A. Malinowski, D. D. C. Bradley, M. Inbasekaran, E. P. Woo, *Chem. Phys. Lett.* **1997**, *272*, 6.
[24] M. N. Shkunov, R. Österbacka, A. Fujii, K. Yoshino, Z. V. Vardeny, *Appl. Phys. Lett.* **1999**, *74*, 1648.
[25] T. Virgili, D. G. Lidzey, D. D. C. Bradley, G. Cerullo, S. Stagira, S. De Silvestri, *Appl. Phys. Lett.* **1999**, *74*, 2767.
[26] F. Hide, M. A. Díaz-García, B. J. Schwartz, M. R. Andersson, Q. Pei, A. J. Heeger, *Science* **1996**, *273*, 1833.
[27] G. H. Gelinck, J. M. Warman, M. Remmers, D. Neher, *Chem. Phys. Lett.* **1997**, *265*, 320.
[28] G. J. Denton, N. Tessler, M. A. Stevens, R. H. Friend, *Adv. Mater.* **1997**, *9*, 547.
[29] B. Schweitzer, G. Wegmann, H. Giessen, H. Bässler, R. F. Mahrt, *Appl. Phys. Lett.* **1998**, *72*, 2933.
[30] G. Wegmann, B. Schweitzer, D. Hertel, M. Oestreich, U. Scherf, K. Müllen, R. F. Mahrt, *Chem. Phys. Lett.* **1999**, *312*, 376.

Received: May 18, 2000 [Z 32]

Chiral J-Aggregates Formed by Achiral Cyanine Dyes**

Stefan Kirstein,*[a] Hans von Berlepsch,[a]
Christoph Böttcher,[b] Christian Burger,[a] Andre Ouart,[c]
Günter Reck,[d] and Siegfried Dähne[d]

KEYWORDS:

chirality · dyes · helical structures · J-aggregates

Self-organization of molecular species into chiral supramolecular structures is a fundamental building principle in living materials and found in various systems ranging from double-stranded DNA to complex structures like the tobacco mosaic virus. In all natural systems, only one type of the two possible enantiomers is found, namely they are enantiomerically pure. Although this observation has attracted much research interest during the last decades, two basic questions are still open: How is the chiral structure of the molecular building block transmitted into a chiral superstructure of large, sometimes micrometer sized, molecular assemblies, and what was the reason for the spontaneous break in symmetry between the two possible enantiomeric structures, which in ancient times must have happened in nature? Both questions are currently addressed by investigating various artificial systems; for example, the spontaneous break in symmetry was mostly studied on crystals formed by nonchiral molecules.[1, 2] Recently, for liquid crystals, a spontaneous formation of macroscopic chiral domains from achiral molecules was reported.[3] Many other systems are known where macroscopic chirality is induced by chirality of the molecules, such as helicenes,[4, 5] helical metal complexes,[6] block copolymers,[7] gemini surfactants,[8] or the coiled aggregates of (crown ether

---

[a] *S. Kirstein,[+] H. von Berlepsch, C. Burger*
Max-Planck-Institute for Colloids and Interfaces
Am Mühlenberg 2, 14476 Golm/Potsdam (Germany)
Fax: (+49) 30-2093-7832
E-mail: kirstein@physik.hu-berlin.de

[b] *C. Böttcher*
Freie Universität Berlin
Takustrasse 3, 14195 Berlin (Germany)

[c] *A. Ouart*
Federal Institute for Materials Research and Testing
Rudower Chaussee 5, 12489 Berlin (Germany)

[d] *G. Reck, S. Dähne*
Institute of Chemistry
Humboldt-Universität zu Berlin
Hessische Strasse 1 – 2, 10115 Berlin (Germany)

[+] *Current address:*
Institute of Physics
Humboldt-Universität zu Berlin
Invalidenstr. 110, 10115 Berlin (Germany)

[**] *This work was supported by the Deutsche Forschungsgemeinschaft (Ki 544/3-1, Da 268/6-2, and Ab 74/5-2) and the Max Planck Society, which we gratefully acknowledge. We thank Professors H. Möhwald, H.-W. Abraham, and J.-H. Fuhrhop for generous support and encouraging discussions. We are also obliged to Christian Spitz for his constructive criticism and contributions.*

phthalocyaninato) polysiloxanes,[9] to name a few. Other systems which have attracted particular interest within this context are Langmuir monolayers, where the influence of the chirality of lipid molecules on the structure formation of crystalline domains has been investigated,[10] where spontaneous chiral segregation from a racemic mixture of lipids was observed.[11] In all cases, the resulting meso- or macroscopic structure is determined by various intermolecular interactions, such as van der Waals and electrostatic forces, covalent and hydrogen bonding, and, in the case of amphiphilic molecules, hydrophobic interactions[12] to include the interactions with surrounding solvent molecules. Therefore, it is a nearly impossible task to predict the structure and morphology of aggregated systems from the molecular structure in spite of the substantial progress made in molecular modelling.

Self-organisation in polar solutions is a common feature of dye molecules which contain extended planar π-electron systems.[13] Compared to surfactants, in dyes the complexity of the intermolecular force balance is increased by very strong dispersion forces, which are induced by fluctuation of the delocalized π-electrons. A peculiar class of aggregating dyes is represented by the cyanine dyes, which form J-aggregates in polar solvents.[14–18] These aggregates are characterized by a new optical absorption band, which is red-shifted and significantly narrowed with respect to the monomeric absorption, accompanied by an intense and nearly resonant fluorescence emission. The spectroscopic behavior of J-aggregates has been extensively investigated[19–21] and is now well understood in terms of molecular excitons.[22, 23] However, the structure and morphology of J-aggregates in solution is still unknown. Structure determinations published so far were performed on J-aggregates immersed into polymeric films[24] or adsorbed on solid/air[25] or liquid/air interfaces.[26] Only very recently the mesoscopic structure of J-aggregates of certain amphiphilic cyanine dyes has been revealed by cryo-transmission electron microscopy (cryo-TEM).[27, 28] Here, helical J-aggregates are presented, which are spontaneously formed by a nonchiral amphiphilic cyanine dye in aqueous sodium hydroxide solution. The reason for the induced chirality is revealed by X-ray structure analysis of a single crystal.

The dye molecule **C8O3** (5,5′,6,6′-tetrachloro-1,1′-dioctyl-3,3′-di-(3-carboxypropyl)-benzimidacarbocyanine; Scheme 1) combines structure formation abilities known from soluble surfactants with the outstanding optical properties of J-aggregates. The molecule is related to the more prominent dye **TDBC** (5,5′,6,6′-tetrachloro-1,1′-diethyl-3,3′-di-(4-sulfobutyl)-benzimidacarbocyanine; Scheme 1). From these dyes, it is known that their J-aggregates exhibit very strong coupling between the transition dipole moments of neighboring molecules and hence, very strong exciton delocalization over at least ten molecules at room temperature[29] and about 100 molecules at 1.5 K.[20] The J-aggregates of **C8O3** show exciton splitting of the J-absorption band combined with optical activity.[30] In Figure 1, the absorption and CD spectra of a 6.5 μM solution of **C8O3** are shown. The J-aggregate is characterized by three strong absorption bands located at 600, 580, and 562 nm, respectively. The J-aggregate spectrum of **TDBC**, indicated by the dashed line, shows a small peak around 520 nm, caused by residual monomers.

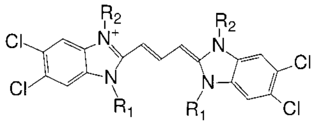

Scheme 1. *Chemical structure of the chromophore of the cyanine dyes.* ***C8O3****:* $R_1 = C_8H_{17}$, $R_2 = C_3H_6COOH$; ***TDBC****:* $R_1 = C_2H_7$, $R_2 = C_4H_8SO_3^-$.

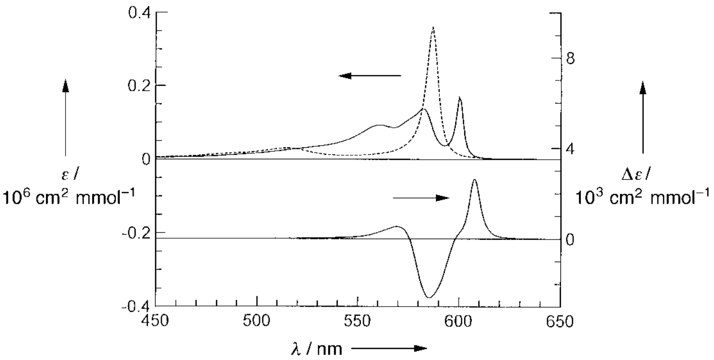

Figure 1. *Absorption (left scale) and CD spectrum (right scale) of a 6.5 μM solution of* ***C8O3*** *dissolved in 0.01 M NaOH. Crystalline material was dissolved directly by stirring for 24 h. The absorption spectrum of* ***TDBC*** *at same concentration is shown by the dashed line as a reference.*

The CD spectra of different solutions always showed the same sign of the bands, whereas the total intensity fluctuated between samples. Two positive bands are present with maxima at 610 and 570 nm and one negative band at 585 nm. The position of CD bands are not identical to the maxima of the absorption bands, which indicates that the CD spectrum is caused by chirality and not by linear dichroism of partially oriented samples. In the latter case, differently polarized absorption bands would appear as positive and negative bands in a CD spectrum, with their maximum at the same position as in the absorption spectrum.[31]

The occurence of the three bands in the absorption spectra of **C8O3** is caused by exciton splitting of the J-aggregate band. The observed optical activity must be due to excitonic coupling between several molecules of a chiral or helical aggregate. The intensity of the CD signal $\Delta\varepsilon$, normalized to the extinction coefficient ε, is in the order of $\Delta\varepsilon/\varepsilon \approx 10^{-3}$ and suggests a nonracemic mixture of right- and left-handed aggregates with a large excess of one type. However, the CD strength varied between samples, to indicate that the aggregate solutions cannot be enantiomerically pure. It is also not possible to conclude unambiguously from the CD spectra on the sense of the helicity because the sign of the CD couplet also depends on the sign of the intermolecular coupling energy and, hence, on the geometrical arrangement of the molecules.[31] Although the molecular structure is still unknown, one can assume from the red-shifted J-aggregate band that an acute angle is formed between the molecular transition moments, which contribute to the chiral excitonic transition.[32] In this case, right-handed aggregates would be predicted from the positive CD couplet at 610 and 585 nm.

The mesoscopic structure of the J-aggregates was resolved with cryo-TEM. Ropelike structures with lengths of several micrometers and diameters ranging from 20 to more than 50 nm were found as presented in Figure 2. The aggregates consist of multiple "strands" twisted around each other. The number of strands was constant within a single aggregate but varied between aggregates from three and more than ten. Occasionally, the splitting of an aggregate into two bundles was observed. At the lower edge of Figure 2 a rarely observed single strand is visible; its shape can be clearly identified as a cylindrical structure.

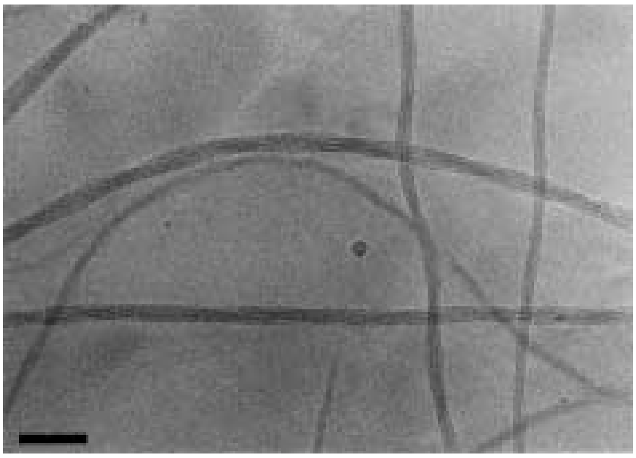

Figure 2. *Cryo-TEM picture of a 2.8 × 10^{-4} M solution of **C8O3**. Ropelike aggregates containing different numbers of individual strands can be identified. The scale bar corresponds to 100 nm.*

The appearance of the aggregates in the TEM pictures was qualitatively modeled by computer simulations. The projection of the electron density of a model superhelix was calculated, which consists of five single hollow cylinders (tubules) with diameters of approximately 10 nm, arranged on a trigonal lattice, and with a left-handed twist around a helical axis. The left-handed helicity was chosen arbitrarily; the same projected view could also be obtained for right-handed aggregates. For this example, the total pitch, defined as the distance over which all cylinders have rotated fully, is in the range of 400 nm. In Figure 3, the original TEM picture (a) of a single superhelix having five single strands is compared with the calculated image (c) obtained from the model (b). The model of a five-stranded superhelix shown here was created by using the same parameters as the model of a four-stranded helix presented in our previous work.[27] The excellent agreement of the calculated and original pictures confirms the validity of the modelling procedure.

Figure 3. *a) Cryo-TEM picture of one **C8O3** J-aggregate that consists of five single strands. b) A simple model, that consists of a bundle of tubules that are packed on a trigonal lattice and twisted around each other. c) The calculated image of the J-aggregate, derived from the model in (b). The scale bar corresponds to 50 nm.*

The handedness of the aggregates was determined by oblique shadowing of samples after their transfer to solid substrates as described in ref. [27]. A majority of left-handed aggregates was found in most of the pictures, although the right-handed type appeared as well. The existence of predominantly left-handed aggregates seems to contradict the conclusion drawn from the CD measurements, which suggests the existence of right-handed helices. However, it is not unlikely that the optical activity is caused by the arrangement of the molecules in the single strands, whose sign might have the opposite sense compared to the mesoscopic structure of the superhelices. A similar behavior has recently been reported for a system of chemically linked porphyrins[9] and is a general feature found in twisted ropes.

To understand the ultimate origin of the spontaneous generation of chiral helices from nonchiral molecules, a detailed structure analysis on a molecular scale would be required. Although no such data are available, valuable information can be drawn from the X-ray structure analysis of a single crystal of **C8O3**;[33] see Figure 4. The triclinic unit cell is composed of two slightly different conformers, A and B, and their centrosymmetric mirror images, A′ and B′. The molecules A and B (A′ and B′) are paired with an average interplanar distance of the chromophores of 3.54 Å, which is a typical value for molecular packing in J-aggregates.[21] The conjugated π-electron system (colored in blue) of the A-type molecules is strictly planar; all dihedral angles are less than 1.7°. However, the B-type chromophores are twisted along the trimethine backbone by an angle of approximately 18° with left-handed symmetry for B but right-handed symmetry for B′. This torsion angle is indicated in Figure 4b by the twisted position of the four green chlorine atoms and is

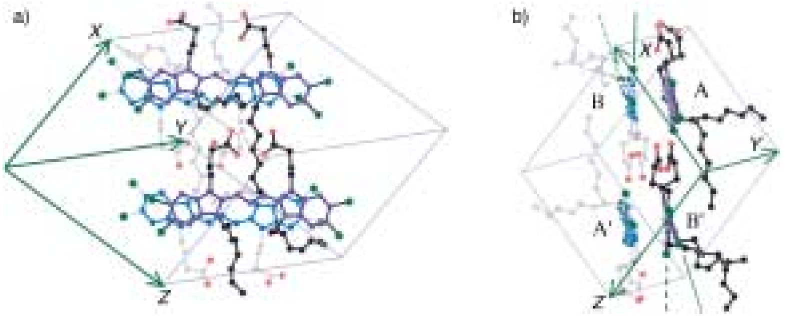

Figure 4. Molecular structure of a single crystal of ***C8O3*** *of dimensions $0.4 \times 0.25 \times 0.2$ mm^3, as revealed by X-ray diffraction analysis. The triclinic unit cell ($a = 16.581$, $b = 17.340$, $c = 19.245$ Å, $\alpha = 64.45$, $\beta = 76.62$, $\gamma = 64.18°$) consists of four molecules, in which two (A′, B′) are point symmetric with respect to the other ones (A, B). a) A view normal to the molecular plane, defined by the π-conjugated chromophore system (marked blue). The molecules in the background are colored in light blue. b) A view on the small edge of the molecular plane. The planar structure of the molecules A, A′ and the twisted structure of B and B′ are clearly visible from the green chlorine atoms and indicated by dashed lines. The average distance between the planes of molecule A to B and A′ to B′ is 3.54 Å. The DMSO molecules, which are also found in the crystal, are not shown here.*

emphasized by the dotted lines. It is important to note that, within the crystal lattice, this molecular twist occurs in a strictly racemic ratio. The coexistence between planar and twisted molecular structures indicates that the activation energy of dihedral torsions along the polymethine chain is low and, thus, the molecules can be easily twisted if it is favorable for the molecular packing.

The reason for the occurance of planar and twisted structures in the crystal lattice is the position and orientation of the carboxy groups. In case of the A type molecules, the carboxy groups are pointing towards a uniform direction, which alternates between A and A′ molecules. The distance between the carboxy groups of A and A′ in two neighboring unit cells is 2.97 Å, which enables *intermolecular* hydrogen bonding. The carboxy groups of the B molecules are directed with their oxygen atoms towards each other, forming *intramolecular* hydrogen bonds. In order to bring the carboxy groups to a close proximity, the trialkyl chains of the B molecules have to be arranged in an antisymmetric orientation, as seen in Figure 4b. It seems that this out-of-plane orientation of the carboxypropyl chains is responsible for the twist of the chromophores. This is supported by a recent investigation of the aggregates and crystallites of a slightly modified molecule, in which these chains are enlarged by one methylene group: In this case, no chirality was observed within the aggregates.[34] It is assumed that the longer carboxybutyl chains are more flexible and, thus, the intramolecular hydrogen bonds between the carboxy groups can be formed without disturbing the planarity of the molecules.

Due to the peculiarities of the aqueous environment, many of the structural features of the crystals may be lost in solution. For example, in the crystal lattice, the octyl chains are packed closely to the carboxypropyl groups in order to bring the chromophoric planes close together in a pairwise arrangement. In aqueous solutions, the preferred structures have the hydrophobic chains covered by hydrophilic moieties, as it is the case of surfactant micelles.[12] Therefore, the amphiphilic dye **C8O3** is expected to form bilayers or micellar structures in solution. However, a micellar structure cannot be judged from the TEM pictures presented in Figure 3, since a 10 nm tubule diameter is contradictory to the assumption of a cylindrical micelle filled with an alkyl chain. Such a model was proposed in our earlier work for similar dyes with longer alkyl chains.[34, 35] Here, the molecular architecture of the aggregates must be more complex than it is expected from models of simple surfactant systems.

The generation of helical aggregates might be explained by the result that part of the molecules are in a twisted state within the crystal (B molecules). Since the molecular chirality is originating from intramolecular hydrogen bonds of the B molecules, it may be conserved even in solution. The twisted molecules may then serve as chiral building units for the growth of helical aggregates. Planar molecules (A molecules) or those of opposite handedness may easily change to the same handedness when they attach to a given aggregate, due to the torsional flexibility of the trimethine chain. However, since the chirality of the B molecules occurs in a strictly racemic ratio, one would expect the growth of J-aggregates with an equal ratio of both handedness and no net CD effect should be observable. Such a racemic ratio of chiral J-aggregates was reported previously for pseudoisocyanine (PIC), whose molecules are strongly twisted due to steric hinderances.[36]

The spontaneous break of symmetry in the formation of J-aggregates from **C8O3** requires an additional explanation. One possibility could be that a certain excess of one enantiomer of the dye is found at the surface of the crystallites, since all solutions are prepared by dissolving crystalline material. In this case, small nuclei are formed from the surface molecules which are dissolved first and, hence, the enantiomeric excess at the crystal surface might be transferred to the aggregate morphology. Another mechanism might be the transfer of chirality from fragments of larger aggregates to newly formed nuclei, as it was proposed for the formation of crystals of sodium chlorate.[1] The suggestion that the chirality of small nuclei is frozen in micrometer long J-aggregates is further supported by the observation that the sense of chirality of the aggregates could not be influenced or reversed by addition of large amounts of enantiomerically pure tartrate.[37] This would require a collective rearrangement of all molecules; however, the energy barrier for such a process is too high and, hence, the initially determined helicity is conserved.

The J-aggregates of **C8O3** presented here are an ideal tool to investigate the influence of the molecular structure and environmental conditions on the asymmetric generation of chiral supramolecular materials. In contrast to other chiral supramolecular systems, the asymmetric generation of helical aggregates is not initiated by chiral auxiliaries. The enantiomeric symmetry is spontaneously broken at a primary state of nucleation which is not hitherto understood. Once generated, the preferred handedness is templated to the J-aggregates during the period of growth to micrometer-long bundles of cylindrical structures. Their morphological complexity was not predictable from the simple one- or two-dimensional J-aggregate models that are usually discussed to describe their optical properties. To our knowledge, it is the first artificial system that shows delocalized excitons and energy migration in a helical arrangement of dye molecules.

Experimental Section

The dye (**C8O3**) was purchased from FEW Chemicals (Wolfen, Germany; Dye S 0250, highest purity available) and used without further purification. The crystalline material was dissolved directly in aqueous sodium hydroxide (1.0×10^{-2} M) by continuous stirring at room temperature for at least 24 h. Aliquots of the 2.5×10^{-2} M stock solution thus formed was diluted by NaOH solution for spectroscopic and cryo-TEM experiments by, typically, a factor of 50. The dye **TDBC** was also purchased from FEW Chemicals (Dye EC 2092) and used without further purification. It was dissolved in aqueous sodium hydroxide at a concentration of 10^{-4} M.

To prepare samples for cryo-TEM, a droplet (5 μL) of the aggregate solution was placed on hydrophilized, perforated, carbon-filmed copper grids. After removal of the excess fluid, an ultrathin layer (100 nm) spanned the holes of the carbon film. These grids were vitrified in liquid ethane (89 K) using a standard plunging device. The vitrified samples were transfered under liquid nitrogen into a TEM (Philips CM12) using the Gatan cryoholder and stage.

Single crystals of **C8O3** were grown from a 100 °C solution of dimethylsulfoxide (DMSO) by slowly cooling to room temperature in a Dewar vessel and stored for several days in a refrigerator. Crystals were investigated at room temperature using a SMART single-crystal diffractometer (Siemens). Absorption spectra were recorded using a spectrophotometer (Varian Cary 4), the CD-spectra from a spectropolarimeter (Jasco J-715).

[1] D. K. Kondepudi, R. Kaufmann, N. Singh, *Science* **1990**, *250*, 975.

[2] E. M. Geertsema, A. Meetsma, B. L. Feringa, *Angew. Chem.* **1999**, *111*, 2902; *Angew. Chem. Int. Ed.* **1999**, *38*, 2738.

[3] D. R. Link, G. Natale, R. Shao, J. E. Maclennan, N. A. Clark, E. Korblova, D. M. Walba, *Science* **1997**, *278*, 1924.

[4] A. E. Rowan, R. J. Nolte, *Angew. Chem.* **1998**, *110*, 65; *Angew. Chem. Int. Ed.* **1998**, *37*, 63.

[5] B. Kiupel, C. Niederalt, M. Nieger, S. Grimme, F. Vögtle, *Angew. Chem.* **1998**, *110*, 3206; *Angew. Chem.* **1998**, *37*, 3031.

[6] J.-M. Lehn, *Supramolecular Chemistry, Concepts and Perspectives*, VCH, Weinheim, **1995**.

[7] K. Jung, V. Abetz, R. Stadler, *Macromolecules* **1996**, *29*, 1076.

[8] R. Oda, I. Huc, M. Schmutz, S. J. Candau, F. C. MacKintosh, *Nature* **1999**, *399*, 566.

[9] H. Engelkamp, S. Middlebeck, R. J. M. Nolte, *Science* **1999**, *284*, 785.

[10] E. Scalas, G. Brezesinski, V. M. Kaganer, H. Möhwald, *Phys. Rev. E.* **1998**, *58*, 2172.

[11] I. Kuzmenko, K. Kjaer, J. Als-Nielsen, M. Lahav, L. Leiserowitz, *J. Am. Chem. Soc.* **1999**, *121*, 2657.

[12] D. Fenell Evans, H. Wennerstroem, *The Colloidal Domain: Where Physics, Chemistry, Biology and Technology Meet*, VCH, New York, **1994**.

[13] J.-H. Furhop, J. Koenig, *Membranes and Molecular Assemblies: The Synkinetic Approach*, The Royal Society of Chemistry, Cambridge, **1994**.

[14] T. Kobayashi, *J-Aggregates*, World Scientific, Singapore, **1996**.

[15] A. H. Herz, *Adv. Colloid Interface Sci.* **1977**, *8*, 237.

[16] S. Dähne, U. De Rossi, J. Moll, *J. Sci. Photogr. Sci. Technol. Jpn.* **1996**, *59*, 250.

[17] E. E. Jelley, *Nature* **1936**, *138*, 1009.

[18] G. Scheibe, A. Mareis, H. Ecker, *Naturwissenschaften* **1937**, *129*, 474.

[19] E. O. Potma, D. A. Wiersma, *J. Chem. Phys.* **1998**, *108*, 4894.

[20] U. De Rossi, S. Daehne, M. Lindrum, *Langmuir* **1996**, *12*, 1159.

[21] H. Kuhn, D. Möbius, *Angew. Chem.* **1971**, *83*, 672; *Angew. Chem.* **1971**, *10*, 620.

[22] V. Czikkely, H. D. Foersterling, H. Kuhn, *Chem. Phys. Lett*. **1970**, *6*, 11.

[23] J. Knoester, *J. Chem. Phys*. **1993**, *99*, 8466.

[24] D. A. Higgins, J. Kerimo, D. A. Vanden Bout, P. F. Barbara, *J. Am. Chem. Soc.* **1996**, *118*, 4049.

[25] J. E. Maskasky, *Langmuir* **1991**, *7*, 407.

[26] S. Kirstein, R. Steitz, R. Garbella, H. Möhwald, *J. Chem. Phys.* **1995**, *103*, 815.

[27] H. von Berlepsch, C. Böttcher, A. Ouart, C. Burger, S. Dähne, S. Kirstein, *J. Phys. Chem. B* **2000**, *104*, 5255.

[28] H. von Berlepsch, C. Böttcher, A. Ouart, M. Regenbrecht, S. Akari, U. Keiderling, H. Schnablegger, S. Dähne, S. Kirstein, *Langmuir* **2000**, *16*, 5908.

[29] M. Van Burgel, D. A. Wiersma, K. Duppen, *J. Chem. Phys.* **1995**, *102*, 20.

[30] U. De Rossi, S. Daehne, S. Meskers, H. Dekkers, *Angew. Chem.* **1996**, *108*, 827; *Angew. Chem. Int. Ed. Engl.* **1996**, *35*, 760.

[31] A. Rodger, B. Norden, *Circular Dichroism and Linear Dichroism*, Oxford University Press, Oxford, **1997**.

[32] S. Kirstein, H. Möhwald, *Adv. Mater.* **1995**, *7*, 460.

[33] Crystallographic data (excluding structure factors) for the structure reported in this paper have been deposited with the Cambridge Crystallographic Data Centre as supplementary publication no. CCDC-14064. Copies of the data can be obtained free of charge on application to CCDC, 12 Union Road, Cambridge CB2 1EZ, UK (fax: (+44) 1223-336-033; e-mail: deposit@ccdc.cam.ac.uk).

[34] A. Pawlik, U. De Rossi, S. Kirstein, S. Daehne, *J. Phys. Chem. B* **1997**, *101*, 5646.

[35] C. Spitz, S. Daehne, *Ber. Bunsen-Ges. Phys. Chem*. **1998**, *102*, 738.

[36] G. Scheibe, F. Haimerl, W. Hoppe, *Tetrahedron Lett*. **1970**, 3067.

[37] This is in contrast to previously reported results.[30] However, in those experiments, the J-aggregates were prepared in a different way: The dye was dissolved in alcohol first to prepare a stock solution which than was titrated into aqueous 10^{-2} M sodium hydroxide. By this procedure, other aggregates are formed, which exhibit optical activity with a statistical distribution of positive and negative couplets in the CD spectra and of which the handedness can be influenced by addition of chiral species. These aggregates were very small and could not be resolved by cryo-TEM. In addition, the dye sample was contaminated with a significant amount of the precursor 5,6-dichloro-1-octyl-2-methyl-3-(3-carboxypropyl)-benzimidazolium bromide.[38]

[38] U. De Rossi, J. Moll, M. Spieles, G. Bach, S. Dähne, J. Kriwanek, M. Lisk, *J. Prakt. Chem.* **1995**, *337*, 203.

Received: April 14, 2000 [Z 3]
Revised: July 28, 2000

A fuel cell stack assembly with the proton exchange membrane (PEM) technology—an option for a pollution-free power supply in the future.

Fuel Cells: Principles, Types, Fuels, and Applications[**]

Linda Carrette,[a] K. Andreas Friedrich,[a] Ulrich Stimming*[a]

During the last decade, fuel cells have received enormous attention from research institutions and companies as novel electrical energy conversion systems. In the near future, they will see application in automotive propulsion, distributed power generation, and in low power portable devices (battery replacement). This review gives an introduction into the fundamentals and applications of fuel cells: Firstly, the environmental and social factors promoting fuel cell development are discussed, with an emphasis on the advantages of fuel cells compared to the conventional techniques. Then, the main reactions, which are responsible for the conversion of chemical into electrical energy in fuel cells, are given and the thermodynamic and kinetic fundamentals are stated. The theoretical and real efficiencies of fuel cells are also compared to that of internal combustion engines. Next, the different types of fuel cells and their main components are explained and the related material issues are presented. A section is devoted to fuel generation and storage, which is of paramount importance for the practical aspects of fuel cell use. Finally, attention is given to the integration of the fuel cells into complete systems.

KEYWORDS:

energy conversion · fuel cells · hydrogen · methane · materials science

1. Introduction

1.1. The Reasons Behind Fuel Cells

1.1.1. History

Fuel cells[1–8] are by no means new devices, although their development has lacked drive during their first century. Their invention was made in the middle of the 19th century by Sir William Grove and are one of the oldest electrical energy-conversion technologies known to man. Their technological development has lagged behind the more well known steam engine and internal combustion engine (ICE). The reasons for the late evolution of fuel cells can be reduced to mainly economic factors, materials problems, and certain inadequacies in the operation of electrochemical devices.

At the beginning of the 20th century, with an increasing use of electricity, the conversion of chemical into electrical energy became important, however, primary energy sources were still abundant, unrestricted, and inexpensive. The impetus to improve the efficiencies of steam cycles or the ICE was absent. Electrical energy conversion systems were introduced initially as small, distributed power generators but soon further developments yielded megawatt-scale centralised plants producing electricity. The world population increase requires bigger, more powerful, and finely distributed power distribution. Furthermore, with a newly deregulated electrical power market in many industrialised countries, a new tendency to increase its flexibility by employing distributed power has emerged. It is expected that decentralised power plants will reduce both the overall capital investment for the installer and improve efficiency due to co-generation of electricity and heat.

The first successful application of fuel cells was achieved with the space technologies. An electrical energy conversion device, which can provide electricity, heat, and potable water for the crew, was significantly more convenient compared to existing power sources, such as batteries. The use of the alkaline fuel cell system in the NASA Apollo space programme from 1960 to 1965 was also the start of a new era for fuel cells. Many research groups started to focus on fuel cells and for applications other than just space vehicles. By the 1970s, a fuel cell car was built by Kordesch to run on alkaline fuel cells combined with a lead – acid battery. Many other applications have now been envisioned for fuel cells and, in a few years time, fuel cells are expected to be used in numerous and diverse power applications, ranging from portable power and vehicle propulsion to distributed electrical power generation.

1.1.2. Environmental Factors

One of the major factors that influenced the development of fuel cells over the last few years is the worldwide concern about the environmental consequences of fossil fuel use in the day-to-day

---

[a] Prof. Dr. U. Stimming, Dr. L. Carrette, Dr. K. A. Friedrich
Physik Department E 19
Technische Universität München
James-Franck-Strasse 1
85748 Garching (Germany)
Fax: (+49) 89-2891-2530
E-mail: stimming@ph.tum.de

[**] The authors' research and this review was funded by the Deutsche Forschungsgemeinschaft, reference 74/8-1 and Sti 74/8-2.

production of electricity and for the propulsion of vehicles. The dependence of the industrialised nations on oil became apparent during the oil crises and, recently, pressure on fossil fuel reserves is a cause for anxiety. More importantly however, is the increasing societal awareness, over the last few decades, concerning issues of environmental pollution. The combustion of fossil fuels releases harmful emissions into the air, which influence the Greenhouse Effect as well as the direct health of people, especially in urban areas.

Linda Carrette
has been researching fuel cells for five years now. She investigated fuel cell electrocatalysts during her PhD research at the University of Southampton (UK). She then moved to Germany to take up a post-doctoral position in Professor Stimmings' group and, under his supervision, she has been working on DMFC anode catalysts and fundamental topics in fuel cell research.

Kaspar Andreas Friedrich
is a senior research associate at the Department of Physics at the Technische Universität München. He studied physics at Universität Frankfurt and obtained his Ph.D. from the Freie Universität Berlin in 1974. His research interests are the proton-exchange membrane fuel cells, electrocatalysis, and interfacial spectroscopy.

Ulrich Stimming
has been involved in fuel cell research for several years. After his time at Columbia University (New York), during which he was also a Guest Professor at the Fritz Haber Institut, Berlin, and the University of Ulm (Germany), he returned to Germany to become Director of the Forschungzentrum Jülich from 1991 to 1997. During this time, his work included SOFC and DMFC research. Currently, he holds the Chair for Interfaces and Energy Conversion at the Technische Universität München, where his group is investigating many fuel cell topics, as well as some fundamental problems in surface science.

Major emissions of NO_x, SO_x, CO_2, and particulate matter are the cause of most concern for pollution of our environment (Figure 1).[9] Particulate matter or soot are airborne particles produced mostly by combustion in vehicle engines, power plants, and industrial processes. Small particles can penetrate deep into the lungs and remain there for months or even years and cause a variety of health problems. Emissions of nitrous oxides (NO_x), together with hydrocarbons, can increase the ozone levels in the lower atmosphere, which is toxic for most animals and humans. Sulphur-containing natural resources (coal, oil, and diesel, for example) can create SO_2 gas upon combustion, which triggers the inflammation of lung tissue and SO_2 causes acid rain, which is destroying our monuments and forests. Carbon dioxide by itself does not directly create hazards for people's health but it contributes to the warming of the atmosphere, the Greenhouse Effect. Although it is true that natural phenomena, such as an outburst of a volcano, can create huge amounts of CO_2 as well, there is a fine line between the stable amount of CO_2 in the atmosphere and a domino effect on climate changes, which could be triggered by an imbalance of CO_2.

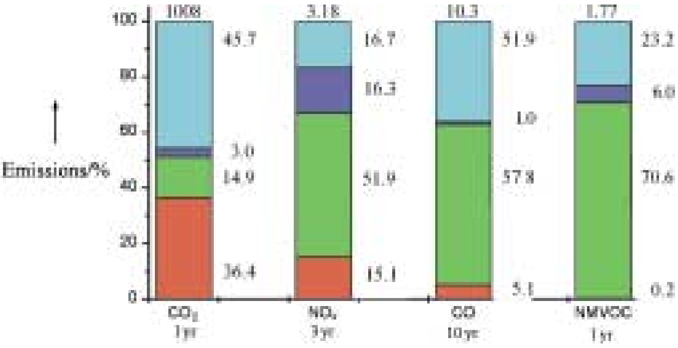

Figure 1. Emissions in West Germany (1990) of NO_x, SO_x, CO_2, and nonmetal volatile organic species (NMVOCs), classed by source (red = heat and power generation, green = road traffic, indigo = commercial vehicles, blue = other sources). The numerical value at total emission (100 %) is their total annual output by mass (Mt year^{-1}).

There are several ways in which the emissions by human activities can be curbed and our dependence on fossil fuels reduced without diminishing the standard of living. Besides the enormous potential for saving energy, the efficiency of end-use equipment, of vehicle propulsion engines, as well as power generation facilities, can be improved. The contribution of renewable energy sources, from wind, sun, and water, could increase but one must remember that the complete generation process should be taken into account when comparing different systems and that these sources are not suited to cover the base load. The combination of these energies to produce hydrogen, in combination with the fuel cell conversion system, may well be an option for future power generation. The main advantage of fuel cells in this respect are their higher efficiencies, compared to an ICE, and their lower emissions.

Another renewable energy source is biomass in its different forms, which range from sewage sludge to municipal waste and forestry residues. Biomass can readily be converted to methane, which can be directly oxidised in high temperature fuel cells (see Section 4) or it can be reformed (converted) into hydrogen for use in other types of fuel cell systems. Nowadays, research into synthetic gases also aims to reduce the use of fossil fuels.

Fuel cells can, thanks to their higher efficiencies (see Section 1.3), contribute to the reduction of emissions. Using pure hydrogen (provided this was generated by a renewable energy source) fuel cells only produce water, thus eliminating all emissions caused by electricity production. No natural sources of pure hydrogen exist on earth, so hydrogen must be generated by chemical reactions and most is still produced from fossil fuels or biomass.

1.2. Important Reactions

1.2.1. General

An electrochemical cell consisting of two electrodes (anode and cathode) has an overall reaction described in Equation (1).

$$a_{ox_1} + b_{red_1} \longrightarrow c_{red_2} + d_{ox_2} \tag{1}$$

The voltage of the cell, ΔU, is represented by the difference between the two half-cell reactions, whereby the equilibrium potential of each half cell reaction is given by the Nernst Equation (2), in which n is the number of electrons involved and F is the Faraday constant.

$$U_0 = U^{\ominus} - \frac{RT}{nF}\frac{[\mathrm{red}]}{[\mathrm{ox}]} \tag{2}$$

The term $U^{\ominus}$ for each half cell reaction is the standard electrode potential and [red] ([ox]) is the activity of reducing (oxidising) species in solution. The cell voltage ΔU, in the absence of current, is thus given by Equation (3).

$$\Delta U = U_{0,1} - U_{0,2} = U_1^{\ominus} - U_2^{\ominus} + \frac{RT}{nF}\frac{[\mathrm{ox}_1]^a\,[\mathrm{red}_2]^b}{[\mathrm{ox}_2]^d\,[\mathrm{red}_1]^c} \tag{3}$$

The Gibbs free energy change ΔG for the same cell reaction is given by Equation (4), in which $\Delta G^{\ominus}$ is the standard Gibbs free energy change.

$$\Delta G = \Delta G^{\ominus} + RT\frac{[\mathrm{ox}_1]^a\,[\mathrm{red}_2]^b}{[\mathrm{ox}_2]^d\,[\mathrm{red}_1]^c} \tag{4}$$

Fuel cells are Galvanic cells, in which the free energy of a chemical reaction is converted into electrical energy (via an electrical current). The Gibbs free energy change of a chemical reaction is related to the cell voltage Equation (5).[10]

$$\Delta G = -nF\Delta U \tag{5}$$

The anodic reaction in fuel cells is either the direct oxidation of hydrogen or the oxidation of methanol. An indirect oxidation, via a reforming step, can also occur (see Section 4). In fuel cells, the cathodic reaction is usually oxygen reduction, in most cases the oxygen source is from air. This reaction has been investigated in numerous studies but the complete mechanism of oxygen reduction is still not fully understood. An introduction to the different possible mechanisms is given here.

1.2.2. Oxygen Reduction

The oxygen reduction reaction (ORR)[11] can proceed by two overall pathways in aqueous electrolytes, shown in Equations (6) and (7) and Equations (8) to (13).

1) Direct four-electron pathway:
   a) either in an alkaline electrolyte

$$O_2 + 2\,H_2O + 4\,e^- \longrightarrow 4\,OH^- \qquad U^{\ominus} = 0.401\ \mathrm{V} \tag{6}$$

   b) or in an acidic electrolyte

$$O_2 + 4\,H^+ + 4\,e^- \longrightarrow 2\,H_2O \qquad U^{\ominus} = 1.229\ \mathrm{V} \tag{7}$$

2) Peroxide pathway:
   a) either in an alkaline electrolyte

$$O_2 + H_2O + 2\,e^- \longrightarrow HOO^- + OH^- \qquad U^{\ominus} = -0.065\ \mathrm{V} \tag{8}$$

followed by either peroxide reduction

$$HOO^- + H_2O + 2\,e^- \longrightarrow 3\,OH^- \qquad U^{\ominus} = 0.867\ \mathrm{V} \tag{9}$$

or peroxide decomposition

$$2\,HOO^- \longrightarrow 2\,OH^- + O_2 \tag{10}$$

   b) or in an acid electrolyte

$$O_2 + 2\,H^+ + 2\,e^- \longrightarrow HOOH \qquad U^{\ominus} = 0.670\ \mathrm{V} \tag{11}$$

followed by either

$$HOOH + 2\,H^+ + 2\,e^- \longrightarrow 2\,H_2O \qquad U^{\ominus} = 1.77\ \mathrm{V} \tag{12}$$

or

$$2\,HOOH \longrightarrow 2\,H_2O + O_2 \tag{13}$$

The direct four-electron pathway is preferable as it does not involve peroxide species in solution and the charge efficiency (Faradaic efficiency) of the reaction is greater. This pathway however, consists of a number of steps in which molecular oxygen dissociates at the surface and combines with hydrogen ions. The adsorption of an oxygen species to the surface of the metal particles is essential for electron transfer. Detailed mechanisms of these steps for the ORR on different catalysts can be found elsewhere.[12–16a]

Other factors can influence the kinetics of a reaction at a particular electrode; an overview was given by Kinoshita[11] on the effects of different properties of the technical electrocatalyts on the ORR and oxygen-evolution reaction kinetics. It is experimentally difficult to obtain the relevant structural information from the complex electrocatalysts used in fuel cells. Therefore, the models derived to explain the structure–activity relationship are often controversial. A particle–crystalline size effect, with respect to oxygen reduction, has been reported by

Takasu et al., Bregoli, and Ross.[16b–d] The optimum particle size was found to be around 5 nm; smaller particles exhibited lower reactivities. This interpretation is disputed by Watanabe et al.,[16e] who claim that the intercrystalline distance on the carbon support is fundamental to the ORR and therefore the reactivity is dependent on platinium loading (see Section 2.2.5).

Another possible explanation[17, 18] states the ORR is structure-sensitive, namely, the reaction only takes place on specific active sites of the catalyst. When the particles are smaller, the amount of surface increases but this does not mean that the number of active sites also increases.

Other influencing factors include the geometry, crystal structure, and d-band vacancy of the metal catalyst. Pretreatment of the catalyst, such as heating under hydrogen or air, or the electrochemical activation of the electrodes can also improve the performance for oxygen reduction.[17–26]

1.2.3. Hydrogen Oxidation

Hydrogen oxidation occurs readily on platinum-based catalysts. The kinetics of this reaction are very fast and, in a fuel cell, hydrogen oxidation is usually controlled by mass transfer limitations. Hydrogen oxidation also involves the adsorption of the gas onto the catalyst surface followed by dissociation of the molecule and an electrochemical reaction to form two protons (acid electrolyte) as follows (Equations (14) and (15)), where $Pt_{(s)}$ is a free surface site and $Pt{-}H_{ads}$ is an adsorbed hydrogen atom on the Pt active site.

$$2\,Pt_{(s)} + H_2 \longrightarrow Pt{-}H_{ads} + Pt{-}H_{ads} \qquad (14)$$

$$Pt{-}H_{ads} \longrightarrow H^+ + e^- + Pt_{(s)} \qquad (15)$$

The overall reaction of hydrogen oxidation is given by Equation (16).

$$H_2 \longrightarrow 2\,H^+ + 2\,e^- \qquad U^{\ominus} = 0\,V \qquad (16)$$

Although this process is a fast electrochemical reaction, with rate constants of about $10^{-5}\,mol\,sec^{-1}\,cm^{-2}$,[27a] some problems may arise in a fuel cell when impure hydrogen is used. Operating a fuel cell with pure hydrogen gives the best performance but pure hydrogen can be expensive and difficult to store. Alternatives to pure hydrogen include natural gas, propane, or alcohols. These substances have to be reformed, however, into hydrogen (see Section 3) and, even after gas clean-up, some contaminants, such as CO species, can persist in the fuel feed. As with the methanol oxidation catalysts, CO poisons the catalyst by blocking active sites. Consequently, sites are no longer available for hydrogen adsorption and subsequent oxidation. So although, in principle, a pure Pt catalyst can be used for hydrogen oxidation, similar studies into alloys for methanol oxidation catalysts (Section 1.2.4) have been carried out to improve the catalyst activity with contaminated hydrogen.[27b, 28] More details about the anodic reaction of hydrogen and CO poisoning are given in Section 2.

1.2.4. Methanol Oxidation

Very few electrode materials have been shown to be capable of adsorbing and oxidising methanol in acidic media at low enough potentials. Platinum-based materials display a sufficiently high stability and activity to be attractive as catalysts. Many studies on the oxidation of organic molecules and specifically on methanol oxidation have been carried out.[29–40] An overview of methanol oxidation and methanol fuel cells has been published.[41] The overall reaction mechanism for methanol oxidation is given by Equation (17).

$$CH_3OH + H_2O \longrightarrow CO_2 + 6\,H^+ + 6\,e^- \qquad U^{\ominus} = 0.046\,V \qquad (17)$$

It is assumed that the oxidation of methanol on platinum-based catalysts proceeds by the adsorption of the molecule followed by several steps of deprotonation. This adsorption/deprotonation process is given in Scheme 1.[42]

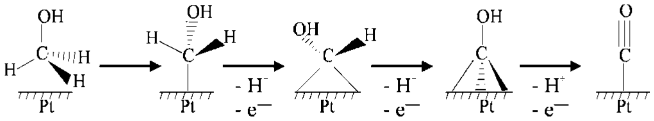

Scheme 1. Adsorption mechanism of methanol on Pt and subsequent oxidation by consecutive stripping of electrons.

Scheme 1 shows that a CO species is formed during the methanol oxidation, a result confirmed by IR spectroscopy. This CO molecule can block the surface of the catalyst and hinder further reaction. For this reason, a number of co-metals are usually added to the catalyst to facilitate CO removal by its oxidation to CO_2. This can be achieved by oxidising the CO species with oxygen, either from the dissociation of water in solution to form, for example, adsorbed OH species on the platinum itself or on a secondary metal.

A series of reaction pathways have been suggested for the methanol oxidation reaction and the subsequent CO oxidation, as given in Equations (18) to (21).

$$Pt_{(s)} + H_2O \longrightarrow Pt{-}OH + H^+ + e^- \qquad (18)$$

$$Pt{-}OH + Pt{-}CO \longrightarrow Pt{-}COOH \qquad (19)$$

or

$$Pt{-}CO + H_2O \longrightarrow Pt{-}COOH + H^+ + e^- \qquad (20)$$

$$Pt{-}COOH \longrightarrow Pt_{(s)} + CO_2 + H^+ + e^- \qquad (21)$$

Additional reactions have also been suggested for this process, as presented in Scheme 2,[43, 44] to show the possible reaction pathways and their products.

Much research is being rendered on catalysts for methanol oxidation (see also Section 2) to find a catalyst which avoids the poisoning effect of the intermediate species.[45–48] Several promoters have been found to increase the activity of the Pt catalyst. One of the most important and most investigated

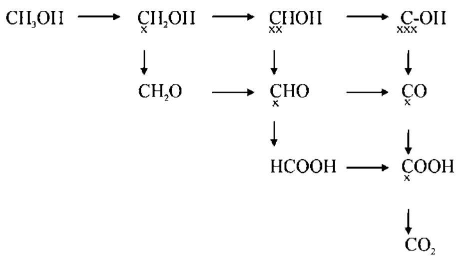

Scheme 2. All possible reaction pathways and intermediates, named the Bagotzky scheme, for the oxidation of methanol to CO_2. Stable compounds in the electrolyte are located on the hypotenuse; dehydration occurs left to right, oxidation occurs top to bottom. Each x denotes a C–Pt bond.

promoter is ruthenium. A bimetallic alloy, consisting of Pt and Ru supported on carbon, has thus far been the most successful catalyst in direct methanol fuel cells (Section 2). Other promoters such as tin, osmium, tungsten, molybdenum, and other metals have also been investigated. More on CO poisoning and other specific system requirements will be discussed in detail in Sections 2 and 4.

1.3. Operation of a Fuel Cell

1.3.1. Schematic

A fuel cell is an electrochemical cell and each electrochemical reaction is characterised by the Nernst Equation (2). When a current flows, a deviation of the potential from the equilibrium value occurs. This corresponds to electrical work performed by the cell; the deviation from the equilibrium value is the overpotential η. For a redox reaction at one electrode, the current density j is given in the simplest case by the Butler–Volmer Equation (22), in which j_0 is the exchange current

$$j = j_0[\exp(\alpha_A nF\eta/RT) - \exp(-\alpha_C nF\eta/RT)] \qquad (22)$$

density and α_A (α_C) is the transfer coefficient for the anodic (cathodic) reaction. This equation holds when the charge transfer dominates the reaction at small values of j and η. Other limiting factors, like mass transport hinderance, are present in real systems and are described in terms of potential losses (concentration, reaction, and resistance overpotentials).

A current density versus overpotential plot is shown in Figure 2. There are different types of overpotential in the system, the main two are losses due to reaction kinetics or mass transfer problems.

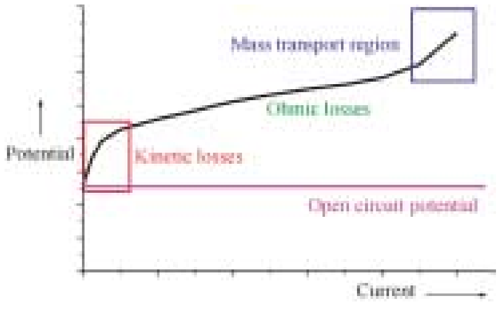

Figure 2. The potential losses for an anodic reaction showing the kinetic, ohmic, and mass transport regions.

The cell voltage of a fuel cell is the difference between the two half-cell potentials and an additional ohmic drop, as shown in Figure 3a. From such a graph, a power density versus current density plot can be obtained (Figure 3b) and this is a useful representation for comparing different fuel cells.

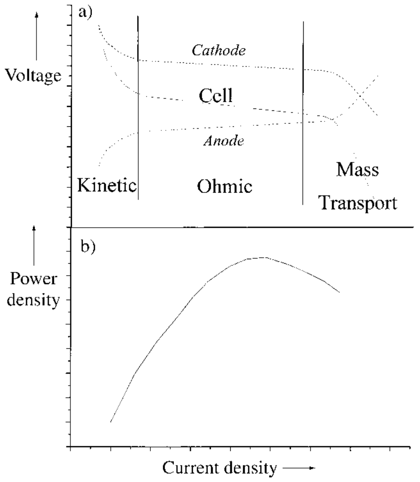

Figure 3. a) The cell voltage consists of the contributions by the anodic and cathodic reactions displaying the kinetic, ohmic, and mass transport regions. b) From the current–voltage data, a power density versus current plot can be derived.

1.3.2. Efficiencies of Fuel Cells

A comparison of fuel cells with other systems, such as the ICE, is usually carried out using maximum efficiencies. An ICE converts chemical energy into mechanical energy, which can then be transformed into electrical energy by means of an alternating current generator, as shown in Figure 4.[49]

The combustion of a hydrocarbon (chemical energy) is accompanied by a rise in temperature, as these reactions are

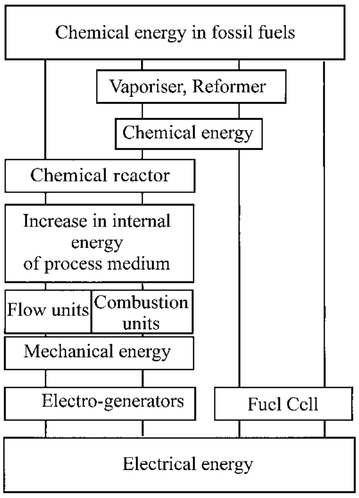

Figure 4. Comparison of the processes involved in an ICE and a fuel cell.

exothermic, and the reaction products are usually gases. The heat increase causes expansion of the gases, which in turn produces mechanical work by causing the pistons in the ICE to move. The maximum efficiency of this system is the Carnot efficiency ε, as given in Equation (23), in which T_1 and T_2 are the source and sink temperatures, respectively. It is clear that $\eta \rightarrow 1$ if T_1 is very high or if T_2 is near zero (impossible in one cycle).

$$\varepsilon = \frac{T_1 - T_2}{T_1} \tag{23}$$

For a fuel cell, the efficiency can be calculated from the changes in Gibbs free energy ΔG and the enthalpy ΔH of the electrochemical reaction. Ideally, the free energy of the reaction can be completely converted into electrical energy; the efficiency is given by Equation (24).

$$\varepsilon_{\text{th}} = \frac{\Delta G}{\Delta H} = 1 - \frac{T\Delta S}{\Delta H} \tag{24}$$

The change in entropy of the reaction ΔS depends, however, on the reactants and products. Often for high temperature fuel cells, theoretical efficiencies close to $\varepsilon = 1$ are attainable steam is produced and no volume changes occur. In practice, however, electrode overpotentials cause the practical efficiencies to be lower. At lower temperatures, the water formed is liquid and the entropy change is negative. For negative ΔS, an increase in temperature causes a decrease in thermodynamic efficiency of the fuel cell.

The electrochemical efficiency is sometimes used to compare fuel cells. Cells composed of different designs and components can be compared by using the same reactions and calculating the electrochemical efficiency, as given by Equation (25).

$$\varepsilon_{\text{el}} = \frac{-nFE}{\Delta G} \tag{25}$$

The (electrochemical) electrical efficiency provides a better means with which to compare different fuel cells than the thermodynamic efficiency, as it is directly related to the performance of the cell. A comparison of electrical system efficiencies is given in Figure 5.[50, 51]

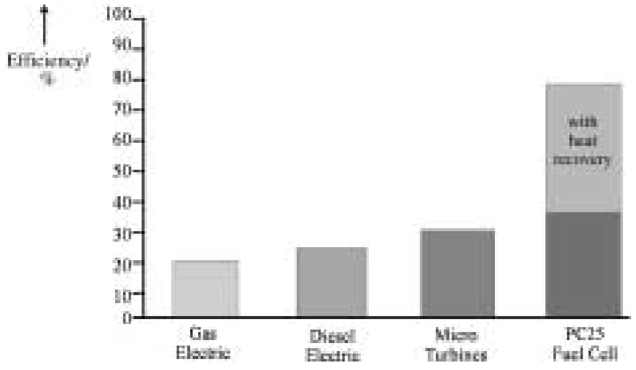

Figure 5. A comparison of the efficiencies of a phosphoric acid fuel cell (with and without heat recovery) versus conventional systems.

1.3.3. Co-Generation of Heat and Power

The simultaneous utilisation of electricity and heat from an energy conversion system is called co-generation. This type of energy utilisation is much more efficient than the single production of electricity, since, in most systems, considerable waste heat is produced. The use of this heat to either produce more electricity (in a gas or steam turbine for instance) or to accommodate the plant with heat and warm water increases the efficiency as shown in Equation (26), in which Q is the energy obtained in heat, E is the electrical energy, and Q_0 the energy inherent in the fuel. For stationary applications especially, co-generation can be used to provide homes with both electricity, heat, and hot water (see Section 4).[52]

$$\varepsilon = \frac{Q + E}{Q_0} \tag{26}$$

1.4. From Fuel to Electricity

The basic principles of fuel cells have been shown in this Introduction but a fuel cell system or power plant is not just a combination of the single components. Careful consideration needs to be taken for all components and their interactions, from the appropriate fuel cell type (with all its own components) to the right fuel and system requirements. This overview is by no means complete but an attempt has been made to cover the different aspects of fuel cell system engineering for possible applications.

The different fuel cell types and their components will be discussed in Section 2. A brief overview on catalysts for the different fuel cells is given and the fuel cell characteristics, such as operating temperature, electrolytes, and specific associated problems with them are also denoted. In Section 3, the importance of fuel processing is elaborated. The reforming of hydrocarbons and alcohols is discussed as well as the storage of hydrogen. Complete systems and applications are discussed in Section 4. A summary of Sections 1 – 4 is given in Section 5 with a complete table of all fuel cell types, their applications, operating temperature range and other specifications.

2. Types of Fuel Cell

Fuel cells are usually classified by the electrolyte employed in the cell. An exception to this classification is the DMFC (Direct Methanol Fuel Cell), which is a fuel cell in which methanol is electrochemically oxidised directly in the fuel cell. A second grouping is by the operating temperature for each of the fuel cells. There are, thus, low and high temperature fuel cells. Low temperature fuel cells are the Alkaline Fuel Cell (AFC), the Proton Exchange Membrane Fuel Cell (PEMFC, also called the Polymer Electrolyte Fuel Cell, PEFC, or the Solid Polymer Electrolyte Fuel Cells, SPEFC), the DMFC, and the Phosphoric Acid Fuel Cell (PAFC). The high temperature fuel cells operate at 500 – 1000 °C and are classed into two different types, the Molten Carbonate Fuel Cell (MCFC) and the Solid Oxide Fuel Cell (SOFC). All types are presented in this Section in order of increasing operating temperature.

2.1. Alkaline Fuel Cells

2.1.1. General

The alkaline fuel cell (Figure 6) is generally regarded as the "ugly duckling" in fuel cell technology. The AFC has the highest electrical efficiencies of all fuel cells but it only works properly with very pure gases, which is considered a major drawback in most applications. The KOH electrolyte, which is used in AFCs (usually in concentrations of 30 – 45 wt%), has an advantage over acidic fuel cells. The oxygen reduction kinetics are much faster in alkaline electrolyte than in acid, which makes the AFC a more efficient system. The AFC was one of the first fuel cells used in space (although a PEM fuel cell was used for the Gemini program, it was soon discovered that the AFC had many advantages over this system). The AFC was used in the Apollo missions, the Space Shuttle program, and was planned to be used in the European Hermes Project.

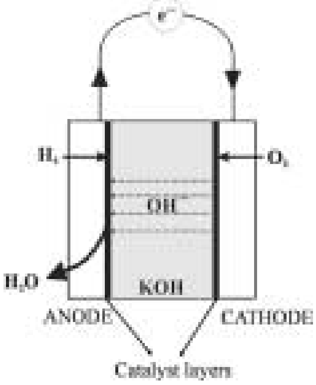

Figure 6. A schematic representation of the reactions in an alkaline fuel cell.

The first AFC (1950s) was a Bacon fuel cell, provided 5 kW power, and used a Ni anode, a lithiated NiO cathode, and 30 wt% aqueous KOH. Its operating temperature and pressure were 200 °C and 5 MPa, respectively. For the Apollo program, an AFC which employed an 85% KOH solution at 200 – 230 °C was used. In the Space Shuttles, the fuel cells are used both for producing energy, cooling the Shuttle compartments, and producing potable water. Three plant modules are used, each with a maximum power output of 12 kW. AFCs are now normally run at operating temperatures below 100 °C, as the high temperature is not needed to improve oxygen reduction kinetics (although higher temperatures are advantageous for the hydrogen oxidation kinetics).

2.1.2. Reactions

In alkaline media, oxygen reduction and hydrogen oxidation involve OH^- ions, Equations (27) to (29). The OH^- species formed by the cathodic reduction of water move through the electrolyte to the anode, where recombination with hydrogen, oxidised at the anode, produces water.

Cathode:

$$\tfrac{1}{2}O_2 + H_2O + 2\,e^- \longrightarrow 2\,OH^- \qquad (27)$$

Anode:

$$H_2 + 2OH^- \longrightarrow 2\,H_2O + 2\,e^- \qquad (28)$$

Overall:

$$H_2 + \tfrac{1}{2}O_2 \longrightarrow H_2O \qquad (29)$$

The advantage of AFCs over the other systems lies in the fact that the reduction of oxygen to OH^- is much faster than the acidic equivalent of oxygen to H_2O due to better kinetics. The hydrogen oxidation reaction in alkaline medium is slower, however.

2.1.3. Electrodes

AFC electrodes began as Ni-based catalysts sometimes activated with platinum. It should be noted, however, that metal loadings are usually lower (0.3 mg cm^{-2} can be attained) than for a PAFC or a PEM fuel cell. The Pt/C gas diffusion electrodes are now generally used for both the anode and cathode, although various groups are investigating other possibilities.

Pt/Co alloys have been suggested[19] and have proved to have a superior activity to Pt for oxygen reduction due to a higher exchange current density. The Tafel slope for oxygen reduction for Pt/Co catalysts is the same as for Pt catalysts (60 mV decade^{-1}). Further work on Ag and Co catalysts is being undertaken to replace some or all of the Pt in the electrodes.[53]

A Pt/Pd anode was tested for stability characteristics in comparison to Raney nickel.[54] It is known that Raney Ni electrodes have a high activity for hydrogen oxidation (see Section 2.5) but, due to the wettability of the inner pores and changes in chemical structure under operation conditions, a decay in performance occurs. The Pt/Pd activity was also seen to have a very rapid decay initially but after a short time the decay stopped and the performance remained constant afterwards.

2.1.4. Electrolyte

The AFCs used in space had KOH in a stabilised matrix, usually gel-like materials, but this is disadvantageous for most applications. It has since been found that a much longer operating lifetime can be obtained with circulating KOH.[55–57] A circulating electrolyte provides a good barrier against gas leakage and it can be used as a cooling liquid in the cell or stack. Other advantages include the use of the electrolyte circulation to clean the cell and remove the water produced at the anode. An early demonstration of the AFC with circulating electrolyte was made by Kordesch et al. in the 1970s.[55] They combined an H_2/air AFC with a lead acid battery in a hybrid vehicle. Between operations, the complete cell was shut down by draining the KOH electrolyte. This improved the life expectancy enormously since the cell voltage is very high (open circuit voltage) when the cell is under no load. High open-circuit voltages can induce carbon oxidation processes to produce carbonates that can destroy the matrix/electrolyte.

One of the most controversial issues in AFCs is the formation of carbonates. It is generally accepted that the CO_2, both originally in the air and formed by reaction, interact with the electrolyte according to Equation (30). The formation of carbonates, via the oxidation of the carbon support material in the electrodes during open circuit conditions, clogs up the pores of the gas diffusion electrodes and the cell performance rapidly decreases. A circulating electrolyte avoids the build up of carbonates.

$$CO_2 + 2\,OH^- \longrightarrow CO_3^{2-} + H_2O \tag{30}$$

Carbon dioxide can be cost-effectively removed from the hydrogen feed and from the air flow by an iron-sponge system, which is similar to the shift reaction in a reformer. This process is used in most ammonia production plants for the same purpose and can be used in AFC applications. Other processes to remove CO_2 are swing adsorption or normal shift reaction, both of which are being used in fuel cell systems.[53–58]

2.2. Proton Exchange Membrane Fuel Cells

2.2.1. General

PEM fuel cells (Figure 7) use a proton-conducting polymer membrane as an electrolyte. They are low temperature fuel cells, generally operating at 85 – 105 °C and were the first to be used in space. The Gemini program employed a 1 kW fuel cell stack as an auxiliary power source. It was also used to provide the astronauts with clean drinking water. The membrane used was a polystyrene sulfonate (PSS) polymer which, however, proved to be insufficiently stable. This was one of the major reasons for NASA to opt for the AFC system for its further missions.

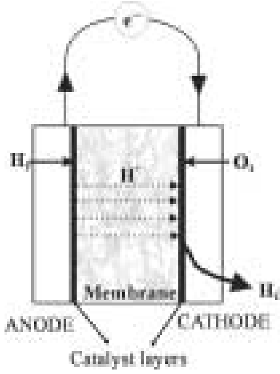

Figure 7. A schematic representation of the reactions in a polymer electrolyte fuel cell.

A major breakthrough in the field of PEM fuel cells came with the use of Nafion membranes (DuPont). These membranes possess a higher acidity, and concurrently conductivity, and are far more stable than the polystyrene sulfonate membranes. Nafion consists of a polytetrafluoroethylene-based (PTFE) structure which is chemically inert in reducing and oxidising environments, in contrast to the PSS membranes.

In 1987, Ballard started using a Dow membrane (Dow Chemicals) in their PEM fuel cells, which gave current densities about four times higher at the same voltage than with Nafion. These membranes, together with Nafion and some other PTFE-based polymers, are still under scrutiny by several research groups over the world. A general overview on polymer electrolytes was published in 1998.[58]

2.2.2. Reactions

The reactions in a PEM fuel cell are the same as in a PAFC (Section 2.4) as they both employ an acidic electrolyte Equations (31) and (32). The anode reaction consists of hydrogen oxidation to protons; the protons migrate through the membrane to the cathode. At the cathode, oxygen is reduced and then recombines with the protons to form water.

Cathode:

$$\tfrac{1}{2}O_2 + 2\,H^+ + 2\,e^- \longrightarrow H_2O \tag{31}$$

Anode:

$$H_2 \longrightarrow 2\,H^+ + 2\,e^- \tag{32}$$

The proton conductivity of the membrane is a very important factor in PEM technology. Better membranes are constantly under investigation and the formation of water at the cathode can also be a determining factor for the future employment of PEM fuel cells.

2.2.3. Membranes

Nafion (Figure 8)[59] is probably the most studied and employed electrolyte for PEM fuel cells but other perfluorocarbonsulfonic acid ionomers, such as the membranes from Dow, Aciplex, Gore, and Asahi Chemical, are also used.[60] Membranes usually have a small temperature range in which they are stable. The upper limit of temperature is dictated by the humidification needs of the membrane, as water is a prerequisite for conduction (Section 2.2.4).

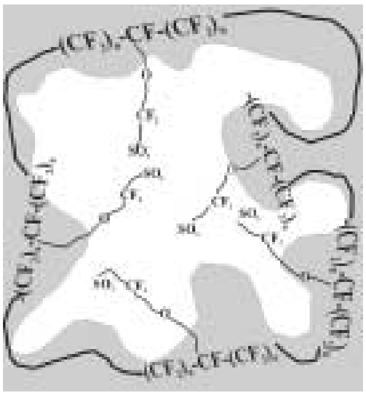

Figure 8. The Nafion structure: the grey zones are the hydrophobic regions consisting of the PTFE backbone and the white zone is the hydrophilic region consisting of the sulphate ions which are involved in the transport of H^+.

Improvements in the membrane structure and conductivity are made by producing composite membranes. This can be done in several ways, one of which consists of reinforcing the perfluorosulfonic membrane with PTFE components, which is the basis of the approaches used successfully by Gore and Asahi Chemicals. Another possibility is to impregnate a membrane with a solution or with a solid powder to decrease the permeability of the reactant gases. Another technique is to dissolve the membrane into an appropriate solvent and to mix it with another substance. After recasting (usually by evaporating the solvent) the composite membrane can be used in a fuel cell.[61]

Impregnation of PTFE films with the Nafion ionomer (18 wt% Nafion in ethanol) to make thinner membranes was carried out, thus reducing the membrane resistance in the system.[62] The conductivity of this membrane was comparable to Nafion 112 ($\kappa = 0.1\,\mathrm{S\,cm^{-1}}$) but its permeability towards gases is much higher.

Poly(ethylene oxide)-like films (PEO) were impregnated with lithium silicates to produce an organic/inorganic composite electrolyte.[63] These composite electrolytes are thermally stable and provide good conductivity and performance in lithium batteries. They have also been investigated for fuel cell applications.

Other composites were formed by swelling of perfluorinated ionomeric membranes with an ionic liquid.[64] These composites were able to attain a similar conductivity as Nafion 117 ($\kappa = 0.1\,\mathrm{S\,cm^{-1}}$) but were simultaneously able to operate at 180 °C, which could substantially improve the oxygen reduction kinetics and the CO poisoning problems (Section 2.2.5.3).

Other membranes were prepared by filling a SiO_2 or Al_2O_3 ceramic phase with H_2SO_4, H_3PO_4, or CF_2SO_3H (TFMSA), whereby the highest conductivity ($\kappa = 0.21\,\mathrm{S\,cm^{-1}}$) was obtained for a SiO_2/poly(vinyl difluoride) (PVDF) binder (10%/15%) filled with a sulphuric acid/H_2O mixture (1/3).[65, 66]

Novel membranes are also prepared by techniques such as plasma polymerisation or radiation grafting.[67, 68] Plasma polymerised membranes were prepared to produce thin ion-exchange films, which are desired in fuel cells to reduce ohmic resistance in the system and to prevent the membrane from drying. Plasma polymerisation is known to give highly cross-linked, uniform, and stable thin films. A plasma polymerised film of hexafluoropropylene and TFMSA showed high cationic permselectivity, stablity, and an ion-exchange capacity similar to Nafion 117 ($0.9\,\mathrm{meq\,g^{-1}}$).[69]

Radiation grafting of PVDF films gave membranes with a lower oxygen solubility but higher diffusion than through Nafion. These membranes are promising for PEM fuel cells as long as they prove to be mechanically and electrochemically stable.[67] Other radiation-grafted membranes are pursued at the Paul-Scherrer Institute (Switzerland).[68]

Some membrane properties, like oxygen diffusion, solubility, and proton transport, have been reported.[59, 67, 69–73] In general, thinner membranes have a lower resistance but may have a higher cross-over of gas, thus reducing their performance.

2.2.4. Water Management

Membranes in PEM fuel cells are generally water filled to keep the conductivity high (Figure 9);[57] a dry membrane possesses a lower conductivity. Water management of the membrane is one of the major issues in PEM technology. Although water, in liquid or gaseous form, is a product of the reactions at the cathode, it is not easy to keep the water in the membrane. Factors influencing the water content in the membrane are (electro-osmotic) water drag through the cell—for every proton, a shell of (around 3.5) H_2O molecules is also transported through the membrane—and, in the opposite direction, back diffusion of water from the cathode can also occur.

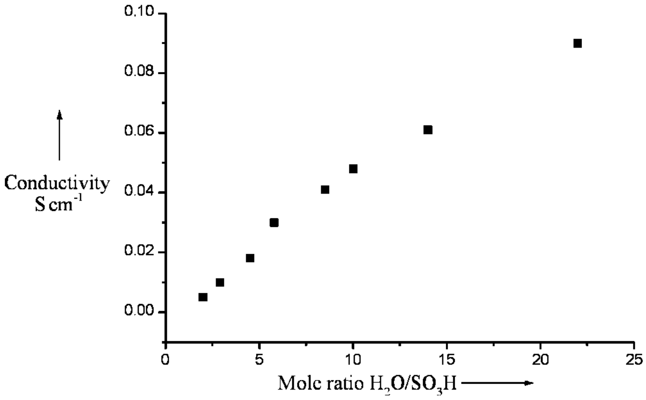

Figure 9. The conductivity of Nafion as a function of water content.

One way to improve water management is to humidify the gases entering the fuel cell. An integrated stack can use cooling water flowing through the stack to humidify the gases.[74] Polysulfonic membranes fabricated for ultrafiltration processes were found to perform better with internal humidification than Nafion 115, as they have a higher water permeability.

Phosphoric acid doped polybenzimidazole (PBI) membranes have an acceptable protonic conductivity and the H^+ transport is not accompanied by an electro-osmotic water drag through the membrane, which makes it a good candidate for fuel cells. PBI membranes also have a low gas permeability and low methanol cross-over, which could render them suitable for the DMFC too (Section 2.3).[38, 75, 76]

Another form of water management can be found in direct hydration of the membrane by mounting porous fibre wicks.[77, 78] Twisted threads of porous polyester fibres are placed between the membrane and a cast thin film of Nafion ionomer and is hot pressed at 150 °C. This ensures a direct water supply from either the humidifiers or from product water at the cathode to the membrane by using a pressure difference.

Self-humidifying membranes were used in a fuel cell which improved the water management. These membranes were made by impregnating a Nafion membrane with a few weight-percentage of SiO_2 or TiO_2. The water formed at the cathode and the water transported by electro-osmotic drag are adsorbed by the oxide particles, to ensure hydration of the membrane at all times. The cell was very stable and a high performance was obtained even under ambient conditions.[79] More literature on water transport and management is available.[59, 73, 80–82]

2.2.5. Electrodes

2.2.5.1. General

Electrodes for PEM fuel cells have to be porous to gas diffusion to ensure the supply of the reactant gases to the active zones, where the noble metal catalyst is in contact with the ionic and electronic conductor. The fabrication of gas diffusion electrodes (GDE), although commercially available, is an intricate process in which all details of the structure is important. The structure of the GDEs is crucial for fuel cell performance and depends strongly on the manufacturing process. The reason for this is that the function of the electrodes is actually far more than just catalysing a reaction which is carried out by the catalyst particles.

The main requirement of a good electrode is a three-phase boundary (Figure 10)[43] between the gas supply on one hand, and the catalyst particle and the ionic conductor on the other.

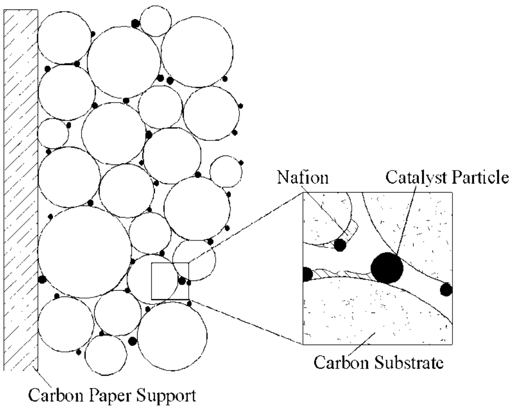

__Figure 10.__ The three-phase boundary in a GDE consisting of the ionomer (ionic conductivity), the pores in the catalyst (gas diffusion), and the catalyst particles (support for electronic conductivity).

The particles must be in direct contact with an electronic conductor to ensure the electrons are supplied to or removed from the reaction site. Electronic conductivity is usually provided by a carbon support onto which the catalyst particles are bound. The three-phase boundary is made by impregnating the catalyst/support powder with some ionomeric binder before pressing the electrode onto the membrane. This ensures good, quantitative contact of most catalyst particles with ionomer chains that have an ionic connection with the membrane.

Gas diffusion occurs through the backing layer and the carbon support to the catalyst particles. When using humidified gases or a methanol/water mixture (see Section 2.3), the catalyst layer must be sufficiently hydrophobic to prevent the pores from flooding. This hydrophobicity can be provided by introducing PTFE as a in combination with Nafion, which is hydrophillic. Although the solubility of oxygen in PTFE is quite high, its diffusivity is rather low and, thus, its permeability (solubility × diffusivity). A high PTFE content of the layer may hinder access of the protons to the catalyst particles.

Usually, the catalyst is made into an ink with water and isopropanol (IPA) and mixed with the binder material. The ink can be cast straight onto the membrane after which a carbon backing layer is pressed on top of the catalyst layer. Alternatively, the ink can also be cast onto the carbon backing layer after which the membrane is pressed onto this. The effect of the binder content on the performance of the electrodes was studied both for the PTFE and the Nafion binders.[83–85]

2.2.5.2. Cathodes

Although a huge variety of non-noble metal catalysts have been investigated, platinum-based catalysts are the superiour materials for the ORR. Platinum dispersed on carbon or other small (such as colloidal) Pt particles exhibit a good performance. Due to the low temperature in a PEMFC, the metal loading for the oxygen catalysts is very high to compensate for the slow kinetics. For practical reasons, fuel cells use air for the cathodic gas supply. The oxygen partial pressure, however, is lower in air so a reduced activity, compared to pure oxygen, is found. Further, when cycling Pt particles over any length of time, the operating conditions induce Ostwald "ripening" of the particles, that manifests in a decrease of active surface area due to the formation of larger particles. More information on the ORR and its kinetics has been published.[11]

Research into less expensive materials and better catalysts for the ORR has been carried out by various groups. Non-noble metal catalysts can be prepared from the pyrolysis of iron acetate adsorbed on perylenetetracarboxylic dianhydride in a $Ar/H_2/NH_3$ gas mixture at 900 °C. A maximum iron content in the catalysts of 0.2 wt% gave a similar current density at 0.5 V as for a 2 wt% Pt/C catalyst.[86]

For improved gas diffusion, it is necessary to assess the carbon backing layer. Several backing layers are commercially available but none of them have the same gas-diffusion properties. Carbon cloth (carbon fibres woven into a clothlike material) backings have 3 – 5 fold higher gas permeation rates than carbon paper (pressed carbon fibres). The use of carbon cloth for cathode backing layers can increase the power density up to 20% more than with carbon paper. The paper backings, however, provide greater stability and rigidity to the electrode. However, the results from different groups are not consistent in this respect and the optimal backing material appears to depend strongly on the cell design.

An optimum porosity of the cathode layer can also be obtained by adding pore-forming substances to the electrode. When an optimum is found, a significant reduction in mass-transport resistance occurs, which improves the overall performance of the electrode.[87]

The effective handling of water through the backing layer is another concern as, in general, backings with thin microporous layers exhibit a better performance. Water is transported through the electrode and backing layer, to thereby avoid complete flooding of the pores.

2.2.5.3. Anodes

The anode catalyst in low temperature fuel cells has to oxidise hydrogen (or methanol in the case of the DMFC; Section 2.3). In an ideal system, the fuel stream only consists of hydrogen, in which case Pt catalysts are ideal. Unfortunately, in most real systems the fuel stream contains traces of certain elements or compounds such as CO, S, and NH_3.

CO is one of the major poisons in low temperature fuel cells.[88, 89] In the PEMFC and PAFC, CO poisoning occurs due to adsorption of the species to the active sites of the catalysts so that no or much fewer sites are available for reaction with H_2; it is a case of site-blocking behaviour. On Pt catalysts, CO adsorbs readily, thus leading to a surface covered with CO. To reactivate the surface, the CO can be oxidised to CO_2. In the AFC, CO is easily oxidised to CO_2 but the electrolyte then becomes contaminated due to carbonate formation (see Section 2.1.4). In the PAFC, CO oxidation is also slightly easier than in the PEM, thanks to the higher operating temperatures.

To avoid CO contamination in the cell, a number of options are available. A gas clean-up can be built in between the reformer and the fuel cell (see Section 3.5), which adds complexity to the system and increases costs. Some research groups added oxygen or hydrogen peroxide to the fuel stream to chemically oxidise the CO to CO_2.[90, 91]

Better catalysts, that oxidise CO at low temperatures, are being investigated by several research groups and give a wide range of options. CO-tolerant anodes usually consist of a Pt-based alloy (for example Pt/Ru). Ternary Pt/Ru/X alloys, in which X is one of a range of other metals, were prepared via a direct-current magnetron sputtering technique to produce thin layers on standard fuel cell electrode substrates. Pt/Ru/W showed an improved CO tolerance over Pt and Pt/Ru catalysts.[92]

The promoting effect of Ru on the catalytic activity of Pt towards the electro-oxidation of methanol has been known since the early 1970s.[93a] Gasteiger et al.[93b–e] correlated the electrocatalytic activity of different polycrystalline Pt/Ru alloys with the analytical ex situ determination of their respective surface composition. Two possible mechanisms have been suggested and the most widely accepted states that the positive influence of Ru is a result of its ability to facilitate dissociated water adsorption.[93f] The bifunctional mechanism involves the adsorption of an oxide species onto the Ru surface, which allows the production of OH_{ads}. This species acts as a source to complete the oxidation of CO into CO_2 (the Ru–O bond is weak enough to allow the OH_{ads} to react with the CO). Several groups studied the effect of electrodeposited Ru upon the catalytic activity of Pt single-crystal electrodes.[94a–d] In these studies, a comparison between single-crystal electrodes, modified by Ru deposition, and Pt/Ru alloys, with a homogenous distribution of Pt and Ru, was made. From STM and IR investigations of the adsorbed CO, it was found that nanostructured Pt/Ru electrodes and alloys show very similar catalytic activity towards CO oxidation. These observations were explained by a cooperative reaction mechanism that shows that CO surface mobility is important for the promoting effect of Pt/Ru and for its superior CO tolerance.

Some studies claim that an electronic promotion is present in the Pt/Ru catalysts, for example, the work by Davies et al.,[94e] states that Ru in the second and third atomic layers (namely, not directly accessible from the surface of an electrode) will still promote the oxidation of CO.

These two mechanisms for the promotion of CO oxidation on Pt/Ru catalysts have also been evaluated for other alloys. Another mechanism to explain the promotional effect of some Pt alloys (for example, some Pt/Sn compounds) is the leaching of the secondary metal out of the alloy, which increases the surface area of the catalyst. The promotional effect is, thus, only due to an increase in surface area and not related to electronic or chemical effects.[95] This type of promotion is not very effective as the effect is only temporary; once all the metal leaches out, no more promotion can be achieved.

2.3. Direct Methanol Fuel Cells

2.3.1. General

The direct methanol fuel cell (Figure 11) is a special form of low temperature fuel cell based on PEM technology. It operates at temperatures similar to PEMFC although it can also run at slightly higher temperatures, dependent on the electrolyte and fuel feed. In the DMFC, methanol is directly fed into the fuel cell without the intermediate step of reforming the alcohol into hydrogen. Methanol is a favoured fuel as it is easily obtained from natural gas or renewable biomass resources, it has a high specific energy density, it is liquid at operating temperatures, and, most of all, the existing infrastructure for transporting petrol may easily be transformed to support methanol. Methanol is one of the few alcohols that can be fed directly into a fuel cell and can be converted electrochemically at the anode.

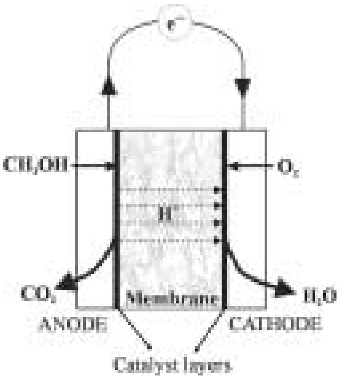

Figure 11. A schematic representation of the reactions in a direct methanol fuel cell.

The DMFC can be fed with a gaseous or liquid fuel feed. The liquid DMFC generally uses methanol diluted in water (typically 1 – 2 M) and only a fraction of the methanol is used at the anode. It is, therefore, important to recycle the effluent and replenish it to keep the concentration in the fuel feed constant. To be able to achieve this, methanol sensors are a very important part of the fuel cell system. Methanol sensors are usually based on an electrochemical system which measures the current from an electro-oxidation of methanol.[96, 97] The gaseous feed of the methanol/water mixture is discussed in Section 2.3.3. Due to their simple system design, DMFCs have attracted considerable interest in the past and reviews on the DMFC are available.[41, 98]

2.3.2. Reactions

As methanol is directly fed to the anode, the anode reaction consists of the oxidation of methanol. Although this reaction occurs in different steps (see Section 1.2.4), the overall anode reaction is given in Equation (33). The protons move from the anode to the cathode via the electrolyte (usually an acidic membrane but liquid-acid DMFCs are under investigation). The cathode reaction does not differ from the normal acidic reaction pathway for oxygen reduction, Equation (34). The overall cell reaction for the DMFC is given by Equation (35).

Anode:

$$CH_3OH + H_2O \longrightarrow CO_2 + 6\,H^+ + 6\,e^- \qquad (33)$$

Cathode:

$${}^{3}\!/_{2}O_2 + 6\,H^+ + 6\,e^- \longrightarrow 3\,H_2O \qquad (34)$$

Overall:

$$CH_3OH + {}^{3}\!/_{2}O_2 \longrightarrow CO_2 + 2\,H_2O \qquad (35)$$

2.3.3. Catalysts

The activity of catalysts for methanol oxidation needs to be improved, although Pt-based compounds have shown the highest activity so far. Compared to hydrogen oxidation, however, the catalytic activity for methanol oxidation is not very effective. It was found early on, that addition of other metals to Pt could enhance the activity of the catalyst dramatically. Species such as Re, Ru, Os, Rh, Mo, Pb, Bi, and Sn have been found to have a positive effect on the catalytic activity towards methanol oxidation.[30, 45, 46, 99–103] For all these metals, it was found that the determining factor for promotion was the formation of an OH^- species on the secondary metal at potentials lower than on Pt. The OH^- species are needed for the oxidation of intermediate adsorbates. It is still necessary, however, to employ higher loadings for the catalysts than for H_2 oxidation.

Other factors that influence the catalytic activity of the electrode are the support, the ionomer content in the active layer, the preparation method, and the fuel feed. It was found that the specific activity of supported Pt/Ru/C is much higher than for the Pt/Ru black. The maximum attainable voltage in the cell is, however, much lower for the supported catalyst. The cell employing the unsupported catalyst also features a lower cross-over rate, to suggest a higher methanol utilisation (Section 2.3.4). The advantage of using a supported metal catalyst lies in the possibility to reduce the metal loadings drastically. The difference in performance may be due to the difference in morphology between the two types of catalyst. It is, therefore, necessary to further investigate the stability of supported and unsupported metal catalysts.[104, 105]

Electrodes can be prepared in a number of different ways (cold spraying and pressing, hot spraying, rolling, among others) and the preparation technique also influences the performance of the electrode. A rolling technique, by which a colloidal dispersion is cast onto a carbon paper substrate, increased the catalytic activity of a Pt/Ru catalyst.[106, 107]

A vapour-fed methanol fuel cell minimises the cross-over effect (Section 2.3.4) and can improve the overall performance of the cell in combination with GDEs. Using a liquid feed arrangement simplifies the design, as no humidification system is necessary. It is, however, necessary to optimise the hydrophobicity of the backing layer and methanol cross-over is easier due to electro-osmotic drag through the system.[108, 109] The system complexity is greater for vapour-fed methanol FCs than the liquid-fed devices.

Several studies on the anodic oxidation of methanol have been reported for a number of catalysts.[31, 34–36, 39] Catalysts for oxygen reduction for DMFCs are mostly identical to those for the PEM fuel cell (methanol-resistant cathode catalysts can be used to avoid methanol cross-over problems; Section 2.3.4). One major problem for the DMFC is the methanol cross-over from the anode to the cathode. This problem, its effects on the cathode, and possible solutions is discussed in the next Section.

2.3.4. DMFCs and Methanol Cross-Over

Most DMFC research nowadays is concentrated on PEM fuel cells fed directly with methanol. The membrane used in DMFCs were developed for PEM applications for optimising the proton condictivity; however, these membranes are not the optimal with regard to methanol blocking. The proton movement across the membrane is associated with water transport in the solvation shells. Due to the similar properties of methanol (such as its dipole moment), methanol is also transported to the cathode by electroosmotic drag. At the cathode, methanol causes a mixed potential due to its oxidation and, consequently, a decrease in cell performance (Figure 12).

The membrane is a very important factor which can be optimised for methanol blocking. Thinner membranes give lower cell resistances but tend to have a higher permeability for liquid methanol. For methanol fuel cells, a thicker membrane, such as Nafion 120, should be used.[110] Another way of improving the permeability of the membrane is to use a Cs^+-doped membrane. Caesium cations were seen to alter the microstructure of the membrane and the conductivity of Cs^+-doped membranes was slightly lower than this for H^+-filled membranes. It is known, however, that Cs^+ has a smaller hydration energy, which ultimately means a reduced affinity for water. The methanol permeability of a Nafion 117 membrane could be lowered by two orders of magnitude by Cs^+ impregnation.[111]

The methanol concentration within the channels of the membrane is equal to the concentration in the methanol feed.

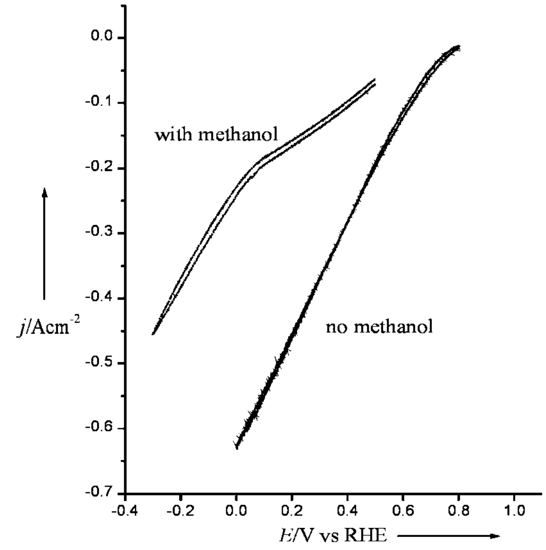

Figure 12. The influence of methanol on the performance of a Pt/C cathode for oxygen reduction. Conditions are standard electrodes from Etek Inc., 0.5 mg cm^{-1} Pt, O_2, in the presence (••••) or absence (——) of methanol. Potentials measured versus a reversible hydrogen electrode (RHE).

The cross-over effect is, thus, dependent on the methanol concentration in the feed. An optimum concentration of methanol was considered to be around 2 M methanol in water (around 6% methanol).[112, 113]

A different approach to cope with the methanol cross-over problem comes with the development of methanol-tolerant cathodes. In this concept, the methanol diffusion is not prevented but, instead, cathodes with catalysts that are inactive towards methanol oxidation are used, thereby preventing the establishment of a mixed potential at the cathode. Different methanol-tolerant cathodes have been investigated. A $Mo_2Ru_5S_5$ catalyst (Chevrel phase) shows inferior performance than Pt for pure oxygen reduction activity but, in the presence of methanol, the activity of the Pt catalyst deteriorated below that of the Mo/Ru/S-based catalyst. A sulfur treatment of the carbon support also increased the performance of the mixed transition metal sulfides (whereas the same treatment for a Pt/C catalyst inhibits the performance). Catalysts of this kind have long been under investigation for their oxygen reduction properties.[114, 115]

Other methanol-tolerant catalysts have been found in iron–porphyrin materials supported on high surface area carbon.[116, 117] These catalysts were tested under fuel cell conditions and it was found that no deterioration of the electrode performance could be seen when methanol was utilised in the cell. These catalysts were also combined with a new cell concept, whereby the anode and cathode reside in the same compartment. Both electrodes were in contact with the same side of the membrane, thus eliminating most of the ohmic resistance in the cell. The fuel efficiency in the cell at low current densities was much higher than for a normal bipolar-plate design. It is clear, however, that a methanol-tolerant cathode is necessary to make this concept feasible.

2.4. Phosphoric Acid Fuel Cells

2.4.1. General

The phosphoric acid fuel cell (Figure 13) is, so far, the most advanced system when it comes to commercial development. It is mainly used in stationary power plants ranging from dispersed power to on-site generation plants. Power plants based on PAFCs are being built around the world with outputs ranging from 0.2–20 MW, to supply cities, shopping malls, and hospitals with electricity, heat, and hot water.

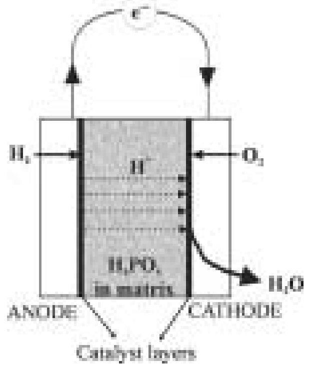

Figure 13. A schematic representation of the reactions in a phosphoric acid fuel cell.

The advantages of the PAFCs, and probably the main factors for its earlier deployment in commercial systems, are its simple construction, its thermal, chemical, and electrochemical stability, and the low electrolyte volatility at operating temperatures (150–200 °C).

In early stages of development, diluted acid was used to avoid corrosion of some of the cell components. Nowadays, with the improved materials available for cell construction, the acid concentration is over 85%. The acid is usually stabilised in a SiC-based matrix. The higher concentration of the acid increases the conductivity of the electrolyte and reduces the corrosion of the carbon-supported electrodes.

In the 1980s, several groups looked into the possibility of using PAFCs for vehicular applications. Further work on PAFCs in the 1990s led to insights into the mechanisms of the electrode reactions, system designs, and, of course, to the ultimate goal of building viable commercial systems.

2.4.2. Reactions

The reactions in the PAFC are the same as in the PEM for the anode and for the cathode reactions, Equations (36) and (37). The cathode reaction in the PAFC is slightly faster than in the PEM, due to the higher operating temperatures (150–200 °C versus 100 °C or less in the PEM).

Anode:

$$H_2 \longrightarrow 2\,H^+ + 2\,e^- \qquad (36)$$

Cathode:

$$\tfrac{1}{2}O_2 + 2H^+ + 2e^- \longrightarrow H_2O \qquad (37)$$

2.4.3. Electrodes

The electrodes used in PAFCs are usually Pt-based catalysts dispersed on a carbon-based support (Section 2.2.5). The hydrogen oxidation reaction at the anode occurs readily over a Pt/C catalyst.

Even at the early stages of the rebirth of fuel cells in the 1960s and 1970s, research for alternative catalysts was carried out to improve the performance to cost ratio. Some studies on nonprecious metal catalysts were reported. Tungsten carbide has been a viable competitor in the race for more suitable catalysts as it is very resistant and stable under PAFC conditions, not contaminated by CO, and has a very long lifetime. Despite all these advantages, Pt is still favoured not only due to its better catalytic properties but mainly because tungsten carbide is very difficult to produce in a manner which will give consistent results. The catalytic properties of tungsten carbide depend erratically on the production process and extraction of the material.[118]

Activated carbon was also suggested for the oxygen reduction reaction. The carbon phase is activated by a sintering in ammonia at high temperatures (900 °C). The activity for oxygen reduction is, however, still too low to be able to compete with Pt.

In PAFCs, it is extremely important to have a hydrophobic backing layer, as a liquid electrolyte is used. To provide hydrophobicity, the backing layer can be immersed in a solution of PTFE. The catalyst layer must also be prevented from pore flooding, which can be obtained by binding the electrode with PTFE. It is difficult, however, to find the optimum amount of PTFE in the electrode, as there is a fine balance between low wettability (and good gas diffusion) and high wettability (and poor gas diffusion).[119]

Electrodes made from Pt/WO_3 have a better performance than those of plain Pt/C by about twice the current density for the same voltage. It was seen, however, that the addition of WO_3 only induces an increase in electrochemically active surface area, which accounts for the increase in performance.[120]

2.5. Molten Carbonate Fuel Cells

2.5.1. General

The development of molten carbonate fuel cells (Figure 14) commenced around the mid-20th century.[121] As all carbonaceous fuels will produce CO_2 along their oxidation pathways, the choice of a molten carbonate for fuel cells was quite logical. Another advantage of the MCFC is its ability to internally reform methane due to the high operating temperatures (600 – 700 °C). In addition to this, the waste heat can be used in combined cycle power plants (see Section 4.3). The high temperatures also increase the oxygen reduction kinetics dramatically, to eliminate the need for very high loading and/or precious metal catalysts.

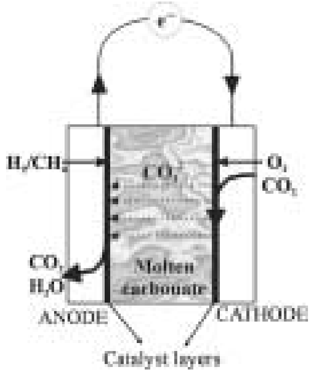

Figure 14. *A schematic representation of the reactions in a molten carbonate fuel cell operated on hydrogen or methane.*

The molten carbonate (usually a LiK or LiNa carbonate) is stabilised in a matrix ($LiAlO_2$), which can be supported with Al_2O_3 fibres for mechanical strength. Finding an optimum electrolyte distribution in the cell is critical, as it is important to balance capillary pressures in order to establish the interfacial boundaries between electrodes and electrolyte.

Molten carbonate fuel cell systems can attain efficiencies of up to 50 %, or up to 70 % when combining the fuel cell with other power generators.[122] MCFCs can operate on a wide range of different fuels and are not prone to CO or CO_2 contamination, as is the case for low temperature cells. For stationary power, molten carbonate fuel cells can play an important role in power conversion units (see Section 4).

2.5.2. Reactions

The high temperature fuel cells have slightly different half-cell reactions due to the difference in electrolyte, however, the overall cell reaction remains the same. When considering the normal half-cell reactions for the MCFC, the anode oxidises hydrogen as given in Equation (38). The carbonate ions used in the oxidation of hydrogen come from the migration through the electrolyte (a molten carbonate) and are formed by the cathode reaction, Equation (39). CO_2 production is, thus, not a problem for the MCFC, in contrast to the AFC (Section 2.4). The anode in the MCFC can also take part in some steps of the internal reforming reaction (Section 4) or can directly oxidise the hydrocarbon or alcohol to CO_2 and H_2O.

Anode:

$$H_2 + CO_3^{2-} \longrightarrow H_2O + CO_2 + 2e^- \qquad (38)$$

Cathode:

$$\tfrac{1}{2}O_2 + CO_2 + 2e^- \longrightarrow CO_3^{2-} \qquad (39)$$

2.5.3. Cathodes

Cathodes for MCFCs are usually NiO, made by an anodic oxidation of a Ni sinter or by an in situ oxidation of Ni metal during the cell start up. NiO cathodes are active enough for oxygen reduction at high temperatures, so that a Pt-based metal is not necessary. A problem with the NiO cathode occurs, however, as the NiO particles grow over time as they leach into the molten carbonate melt, which reduces the active surface area and may cause short circuiting of the cell. Solutions for this problem are the addition of small amounts of magnesium metal to the cathode and the electrolyte for stability. The use of a different electrolyte, which decreases the dissolution of the NiO cathode, is also possible (see Section 2.5.5).

Alternatives for MCFC cathodes have been found in doped lithium oxide materials, such as $LiFeO_2$, Li_2MnO_3, and $LiCoO_2$, also in combination with NiO materials to form double-layer electrodes. A tape casting of a $NiO/LiCoO_2$ double-layer electrode improved the stability tremendously. The ORR was improved at these double-layer cathodes and the resistance decreased.[123, 124]

2.5.4. Anodes

Ni/Al or Ni/Cr alloys have been employed as MCFC anodes. These materials are used since Ni anodes are not stable enough under the MCFC operating conditions as Ni leaches out (see Section 2.5.3).[121, 124] Ceramic – metallic (Cermet) materials avoid sintering, pore growth, and shrinkage of the Ni metal, so that a loss of surface area does not occur. A low cost process is necessary, however, as these materials are expensive to fabricate.

2.5.5. Electrolyte and Matrix

The electrolyte for MCFCs is a molten carbonate stabilised by an alumina-based matrix. Initially, Li_2CO_3/K_2CO_3 materials were used as electrolytes. It was soon found, however, that most fuel cell components degraded in this melt. A Li_2CO_3/Na_2CO_3 melt provides the advantage of a slightly more alkaline system, in which the cathode and anode dissolution is lower, as it prevents a dendritic growth of the Ni metal. Li_2CO_3/Na_2CO_3 electrolytes are expected to have a longer endurance and a lower decay rate than Li_2CO_3/K_2CO_3 melts.

The matrix, which stabilises the electrolyte, consists of either an alumina phase or a ceria-based material. Usually a γ-$LiAlO_2$ phase is used but a transformation into an α-phase during operation is observed. The stability of the α-phase was investigated, and it was suggested that the α-phase may actually be more stable for long term operation than the γ-phase. Ceria-based materials are more stable than alumina-based matrices but they are also more expensive. Reinforcements can be built into the matrix in the form of particulates or fibres. These reinforcements act as crack deflectors to avoid dissolution in the carbonate melt.[122, 124]

2.5.6. Cell Materials

Material selection is far more important in high temperature fuel cells due to degradation, sealing, and thermal expansion properties. There are some high temperature stainless steel alloys available for use in fuel cells. Ni-, Co-, and Fe-based alloys or Cr/Al alloys have proven to be more stable than normal stainless steel (SS). An Fe/Cr ferritic SS material was used in fuel cell components, as the materials are low cost, but it was found that the corrosion resistance was not sufficient. An Fe/Ni/Cr austenitic material was also used and found to be very resistant for the cathodic reduction but not towards anodic oxidation. An Ni coating is necessary to reduce anodic corrosion. The Cr content in the stainless steel compound influences the corrosion resistance the most: The higher the Cr content, the lower the corrosion rate. Chromium-containing SS forms a $LiCrO_2$ inner layer under operating conditions, which is a barrier against Fe^{3+} diffusion, thus decreasing the corrosion.[124, 125] Cost reduction is still a major factor in the fabrication of fuel cell components. An overview on molten carbonate fuel cell materials has been published.[124]

2.6. Solid Oxide Fuel Cells

2.6.1. General

Solid oxide fuel cells (Figure 15) employ a solid oxide material as electrolyte and are, thus, more stable than the molten carbonate fuel cells because no leakage problems, due to a liquid electrolyte, can occur. The SOFC is a straightforward two-phase gas – solid system, so it has no problems with water management, flooding of the catalyst layer, or slow oxygen reduction kinetics. On the other hand, it is difficult to find suitable materials which have the necessary thermal and chemical stability properties for operating at high temperatures (see also Section 2.5.6).

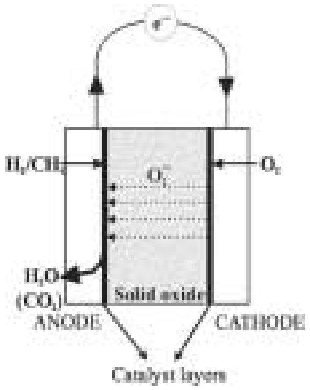

Figure 15. *A schematic representation of the reactions in a solid oxide fuel cell operated on hydrogen or methane.*

Internal reforming is possible in the SOFC over the anode catalyst; partial oxidation reactions and direct oxidation of the fuel have been observed.[126–129] Different concepts for solid oxide fuel cells have been developed. Flat plates stack easily while tubular designs have a smaller sealing problem. Monolithic plate and even single-chamber designs have been considered and investigated for SOFC use. Further, the high power density of the SOFCs mean compact designs are feasible. For the SOFC, the better use of internal reforming and higher temperature waste and exhaust heat can, in combination with co-generation cycles, also provide a high efficiency (up to 70% in a combined cycle system). For example, by pressurising an SOFC module and combining it with a gas turbine, electrical efficiency increases dramatically; in a highly integrated system, air is pressurized by the turbine's compressor and heated in a recuperator before entering the fuel cell module.

2.6.2. SOFC Cell Designs

Different SOFC designs have been developed to implement the fuel cell and reformers into the stack and, ultimately, the complete system. An overview of the different systems is presented in Figures 16 – 20. SOFC designs can be split into two different concepts, the supported and the self-supporting structures. In the supported design, a substrate is used to provide the cell and later stack with the necessary mechanical stability. The self-supporting concept is based on the possibility of using the anode or cathode as a support structure for the other cell components. In this case, the anode or cathode has to be much thicker than in the substrate-supported cells to provide a sufficiently high mechanical stability.

The tubular design is probably the best known design. It has been developed by Westinghouse (now Siemens – Westinghouse). Tubular designs have a self-sealing structure which improves thermal stability and makes the need for good sealants superfluous. The tubular design can be split into two systems, in which the gas flow is parallel (Figure 16)[130] or perpendicular (Figure 17)[131] to the axis of the tube. The first concept was pursued by Westinghouse and consisted of an air-electrode fuel cell. In earlier days, the tubes were made from a calcium-stabilised zirconia on which the active cell components were sprayed (supported configuration). Nowadays, the porous supported tube (PST) is replaced by a doped lanthanum manganite air-electrode tube (AES, self-supporting configuration), which increased the power density by about 35%. The tubes are extruded and sintered and serve as the air electrode. The other cell components are a layered thinly on this construction by electrochemical vapour deposition (EVD). EDV of the electrolyte produces a gas-tight film with a uniform thickness but other deposition methods, such as a colloidal electrophoresis, are also under investigation.[130]

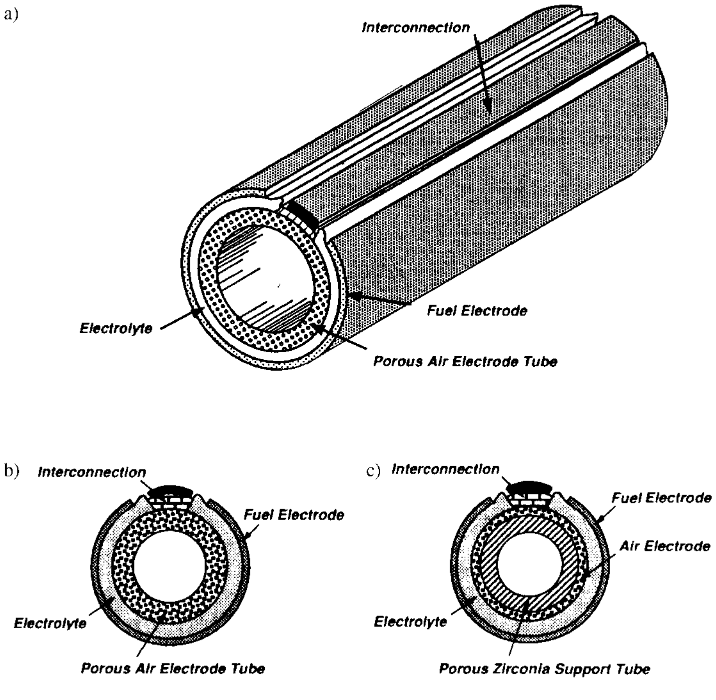

Figure 16. *SOFC cell designs: a) the Siemens – Westinghouse tubular design and the difference between b) a self-supported and c) a substrate-supported structure.*

A different type of SOFC design is under investigation by Sulzer – Hexis (Hexis = Heat Exchanger Integrated Stack; the concept is shown in Figure 17). It can be used for small co-generation plants. The interconnection (see Section 2.6.7) in this case serves as a heat exchanger as well as a current collector and is made by Plansee (Reutte, Austria). Thermal spray coatings on the current collector can improve the stability of the system and performances were tested for 3000 h.[131]

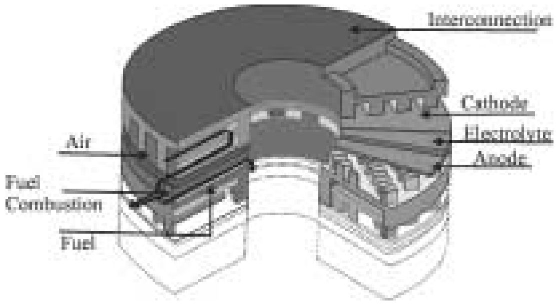

Figure 17. *SOFC cell designs: the Sulzer – Hexis tubular design.*

The planar design (Figure 18)[111] is more efficient and cheaper than the tubular, as the current path is shorter and it is easier to stack. It is, however, still a problem to find good sealants and interconnection materials. Interconnection materials for planar SOFCs have been investigated: For lower temperatures, it was found that stainless steel had the best performance (also better stabilities were reported when doping the stainless steel; see Section 2.6.7), but for higher temperatures, an alloyed metal or a lanthanium – chromite material has been used. Heat removal in a planar design can be achieved by using the cathode air flow and internal reforming; small size cells make this heat exchange easier.

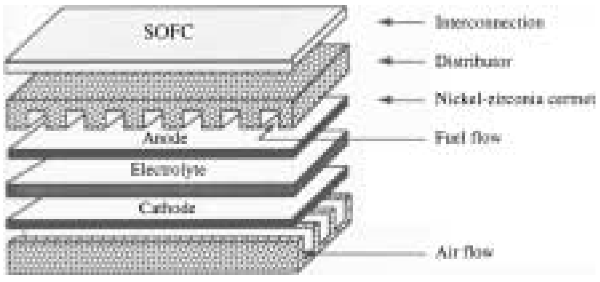

Figure 18. *SOFC cell designs: the planar design.*

The long, monolithic planar cell (LMP)[132] combines the advantages of both tubular and planar cell concepts (Figure 19). The support body consists of the cathode and the interconnection material and is shaped into a long planar structure. The electrolyte is then sprayed onto the support body covering the cathode completely. The anode is then fabricated onto the electrolyte film. The thin planar structure allows a short current path, as for all planar designs, and it is also easy to stack. The oxidant gas is sealed on the inside by the interconnection material, so there is no need for an extra sealant structure. The fuel is supplied to the outside and Ni felts are used as flow fields to provide the anode with sufficient gas.

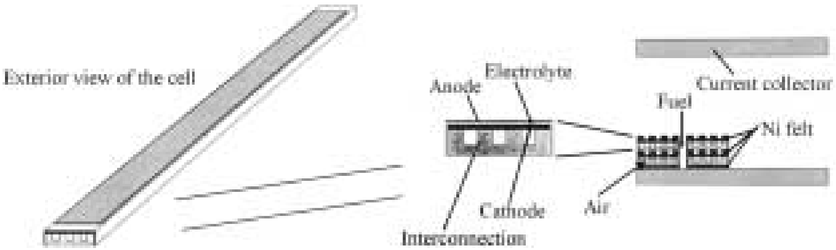

Figure 19. *SOFC cell designs: the long, monolithic planar design.*

The single-chamber design comes in two forms (Figure 20),[133] dependent on the arrangement of the electrodes onto the electrolyte. In Figure 20 a, the power density increases with a decrease in electrolyte thickness, as the electrodes are arranged as normal on either side of the electrolyte. In Figure 20 b, the electrodes are placed on the same side of the electrolyte with a small gap in between. For this design, the power density increases with a decrease in gap between the two electrodes, although an optimum is found around 0.5 mm. A single-chamber design overcomes the sealant problem, as anode and cathode are supplied with the same fuel. For the second system, the electrolyte thickness is not an issue, which is an advantage for the fabrication of electrolytes. As both electrodes see the same mixture of fuel and air it is necessary to have a cathode which does not oxidise the fuel. Cathodes of $LaSrMnO_3$ (LSM) are used for this purpose. The anode for the single-chamber design was a Ni/GDC (gallium-doped cerium oxide) electrode. The performance of this cell was rather low, however, due to the high overpotentials of the catalysts for the reactions and the formation of mixed potentials. The combustion process also needs to be kinetically inhibited to ensure the electrochemical reaction occurs: This can be achieved by lowering the temperatures.[133]

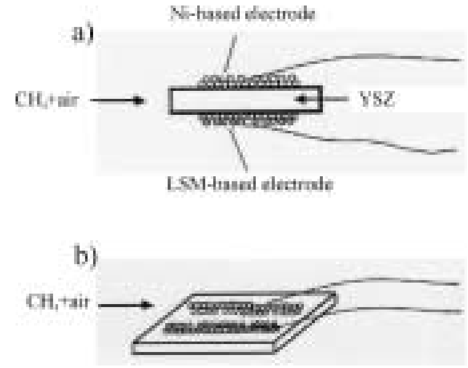

Figure 20. *SOFC cell designs: the single-chamber design.*

Different concepts for the electrode/electrolyte assembly of SOFCs have been investigated (see Section 4). The main differences consist of the fact that the whole cell can be made self-supporting (namely, the assembly supports the structure of the cell and no substrate is used) or supported (whereby the electrodes and electrolyte are cast onto a substrate).

2.6.3. Reactions

The SOFC half cell reactions are different from the low temperature fuel cells due to the conductivity of the solid oxide electrolyte for oxygen ions. The anode reaction is given in Equation (40). The oxygen ions are produced at the cathode and migrate through the solid oxide (migration occurs by oxygen vacancies in the crystal structure) to the anode; the cathode reaction is given in Equation (41).

Anode:

$$H_2 + O^{2-} \longrightarrow H_2O + 2\,e^- \tag{40}$$

Cathode:

$$\tfrac{1}{2}O_2 + 2\,e^- \longrightarrow O^{2-} \tag{41}$$

Solid oxide fuel cells have the same advantages as MCFCs, where CO and CO_2 are not a problem for operation of the fuel cell. The high temperatures also makes expensive, high loading catalysts unnecessary. The advantage SOFCs have over MCFCs is the solid oxide electrolyte, which is very stable and will not leak, which can be a problem with the molten carbonate electrolyte of MCFCs. SOFC systems can be made smaller (1 kW range) than MCFCs because of the latter's requirement to recycle CO_2. The SOFC anode can, like the MCFC anode, take part in internal reforming reactions (see Section 4).

2.6.4. Cathodes

From the beginning of SOFC development, it was found that LSM electrodes had a high activity for oxygen reduction at high temperatures and were stable under SOFC operating conditions. Single-phase LSM cathodes show low oxide diffusion coefficients, so it is better to use a two-phase cathode, which results in a lower overpotential for the oxygen reduction reaction. Yttrium-stabilised zirconia (YSZ) was used as electrolyte in the SOFC (Section 2.6.6) and a composite LSM/YSZ cathode gave a better O^{2-} conductivity and the active area was greater, thus improving the overall catalytic activity even at lower temperatures.[134, 135] The YSZ powder size affects the structure of the cathode, which in turn affects the ionic conductivity.

Perovskite-type materials have been investigated as cathodes for SOFCs as well. Iron-doped cobaltates ($Y_{0.8}Ca_{0.2}Co_{1-x}Fe_xO_3$/YSZ) exhibited a better thermal stability than undoped cobaltates and their activity for oxygen reduction was superior to LSM cathodes. The thermal expansion coefficient of these types of materials is similar to that of the YSZ electrolyte, thereby avoiding discrepancies and cell cracking.[134] Lanthanide-based perovskites showed a high conductivity and a high catalytic activity for oxygen reduction. Several types have been investigated and the best performance was exhibited by a $Sm_{0.2}Sr_{0.8}CoO_3$ cathode.[136] A problem with Co-containing catalysts is that Co can react with the electrolyte. For this reason, these catalysts have to be used at lower temperatures.

2.6.5. Anodes

Anodes for SOFC are usually stabilised Ni cermets. NiO anodes are slightly soluble in the YSZ electrolyte but this stabilises the cubic phase of the electrolyte. A NiO powder mixed with an YSZ powder and a resin binder produces an anode functional layer, onto which the YSZ electrolyte can be deposited and sintered. The cathode can then be sprayed onto this layer to form an anode-supported planar SOFC structure.[137] YSZ/Ni anodes can also be produced by vacuum plasma spraying. To overcome the thermal expansion mismatch that can occur between the anode and the electrolyte, a zirconia-stabilised anode is preferable. The performance of plasma-sprayed electrodes is similar to that of the more common screen-printed anodes.[138]

The anode in the SOFC can take part in the internal reforming process or in a direct oxidation of the fuel. Carbon formation (coking; see Section 3.1.4) on the anode can be reduced by catalyst optimisation and by introducing small quantities of additives to the anode (such as Mo particles).[139] Ruthenium electrodes, supported on TiO_2 or $LaCrO_3$, have been found to locally reform CH_4 with steam produced by the oxidation of hydrogen which occurred at the anode phase boundary.[140]

Doped cerium oxide based YSZ anodes were seen to have a higher catalytic activity and a better ionic and electronic conductivity than a nickel-based anode. It was also less susceptible to carbon formation. Addition of MnO_2 to this anode improved the adhesion between the anode and the YSZ electrolyte but decreased the performance of the electrode.

2.6.6. Electrolytes

For high temperature operation, most ceramics are sufficiently conductive to give a good overall cell performance. Zirconia-supported electrolytes have been found to be stable and they give a reasonable conductivity. Special metallic or ceramic materials are necessary, however, for fabrication of the cell components to sustain the high operating temperatures and to avoid discrepancies in the thermal expansion coefficients. For applications, it would be advantageous to use lower operating temperatures. At these temperatures, however, better cathodes and more conductive electrolytes need to be considered. Ceria-based electrolytes are more conductive than yttria-stabilised electrolytes and, in conjunction with ferritic stainless steel materials, they can provide a competitive model for SOFCs.[135, 141–143]

2.6.7. Other Cell Components

The interconnection material (ICM) is another important issue in SOFC development: It forms the connection between the anode of one cell and the cathode of the next in a stack arrangement (see Section 4.1). The ICM has to be electrically conductive but it must also seal the gas chambers towards the oxygen and fuel feed gases at either the anode or the cathode. Different possibilities for the material depending on the stack design are possible. No systematic procedures exist, however, to determine the suitability of a material in a fuel cell or stack because hardly any data on degradation of interconnection and sealant materials is available.

Chromium-based alloys for bipolar plates are easy to machine, have a high conductivity, and corrosion resistance at high temperatures.[126] Calcium-doped lanthanum plates, combined with small amounts of yttrium binder, were also employed as bipolar plate materials.[145] Iron-based alloys are not stable enough at high temperatures but chromium-doped ferritic steels are sufficiently conductive for lower temperature applications and, when made by vacuum plasma spraying, the evaporation of chromium oxides is suppressed.[146, 147]

Bipolar plates fabricated from $LaCrO_3$-based ceramics have a thermal expansion coefficient similar to ZrO_2 but can only provide a high enough conductivity if a Cr_2O_3 layer is formed on the surface of the material.[148] An alloy with high Cr content made by Plansee was found to have a high corrosion resistance and good thermal conductivity combined with a high mechanical strength and a low expansion coefficient. The metal/cermet alloy is based on a CrFe stainless steel metallic component mixed with an yttrium oxide ceramic. A protective layer of $LaSrCrO_3$ was (vacuum plasma) sprayed on top of the plates to prevent the evaporation of chromium (which is a poison for the catalysts). The machining of this type of material is demanding and therefore costly.

Sealing the SOFC compartments is still a major problem due to the high temperatures, for which not many sealing materials are available. The most commonly used material for this purpose is glass (SiO_2). Normal glass, however, can evaporate and soften with a higher likelihood of leakages as a result. Pyrex seals can be used to avoid evaporation and glass ceramic sealants have been proven to have the necessary stability at high temperatures and pressures so that the probability of leakages can be reduced dramatically.[149, 150]

Ceramic foams consisting of cobalt-doped LSM materials were proven to have a high electrical conductivity and a reasonable compression strength but, most of all, the material does not creep.[151] A survey of materials for electrolytes and interconnection materials for ceramic fuel cells has been published.[141]

3. Fuel Processing

3.1. General

The main fuel for fuel cells is hydrogen (Scheme 3) but its storage is a major issue. Hydrogen has been stored in materials, such as nanotubes, carbon fibres, metal hydrides, and in a number of chemical compounds. Hydrogen stored in alcohols or hydrocarbons, such as methanol or methane, can be an option. Such alcohols and hydrocarbons are usually reformed into hydrogen-rich synthesis gases by several methods, the main processes are catalytic steam reforming (CSR), partial oxidation (POX), and autothermal reforming (ATR).

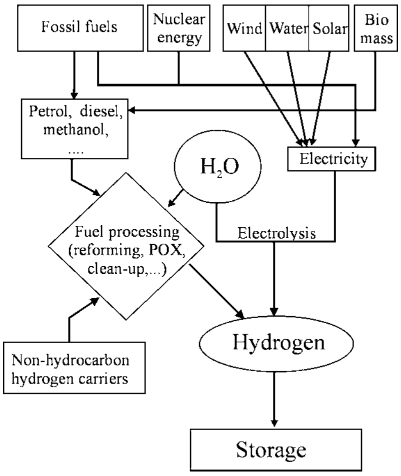

Scheme 3. The different pathways of hydrogen production.

Apart from these techniques, some of the other hydrogen storage forms will be discussed in Section 3.6. CSR is usually performed to obtain hydrogen from light hydrocarbons or alcohols. As it is an endothermic process, energy must be supplied to the system. Steam reforming is the most common reforming process because it yields the highest amount of hydrogen. In contrast, POX is an exothermic process and can be initiated by a simple combustion process. The POX of heavier hydrocarbons is carried out where natural gas is not readily available or where an abundance of oil is predominant. Coal gasification is a similar process, which can also deliver hydrogen, although this reaction is again endothermic. Reviews of on-board hydrogen generation have been published.[152, 153]

Ideally, after reformation, only H_2 and CO_2 should be present but because of the water gas shift reaction (Section 3.2.3), CO is also present, which poisons the catalysts in most fuel cells that operate below 250 °C. A gas clean-up is therefore necessary. After the reformer system, a high and low temperature reactor shifts the reaction equilibrium towards H_2 formation. A preferential oxidation (PROX) reactor can then be used, which selectively oxidises the CO to CO_2, to reduce the CO content in the fuel stream to as low as 5 ppm, dependent on the number of PROX reactors. A membrane can also be used which selectively blocks the permeation of CO (usually a Pd/Ag membrane). The CO can then be burnt to CO_2 and removed from the system. Methanation is another form of gas clean-up (see Section 3.5).

The electrolysis of water is one of the few processes which does not rely on fossil fuels to produce hydrogen. It is also one of the cleanest methods and pure hydrogen (and oxygen) is obtained. Hydrogen may be generated from other carriers, such as ammonia (NH_3), hydrazine (N_2H_4), carbon fibres, and metal hydrides.

Hydrogen is inherently present in fossil fuels, in water, and in secondary sources like biogas and waste materials. It is also a main or by-product in many chemical reactions. It is, however, important to be able to produce hydrogen as economically as possible in fuel cell applications.

3.2. Producing Hydrogen from Alcohols

3.2.1. General

Alcohols, and more specifically methanol, are convenient storage systems for hydrogen (see also the DMFC; Section 2.3). These liquids can easily be transported through the existing infrastructure and have fewer constraints concerning safety than, for instance, gaseous hydrogen storage. The technical synthesis of methanol is base on natural gas, which is readily available. A direct conversion of methanol in fuel cells is attractive, due to the simplicity of the system without the need for a reformer, and can be achieved in MCFCs and SOFCs or DMFCs. However, a research effort is in progress, which, if successful, will diminish considerably the capital costs of small reforming reactors.

Methanol steam reforming can be considered to consist of either the decomposition of methanol followed by the water gas shift reaction or as the reaction of methanol with steam to form CO_2, which can be followed by a reverse shift reaction; both mechanisms are explained in Sections 3.2.2 and 3.2.3. The partial oxidation of methanol is usually not preferred, as steam reforming is more effective for hydrogen production.

3.2.2. Partial Oxidation

Partial oxidation[154] of methanol, Equation (42), is exothermic and occurs over ZnO-supported Pd catalysts with a very high

$$CH_3OH + {}^1\!/_2O_2 \longrightarrow CO_2 + 2\,H_2 \qquad \Delta H_0 = -66.7\ \mathrm{kJ\,mol^{-1}} \qquad (42)$$

selectivity towards hydrogen production. It was found, though, that at higher temperatures the selectivity for H_2 improved but the overall catalytic activity decreased. Methanol reforming over Pd/ZnO catalysts also seems to agree with a partial oxidation scheme followed by a steam reforming step, which improves the selectivity. Methanol decomposition may also play a role in the methanol reforming reaction over this type of catalyst.

3.2.3. Steam Reforming

As mentioned before, the steam reforming[154–156] of methanol can follow two different pathways. The first involves the decomposition of methanol into CO and hydrogen, Equation (43), followed by a water gas shift reaction, Equation (44).

$$CH_3OH \rightleftharpoons CO + 2H_2 \qquad (43)$$

$$CO + H_2O \rightleftharpoons CO_2 + H_2 \qquad \Delta H_0 = -41.2\ \mathrm{kJ\,mol^{-1}} \qquad (44)$$

The second mechanism consists of the reaction of water and methanol to CO_2 and hydrogen, Equation (45), which can be followed by a reverse shift reaction, Equation (46).

$$CH_3OH + H_2O \rightleftharpoons CO_2 + 3H_2 \qquad \Delta H_0 = 49\ \mathrm{kJ\,mol^{-1}} \qquad (45)$$

$$CO_2 + H_2 \rightleftharpoons CO + H_2O \qquad (46)$$

Methanol steam reforming (Scheme 4)[157] occurs when methanol and water are mixed then vapourised and heated to about 300 °C. The vapour mixture is passed over a catalyst, where the reaction occurs. At 300 °C, the decomposition of methanol readily occurs, as well as the two steam-reforming reaction pathways described above, to convert methanol into hydrogen.

Steam reforming of methanol is usually catalysed by Cu/ZnO-type catalysts and can be performed in fixed-bed reactors. The catalytic burner provides the heat for the reaction. The basic burner structure is a ceramic hollow cylinder to which fuel gas mixed with air is supplied. Pure methanol from the tank is used for start-up operation but during continuous operation the methanol feed can be diluted with retentate from the anode off-gas (when connected to a fuel cell system). The products can be separated as necessary.

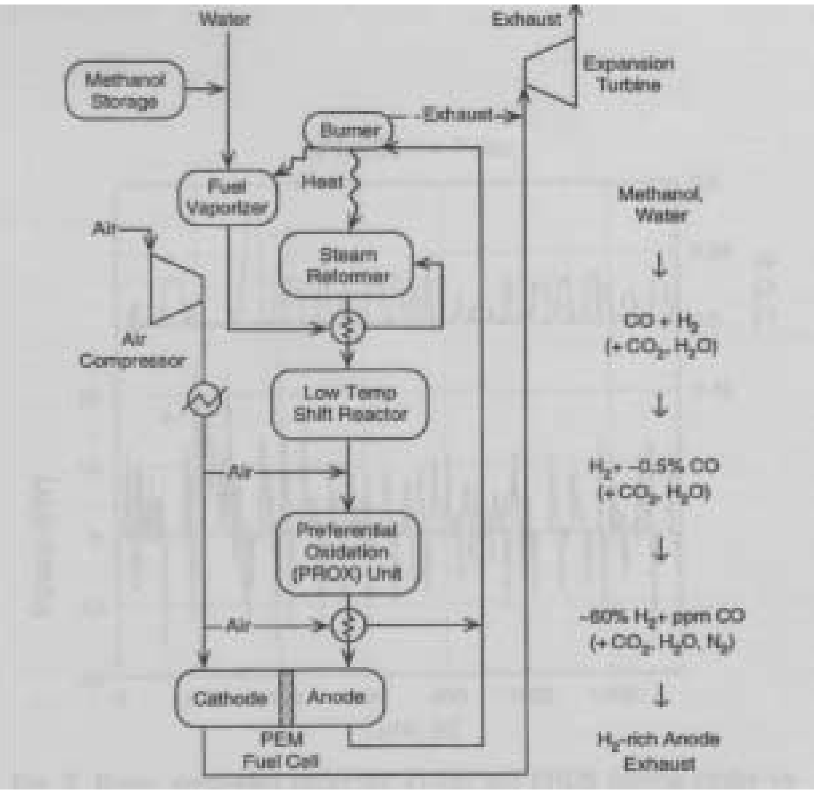

Scheme 4. The methanol steam reforming reaction.

3.2.4. Autothermal Reforming

This type of methanol reforming combines the endothermic steam reforming reaction with the partial oxidation of methanol in an adiabatic system (see Equations (42)–(46)). A spherical reactor system was calculated to be the most attractive configuration for an autothermal process. In this configuration, an inner oxidation catalyst bed is combined with an outer sphere for steam reforming to promote internal heat exchange and maximise the product selectivity.[158]

Autothermal systems can be very productive, fast starting, and compact. A single compact catalyst bed, which converts methanol, water, and air into a reformate composed mostly of CO_2 and H_2, has been built. The Johnson Matthey (Reading, UK) "HotSpot" methanol processor uses a combination of POX and CSR, whereby the relative contributions of the two reactions can be tuned as necessary.[159]

3.2.5. Membrane Reactors

This type of reforming unit combines the process of steam reforming (or cracking, dependent on the conditions) with a semipermeable membrane, which extracts the product, reducing its concentration, and thereby the reaction yields are higher. For the methanol reforming reaction, the hydrogen partial pressure in the product depends less on the reaction and more on the backpressure across the membrane. With a membrane reactor, pure hydrogen was obtained[160] with a total efficiency of 80%. With better membranes and catalysts, the loss of hydrogen could be kept to 5%.

3.3. Producing Hydrogen from Hydrocarbons

Natural gas is abundant in most places over the world as a fossil fuel. Other natural resources, such as oil, coals, and coal gas, can also be found in most regions. As was the case for methanol, hydrogen has to be liberated from the hydrocarbons by one of the mentioned processes: CSR, POX, or ATR. Natural gas can be used directly without external reforming in the high temperature fuel cells.

3.3.1. Catalytic Steam Reforming

3.3.1.1. General

Catalytic steam reforming[161] (Scheme 5)[162] was recognised as a process in the early 19th century and has been developed since. A series of patents were filed in the 1920s when researchers in the US were interested in broadening the possible uses of CSR into different fields. Europe and Japan quickly followed and new routes for the CSR of different hydrocarbons were found. Nowadays, CSR is one of the principal processes for the production of H_2

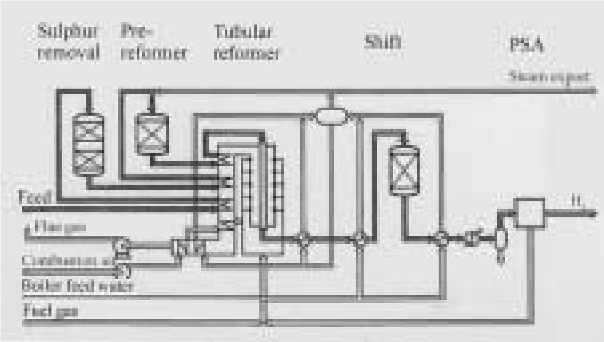

Scheme 5. *The hydrocarbon steam reforming reaction.*

and syngas (synthetic gas; a mixture of H_2 and CO). Although partial oxidation and coal gasification also play a vital role in hydrogen production, CSR is cheaper and more energy efficient than the former two methods.[163]

3.3.1.2. Reactions

The general reaction mechanism for steam reforming of a hydrocarbon into syngas is given in Equation (47).

$$C_nH_m + n\,H_2O \rightleftharpoons n\,CO + (n + {}^1\!/\!_2 m)\ H_2 \qquad (47)$$

This reaction is endothermic and needs an energy input to work. Further reactions of CO can be the water gas shift reaction to CO_2 or the methanation reaction to methane (which are also used in the reformer unit to clean the effluent gas; see Section 3.5). The water gas shift reaction is given in Equation (48).

$$CO + H_2O \rightleftharpoons CO_2 + H_2 \qquad (48)$$

This reaction is reversible, so a mixture of CO_2 and hydrogen can produce more CO by the reverse water gas shift reaction. The same can occur in the methanation process, Equation (49), which is also reversible.

$$CO + 3\,H_2 \rightleftharpoons CH_4 + H_2O \qquad (49)$$

3.3.1.3. Catalysts

Steam reforming of most hydrocarbons occurs only over appropriate catalysts (therefore, catalytic SR), apart from at very high temperatures, where, in some cases, steam reforming can occur without a catalyst (methanol decomposition can be carried out above a certain temperature without catalyst; see Section 3.2.3). Catalysts for SR are usually group VIII metals, in which Ni appears to be the most active of this group. The addition of ceramic oxide stabilisers (α-Al_2O_3 and other oxides) can improve the catalytic activity and can prevent coke formation (Section 3.3.1.4). Catalysts appear in their oxide form and can be activated by some reducing agents like H_2 and NH_3. Reduction of the metal oxide results in free metal particles, which can take part in the reaction to produce more free metal sites and so on.

3.3.1.4. Coke Formation

Depending on the catalytic selectivity and on the saturation (carbon to hydrogen ratio) of the hydrocarbons, the decomposition of the hydrocarbon may be favoured over the reaction with steam. This process, called coke formation, can deactivate the catalyst in different ways. The carbon so formed can diffuse through the metal crystal and disrupt the catalyst structure but the catalyst surface properties remain unchanged. A slow polymerisation of $^{\bullet}C_nH_m$ radicals can also occur, which causes a progressive deactivation of the catalyst. An encapsulation of the catalyst particles by carbon precursors limits the catalytic activity by blocking the active sites.

To avoid coke formation, an optimum fuel to steam ratio must be maintained throughout the entire system. The affinity for hydrocarbon decomposition also induces the need for a heat flux, whereby the temperature of the catalyst at the tube walls should be lower than the carbon limit temperature. Smaller metal crystallites (<2 nm) or promotion of the catalysts with alkaline material also reduces coke formation.

3.3.2. Partial Oxidation

Methane and other hydrocarbons can be converted to hydrogen by partial oxidation,[155, 164–166] which may be catalysed or uncatalysed. Partial oxidation (Scheme 6)[157] is a reforming

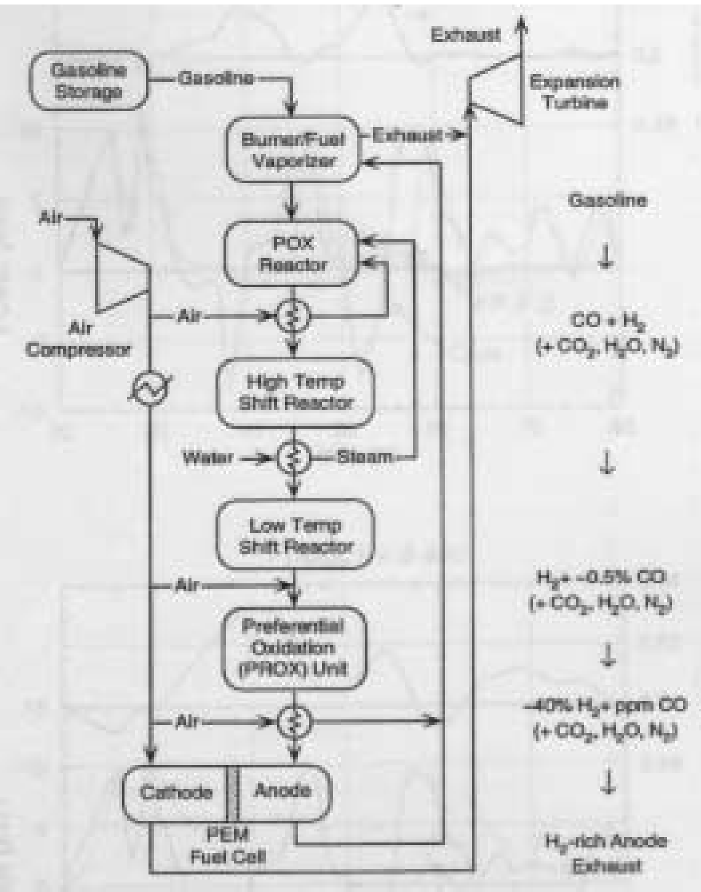

Scheme 6. *The partial oxidation of hydrocarbons to hydrogen.*

process in which the fuel is partially combusted; it is exothermic and provides heat for other reactions in the reforming system (usually in combination with steam reforming). The oxygen fed into the system is substoichiometric, so that both CO and CO_2 are formed.

A gas shift reaction can transform the CO from the first reaction further into CO_2 (Section 3.5). The principle reactions are given in Equations (50) and (51).

$$CH_4 + {}^1\!/\!_2 O_2 \rightleftharpoons CO + 2\,H_2 \qquad (50)$$

$$CH_4 + O_2 \rightleftharpoons CO_2 + 2\,H_2 \qquad (51)$$

When using air as the oxidant, NO_x components can be formed at high temperatures (> 1400 °C). Methane POX occurs over heterogeneous selective catalysts, whereby Ni/Al_2O_3 has a high selectivity for CO_2/H_2 at reforming temperatures of 850 °C. $Ni/La/Al_2O_3$ was found to have a lower activity and selectivity. At lower temperatures, different catalyst were tested and it was shown that $Co/La/Al_2O_3$ is active at 750 °C but not at lower temperatures, whilst an $Fe/La/Al_2O_3$ catalyst could be used at 600 °C but provided a low conversion and low selectivity.[165]

3.3.3. *Autothermal Reforming*

Autothermic conversion of methane to hydrogen occurs readily at 850 °C, where a partial oxidation process is combined with a catalytic steam reforming process. An improved performance was found for single-bed configurations, as opposed to two-bed systems, due to the better heat exchange possibilities in a single-bed reactor. A 60–65 % methane conversion could be attained with a selectivity of 80 % towards hydrogen production. Systems employing the autothermic conversion of hydrocarbons are being used internally for MCFCs and SOFCs and can be used externally for other fuel cell systems (see Section 4).

3.3.4. *Membrane Reactors*

It is also possible for the reforming of hydrocarbons to be combined directly, as described for methanol reforming (Section 3.2.5), using a membrane in order to selectively shift the reforming reactions towards formation of the product. Membrane reactors[162] are more economic at lower temperatures but they need a minimum temperature of around 650 °C, otherwise their fuel consumption and feed supply pressure is too high. A very selective membrane is needed to perform the separation of the substances.

3.3.5. *Propane Cracking*

The decomposition of hydrocarbons (propane, methane, and so forth) is endothermic but provides some advantages to the reactor design. A simple design can be chosen, as no shift converter or steam generator is necessary. The reaction for propane cracking[167] is given by Equation (52).

$$C_3H_8 \rightleftharpoons 3\,C + 4\,H_2 \qquad \Delta H_0 = 103.8\ \text{kJ}\,\text{mol}^{-1} \qquad (52)$$

This reaction occurs at above 800 °C, so a heat source (such as a propane burner) is needed. The carbon by-product accumulates on the surface of the catalysts, thus eventually blocking the whole surface area. The catalyst can be regenerated, however, by passing air over the surface to burn off the carbon. Some small amounts of CO and CO_2 are produced during the cracking process, which can be removed by methanation, selective oxidation, or catalytic burning (Section 3.5).

3.3.6. *Coal Gasification*

This process is endothermic and a high temperature is needed for the reaction to proceed. Solid coal is treated with oxygen and steam to produce a syngas mixture according to Equation (53). The reaction process can be very complex, however, as coal comes in many forms and compositions. The process, therefore, has to be adjusted for each type of coal mined. This type of hydrogen production is mainly used in large powerplants (> 20 MW).

$$C + H_2O \longrightarrow CO + H_2 \qquad (53)$$

3.4. Hydrogen from Other Sources

Ammonia (NH_3) is an easily liquefied gas produced by the reaction of methane with steam and air. It is easy to find transport facilities, as ammonia is widely used in many applications (fertilisers, for instance). Decomposition of NH_3 occurs according to Equation (54), to produces hydrogen by cracking at high temperatures.

$$2\,NH_3 \rightarrow N_2 + 3\,H_2 \qquad (54)$$

An ammonia fuel cell power plant was developed by the Analytical Power Corporation (Boston, MA, USA) using an ammonia cracker to power the fuel cells. The biggest advantage to ammonia over hydrocarbons is the lack of carbonaceous species, which can decompose alkaline fuel cells or poison the other low temperature fuel cells.[168]

Electrolysis of water is a major issue in hydrogen production: Hydrogen produced by water electrolysis is pure and, most of all, the process can be completely emission free if the electricity used to electrolyse the water is from a renewable source, such as hydropower or wind energy. Hydro-electric power plants could enhance the energy storage by using the electricity to produce hydrogen. Solar energy is also a clean method for water electrolysis.

Another renewable method to produce hydrogen comes in a rather unlikely form. It was recently reported that some type of algae can be tricked into producing hydrogen instead of their normal photosynthesis processes that lead to oxygen. The plants utilise stored carbohydrates and other biochemical materials to generate hydrogen using just sunlight and water. It should, therefore, be possible to extract hydrogen from these algae by growing them in a closed system and venting off the produced hydrogen.[169]

3.5. Gas Clean-Up

Reforming hydrocarbons into hydrogen always produces small amounts of CO in the gas stream. This contaminant must be taken out of the fuel stream before being fed into low temperature fuel cells. The gas clean-up can be done in several ways. The first step is a water gas shift conversion of some of the CO into CO_2, thereby producing more hydrogen, which is the reason why this is called the shift reaction. The next step, to reduce the CO level, can be carried out by different techniques. The three most common ones are selective oxidation, methanation, and the use of a selective membrane.

3.5.1. The Shift Reaction

The shift reaction involves the conversion of CO into CO_2 using steam as an oxidant according to Equation (55). This reaction is hydrogen-forming reaction is exothermic and usually carried out over a catalyst. The reformate clean-up includes both a high and low temperature shift step. The high temperature shift reactor uses Fe_3O_4 catalysts and temperatures above 350 °C to produce CO_2 and H_2 from CO and steam. The low temperature reactors operate at around 200 °C and employ CuO/ZnO catalysts.

$$CO + H_2O \rightleftharpoons CO_2 + H_2 \qquad \Delta H_0 = -41.2\ \mathrm{kJ\,mol^{-1}} \qquad (55)$$

For SOFCs and MCFCs, a separate shift reactor is not necessary, as CO can be used in the cell by direct oxidation or an internal shift reaction can occur in these systems. When using an internal reforming system, the H_2 produced by the reforming step is directly used at the anode, thereby shifting the reforming step towards hydrogen. The produced CO can also be directly oxidised or shifted with steam to hydrogen and CO_2.

After the low temperature shift reactor, the fuel stream still contains CO (0.5 – 1 %), still too high for low temperature fuel cells. Therefore, a further clean-up has to be carried out.

3.5.2. Selective Oxidation

Selective removal of CO occurs over some catalysts, which only oxidise CO and not hydrogen. The fuel stream is fed in a bed over these catalysts and oxygen is introduced. Catalysts used for this purpose are usually alumina-supported structures: Ruthenium and rhodium supported on alumina are amongst the most active catalysts. Near to complete CO conversion can be achieved at temperatures as low as 100 °C. Copper particles dispersed on alumina are cheaper, easier to make, and, combined with ZnO, they also have a high catalytic activity for CO oxidation. The activity depends on the Cu particle size, with smaller particles being more active. Selective oxidation prevents the loss of hydrogen, as opposed to the methanation process (Section 3.5.3).[170, 171]

3.5.3. Methanation

A different approach to CO removal is taken by the methanation process.[159] In this process, CO is treated with hydrogen to form methane and water. The amount of hydrogen needed to carry out this reaction is, however, three times the amount of CO removed, as shown in Equation (56).

$$CO + 3\,H_2 \rightleftharpoons CH_4 + H_2O \qquad \Delta H_0 = -206.2\ \mathrm{kJ\,mol^{-1}} \qquad (56)$$

CO_2 present in the gas stream can, however, react with the hydrogen produced in a reverse shift reaction (see Section 3.5.1); the CO produced thereby would defeat the purpose of the whole process. Methanation can remove CO but severe restrictions are necessary to make this process viable in a gas clean-up system.

3.5.4. Membranes

Palladium-alloy membranes can be very effective in the removal of CO from the fuel stream. The gas is fed through the membrane but only the hydrogen can permeate. They require rather large pressure differences and a relatively high temperature, which could make them less efficient depending on whether the heat can be provided by the fuel cell system or not. The use of membranes was already mentioned (Section 3.2.5), whereby the methanol steam reforming and the reforming of hydrocarbons can be directly combined with a membrane to produce clean hydrogen.[160, 162, 172]

A combined system with different catalytic stages can prove to be the best answer to the problem of gas clean-up. The second cleaning step should take the CO level down to around 10 – 100 ppm, which can then be fed through the fuel cell with minimal losses.

3.6. Hydrogen Storage

Hydrogen can be stored either as a pure compound in gaseous or liquid form and also as hydrogen bound in metals and chemicals. Hydrogen storage in hydrocarbons and other energy carriers such as ammonia and hydrazine was discussed in Section 3.1. Other, mostly physical, forms of hydrogen storage will be shown here.

3.6.1. Pure Hydrogen

It is well known that hydrogen/air mixtures are explosive and most people still have the images of the Hindenburg or the Challenger disaster imprinted in their minds. Most other gases, however, are far more explosive than hydrogen and, in case of a leak, hydrogen disperses so quickly that it is very difficult to ignite. Safety measures are one of the major implications when it comes to commercialisation of hydrogen fuel cells, although necessary safety measures can easily be taken and implemented in all applications.

For simplicity, it would be best to store hydrogen directly on board the vehicle or next to the stationary application. In this way, problems with reformed hydrogen, which contains contaminants that can degrade the fuel cell performance, are avoided. Unfortunately, the storage of gaseous hydrogen is not an easy task. Compressing hydrogen into a tank can be achieved but a restricting factor, especially for transportation applications, is the size and mass of these tanks. With tanks of acceptable size and mass, the driving range of vehicles is restricted and much lower compared to the prevailing systems. Gaseous hydrogen is used, however, to fuel buses and on-site cars, as long ranges are not required and small tanks can be used.

Liquid hydrogen has the highest energy density of any form of hydrogen storage. Liquid hydrogen tanks should be extremely well insulated (boiling point is $-253\,^{\circ}$C) and even then a loss of around 1 – 2% per day of the stored hydrogen by evaporation occurs. Another problem with liquid hydrogen storage is the amount of energy necessary to convert the hydrogen into a liquid.

Although existing refuelling stations could be employed for refilling hydrogen tanks in both liquid and gaseous forms, it is still necessary to completely reorganise these stations, which could be rather expensive and time consuming. Localised refilling stations can be employed especially for fleet refill purposes. A project running at the Munich airport (Germany) uses cars running on hydrogen for special transports from the terminal to the plane. The filling station is one of Europe's first and also provides hydrogen for a fleet of buses running at the same airport. The NECAR4 prototype hydrogen car from Daimler – Chrysler (see Section 4.3.2) was also a guest at the hydrogen refuelling station.

3.6.2. Hydrogen in Other Structures

The storage of hydrogen in metals or other structures is sometimes incorrectly called solid hydrogen. In principle, the hydrogen is stored as atomic hydrogen or as a gas absorbed into the structure. Metal hydrides are commonly used for hydrogen storage: A metal alloy exposed to hydrogen can form a metal hydride. The conditions under which a metal alloy forms a metal hydride depends on the type of alloy. The release of hydrogen usually involves the heating of the metal hydride. Metal hydrides are common and can be used for different applications; hydrogen storage is only one of them. A database with properties, processing details, and applications of metal hydrides can be found on the Internet.[173]

A special case of metal hydride storage is found in the so-called powerballs. These powerballs store sodium hydride very effectively: They are produced by coating sodium hydride pellets in a waterproof skin and the balls are then stored in water. To release the fuel, mechanical breakage of the skin of individual balls releases fuel as necessary. The reaction of the stored NaH with water produces hydrogen and sodium hydroxide. The released hydrogen bubbles to the top of the containing vessel and can be used for fuel cells.[174]

Another hot topic in hydrogen storage is the use of graphite nanostructures, which store hydrogen in gaseous form within their crystal structure. These graphite structures can be obtained in tubular form (nanotubes) or as fibres. Both forms are highly conductive, flexible, and mechanically stable. The storage of hydrogen is achieved by absorption of the hydrogen gas in the crystal structure under elevated pressures and temperatures. The absorbed hydrogen is claimed to be more densely packed in the material than is possible by compressing hydrogen gas.[175]

Nanotubes can be considered elongated fullerenes with open ends, in which all carbon atoms are arranged in a sheet of hexagons. This sheet of hexagons can be rolled along its main axis to form an electrically conducting tube or perpendicular to this axis to form an insulator. Controversial reports state that single-walled nanotubes have a hydrogen storage capacity of 4.2 wt% (a H:C atomic ratio of 0.52). Most of the absorbed hydrogen is claimed to be released at ambient pressure and temperature, whilst the residual hydrogen could be obtained by slightly heating the samples.[176, 177] Multiple walled nanotubes are reported to be even more promising.

Other, also controversial, studies report graphite nanofibres are even better than nanotubes.[178] They have been reported to store about 20 – 30 L of hydrogen per gram of material, which is about ten times as much compared to metal hydrides. Carbon nanofibres are predicted to store up to three times their own mass in hydrogen under pressure at room temperature. This would be far more than any natural hydrogen storage in hydrocarbons (the highest storage, methane, is 25 wt%). The key to this enormous storage capacity is believed to be the regular, close-packed structure of the nanofibres. The fibres pack into dense, layered plates with gaps in between. Multiple layers of hydrogen could fit into these spaces (Figure 21)[179a] if the interaction with the carbon molecules is strong enough. However, several groups could not confirm the spectacular claims and therefore caution is advised with respect to these storage materials.[179b]

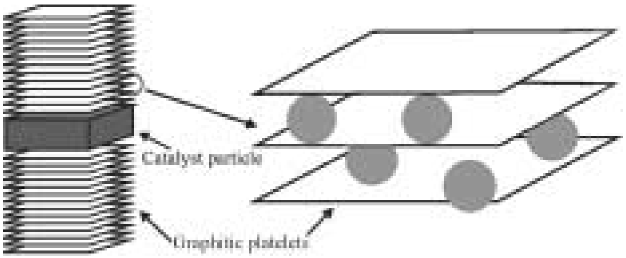

Figure 21. *Hydrogen absorption (grey circles) in graphite (platelike) nanofibre multilayers.*

Carbon nanomaterials could be cost-effective as long as an efficient production method can be found. Scaling up the production process is necessary to attain economical feasibility. Charging the materials with hydrogen still takes quite a long time and the pressures employed to pack the hydrogen in the crystal structure can be rather high. Reproducibility is also a factor which needs to be approached for commercialising this technique; thus far, many results have been published and, while some are very promising, many of them have proved to be irreproducible. Nevertheless, nanostructured carbon materials could prove to play an important role in hydrogen storage systems.

Glass microspheres[175] have been used for the purpose of hydrogen storage as well. At high temperatures, hydrogen gas can permeate through glass, so that the glass microspheres can store hydrogen under pressure when the temperature is lowered. At lower temperatures, the gas is locked in the structure until the microspheres are heated and release the trapped hydrogen. The storage capacity of these structures is smaller than for the carbon nanofibres but could compete as a more reliable method.

Zeolites can store hydrogen in a similar manner. The gas can be forced into the pores of the molecular sieves under elevated temperatures and pressures. Cooling the matrix again traps the hydrogen, which can be released by heating. The amount of hydrogen which can be stored depends on the cation of the zeolite. Potassium zeolites have been found to store more hydrogen than rubidium- and still more than sodium zeolites.[180, 181]

The entire scope, from fuel to fuel cell system to vehicle to infrastructure, has to be taken into account when comparing different storage forms and fuel processing techniques for fuel cells. A combination of existing technologies should be feasible to design a system which is compatible with every one of the fuel cell applications. With modern and future technologies, it should be possible to find enough options for hydrogen production and storage to avoid hydrogen storage hindering the commercialisation of fuel cells.

4. Systems and Applications

In order to fulfil the requirements of a specific application with fuel cells, smart system engineering, which considers all aspects from safety regulations to user comfort and attainable power densities, is necessary. Therefore the fuel cells always need to be integrated into a system in which the components are matched. A fuel cell alone delivers insufficient voltage for most applications, which is why they are combined together in series into stacks. These stacks need peripheral components (fuel processing, power conditioning, heat recovery, cooling, and so forth) to operate the fuel cell and to control certain parameters, as well as to ensure a supply of fuel and oxidant. The stacks can themselves be combined into modules, which can then be used in an application. The complexity of systems with fuel cells is described in this Section.

4.1. Stack Engineering

Single cells do not deliver the necessary power output; the voltage of a single cell cannot be used for normal applications. Therefore the cells are connected in arrays where the cell voltages are added in series (Figure 22).[182] The cell current is constant over all cells. To be able to operate a stack efficiently, careful design of the flow fields is required, as the pressure and pressure drop over the flow field of the gases in all cells needs to be the same. The connection of the single cells is also important.

The multifunctional current collector plates facilitate the coupling of single cells into a stack. Not only do these plates act as flow fields for the reactant gases and as current collectors in the single fuel cells, when combined into a stack the current collector plates become bipolar plates. These plates must be both gas-tight, as the gases stream on either side of the plate, and they must be able to separate the single cells electrically.

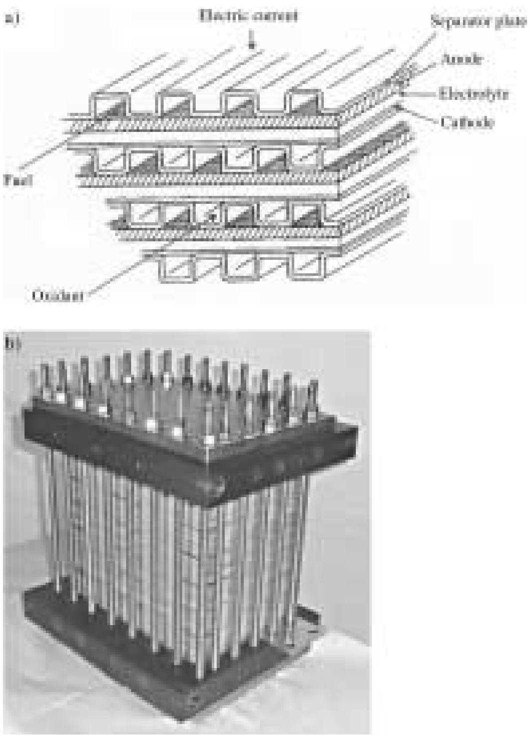

Figure 22. The formation of a stack (a) schematically and b) in practise) showing the array of single cells connected by bipolar plates.

Usually single cells are assembled “vertically” to form a stack, although some lateral expansion has also been implemented, especially for small applications. The insulation of all the cells from each other is, of course, important to avoid a short circuit. It is also important to be able to produce MEAs with similar characteristics. Water management in the stack can also be difficult.

4.2. Fuel Processing Systems

The reforming of hydrocarbons and alcohols was discussed in Section 3. In this Section, the three methods to incorporate reformation into the system will be discussed. Of these reforming types, the external reforming takes place outside the stack, whereas the internal and integrated reforming take place within the stack. For external reforming, the hydrocarbon is converted into a hydrogen-rich gas stream outside the fuel cell and the hydrogen is fed into a fuel cell stack. The reformer operates at temperatures of 800 – 1000 °C, as the reforming process is highly endothermic. The heat supplied by the burning of the anode gas exhaust (sometimes mixed with a supplement of the hydrocarbon fuel, for instance, at start-up of the appliance) can be used for the reforming process.[121]

The integrated reformation involves a chemical reactor in thermal contact with either the complete or a part of the fuel cell stack. The cells can be fed separately, whereby each individual cell contains a reformer unit. Alternatively, there could be one reforming unit per block of cells, which can then supply the cells with hydrogen. A combination of both is also possible, of course. The extra advantages of integrated reforming is that the waste heat from the fuel cell can be directly used to provide the heat necessary for the reforming process and concurrently the stack is cooled efficiently. An integrated reformation improves the overall efficiency of the system. External reforming units add mass and volume to the system but the main disadvantage is the increased complexity and slowed response time.

The direct fuel cells (MCFC and SOFC) with internal refomation differ from the above systems in that the fuel is supplied to the anode compartment of the fuel cell and is there either directly oxidised to CO_2 and water or the fuel can be reformed and a water gas shift reaction can shift the reaction in favour of hydrogen. The hydrogen obtained in the reforming step can then be used by the anode to produce protons and electrons. This internal reforming has even more advantages than the integrated reforming, as the heat exchange between the different components can be achieved more easily and the need for gas clean-up is superfluous in these systems. In this respect, internal reformation is a very attractive option, as the fuel cell system can be compact and simple.

4.3. Power Plants

4.3.1. Stationary Power

The most important attributes of fuel cells for stationary power generation are the high efficiencies for relatively small systems and the possibility for distributed power generation. Both low and high temperature fuel cells could, in principle, be utilised for stationary applications. The low temperature fuel cells are advantageous in that a quicker start-up can usually be achieved. The high temperature systems, such as SOFCs and MCFCs, generate high grade heat, which can directly be used as process heat, usually as steam or indirectly by incorporating the fuel cell system into a combined cycle. SOFCs and MCFCs also have the advantage that they can operate directly on available fuels without the need for external reforming.

For a small, distributed power system, such as single or multiple home power generation, a PEMFC or PAFC combined with a heat cycle could be used to provide all the energy requirements for residential use (Figure 23 a, b).[183] The PAFC start-up time is much faster than high temperature systems, which makes it more attractive for small-scale power generation. The heat generated by the fuel cell system can be employed for heating purposes and for providing hot water. The PAFC produces enough steam to operate a steam reforming system, whereas the PEMFC system operates at lower temperatures without producing much steam. The SOFC system can also be used for this type of application, as it produces enough power and heat.

Larger scale power plants (> 250 kW) can use both high and low temperature fuel cell systems. The high grade heat obtained from the high temperature systems can be exchanged over a broad temperature range to provide the possibility of direct heat use and further electricity production from the generated heat remains open to the user. The start-up time of these systems is longer than for low temperature systems but the advantages of being able to operate the system without external reforming and the higher efficiencies of SOFCs and MCFCs makes these systems more suitable for large-scale power plants.

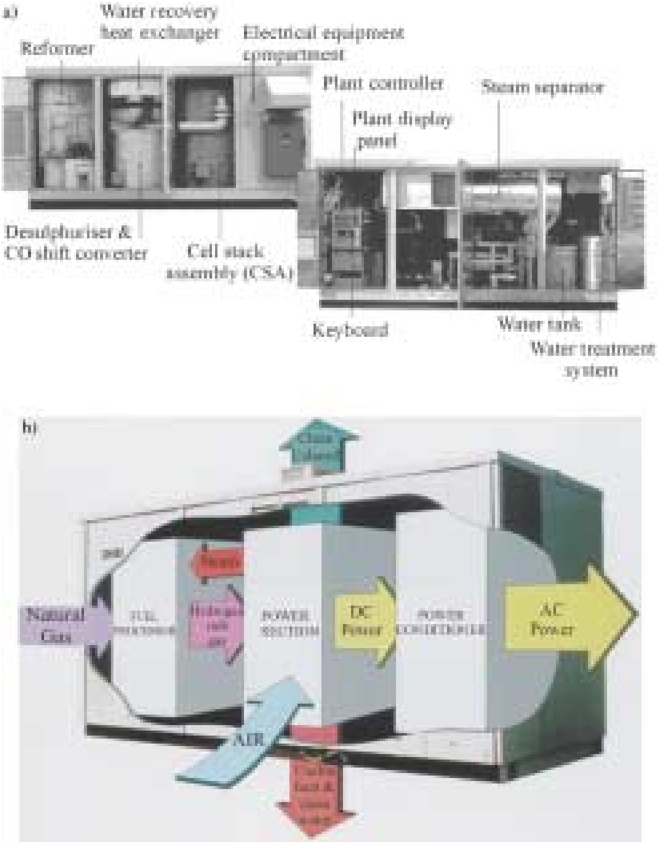

Figure 23. a) *The Toshiba ONSI PC25 PAFC system showing the different parts to the system (fuel cell, gas processing, control units, and so forth).* b) *The overall integration into other household systems.*

4.3.2. Vehicle Propulsion

For vehicular applications, fuel cell systems need to differ from stationary power generation. The available space in vehicles is much more critical and fast response and start-up times are required. Thus, only the low temperature systems seem applicable for vehicles.

The controversial AFC has proven to be a suitable system for hybrid vehicles, as long as a circulating electrolyte is used and pure hydrogen is supplied to the fuel cell. Pure hydrogen distribution centres are not widely available and, thus, it is predicted that AFC vehicles will be limited to specific types (such as fleet buses and other centralised vehicles). For space vehicles, AFCs have shown their worth and, although the tendency to change to PEM fuel cells is also penetrating the space industry, it is likely that AFC systems will be employed for many more years in space because system reliability is of paramount importance and the introduction of new technologies is therefore inhibited.

For car propulsion, PEM fuel cells are being tested all over the world (Figure 24 a – c).[184–186] The PEFC has very fast start-up and response times. The major problem with the implementation of PEM fuel cells in vehicles is the fuel supply. Liquid fuels are easier to handle, transport, and have a high energy density, which is essential for driving ranges of modern cars (in the order of 500 km). Hydrogen in the liquid form is not obtained easily and requires much energy to generate. Methanol is one of the ideal candidates for vehicle use but fuel reforming leads to slower response times and extensive gas clean-up procedures are needed to supply the fuel cell with CO-free hydrogen. A direct methanol supply into the anode of a DMFC is considered more suited to vehicles and portable applications but, as was mentioned before, the DMFC system has to be developed further to achieve higher power densities and better stability. Based on state-of-the-art technology, it is foreseen that the first fuel cell vehicles will be fuelled with liquid hydrogen. The fortune of the methanol-fuelled vehicles depends crucially on the choices of the mineral oil industry and their willingness to support this fuel. Advances in DMFC technology might give an impetus to these systems, although reforming technology will also advance. Gasoline-supplied cars are also under investigation but gasoline reforming still poses problems of fuel reformation and response time, and work is still required to make this option viable for vehicle propulsion.

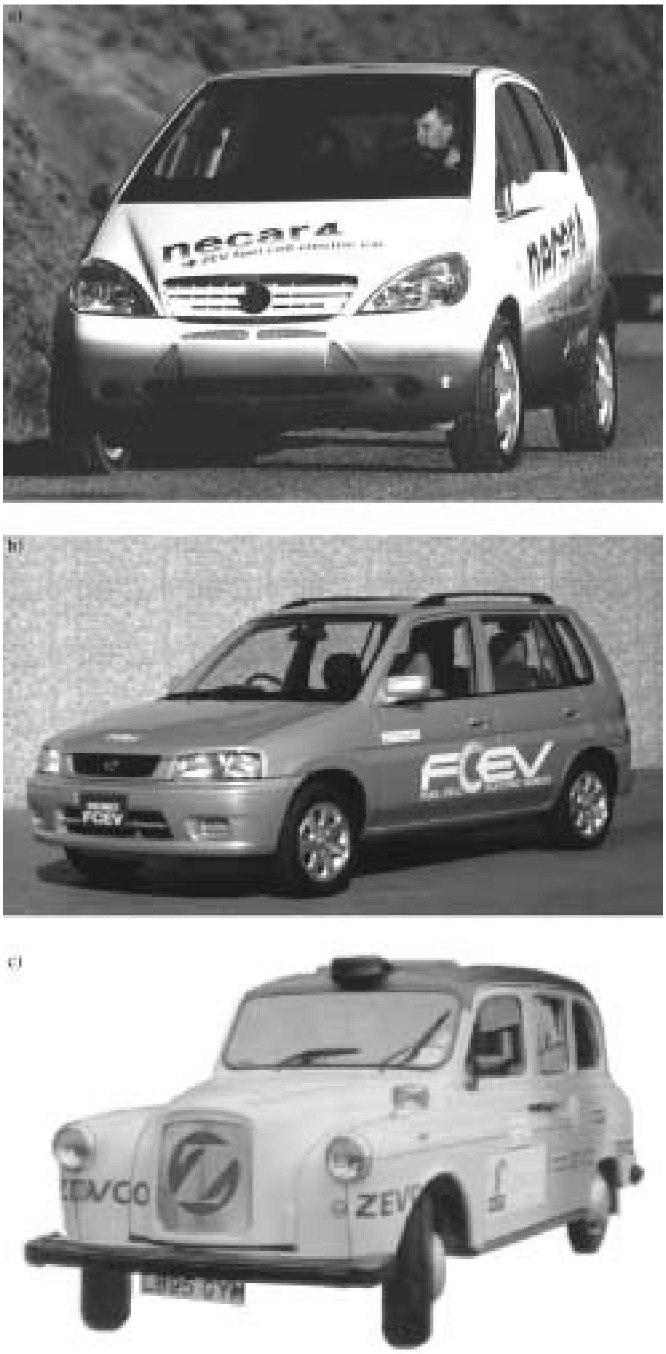

Figure 24. *Fuel cells used in vehicular systems: a) NECAR 4 (Daimler – Chrysler); b) Demio FCEV (Mazda); c) an alkaline fuel cell vehicle (the ZEVCO London Cab).*

4.3.3. Portable Applications

For small power applications,[187, 188] like laptops, camcorders, mobile phones, and so forth, the specifications of the fuel cell systems are quite different and compete mainly with batteries. The systems utilised thus far are PEM fuel cells, combined with metal hydride or another form of pure hydrogen storage, or direct methanol fuel cells (Figure 25). The requirements for portable applications are mostly focused on system size and mass, as well as the temperature. Other fuel cells are, therefore, not suitable for these applications. Portable devices need less power than other applications and, thus, DMFC systems are well suited if power densities can be improved. With further improvements in technology and storage systems, PEM fuel cells and DMFC systems will continue to compete in this market.

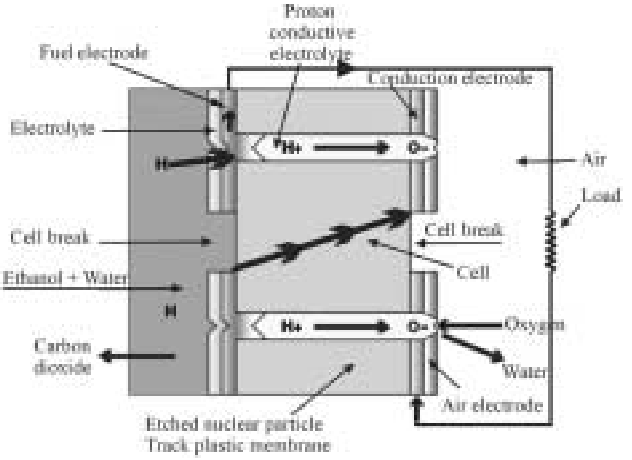

Figure 25. *The Micro Fuel Cell from Manhattan Scientific (New York, USA).*

5. Summary and Future Technologies

Looking at fuel cells, it can be seen that these devices will make a valuable contribution to future power generation facilities. Both the low and high temperature fuel cells have their advantages and disadvantages and, depending on the application, they can both be implemented in a variety of systems. Fuel cells with their high efficiency, low emissions, and high reliability are ideal candidates for distributed power generation. The modularity of fuel cells makes them suitable for a wide range of applications, as the power needed can easily be attained by changing the number of modules. An overview of all fuel cells specifying current applications, operating temperatures, reactions, and some advantages and disadvantages for each type is listed in Table 1.[3, 7, 8, 70, 189]

Twenty years ago, mainly universities and research institutions—but only a few companies—conducted fuel cell research on the fundamentals of fuel cells. Nowadays, due to the commercial interest, innumerable research groups and companies have fuel cell activities ranging from catalyst studies to the development of novel PEMFC and DMFC membranes and the development other components for fuel cells. Optimisation of flow field structures, backing layers, and other units of the single cells have intensified.

The work carried out on stack performance is also considerable. Institutions are investigating different arrangements, better reactant manifolds, and the general optimisation of stacking single cells into operational modules. The combination of these modules, together with their peripheral components, leads to full working systems currently being tested all over the world.

When looking at the fuel cell systems, it was noted that the fuel cells themselves need optimisation but the peripheral components especially are not up to commercialisation standards. More efficient reformers are necessary to bring the cost of systems down. Fuel processing also demands a major part of the system, especially for low temperature systems. Optimisation of the catalysts may reduce the need for more efficient gas clean-up systems, although, considering environmental factors, it will still be necessary to have sufficient gas processing.

There is no ideal fuel cell for all applications. As shown in Section 4, the most suited system depends on the application requirements. Not only the fuel cell itself but the entire system has to be under investigation when customising fuel cells for specific purposes. It may seem that a certain type of fuel cell is better suited for a certain application but, when taking the hydrogen storage and/or the reforming into account, the picture can change dramatically. For high power systems, high temperature fuel cells with internal reforming offer more efficient electrical systems than low temperature fuel cells. For vehicular applications, the judgement depends strongly on the future fuel; for hydrogen fuelled vehicles, low temperature systems are ideal, however, the use of fossil fuels may favour the high

Table 1. *An overview of all fuel cells, giving cell reactions, operating temperatures, applications, and specifications.*

	AFC Alkaline	PEMFC Polymer Electrolyte Membrane	DMFC Direct Methanol	PAFC Phosphoric Acid	MCFC Molten Carbonate	SOFC Solid Oxide
Temperature [°C]	60–90	80–110	80–110	160–200	600–800	800–1000; 500–600 possible
Anode reaction	$H_2 + 2OH^- \rightarrow 2H_2O + 2e^-$	$H_2 \rightarrow 2H^+ + 2e^-$	$CH_3OH + H_2O \rightarrow CO_2 + 6H^+ + 6e^-$	$H_2 \rightarrow 2H^+ + 2e^-$	$H_2 + CO_3^{2-} \rightarrow H_2O + CO_2 + 2e^-$	$H_2 + O^{2-} \rightarrow H_2O + 2e^-$
Cathode reaction	$\frac{1}{2}O_2 + H_2O + 2e^- \rightarrow 2OH^-$	$\frac{1}{2}O_2 + 2H^+ + 2e^- \rightarrow H_2O$	$\frac{3}{2}O_2 + 6H^+ + 6e^- \rightarrow 3H_2O$	$\frac{1}{2}O_2 + 2H^+ + 2e^- \rightarrow H_2O$	$\frac{1}{2}O_2 + CO_2 + 2e^- \rightarrow CO_3^{2-}$	$\frac{1}{2}O_2 + 2e^- \rightarrow O^{2-}$
Example applications						
Transport	London Taxi (Zevco)	NECAR series, Ford P2000, Toyota,...	high possibility for vehicles	golf cart hybrid		
Stationary	Astris	Plug Power		ONSI PC 25 (UTX)	ERC (Santa Clara)	Siemens–Westinghouse (Westervoort)
	residential plants	residential unit			M-C Power Corp. (Miramar)	+ projects with Norske Shell, SCE,... Global Thermoelectric residential unit
Portable		Fraunhofer ISE	Micro Fuel Cell (Manhattan Scientific) Darpa (JPL) for low power applications			
Space	Apollo, Space Shuttle (IFC)	Gemini, Mars missions				
Advantages	Simple system design	Faster start-up no leakage of electrolyte	Methanol is easier to store	Higher operating temp reduces CO problems	High efficiencies possible, especially combined with gas turbine, internal reforming possible, CO and CO_2 tolerant	no electrolyte creeping, high efficiencies possible (co-generation), internal reforming possible, CO and CO_2 tolerant
Disadvantages	Not CO_2 tolerant	Not CO tolerant, water management problem in membranes	Not CO tolerant water management problems, methanol cross-over	Liquid electrolyte leaks, lower phosphoric acid conductivity	Longer start-up, electrolyte creep possible, NiO cathode can creep and cause short circuit	Longer start-up, high operating temperatures need different materials

temperature systems for mobile applications. For portable devices, a low operation temperature is crucial and only the PEM and DMFC systems appear realistic.

The fuel flexibility and compatibility with existing fuel infrastructure are requirements which can be met by most fuel cells. The overall efficiencies attained are much higher than for conventional systems and it can be seen that fuel cells are entering the market as additions to conventional systems and may start to compete, in a couple of years, when capital costs can be reduced due to technological advances and increase in production volumes.

There are few commercial fuel cells on the market so far. The PAFC system marketed by ONSI (Figure 23) is the sole system which can be purchased for relatively small power applications. Companies such as H-Power, Ballard, and Plug Power are currently developing their products to commercial standards. Fuel cells for laboratory demonstrations can be purchased. A full list of all developers and their contact details can be found on the Internet.[190, 191] The market introduction of other applications will not take long and it is important to face the facts: Fuel cells are coming our way; we should be ready.

The research was funded by the Deutsche Forschungsgemeinschaft, reference 74/8-1 and Sti 74/8-2.

[1] B. M. Barnett, W. P. Teagan, *J. Power Sources* **1992**, *37*, 15.
[2] F. D. Melle, *J. Power Sources* **1998**, *71*, 7.
[3] D. Hart, *J. Power Sources* **2000**, *86*, 23.
[4] G. D. Callow, *J. Power Sources* **1999**, *80*, xvii.
[5] A. Bauen, D. Hart, *J. Power Sources* **2000**, *86*, 482.
[6] "Clean fuel cell energy for today": *Platinum Met. Rev.* **1999**, *43*, 14.
[7] S. G. Chalk, J. F. Miller, F. W. Wagner, *J. Power Sources* **2000**, *86*, 40.
[8] A. U. Dufour, *J. Power Sources* **1998**, *71*, 19.
[9] *Energiedaten*, Bundesministerium für Wirtschaft und Technologie, Magdeburg, **1999**.
[10] P. W. Atkins, *Physical Chemistry*, Oxford University Press, Oxford, **1994**.
[11] K. Kinoshita, *Electrochemical Oxygen Technology*, Wiley, New York, **1992**.
[12] A. Damjanovic, M. A. Genshaw, J. O. M. Bockris, *J. Chem. Phys.* **1966**, *45*, 4057.
[13] H. S. Wroblowa, Y. C. Pan, G. Razumney, *J. Electroanal. Chem.* **1976**, *69*, 195.
[14] A. J. Appleby, M. Savy, *J. Electroanal. Chem.* **1978**, *92*, 15.
[15] R. W. Zurilla, R. K. Sen, E. Yeager, *J. Electrochem. Soc.* **1978**, *125*, 1103.
[16] a) V. S. Bagotskii, M. R. Tarasevich, V. Y. Filinovskii, *Elektrochimiya* **1969**, *5*, 1218; b) M. L. Sattler, P. N. Ross, *Ultramicroscopy* **1986**, *20*, 21; c) L. J. Bregoli, *Electrochim. Acta* **1978**, *23*, 489; d) Y. Takasu, N. Ohashi, X.-G. Zhang, Y. Murakawi, H. Minagawa, S. Sato, K. Yahikozawa, *Electrochim. Acta* **1996**, *41*, 2595; e) M. Watanabe, H. Sei, P. Stonehart, *J. Electroanal. Chem.* **1989**, *261*, 375.
[17] K. Kinoshita, *J. Electrochem. Soc.* **1990**, *137*, 845.
[18] N. Giordano, E. Passalacqua, L. Pino, A. S. Arico, V. Antonucci, M. Vivaldi, K. Kinoshita, *Electrochim. Acta* **1991**, *36*, 1979.
[19] Y. Kiros, *J. Electrochem. Soc.* **1996**, *143*, 2152.
[20] Y. F. Yang, Y. H. Zhou, C. S. Cha, *Electrochim. Acta* **1995**, *40*, 2579.
[21] M. Peuckert, T. Yoneda, R. A. Dalla Betta, M. Boudart, *J. Electrochem. Soc.* **1986**, *133*, 944.
[22] Y. Takasu, N. Ohashi, X. G. Zhang, Y. Murakami, H. Minagawa, S. Sato, K. Yahikozawa, *Electrochim. Acta* **1996**, *41*, 2595.
[23] R. S. Weber, M. Peuckert, R. A. Dallabetta, M. Boudart, *J. Electrochem. Soc.* **1988**, *135*, 2535.
[24] M. Watanabe, S. Saegusa, P. Stonehart, *Chem. Lett.* **1988**, 1487.
[25] D. R. de Sena, E. R. Gonzalez, E. A. Ticianelli, *Electrochim. Acta* **1992**, *37*, 1855.
[26] S. J. Clouser, J. C. Huang, E. Yeager, *J. Appl. Electrochem.* **1993**, *23*, 597.
[27] a) J. Barber, S. Morin, B. E. Conway, *Electrochem. Soc. Proc.*, **1997**, *97*, 101; b) B. N. Grgur, N. M. Markovic, P. N. Ross, *Electrochim. Acta* **1998**, *43*, 3631.
[28] B. N. Grgur, N. M. Markovic, P. N. Ross, *J. Electrochem. Soc.* **1999**, *146*, 1613.
[29] L. J. Burcham, I. E. Wachs, *Catal. Today* **1999**, *49*, 467.
[30] L. Liu, R. Viswanathan, R. Liu, E. S. Smotkin, *Electrochem. Solid State Lett.* **1998**, *1*, 123.
[31] R. W. McCabe, D. F. McCready, *J. Phys. Chem.* **1986**, *90*, 1428.
[32] G. T. Burstein, C. J. Barnett, A. R. Kucernak, K. R. Wiliams, *Catal. Today* **1997**, *38*, 425.
[33] A. Hamnett, *Catal. Today* **1997**, *38*, 445.
[34] J. Sobkowski, K. Franaszczuk, K. Dobrowolska, *J. Electroanal. Chem.* **1992**, *330*, 529.
[35] H. Matsui, A. Kunugi, *J. Electroanal. Chem.* **1990**, *292*, 103.
[36] X. H. Xia, T. Iwasita, F. Ge, W. Vielstich, *Electrochim. Acta* **1996**, *41*, 711.
[37] A. Wieckowski, M. Rubel, C. Gutierrez, *J. Electroanal. Chem.* **1995**, *382*, 97.
[38] C. He, H. R. Kunz, J. M. Fenton, *J. Electrochem. Soc.* **1997**, *144*, 970.
[39] M. Watanabe, S. Saegusa, P. Stonehart, *J. Electroanal. Chem.* **1989**, *271*, 213.
[40] R. Parsons, T. Vandernoot, *J. Electroanal. Chem.* **1988**, *257*, 9.
[41] S. Wasmus, A. Küver, *J. Electroanal. Chem.* **1999**, *461*, 14.
[42] M. P. Hogarth, G. A. Hards, *Platinum Met. Rev.* **1996**, *40*, 150.
[43] A. J. Dickinson, Ph.D. thesis, University of Newcastle-upon-Tyne (UK), **2000**, p. 250.
[44] a) A. Hamnett in *Comprehensive Chemical Kinetics*, *Vol. 37* (Ed.: R. G. C. G. Hancock), Elsevier, Amsterdam, **1999**, p. 635; b) V. S. Bagotzky, Yu. B. Vassiliev, O. A. Khazova, *J. Electroanal. Chem.* **1977**, *81*, 229.
[45] K. L. Ley, R. Liu, C. Pu, Q. Fan, N. Leyarovska, C. Segre, E. S. Smotkin, *J. Electrochem. Soc.* **1997**, *144*, 1543.
[46] Y. Morimoto, E. B. Yeager, *J. Electroanal. Chem.* **1998**, *444*, 95.
[47] M. Watanabe, M. Uchida, S. Motoo, *J. Electroanal. Chem.* **1987**, *229*, 395.
[48] Z. Wei, H. Guo, Z. Tang, *J. Power Sources* **1996**, *58*, 239.
[49] P. Biedermann, B. Höhlein, B. Sackmann, *Electro-Chemical Engineering and Energy* (Eds.: F. Lapicque, A. Storek, A. A. Wragg), Plenum, New York, **1995**.
[50] L. J. M. J. Blomen, M. N. Mugerwa, *Fuel Cell Systems*, Plenum, New York, **1993**.
[51] J. Appleby, F. R. Foulkes, *Fuel Cell Handbook*, Krieger, Melbourne, FL, **1993**.
[52] F. Albisu, *European Seminar on Combined Production of Heat and Power (Co-Generation)* (Ed.: J. Sirchis) Elsevier Applied Science **1989**, p. 10.
[53] E. D. Geeter, M. Mangan, S. Spaepen, W. Stinissen, G. Vennekens, *J. Power Sources* **1999**, *80*, 207.
[54] Y. Kiros, S. Schwartz, *J. Power Sources* **2000**, *87*, 101.
[55] K. Kordesch, J. Gsellmann, M. Cifrain, S. Voss, V. Hacker, R. R. Aronson, C. Fabjan, T. Hezje, J. Daniel-Ivad, *J. Power Sources* **1999**, *80*, 190.
[56] K. Kordesch, V. Hacker, J. Gsellmann, M. Cifrain, G. Faleschini, P. Enzinger, R. Fankhauser, M. Ortner, M. Muhr, R. R. Aronson, *J. Power Sources* **2000**, *86*, 162.
[57] K. Kordesch, G. Simader, *Fuel Cells and Their Applications*, VCH, Weinheim, **1996**.
[58] P. V. Wright, *Electrochim. Acta* **1998**, *43*, 1137.
[59] H. L. Yeager, A. Steck, *J. Electrochem. Soc.* **1981**, *128*, 1880.
[60] M. Wakizoe, O. A. Velev, S. Srinivasan, *Electrochim. Acta* **1995**, *40*, 335.
[61] B. Baradie, C. Poinsignon, J. Y. Sanchez, Y. Piffard, G. Vitter, N. Bestaoui, D. Foscallo, A. Denoyelle, D. Delabouglise, M. Vaujany, *J. Power Sources* **1998**, *74*, 8.
[62] K. M. Nouel, P. S. Fedkiw, *Electrochim. Acta* **1998**, *43*, 2381.
[63] K. M. Abraham, V. R. Koch, T. J. Blakley, *J. Electrochem. Soc.* **2000**, *147*, 1251.
[64] M. Doyle, S. K. Choi, G. Proulx, *J. Electrochem. Soc.* **2000**, *147*, 34.
[65] E. Peled, T. Duvdevani, A. Melman, *Electrochem. Solid State Lett.* **1998**, *1*, 210.
[66] E. Peled, T. Duvdevani, A. Melman in *Second Int. Symp. Proton Conducting Membrane Fuel Cells II* (Eds.: S. Gottesfeld, T. F. Fuller), Boston, MA, **1998**, p. 6.

[67] T. Lehtinen, G. Sundholm, S. Holmberg, F. Sundholm, P. Björnbom, M. Bursell, *Electrochim. Acta* **1998**, *43*, 1881.

[68] H. P. Brack, F. N. Büchi, J. Huslage, G. G. Scherer in *Second Int. Symp. Proton Conducting Membrane Fuel Cells II* (Eds.: S. Gottesfeld, T. F. Fuller), Boston, MA, **1998**, p. 52.

[69] K. Yasuda, O. Uchimoto, Z. Ogumi, Z.-i. Takehara in *Symp. Batteries and Fuel Cells for Stationary and Electric Vehicle Applications*, (Eds.: A. Langrebe, Z. Takehara), Honolulu, HI, **1993**, p. 292.

[70] T. Okada, S. Moller-Holst, O. Gorseth, S. Kjelstrup, *J. Electroanal. Chem.* **1998**, *442*, 137.

[71] Z. Ogumi, Z. Takehara, S. Yoshizawa, *J. Electrochem. Soc.* **1984**, *131*, 769.

[72] C. L. Gardner, A. V. Anantaraman, *J. Electroanal. Chem.* **1998**, *449*, 2009.

[73] C. A. Edmondson, P. E. Stallworth, M. C. Wintersgill, J. J. Fontanella, Y. Dai, S. G. Greenbaum, *Electrochim. Acta* **1998**, *43*, 1295.

[74] K. H. Choia, D. J. Park, Y. W. Rho, Y. T. Kho, T. H. Lee, *J. Power Sources* **1998**, *74*, 146.

[75] R. F. Savinell, J. S. Wainwright, M. Litt in *Second Int. Symp. Proton Conducting Membrane Fuel Cells II* (Eds.: S. Gottesfeld, T. F. Fuller), Boston, MA, **1998**, p. 81.

[76] J. S. Wainwright, J.-T. Wang, D. Weng, R. F. Savinell, M. Litt, *J. Electrochem. Soc.* **1995**, *142*, L121.

[77] M. S. Wilson, C. Zawodzinski, S. Gottesfeld in *Second Int. Symp. Proton Conducting Membrane Fuel Cells II* (Eds.: S. Gottesfeld, T. F. Fuller), Boston, MA, **1998**, p. 424.

[78] M. Watanabe, Y. Satoh, C. Shimura, *Symp. Batteries and Fuel Cells for Stationary and Electric Vehicle Applications* (Eds.: A. R. Landgrebe, Z.-I. Takehara), Honolulu, HI, **1993**, p. 302.

[79] M. Watanabe, H. Uchida, Y. Seki, M. Emori, *J. Electrochem. Soc.* **1996**, *143*, 3847.

[80] T. Okada, G. Xie, O. Gorseth, S. Kjelstrup, N. Nakamura, T. Arimura, *Electrochim. Acta* **1998**, *43*, 3741.

[81] T. A. J. Zawodzinski, T. E. Springer, F. Uribe, S. Gottesfeld, *Solid State Ionics* **1993**, *60*, 199.

[82] K. H. Choi, D. J. Park, Y. W. Rho, Y. T. Kho, T. H. Lee, *J. Power Sources* **1998**, *74*, 146.

[83] Z. Poltarzewski, P. Staiti, V. Alderucci, W. Wieczorek, N. Giordano, *J. Electrochem. Soc.* **1992**, *139*, 761.

[84] O. Teschke, *J. Electrochem. Soc.* **1983**, *131*, 1095.

[85] S. J. Lee, S. Mukerjee, J. McBreen, Y. W. Rho, Y. T. Kho, T. H. Lee, *Electrochim. Acta* **1998**, *43*, 3693.

[86] G. Faubert, R. Cote, J. P. Dodelet in *Second Int. Symp. Proton Conducting Membrane Fuel Cells II* (Eds.: S. Gottesfeld, T. F. Fuller), Boston, MA, **1998**, p. 30.

[87] S. Gamburzev, C. Boyer, A. J. Appleby in *Second Int. Symp. Proton Conducting Membrane Fuel Cells II* (Eds.: S. Gottesfeld, T. F. Fuller), Boston, MA, **1998**, p. 23.

[88] H.-F. Oetjen, V. M. Schmidt, U. Stimming, F. Trila, *J. Electrochem. Soc.* **1996**, *143*, 3838.

[89] R. Ianiello, V. M. Schmidt, U. Stimming, J. Stumper, A. Wallau, *Electrochim. Acta* **1994**, *39*, 1863.

[90] J. Divisek, H.-F. Oetjen, V. Peinecke, V. M. Schmidt, U. Stimming, *Electrochim. Acta* **1998**, *43*, 3811.

[91] S. Gottesfeld, J. Pafford, *J. Electrochem. Soc.* **1988**, *135*, 2651.

[92] G. Holleck, D. Pasquariello, S. Clauson in *Second Int. Symp. Proton Conducting Membrane Fuel Cells II* (Eds.: S. Gottesfeld, T. F. Fuller), Boston, MA, **1998**, p. 150.

[93] a) H. Binder, A. Köhling, G. Sandstede in *From Electrocatalysis to Fuel Cells* (Ed.: G. Sandstede), University of Washington Press, Seattle, WA, **1972**, pp. 43-57; b) H. A. Gasteiger, N. Markovic, P. N. Ross, E. J. Cairns, *J. Phys. Chem.* **1993**, *97*, 12020; c) H. A. Gasteiger, N. Markovic, P. N. Ross, E. J. Cairns, *J. Phys. Chem*. **1994**, *98*, 617; d) H. A. Gasteiger, N. M. Markovic, J. P. N. Ross, *J. Phys. Chem.* **1995**, *99*, 8290; e) H. A. Gasteiger, N. M. Markovic, J. P. N. Ross, *J. Phys. Chem*. **1995**, *99*, 8945; f) M. Watanabe, S. Motoo, *J. Electroanal. Chem.* **1975**, *60*, 275.

[94] a) E. Herrero, K. Franaszczuk, A. Wieckowski, *J. Electroanal. Chem.* **1993**, *361*, 269; b) K. A. Friedrich, K.-P. Geyzers, U. Linke, U. Stimming, J. Stumper, *J. Electroanal. Chem*. **1996**, *402*, 123; c) K. A. Friedrich, K.-P. Geyzers, U. Stimming, J. Stumper, R. Vogel, *Electrochem. Soc. Proc.* **1995**, *95*, 299; d) K. A. Friedrich, K.-P. Geyzers, A. Marmann, U. Stimming, R. Vogel, *Z. Phys. Chem*. **1999**, *208*, 137; e) J. Davies, B. E. Hayden, D. J. Pegg, *Electrochim. Acta* **1998**, *44*, 1181.

[95] J. Solokowski, K. Franaszuzuk, A. Piasek, *J. Electroanal. Chem.* **1985**, *196*, 145.

[96] S. A. C. Barton, B. L. Murach, T. F. Fuller, A. C. West, *J. Electrochem. Soc.* **1998**, *145*, 3783.

[97] W. E. O'Grady, X. Qian, D. E. Ramaker, *J. Phys. Chem. B* **1997**, *101*, 5624.

[98] B. D. McNicol, D. A. J. Rand, K. R. Williams, *J. Power Sources* **1999**, *83*, 15.

[99] N. A. Hampson, M. J. Willars, B. D. McNicol, *J. Power Sources* **1979**, *4*, 191.

[100] B. D. McNicol, R. T. Short, A. G. Chapman, *J. Chem. Soc. Faraday Trans. 1* **1976**, *72*, 2735.

[101] A. Hamnett, B. J. Kennedy, *Electrochim. Acta* **1988**, *33*, 1613.

[102] A. S. Arico, Z. Poltarzewski, H. Kim, A. Morana, N. Giordano, V. Antonucci, *J. Power Sources* **1995**, *55*, 159.

[103] M. Götz, H. Wendt, *Electrochim. Acta* **1998**, *43*, 3637.

[104] A. S. Arico, A. K. Shukla, K. M. El-Khatib, P.Creti, V. Antonucci, *J. Appl. Electrochem*. **1999**, *29*, 671.

[105] L. Liu, C. Pu, R. Viswanathan, Q. Fan, R. Liu, E. S. Smotkin, *Electrochim. Acta* **1998**, *43*, 3657.

[106] R. Ramkumar, S. Dheenadayalan, R. Pattabiraman, *J. Power Sources* **1997**, *69*, 75.

[107] Deutsches Zentrum für Luft- und Raumfahrt, Institut für Technische Thermodynamik, Stuttgart, Germany, personal communication.

[108] W. Vielstich, A. Kuver, M. Krausa, A. C. Ferreira, K. Petrov, S. Srinivasan in *Symp. Batteries and Fuel Cells for Stationary and Electric Vehicle Applications* (Eds.: A. R. Landgrebe, Z.-I. Takehara), Honolulu, HI, **1993**, p. 269.

[109] A. K. Shukla, P. A. Christensen, A. J. Dickinson, A. Hamnett, *J. Power Sources* **1998**, *76*, 54.

[110] X. Ren, T. E. Springer, S. Gottesfeld, *J. Electrochem. Soc.* **2000**, *147*, 92.

[111] V. Tricoli in *Second Int. Symp. Proton Conducting Membrane Fuel Cells II* (Eds.: S. Gottesfeld, T. F. Fuller), Boston, MA, **1998**, p. 358.

[112] A. Küver, W. Vielstich, *J. Power Sources* **1998**, *74*, 211.

[113] M. K. Ravikumar, A. K. Shukla, *J. Electrochem. Soc.* **1996**, *143*, 2601.

[114] N. Alonso-Vante, H. Tributsch, O. Solorza-Feria, *Electrochim. Acta* **1995**, *40*, 567.

[115] O. Solorza-Feria, K. Ellmer, M. Giersig, N. Alonso-Vante, *Electrochim. Acta* **1994**, *39*, 1647.

[116] S. Gupta, D. Tryk, S. K. Zecevic, W. Aldred, D. Guo, R. F. Savinell, *J. Appl. Electrochem.* **1998**, *28*, 673.

[117] S. C. Barton, T. Patterson, E. Wang, T. F. Fuller, A. C. West in *Second Int. Symp. Proton Conducting Membrane Fuel Cells II* (Eds.: S. Gottesfeld, T. F. Fuller), Boston, MA, **1998**, p. 238.

[118] H. Böhm, *J. Power Sources* **1967/77**, *1*, 177.

[119] D. S. Chan, C. C. Wan, *J. Power Sources* **1994**, *50*, 163.

[120] O. Savadogo, P. Beck, *J. Electrochem. Soc.* **1996**, *143*, 3842.

[121] B. S. Baker, H. C. Maru in *Fourth Int. Symp. Carbonate Fuel Cell Technology* (Eds.: J. R. Selman, I. Uchida, H. Wendt, D. A. Shores, T. F. Fuller), Montréal, PQ, **1997**, p. 14.

[122] K.-I. Ota in *Fourth Int. Symp. Carbonate Fuel Cell Technology* (Eds.: J. R. Selman, I. Uchida, H. Wendt, D. A. Shores, T. F. Fuller), Montréal, PQ, **1997**, p. 238.

[123] B. Rohland, U. Jantsch in *Fourth Int. Symp. Carbonate Fuel Cell Technology* (Eds.: J. R. Selman, I. Uchida, H. Wendt, D. A. Shores, T. F. Fuller), Montréal, PQ, **1997**, p. 212.

[124] C. Yuh, R. Johnsen, M. Farooque, H. Maru, *J. Power Sources* **1995**, *56*, 1.

[125] A. C. Schoeler, T. D. Kaun, I. Bloom, M. Lanagan, M. Krumpelt, *J. Electrochem. Soc.* **2000**, *147*, 916.

[126] S. Hamakawa, R. Shiozaki, T. Hayakawa, K. Suzuki, K. Murata, K. Takehira, M. Koizumi, J. Nakamura, T. Uchijima, *J. Electrochem. Soc.* **2000**, *147*, 839.

[127] M. Ihara, C. Yokoyama, A. Abudula, R. Kato, H. Komiyama, K. Yamada, *J. Electrochem. Soc.* **1999**, *146*, 2481.

[128] S. Park, J. M. Vohs, R. J. Gorte, *Nature* **2000**, *404*, 265.

[129] U. Birnbaum, E. Riensche, U. Stimming in *Proc. Fifth Int. Symp. Solid Oxide Fuel Cells* (Eds.: U. Stimming, S. C. Singhal, H. Tagawa, W. Lehnert), Aachen, Germany, **1997**, p. 112.

[130] S. C. Singhal in *Proc. Fifth Int. Symp. Solid Oxide Fuel Cells* (Eds.: U. Stimming, S. C. Singhal, H. Tagawa, W. Lehnert), Aachen, Germany, **1997**, p. 37.

[131] R. Diethelm, J. Brun, T. Gamper, M. Keller, R. Kruschwitz, D. Lenel in *Proc. Fifth Int. Symp. Solid Oxide Fuel Cells* (Eds.: U. Stimming, S. C. Singhal, H. Tagawa, W. Lehnert), Aachen, Germany, **1997**, p. 79.

[132] S. Kawasaki, K. Okumura, Y. Esaki, M. Hattori, Y. Sakaki, J. Fujita, S. Takeuchi in *Proc. Fifth Int. Symp. Solid Oxide Fuel* (Eds.: U. Stimming, S. C. Singhal, H. Tagawa, W. Lehnert), Aachen, Germany, **1997**, p. 171.

[133] T. Hibino, H. Tsunekawa, S. Tanimoto, M. Sano, *J. Electrochem. Soc.* **2000**, *147*, 1338.

[134] Y. Shibuya, H. Nagamoto in *Proc. Fifth Int. Symp. Solid Oxide Fuel Cells* (Eds.: U. Stimming, S. C. Singhal, H. Tagawa, W. Lehnert), Aachen, Germany, **1997**, p. 510.

[135] R. Doshi, V. L. Richards, M. Krumpelt in *Proc. Fifth Int. Symp. Solid Oxide Fuel Cells* (Eds.: U. Stimming, S. C. Singhal, H. Tagawa, W. Lehnert), Aachen, Germany, **1997**, p. 379.

[136] H. Y. Tu, Y. Takeda, N. Imanishi, O. Yamamoto in *Proc. Fifth Int. Symp. Solid Oxide Fuel Cells* (Eds.: U. Stimming, S. C. Singhal, H. Tagawa, W. Lehnert), Aachen, Germany, **1997**, p. 394.

[137] H. P. Buchkremer, U. Diekmann, L. G. J. de Haart, H. Kabs, U. Stimming, D. Stöver in *Proc. Fifth Int. Symp. Solid Oxide Fuel Cells* (Eds.: U. Stimming, S. C. Singhal, H. Tagawa, W. Lehnert), Aachen, Germany, **1997**, p. 160.

[138] M. Lang, R. Henne, G. Schiller, N. Wagner in *Proc. Fifth Int. Symp. Solid Oxide Fuel Cells* (Eds.: U. Stimming, S. C. Singhal, H. Tagawa, W. Lehnert), Aachen, Germany, **1997**, p. 461.

[139] A. Gubner, H. Landes, J. Metzger, H. Seeg, R. Stübner in *Proc. Fifth Int. Symp. Solid Oxide Fuel Cells* (Eds.: U. Stimming, S. C. Singhal, H. Tagawa, W. Lehnert), Aachen, Germany, **1997**, p. 844.

[140] P. Vernoux, J. Guindet, E. Gehain, M. Kleitz in *Proc. Fifth Int. Symp. Solid Oxide Fuel Cells* (Eds.: U. Stimming, S. C. Singhal, H. Tagawa, W. Lehnert), Aachen, Germany, **1997**, p. 219.

[141] B. C. H. Steele in *British Ceramic Proceedings* (Ed.: B. C. H. Steele), The Institute of Materials, London, UK, **1996**, p. 151.

[142] R. Doshi, V. L. Richards, J. D. Carter, X. Wang, M. Krumpelt, *J. Electrochem. Soc.* **1999**, *146*, 1273.

[143] J. P. P. Huijsmans, F. P. F. van Berkel, G. M. Christie, *J. Power Sources* **1998**, *71*, 107.

[144] M. Janousek, W. Köck, M. Baumgärtner, H. Greiner in *Proc. Fifth Int. Symp. Solid Oxide Fuel Cells* (Eds.: U. Stimming, S. C. Singhal, H. Tagawa, W. Lehnert), Aachen, Germany, **1997**, p. 1225.

[145] B. Krogh, M. Brustad, M. Dahle, J. L. Eilertsen, R. Ödegärd in *Proc. Fifth Int. Symp. Solid Oxide Fuel Cells* (Eds.: U. Stimming, S. C. Singhal, H. Tagawa, W. Lehnert), Aachen, Germany, **1997**, p. 1234.

[146] T. Malkow, U. van de Crone, A. M. Laptev, T. Koppitz, U. Breuer, W. J. Quadakkers in *Proc. Fifth Int. Symp. Solid Oxide Fuel Cells* (Eds.: U. Stimming, S. C. Singhal, H. Tagawa, W. Lehnert), Aachen, Germany, **1997**, p. 1244.

[147] R. Rückdäschel, R. Henne, G. Schiller, H. Greiner in *Proc. Fifth Int. Symp. Solid Oxide Fuel Cells* (Eds.: U. Stimming, S. C. Singhal, H. Tagawa, W. Lehnert), Aachen, Germany, **1997**, p. 1273.

[148] H. P. Buchkremer, *SOFC-Industrieseminar*, KFA, Jülich, Germany, **1995**, p. 166.

[149] Y. Sakaki, M. Hattori, Y. Esaki, S. Ohara, T. Fukui, K. Kodera, Y. Kubo in *Proc. Fifth Int. Symp. Solid Oxide Fuel Cells* (Eds.: U. Stimming, S. C. Singhal, H. Tagawa, W. Lehnert), Aachen, Germany, **1997**, p. 652.

[150] A. Momma, Y. Kaga, K. Fujii, K. Hohjyo, M. Kanazawa, T. Okuo in *Proc. Fifth Int. Symp. Solid Oxide Fuel* (Eds.: U. Stimming, S. C. Singhal, H. Tagawa, W. Lehnert), Aachen, Germany, **1997**, p. 311.

[151] J. Will, L. J. Gauckler in *Proc. Fifth Int. Symp. Solid Oxide Fuel Cells* (Eds.: U. Stimming, S. C. Singhal, H. Tagawa, W. Lehnert), Aachen, Germany, **1997**, p. 757.

[152] Y. Jamal, M. L. Wyszynski, *Int. J. Hydrogen Energy* **1994**, *19*, 557.

[153] P. Sharke, *Mech. Engl.* **1999**, *121*, 46.

[154] M. L. Cubiero, J. L. G. Fierro, *J. Catal.* **1998**, *179*, 150.

[155] Environex, Inc., Fuel Cells for Vehicles, Wayne, PA, USA, **1995**.

[156] B. Emonts, J. B. Hansen, S. L. Jörgensen, B. Höhlein, R. Peters, *J. Power Sources* **1998**, *71*, 288.

[157] J. M. Ogden, M. M. Steinbugler, T. G. Kreutz, *J. Power Sources* **1999**, *79*, 143.

[158] L. Ma, C. Jiang, A. A. Adesina, D. L. Trimm, M. S. Wainwright, *Chem. Eng. J.* **1996**, *62*, 103.

[159] N. Edwards, S. R. Ellis, J. C. Frost, S. E. Golunski, A. N. J. van Keulen, N. G. Lindewald, J. G. Reinkingh, *J. Power Sources* **1998**, *71*, 123.

[160] R. Buxbaum, *REB Research and Consulting*, http://www.rebresearch.com/MRessay.html.

[161] J. R. Rostrup-Nielsen, *Catalytic Steam Reforming*, *Vol. 5*, Springer, Berlin, **1984**.

[162] K. Aasberg-Petersen, C. S. Nielsen, S. L. G. Jörgensen, *Catal. Today* **1998**, *46*, 193.

[163] E. A. Gilles, *Chem. Eng. Prog.* **1980**, *76*, 88.

[164] V. Recupero, L. Pino, R. D. Leonardo, M. Lagana, G. Maggio, *J. Power Sources* **1998**, *71*, 208.

[165] Ä. Slagtern, H. M. Swaan, U. Olsbye, I. M. Dahl, C. Mirodatos, *Catal. Today* **1998**, *46*, 107.

[166] O. Deutschmann, L. D. Schmidt, *AIChE J.* **1998**, *44*, 2465.

[167] K. Ledjeff-Hey, T. Kalk, F. Mahlendorf, O. Niemzig, J. Roes, *Portable Fuel Cells*, Lucerne, Switzerland, **1999**, p. 193; K. Ledjeff-Hey, T. Kalk, F. Mahlendorf, O. Niemzig, A. Trautmann, J. Roes, *J. Pow. Sources*, **2000**, *86*, 166.

[168] L. Yang, D. P. Bloomfield, *Fuel Cell Seminar*, Palm Springs, CA, **1998**.

[169] P. Hoffmann, *The Hydrogen and Fuel Cell Letter* **2000**, *15*, 1.

[170] K. Sekizawa, S.-i. Yano, K. Eguchi, H. Arai, *Appl. Catal. A* **1998**, *169*, 291.

[171] S. H. Oh, R. M. Sinkevitch, *J. Catal.* **1993**, *142*, 254.

[172] A. Heinzel, R. Nolte, K. Ledjeff-Hey, M. Zedda, *Electrochim. Acta* **1998**, *43*, 3817.

[173] Sandia National Laboratories, *Metal Hydride Applications*, http://146.246.239.9:591/FMPro.

[174] Powerball Technologies, *The Concept of Powerball Technology*, http://www.powerball.net/inside/concept/index.shtml, **2000**.

[175] "Hydrogen, the fuel for the future": DOE National Renewable Energy Laboratory, DE-B 95004024, **1995**.

[176] C. Liu, Y. Y. Fan, M. Liu, H. T. Cong, H. M. Cheng, M. S. Dresselhaus, *Science* **1999**, *286*, 1127.

[177] "Atomic-sized carbon nanotubes show promising tunable structure, electronic properties", University of North Carolina at Chapel Hill, *Science Daily* **2000**.

[178] S. Hill, *New Scientist* **1996**, *152* (2061), 20.

[179] a) R. T. K. Baker, *Synthesis*, *Properties and Applications of Graphite Nanofibers*, http://itri.loyola.edu/nano/us_r_n_d/09_03.htm, **2000**; b) M. Rzepka, P. Lamp, M. A. De La Casallilo, *J. Phys. Chem. B*, **1998**, *102*, 10894, and references therein.

[180] D. Chu, R. Jiang, *J. Power Sources* **1999**, *80*, 226.

[181] J. Weitkamp, *Zeolites as Media for Hydrogen Storage*, Universität Stuttgart, http://www.uni-stuttgart.de/sfb270/B7_E.htm, **2000**.

[182] K. Joon, *J. Power Sources* **1998**, *71*, 12.

[183] Toshiba Corp., *Environmentally Friendly Co-Generation Package—200 kW Fuel Cell Power Plant*, personal communication.

[184] Daimler – Chrysler, http://www.daimlerchrysler.com, **1999**.

[185] Mazda Technology, company brochure.

[186] Zevco, company brochure.

[187] R. G. Hockaday in *Fuel Cell Conference*, New Orleans, LA; http://sites.netscape.net/etsoupanarias/mhtx2.html.

[188] Fraunhofer Institut, *Fuel Cell Supplies Electricity for Laptop*, http://www.ise.fhg.de/Products/brennstoffzelle.html, **2000**.

[189] H. Wendt, M. Götz, *Chem. Unserer Zeit* **1997**, *31*, 301.

[190] *Fuel Cells 2000*, http://www.fuelcells.org/.

[191] http://www.h2fc.com/.

Long Distance Charge Transport through DNA: Quantification and Extension of the Hopping Model**

Bernd Giese[a]* and Martin Spichty[a]

Long distance charge transport through DNA occurs by a hopping mechanism. If the positive charge is injected into a guanine base, all guanines act as charge carriers. Because of the strong influence that the distance has on the charge-transfer step, DNA strands with long adenine:thymine sequences also involve adenine as charge carriers. A prerequsite for this mechanism is that the electron transfer to an adjacent adenine base is faster than the H_2O trapping reaction of the guanine radical cation. We have developed a model that can explain and qualitatively predict the product yields.

KEYWORDS:

adenosine · charge transfer · DNA oxidation · guanidine · kinetics

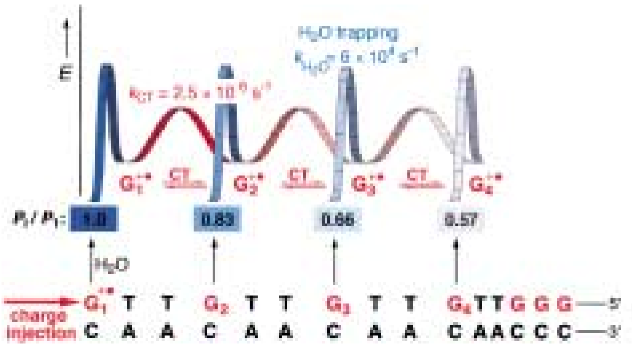

1

Figure 1. *Curtin – Hammett picture of the charge transfer (CT, red) from a guanine radical cation ($G^{\bullet+}$) to guanine bases (G) and the competing water-trapping processes (blue) along double strand **1** (pH = 7). The yields of the water-trapped products at the guanine bases are given as P_i/P_1 ratios.*

Experiments on very long distance charge transport through DNA raised a controversial discussion in the last years.[1] Today, there is no doubt that transport of a positive charge over 50 Å and more along DNA in water is possible and that it occurs via a multistep "hopping" mechanism.[2] Two years ago, we suggested that all guanine bases (G) are the charge carriers of the hole transfer, if a guanine radical cation ($G^{\bullet+}$) is formed in the injection step.[3] The charge tunnels reversibly between the guanine bases and can be detected by water-trapping of the guanine radical cation ($G^{\bullet+}$), which leads to product *P*. The efficiency of the charge transport is given by P_i/P_1, where P_i is the yield at the end and P_1 the yield at the start of the charge transport. According to the Marcus-Levich-Jortner Equation (1), the charge transfer rate k_{CT} of each hopping step is strongly distance (Δr) dependent, whereas the number of the hopping steps *N*, Equation (2), only slightly influences the efficiency of the charge transport (β and η are proportionality factors).[4]

$$\ln k_{CT} \; \propto \; -\beta \Delta r \tag{1}$$

$$\ln P_i/P_1 \; \propto \; -\eta \ln N \tag{2}$$

Thus in double strand **1**, the yields of $G^{\bullet+}$-trapping products P_i/P_1 decreased only slightly along the strand (Figure 1).[5] The rates of the charge-transfer processes between guanine bases have been measured recently by Lewis and Wasielewski.[6] It turned out that GG and GGG sequences react with a guanine radical cation ($G^{\bullet+}$) about 1.5 times faster than G.[6, 7] The equilibrium constants *K* for the charge equilibration between $G^{\bullet+}$ and GG or GGG are 7.7 and 20, respectively.[6] With these data, and a value for β of 0.7 Å^{-1},[3, 8] the rate for the hole transfer between single guanine units over two A:T base pairs in strand **1** is $k_{CT} = 2.5 \times 10^6\,s^{-1}$. The rate of water-trapping of $G^{\bullet+}$ has not been measured yet, but one can determine its pseudo first-order rate constant as $k_{H_2O} = 6 \times 10^4\,s^{-1}$ by a fit using the known charge transfer rates and the product yields of double strand **1** at pH 7.[9] With the rate constants for k_{CT} and k_{H_2O}, one arrives at the Curtin – Hammett situation of Figure 1. As discussed recently,[5] the influence of the distance on the product yields must not be confused with the distance dependence of the charge-transfer rates (k_{CT}) because the rate of the water trapping (k_{H_2O}) plays a major role in the formation of the products *P*.

In addition, our analysis has shown that the ratio k_{CT}/k_{H_2O} seems to depend upon the pH value of the solution. The results described in Figure 1 were carried out at pH 7.0.[4b, 5] For fitting the data measured at pH values of 5.0[3] and 8.0,[2c] we artificially kept the charge-transfer rates constant and determined the ratios k_{CT}/k_{H_2O} for experiments at different pH values. As an example, the experiments of Barton[2c] with strand **2** were used for the fitting process at pH 8.0 (Figure 2).

---

[a] *Prof. Dr. B. Giese, Dipl.-Chem. M. Spichty*
Department of Chemistry
University of Basel
St. Johanns Ring 19, 4056 Basel (Switzerland)
Fax: (+41) 61-267-1105
E-mail: bernd.giese@unibas.ch

[**] *This work was supported by the Swiss National Science Foundation and the Volkswagen Foundation. We thank G. B. Schuster for very fruitful discussions.*

Figure 2. *Fits of the experimental yield data at the GG positions of double strand* ***2*** *(pH 8.0) using the guanine radical cation ($G^{\bullet +}$) as the charge carrier. One of the strands is ^{32}P radiolabeled.*

The analysis of experimental data with several DNA strands yielded k_{CT}/k_{H_2O} ratios, in which k_{CT} describes the charge transfer between single guanine bases, separated from each other by two A:T base pairs. The values are $k_{CT}/k_{H_2O} = 4.0$ (pH 5.0), 40 (pH 7.0), and 200 (pH 8.0).

Another result of this fitting process is that $G^{\bullet +}$ reacts 1.5 times faster than $GG^{\bullet +}$ and 3.0 times faster than $GGG^{\bullet +}$ with water. For the Curtin–Hammett situation, the ratio of the competing processes k_{CT}/k_{H_2O} is the most important value, therefore its dependence on the experimental conditions has to be taken into account. We have applied these data, together with the value $\beta = 0.7$ Å^{-1}, for the calculation of product yields in different double strands. One test system uses compounds **3a–f** from Barton et al.[2c] (Scheme 1). This drastic increase of the distance between the two GG groups caused only a 10–20% decrease of the efficiency P_i/P_1. Our calculations gave the same result! As an example, the relative rates of the individual steps for strand **3d** are shown in Figure 3 and a graphical representation of this situation is given in Figure 4.

Scheme 1. *Strands* ***3a–f*** *from Barton et al,[2c] in which n, the number of base pairs X:Y between the GG sequences, increases from 6 (****3a****) to 16 (****3f****).*

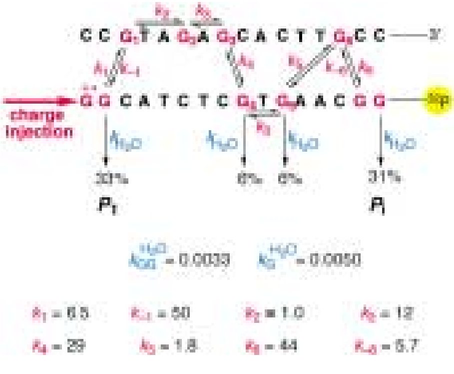

Figure 3. *Calculated product yields and relative rates (red) of electron transfer, as well as of the water-trapping processes (blue), of each guanine radical cation ($G^{\bullet +}$) in double stranded* ***3d****, using the data fitted to strand* ***2****.*

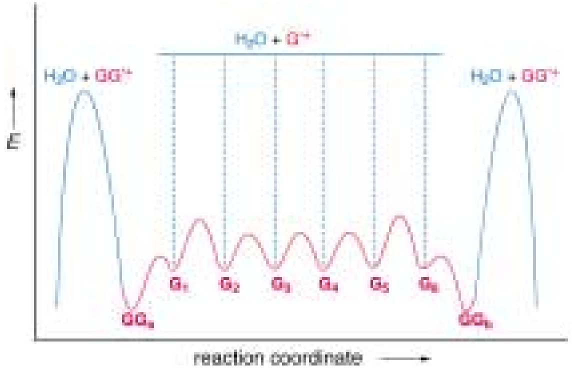

Figure 4. *Curtin–Hammett representation of the charge-transport and water-trapping processes in double strand* ***3d****.*

Figures 3 and 4 demonstrate that only small amounts of charges are trapped at the single guanine bases (G) because the constant K for the charge equilibriation between G and GG is 7.7,[6] whereas water reacts only 1.5 times faster with $G^{\bullet +}$ than with $GG^{\bullet +}$. Thus, the transition states of the water-trapping processes of $G^{\bullet +}$ are higher than those of the GG trapping. Therefore, in strands like **3**, where the charge transfer is much faster than the water trapping process, the number of hopping steps between the guanines only slightly influences the efficiency of the charge transport.

This picture changes dramatically when the charge transfer becomes slower than the water-trapping process. At pH 7, this is the case if the bridge between the guanines contains four ($k_{CT} = 2 \times 10^4\ s^{-1}$) or more A:T base pairs. Nevertheless, Schuster[2a] has demonstrated that efficient charge transport occurs also in these strands at pH 7.

Strand **4** (Figure 5), as an example, contains $(A{:}T)_n$ sequences, with $n \leq 3$ as well as $n \geq 4$, between the guanine units. The efficiency of the charge transport from GG_1 to GG_2 for short $(A{:}T)_n$ bridges ($n = 0-3$) are correctly calculated by the above-described data for the $G^{\bullet +}$ and $GG^{\bullet +}$ processes. On the other hand, the charge transport between GG_2 and GG_3 over two long A:T sequences ($n = 4$, 5) cannot be predicted by a mechanism in which only hopping steps between guanine bases occur (Figure 5). We assume, that in strands with long $(A{:}T)_n$ sequences ($n \geq 4$), an oxidation of adenine by a guanine radical cation might occur. This would lead to a situation where not only

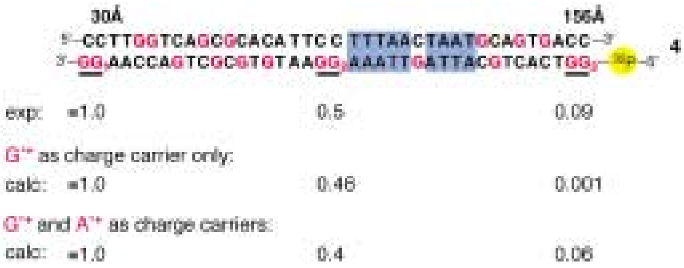

Figure 5. *Experimental and calculated product ratios in double strand* ***4****. The calculations were performed using only $G^{\bullet +}$, or $G^{\bullet +}$ and $A^{\bullet +}$, as charge carriers.*

guanine radical cations ($G^{\bullet +}$) but also adenine radical cations ($A^{\bullet +}$) are charge carriers. The slowest step in this process is the electron transfer from A to $G^{\bullet +}$. This process is then followed by fast electron-transfer steps induced by $A^{\bullet +}$. Because rates for the formation and the reaction of $A^{\bullet +}$ are not known, we will describe the charge transport between two guanine units separated by a long $(A{:}T)_n$ sequence ($n \geq 4$) by Equation (3).

$$k_{obs} = K_{th} k_{CT} \tag{3}$$

In Equation (3), k_{obs} is the overall rate constant for the charge transport between the guanine bases, K_{th} describes the thermal equilibration of the positive charge between G and A, and k_{CT} is the slowest subsequent charge-transfer step between the adenine bases. This situation will be demonstrated by sequence **5** (Figure 6).

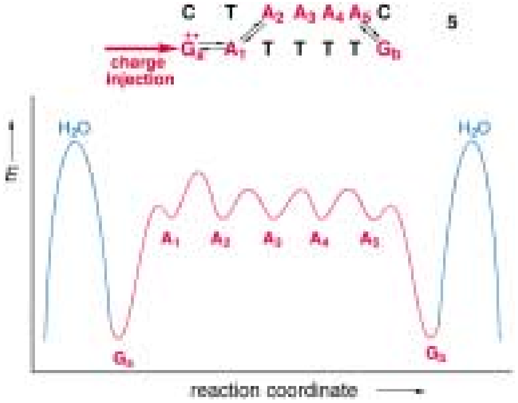

Figure 6. *Curtin – Hammett representation of the charge transport through long A:T sequences using $G^{\bullet +}$ and $A^{\bullet +}$ as charge carriers.*

The charge is distributed over G_a and A_1 in a pre-equilibrium. The slowest charge transfer step between the adenine bases of **5** is the *interstrand* hopping step between A_1 and A_2. *Intrastrand* charge transfer rates are faster because the distance between adjacent adenines in one strand is shorter than those between complementary strands.[10] The fastest charge-transfer steps are those between $A_1^{\bullet +}$ and G_a as well as between $A_5^{\bullet +}$ and G_b.

The fit of the efficiencies of the charge transport from GG_1 to GG_2 and GG_3 in strand **4**, in which the rate data for $G^{\bullet +}$ in short $(A{:}T)_n$ sequences ($n = 0 – 3$) is used and Equation (3) for long $(A{:}T)_n$ sequences ($n = 4,5$), leads to a rate coefficient $k_{obs} = 2.5 \times 10^5\,s^{-1}$ for both long A:T sequences (Figure 5).[11] The slowest step after the ionization of A by $G^{\bullet +}$ is the interstrand charge transfer from an $A^{\bullet +}$ to the adjacent A of the complementary strand. This rate should be in the order of $k_{CT} = 10^8\,s^{-1}$,[12] which leads to a reasonable equilibrium constant K of about 10^{-3}.[13]

As long as the water-trapping process of $G^{\bullet +}$ is slower than the ionization of A by $G^{\bullet +}$ and the subsequent charge transfer between the adjacent adenine bases, the efficiency of the charge transport between guanine bases over long $(A{:}T)_n$ sequences ($n \geq 4$) depends only slightly on n. This is because the transition state for the water-trapping process of $A^{\bullet +}$ should be much higher in energy than the transition state for the water trapping of $G^{\bullet +}$ (Figure 6) and almost no charge is lost by water trapping of the charge carrier $A^{\bullet +}$. Actually, Barton et al.[14] have recently shown that the efficiency of the charge transport between guanine units over longer $(A{:}T)_n$ sequences ($n \geq 4$) is only slightly influenced by the number of the A:T base pairs. In strands **5 a – d** for example (Scheme 2), n increases from 4 to 10, which barely affects the efficiency P_2/P_1 of the charge transport.

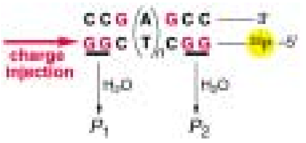

5	n	P_2/P_1
a	4	0.9 ± 0.1
b	6	1.2 ± 0.3
c	8	2.2 ± 0.4
d	10	0.4 ± 0.3

Scheme 2. *Double strands **5 a – d** and the influence of the length (n) of the $(A{:}T)_n$ sequence on the efficiency of the charge transport (P_2/P_1) between the guanine bases.*

In experiments where the water trapping of $G^{\bullet +}$ has a similar rate as the ionization of A by $G^{\bullet +}$, the sequence of the A:T base pairs between the guanines should play a role because one can no longer neglect a) the influence of the neighboring bases on the redox potentials of A and G, and b) the difference between *intra-* and *interstrand* hole transfer rates. Recent work by Schuster[15] is in accord with this prediction. Furthermore, if the water trapping of $G^{\bullet +}$ is faster than the ionization of A by $G^{\bullet +}$, the efficiency of the long range charge transport should drop dramatically when the number of the A:T base pairs is increased.

Thus, the influence of the experimental conditions on the rate ratio between the water trapping and the charge transfer (k_{H_2O}/k_{CT}) is an important parameter for the efficiency of the long distance charge transport through DNA. For instance, as we have discussed above, the pH of the reaction medium could play a role.

In conclusion, long distance charge transport occurs by a hopping mechanism and the product formation by water trapping of the charge can be explained by the Curtin – Hammett principle. If $G^{\bullet +}$ is formed in the injection step, charge hopping occurs between the guanine bases as long as the intervening $(A{:}T)_n$ bridge is short. Under these circumstances, a variation of the $(A{:}T)_n$ bridge length dramatically influences the rate of the charge transfer between the guanine bases (Figure 7). The decrease of the charge transfer rate by elongation of the bridge can lead to a situation where the endothermic electron transfer from an adjacent A to $G^{\bullet +}$ is as fast as (or faster than) the thermoneutral, long distance electron transfer from the distal G. At pH 7, this occurs if the number n of the $(A{:}T)_n$ base pairs is about four and, for $n \geq 4$, adenine bases also become charge carriers. In this region, an increase of n only slightly reduces the rate because the charge transfer between $A^{\bullet +}$ and the adjacent A is very fast (Figure 7).

Thus, under experimental conditions, where the water-trapping process of $G^{\bullet +}$ is slower than the oxidation of A by $G^{\bullet +}$, the charge can travel over very long $(A{:}T)_n$ sequences via a multistep hopping mechanism involving adenine and guanidine bases as charge carriers. In the extreme case (very slow water trapping), the charge equilibrates over the DNA strand.

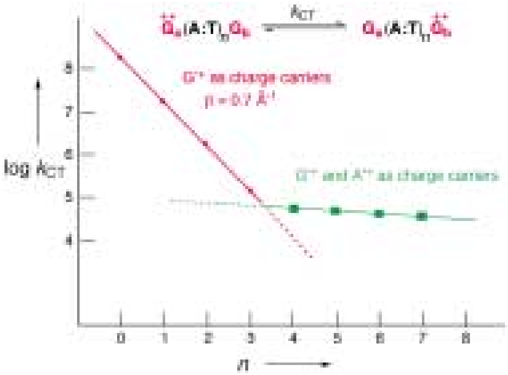

Figure 7. *Influence of the number of (A:T)*$_n$ *base pairs on the charge transport rate (k*$_{CT}$*) between guanine bases in DNA double strands.*

[1] Commentaries on hole transfer in DNA: a) U. Diederichsen, *Angew. Chem.* **1997**, *107*, 2411; *Angew. Chem. Int. Ed. Engl.* **1997**, *36*, 2317; b) E. K. Wilson, *Chem. Eng. News* **1999**, *77*(34), 43; c) M. Ratner, *Nature* **1999**, *397*, 480; d) M. W. Grinstaff, *Angew. Chem.* **1999**, *111*, 3845; *Angew. Chem. Int. Ed.* **1999**, *38*, 3629. For electron transfer, see: e) M. G. Debije, M. T. Milano, W. A. Bernhard, *Angew. Chem.* **1999**, *111*, 2926; *Angew. Chem. Int. Ed.* **1999**, *38*, 2752; f) Y. Razskazovskii, S. Swarts, J. Falcone, C. Taylor, M. Sevilla, *J. Phys. Chem.* **1997**, *101*, 1460.

[2] a) G. B. Schuster, *Acc. Chem. Res.* **2000**, *33*, 253; b) B. Giese, *Acc. Chem. Res.* **2000**, *33*, 631; c) M. E. Nuñez, D. B. Hall, J. K. Barton, *Chem. Biol.* **1999**, *6*, 85.

[3] E. Meggers, M. E. Michel-Beyerle, B. Giese, *J. Am. Chem. Soc.* **1998**, *120*, 12950.

[4] a) J. Jortner, M. Bixon, T. Langenbacher, M. E. Michel-Beyerle, *Proc. Natl. Acad. Sci. US* **1998**, *95*, 12759; b) B. Giese, S. Wessely, M. Spormann, U. Lindemann, E. Meggers, M. E. Michel-Beyerle, *Angew. Chem.* **1999**, *111*, 1050; *Angew. Chem. Int. Ed.* **1999**, *38*, 996.

[5] B. Giese, S. Wessely, *Angew. Chem.* **2000**, *112*, 3632; *Angew. Chem. Int. Ed.* **2000**, *39*, 3490.

[6] a) F. D. Lewis, X. Liu, J. Liu, S. E. Miller, R. T. Hayes, M. R. Wasielewski, *Nature* **2000**, *406*, 51; b) F. D. Lewis, X. Liu, J. Liu, R. T. Hayes, M. R. Wasielewski, private communication.

[7] For related systems, see: a) E. Meggers, D. Kusch, M. Spichty, U. Wille, B. Giese, *Angew. Chem.* **1998**, *110*, 473; *Angew. Chem. Int. Ed.* **1998**, *37*, 460; b) W. B. Davies, J. Naydenova, R. Haselsberger, A. Ogrodnik, B. Giese, M. E. Michel-Beyerle, *Angew. Chem.* **2000**, *112*, 3795; *Angew. Chem. Int. Ed.* **2000**, *39*, 3649.

[8] F. D. Lewis, T. Wu, Y. Zhang, R. L. Letsinger, S. R. Greenfield, M. R. Wasielewski, *Science* **1997**, *277*, 673.

[9] In order to simulate the product yields of strand **1**, we solved the differential equations for the intermediates $G^{\bullet+}$ and $GGG^{\bullet+}$, as well as for the products, numerically. The water-trapping rates are variables in this fitting process. See also: M. Bixon, B. Giese, S. Wessely, T. Langenbacher, M. E. Michel-Beyerle, J. Jortner, *Proc. Natl. Acad. Sci. US* **1999**, *96*, 11713.

[10] We have defined the distance for the *intrastrand* and *interstrand* charge transfer between purine bases as the distance between the centers of their 4,5-bonds.

[11] The rate coefficient $k_{obs} = 2.5 \times 10^5\ s^{-1}$ [Eq. 3] describes the charge-transfer rate starting from $G^{\bullet+}$. Starting from $GG^{\bullet+}$, k_{obs} is $3.2 \times 10^4\ s^{-1}$.

[12] We assume that the rate of the thermoneutral charge transfer from $A^{\bullet+}$ to an A is comparable to the charge transfer from $G^{\bullet+}$ to a G.

[13] Exact ionization potentials for the nucleotides in DNA double strands are not known; only the ionization potentials of the monomers have been measured. See: a) S. Steenken, S. V. Jovanovic, *J. Am. Chem. Soc.* **1997**, *119*, 617. The equilibrium constants K are slightly different for *intra-* and *interstrand* hole transfer between G and A bases because the neighboring bases influence the ionization potentials of G and A: b) A. A. Voityuk, J. Jortner, M. Bixon, N. Rösch, *Chem. Phys. Lett.* **2000**, *324*, 430; c) I. Saito, T. Nakamura, K. Nakatani, Y. Yoshioka, K. Yamaguchi, H. Sugiyama, *J. Am. Chem. Soc.* **1998**, *120*, 12686.

[14] T. T. Williams, D. T. Odom, J. K. Barton, *J. Am. Chem. Soc.* **2000**, *122*, 9048. In some experiments, the product ratios P_i/P_1 are greater than unity. We assume that this might be caused by the bulky charge-injection complex. If this complex is close to the proximal guanine bases, their water-trapping rates could be slower than those of the distal guanine bases because of steric effects.

[15] G. B. Schuster, private communication. The data will be described in a separate publication.

CHEMPHYSCHEM

Quantum Yields Lower than Unity in Photoinduced Dissociative Electron Transfers: The Reductive Cleavage of Carbon Tetrachloride

Laurence Pause,[a] Marc Robert,[a] and Jean-Michel Savéant*[a]

It has been shown recently that the electrochemical reduction of carbon tetrachloride in N,N′*-dimethylformamide follows a mechanism in which electron transfer and bond cleavage are concerted. We report here results concerning photoinduced electron transfer from the singlet excited state of two aromatic molecules, 2-ethyl-9,10-dimethoxyanthracene and perylene, to* CCl_4*, which is characterised by a quantum yield of complete quenching fragmentation ranging from 0.7 to 0.8. It is shown that a quantum yield below unity is compatible with a dissociative mechanism and arises from partitioning of the system at the intersection of the product- and ground-state potential energy surfaces. This phenomenon predominates over back electron transfer from the clustered fragments state. The photoinduced reductive cleavage of* CCl_4 *thus provides a clear illustration of the recent theoretical prediction, that photoinduced dissociative electron transfers are not necessarily endowed with a unity quantum yield. This offers an opportunity to estimate the magnitude of the electronic matrix element that couples the fragmented product state and the ground reactant state.*

KEYWORDS:

dissociative electron transfer · electron transfer · photochemistry · quantum yields

Introduction

Bond breaking and bond making are quite often associated with electron-transfer reactions. Understanding how these events are dynamically coupled is thus an important issue in the description of reactivity in electron-transfer chemistry. Focusing on the coupling between electron transfer and bond cleavage, the reaction mechanism (Scheme 1) may involve two successive steps (stepwise mechanism) or a single step, in which electron transfer and bond breaking are concerted according to what is usually designated as a dissociative electron-transfer reaction. The existence of two different pathways and the factors that govern the passage from one to the other are well documented for homogeneous and heterogeneous (electrochemical) thermal reactions.[1] The molecular structure of the cleaving acceptor is one of these factors and the main controlling structural parameters have been identified.[2] The passage between one mechanism and the other may also be observed experimentally with the same cleaving substrate upon changing the thermodynamic driving force offered to the reaction,[3a] as exemplified by an increasing number of cleaving substrates.[2c, 3b–d] The observation of such mechanistic transitions leaves little doubt as to the existence of both mechanisms.

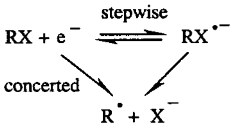

Scheme 1. An example reduction, illustrating the possible stepwise and concerted mechanisms.

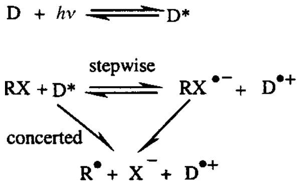

Scheme 2. The stepwise and concerted mechanisms of photoinduced electron transfer.

In photoinduced electron-transfer studies too, attention is being paid to the concerted versus stepwise issue (Scheme 2) for reactions where bond breaking is associated with electron transfer. Indeed, an attractive way of fighting the energy-wasting back electron transfer in photoinduced electron-transfer reactions is to use a system in which the acceptor, the donor, or both, in the resulting ion-pair undergoes a fast cleavage reaction.[4] Concerted electron transfer/bond breaking reactions would thus intuitively appear as an ideal means of suppressing back electron

---

[a] *Prof. J.-M. Savéant, L. Pause, Dr. M. Robert*
Laboratoire d'Electrochimie Moléculaire
Unité Mixte de Recherche Université - CNRS No 7591
Université de Paris 7 - Denis Diderot
2 place Jussieu, 75251 Paris Cedex 05 (France)
Fax: (+33) 1-44-27-76-25
E-mail: saveant@paris7.jussieu.fr

transfer. If this intuition is correct, the complete quenching fragmentation quantum yield, Φ_∞, should be unity in the concerted case. The observation of a quantum yield less than unity would therefore prove that the reaction follows a stepwise, rather than a concerted, mechanism.[4, 5] There are several examples where quantum yields smaller than unity have been found,[5] whereas the electrochemical reaction was reported to follow a concerted mechanism.[2a,c] Among these, the reductive cleavage of the 4-cyanobenzylmethylphenyl sulfonium cation by the excited singlets of a series of aromatic compounds is particularly noteworthy. Great care was indeed taken, by appropriate choice of the donors, to avoid the side reactions that waste photochemical energy, such as electron transfer between the donor radical cation and the 4-cyanobenzyl radical, followed by regeneration of the starting sulfonium cation by coupling the resulting 4-cyanobenzyl cation with methylphenyl sulfide.[5d]

More recently however, it has been shown, on theoretical grounds, that a concerted dissociative electron transfer reaction is *not necessarily* endowed with a unity quantum yield if due account is taken of the possible partitioning of the system at the intersection of the product- and ground-state potential energy surfaces.[6] The partitioning is an increasing function of the electronic matrix-element coupling the two states. A relationship was thus established between the quantum yield and the electronic matrix-element that couples the ground- and the fragmented-product states at the intersection of their zero-order potential energy surfaces. The purpose of the work reported herein was to give an example of a photoinduced, dissociative electron-transfer reaction that gives rise to a quantum yield less than one.

Carbon tetrachloride was selected in this purpose for several reasons. It is a commonly used oxidative quencher of excited states and several quantum yield determinations have been reported.[4c, 5a–c, 7] Since the $Cl_3C^\bullet$ radical is not easily oxidised, it should be possible to select donors fulfilling two necessary and somewhat contradictory requirements, namely, a) that their cation radical does not oxidise $Cl_3C^\bullet$ rapidly, and b) the singlet excited state does not reduce the solvent to an appreciable extent. Recent work on thermal electron transfer to CCl_4 in solution demonstrated the dissociative character of single electron transfer to this molecule and revealed that a small but significant interaction between the Cl^- and $Cl_3C^\bullet$ fragments exists in the product state.[8]

Editorial Advisory Board Member:[*]
Jean-Michel Savéant,
is currently Directeur de Recherche au Centre National de la Recherche Scientifique. His research interests involve all aspects of molecular electrochemistry (organic, inorganic, enzymatic), as well as mechanisms and reactivity in thermal and photoinduced electron transfers.

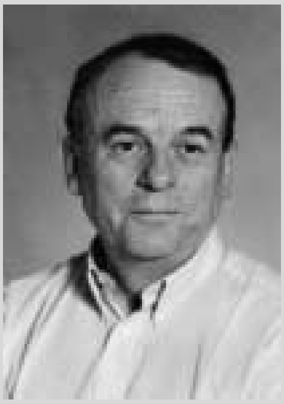

Results

We investigated the reductive cleavage of CCl_4 by the excited singlets of two donors (D*), perylene and 2-ethyl-9,10-dimethoxyanthracene (EDA), and determined the corresponding quantum yields. These two particular molecules were selected for the following reasons. One was the large driving force, $-\Delta G^{0,*}$ offered by their singlet towards dissociative electron transfer to CCl_4, Equation (1), where the first term is the excitation energy from the ground state to the singlet and the two E^0 values are the standard potentials of the subscript couples.

$$-\Delta G^{0,*} = -E_{D/D^*} + E^0_{D^{\bullet+}/D} + E^0_{CCl_4/CCl_3^\bullet + Cl^-} \quad (1)$$

The cyclic voltammetric oxidation wave of perylene is reversible at a scan rate as low as $0.2\,V\,s^{-1}$ from which $E^0_{D^{\bullet+}/D}$ is found equal to 1.03 V versus SCE. With EDA, reaching reversibility requires much higher scan rates ($27\,000\,V\,s^{-1}$ with a $10\,\mu m$ diameter carbon electrode). The value of $E^0_{D^{\bullet+}/D}$ is then found equal to 1.00 V versus SCE. The values for E_{D/D^*} may be estimated as 2.84[9] and 3.01 eV,[5d] respectively, and $E^0_{CCl_4/CCl_3^\bullet + Cl^-}$, the standard potential for the dissociative electron-transfer reaction, can be obtained from the thermodynamic parameters present in Equation (2).

$$E^0 = -D_R + E^0_{Cl^\bullet/Cl^-} + T(S_{CCl_3^\bullet} + S_{Cl^\bullet} - S_{CCl_4}) \quad (2)$$

Estimation of the bond dissociation energy D_R (2.84 eV),[10a] of the entropic term (0.381 eV)[10e] and of the standard potential of the $Cl^\bullet/Cl^-$ couple in DMF (1.81 V versus SCE)[11] thus leads to $E^0_{CCl_4/CCl_3^\bullet + Cl^-} = -0.649$ V versus SCE. It follows that $\Delta G^{0,*} = -1.161$ and -1.361 eV for perylene and EDA, respectively. With such large driving forces, the dissociative electron-transfer quenching of fluorescence (Scheme 2) of the two compounds is expected to be fast, faster than the energy transfer between D* and CCl_4.[12] We may also exclude the participation of the triplet state to the reaction along the same lines as for the 4-cyanobenzyl-methylphenyl sulfonium cation.[5d] Indeed, electron transfer from $^3D^*$ to CCl_4 is an unfavourable reaction (by 0.13 eV for perylene), and thus unable to compete with the favoured $^1D^* + CCl_4$ reaction. Taking into account that $^3D^*/^1D^* = 10^{-2}$ at equilibrium (measured from the fluorescence quantum efficiency[9]), the $^1D^* + CCl_4$ reaction is so rapid that it prevents any catalysis of intersystem crossing of $^1D^*$ to $^3D^*$, as confirmed by the fact that no triplet transpires in the laser flash study of the reaction (see below).

Our main goal is to test the idea that a purely dissociative photoinduced electron transfer (see Scheme 2) may have a quantum yield lower than unity because of partitioning at the

---

[*] *Members of the Editorial Advisory Board will be introduced to the readers with their first manuscript.*

intersection of the ground- and product-state potential energy surfaces.[6] We must therefore select a system in which electron transfer within the product solvent cage, which regenerates the ground-state reactants, is negligible. These reactions may concern electron transfer from Cl^- to $D^{\bullet+}$ producing $Cl^\bullet$, which would then combine with $Cl_3C^\bullet$ yielding back CCl_4 and also electron transfer from $Cl_3C^\bullet$ to $D^{\bullet+}$ producing Cl_3C^+, which would then combine with Cl^- to return CCl_4. The standard potential of the $Cl^\bullet/Cl^-$ couple in DMF, 1.81 V versus SCE,[11] is much more positive than the two $E^0_{D^{\bullet+}/D}$ values, which renders the first reaction negligible. The standard potential of the $Cl_3C^+/Cl_3C^\bullet$ couple was estimated as follows. The standard free enthalpy of the reaction $Cl_3C^\bullet + tBu^+ \rightarrow Cl_3C^+ + tBu$ was obtained from a quantum chemical, ab initio calculation that involved geometry optimisation and energy calculation at the UHF–MP2 level followed by a calculation of the standard free enthalpy of solvation according to the IPCM method.[14] We thus found $E^0_{Cl_3C^+/Cl_3C^\bullet} = 1.33$ V versus SCE, to show that electron transfer from $Cl_3C^\bullet$ to $D^{\bullet+}$ is negligible in both cases.

Stationary fluorescence quenching experiments showed that CCl_4 is a powerful quencher in both cases. The corresponding Stern–Volmer plots, based on Equation (3), in which I_F and I^0 are fluorescence intensities in the presence and absence of CCl_4 and K_Q is the quenching constant, indeed indicate large quenching constants, $K_Q = 88.5$ and $18.4\,M^{-1}$ for EDA and perylene, respectively.

$$\frac{I^0}{I_F} = 1 + K_Q[CCl_4] \qquad (3)$$

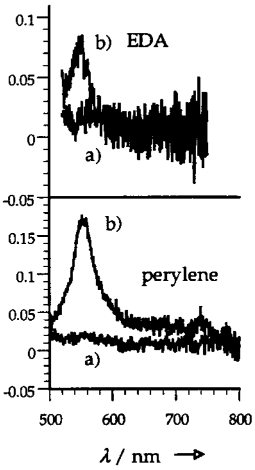

Figure 1. Laser flash induced reductive cleavage of CCl_4 in DMF. Above: absorption spectrum of a 2.2 mM EDA solution in the a) absence and b) presence of 0.1 M CCl_4, which were recorded over 100 ns starting 570 ns after the pulse. Below: absorption spectrum of a 1.5 mM perylene solution in the a) absence and b) presence of 0.25 M CCl_4 recorded over 100 ns starting 340 ns after the pulse.

Laser flash experiments confirmed that quenching of the excited states does result from electron transfer. Indeed, as seen in Figure 1, the characteristic spectrum of the cation radicals appears upon irradiating the solution in the presence of CCl_4.[15] Since the radicals $Cl_3C^\bullet$ and $D^{\bullet+}$ may couple, the quantum yield of the reductive cleavage cannot be securely derived from the intensity of this cation radical spectrum. Reliable results may only be derived from the titration of the stable ion Cl^- produced after continuous irradiation. Ion chromatography was used in this purpose (see Experimental Section).

Figure 2 depicts the strategy we employed to derive the value of the complete quenching quantum yield, Φ_∞. This was measured at concentrations of CCl_4, at which complete fluorescence quenching is achieved. We thus found $\Phi_\infty = 0.77 \pm 0.10$ and 0.70 ± 0.09 for EDA and perylene, respectively. Before the quantum yields for the production of free Cl^- ion can be equated to quantum yields for the photoinduced reductive–cleavage reaction, we must ascertain that a) the cation Cl_3CD^+, which results from the reaction of $Cl_3C^\bullet$ with $D^{\bullet+}$, does not couple significantly with Cl^- and b) Cl^- do not couple significantly with $D^{\bullet+}$ before escaping from the solvent cage.

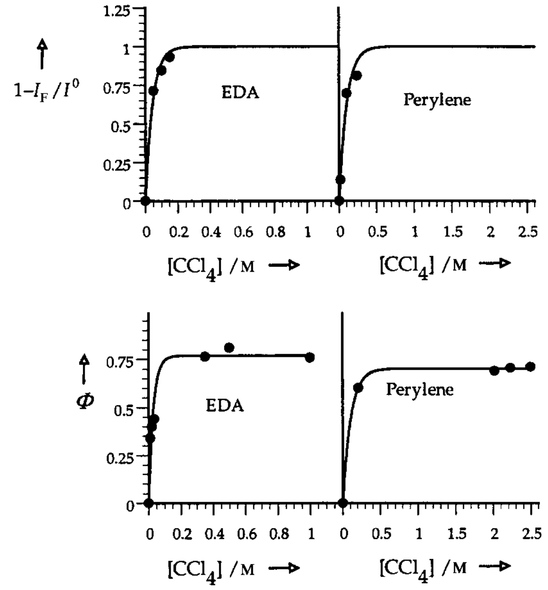

Figure 2. Photoinduced reductive cleavage of CCl_4 by EDA (2.2 mM) and perylene (3.3 mM). The fraction of fluorescence quenching (above) and quantum yield (below) is presented as a function of CCl_4 concentration.

That the first of these conditions is fulfilled results from the results depicted in Figure 3, where the sum of the CCl_4 and Cl^- concentrations remains constant. The amount of Cl^- produced during these experiments, as well as during the complete fluorescence quenching experiments, in which Φ_∞ was measured, corresponds to less than 10% of the initial quantity of sentitiser (8–10% with EDA and around 8% with perylene). With such conversion ratios, we expect the increase in $[Cl^-]$ and the decay of $[CCl_4]$ to be linear functions of time, as indeed can be

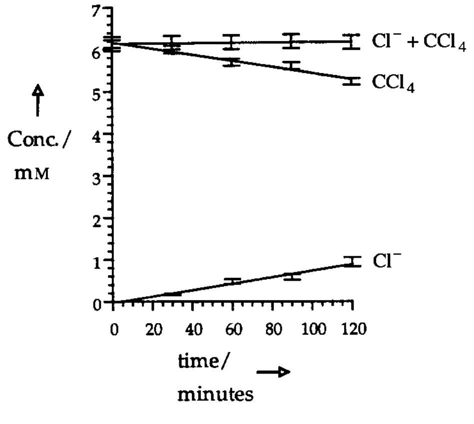

Figure 3. Photoinduced reductive cleavage of CCl_4 by EDA (initial concentrations 6.14 and 10 mM, respectively).

seen. For the same reason, the values of Φ_∞ are predicted to be time independent, which is the case between 6 and 10 min.

The fulfillment of the second condition was checked as follows. Cyclic voltammetric determination to ascertain the bimolecular rate constants of the reaction of Cl^- with the two cation radicals gave values of 1×10^6 and $3 \times 10^6\,\mathrm{M^{-1}\,s^{-1}}$ for perylene and EDA, respectively. The rate constants of the reaction of the cation radical with the solvent medium (including residual water) is $5 \times 10^5\,\mathrm{s^{-1}}$ with EDA and less than $1\,\mathrm{s^{-1}}$ with perylene. Starting from a lower limit of the size of the solvent cage, as estimated by calculations, indicates that the concentrations of Cl^- in the cage are about 0.6 and 0.5 M for perylene and EDA, respectively. Cage coupling of the cation radical with Cl^- (0.6×10^6 and $1.5 \times 10^6\,\mathrm{s^{-1}}$, respectively, as compared to $1 \times 10^8 - 1 \times 10^{10}\,\mathrm{s^{-1}}$ for cage escape) is thus negligible.

We may thus conclude that that the values of Φ_∞, 0.77 ± 0.10 and 0.70 ± 0.09 for EDA and perylene, respectively, do represent the values of the quantum yield of complete quenching for the photoinduced reductive cleavage of the two sentitisers.

Although not appropriate for the determination of the quantum yield of the photoinduced reductive cleavage, the laser flash experiments described above may be used to obtain an estimate of the ratio between the rate constants of separation of the fragments, k_{sp}, and of coupling of the two radicals in the solvent cage, k_{cc}. We measured the amounts of $D^{\bullet+}$ that escaped from the solvent cage without coupling with $Cl_3C^\bullet$, using previously determined values of the molar extinction coefficient and the optical densities at the maximum absorption peak of the cation radical. The quantum yield for the formation of $D^{\bullet+}$, $\Phi_{D^{\bullet+}}$, may thus be determined and lead to $\Phi_{D^{\bullet+}}$ values of 0.42 and 0.1 for EDA and perylene, respectively. For EDA, since measurements were made 670 ns after the laser pulse, the experimental value of 0.3 was corrected from the first-order decay of the cation radical through reaction with the solvent medium, which occurs at a rate of $5 \times 10^5\,\mathrm{s^{-1}}$. Combining these values to those of the quantum yield for the formation of chloride ion, Φ_{Cl^-}, obtained from continuous irradiation experiments at the same CCl_4 concentration, allowed the determination of the ratio k_{cc}/k_{sp} by means of Equation (4).

$$\frac{\Phi_{D^{\bullet+}}}{\Phi_{Cl^-}} = \frac{k_{sp}}{k_{sp} + k_{cc}} \tag{4}$$

We thus found $k_{cc}/k_{sp} = 0.6$ and 1.0 for EDA and perylene, respectively.

Discussion

Are the observed quantum yields consistent with a dissociative electron transfer mechanism?

Although large, the complete quenching quantum yields are clearly below unity. As shown recently, the theoretical analysis of photoinduced dissociative electron transfer predicts,[6] against common intuition, that such values are perfectly compatible with a dissociative electron-transfer mechanism in which electron transfer and bond breaking are concerted. The quantum yield is given by Equation (5), where *1 − P* is the probability that the system remains on the zero-order curve of the fragmented product (shown in Figure 4).

$$\Phi_\infty = \frac{1}{(1+P)\left(1 + \dfrac{2P}{1+P}\dfrac{k_{-act}}{k_{sp}+k_{cc}}\right)} \tag{5}$$

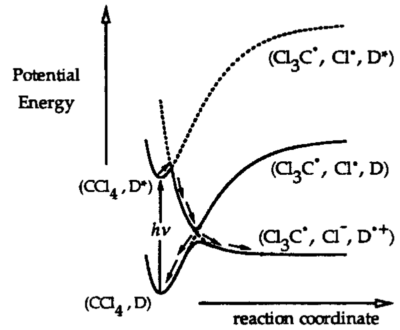

Figure 4. Photoinduced dissociative electron transfer. Curve crossing allows the partitioning of the system between fragmentation and back electron transfer.

In Equation (5), the partition of the system at the crossing between the fragmented product- and the ground-state reactant potential energy surfaces is expressed by the term $1/(1+P)$. The second parenthesis in the denominator represents the possibility that back electron transfer from the caged fragments, with rate constant k_{-act}, could compete with cage escape (k_{sp}) and cage coupling of the radicals $Cl_3C^\bullet$ and $D^{\bullet+}$ (k_{cc}). If the two latter events are faster than the former, the complete quenching quantum yield is simply given by Equation (6).

$$\Phi_\infty = \frac{1}{1+P} \tag{6}$$

In the present case, we may infer from the quantum yields values that $P \leq 0.30$ and $P \leq 0.43$ with EDA and perylene, respectively. The probability P is an increasing function of the electronic coupling matrix element at the crossing between the fragmented product- and the ground-state reactant potential energy surfaces, H, according to Equation (7), in which D_R is the bond dissociation energy and ν_{eff} the effective frequency at which the intersection region is crossed.

$$1P = 1 - \exp[-\pi^{3/2} H^2 / h\nu_{eff}(RTD_R)^{1/2}] \tag{7}$$

From estimations of D_R and ν_{eff}, detailed further, we infer that $H \leq 23$ and 28 meV with EDA and perylene, respectively. These values correspond to a moderately nonadiabatic electron transfer at the ground state (the electronic factor is $\kappa_{el} = 2P/(1+P)$ has values 0.5 and 0.6 for EDA and perylene, respectively).[6]

Does partitioning at the potential energy surface crossing and/or back electron transfer from the fragment cluster occur?

The expression of the complete quenching quantum yield in Equation (5) summarises the two reasons that may lower it value below unity. The first, represented by the second parenthesis in the denominator, involves back electron transfer from the fragmented product cluster which regenerates the ground-state system. It depends on the competition between back electron transfer ($k_{-\mathrm{act}}$) on the one hand and, on the other, of both the escape from the cluster (k_{sp}) and coupling of the radicals $\mathrm{Cl_3C^\bullet}$ and $\mathrm{D^{\bullet+}}$ in the solvent cage (k_{cc}). The other, represented by the term $1+P$, deals with the partitioning of the system at the intersection of the product- and ground-state potential energy surfaces. For estimating the relative importance of these two processes, we have to estimate $k_{-\mathrm{act}}$. The dissociative electron transfer from the ground state is a very unfavourable reaction, with a standard free energy, $\Delta G^0_{\mathrm{get}}$, equal to 1.649 and 1.652 eV with EDA and perylene, respectively. The free energy of activation for this reaction $\Delta G^{\neq}_{\mathrm{get}}$ is obtained from the minimisation of Equations (8) and (9), subject to the condition $G_{\mathrm{CCl_4+D}} = G_{\mathrm{Cl_3C^\bullet,\,Cl^-+D^{\bullet+}}}$.[8]

$$G_{\mathrm{CCl_4+D}} = D_{\mathrm{R}} Y^2 + \lambda_0(Y) X^2 \tag{8}$$

$$G_{\mathrm{Cl_3C^\bullet,\,Cl^-+D^{\bullet+}}} = \Delta G^0 - \Delta G^0_{\mathrm{sp}} + D_{\mathrm{R}}\left[\left(1-\sqrt{\frac{D_{\mathrm{P}}}{D_{\mathrm{R}}}}\right) - Y\right]^2 + \lambda_0(Y)(1-X)^2 \tag{9}$$

The term $Y = -\exp[-\beta(y-y_{\mathrm{R}})]$, in which y is the length of the cleaving C$\cdots$Cl bond and y_{R} (1.77 Å) its equilibrium value in the reactant system. The term D_{R} (2.84 eV) is the dissociation energy of the cleaving bond and D_{P} (0.062 eV) is the deepness of the shallow minimum in the potential energy of the products versus the C$\cdots$Cl distance, a minimum due to the small attractive attraction between the polarised radical $\mathrm{Cl_3C^\bullet}$ and $\mathrm{Cl^-}$.[8] The standard free energy of the reaction ΔG^0 leads to the separated fragments and $\Delta G^0_{\mathrm{sp}} = D_{\mathrm{P}} - T\Delta S^0_{\mathrm{sp}} \approx D_{\mathrm{P}}$ is the difference between the standard free energies of the separated and the caged fragments. The term X is a fictitious charge, which varies between 0 and 1 and serves as a solvation index. The solvent reorganisation energy λ_0, in eV, was obtained from the Marcus–Hush approximation,[17] Equation (10), where the equivalent sphere radius of the donor, $a_{\mathrm{D}} = 3.8$ and 4.3 Å for EDA and perylene, respectively, and a_{R}, the radius of the sphere equivalent to the cleaving molecule $\mathrm{CCl_4}$, is a function of the C$\cdots$Cl distance.

$$\lambda_0 = 3.376\left(\frac{1}{a_{\mathrm{R}}} + \frac{1}{a_{\mathrm{D}}} - \frac{1}{a_{\mathrm{R}} + a_{\mathrm{R}}}\right) \tag{10}$$

The value for a_{R} is obtained from $a_{\mathrm{R}} = 3/\lambda_0^{\mathrm{el}}$, where λ_0^{el} is the solvent reorganisation energy around $\mathrm{CCl_4}$ and depends of the progress of bond cleavage (see reference [8] for an exact determination of λ_0^{el} out from electrochemical data and ab initio calculations). We obtained $\Delta G^{\neq}_{\mathrm{get}} = 1.784$ and 1.774 eV for EDA and perylene, respectively. Taking the collision frequency, $2\times 10^{11}\,\mathrm{M^{-1}\,s^{-1}}$, as a pre-exponential factor, it follows that $k_{\mathrm{act}} = 5.3\times 10^{-20}$ and $1.2\times 10^{-20}\,\mathrm{M^{-1}\,s^{-1}}$. Thus, with the values of the standard free energies for passing from the ground state to the cluster, $k_{-\mathrm{act}} = 8.5\times 10^7$ and $2.1\times 10^8\,\mathrm{s^{-1}}$ for EDA and perylene, respectively.

In evaluating k_{sp}, we have to take account that the standard free energy of the cluster is slightly below the standard free energy of the separated fragments by 0.062 meV, namely 0.09 M in terms of equilibrium constant for separation. Since the separation does not involve an activation barrier, we may obtain k_{sp} from the diffusion-limited escape rate constant, $k_{\mathrm{dif}} = 10^{10}\,\mathrm{s^{-1}}$, given in Equation (11), which leads to $k_{\mathrm{sp}} = 8\times 10^8\,\mathrm{s^{-1}}$.

$$\frac{1}{k_{\mathrm{sp}}} = \frac{1}{k_{\mathrm{dif}}} - \frac{1}{K\,k_{\mathrm{dif}}} \tag{11}$$

It follows that the competition between back electron transfer on the one hand, and, on the other, cage escape and coupling may be expressed as $k_{-\mathrm{act}}/(k_{\mathrm{sp}} + k_{\mathrm{cc}}) = 0.10$ and 0.23 for EDA and perylene, respectively. In both cases, the main cause for observing a less-than-unity quantum yield derive from the partitioning of the system at the intersection of the product- and ground-state potential energy surfaces with a minor contribution of back electron transfer from the fragments cluster to the ground state reactant system. Application of Equation (5) thus leads to $P = 0.25$ and 0.29 for EDA and perylene, respectively (the values would have been 0.3 and 0.43, respectively, if back electron transfer would have been neglected).

In the application of Equation (7) for deriving the magnitude of the electronic coupling matrix element from P, the effective frequency, ν_{eff}, is practically the same for EDA and perylene ($\nu_{\mathrm{eff}} = 8.5\times 10^{12}\,\mathrm{s^{-1}}$).[18] The electronic coupling matrix element is therefore $H = 21$ and 23 meV for EDA and perylene, respectively.

Conclusions

Photoinduced electron transfer with 2-ethyl-9,10-dimethoxyanthracene or perylene as electron donors is a fast reaction exhibiting complete quenching quantum yields in the range 0.7–0.8. These values, albeit large, are clearly below unity. According to recent theory, quantum yields below unity are compatible with a dissociative electron transfer reaction and may be caused both by partitioning of the system at the intersection of the product- and ground-state potential energy surfaces and/or by back electron transfer from the clustered fragments state. The former phenomenon predominates over the later as shown by application of the model validated by the electrochemical data. The photoinduced reductive cleavage of $\mathrm{CCl_4}$ thus provides a clear illustration of the recent theoretical prediction that photoinduced dissociative electron transfers are not necessarily endowed with a unity quantum yield. It offers an opportunity to estimate the magnitude of the electronic matrix element coupling the fragmented product state and the ground reactant state.

Computational Methods

All calculations were carried out with the Gaussian 94 or Gaussian 98 packages.[19] The unrestricted Hartree–Fock method was used for all open shell systems with a 6-31G* basis set. Correlation energy was introduced according to the Møller–Plesset perturbation treatment up to second order (MP2). All geometries were optimised at the MP2 level (calculations are quoted as either UHF–MP2 or MP2). No imaginary frequencies were found from the analytical second derivatives of the energies, to confirm that stationary points are true minimum on potential energy surfaces. The second derivatives were also used to obtain various thermodynamic parameters, which included the zero-point energy and the entropy term from the usual relationships within the ideal gas, rigid rotor and harmonic oscillator models. The standard enthalpies, free enthalpies and molar entropies were corrected by a scaling factor (0.9646) applied to the zero-point energies and thermal energy corrections.

Concerning carbon tetrachloride, bond dissociation energy for C–Cl bond was obtained as the ΔH^0 value of the reaction starting from CCl_4 and becoming the two fragments $Cl^{\bullet} + CCl_3{}^{\bullet}$ (fully optimised at the MP2 level).

Experimental Section

N,N′-Dimethylformamide (Fluka, >99.5%), carbon tetrachloride (Acros, 99.8%) and perylene (Acros, 99+ %) were used as received. 2-Ethyl-9,10-dimethoxyanthracene (EDA; Aldrich, 97%) was recrystallised twice from Et_2O before use.

For laser flash photolysis, samples were irradiated with an intense nanosecond excimer laser (XeCl, $\lambda = 308$ nm, $E = 110$ mJ). Optical detection of transient species was performed perpendicular to the laser beam with an OMA system (Optical Multichannel Analyzer, Princeton Instruments), allowing one to obtain absorption spectra a few tens of nanoseconds after the pulse. Acquisition of each spectrum was made on a time window of 100 ns. Quantum yields for radical cation formation ($\Phi_{D^{\bullet+}}$) were estimated using the benzophenone triplet as a standard. The ΔOD (absorbance) values of the benzophenone triplet (monitored at 520 nm) and of the radical cations (monitored at 550 nm for $EDA^{\bullet+}$ and 554 nm for $perylene^{\bullet+}$) immediately after excitation were measured as a function of laser intensity, which was modulated by appropriate filters. Both solutions of benzophenone and aromatic donors were optically matched at 308 nm. The plots of ΔOD versus laser dose were linear at low laser power only. The quantum yields were thus obtained using the slopes extrapolated at zero intensity ($S^{\bullet+}$ for the radical cation, S^{benz} for benzophenone) and by using the molar extinction coefficient of the two species ($\varepsilon^{\bullet+}$ for the radical cation and $\varepsilon_{benz} = 7200\ \mathrm{M^{-1}\,cm^{-1}}$ for benzophenone),[20, 21] while the quantum yield for benzophenone formation Φ_{benz} was equal to unity, Equation (12).[9]

$$\Phi_{D^{\bullet+}} = \frac{S^{\bullet+}\varepsilon_{benz}\Phi_{benz}}{S^{benz}\varepsilon^{\bullet+}} \qquad (12)$$

Stationary fluorescence quenching experiments used a fluorimeter (Perkin–Elmer LS5). Perylene fluorescence extends from 450 to 600 nm, while EDA fluorescence extends from 425 to 575 nm. Stern–Volmer plots were obtained by adding increasing amounts of carbon tetrachloride and measuring the decrease of the fluorescence emission band at 480 and 508 nm with perylene and at 445 nm with EDA. It is worth noting that no new emission bands appear upon addition of quencher.

Quantum yields of chloride formation were measured from a solutions containing the aromatic donor (typically 3.3 mM with perylene and between 2 and 2.5 mM with EDA) and quencher were irradiated with filtered UV light (321 ± 10 nm from an interferometric filter) coming from a high pressure, short arc xenon lamp (150 W). Solutions were carefully deaerated with an argon purge prior to irradiation and the chloride anion yields were measured for illumination times varying between 6 and 10 min.

Chloride concentration was determined by ion chromatography (Dionex DX100 with a conductimetric detector, a conductivity suppresser (ASRS-I 4 mm) and an ion exchanger (Dionex IonPac AS14-SC column, 4 mm)). Samples were diluted 1/50 in ultra-pure water prior to analysis. Tetraethylammonium chloride was used as a chloride standard. In all experiments, the chloride concentrations remained below 30 μM after dilution. The integrated signal to chloride concentration was linear to at least 35 μM.

To obtain the quantum yield, the concentration of photons absorbed during irradiation must be known, which was achieved by measuring light intensity with a chemical actinometer (Aberchrome 540, Aberchromics) and Equation (13), where I is the light intensity Einstein A^{-1}), ΔOD is the increase in absorbance at 494 nm, V is the volume of the irradiated solution (10 mL), t is the irradiation time, $\Phi_0 = 0.20$ and $\varepsilon = 8200\ \mathrm{M^{-1}\,cm^{-1}}$.[22]

$$I = \frac{\Delta OD\, V}{\Phi_0\, \varepsilon\, t}; \qquad \Phi_{Cl^-} = \frac{[Cl^-]\,V}{I\,t} \qquad (13)$$

The amount of photons was measured after each experiment and care was taken that all incident light was absorbed. Infinite quantum yields (at complete fluorescence quenching) were measured five times for each aromatic donor. Accuracy of the measured quantum yields could be estimated as between 10 and 13% (8–10% for $[Cl^-]$ and 2–3% for photon concentration).

[1] a) "Single Electron Transfer and Nucleophilic Substitution": J.-M. Savéant in *Advances in Physical Organic Chemistry, Vol. 26* (Ed.: D. Bethel), Academic Press, New York, **1990**, pp. 1–130; b) "Dissociative Electron Transfer": J.-M. Savéant in *Advances in Electron Transfer Chemistry, Vol. 4* (Ed.: P. S. Mariano), JAI, New York, **1994**, pp. 53–116; c) J.-M. Savéant, *Acc. Chem. Res.* **1993**, *26*, 455; d) H. Lund, K. Daasbjerg, T. Lund, S. U. Pedersen, *Acc. Chem. Res.* **1995**, *28*, 313; e) H. Lund, K. Daasbjerg, T. Lund, D. Occhialini, S. U. Pedersen, *Acta. Chem. Scand.* **1997**, *51*, 135.

[2] a) C. P. Andrieux, A. Le Gorande, J.-M. Savéant, *J. Am. Chem. Soc.* **1992**, *114*, 6892; b) C. P. Andrieux, E. Differding, M. Robert, J.-M. Savéant, *J. Am. Chem. Soc.* **1993**, *115*, 6592; c) C. P. Andrieux, M. Robert, F. D. Saeva, J.-M. Savéant, *J. Am. Chem. Soc.* **1994**, *116*, 7864; d) C. P. Andrieux, A. Tallec, R. Tardivel, J.-M. Savéant, C. Tardy, *J. Am. Chem. Soc.* **1997**, *119*, 2420.

[3] a) C. P. Andrieux, J.-M. Savéant, *J. Electroanal. Chem.* **1986**, *205*, 43; b) S. Antonello, F. Maran, *J. Am. Chem. Soc.* **1997**, *119*, 12595; c) L. Pause, M. Robert, J.-M. Savéant, *J. Am. Chem. Soc.* **1999**, *121*, 7158; d) S. Antonello, F. Maran, *J. Am. Chem. Soc.* **1999**, *121*, 9668.

[4] a) F. D. Saeva, *Top. Curr. Chem.* **1990**, *156*, 61; b) "Intramolecular Photochemical Electron Transfer (PET)—Induced Bond Cleavage Reactions in some Sulfonium Salts Derivatives": F. D. Saeva in *Advances in Electron Transfer Chemistry, Vol. 4* (Ed.: P. S. Mariano), JAI, New York, **1994**, pp. 1–25; c) E. R. Gaillard, D. G. Whitten, *Acc. Chem. Res.* **1996**, *29*, 292.

[5] a) B. R. Arnold, J. C. Scaiano, W. G. McGimpsey, *J. Am. Chem. Soc.* **1992**, *114*, 9978; b) L. Chen, M. S. Farahat, E. R. Gaillard, H. Gan, S. Farid, D. G. Whitten, *J. Am. Chem. Soc.* **1995**, *117*, 6398; c) L. Chen, M. S. Farahat, E. R. Gaillard, S. Farid, D. G. Whitten, *J. Photochem. Photobiol. A* **1996**, *95*, 21; d) X. Wang, F. D. Saeva, J. A. Kampmeier, *J. Am. Chem. Soc.* **1999**, *121*, 4364.

[6] a) M. Robert, J.-M. Savéant, *J. Am. Chem. Soc.* **2000**, *122*, 514; b) C. Costentin, M. Robert, J.-M. Savéant, *J. Phys. Chem. A* **2000**, *104*, 7492.

[7] A. Anne, P. Hapiot, J. Moiroux, P. Neta, J.-M. Savéant, *J. Phys. Chem.* **1991**, *95*, 2370.

[8] L. Pause, M. Robert, J.-M. Savéant, *J. Am. Chem. Soc.* **2000**, *122*, 9829.

[9] S. V. Murov, I. Carmichael, G. L. Hug, *Handbook of Photochemistry*, 2nd ed., Marcel Dekker, New York, **1993**.

[10] a) Ab initio quantum chemical calculation of D_R (UHF-MP2 level) gave a value of 2.84 eV, in fair agreement with the experimentally determined values, 2.86,[10b] 2.99[10c] and 3.08,[10d]; b) *Handbook of Chemistry and Physics*, 78th ed., CRC, Cleveland, OH, **1997–1998**.; c) J. W. Hudgens, R. D. Johnson III, R. S. Timonen, J. A. Seetula, D. Gutman, *J. Phys. Chem.* **1991**, *95*, 4400; d) M. W. Chase, *J. Phys. Chem. Ref. Data, Monograph 9, Part 1*, 4th ed., The American Chemical Society and The American Institute of Physics, **1998**; e) From ab initio quantum chemical calculations (UHF–MP2 level), $T(S_{CCl_3} + S_{Cl^{\bullet}} - S_{CCl_4}) = 0.381$ eV at the measurement temperature, 21 °C, taking into account that the standard states refer to 1 mol L^{-1}.

[11] Standard redox potentials of the $Cl^{\bullet}/Cl^{-}$ couple in DMF versus aqueous SCE was derived from the following derivation.

$$\begin{aligned} E^{0,\mathrm{DMF}}_{\mathrm{Cl}\bullet/\mathrm{Cl}^-}\ (\text{vs. SCE}) &= E^{0,\mathrm{DMF}}_{\mathrm{Cl}\bullet/\mathrm{Cl}^-}\ (\text{vs. Ag/Ag}^+) + E^{0,\mathrm{DMF}}_{\mathrm{Ag}^+/\mathrm{Ag}}\ (\text{vs. SCE}) \\ &= \mu^{0,\mathrm{DMF}}_{\mathrm{Cl}\bullet} - \mu^{0,\mathrm{DMF}}_{\mathrm{Cl}^-} - \mu^{0,\mathrm{DMF}}_{\mathrm{Ag}^+} + \mu^{0,\mathrm{DMF}}_{\mathrm{Ag}} + 0.44 \\ &= \mu^{0,\mathrm{H_20}}_{\mathrm{Cl}\bullet} - (\mu^{0,\mathrm{H_20}}_{\mathrm{Cl}^-} + \Delta_{\mathrm{trn}}G^0_{\mathrm{Cl}^-,\mathrm{H_2O}\rightarrow\mathrm{DMF}}) \\ &\quad - (\mu^{0,\mathrm{H_2O}}_{\mathrm{Ag}^+} + \Delta_{\mathrm{trn}}G^0_{\mathrm{Ag}^+,\mathrm{H_2O}\rightarrow\mathrm{DMF}}) + \mu^0_{\mathrm{Ag}} + 0.44 \\ &= E^{0,\mathrm{H_2O}}_{\mathrm{Cl}\bullet/\mathrm{Cl}^-}\ (\text{vs. SCE}) - E^{0,\mathrm{H_2O}}_{\mathrm{Ag}^+/\mathrm{Ag}}\ (\text{vs. SCE}) \\ &\quad - (\Delta_{\mathrm{trn}}G^0_{\mathrm{Cl}^-,\mathrm{H_2O}\rightarrow\mathrm{DMF}} + \Delta_{\mathrm{trn}}G^0_{\mathrm{Ag}^+,\mathrm{H_2O}\rightarrow\mathrm{DMF}}) + 0.44 \end{aligned}$$

Standard redox potentials in water versus SHE and standard free enthalpies of transfer from water to DMF, $\Delta_{\mathrm{trn}}G^0_{\mathrm{X},\mathrm{H_2O}\rightarrow\mathrm{DMF}}$, were calculated based on references [10b] and [13].

[12] The reaction, $D^* + CCl_4 \rightarrow D + CCl_4{}^*$ is unfavorable in the indicated direction, since CCl_4 does not absorb above 300 nm, that is, 4.1 eV (compared with E_{D/D^*}).

[13] Y. Marcus, *Ion Properties*, Marcel Dekker, New York, **1997**.

[14] The solvation term is small, 0.067 eV over a total of 1.24 eV, because the positive charge is delocalised over a similar volume in the two carbocations.

[15] a) Absorption spectrum for the radical cation of perylene is similar to the spectrum obtained in 2-propanol;[15c] b) The absorption spectrum of the radical cation of 9-methoxyanthracene has been observed in dichloromethane with a maximum absorption band at 610 nm, blue shifted by 100 nm compared to unsubstituted anthracene.[15d] Thus the maximum absorption band found at 550 nm and assigned to the radical cation of EDA seems very plausible; c) A. Liu, D. M. Loffredo, A. D. Trifunac, *J. Phys. Chem*. **1993**, *97*, 3791; d) J. M. Masnovi, J. K. Kochi, *J. Am. Chem. Soc.* **1985**, *107*, 7880.

[16] The concentration of CCl_4 was derived from the cyclic voltammetric current of its first peak, which is proportional to the concentration, as checked independently.

[17] a) R. A. Marcus, *J. Chem. Phys*. **1956**, *24*, 4966; b) N. S. Hush, *J. Chem. Phys*. **1958**, *28*, 962; c) R. A. Marcus in *Special Topics in Electrochemistry* (Ed.: P. A. Rock), Elsevier, New York, **1977**, pp. 161–179.

[18] Adapting the analysis in reference [6] to the present model, Equation (14), where ν_c, the asymmetric stretching frequency of the cleaving bond, is equal to 776 cm^{-1},[10d] it follows that $\nu_{\mathrm{eff}} = 8.5 \times 10^{12}\ s^{-1}$.

$$\nu_{\mathrm{eff}} = (\nu_c/2)[1 - \{\Delta G^0_{\mathrm{get}}/[(\sqrt{D_R}) - (\sqrt{D_P})^2 + \lambda_0]\}^2] \qquad (14)$$

[19] a) M. J. Frisch, G. W. Trucks, H. B. Schlegel, P. M. W. Gill, B. G. Johnson, M. A. Robb, J. R. Cheeseman, T. Keith, G. A. Petersson, J. A. Montgomery, K. Raghavachari, M. A. Al-Laham, V. G. Zakrzewski, J. V. Ortiz, J. B. Foresman, J. Cioslowski, B. B. Stefanov, A. Nanayakkara, M. Challacombe, C. Y. Peng, P. Y. Ayala, W. Chen, M. W. Wong, J. L. Andres, A. S. Replogle, R. Gomperts, R. L. Martin, D. J. Fox, J. S. Binkley, D. J. Defrees, J. Baker, J. P. Stewart, M. Head-Gordon, C. Gonzalez, J. A. Pople, *Gaussian 94*, Revision E.1, Gaussian Inc., Pittsburgh, PA, **1995**; b) M. J. Frisch, G. W. Trucks, H. B. Schlegel, M. A. Scuseria, P. M. W. Gill, B. G. Johnson, M. A. Robb, J. R. Cheeseman, T. Keith, G. A. Petersson, J. A. Montgomery, R. E. Stratmann, J. C. Burant, S. Dapprich, J. M. Millam, A. D. Daniels, K. N. Kudin, M. C. Strain, O. Farkas, J. Tomasi, V. Barone, M. Cossi, R. Cammi, B. Mennuci, C. Pomelli, C. Adamo, S. Clifford, G. Ochterski, Q. Cui, K. Morokuma, D. K. Malick, A. D. Rabuck, K. Raghavachari, M. A. Al-Laham, V. G. Zakrzewski, J. V. Ortiz, J. B. Foresman, J. Cioslowski, B. B. Stefanov, G. Liu, A. Liashenko, P. Piskorz, I. Komaromi, A. Nanayakkara, M. Challacombe, C. Y. Peng, P. Y. Ayala, W. Chen, M. W. Wong, J. L. Andres, A. S. Replogle, R. Gomperts, R. L. Martin, D. J. Fox, J. S. Binkley, D. J. Defrees, J. Baker, J. P. Stewart, M. Head-Gordon, C. Gonzalez, J. A. Pople, *Gaussian 98*, Revision A.1, Gaussian Inc., Pittsburgh, PA, **1998**.

[20] R. Bonneau, I. Carmichael, G. L. Hug, *Pure Appl. Chem.* **1991**, *63*, 289.

[21] a) For EDA, $\varepsilon = 5000\ \mathrm{M}^{-1}\,\mathrm{cm}^{-1}$ in acetonitrile;[21b] for perylene, $\varepsilon = 34\,800\ \mathrm{M}^{-1}\,\mathrm{cm}^{-1}$ in ethanol;[15c] b) M. Robert, unpublished results.

[22] a) C. G Hatchard, C. A. Parker, *Proc. R. Soc. London A* **1956**, *235*, 518; b) H. G. Heller, J. R. Langan *J. Chem. Soc. Perkin Trans. 2* **1981**, 341.

Received: May 8, 2000 [F 36]
Revised: October 5, 2000

and calcium was deposited as the cathode. PEDOT layers were obtained by spin coating the as-received aqueous suspension.[30] The characterization of the devices was performed by a custom-made voltage generator using a calibrated ammeter and a calibrated photodiode.

All chemicals were purchased (Aldrich, Lancaster, or Strem) and were used without further purification. 3-Chloromethyl-3-ethyloxetane **2** and the photoacid 4-(thio-phenoxyphenyl)diphenylsulfonium hexafluoroantiomonate **10** were prepared according to ref. [31] and [16], respectively. Further characterization and preparation data may be found in the Supporting Information.

[1] R. H. Friend, R. W. Gymer, A. B. Holmes, J. H. Burroughes, R. N. Marks, C. Taliani, D. D. C. Bradley, D. A. Dos Santos, J. L. Brédas, M. Lögdlund, W. R. Salaneck, *Nature* **1999**, *397*, 121.

[2] A. J. Heeger, *Solid State Commun.* **1998**, *107*, 673.

[3] J.Salbeck, *Ber. Bunsenges. Phys. Chem.* **1996**, *100*, 1667.

[4] V. R. Nikitenko, V. I. Arkhipov, Y.-H. Tak, J. Pommerehne, H. Bässler, H.-H. Hörhold, *J. Appl. Phys.* **1997**, *81*, 7414.

[5] T. Virgili, D. G. Lidzey, D. D. C. Bradley, *Adv. Mat.* **2000**, *12*, 58.

[6] J. H. Burroughes, D. D. C. Bradley, A. R. Brown, R. N. Marks, K. McKay, R. H. Friend, P. N. Burns, A. B. Holmes, *Nature* **1990**, *341*, 539.

[7] X. C. Li, T. M. Yong, J. Grüner, A. B. Holmes, S. C. Moratti, F. Cacialli, R. H. Friend, *Synth. Met.* **1997**, *84*, 437.

[8] P. Le Barney, C. M. Bouche, H. Facoetti, F. Soyer, P. Robin, *Proc. SPIE* **1997**, *3148*, 160.

[9] E. Bellmann, S. E. Shaheen, S. Thayumanavan, S. Barlow, R. H. Grubbs, S. R. Marder, B. Kippelen, N. Peyghambarian, *Chem. Mater.* **1998**, *10*, 1668.

[10] X. Jiang, S. Liu, H. Ma, A. K. Jen, *Appl. Phys. Lett.* **2000**, *76*, 1813.

[11] M. S. Bayerl, T. Braig, O. Nuyken, C. D. Müller, M. Gross, K. Meerholz, *Macromol. Rapid Commun.* **1999**, *20*, 224.

[12] A. Bacher, C. H. Erdelen, W. Paulus, H. Ringsdorf, H. W. Schmidt, P. Schuhmacher, *Macromolecules* **1999**, *32*, 4551.

[13] W. Li, Q. Wang, J. Cui, H. Chou, S. E. Shaheen, G. E. Jabbour, J. Anderson, P. Lee, B. Kippelen, N. Peyghambarian, N. R. Armstrong, T. J. Marks, *Adv. Mater.* **1999**, *11*, 730.

[14] J. P. Chen, G. Klärner, J. I. Lee, D. Markiewicz, V. Y. Lee, R. D. Miller, J. C. Scott, *Synth. Met.* **1999**, *107*, 129.

[15] R. Böhner, C. Erdmann, O. Nuyken, *Macromol. Symp.* **1996**, *107*, 125.

[16] J. V. Crivello, J. H. W. Lam, *J. Polym. Chem. Ed.* **1980**, *18*, 2697.

[17] a) M. S. Driver, J. F. Hartwig, *J. Am. Chem. Soc.* **1996**, *118*, 7217; b) J. P. Wolfe, S. Wagaw, S. L. Buchwald, *J. Am. Chem. Soc.* **1996**, *118*, 7215.

[18] a) Bayer AG, DE 1021858, **1958** [K. Bodenbrenner, R. Wegler, *Chem. Abstr.* **1960**, *54*, 4617]; b) M. Miura, T. Aoyagi, T. Hirai, *J. Chem. Soc. Jpn. Ind. Chem. Sect.* **1964**, *67*, 485.

[19] a) T. Nishiyama, T. Yamamoto, Y. Koie, *Tetrahedron Lett.* **1998**, *39*, 617; b) T. Yamamoto, T. Nishiyama, Y. Koie, *Tetrahedron Lett.* **1998**, *39*, 2367.

[20] T. Braig, Ph.D. thesis, Technical University München (Germany), **2000**.

[21] a) D. Müller, M. Gross, K. Meerholz, T. Braig, M. Bayerl, F. Bielefeldt, O. Nuyken, *Synth. Met.* **2000**, *111 – 112*, 31; b) T. Braig, D. Müller, M. Gross, K. Meerholz, O. Nuyken, unpublished results.

[22] M. Gross, D. C. Müller, H.-G. Nothofer, U. Scherf, D. Neher, C. Bräuchle, K. Meerholz, *Nature* **2000**, *405*, 661.

[23] A. W. Grice, D. D. C. Bradley, M. T. Bernius, M. Inbasekaran, W. W. Wi, E. P. Woo, *Appl. Phys. Lett.* **1998**, *73*, 629.

[24] S. Janiez, D. D. C. Bradley, M. Grell, C. Giebeler, M. Inbasekaran, E. P. Woo, *Appl. Phys. Lett.* **1998**, *73*, 2453.

[25] a) F. Nuesch, L. J. Rothberg, E. W. Forsythe, Q. Toan, Y. A. Gao, *Appl. Phys. Lett.* **1999**, *74*, 880; b) J. S. Kim, M. Granström, R. H. Friend, N. Johansson, W. R. Salanek, R. Daik, W. J. Feast, F. Carcialli, *J. Appl. Phys.* **1998**, *84*, 6859.

[26] a) K. Z. Xing, M. Fahlman, X. W. Chen, O. Inganäs, W. R. Salaneck, *Synth. Met.* **1997**, *89*, 161; b) T. M. Brown, J. S. Kim, R. H. Friend, F. Cacialli, R. Daik, W. J. Feast, *Appl. Phys. Lett.* **1999**, *75*, 1679.

[27] a) H.-G. Nothofer, A. Meisel, T. Miteva, D. Neher, M. Forster, M. Oda, G. Lieser, D. Sainova, A. Yasuda, D. Lupo, W. Knoll, U. Scherf, *Macromol. Symp.* **2000**, *154*, 139; b) T. Miteva, A. Meisel, W. Knoll, H.-G. Nothofer, U. Scherf, A. Yasuada, D. Müller, K. Meerholz, D. Neher, *Adv. Mater.*, in press.

[28] a) V. N. Bliznuyk, S. A. Carter, J. C. Scott, G. Klärner, R. D. Miller, D. C. Miller, *Macromolecules* **1999**, *32*, 361; b) D. Sainova, T. Miteva, H. G. Nothofer, U. Scherf, I. Glowacki, J. Ulanski, H. Fujikawa, D. Neher, *Appl. Phys. Lett.* **2000**, *76*, 1810.

[29] V. Bulovic, S. R. Forrest, *Semicond. Semimet.* **2000**, *65*, 1, and references therein.

[30] *Baytron P®*, Bayer Corporation..

[31] A. C. Farthing, *J. Chem. Soc.* **1955**, 3648.

[32] A. J. Bard, L. A. Faulkner, *Electrochemical Methods –-Fundamentals and Applications*, Wiley, New York, **1984**.

Received: July 13, 2000 [Z 70]

Intrazeolite Diffusion Kinetics of Dye Molecules in the Nanochannels of Zeolite L, Monitored by Energy Transfer[**]

Michel Pfenniger[a] and Gion Calzaferri*[a]

KEYWORDS:

dyes · energy transfer · fluorescence · mass transport · zeolites

The strongly fluorescent dyes oxonine (Ox^+) and pyronine (Py^+) have been observed to enter the main channels of zeolite L at approximately the same speed when ion exchanged from an aqueous solution. Energy transfer from excited Py^+ (donor) to Ox^+ (acceptor) is very efficient, due to the large spectral overlap between the fluorescence of Py^+ and the absorption of Ox^+.[1, 2] This can be used to monitor the transport of these dyes. Interference microscopy was used to investigate intracrystalline

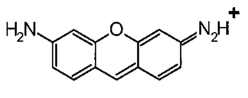

Pyronine

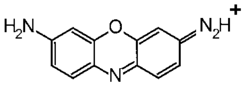

Oxonine

---

[a] G. Calzaferri, M. Pfenniger
Department of Chemistry and Biochemistry
University of Berne
Freiestrasse 3, 3000 Bern 9 (Switzerland)
Fax: (+41) 31 631 3994
E-mail: Gion.Calzaferri@iac.unibe.ch

[**] This work was supported by the Swiss National Science Foundation, Projects NFP 4047-057481 and NF 2000-053414/98/1. We would like to thank Drs. Silke Megelski and Niklaus Gfeller for their contributions and fruitful discussions.

transport, thus extending the information obtained from classical methods.[3] We have recently shown that quenching of the fluorescence of the resorufin anion inside the zeolite L channels can be used to study the exit kinetics of the inserted molecules. From this, information about the intrazeolite transport processes was deduced.[4] In situ FTIR spectroscopy of very thin zeolite layers is another powerful method.[5] In this study, we show that using the pronounced distance dependence of electronic excitation energy transfer leads to new insight into intrazeolite transport processes; the geometry of the zeolite L framework is illustrated in Figure 1.

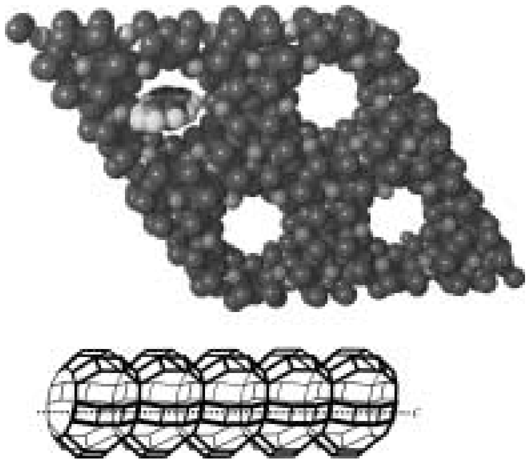

Figure 1. Framework of zeolite L. Above: A view, perpendicular to the c-axis of the hexagonal structure, as a space-filling model with a Py^+ or an Ox^+ entering a channel. Below: Side view of a channel.

Zeolite L has cylinder morphology. The primitive vector ***c*** corresponds to the channel axis while the primitive vectors ***a*** and ***b*** are perpendicular to it enclosing an angle of 120°.[6–11] The number of parallel channels n_{cha} of a zeolite L crystal depends on the radius r_{cyl} (in nanometers) by Equation (1).[2]

$$n_{cha} \approx 1.07\, r_{cyl}^2 \qquad (1)$$

This means that a zeolite L crystal of 900 nm diameter and 1500 nm length gives rise to about 217 000 parallel channels, each of which consists of 3000 unit cells. The dye molecules are at sites along the linear channels. The sites do not overlap. Their length is equal to the length of two unit cells along the *c*-axis ($|\boldsymbol{c}| = 7.5$ Å). All sites have the same geometrical properties. The first electronic transitions of Py^+ and Ox^+ are of $\pi^* \leftarrow \pi$ type with transition moments oriented along their long axis. Equivalent sites *i* have the same probability p_i to be occupied by a dye molecule. The occupation probability *p* is equal to the ratio between the occupied and the total number of equivalent sites. In Figure 2, the absorption and fluorescence spectra of Py^+ and Ox^+ are shown. These dyes are well suited for the envisaged experiments because of the large Py^+/Ox^+ spectral overlap J_{PyOx}, which is 1.5×10^{-13} $cm^3 M^{-1}$.[2] Hence, the Förster radius[12, 13] is about 60 Å for random orientation.

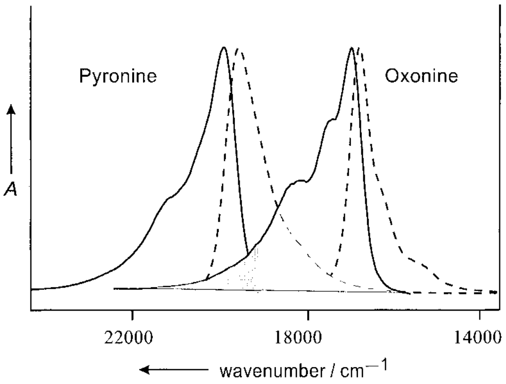

Figure 2. Absorption A (——) and fluorescence F (- - - -) spectra of Py^+ – zeolite L and Ox^+ – zeolite L suspended in water. The maxima of all spectra were adjusted to equal height. The spectral overlap region of the Py^+ emission and the Ox^+ absorption is shaded.

Energy transfer processes in a zeolite containing a random mixture of strongly luminescent donor and acceptor molecules are explained in Figure 3. We show a situation in which a donor has been electronically excited; the excitation energy can then be emitted as fluorescence, decay thermally, or it can be transferred radiationlessly to a neighboring acceptor. This means that the energy transfer can be monitored by the fluorescence of the donor and the acceptor.

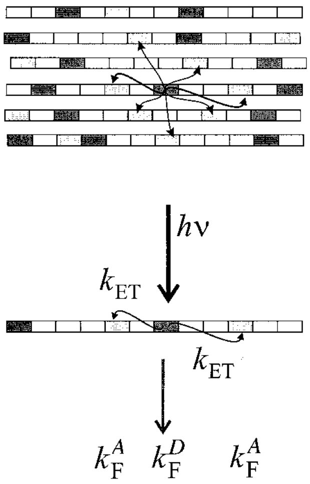

Figure 3. Scheme of a few channels of a zeolite L crystal containing acceptor A (light gray rectangles) and donor D (dark gray rectangles) molecules. Each rectangle marks a site. Main processes taking place after excitation of a donor are indicated: k_{ET} is the energy-transfer rate constant, k_F^A and k_F^D are the fluorescence rate constants.

Taking into account radiationless processes, namely internal conversion k_{IC}, intersystem crossing k_{ISC}, and bimolecular quenching $k_Q[Q]$ with a quencher *Q*, the time-dependent concentrations of the donor *D* and the acceptor *A* in the excited singlet state S_1, $[D_{S_1}]$ and $[A_{S_1}]$, can be expressed as in Equations (2) and (3). The term j_{abs} is the number of photons absorbed per unit time.

$$\frac{\mathrm{d}[D_{S_1}]}{\mathrm{d}t} = j_{\mathrm{abs}} - (k_{\mathrm{ET}} + k_{\mathrm{F}}^{D} + k_{\mathrm{IC}}^{D} + k_{\mathrm{ISC}}^{D} + k_{\mathrm{Q}}^{D}[Q])[D_{S_1}] = j_{\mathrm{abs}} - [D_{S_1}]\sum_{d} k_{d}^{D} \quad (2)$$

$$\begin{aligned}\frac{\mathrm{d}[A_{S_1}]}{\mathrm{d}t} &= k_{\mathrm{ET}}[D_{S_1}] - (k_{\mathrm{F}}^{A} + k_{\mathrm{IC}}^{A} + k_{\mathrm{ISC}}^{A} + k_{\mathrm{Q}}^{A}[Q])[A_{S_1}] \\ &= k_{\mathrm{ET}}[D_{S_1}] - [A_{S_1}]\sum_{a} k_{a}^{A} \end{aligned} \quad (3)$$

The fluorescence quantum yield of the donor Φ_{F}^{D} and of the acceptor Φ_{F}^{A} under stationary conditions is therefore given by Equations (4) and (5), in which η_{F}^{D}, η_{F}^{A}, and η_{ET} denote the efficiencies for the fluorescence of D and A, and for the energy transfer.

$$\Phi_{\mathrm{F}}^{D} = \eta_{\mathrm{F}}^{D} = \frac{k_{\mathrm{F}}^{D}}{\sum_{d} k_{d}^{D}} \quad (4)$$

$$\Phi_{\mathrm{F}}^{A} = \eta_{\mathrm{ET}}\eta_{\mathrm{F}}^{A} = \frac{k_{\mathrm{ET}}}{\sum_{d} k_{d}^{D}} \cdot \frac{k_{\mathrm{F}}^{A}}{\sum_{a} k_{a}^{A}} \quad (5)$$

A quantity we can measure with good accuracy, even in a heterogeneous system, is the ratio between the two fluorescence quantum yields Φ_{F}^{D} and Φ_{F}^{A}, Equation (6).

$$\frac{\Phi_{\mathrm{F}}^{A}}{\Phi_{\mathrm{F}}^{D}} = k_{\mathrm{ET}} \frac{k_{\mathrm{F}}^{A}}{k_{\mathrm{F}}^{D}\sum_{a} k_{a}^{A}} \quad (6)$$

Equation (6) shows that the ratio between the fluorescence quantum yields is directly proportional to the rate constant for energy transfer k_{ET}. We have shown that k_{ET} for an energy transfer from an excited donor D to an acceptor A is proportional to the occupation probability of A, which we denote as p_A; $k_{\mathrm{ET}} \propto p_A$.[1, 2] Inserting this expression into Equation (6) leads to Equation (7).

$$\frac{\Phi_{\mathrm{F}}^{A}}{\Phi_{\mathrm{F}}^{D}} = C p_A \quad (7)$$

An expression for the proportionality constant C was derived in reference [2]. Its dimension is site. Constant C can be determined by measuring the ratio of acceptor to donor fluorescence emission intensity at different occupation probabilities.

The energy transfer in the channels of zeolite L can be used for measuring the diffusion kinetics. We assume that a situation, as illustrated in Figure 4a, can be prepared at the beginning of the experiment. Immediately after all dye molecules have entered the zeolite channels, the maximum energy transfer is observed because the donor to acceptor distance is short. The donor to acceptor distance increases, and hence the energy transfer rate decreases, when the molecules diffuse deeper into the channels. From this, the diffusion kinetics can be derived. The ratio of the acceptor to donor fluorescence yield, which is equal to the ratio of the corresponding intensities I at position z in a microcrystal at time t, is given by Equation (8). Terms $p_A(z,t)$ and $p_D(z,t)$ are the position and time dependent occupation probabilities of D and A.

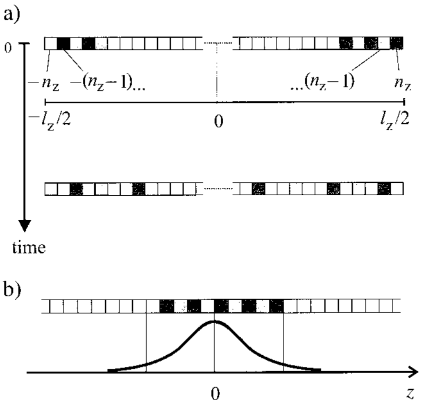

Figure 4. *Diffusion of dye molecules in the channels of zeolite L. a) Idealized initial state of a channel and state after diffusion has occurred for some time. b) Model of the initial Gaussian distribution for an infinitely long channel.*

$$\frac{\Phi_{\mathrm{F}}^{A}}{\Phi_{\mathrm{F}}^{D}}(z,t) = \frac{I_{\mathrm{F}}^{A}}{I_{\mathrm{F}}^{D}}(z,t) = C p_A(z,t)\, p_D(z,t) \quad (8)$$

What we actually observe is an average over the whole microcrystal, which means an average over z. If experiments are carried out with many crystals, an average over them is observed. We express this as Equation (9).

$$\frac{I_{\mathrm{F}}^{A}}{I_{\mathrm{F}}^{D}}(t) = \left\langle \frac{I_{\mathrm{F}}^{A}}{I_{\mathrm{F}}^{D}}(z,t) \right\rangle = C \langle p_A(z,t)\, p_D(z,t) \rangle \quad (9)$$

If an experiment is carried out so that the occupation probabilities $p_A(z,t)$ and $p_D(z,t)$ have the same value, $p(z,t)$, then Equation (10) follows, where D_0 is the dye diffusion coefficient, t the time, p^0 the local distribution at both ends of the channels at time $t = 0$, and $2n_z + 1$ is the number of sites in a channel.

$$p(z,t) = \frac{p^0}{\sqrt{4\pi D_0 t}} \sum_{-n_z}^{n_z} \mathrm{e}^{-(z-n_z)^2/(4D_0 t)} \quad (10)$$

If the channels used in an experiment are long enough, so that they consist of a few thousand sites, the reasoning can be simplified as follows: Firstly, we assume that at time $t = 0$ the system is prepared so that the initial distributions of the donor and the acceptor molecules are the same, $p_D^0 \approx p_A^0$, denoted as p^0. Then we assume that the number of sites in the channels extends to infinity, so that the idealized initial state can be described as in Figure 4b. Applying these assumptions, the donor and the acceptor distributions can be expressed by Equations (11) and (12).

$$p_D(z,t) = \frac{p_D^0}{\sqrt{4\pi D_0 t}} \mathrm{e}^{-z^2/4D_0 t} \quad (11)$$

$$p_A(z,t) = \frac{p_A^0}{\sqrt{4\pi D_0 t}} \mathrm{e}^{-z^2/4D_0 t} \quad (12)$$

Inserting these into Equation (9) results in Equation (13).

$$\frac{I_{\mathrm{F}}^{A}}{I_{\mathrm{F}}^{D}}(t) = C\frac{(p^0)^2}{4\pi D_0 t} \int_{-\infty}^{\infty} \mathrm{e}^{-z^2/2D_0 t}\,\mathrm{d}z = C\frac{(p^0)^2}{\sqrt{8\pi}} \frac{1}{\sqrt{D_0 t}} \quad (13)$$

The ratio of the acceptor to donor fluorescence intensities is proportional to the inverse square root of time, when the above-mentioned conditions are fulfilled. Energy transfer does not only occur between dye molecules located in the same channel but also among donors and acceptors located in different channels. This averages out, so that Equation (13) is expected to remain valid because of the cylindric morphology of the host. Equations (6) and (13) were derived by assuming Förster energy transfer.[14] The specific form of the rate constant is, however, not important as long as the rate constant k_{ET}^{ij} for energy transfer of an excited molecule *i* to an unexcited one *j* is proportional to the occupation probabilities p_i and p_j of the respective sites. A general discussion of energy-transfer properties of electronically excited molecules can be found in reference [15].

Several experimental conditions must be realized for the application of Equation (13). The donor and acceptor molecules should enter the channels at about the same rate, so that the assumptions made for the initial state are sufficiently well fulfilled. They should not be able to glide past each other once they are inside the channels. The crystals should be so long that molecules entering from both sides do not reach each other in the middle part of the channels during the time of observation. These constraints can only be realized when avoiding an excessive loading.

Crystals of about 1500 nm average length (900 nm diameter) have been investigated at four temperatures and crystals of about 700 nm average length (600 nm diameter) were studied at two temperatures. An SEM picture of the long zeolite L crystals is given in Figure 5; the morphology of the short crystals is similar.

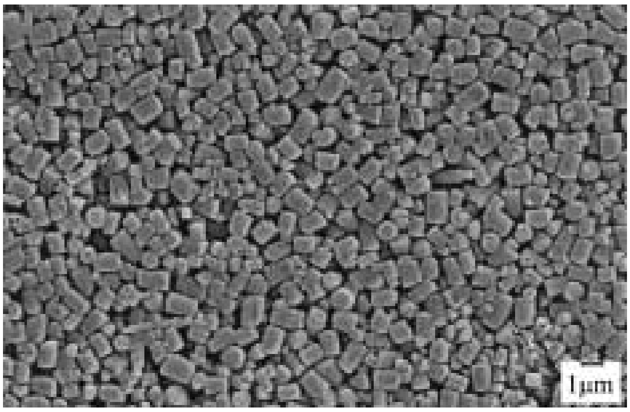

***Figure 5.** Scanning electron microscopy (SEM) image of the long zeolite L crystals. The scale bar is 1 µm.*

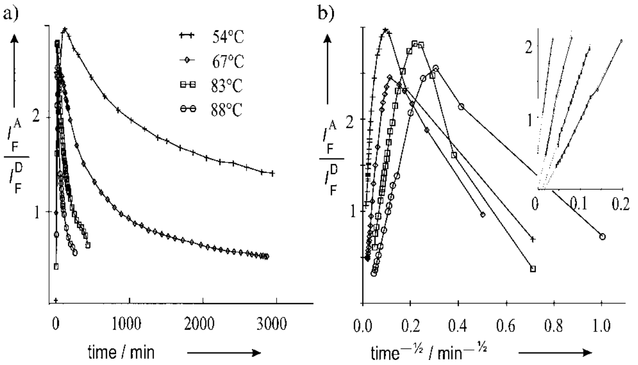

***Figure 6.** The fluorescence intensity ratios of acceptor Ox^+ to donor Py^+ versus a) time and b) the inverse square root of time, both for the long zeolite L crystals. The insert shows the linear region, magnified.*

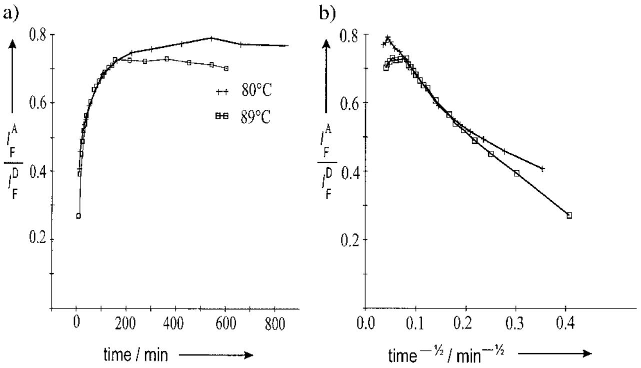

***Figure 7.** The fluorescence intensity ratios of acceptor Ox^+ to donor Py^+ versus a) time and b) the inverse square root of time, both for the short zeolite L crystals.*

In all cases, the amount of donor and acceptor molecules was in the order of $p_{\mathrm{Py}} \approx 0.008$ and $p_{\mathrm{Ox}} \approx 0.008$, so that only 1.6% of the sites were filled with either a donor or an acceptor. Py^+ was specifically excited at 470 nm, where the light absorption by Ox^+ is negligible. The fluorescence spectra were recorded from 480 nm to 700 nm. Figures 6 and 7 show, for both crystal lengths, the fluorescence intensity ratios $I_\mathrm{F}^\mathrm{A}/I_\mathrm{F}^\mathrm{D}$ between the acceptor Ox^+ and the donor Py^+ as functions of time and of the inverse square root of time. We notice in each case a rapid increase of $I_\mathrm{F}^\mathrm{A}/I_\mathrm{F}^\mathrm{D}$ at the beginning. This ratio goes through a sharp maximum and then decreases for the 1500 nm crystals; it remains nearly constant after having reached the maximum for the 700 nm crystals. Immediately after mixing the aqueous solution of Ox^+ and Py^+ with the zeolite suspension, nonluminescent aggregates are formed at the surface of the crystals.[2, 16] Therefore not only the intensity ratio is small but also the total emission is weak. Only after the dyes have entered the channels are they present as monomers. Hence, the total intensity increases. At this stage, the donor to acceptor distances are short and the energy transfer is efficient. Later, the dyes diffuse deeper into the crystal and the intermolecular distances increase with time. The sharp decrease in the value of $I_\mathrm{F}^\mathrm{A}/I_\mathrm{F}^\mathrm{D}$ after passing the maximum in case of the long crystals—but not in case of the short ones—means that, in the 700 nm crystals, the dyes approaching from both ends do interact via energy transfer. In addition, the ratio between the number of dye molecules with respect to the number of channels is two-fold smaller for the short crystals. The two-fold greater number of channels for each entering molecule leads to faster diffusion of the dye molecules, so that the initial situation of close-packed molecules, illustrated in Figure 4, is bypassed. The large difference in the intensity ratios between the long and the short crystals appears even greater when plotted versus inverse square root of time (Figures 6b and 7b). The behavior of the 1500 nm crystals after an initial preparation time follows Equation (13). We also observe that the transport becomes faster with increasing temperature. The enlargement of the linear part, magnified in the inset of Figure 6, shows that the extrapolation to the origin is reasonable. The deviations from what we would expect for "infinitely" long crystals are within an error range we can accept. The 700 nm crystals do not show this behavior under the conditions we have tested. We also note that the maximum intensity ratio is about four times smaller than that for the longer crystals. This means that the initial situation needed to fulfill Equation (13) was not reached.

Different stages of the diffusion can be observed by means of an optical microscope. We show, in Figure 8, fluorescence microscopy images of a sample which corresponds to the 88 °C curve in Figure 6 after 20, 60, and 470 min, and 162 h reaction time. Two selected crystals are framed, to represent what we observed for most crystals.

When comparing the images 1, 2, 3 a, and 4 in Figure 8 (increasing reaction times), we first notice the progress of the insertion (1 →2) of the dye molecules and then their diffusion inside of the zeolite channels by considering both the size and the colour of the fluorescent spots. The fluorescence of Py^+ appears green and that of Ox^+ deep red, while yellows are due to mixtures of red and green. Since specifically Py^+ was excited, the red contribution is due to energy transfer from the exited Py^+ to Ox^+. We observe two yellow-red spots on both sides of the crystals in image 1, which corresponds to a situation close to the maximum of the 88 °C curve in Figure 6. In image 2, the spots have extended and, in the middle part, a weak green region appears. While it is hardly visible in 2, it becomes obvious in 3 a. If Ox^+ is excited specifically, as illustrated in image 3 b, its presence in the inner region of the channel can be seen. This also shows that the mean distance between the donor and acceptor molecules is greater in the middle than at the ends of the channels. The green colour dominates after the very long reaction time and extends over the whole crystal, as in 4. The intensity distribution shows that the equilibrium has not yet been reached. Red fluorescence of the same shape is observed if specifically Ox^+ is excited. This means that the distribution of Py^+ and Ox^+ in the crystals is the same or at least similar. The images in Figure 8 support the assumption made, that Py^+ and Ox^+ enter the channels of zeolite L at about the same rate.

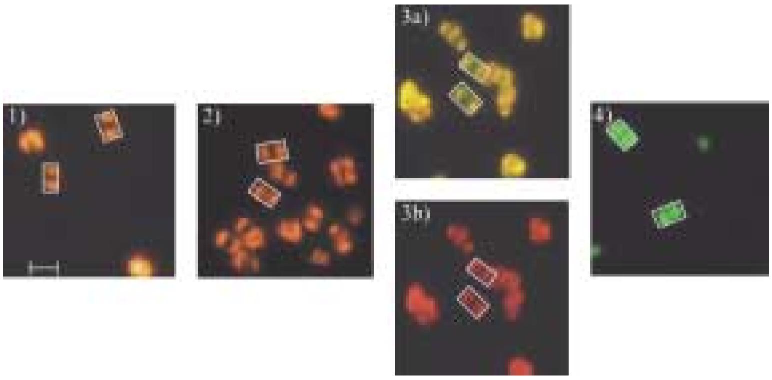

Figure 8. *Fluorescence microscopy pictures to visualize the diffusion of Ox^+ to Py^+ in zeolite L. The images were taken after 1) 20, 2) 60, and 3) 470 min, and 4) 162 h, respectively. The images were obtained by specifically exciting Py^+ at λ = 470 – 490 nm, with the exception of 3 b, in which Ox^+ was specifically excited at λ = 545 – 580 nm. Two crystals of each image are framed. The scale, given in 1, corresponds to a length of 1.5 μm.*

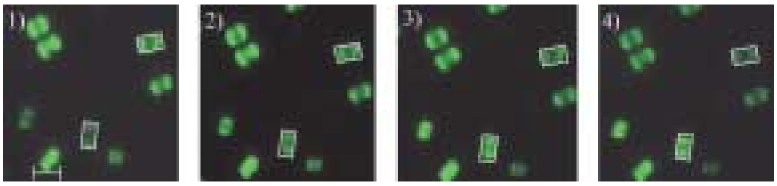

Figure 9. *Fluorescence microscopy pictures to visualize the polarization of the crystals' fluorescence after 48 h diffusion of Ox^+ to Py^+. Py^+ was specifically excited. The fluorescence was observed at angles (anticlockwise) of 1) 30°, 2) 60°, 3) 90°, and 4) 120°, from left to right, with respect to the base of the images. 0° means polarization parallel to horizontal axis and 90° parallel to the vertical axis. The same two crystals are framed in the four pictures. The scale, given in 1, corresponds to a length of 1.5 μm.*

A sample taken after 48 h of reaction time was examined with a polarization filter. Pictures obtained after specifically exciting Py^+ are shown in Figure 9. The polarization filter was set at angles of 30°, 60°, 90°, and 120°. The fluorescence is strongly polarized, nearly perpendicular to the crystal *c*-axis. The luminescence intensity of the framed crystal in the upper right edge of the pictures decreases with increasing polarization angle, while the opposite behavior is adopted by the framed crystal in the lower half of the pictures. The red luminescence, which appears when selectively observing Ox^+, shows the same behavior. A detailed study of this pronounced fluorescence anisotropy is reported in reference [17].

Experimental determination of the constant *C* is possible by means of Equation (7), which has been tested by measuring a series of suspensions with identical amounts of zeolite L but varying the occupation probabilities of Py^+ and Ox^+.[1, 2] The results of such an experiment are illustrated in Figure 10. The experiment was carried out with zeolite L of 700 nm average length. The fluorescence spectra on the left side of Figure 10, measured after

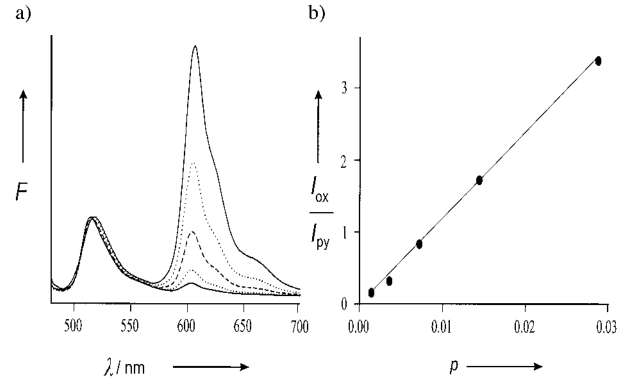

Figure 10. *Fluorescence of five suspensions with occupational probabilities p = 0.0014, 0.0036, 0.0072, 0.0144, and 0.0288 after specific excitation of Py^+ at 465 nm. The values of p ($p_{Ox} = p_{Py}$) are approximately $2^a \times 0.0015$ for a = 0...4, which correspond to dye concentrations inside of each nanocrystal of $2^a \times 0.6$ mM. a) Fluorescence spectra normalized to the same peak height for the Py^+ emission at about λ = 520 nm. The intensity of the oxonine emission (peak on the right) increases with increasing p. b) Ratio of the fluorescence intensities I_{Ox}/I_{Py} as a function of the loading of Ox^+ and Py^+.*

specific excitation of Py^+, show that at the lowest loading the green emission of Py^+, with a maximum at about 520 nm, dominates. An increase of the loading causes this emission to decrease and the Ox^+ emission, with a maximum at about 605 nm, to increase. The Ox^+ emission clearly dominates at $p = 0.0288$. The ratio of the acceptor to donor fluorescence intensity, I_{Ox}/I_{Py}, illustrated on the right side of Figure 10, shows that Equation (7) holds, with a constant $C = 121$ sites. This value is used to estimate the diffusion coefficient.

In order to estimate the diffusion coefficient from the data given in Figure 6 based on Equation (13), the value of C and that of the initial local loading p^0, extrapolated to ideal initial conditions, are needed. The upper limit of p^0 is unity. From this, we obtain an upper limit of the diffusion coefficients D_0, listed in Table 1. Diffusion coefficients of molecules of similar size in water at room temperature are in the order of 10^{-6} cm^2 s^{-1}[18] and that of $[Mo(CO)_6]$ in zeolite Y is of the order 10^{-13} cm^2 s^{-1}.[5] The values in Table 1 are about three orders of magnitude smaller: Zeolite L is one dimensional, while zeolite Y has a three-dimensional framework. In addition, we must consider that counter diffusion of water molecules and of solvated potassium ions is correlated with the diffusion of the cationic dye molecules. We have good qualitative information concerning the influence of counter diffusion of the solvent molecules from studies carried out on the exit kinetics of the resorufin anion.[4] A simplified view of these processes is illustrated in Scheme 1. We conclude that energy-transfer measurements can provide details of intrazeolite diffusion kinetics with a sensitivity and a spatial resolution which has otherwise not yet been accessible.

Table 1. Diffusion coefficients of the Ox^+ and Py^+ in zeolite L at different temperatures.

T [°C]	Diffusion coefficients D_0 [site^2 min^{-1}]	[cm^2 s^{-1}]
54	0.27	1.0×10^{-16}
67	0.74	2.8×10^{-16}
83	1.8	6.7×10^{-16}
88	4.4	1.7×10^{-15}

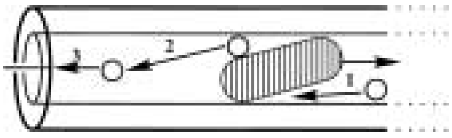

Scheme 1. Counter diffusion of dye (hatched block) and water molecules (circles) in a one-dimensional channel. The solvent molecules have to pass the dye molecule in a first step (1). This step is decisive for the rate of the solvent counter diffusion: After passing the dye molecule (2), the solvent molecules freely drift (3), until they encounter the next dye molecule.

Experimental Section

The pure potassium form of zeolite L, $K_9(AlO_2)_9(SiO_2)_{27} \cdot 21\,H_2O$, was synthesized as described in references [19, 20]. The average dimensions of the short and the long crystals are (length, diameter) 700 and 600 nm, and 1500 and 900 nm, respectively. Py^+ and Ox^+ were synthesized as reported in reference [19]. The integrity of the zeolite samples during different stages of the experiments was checked by X-ray powder diffraction.

Fluorescence spectra were recorded on a luminescence spectrometer (LS 50B, Perkin Elmer) with a resolution of 5 nm. 10 mm path length quartz cuvettes were used. The temperature was held constant by a closed water circulation and measured inside the cuvettes by means of a calibrated Pt-100 thermocouple. Optical microscopy images of fluorescent samples were taken with 2000-fold magnification using a microscope (Olympus BX 60) and a CCD camera (Kappa CF 20 DCX Air K2). Light, from a 100 W halogen lamp, passed through appropriate excitation cubes comprised of a narrow band excitation filter, a dichroic mirror, and a cut-off barrier filter. For the fluorescence observations, the appropriate cubes were selected for specific excition of the molecules and the region of the first π,π^* absorption band: U-MNB (470 – 490 nm) for Py^+ and U-MWIY (545 – 580 nm) for Ox^+. Images were recorded with Kappa ImageBase software.

Diffusion kinetics experiments were performed over a temperature range 50 – 90 °C into long and short zeolite L crystals. The amounts of zeolite, Py^+, and Ox^+ were identical for every experiment. Zeolite stock suspensions were prepared by adding doubly distilled water (10 mL) to zeolite (0.2 g). The kinetic mixtures were prepared as follows. Equal amounts of Py^+ and Ox^+ (1.11 nmol) were dissolved together in doubly distilled water (1 mL), then added to a quartz cuvette equipped with a magnetic stirring bar. The zeolite stock suspension was, in the meantime, pretreated in an ultrasonic bath for 20 min. A sample of suspension (40 μL) was taken and added to the preheated dye solution in the cuvette and diluted with doubly distilled water (1.5 mL). Measurements commenced 2 min after the zeolite was added to the dye. Fluorescence spectra were recorded over $\lambda = 480 - 700$ nm, with $\lambda_{ex} = 470$ nm, at intervals dependant on the progress of the diffusion; at 50 °C, the spectra were taken typically every 30 min for the first 30 h and then every 60 min, while at 90 °C, spectra were taken every 5 min for 3 h and then every 30 min afterwards.

[1] N. Gfeller, S. Megelski, G. Calzaferri, *J. Phys. Chem. B* **1998**, *102*, 2433 – 2436.
[2] G. Calzaferri, D. Brühwiler, S. Megelski, M. Pfenniger, M. Pauchard, B. Hennessy, H. Maas, A. Devaux, U. Graf, *Solid State Sciences* **2000**, *2*, 421 – 447.
[3] U. Schemmert, J. Käger, J. Weitkamp, *Microporous Mesoporous Mater.* **1999**, *32*, 101 – 110.
[4] D. Brühwiler, N. Gfeller, G. Calzaferri, *J. Phys. Chem. B* **1998**, *102*, 2923 – 2929.
[5] B. R. Müller, G. Calzaferri, *Microporous Mesoporous Mater.* **1998**, 21, 59 – 66.
[6] R. M. Barrer, H. Villiger, *Z. Kristallogr.* **1969**, *128*, 352.
[7] S. Ernst, J. Weitkamp, *Catal. Today* **1994**, *19*, 27 – 60.
[8] M. Tsapatsis, T. Okubo, M. Lovallo, M. E. Davis, *Mat. Res. Soc. Symp. Proc.* **1995**, *371*, 21 – 26.
[9] W. M. Meier, D. H. Olson, C. Bärlocher, *Atlas of Zeolite Structure Types,* 4th ed., Elsevier, London, **1996**, p. 17.
[10] T. Ohsuna, Y. Horikawa, K. Hiraga, *Chem. Mater.* **1998**, *10*, 688 – 691.
[11] B. Hennessy, S. Megelski, C. Marcolli, V. Shklover, C. Bärlocher, G. Calzaferri, *J. Phys. Chem. B* **1999**, *103*, 3340 – 3351.
[12] a) T. Förster, *Ann. Phys. (Leipzig)* **1948**, *2*, 55; b) T. Förster, *Fluoreszenz organischer Verbindungen*, Vandenhoeck und Ruprecht, Göttingen, **1951**.
[13] J. R. Lacowicz, *Principles of Fluorescence Spectroscopy,* 2nd ed., Kluver Academic/Plenum, New York, **1999**.
[14] N. Gfeller, G. Calzaferri, *J. Phys. Chem. B* **1997**, *101*, 1396 – 1408.
[15] G. Juzeliûnas, D. L. Andrews in *Resonance Energy Transfer* (Eds.: D. L. Andrews, A. A. Demidov), Wiley, New York, NY, **1999**, Chap. 2, p. 65.

[16] F. Binder, G. Calzaferri, N. Gfeller, *Sol. Energy Mater. Sol. Cells* **1995**, *38*, 175 – 186.

[17] S. Megelski, A. Lieb, M. Pauchard, A. Drechsler, S. Glaus, C. Debus, A. J. Meixner, G. Calzaferri, *J. Phys. Chem. B*, in press.

[18] *Landolt-Börnstein*, *Vol. 2*, Sect. 5a, 6th ed. (Eds.: H. Borchens, H. Hausen, K. H. Hellwege, K. Schäfer, E. Schmidt), Springer, Berlin, **1969**.

[19] N. Gfeller, S. Megelski, G. Calzaferri, *J. Phys. Chem. B* **1999**, *103*, 1250 – 1257.

[20] S. Megelski, PhD thesis, University of Berne (Switzerland) **2000**.

Received: July 17, 2000 [Z 72]

Single-Transition Coherence Transfer by Adiabatic Cross Polarization in NMR**

Thomas R. Eykyn,[a, b] Fabien Ferrage,[a]
Emanuel Winterfors,[a] and Geoffrey Bodenhausen*[a, b]

KEYWORDS:

coherence transfer · cross polarization · NMR spectroscopy · peptides

The interest shown in the manipulation of single-transition coherences in nuclear magnetic resonance (NMR) has increased greatly since it was recognised that cross-correlated relaxation phenomena could lead to line-narrowing effects. In transverse relaxation-optimised spectroscopy (TROSY),[1] the fluctuations of a dipolar interaction and an anisotropic chemical shift tensor mutually cancel so that, in large molecules with long rotational correlation times at elevated magnetic field strengths, some single-transition coherences can have very long lifetimes. Many coherence-transfer methods have been developed[2–4] to obviate mixing of single-transition coherences. Most of these methods employ nonselective pulses. Recently, another approach, single-transition cross polarization (ST-CP) has been introduced[5] to enable a transfer between single-transition coherences without mixing parallel transitions by employing radio frequency (RF) fields that are weaker than the scalar coupling constant. The original version of ST-CP employed spin-lock fields of constant amplitude to achieve coherence transfer via zero- or double-quantum coherences. We propose herein an adiabatic version, where the density operator is confined to a subspace spanned by single-quantum coherences, which we shall refer to as single-transition adiabatic cross polarization (ST-ACP).

Adiabatic transformations have been extensively employed in solid-state NMR for the enhancement of cross polarization efficiency,[6–10] to achieve excitation of both quadrupolar order[11] and multiple quantum coherences[12] in $I > {}^1\!/_2$ systems. Adiabatic coherence transfer has also been used in liquid-state NMR[13, 14] and a number of methods have been proposed for achieving adiabatic inversions.[15, 16] Many theoretical studies of the adiabaticity of such methods have been carried out.[15, 17] We present the use of adiabatic coherence transfer in a four-level system of two J-coupled spin-${}^1\!/_2$ nuclei to achieve spin-state selective coherence transfer. A theoretical treatment is given for the conditions under which the transfer is adiabatic and different limiting cases are considered. We have also developed an experimental test of the reversibility of the transfer which reveals violations of adiabaticity.

We consider a scalar-coupled two-spin-${}^1\!/_2$ system, IS (Figure 1). Coherence transfer can be achieved by irradiating simultaneously two connected transitions with low amplitude RF fields. It has been demonstrated[5] that two processes occur simultaneously: an on-resonance transfer, between the two irradiated transitions, and an off-resonance transfer, between the other two transitions. These two processes have been shown to be confined in two mutually exclusive three-dimensional subspaces of the Liouville space, provided the scalar coupling constant J_{IS} is large enough compared to the RF field amplitude and relaxation coupling terms.

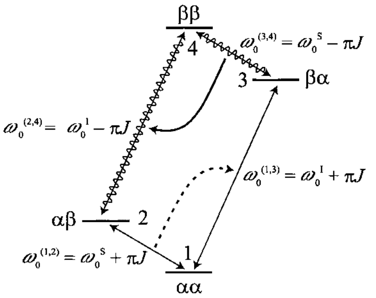

Figure 1. Energy-level diagram for a scalar-coupled two-spin system, IS, such as is found in ${}^{15}N-{}^{1}H$ pairs. The nitrogen doublet components correspond to transitions (1,2) and (3,4), while the proton doublet components correspond to transitions (1,3) and (2,4). Also shown is a schematic representation of single-transition cross polarization (ST-CP) transfer. If irradiation is truly selective, so that the secular approximation is fulfilled, both the on-resonance (solid arrow) and off-resonance transfers (dashed arrow) occur. The energy levels have been drawn for a system where both nuclei have positive gyromagnetic ratios although $\gamma(^{15}N) < 0$. However, if the order of the energy levels were swapped, this might create confusion, especially between "zero" and "double" quantum coherences.

The whole discussion will take place, unless otherwise indicated, in the interaction frame (IF) where the Zeeman and scalar coupling terms of the static Hamiltonian are taken into account, so that all coherences appear stationary. In the following, we consider the transfer (Figure 1) from the coherence $I_x^{(3,4)}$ of the S nucleus (for example, ${}^{15}N$) to the coherence $I_x^{(2,4)}$ of

---

[a] *Prof. G. Bodenhausen, T. R. Eykyn, F. Ferrage, E. Winterfors*
Département de Chimie, associé au CNRS
Ecole Normale Supérieure
24, rue Lhomond, 75231 Paris cedex 05 (France)
Fax: (+33) 1-44-32-33-97
E-mail: Geoffrey.Bodenhausen@ens.fr

[b] *Prof. G. Bodenhausen, T. R. Eykyn*
Section de Chimie, Université de Lausanne
BCH, 1015 Lausanne (Switzerland)

[**] *This work was supported by the Centre National de la Recherche Scientifique (CNRS) of France, and by the Fonds National de la Recherche Scientifique (FNRS) and the Commission pour la Technologie et l'Innovation (CTI) of Switzerland.*

Efficient Blue Organic Light-Emitting Diodes with Graded Hole-Transport Layers**

David C. Müller,[a] Thomas Braig,[b] Heinz-Georg Nothofer,[c] Markus Arnoldi,[d] Markus Gross,[a] Ulrich Scherf,[c] Oskar Nuyken,*[b] and Klaus Meerholz*[a]

KEYWORDS:

hole transport · luminescence · oxetanes · semiconductors · thin films

Organic light-emitting diodes (OLEDs) represent a promising technology for large, flexible, lightweight, flat-panel displays.[1–3] Such devices consist of one or several semiconducting organic layer(s) with an overall thickness of about 100 nm sandwiched between two electrodes. The organic layers are commonly deposited either by sublimation of small molecules in vacuum or by solution casting of polymers. The latter route has many advantages for the industrial mass production of OLED devices compared with vacuum deposition technique, including the lower cost of the equipment, faster and simpler layer deposition even on curved surfaces, and generally better performance in single-layer devices. However, the most important disadvantage at this point is the shorter device lifetime compared with small-molecule devices. This is generally attributed to the difficulty in rigorously purifying polymers and in removing residual solvent from the casting process.

The key to obtain efficient blue OLEDs is the deposition of several layers. In contrast to the vacuum deposition route, this is much more challenging in solution casting due to the risk of partially dissolving the previous layer while depositing the next. In order to make solution processing suitable for preparation of multilayer organic devices, either "orthogonal" solvents have to be used (allowing, in the ideal case, deposition of only two or three layers)[4, 5] or, alternatively, the solubility of the layers has to be reduced after their deposition. One possibility for the latter approach is to use soluble precursor polymers, which can be converted into an insoluble form afterwards. This concept has been extensively used, for example, with poly(*p*-phenylenevinylene) (PPV).[6] Other authors have proposed soluble precursors with pendent polymerizable moieties to be crosslinked after deposition. One can distinguish reactive side- or main-chain polymers[7–10] and monomers with several reactive groups;[11–14] both lead to polymer networks. Generally, whenever a direct comparison was attempted, the performance of devices containing a crosslinked layer was less compared with a reference device based on the noncrosslinked material.[8, 9] One probable reason is that, upon crosslinking, not only the desired polymerization/crosslinking reaction took place but also side reactions, which reduced the concentration of the electrical functional moieties (for example, hole- or electron-transport site or emitter).[7] Another possiblity for the reduced performance might also be the distinct shrinkage which occurs upon polymerization (about 10 – 20% for acrylates and epoxides), leading, in the thin films, to microcrack formation and thereby to current leak and eventually to a short circuit. The challenges from a synthetic standpoint are: a) to develop compounds with good solubility and film-forming properties; b) establish polymerization conditions which leave the desired electrical and optical functionality unaffected; c) to minimize the volume shrinkage upon crosslinking, and d) to reach complete insolubility.

Herein, we demonstrate how these challenges can be overcome by using low-molecular weight "monomers" with two oxetane groups[11] as the reactive, polymerizable group. Oxetanes exhibit an extremely low shrinkage during the crosslinking process,[15] are chemically stable, and can be cationically polymerized in bulk at high rates and with high conversions to form polyethers.[16] Furthermore, oxetanes are stable even under the strongly basic conditions (NaO*t*Bu) under which the C—N coupling reaction employed proceeds (see below). We restrict ourselves to crosslinkable hole-transporting agents (HTA) with a variable HOMO level, which allows "electronic stairs" to be built towards a poly(9,9′-dialkylfluorene) (PF) derivative. PFs have recently attracted much interest as polymeric materials for blue emission.

Three oxetane-functionalized hole-transporting triarylamines (monomers **7** – **9**, Scheme 1) with different electronic levels were synthesized by Pd-catalyzed C—N coupling (Hartwig – Buchwald amination)[17] of bromoarenes with secondary amines. The length of the spacer between the oxetane group and the triarylamine core determines the film-forming properties and glass-transition temperature T_g of the monomers. The film-forming and wetting properties are reduced for very low T_g. On the other hand, since T_g can be regarded as a measure for the diffusional mobility of the reactive oxetane groups, a low T_g

---

[a] Priv.-Doz. Dr. K. Meerholz, Dipl.-Chem. D. C. Müller, Dipl.-Chem. M. Gross
Department Chemie
Lehrbereich Physikalische Chemie
Ludwig-Maximilians-Universität München
Butenandtstrasse 11, 81377 München (Germany)
Fax:(+49) 89-2180-7565
E-mail: klaus.meerholz@cup.uni-muenchen.de

[b] Prof. Dr. O. Nuyken, Dr. T. Braig
Lehrstuhl für Makromolekulare Stoffe
Technische Universität München
Lichtenbergstrasse 4, 85747 Garching (Germany)
Fax: (+49) 89-2891-3562
E-mail: nuyken@ch.tum.de

[c] Priv.-Doz. Dr. U. Scherf, Dipl.-Chem. H.-G. Nothofer
Max Planck Institute for Polymer Research
Ackermannweg 10, 55037 Mainz (Germany)

[d] Dipl.-Phys. M. Arnoldi
Physik-Department der TU München
Institut für Biophysik
James-Franck-Strasse, 85747 Garching (Germany)

[**] This work was supported by the Bavarian government through the "Neue Werkstoffe" program. We express our thanks to Francisco Gallego-Gomez (LMU) for measuring the glass-transition temperatures. We also acknowledge a donation of Baytron P® from Bayer AG (Leverkusen).

Supporting information for this article is available on the WWW under http://www.wiley-vch.de/home/chemphyschem/ or from the author.

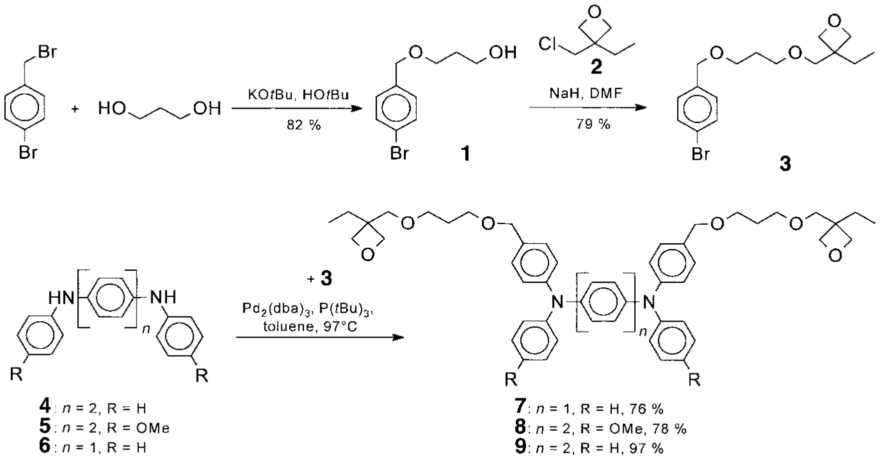

Scheme 1. Synthesis of oxetane-functionalized N,N′*-tetraphenylbenzidine and* N,N′*-tetraphenylphenylene diamine derivatives **7**–**9** via a palladium-catalyzed C—N coupling reaction.*

enables fast kinetics and high yield of the crosslinking process. As a compromise, propyl spacers were introduced, to yield T_g values in the range -10– $+10\,^\circ$C (Table 1).

Table 1. *Material-related physical properties of the monomeric hole-transport agents **7**–**9**.*

HTA	T_g [°C]	E_0^1 [a] [V]	E_0^2 [a] [V]	E_{HOMO} [b] [eV]
7	-9	0.49	0.96	-5.29
8	$+8$	0.61	0.76	-5.41
9	$+7$	0.68	0.84	-5.48

[a] Oxidation potential versus Ag/AgCl, determined by cyclic voltammetry in acetonitrile/$[N(C_4H_9)_3][PF_6]$ (0.1 M). Internal calibration was performed using the ferrocene/ferrocenium redox couple. [b] HOMO energy estimated according to $E_{HOMO} = -(E_0^1 + 4.8)$.[32]

The oxetane-functionalized bromoarene precursor **3** was synthesized in two steps (Scheme 1). 4-Bromobenzyl bromide was treated with an excess of 1,3-propanediol to 3-(4-bromobenzyloxy)propanole **1** in 82% yield. Final conversion of **1** with 3-chloromethyl-3-ethyloxetane **2**[18] yielded 79% of the oxetane-functionalized bromoarene precursor **3**. An alternative route, using the oppositely functionalized educts 1,3-dibromopropane, 4-bromobenzyl alcohol, and 3-ethyl-3-hydroxyoxetane, which was previously reported for the synthesis of homologue **2** containing a hexyl spacer,[11] could not be applied successfully, since severe elimination of HBr occurred in both steps to afford allylic systems.

Tris(*tert*-butyl)phosphine, P(*t*Bu)$_3$,[19] was used as ligand in the presence of $[Pd_2(dba)_3]$ for the C—N coupling reaction of **3** with the aromatic secondary diamines **4**–**6** (dba = dibenylideneacetone). Compounds **4** and **6** are commercially available; **5** was obtained by coupling of 4,4′-dibromobiphenyl with two equivalents of 4-methoxyaniline. The formation of the *N,N*′-tetraphenylbenzidine derivative **7** proceeded in excellent yield (97%) and in good yield for **8** and **9** (78% and 76%, respectively). The compounds were purified by flash chromatography.

Thin films were prepared by spin coating the monomers from a THF solution, which additionally contained 2 wt% of the photoacid 4-(thio-phenoxyphenyl)-diphenylsulfonium hexafluoroantiomonate (**10**).[16] The UV-activated acid is the initiatior for the cationic polymerization. We point out that the decomposition products of **10** are soluble and volatile, that is, they can be removed by rinsing or simply evaporate upon curing at elevated temperature.[20] Furthermore, they should be removed during the period vacuum is applied for depositing the top electrode.

UV illumination ($\lambda > 280$ nm) was performed in bulk at room temperature for about 10 s. To further advance the crosslinking process in the growing network, the films were afterwards cured at 150 °C in an inert gas atmosphere for 5 min, which increased both the diffusional mobility of the oxetane groups and the degree of crosslinking. The resulting polymer networks were found to be completely insoluble. IR investigations[21] indicated a high conversion (> 80%) and, most importantly, no degradation of the triarylamine cores. Films spin coated on indium tin oxide (ITO) exhibited an root-mean square surface roughness $\bar{x}_{RMS}$ of only 0.5 nm, as determined by atomic-force microscopy. However, the surface roughness of the bare ITO substrate was more than one order of magnitude greater ($\bar{x}_{RMS} = 10$ nm); the films smoothly cover the rough substrates.

We first investigated "hole only" devices to study the suitability of the novel compounds for hole transport. The hole-transport layer (HTL) was sandwiched between ITO and aluminum electrodes. Four different types of devices were studied:

a) "Simple" devices consisting of one "thick" crosslinked layer (≈ 100 nm) of each of the HTAs (**7**–**9**);
b) "Control" devices consisting of three "thin" layers (30–35 nm each) of the same HTA deposited one after the other;
c) "Mixed" devices consisting of one "thick" layer (≈ 100 nm) of a 1:1:1 mixture by weight of the three HTAs;
d) "Graded" devices consisting of three "thin" layers (30–35 nm) of each of the three HTAs in the sequence **7** → **8** → **9**.

A linear relationship between the film thickness and the onset voltage was observed in all cases, which indicates that charge injection is field dependent. However, due to the lack of suitable analytical models describing charge injection into amorphous organic semiconductors, a quantitative determination of the barrier for hole injection is impossible at this point.[22] The performance of the "simple" and the "control" devices was found to be identical, that is, it did not matter whether the overall thickness was achieved in one or several steps. This indicated that the successive deposition of several layers did not lead to internal barriers for charge transport. Furthermore, the hole-transport properties of the layers deposited first was clearly not affected by the subsequent deposition steps. It is interesting to note, that the current throughput in fully cured devices was higher than those that were incompletely cured.

Within the series of devices with only one crosslinked HTA, the onset field decreases in the sequence "simple-**9**" > "simple-**8**" > "mixed" > "simple-**7**" (Figure 1). Assuming similar hole mobilities, this reflects the decreasing height of the injection barrier between ITO and the HTL, in agreement with the electrochemical redox potentials E^0 and estimated HOMO levels, respectively (Table 1). The rather good performance of the "mixed" device impressively demonstrates the copolymerization capability of the oxetane-functionalized monomers. AFM investigations of the surface did not indicate signs of phase separation. Finally, the "graded" device showed slightly lower current density than the "mixed" device but higher than the "simple-**8**" device.

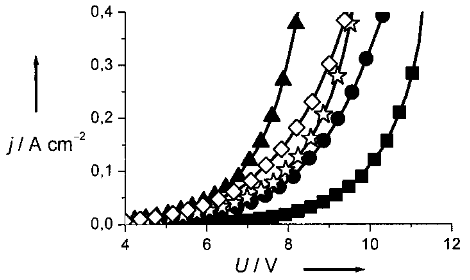

Figure 1. *Performance of "hole only" devices: Dependence of the current density* j *on the applied voltage* U *in devices containing the hole-transport layers "simple-**7**" (▲), "simple-**8**" (●), "simple-**9**" (■), "mixed" (◇), and "graded" (☆).*

After having demonstrated the excellent HTL properties of the compounds, we checked their suitability in multilayer OLEDs. A very attractive material class of blue-emitting polymers are the poly(9,9′-dialkyl-fluorenes) (PFs).[23] Due to their high HOMO energy ($E_{HOMO} \approx -5.8$ eV)[24] hole injection from commonly used ITOs (φ_w varies between -4.1 and -4.9 eV, depending on the pretreatment)[25] or from poly(3,4-ethylendioxythiophene) doped with polystyrene sulfonate (PEDOT/PSS; $\varphi_w \approx -5.1$ eV)[26] is inefficient, thereby limiting the number density of holes in the emission layer (EML). This is considered responsible for the rather poor performance of single-layer OLEDs based on PF derivatives. By contrast, in bilayer devices with an additional HTL, improved performance was achieved.[23] Thus, deposition of multiple organic layers by solution casting is an important task in the optimization of blue-emitting OLEDs.

We selected the PF derivative α,ω-4-(bis(methylphenyl)aminophenylene)-poly(9,9-bis(2-ethylhexyl)fluorene-2,7-diyl) (**11**; see Scheme 2; the feed ratio of the triphenylamine endcaps upon polymerization was about 0.3%).[27b] Among the HTAs under consideration, the HOMO energy of **9** is closest to that of the PF emissive layer, in other words, the barrier for injecting holes is the smallest. Therefore, only those OLED devices were investigated here, which involved compound **9** in the HTL (HTL-OLED "simple-**9**", "mixed", and "graded"). In all HTL-OLEDs, the HTL and EML were 40 and 60 nm thick, respectively. For comparison, the commonly used OLEDs with a PEDOT injection layer ($d = 40$ nm) were investigated.[22, 26] In this case, the EML thickness was 90 nm, that is, slightly less than the 100 nm total layer thickness in the HTL-OLEDs.

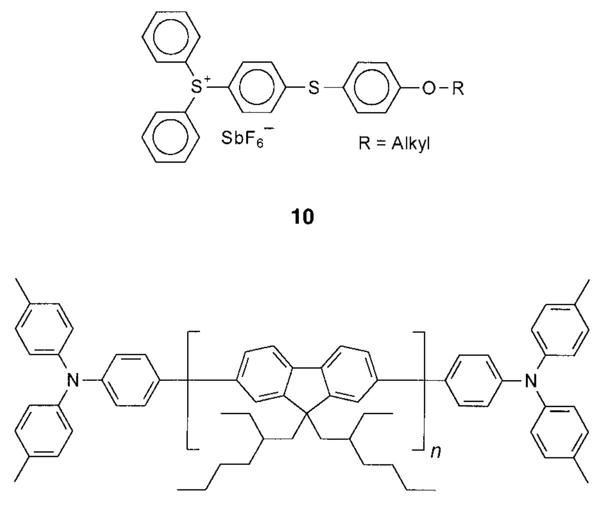

10

11

Scheme 2. *Structures of the photoacid* ***10***[16] *and the polyfluorene derivative* ***11***.[27]

At low current densities, all devices showed stable blue emission with peaks at about 420 and 445 nm (Figure 2), which indicates that charge-carrier recombination and emission takes place exclusively in the EML. The broad emission band at around 475 nm is generally attributed to aggregate formation between the PF chains.[28] By contrast, at high current densities this feature became more dominant (yielding a green impression), presumably as a result of thermal annealing of the layer due to Coulomb heating. We will discuss herein only data, where the original blue emission was maintained, as verified by the EL spectra. The performance parameters of all devices are summarized in Table 2.

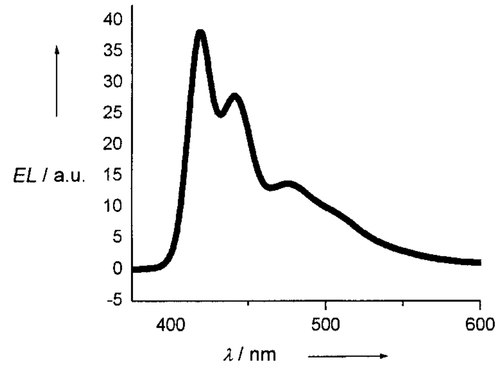

Figure 2. *Normalized electroluminescence spectrum of a "graded" OLED based on the PF derivative* ***11***. *The brightness was approximately 1000 cd m^{-2}.*

Overall, the devices show rather promising performance compared with other blue-emitting devices known in the literature.[23, 29] The "graded" OLED clearly shows the best EL efficiency η (Figure 3c and d). This is a result of both a lower EL onset voltage and low current density. The "mixed" OLED is less

Table 2. OLED performance parameters, measured by electroluminescent efficiency η at a given applied potential, for two brightness levels.

	100 cd m^{-2}		1000 cd m^{-2}	
Device	η [cd A^{-1}]	at Potential [V]	η [cd A^{-1}]	at Potential [V]
"graded"	2.7	5.4	2.45	7.7
"mixed"	1.8	6.1	1.66	8.9
"simple-**9**"	0.64	8.4	0.70	11.5
PEDOT	0.63	6.9	0.75	9.0

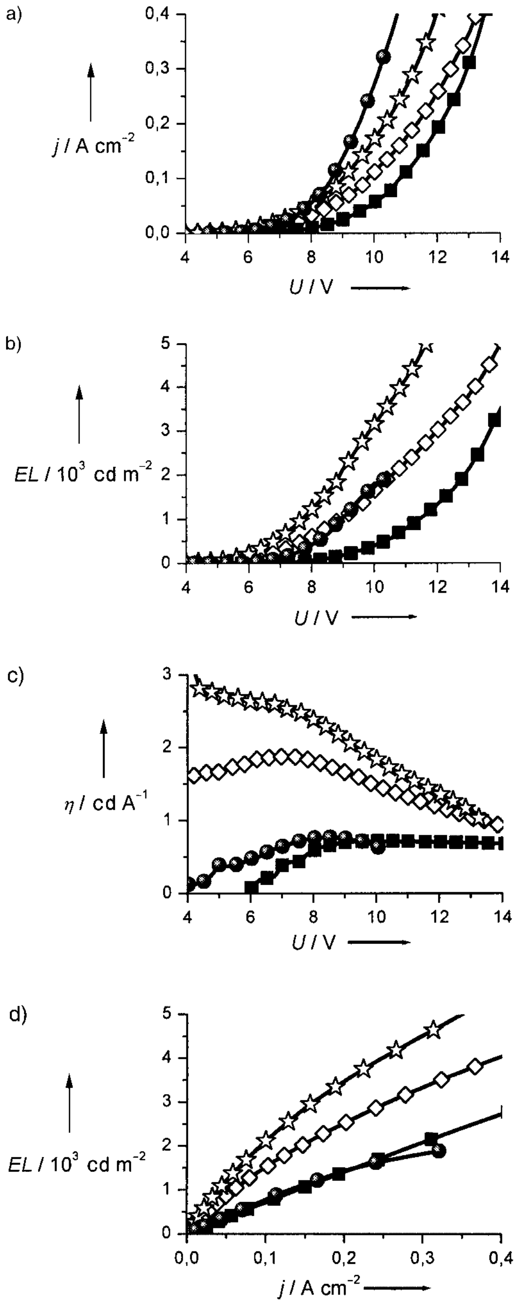

***Figure 3.** Performance of OLEDs based on the PF derivative **11**. Devices contained the hole-transport layers "simple-**9**" (■), "mixed" (◇), "graded" (☆), or a PEDOT injection layer (●). The dependencies of a) the current density j, b) the light output EL, and c) the electroluminescence efficiency η on the applied voltage U are shown, and d) the light output on the current density.*

efficient, which we explain by the lower concentration of **9** at the internal HTL/PF interface (only one third of the other cases) and the fact that the HOMO of **9** is situated above the average hole-transport level of the "mixed" layer, that is, there are few carriers in this level. Finally, the "simple-**9**" HTL OLED shows the poorest performance among the HTL-OLEDs. This is a result of the higher onset fields necessary to inject holes from ITO into the HTL, which leads to improved electron injection at the cathode and, thus, more unbalanced carrier densities than in the "graded" device.

In the PEDOT reference device, the current increases much more rapidly than in any of the HTL-OLEDs when the field is increased, which indicates very efficient injection of holes (Figure 3 a). However, the light output remained relatively low, to yield a rather low efficiency (comparable to the "simple-**9**" HTL-OLED). This behavior suggests some interaction between **11** and the PEDOT injection layer and quenching of excitons at the interface. Indeed, if a thin (10 nm) layer of **9** is introduced between PEDOT and **11**, the efficiency approximately doubles, yielding similar performance as the "mixed" OLED (data not shown).

In conclusion, we successfully demonstrated the use of electrically semiconducting networks obtained by crosslinking monomers functionalized with two oxetane units. The crosslinked films withstand higher current throughput than non-crosslinked films, exhibit excellent surface qualities with a roughness below 1 nm, and are absolutely insoluble even at high temperature in an ultrasonic bath. Furthermore, they are mechanically durable and morphologically stable which are important prerequisites for the long-term stability of OLEDs.

We successfully realized a "graded" HTL consisting of three electronic levels by solution casting only. Layer-by-layer deposition did not lead to internal barriers. Copolymerization of the monomers is also possible. The performance of our best solution-processed four-layer OLEDs based on a PF-derivative (2.7 cd A^{-1} at a brightness of 100 cd m^{-2}) compares favorably with the best performance of similar blue-emitting devices fabricated by vacuum deposition. EL efficiencies higher than 3 cd A^{-1} were obtained for thicker EML but this required higher voltages and, thus, reduced the power efficiency of the devices. Further work is required to optimize the thickness of the individual layers. Our concept may become important for the future realization of electrically driven organic lasers. In this case, the layers perform electrical and optical functions (waveguiding) simultaneously.

Experimental Section

Device preparation and physical characterization: ITO-coated glass substrates were purchased from Applied Films Corporation (resistivity 20 Ω) and carefully cleaned and dried prior to use. No further treatment, such as with ozone plasma,[25] was undertaken. Hole-only devices were fabricated by first spin coating the monomers from THF onto the ITO-substrates, crosslinking the films, rinsing the films with THF, and finally depositing Al as the top electrode. For the OLEDs, the polyfluorene derivative **11** was spin coated from toluene solution and calcium was deposited as the cathode. PEDOT layers were obtained by spin coating the as-received aqueous suspension.[30] The characterization of the devices was performed by a custom-made voltage generator using a calibrated ammeter and a calibrated photodiode.

All chemicals were purchased (Aldrich, Lancaster, or Strem) and were used without further purification. 3-Chloromethyl-3-ethyloxetane **2** and the photoacid 4-(thio-phenoxyphenyl)diphenylsulfonium hexafluoroantiomonate **10** were prepared according to ref. [31] and [16], respectively. Further characterization and preparation data may be found in the Supporting Information.

[1] R. H. Friend, R. W. Gymer, A. B. Holmes, J. H. Burroughes, R. N. Marks, C. Taliani, D. D. C. Bradley, D. A. Dos Santos, J. L. Brédas, M. Lögdlund, W. R. Salaneck, *Nature* **1999**, *397*, 121.

[2] A. J. Heeger, *Solid State Commun.* **1998**, *107*, 673.

[3] J.Salbeck, *Ber. Bunsenges. Phys. Chem.* **1996**, *100*, 1667.

[4] V. R. Nikitenko, V. I. Arkhipov, Y.-H. Tak, J. Pommerehne, H. Bässler, H.-H. Hörhold, *J. Appl. Phys.* **1997**, *81*, 7414.

[5] T. Virgili, D. G. Lidzey, D. D. C. Bradley, *Adv. Mat.* **2000**, *12*, 58.

[6] J. H. Burroughes, D. D. C. Bradley, A. R. Brown, R. N. Marks, K. McKay, R. H. Friend, P. N. Burns, A. B. Holmes, *Nature* **1990**, *341*, 539.

[7] X. C. Li, T. M. Yong, J. Grüner, A. B. Holmes, S. C. Moratti, F. Cacialli, R. H. Friend, *Synth. Met.* **1997**, *84*, 437.

[8] P. Le Barney, C. M. Bouche, H. Facoetti, F. Soyer, P. Robin, *Proc. SPIE* **1997**, *3148*, 160.

[9] E. Bellmann, S. E. Shaheen, S. Thayumanavan, S. Barlow, R. H. Grubbs, S. R. Marder, B. Kippelen, N. Peyghambarian, *Chem. Mater.* **1998**, *10*, 1668.

[10] X. Jiang, S. Liu, H. Ma, A. K. Jen, *Appl. Phys. Lett.* **2000**, *76*, 1813.

[11] M. S. Bayerl, T. Braig, O. Nuyken, C. D. Müller, M. Gross, K. Meerholz, *Macromol. Rapid Commun.* **1999**, *20*, 224.

[12] A. Bacher, C. H. Erdelen, W. Paulus, H. Ringsdorf, H. W. Schmidt, P. Schuhmacher, *Macromolecules* **1999**, *32*, 4551.

[13] W. Li, Q. Wang, J. Cui, H. Chou, S. E. Shaheen, G. E. Jabbour, J. Anderson, P. Lee, B. Kippelen, N. Peyghambarian, N. R. Armstrong, T. J. Marks, *Adv. Mater.* **1999**, *11*, 730.

[14] J. P. Chen, G. Klärner, J. I. Lee, D. Markiewicz, V. Y. Lee, R. D. Miller, J. C. Scott, *Synth. Met.* **1999**, *107*, 129.

[15] R. Böhner, C. Erdmann, O. Nuyken, *Macromol. Symp.* **1996**, *107*, 125.

[16] J. V. Crivello, J. H. W. Lam, *J. Polym. Chem. Ed.* **1980**, *18*, 2697.

[17] a) M. S. Driver, J. F. Hartwig, *J. Am. Chem. Soc.* **1996**, *118*, 7217; b) J. P. Wolfe, S. Wagaw, S. L. Buchwald, *J. Am. Chem. Soc.* **1996**, *118*, 7215.

[18] a) Bayer AG, DE 1021858, **1958** [K. Bodenbrenner, R. Wegler, *Chem. Abstr.* **1960**, *54*, 4617]; b) M. Miura, T. Aoyagi, T. Hirai, *J. Chem. Soc. Jpn. Ind. Chem. Sect.* **1964**, *67*, 485.

[19] a) T. Nishiyama, T. Yamamoto, Y. Koie, *Tetrahedron Lett.* **1998**, *39*, 617; b) T. Yamamoto, T. Nishiyama, Y. Koie, *Tetrahedron Lett.* **1998**, *39*, 2367.

[20] T. Braig, Ph.D. thesis, Technical University München (Germany), **2000**.

[21] a) D. Müller, M. Gross, K. Meerholz, T. Braig, M. Bayerl, F. Bielefeldt, O. Nuyken, *Synth. Met.* **2000**, *111 – 112*, 31; b) T. Braig, D. Müller, M. Gross, K. Meerholz, O. Nuyken, unpublished results.

[22] M. Gross, D. C. Müller, H.-G. Nothofer, U. Scherf, D. Neher, C. Bräuchle, K. Meerholz, *Nature* **2000**, *405*, 661.

[23] A. W. Grice, D. D. C. Bradley, M. T. Bernius, M. Inbasekaran, W. W. Wi, E. P. Woo, *Appl. Phys. Lett.* **1998**, *73*, 629.

[24] S. Janiez, D. D. C. Bradley, M. Grell, C. Giebeler, M. Inbasekaran, E. P. Woo, *Appl. Phys. Lett.* **1998**, *73*, 2453.

[25] a) F. Nuesch, L. J. Rothberg, E. W. Forsythe, Q. Toan, Y. A. Gao, *Appl. Phys. Lett.* **1999**, *74*, 880; b) J. S. Kim, M. Granström, R. H. Friend, N. Johansson, W. R. Salanek, R. Daik, W. J. Feast, F. Carcialli, *J. Appl. Phys.* **1998**, *84*, 6859.

[26] a) K. Z. Xing, M. Fahlman, X. W. Chen, O. Inganäs, W. R. Salaneck, *Synth. Met.* **1997**, *89*, 161; b) T. M. Brown, J. S. Kim, R. H. Friend, F. Cacialli, R. Daik, W. J. Feast, *Appl. Phys. Lett.* **1999**, *75*, 1679.

[27] a) H.-G. Nothofer, A. Meisel, T. Miteva, D. Neher, M. Forster, M. Oda, G. Lieser, D. Sainova, A. Yasuda, D. Lupo, W. Knoll, U. Scherf, *Macromol. Symp.* **2000**, *154*, 139; b) T. Miteva, A. Meisel, W. Knoll, H.-G. Nothofer, U. Scherf, A. Yasuada, D. Müller, K. Meerholz, D. Neher, *Adv. Mater.*, in press.

[28] a) V. N. Bliznuyk, S. A. Carter, J. C. Scott, G. Klärner, R. D. Miller, D. C. Miller, *Macromolecules* **1999**, *32*, 361; b) D. Sainova, T. Miteva, H. G. Nothofer, U. Scherf, I. Glowacki, J. Ulanski, H. Fujikawa, D. Neher, *Appl. Phys. Lett.* **2000**, *76*, 1810.

[29] V. Bulovic, S. R. Forrest, *Semicond. Semimet.* **2000**, *65*, 1, and references therein.

[30] *Baytron P®*, Bayer Corporation..

[31] A. C. Farthing, *J. Chem. Soc.* **1955**, 3648.

[32] A. J. Bard, L. A. Faulkner, *Electrochemical Methods --‐Fundamentals and Applications*, Wiley, New York, **1984**.

Received: July 13, 2000 [Z 70]

Intrazeolite Diffusion Kinetics of Dye Molecules in the Nanochannels of Zeolite L, Monitored by Energy Transfer**

Michel Pfenniger[a] and Gion Calzaferri*[a]

KEYWORDS:

dyes · energy transfer · fluorescence · mass transport · zeolites

The strongly fluorescent dyes oxonine (Ox^+) and pyronine (Py^+) have been observed to enter the main channels of zeolite L at approximately the same speed when ion exchanged from an aqueous solution. Energy transfer from excited Py^+ (donor) to Ox^+ (acceptor) is very efficient, due to the large spectral overlap between the fluorescence of Py^+ and the absorption of Ox^+.[1, 2] This can be used to monitor the transport of these dyes. Interference microscopy was used to investigate intracrystalline

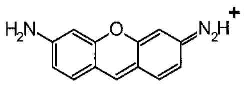

Pyronine

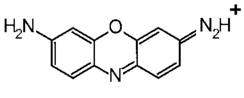

Oxonine

---

[a] G. Calzaferri, M. Pfenniger
Department of Chemistry and Biochemistry
University of Berne
Freiestrasse 3, 3000 Bern 9 (Switzerland)
Fax: (+41) 31 631 3994
E-mail: Gion.Calzaferri@iac.unibe.ch

[**] This work was supported by the Swiss National Science Foundation, Projects NFP 4047-057481 and NF 2000-053414/98/1. We would like to thank Drs. Silke Megelski and Niklaus Gfeller for their contributions and fruitful discussions.

[16] F. Binder, G. Calzaferri, N. Gfeller, *Sol. Energy Mater. Sol. Cells* **1995**, *38*, 175–186.
[17] S. Megelski, A. Lieb, M. Pauchard, A. Drechsler, S. Glaus, C. Debus, A. J. Meixner, G. Calzaferri, *J. Phys. Chem. B*, in press.
[18] *Landolt-Börnstein*, *Vol. 2*, Sect. 5a, 6th ed. (Eds.: H. Borchens, H. Hausen, K. H. Hellwege, K. Schäfer, E. Schmidt), Springer, Berlin, **1969**.
[19] N. Gfeller, S. Megelski, G. Calzaferri, *J. Phys. Chem. B* **1999**, *103*, 1250–1257.
[20] S. Megelski, PhD thesis, University of Berne (Switzerland) **2000**.

Received: July 17, 2000 [Z 72]

Single-Transition Coherence Transfer by Adiabatic Cross Polarization in NMR**

Thomas R. Eykyn,[a, b] Fabien Ferrage,[a]
Emanuel Winterfors,[a] and Geoffrey Bodenhausen*[a, b]

KEYWORDS:

coherence transfer · cross polarization · NMR spectroscopy · peptides

The interest shown in the manipulation of single-transition coherences in nuclear magnetic resonance (NMR) has increased greatly since it was recognised that cross-correlated relaxation phenomena could lead to line-narrowing effects. In transverse relaxation-optimised spectroscopy (TROSY),[1] the fluctuations of a dipolar interaction and an anisotropic chemical shift tensor mutually cancel so that, in large molecules with long rotational correlation times at elevated magnetic field strengths, some single-transition coherences can have very long lifetimes. Many coherence-transfer methods have been developed[2–4] to obviate mixing of single-transition coherences. Most of these methods employ nonselective pulses. Recently, another approach, single-transition cross polarization (ST-CP) has been introduced[5] to enable a transfer between single-transition coherences without mixing parallel transitions by employing radio frequency (RF) fields that are weaker than the scalar coupling constant. The original version of ST-CP employed spin-lock fields of constant amplitude to achieve coherence transfer via zero- or double-quantum coherences. We propose herein an adiabatic version, where the density operator is confined to a subspace spanned by single-quantum coherences, which we shall refer to as single-transition adiabatic cross polarization (ST-ACP).

Adiabatic transformations have been extensively employed in solid-state NMR for the enhancement of cross polarization efficiency,[6–10] to achieve excitation of both quadrupolar order[11] and multiple quantum coherences[12] in $I > {}^1/_2$ systems. Adiabatic coherence transfer has also been used in liquid-state NMR[13, 14] and a number of methods have been proposed for achieving adiabatic inversions.[15, 16] Many theoretical studies of the adiabaticity of such methods have been carried out.[15, 17] We present the use of adiabatic coherence transfer in a four-level system of two J-coupled spin-${}^1/_2$ nuclei to achieve spin-state selective coherence transfer. A theoretical treatment is given for the conditions under which the transfer is adiabatic and different limiting cases are considered. We have also developed an experimental test of the reversibility of the transfer which reveals violations of adiabaticity.

We consider a scalar-coupled two-spin-${}^1/_2$ system, IS (Figure 1). Coherence transfer can be achieved by irradiating simultaneously two connected transitions with low amplitude RF fields. It has been demonstrated[5] that two processes occur simultaneously: an on-resonance transfer, between the two irradiated transitions, and an off-resonance transfer, between the other two transitions. These two processes have been shown to be confined in two mutually exclusive three-dimensional subspaces of the Liouville space, provided the scalar coupling constant J_{IS} is large enough compared to the RF field amplitude and relaxation coupling terms.

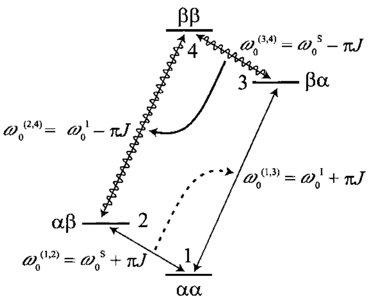

Figure 1. Energy-level diagram for a scalar-coupled two-spin system, IS, such as is found in ${}^{15}N-{}^{1}H$ pairs. The nitrogen doublet components correspond to transitions (1,2) and (3,4), while the proton doublet components correspond to transitions (1,3) and (2,4). Also shown is a schematic representation of single-transition cross polarization (ST-CP) transfer. If irradiation is truly selective, so that the secular approximation is fulfilled, both the on-resonance (solid arrow) and off-resonance transfers (dashed arrow) occur. The energy levels have been drawn for a system where both nuclei have positive gyromagnetic ratios although $\gamma(^{15}N) < 0$. However, if the order of the energy levels were swapped, this might create confusion, especially between "zero" and "double" quantum coherences.

The whole discussion will take place, unless otherwise indicated, in the interaction frame (IF) where the Zeeman and scalar coupling terms of the static Hamiltonian are taken into account, so that all coherences appear stationary. In the following, we consider the transfer (Figure 1) from the coherence $I_x^{(3,4)}$ of the S nucleus (for example, ^{15}N) to the coherence $I_x^{(2,4)}$ of

---

[a] Prof. G. Bodenhausen, T. R. Eykyn, F. Ferrage, E. Winterfors
Département de Chimie, associé au CNRS
Ecole Normale Supérieure
24, rue Lhomond, 75231 Paris cedex 05 (France)
Fax: (+33) 1-44-32-33-97
E-mail: Geoffrey.Bodenhausen@ens.fr

[b] Prof. G. Bodenhausen, T. R. Eykyn
Section de Chimie, Université de Lausanne
BCH, 1015 Lausanne (Switzerland)

[**] This work was supported by the Centre National de la Recherche Scientifique (CNRS) of France, and by the Fonds National de la Recherche Scientifique (FNRS) and the Commission pour la Technologie et l'Innovation (CTI) of Switzerland.

the I nucleus (for example, ^{1}H). The density operator evolves in the subspace $\{2I_x^{(2,4)}, 2I_x^{(3,4)}, 2I_y^{(2,3)}\}$, where these operators fulfil the cyclic relationship[18, 19] $[2I_x^{(2,4)}, 2I_x^{(3,4)}] = \mathrm{i}2I_y^{(2,3)}$. The aim of the adiabatic transfer is to confine the density operator to the single-quantum plane by slowly rotating the Hamiltonian which must initially be parallel to the density operator (Figure 2 a). Strictly, the density operator should commute with the Hamiltonian at all times, Equation (1).

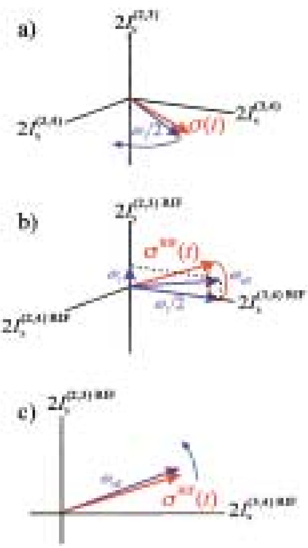

Figure 2. *Evolution of the Hamiltonian (blue arrow) and the density operator (red arrow) during single-transition adiabatic cross polarization (ST-ACP). a) In the interaction frame (IF), the density operator should ideally follow the Hamiltonian. b) In the rotating interaction frame (RIF), one may observe a rotation ($\omega_{eff} = \frac{1}{2}(\omega_1^2 + 4\omega_r^2)^{1/2}$) of the density operator around the Hamiltonian. c) If the deviation from adiabaticity gradually increases (if there is an acceleration of the motion of the Hamiltonian), the density operator is partly converted into the zero-quantum coherence $2I_y^{(2,3)}$.*

$$[H(t), \sigma(t)] = 0 \tag{1}$$

This can be achieved by modulating the amplitude of the RF fields on the I and S spins in a number of different fashions. In the simplest case, the Hamiltonian rotates with a constant angular velocity ω_r, which can be achieved if the ^{15}N and ^{1}H RF fields are modulated in amplitude by cosine and sine envelopes, respectively. In the interaction frame, the Hamiltonian is then given by Equation (2), where $\omega_1^{\mathrm{I,S}}$ are the maximum amplitudes of the RF fields on the I and S spins, respectively.

$$H^{\mathrm{IF}} = \omega_1^{\mathrm{S}} \cos(\omega_r t) I_x^{(3,4)} + \omega_1^{\mathrm{I}} \sin(\omega_r t) I_x^{(2,4)} \tag{2}$$

When $\omega_1^{\mathrm{I}} = \omega_1^{\mathrm{S}} = \omega_1$, the vector representing the Hamiltonian evolves on a circle, otherwise it describes an ellipse. We will consider the former case in order to have a Hamiltonian with a constant norm and constant adiabaticity. In order to remain spin-state selective, the secular condition $\omega_1 \ll 2\pi J_{\mathrm{IS}}$ must be fulfilled, which places an upper limit on the norm of the Hamiltonian.

One can describe relaxation effects using a Liouvillian superoperator $\hat{\hat{L}}$. The evolution of the system is described by the Liouville–von Neumann equation, Equation (3).

$$\frac{\mathrm{d}\sigma}{\mathrm{d}t} = -\hat{\hat{L}}\sigma \tag{3}$$

In the interaction frame IF, that is, in the basis $\{2I_x^{(2,4)}, 2I_x^{(3,4)}, 2I_y^{(2,3)}\}$, the Liouvillian superoperator is given by Equation (4),[5] in

$$\hat{\hat{L}}^{\mathrm{IF}} = \begin{pmatrix} \rho^I & 0 & -\frac{\omega_1}{2}\cos(\omega_r t) \\ 0 & \rho^S & \frac{\omega_1}{2}\sin(\omega_r t) \\ \frac{\omega_1}{2}\cos(\omega_r t) & -\frac{\omega_1}{2}\sin(\omega_r t) & \rho^{ZQC} \end{pmatrix} \tag{4}$$

which $\rho^{\mathrm{I,S}} = \rho_{\mathrm{av}}^{\mathrm{I,S}} - \delta^{\mathrm{I,S}}$, where $\rho_{\mathrm{av}}^{(\mathrm{I,S})}$ are the average relaxation rates of the in-phase and anti-phase coherences $\{I_x, 2I_xS_z\}$ and $\{S_x, 2S_xI_z\}$, $\delta^{\mathrm{I,S}}$ are the cross-correlation rates due to interference between dipolar coupling and CSA[20, 21] of the I and S spins respectively, and ρ^{ZQC} is the relaxation rate of the zero-quantum coherence $I_y^{(2,3)}$.

Transformation into a rotating interaction frame (RIF),[12] that is, in the basis $\{2I_x^{(2,4)\,\mathrm{RIF}}, 2I_x^{(3,4)\,\mathrm{RIF}}, 2I_y^{(2,3)\,\mathrm{RIF}}\}$, where the Hamiltonian of Equation (2) appears stationary, one obtains Equation (5), as is demonstrated in the Appendix.

$$\hat{\hat{L}}^{\mathrm{RIF}} = \begin{pmatrix} \rho^I\cos^2(\omega_r t) + \rho^S\sin^2(\omega_r t) & \omega_r + \frac{\rho^I - \rho^S}{2}\sin(2\omega_r t) & -\frac{\omega_1}{2} \\ -\omega_r + \frac{\rho^I - \rho^S}{2}\sin(2\omega_r t) & \rho^I\sin^2(\omega_r t) + \rho^S\cos^2(\omega_r t) & 0 \\ \frac{\omega_1}{2} & 0 & \rho^{ZQC} \end{pmatrix} \tag{5}$$

In this frame, the diagonal relaxation rates become oscillatory since the quasi-stationary coherence $I_x^{(3,4)\,\mathrm{RIF}}$ actually oscillates between $I_x^{(3,4)}$ and $I_x^{(2,4)}$. The transfer is adiabatic if $I_x^{(3,4)\,\mathrm{RIF}}$ is an eigenvector of the Liouvillian superoperator, which is true if the off-diagonal terms $\pm\omega_r + \frac{1}{2}(\rho^{\mathrm{I}} - \rho^{\mathrm{S}})\sin(2\omega_r t)$ can be neglected. The time-independent terms proportional to ω_r represent the fact that the Hamiltonian is tilted in the three-dimensional subspace (Figure 2 b). If the transformation is to be confined to the plane spanned by the terms $\{I_x^{(2,4)}, I_x^{(3,4)}\}$, the following condition of adiabaticity must be fulfilled, Equation (6).

$$\omega_r \ll \omega_1 \tag{6}$$

Returning to the interaction frame, the density operator is comprised of a time-dependent linear combination of the two vectors $I_x^{(3,4)}$ and $I_x^{(2,4)}$, which have different relaxation rates. Thus, the angular velocity is also affected by an asymmetric decay of these expectation values leading to a second adiabatic condition, Equation (7).

$$\rho^{\mathrm{I}} - \rho^{\mathrm{S}} \ll \omega_1 \tag{7}$$

One should notice that the effective relaxation rate is oscillating and therefore need only be considered if the angular velocity ω_r of the Hamiltonian is slow. In fact, it is very hard to realise this second requirement experimentally.

As one may see in Figure 2 b, the density operator tends to move away from the plane $\{I_x^{(3,4)}, I_x^{(2,4)}\}$ and acquires a component $I_y^{(2,3)}$, which corresponds to zero-quantum coherence, even if the first condition of adiabaticity (namely, $\omega_r \ll \omega_1$) is correctly fulfilled. The zero-quantum coherence decays faster than the single-quantum coherences so that this component of the density operator tends to disappear rapidly. One may ask whether the relaxation of the zero-quantum coherence makes the transfer truly adiabatic or merely inefficient. An answer may be found in Figure 3. Simulations were carried out using the platform GAMMA.[22] For an ST-CP transfer, the norm of the density operator initially decreases rapidly as it is partly transformed into rapidly relaxing zero-quantum coherence. Due to this dissipative effect, the angle between the Hamiltonian and the density operator decreases, so that the vector representing the density operator can never achieve a pure state, $I_x^{(3,4)}$ or $I_x^{(2,4)}$. As a result, after a long transfer time, one observes a pseudostationary state.

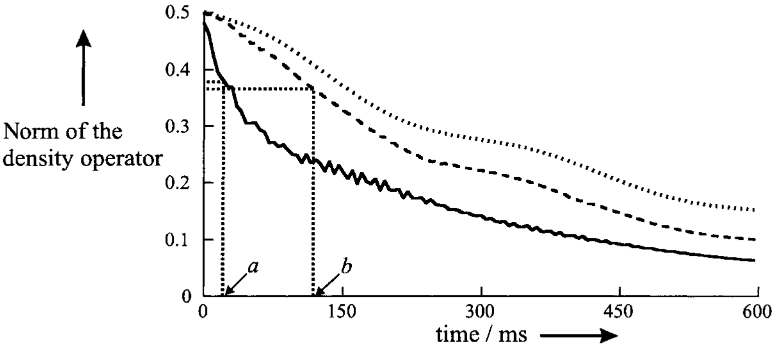

Figure 3. Simulations of the decay of the norm of the density operator due to relaxation. For ideal, adiabatic cross polarization (where Equation (1) is fulfilled at all times) with $\omega_r/2\pi = 1.67$ Hz (dotted line), the density operator strictly follows the Hamiltonian, hence the decrease of the norm is only due to the oscillating diagonal term associated with $2I_x^{(3,4)\,RIF}$ in Equation (5). The relaxation times used were $T_2^S = 1/\rho_{av}^S = 1.12$ s for both nitrogen transitions, $T_2^I = 1/\rho_{av}^I = 325$ ms for both proton transitions and $T_2^{ZQC} = 1/\rho^{ZQC} = 30$ ms, corresponding to the ^{15}N – ^{1}H pair of tBoc-protected glycine in DMSO at 300 K. For semiadiabatic cross polarization (dashed lines), the ^{15}N and ^{1}H RF fields are modulated by cosine and sine functions, respectively, with $\omega_1^{max}/2\pi = 27$ Hz and $\omega_r/2\pi = 1.67$ Hz, so that a complete rotation of the Hamiltonian is achieved after 600 ms. For ST-CP with constant amplitude pulses (solid line), the amplitudes of the proton and ^{15}N RF fields are both 27 Hz. At time points a and b, the expectation value $\langle I_x^{(2,4)} \rangle (t)$ reaches a maximum value for ST-CP and ST-ACP, respectively. Although their durations are very different, the conservation of the norm is almost the same.

If the most rigorous condition of adiabaticity, Equation (1), is fulfilled at all times, one can observe the oscillatory effects of relaxation when the density operator alternates between $I_x^{(3,4)}$ (^{15}N) and $I_x^{(2,4)}$ (^{1}H) coherences. This corresponds to an optimum conservation of the norm of the density operator. By contrast, in ST-ACP, one notices a faster decrease of the norm, which is due to the involvement of the zero-quantum coherence. We can conclude that the transfer is nearly adiabatic when the first condition $\omega_r \ll \omega_1$ is fulfilled.

One can also minimise the contribution of the zero-quantum coherence $I_y^{(2,3)}$ to the density operator by tilting the Hamiltonian adiabatically in the rotating interaction frame. Indeed, if one increases the angular velocity of the Hamiltonian adiabatically, the density operator follows the Hamiltonian (Figure 2 c) which avoids the oscillatory behaviour of Figure 2 b. To achieve an adiabatic transfer, the maximum angular velocity in the rotating interaction frame has to remain appreciably inferior to ω_1. Alternatively, if one continues increasing the angular velocity of the Hamiltonian, one may achieve efficient zero-quantum excitation, in analogy to Ermakov's controlled violation of adiabaticity.[12]

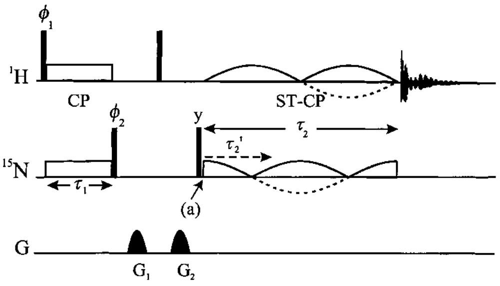

Figure 4. Pulse sequence used to study ST-ACP and to test its reversibility. The first semiselective conventional cross-polarization (CP) period has a duration $\tau_1 = |J_{NH}|^{-1} = 10.9$ ms with constant matched RF amplitudes $\omega_1^I/2\pi = \omega_1^S/2\pi \approx 70$ Hz. The carrier frequencies are positioned at the midpoints of the proton and nitrogen doublets. The resulting nitrogen magnetization is temporarily converted into longitudinal Zeeman order ($S_x \rightarrow \pm S_z$) by applying a $(\pi/2)^S$ pulse of phase Φ_2. Remaining proton Zeeman order is converted into transverse magnetization ($I_z \rightarrow I_x$) by a $(\pi/2)^I$ pulse. Residual coherences S_x and I_x are dephased by pulsed field gradients G_1 and G_2. During the adiabatic single-transition cross-polarization (ST-ACP) period τ_2, the maximum RF amplitudes are reduced to $\omega_1^{I\,max}/2\pi = \omega_1^{S\,max}/2\pi \approx 26$ Hz and the carrier frequencies moved on-resonance with a pair of connected transitions which appear in the undecoupled multiplet $\omega_0^{(1,2)} = \omega_0^S + \pi J$ or $\omega_0^{(3,4)} = \omega_0^S - \pi J$ and $\omega_0^{(1,3)} = \omega_0^I + \pi J$ or $\omega_0^{(2,4)} = \omega_0^I - \pi J$ ($\omega_0^I = -\gamma_I B_0 < 0$ for ^{1}H, $\omega_0^S = -\gamma_S B_0 > 0$ for ^{15}N, $J_{NH} = -94$ Hz). The precise proton and nitrogen resonance frequencies may be taken from a heteronuclear correlation experiment. The phase cycling is: $\Phi_1 = y, y, -y, -y$; $\Phi_2 = y, -y, -y, y$; receiver $\Phi_{rec} = x, -x, x, -x$. The dashed lines correspond to a complete 2π rotation of the Hamiltonian in a period $\tau_2 = 2\pi/\omega_r$. To test the reversibility, the angular velocity may be inverted every $n\pi/2$, which is equivalent to using $|\sin|$ and $|\cos|$ modulations (solid lines).

All experiments were performed on a Bruker DRX 600 MHz spectrometer with a TBI probe equipped with three orthogonal pulsed-field gradients. In ^{15}N-enriched *t*Boc-protected glycine (100 mM; *t*Boc = *tert*-butoxycarbonyl) in DMSO, the coupling constant is $J_{NH} = -94$ Hz, which permits the use of RF field amplitudes up to 40 Hz without significantly affecting the parallel transitions. The study of adiabatic ST-CP has been carried out using the pulse sequences of Figure 4. Semiselective cross polarization[23, 24] was used to transfer the proton coherence $I_x = I_x^{(1,3)} + I_x^{(2,4)}$ to the nitrogen coherence $S_x = I_x^{(1,2)} + I_x^{(3,4)}$. ST-ACP coherence transfer starts at point (a) and is achieved by irradiating a selected pair of connected single-quantum transitions with very weak RF fields. The adiabatic transfer requires the modulation of both proton and nitrogen spin-lock amplitudes. The main problem posed by ST-CP if one uses constant amplitude pulses is the loss of signal due to relaxation. Indeed, for a ^{15}N – ^{1}H pair, the duration of ST-CP is as long as 20 ms for

$\omega_1/2\pi = 35$ Hz. Moreover, during the transfer, the density operator is partly converted into multiple quantum coherences with relaxation rates that may be an order of magnitude greater than those of single-quantum coherences. For example, we have measured the following rates[5] in our system: $\rho^{\mathrm{I}}_{\mathrm{av}} = 3.1$, $\rho^{\mathrm{S}}_{\mathrm{av}} = 0.89$ and $\rho^{\mathrm{ZQC}} > 30\ \mathrm{s}^{-1}$. The cross-correlation rates $\delta^{\mathrm{I}} \approx \delta^{\mathrm{S}} \approx 0$ are negligible, since the rotational correlation time of this small molecule is very short.

The adiabatic transfer allows one to avoid the resulting loss of signal by confining the density operator to the single-quantum plane. In Figure 5, the efficiency of constant-amplitude ST-CP is compared to ST-ACP. Even though the duration of the adiabatic transfer is about three times longer, the efficiency is the same in *t*Boc-glycine. This is in agreement with the behaviour predicted by the simulations in Figure 3, where the decrease of the norm of the density operator is faster for constant amplitude pulses, particularly at the beginning. However, the adiabatic condition imposes a limitation, since it prevents us from achieving fast transfers. Even if the effects of relaxation are greatly minimised, the absolute efficiency of the transfer is not improved.

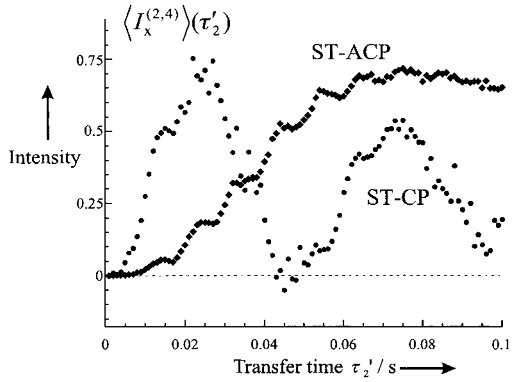

Figure 5. *Experimental signal intensities of selected doublet components in* t*Boc-protected* ^{15}*N-enriched glycine as a function of the spin-lock duration* τ_2' *(see Figure 4). The experimental points correspond to cross polarization from the high-frequency nitrogen transition* $I_x^{(3,4)}$ *to the low-frequency* $I_x^{(2,4)}$ *proton component. For constant amplitude ST-CP transfer (●), the amplitudes of both* ^{1}*H and* ^{15}*N RF fields were set to about 27 Hz. For ST-ACP (◆), the angular velocity of the Hamiltonian was* $\omega_r/2\pi = 2.5$ *Hz so that the density operator would be completely converted into* $I_x^{(2,4)}$ *at* $\tau_2' = \pi/2\omega_r = 0.1$ *s corresponding to the first quarter of the pulse shape in Figure 4 with* $\tau_2 = 2\pi/\omega_r = 0.4$ *s. The intensity is normalized with respect to a signal from the same transition excited after a 90° pulse under identical conditions.*

By definition, a transfer is truly adiabatic only if it is reversible. We have developed a test of reversibility, consisting of consecutive steps combining forward and back transfer. Simulations without relaxation (data not shown) have demonstrated that the amplitude of the oscillations of the zero quantum component $I_y^{(2,3)}$ increases with each $\pi/2$ rotation of the Hamiltonian. When the angular velocity of the Hamiltonian is too large, the density operator deviates from the single-quantum plane. The criterion of adiabaticity in Equation (1) is therefore violated and the expectation value $\langle I_x^{(2,4)}\rangle(t)$ does not follow the shape of the RF field applied to the (2,4) transition.

In Figures 6a–6d, the angular velocity ω_r is progressively decreased. For fast rotations of the Hamiltonian, Figure 6a, the adiabatic condition of Equation (6) is severely violated and the evolution can be explained in terms of an average Hamiltonian. When $\omega_r \gg \omega_1$, the cycle period $\tau_r = 2\pi/\omega_r$, after which one can consider that the evolution is due to an average Hamiltonian $\bar{H}$, is very short with respect to the evolution of the density operator. Therefore, this evolution seems to be controlled, at integer multiples of τ_r, by the average Hamiltonian. In other terms, we can write the Hamiltonian $H(t) = \bar{H} + H_{\mathrm{osc}}(t)$, where the oscillating part $H_{\mathrm{osc}}(t)$ can be neglected for $\omega_r \gg \omega_1$ by invoking the secular approximation. In Figures 6b and c, significant deviations between the Hamiltonian and the density operator are still observed. The transfer is truly adiabatic in Figure 6d where $\omega_r/\omega_1 = 0.11$. The limit of adiabaticity is approximately $\omega_r/\omega_1 = 0.15$, which is quite stringent, since we must also have $|\omega_1/2\pi| \ll |J_{\mathrm{IS}}|$. Typically, if $|J_{\mathrm{IS}}| = 100$ Hz, $\omega_1/2\pi = 30$ Hz and $\omega_r/2\pi = 3$ Hz, the transfer is completed at $\tau_2 = \pi/2\omega_r = 83$ ms.

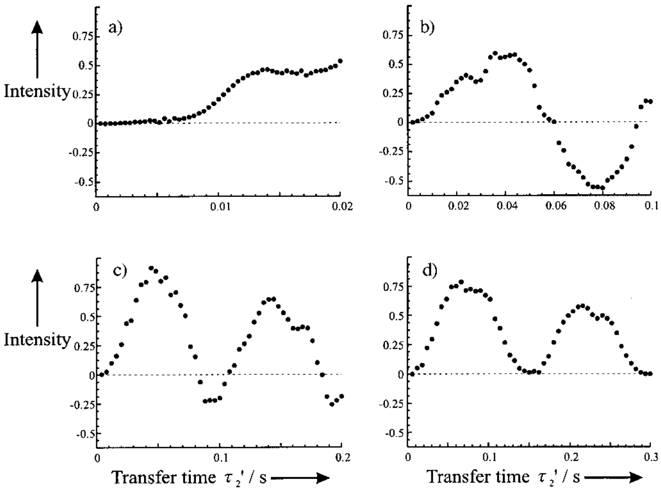

Figure 6. *Experimental test of the reversibility of the transfer showing the expectation value* $\langle I_x^{(2,4)}\rangle(\tau_2')$ *at the end of the irradiation period. The angular velocities* $\omega_r/2\pi$ *were a) 50, b) 10, c) 5, and d) 3.33 Hz. The pulse shapes employed correspond to a full cycle* $\tau_2 = 2\pi/\omega_r$ *of the Hamiltonian with three inversions of the sign of the angular velocity* ω_r *when* $|\omega_r\tau_2'| = \pi/2, \pi, 3\pi/2$*, as shown in Figure 4. The pulse shapes have been recalculated for each point so that* ω_r *is constant. To enable comparison, the same normalisation is used as in Figure 5.*

We have introduced a new method for spin-state selective coherence transfer relying on the principles of adiabatic cross polarization. Relaxation leads to additional constraints but also provides a means to improve adiabaticity. Although adiabatic transfer may be very slow, it can be as efficient as much faster oscillatory transfer processes. A good experimental criterion of adiabaticity is the reversibility of the transfer.

Appendix

The transformation of the matrix representation of a Liouvillian superoperator from one frame to another can be accomplished in analogy to Hamiltonians.[25] One may write the Liouville–von Neuman equation either in the initial interaction frame, Equation (A1), or in the new, rotating interaction frame, Equation (A2).

$$\frac{d\sigma^{IF}(t)}{dt} = -\hat{\hat{L}}^{IF}\sigma^{IF}(t) \tag{A1}$$

$$\frac{d\sigma^{RIF}(t)}{dt} = -\hat{\hat{L}}^{RIF}\sigma^{RIF}(t) \tag{A2}$$

We define the transformation of the density operator by Equations (A3) and (A4).[26, 27]

$$\sigma^{RIF}(t) = \hat{\hat{U}}_0(t)\,\sigma^{IF}(t) \tag{A3}$$

where

$$\hat{\hat{U}}_0(t) = \exp(\hat{\hat{L}}_0 t) \tag{A4}$$

Since the superoperator $\hat{\hat{L}}_0$ is time-independent, it follows that Equation (A5) is:

$$\frac{d\hat{\hat{U}}_0(t)}{dt} = \hat{\hat{L}}_0\,\hat{\hat{U}}_0(t) \tag{A5}$$

The derivative of Equation (A3) yields Equation (A6).

$$\frac{d\sigma^{RIF}(t)}{dt} = \frac{d\hat{\hat{U}}_0(t)}{dt}\sigma^{IF}(t) + \hat{\hat{U}}_0(t)\frac{d\sigma^{IF}(t)}{dt} \tag{A6}$$

Equation (A6) can be simplified with Equations (A1) and (A5) to give Equation (A7).

$$\frac{d\sigma^{RIF}(t)}{dt} = \hat{\hat{L}}_0\,\hat{\hat{U}}_0(t)\,\sigma^{IF}(t) - \hat{\hat{U}}_0(t)\,\hat{\hat{L}}^{IF}\sigma^{IF}(t) \tag{A7}$$

Since $(1/i)\hat{\hat{L}}_0$ is hermitic, $\hat{\hat{U}}_0(t)$ is unitary, so that one can insert $\hat{\hat{U}}_0^{\dagger}(t)\,\hat{\hat{U}}_0(t) = \hat{\hat{E}}$ into Equation (A7) to yield Equation (A8).

$$\frac{d\sigma^{RIF}(t)}{dt} = \hat{\hat{L}}_0\,\hat{\hat{U}}_0(t)\,\sigma^{IF}(t) - \hat{\hat{U}}_0(t)\,\hat{\hat{L}}^{IF}\,\hat{\hat{U}}_0^{\dagger}(t)\,\hat{\hat{U}}_0(t)\,\sigma^{IF}(t) \tag{A8}$$

With Equation (A3), one obtains, in comparison to Equation (A2), Equation (A9).

$$\hat{\hat{L}}^{RIF} = \hat{\hat{U}}_0(t)\,\hat{\hat{L}}^{IF}\,\hat{\hat{U}}_0^{\dagger}(t) - \hat{\hat{L}}_0 \tag{A9}$$

In the transformation from Equation (4) to Equation (5), $\hat{\hat{L}}_0$ represents a rotation about the $I_y^{(2,3)}$ operator, shown in Equation (A10).

$$\hat{\hat{L}}_0 = i\omega_r(I_y^{(2,3)} \oplus E - E \oplus I_y^{(2,3)}) \tag{A10}$$

Equation (A10) yields a matrix representation in the Liouville subspace spanned by the operators $\{2I_x^{(2,4)}, 2I_x^{(3,4)}, 2I_y^{(2,3)}\}$, Equation (A11).

$$\hat{\hat{L}}_0 = \begin{pmatrix} 0 & -\omega_r & 0 \\ -\omega_r & 0 & 0 \\ 0 & 0 & 0 \end{pmatrix} \tag{A11}$$

[1] K. Pervushin, R. Riek, G. Wider, K. Wüthrich, *Proc. Natl. Acad. Sci. USA* **1997**, *94*, 12366 – 12371.
[2] M. D. Sørensen, A. Meissner, O. W. Sørensen, *J. Biomol. NMR* **1997**, *10*, 181 – 186.
[3] P. Andersson, A. Annila, G. Otting, *J. Magn. Reson.* **1998**, *133*, 364 – 367.
[4] K. Pervushin, G. Wider, K. Wüthrich, *J. Biomol. NMR* **1998**, *12*, 345 – 348.
[5] F. Ferrage, T. R. Eykyn, G. Bodenhausen, *J. Chem. Phys.* **2000**, *113*, 1081 – 1087.
[6] A. Pines, M. G. Gibby, J. S. Waugh, *J. Chem Phys.* **1973**, *59*, 569 – 595.
[7] M. Mehring, *Principles of High Resolution NMR in Solids*, 2nd ed., Springer, Berlin, **1983**.
[8] S. Hediger, B. H. Meier, N. D. Kurur, G. Bodenhausen, R. R. Ernst, *Chem. Phys. Lett.* **1994**, *223*, 283 – 288.
[9] S. Hediger, B. H. Meier, R. R. Ernst, *Chem. Phys. Lett.* **1995**, *240*, 449 – 456.
[10] R. Fu, P. Pelupessy, G. Bodenhausen, *Chem. Phys. Lett.* **1997**, *264*, 63 – 69.
[11] C. E. Hughes, R. Kemp-Harper, S. Wimperis, *J. Chem. Phys.* **1998**, *108*, 876 – 889.
[12] V. L. Ermakov, G. Bodenhausen, *J. Chem. Phys.* **1995**, *103*, 136 – 143.
[13] G. C. Chingas, A. N. Garroway, W. B. Moniz, R. D. Bertrand, *J. Am. Chem. Soc.* **1980**, *102*, 2526 – 2528.
[14] N. D. Kurur, G. Bodenhausen, *J. Magn. Reson. A* **1995**, *114*, 163 – 173.
[15] J. Baum, R. Tycko, A. Pines, *Phys. Rev. A* **1985**, *32*, 3435 – 3447.
[16] D. Rosenfeld, S. L. Panfil, Y. Zur, *J. Magn. Reson.* **1997**, *129*, 115 – 124.
[17] D. Rosenfeld, Y. Zur, *J. Magn. Reson.* **1998**, *132*, 102 – 108.
[18] A. Wokaun, R. R. Ernst, *J. Chem. Phys.* **1977**, *67*, 1752 – 1758.
[19] S. Vega, *J. Chem. Phys.* **1978**, *68*, 5518 – 5527.
[20] M. Guéron, J. L. Leroy, R. H. Griffey, *J. Am. Chem. Soc.* **1983**, *105*, 7262 – 7266.
[21] M. Goldman, *J. Magn. Reson.* **1984**, *60*, 437 – 452.
[22] S. A. Smith, T. O. Levante, B. H. Meier, R. R. Ernst, *J. Magn. Reson. A* **1994**, *106*, 75 – 105.
[23] E. Chiarparin, P. Pelupessy, G. Bodenhausen, *Mol. Phys.* **1998**, *95*, 759 – 767.
[24] P. Pelupessy, E. Chiarparin, *Concepts Magn. Reson.* **2000**, *12*, 103 – 124.
[25] C. P. Slichter, *Principles of Magnetic Resonance*, 3rd ed., Springer, Berlin, **1990**, p. 157.
[26] M. Goldman, *Quantum Description of High-Resolution NMR in Liquids*, Oxford University Press, Oxford, **1988**, p. 110.
[27] C. L. Mayne, in *Encyclopedia of Nuclear Magnetic Resonance*, *Vol. 4* (Eds.: D. M. Grant, R. K. Harris), Wiley, New York, **1996**, p. 2717.

Received: July 24, 2000 [Z 76]

Can Monoatomic Xenon Become Chiral?**

Kristin Bartik,[a] Mustapha El Haouaj,[a] Michel Luhmer,[a] André Collet,[a] and Jacques Reisse*[a]

In memory of André Collet

KEYWORDS:

chirality · NMR spectroscopy · xenon

Mislow and Siegel characterize as chirotopic any point of a molecule, whether occupied by an atom or not, that resides within a chiral environment.[1] They point out that all segments of a chiral molecule are chirotopic and that chirality is an all-

---

[a] *Prof. J. Reisse, Dr. K. Bartik, M. El Haouaj, Dr. M. Luhmer*
Laboratoire de Chimie Organique CP 165/64
Université Libre de Bruxelles
50 av. F.D. Roosevelt, 1050 Bruxelles (Belgium)
Fax: (+32) 2-650-3606
E-mail: jreisse@ulb.ac.be

[**] *K.B., M.L., and J.R. thank the Belgian "Fonds National de la Recherche Scientifique" and the French "Centre National de la Recherche Scientifique" (LEA 1996-2000) for financial support. M.El H. thanks the "Fondation Van Buren" for financial support.*

Equation (A1), or in the new, rotating interaction frame, Equation (A2).

$$\frac{d\sigma^{\mathrm{IF}}(t)}{dt} = -\hat{\hat{L}}^{\mathrm{IF}}\sigma^{\mathrm{IF}}(t) \tag{A1}$$

$$\frac{d\sigma^{\mathrm{RIF}}(t)}{dt} = -\hat{\hat{L}}^{\mathrm{RIF}}\sigma^{\mathrm{RIF}}(t) \tag{A2}$$

We define the transformation of the density operator by Equations (A3) and (A4).[26, 27]

$$\sigma^{\mathrm{RIF}}(t) = \hat{\hat{U}}_0(t)\,\sigma^{\mathrm{IF}}(t) \tag{A3}$$

where

$$\hat{\hat{U}}_0(t) = \exp(\hat{\hat{L}}_0 t) \tag{A4}$$

Since the superoperator $\hat{\hat{L}}_0$ is time-independent, it follows that Equation (A5) is:

$$\frac{d\hat{\hat{U}}_0(t)}{dt} = \hat{\hat{L}}_0\,\hat{\hat{U}}_0(t) \tag{A5}$$

The derivative of Equation (A3) yields Equation (A6).

$$\frac{d\sigma^{\mathrm{RIF}}(t)}{dt} = \frac{d\hat{\hat{U}}_0(t)}{dt}\sigma^{\mathrm{IF}}(t) + \hat{\hat{U}}_0(t)\frac{d\sigma^{\mathrm{IF}}(t)}{dt} \tag{A6}$$

Equation (A6) can be simplified with Equations (A1) and (A5) to give Equation (A7).

$$\frac{d\sigma^{\mathrm{RIF}}(t)}{dt} = \hat{\hat{L}}_0\,\hat{\hat{U}}_0(t)\,\sigma^{\mathrm{IF}}(t) - \hat{\hat{U}}_0(t)\,\hat{\hat{L}}^{\mathrm{IF}}\sigma^{\mathrm{IF}}(t) \tag{A7}$$

Since $(1/i)\hat{\hat{L}}_0$ is hermitic, $\hat{\hat{U}}_0(t)$ is unitary, so that one can insert $\hat{\hat{U}}_0^{\dagger}(t)\,\hat{\hat{U}}_0(t) = \hat{\hat{E}}$ into Equation (A7) to yield Equation (A8).

$$\frac{d\sigma^{\mathrm{RIF}}(t)}{dt} = \hat{\hat{L}}_0\,\hat{\hat{U}}_0(t)\,\sigma^{\mathrm{IF}}(t) - \hat{\hat{U}}_0(t)\,\hat{\hat{L}}^{\mathrm{IF}}\,\hat{\hat{U}}_0^{\dagger}(t)\,\hat{\hat{U}}_0(t)\,\sigma^{\mathrm{IF}}(t) \tag{A8}$$

With Equation (A3), one obtains, in comparison to Equation (A2), Equation (A9).

$$\hat{\hat{L}}^{\mathrm{RIF}} = \hat{\hat{U}}_0(t)\,\hat{\hat{L}}^{\mathrm{IF}}\,\hat{\hat{U}}_0^{\dagger}(t) - \hat{\hat{L}}_0 \tag{A9}$$

In the transformation from Equation (4) to Equation (5), $\hat{\hat{L}}_0$ represents a rotation about the $I_y^{(2,3)}$ operator, shown in Equation (A10).

$$\hat{\hat{L}}_0 = i\omega_r(I_y^{(2,3)} \oplus E - E \oplus I_y^{(2,3)}) \tag{A10}$$

Equation (A10) yields a matrix representation in the Liouville subspace spanned by the operators $\{2I_x^{(2,4)}, 2I_x^{(3,4)}, 2I_y^{(2,3)}\}$, Equation (A11).

$$\hat{\hat{L}}_0 = \begin{pmatrix} 0 & -\omega_r & 0 \\ -\omega_r & 0 & 0 \\ 0 & 0 & 0 \end{pmatrix} \tag{A11}$$

[1] K. Pervushin, R. Riek, G. Wider, K. Wüthrich, *Proc. Natl. Acad. Sci. USA* **1997**, *94*, 12366 – 12371.

[2] M. D. Sørensen, A. Meissner, O. W. Sørensen, *J. Biomol. NMR* **1997**, *10*, 181 – 186.

[3] P. Andersson, A. Annila, G. Otting, *J. Magn. Reson.* **1998**, *133*, 364 – 367.

[4] K. Pervushin, G. Wider, K. Wüthrich, *J. Biomol. NMR* **1998**, *12*, 345 – 348.

[5] F. Ferrage, T. R. Eykyn, G. Bodenhausen, *J. Chem. Phys.* **2000**, *113*, 1081 – 1087.

[6] A. Pines, M. G. Gibby, J. S. Waugh, *J. Chem Phys.* **1973**, *59*, 569 – 595.

[7] M. Mehring, *Principles of High Resolution NMR in Solids*, 2nd ed., Springer, Berlin, **1983**.

[8] S. Hediger, B. H. Meier, N. D. Kurur, G. Bodenhausen, R. R. Ernst, *Chem. Phys. Lett.* **1994**, *223*, 283 – 288.

[9] S. Hediger, B. H. Meier, R. R. Ernst, *Chem. Phys. Lett.* **1995**, *240*, 449 – 456.

[10] R. Fu, P. Pelupessy, G. Bodenhausen, *Chem. Phys. Lett.* **1997**, *264*, 63 – 69.

[11] C. E. Hughes, R. Kemp-Harper, S. Wimperis, *J. Chem. Phys.* **1998**, *108*, 876 – 889.

[12] V. L. Ermakov, G. Bodenhausen, *J. Chem. Phys.* **1995**, *103*, 136 – 143.

[13] G. C. Chingas, A. N. Garroway, W. B. Moniz, R. D. Bertrand, *J. Am. Chem. Soc.* **1980**, *102*, 2526 – 2528.

[14] N. D. Kurur, G. Bodenhausen, *J. Magn. Reson. A* **1995**, *114*, 163 – 173.

[15] J. Baum, R. Tycko, A. Pines, *Phys. Rev. A* **1985**, *32*, 3435 – 3447.

[16] D. Rosenfeld, S. L. Panfil, Y. Zur, *J. Magn. Reson.* **1997**, *129*, 115 – 124.

[17] D. Rosenfeld, Y. Zur, *J. Magn. Reson.* **1998**, *132*, 102 – 108.

[18] A. Wokaun, R. R. Ernst, *J. Chem. Phys.* **1977**, *67*, 1752 – 1758.

[19] S. Vega, *J. Chem. Phys.* **1978**, *68*, 5518 – 5527.

[20] M. Guéron, J. L. Leroy, R. H. Griffey, *J. Am. Chem. Soc.* **1983**, *105*, 7262 – 7266.

[21] M. Goldman, *J. Magn. Reson.* **1984**, *60*, 437 – 452.

[22] S. A. Smith, T. O. Levante, B. H. Meier, R. R. Ernst, *J. Magn. Reson. A* **1994**, *106*, 75 – 105.

[23] E. Chiarparin, P. Pelupessy, G. Bodenhausen, *Mol. Phys.* **1998**, *95*, 759 – 767.

[24] P. Pelupessy, E. Chiarparin, *Concepts Magn. Reson.* **2000**, *12*, 103 – 124.

[25] C. P. Slichter, *Principles of Magnetic Resonance*, 3rd ed., Springer, Berlin, **1990**, p. 157.

[26] M. Goldman, *Quantum Description of High-Resolution NMR in Liquids*, Oxford University Press, Oxford, **1988**, p. 110.

[27] C. L. Mayne, in *Encyclopedia of Nuclear Magnetic Resonance*, *Vol. 4* (Eds.: D. M. Grant, R. K. Harris), Wiley, New York, **1996**, p. 2717.

Received: July 24, 2000 [Z 76]

Can Monoatomic Xenon Become Chiral?[**]

Kristin Bartik,[a] Mustapha El Haouaj,[a] Michel Luhmer,[a] André Collet,[a] and Jacques Reisse*[a]

In memory of André Collet

KEYWORDS:

chirality · NMR spectroscopy · xenon

Mislow and Siegel characterize as chirotopic any point of a molecule, whether occupied by an atom or not, that resides within a chiral environment.[1] They point out that all segments of a chiral molecule are chirotopic and that chirality is an all-

---

[a] *Prof. J. Reisse, Dr. K. Bartik, M. El Haouaj, Dr. M. Luhmer*
Laboratoire de Chimie Organique CP 165/64
Université Libre de Bruxelles
50 av. F.D. Roosevelt, 1050 Bruxelles (Belgium)
Fax: (+32) 2-650-3606
E-mail: jreisse@ulb.ac.be

[**] *K.B., M.L., and J.R. thank the Belgian "Fonds National de la Recherche Scientifique" and the French "Centre National de la Recherche Scientifique" (LEA 1996-2000) for financial support. M.El H. thanks the "Fondation Van Buren" for financial support.*

pervasive property. The aim of this work was to probe the chirotopicity of the internal cavity of a chiral molecule using a spherical, and therefore achiral, neutral atom as a probe.

Xenon can be seen as the perfect probe. Indeed, it is chemically inert yet exhibits NMR parameters that are highly sensitive to its chemical environment. For example, the chemical shift range of xenon dissolved in organic solvents is about 200 ppm.[2] Considerable work has capitalized on the utility of ^{129}Xe ($I = 1/2$) as a probe of host systems ranging from zeolites, clathrates, and polymers to organic cavitands and even biological systems.[3] Recently, using optical pumping methods, it has been possible to increase the nuclear spin polarization of ^{129}Xe by four to five orders of magnitude, to provide significantly enhanced sensitivity for a variety of NMR and MRI experiments.[4]

Cryptophane-A (CA; **1**) is a chiral molecule and we have shown, working with the racemic mixture, that it complexes xenon in $C_2D_2Cl_4$ with an association constant that is greater than $3000\,\text{M}^{-1}$.[5] The complexation equilibrium is slow on the ^{129}Xe chemical shift time scale at the temperatures studied (245 – 305 K). The ^{129}Xe NMR spectrum of the CA/Xe system exhibits, at 278 K, a resonance line at $\delta = 62.3$ ppm for the complexed xenon and, if the amount of xenon in solution is sufficient, a resonance line at $\delta = 229.5$ ppm for the uncomplexed xenon. Of course, the chemical shift of the complexed xenon is identical for the two enantiomers of the chiral host. However, if the complexed xenon atom is chirotopic, it will become diasteriotopic as soon as the chiral host, with its guest, is immersed in a chiral solvent or placed in the presence of a chiral partner which is not encaged within the host system. This is true even if the solvent or chiral partner does not covalently bond with the chiral host. A chemical shift difference should therefore be observed for the complexed xenon in the two CA enantiomers when a chiral chemical shift reagent (CSR) is added to the medium.

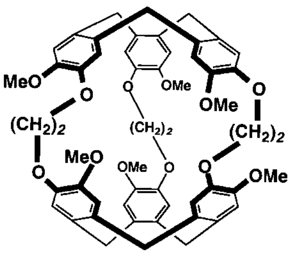

1

The ^{129}Xe NMR spectra of a racemic solution of CA in $C_2D_2Cl_4$ (approximately 0.05 M) containing xenon and increasing amounts of a chiral, europium-based CSR are shown in Figure 1. In the presence of the CSR, two resonance lines are observed for the complexed xenon. The resonance line corresponding to the uncomplexed xenon is not observed in these spectra because only a small amount of xenon was added to the solutions, to ensure that the line widths of the complexed xenon signals, which increase with xenon concentration, are not too broad. The linewidths of the two signals are significantly different and the difference between their chemical shifts increases as the CSR/CA ratio increases.

The ^{129}Xe NMR spectra of a solution of one of the enantiomers of CA (approximately 0.035 M) in $C_2D_2Cl_4$ containing xenon and 0.4 equivalents of the CSR is shown in Figure 2a. A single resonance line is observed for the complexed xenon. The solution containing the pure enantiomer was mixed with a 0.035 M solution of racemic CA containing 0.4 equivalents of CSR. The comparison of the ^{129}Xe spectra of the racemic solution (Figure 2b) and of the mixed solutions (Figure 2c) clearly confirms that the signal of xenon complexed in the pure enantiomer is the broader of the two signals observed in the spectrum of the racemic mixture.

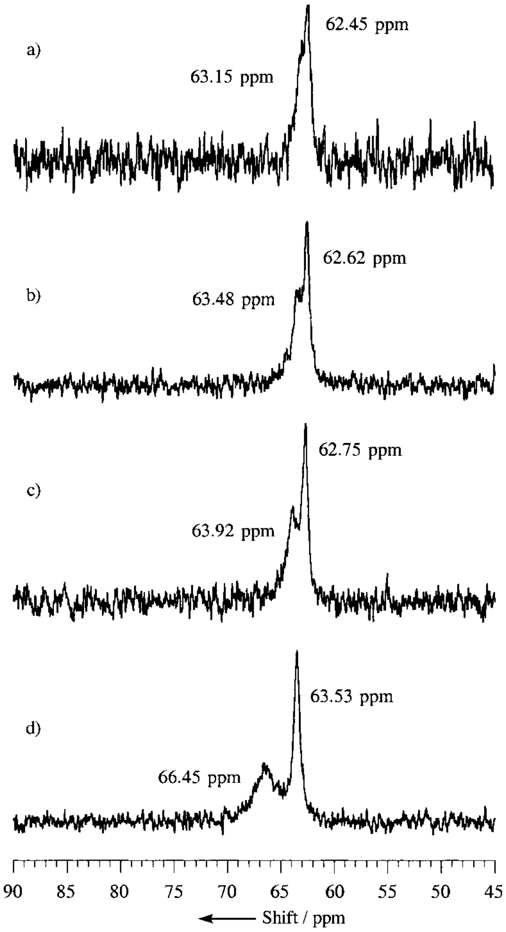

Figure 1. *^{129}Xe NMR spectrum of xenon dissolved in a racemic solution of the two enantiomers of CA in $C_2D_2Cl_4$ at 278 K in the presence of increasing amounts of a chiral CSR. Ratios [CSR]/[CA] are a) 0.08, b) 0.16, c) 0.24, and d) 0.52.*

The CA/Xe/CSR/$C_2D_2Cl_4$ system is complex even if, due to steric constraints, CA cannot make a host – guest complex with the solvent or the CSR. Different equilibria are present, as schematically summarized in Scheme 1. From our previous study, we know that equilibria **I** and **I′** are slow on the ^{129}Xe NMR time scale.[5] Equilibria **III** and **III′** are also slow on the ^{129}Xe NMR time scale, since two signals are observed at 278 K for the complexed xenon when the CSR is added to the CA/Xe system. The chemical shift difference between these two signals is function of the amount of added CSR. This indicates that equilibria **II** and **II′** are fast on the ^{129}Xe NMR time scale. The chemical shifts of the observed signals ($\delta_{2'}$ and $\delta_{3'}$) are therefore the averaged values between the chemical shift of xenon in the CA/CSR/Xe ternary

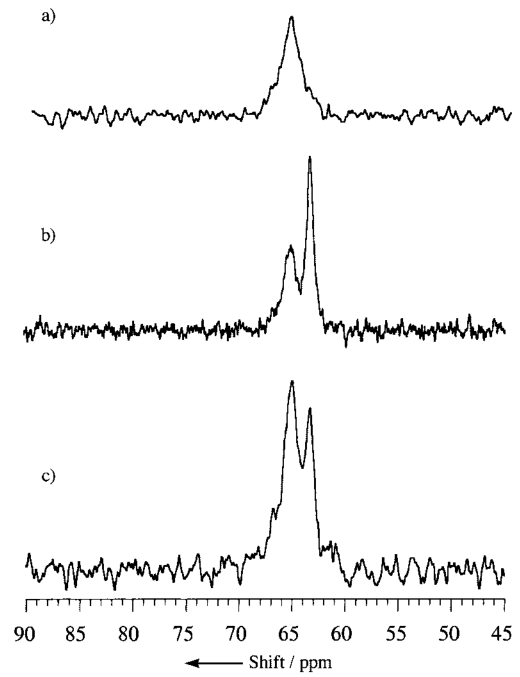

Figure 2. *^{129}Xe NMR spectrum at 278 K of xenon in a $C_2D_2Cl_4$ solution of a) one of the enantiomers of CA, b) a racemic mixture of the two CA enantiomers, and c) a mixture of the two enantiomers with an excess of the pure enantiomer, all in the presence of a chiral CSR.*

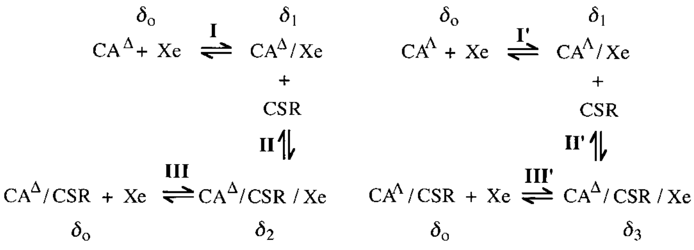

Scheme 1. *The different equilibria present for the two enantiomers of cryptophane-A (CA^{Δ} and CA^{Λ}) in the presence of xenon and the chiral CSR.*

supermolecule (δ_2 and δ_3) and the chemical shift of xenon in the CA/Xe host–guest complex ($\delta_1 = 62.3$ ppm, see above). Due to the high noise level in the different spectra, it was not possible to obtain the ratio of the integrals of the two signals with good precision. If the affinity of xenon for the two CA/CSR systems is the same ($K_{III} = K_{III'}$), the ratio in the spectra in Figure 1 and Figure 2 b would be unity. The ratio would be three for the spectra in Figure 2 c, which is the spectra of a solution containing equal amounts of the racemic mixture and of one of the enantiomers. The half widths of the two signals are not the same. This can be related to difference in the Xe exchange rates ($Xe_{in} \rightleftharpoons Xe_{out}$) in the two diastereotopic supermolecules but can also be due to differences in the transverse relaxation times. Indeed, the dominant relaxation mechanism is certainly the dipole–electronic dipole mechanism which can be different in the two diastereotopic complexes.

The observed splitting of the ^{129}Xe NMR signal of complexed xenon in the chiral host molecule in the presence of a chiral CSR is the experimental proof that an atom can be chirotopic even if it is nonbonded. It can be said that the encaged xenon atom has become chiral. It could be argued that the xenon atoms are diastereotopic in the two ternary complexes. However, if they are diastereotopic in the ternary complexes, it is because they are enatiotopic in the binary Xe/CA complexes. Except in cases of parity violation, never observed until now at the molecular level,[6] the observation of physical differences between enantiomers always requires chiral tools. In this case, the chiral tool is the CSR.

This first example of the "chiralization" of a spherical and neutral atom presents analogies with the work of Hosseini and co-workers on the chiralization of a monoatomic cation (Cs) by a chiral polyatomic anion (borocryptate) in oriented chiral liquid crystals.[7] Their systems were investigated by ^{133}Cs NMR and two sets of signals are observed for the cation, one for each of the enantiomers of the borocrytptate. The chirality is imposed on the labile and exchangable complexed cation by the chiral cavity of the receptor and is described as peristatic chirality. The authors state that the chirality is imposed through noncovalent interactions but the achiral cation and the chiral anion are actually chemically bonded through electrostatic bonds and also through coordination bonds between the metal cation and various heteroatoms of the complexed anion. In the Xe/CA system, the noble gas and the cryptophane are definitely not chemically bonded. The major interactions which exist are physical interactions: essentially attractive London energies and repulsive Pauli energies.

It can therefore be concluded that the all-pervasive character of chirality is associated to detectable experimental differences in supramolecular systems even when the guest molecule is a noble gas. Chemists usually consider that, among the nonbonding interactions, hydrogen bonds, electrostatic interactions, and charge transfers are the most important ones but this is not necessarily the case. It is good to be reminded that the van der Waals energies, especially the attractive London energies, are often dominant and are, furthermore, always present. This work shows that they can be at the origin of interesting phenomena.

Experimental Section

^{129}Xe NMR spectra were recorded on a Unity 600 spectrometer (Varian, nominal frequency = 165.997 MHz). Spectra were recorded with the use of a 30° pulse, a 6 s repetition time, and a spectral width of 42 450 Hz. The number of scans recorded varied from spectrum to spectrum to obtain reasonable signal-to-noise ratios. Spectra were weighted with an exponential line broadening that corresponds to 10% of the natural line width of the narrowest signal. ^{129}Xe chemical shifts are referenced to pure xenon gas extrapolated to zero pressure.

Cryptophane-A was synthesized in the laboratory of Prof. A. Collet (Lyon, France) as per a literature procedure.[8] Deuterated 1,1,2,2-tetrachloroethane and the chiral europium reagent tris[3-(heptafluoropropylhydroxymethylene)-(+)-camphorato] europium(III) were purchased from Janssen Chimica. Xenon gas at its natural isotope abundance was purchased from Air Liquide.

Samples were prepared at room temperature. For the experiments undertaken as a function of the amount of added chiral CSR, 0.5 mL of a known concentration of the racemic mixture of CA in $C_2D_2Cl_4$ (approximately 0.05 M) was placed in a 5 mm NMR tube equipped with a Young valve. Aliquots of a 0.05 M solution of the CSR were added to the same sample in order to achieve the desired [CSR]/[CA] ratios. To achieve [CSR]/[CA] = 0.52, a known amount of solid CSR was added to the solution of [CSR]/[CA] = 0.24. After each addition of CSR, the sample was degassed by several freeze – thaw cycles on a vacuum line. Xenon gas was then added to the sample by condensation and the ^{129}Xe NMR spectrum was recorded. The amount of xenon was controlled so as to have a small Xe:CA mole ratio, in order to ensure that the xenon linewidths are not too broad.

A 3.5×10^{-2} M solution of one of the pure enantiomers of CA was prepared in $C_2D_2Cl_4$. The solution was placed in a 5 mm NMR tube equipped with a Young valve. Xenon gas was bubbled in the solution for approximately 1 min and the solution was then partially degassed on a vacuum line in order to have a small Xe:CA mole ratio. After recording the ^{129}Xe NMR spectrum, 0.4 equiv of CSR was added to the solution. Xenon gas was again bubbled in the solution which was then partially degassed before recording the ^{129}Xe NMR spectrum. This solution was then mixed with an equal volume of a 3.5×10^{-2} M solution of the racemic mixture of CA containing 0.4 equivalents of CSR. Xenon gas was bubbled in the solution which was then partially degassed before recording the ^{129}Xe NMR spectrum.

[1] K. Mislow, J. Siegel, *J. Am. Chem. Soc.* **1984**, *106*, 3319 – 3328.
[2] K. W. Miller, N. V. Reo, A. J. M. Schoot Uiterkamp, D. P. Stengle, T. R. Stengle, K. L. Williamson, *Proc. Natl. Acad. Sci. USA* **1981**, *78*, 4946 – 4949.
[3] For relevant reviews, see: J. Reisse, *New J. Chem.* **1986**, *10*, 665 – 672; C. Dybowski, N. Bansal, *Annu. Rev. Phys. Chem.* **1991**, *42*, 433 – 463; P. J. Barrie, J. Klinowski, D. Raftery, *Prog. Nucl. Magn. Reson. Spectros.* **1992**, 91 – 108; D. Raftery, B. F. Chmelka, *NMR Basic Principles and Progress. Solid-State NMR I: Methods*, *Vol. 30*, Springer, Berlin, **1994**, pp. 111 – 157.
[4] M. Luhmer, B. M. Goodson, Y. Q. Song, D. D. Laws, L. Kaiser, M. C. Cyrier, A. Pines, *J. Am. Chem. Soc.* **1999**, *121*, 3502 – 3512, and references therein.
[5] K. Bartik, M. Luhmer, J. P. Dutasta, A. Collet, J. Reisse, *J. Am. Chem. Soc.* **1998**, *120*, 784 – 791.
[6] A. L. Bara, J. B. Robert, *Molec. Phys.* **1996**, 875 – 886.
[7] E. Graf, R. Graff, M. W. Hosseini, C. Huguenard, F. Taubelle, *Chem. Commun.* **1997**, 1459 – 1460; C. Huguenard, F. Taulelle, E. Graf, M. W. Hosseini, *J. Chim. Phys.* **1998**, *95*, 341 – 349.
[8] J. Canceill, A. Collet, *J. Chem. Soc. Chem. Commun.* **1988**, 582 – 584; J. Canceill, A. Collet, G. Gottarelli, P. Palmieri, *J. Am. Chem. Soc.* **1987**, *109*, 582 – 584; J. Gabard, A. Collet, *J. Chem. Soc. Chem. Commun.* **1981**, 1137 – 1139.

Received: August 15, 2000 [Z 92]

Eosin Molecules Hosted into a Dendrimer Which Carries Thirty-Two Dansyl Units in the Periphery: A Photophysical Study**

Vincenzo Balzani,*[a] Paola Ceroni,[a] Sven Gestermann,[b]
Marius Gorka,[b] Christopher Kauffmann,[b]
Mauro Maestri,[a] and Fritz Vögtle[b]

KEYWORDS:

dendrimers · dyes · energy transfer · fluorescence · host – guest systems

Dendrimers are attracting increasing attention because of their unique structures and properties.[1] Dendrimers containing photoactive components[2, 3] are particularly interesting because a) luminescence signals offer a handle to better understand the dendritic structures and superstructures, b) cooperation among the photoactive components can allow the dendrimer to perform useful functions, such as light harvesting, and c) changes in the photophysical properties can be exploited for sensing purposes with signal amplification.

Continuing our studies in the field of photoactive dendrimers,[3] we have investigated the photophysical behavior of the supramolecular host – guest species obtained when eosin Y (**E**, as disodium salt) is extracted from water by a fourth-generation poly(propylene amine) dendrimer (POPAM) decorated at the periphery with strongly fluorescent dansyl units[3f,g] (**4D**). The use of dendrimers as extracting agents is a topic of current interest.[4, 5] Particularly worth mentioning in this field are the investigations on the extraction of dyes performed by Meijer et al.[5]

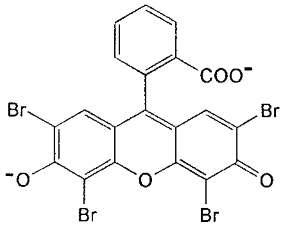

E

---

[a] Prof. Dr. V. Balzani, Dr. P. Ceroni, Prof. Dr. M. Maestri
Dipartimento di Chimica "G. Ciamician"
Università di Bologna
via Selmi 2, 40126 Bologna (Italy)
Fax: (+39) 0-51-2099456
E-mail: vbalzani@ciam.unibo.it

[b] Dr. S. Gestermann, Dr. M. Gorka, Dr. C. Kauffmann, Prof. Dr. F. Vögtle
Kekulé-Institut für Organische Chemie und Biochemie der Universität Bonn
Gerhard Domagk Strasse 1, 53121 Bonn (Germany)

[**] This work has been supported in Italy by MURST (Supramolecular Devices Project), University of Bologna (Funds for Selected Topics), and CNR (Sensori Fluorescenti Supramolecolari).

Samples were prepared at room temperature. For the experiments undertaken as a function of the amount of added chiral CSR, 0.5 mL of a known concentration of the racemic mixture of CA in $C_2D_2Cl_4$ (approximately 0.05 M) was placed in a 5 mm NMR tube equipped with a Young valve. Aliquots of a 0.05 M solution of the CSR were added to the same sample in order to achieve the desired [CSR]/[CA] ratios. To achieve [CSR]/[CA] = 0.52, a known amount of solid CSR was added to the solution of [CSR]/[CA] = 0.24. After each addition of CSR, the sample was degassed by several freeze–thaw cycles on a vacuum line. Xenon gas was then added to the sample by condensation and the ^{129}Xe NMR spectrum was recorded. The amount of xenon was controlled so as to have a small Xe:CA mole ratio, in order to ensure that the xenon linewidths are not too broad.

A 3.5×10^{-2} M solution of one of the pure enantiomers of CA was prepared in $C_2D_2Cl_4$. The solution was placed in a 5 mm NMR tube equipped with a Young valve. Xenon gas was bubbled in the solution for approximately 1 min and the solution was then partially degassed on a vacuum line in order to have a small Xe:CA mole ratio. After recording the ^{129}Xe NMR spectrum, 0.4 equiv of CSR was added to the solution. Xenon gas was again bubbled in the solution which was then partially degassed before recording the ^{129}Xe NMR spectrum. This solution was then mixed with an equal volume of a 3.5×10^{-2} M solution of the racemic mixture of CA containing 0.4 equivalents of CSR. Xenon gas was bubbled in the solution which was then partially degassed before recording the ^{129}Xe NMR spectrum.

[1] K. Mislow, J. Siegel, *J. Am. Chem. Soc.* **1984**, *106*, 3319–3328.
[2] K. W. Miller, N. V. Reo, A. J. M. Schoot Uiterkamp, D. P. Stengle, T. R. Stengle, K. L. Williamson, *Proc. Natl. Acad. Sci. USA* **1981**, *78*, 4946–4949.
[3] For relevant reviews, see: J. Reisse, *New J. Chem.* **1986**, *10*, 665–672; C. Dybowski, N. Bansal, *Annu. Rev. Phys. Chem.* **1991**, *42*, 433–463; P. J. Barrie, J. Klinowski, D. Raftery, *Prog. Nucl. Magn. Reson. Spectros.* **1992**, 91–108; D. Raftery, B. F. Chmelka, *NMR Basic Principles and Progress. Solid-State NMR I: Methods*, *Vol. 30*, Springer, Berlin, **1994**, pp. 111–157.
[4] M. Luhmer, B. M. Goodson, Y. Q. Song, D. D. Laws, L. Kaiser, M. C. Cyrier, A. Pines, *J. Am. Chem. Soc.* **1999**, *121*, 3502–3512, and references therein.
[5] K. Bartik, M. Luhmer, J. P. Dutasta, A. Collet, J. Reisse, *J. Am. Chem. Soc.* **1998**, *120*, 784–791.
[6] A. L. Bara, J. B. Robert, *Molec. Phys.* **1996**, 875–886.
[7] E. Graf, R. Graff, M. W. Hosseini, C. Huguenard, F. Taubelle, *Chem. Commun.* **1997**, 1459–1460; C. Huguenard, F. Taulelle, E. Graf, M. W. Hosseini, *J. Chim. Phys.* **1998**, *95*, 341–349.
[8] J. Canceill, A. Collet, *J. Chem. Soc. Chem. Commun.* **1988**, 582–584; J. Canceill, A. Collet, G. Gottarelli, P. Palmieri, *J. Am. Chem. Soc.* **1987**, *109*, 582–584; J. Gabard, A. Collet, *J. Chem. Soc. Chem. Commun.* **1981**, 1137–1139.

Received: August 15, 2000 [Z 92]

Eosin Molecules Hosted into a Dendrimer Which Carries Thirty-Two Dansyl Units in the Periphery: A Photophysical Study**

Vincenzo Balzani,*[a] Paola Ceroni,[a] Sven Gestermann,[b] Marius Gorka,[b] Christopher Kauffmann,[b] Mauro Maestri,[a] and Fritz Vögtle[b]

KEYWORDS:

dendrimers · dyes · energy transfer · fluorescence · host–guest systems

Dendrimers are attracting increasing attention because of their unique structures and properties.[1] Dendrimers containing photoactive components[2, 3] are particularly interesting because a) luminescence signals offer a handle to better understand the dendritic structures and superstructures, b) cooperation among the photoactive components can allow the dendrimer to perform useful functions, such as light harvesting, and c) changes in the photophysical properties can be exploited for sensing purposes with signal amplification.

Continuing our studies in the field of photoactive dendrimers,[3] we have investigated the photophysical behavior of the supramolecular host–guest species obtained when eosin Y (**E**, as disodium salt) is extracted from water by a fourth-generation poly(propylene amine) dendrimer (POPAM) decorated at the periphery with strongly fluorescent dansyl units[3f,g] (**4D**). The use of dendrimers as extracting agents is a topic of current interest.[4, 5] Particularly worth mentioning in this field are the investigations on the extraction of dyes performed by Meijer et al.[5]

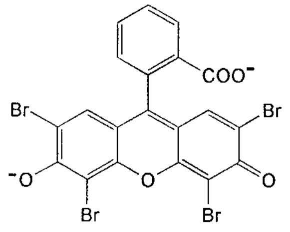

E

---

[a] Prof. Dr. V. Balzani, Dr. P. Ceroni, Prof. Dr. M. Maestri
Dipartimento di Chimica "G. Ciamician"
Università di Bologna
via Selmi 2, 40126 Bologna (Italy)
Fax: (+39) 0-51-2099456
E-mail: vbalzani@ciam.unibo.it

[b] Dr. S. Gestermann, Dr. M. Gorka, Dr. C. Kauffmann, Prof. Dr. F. Vögtle
Kekulé-Institut für Organische Chemie und Biochemie der Universität Bonn
Gerhard Domagk Strasse 1, 53121 Bonn (Germany)

[**] This work has been supported in Italy by MURST (Supramolecular Devices Project), University of Bologna (Funds for Selected Topics), and CNR (Sensori Fluorescenti Supramolecolari).

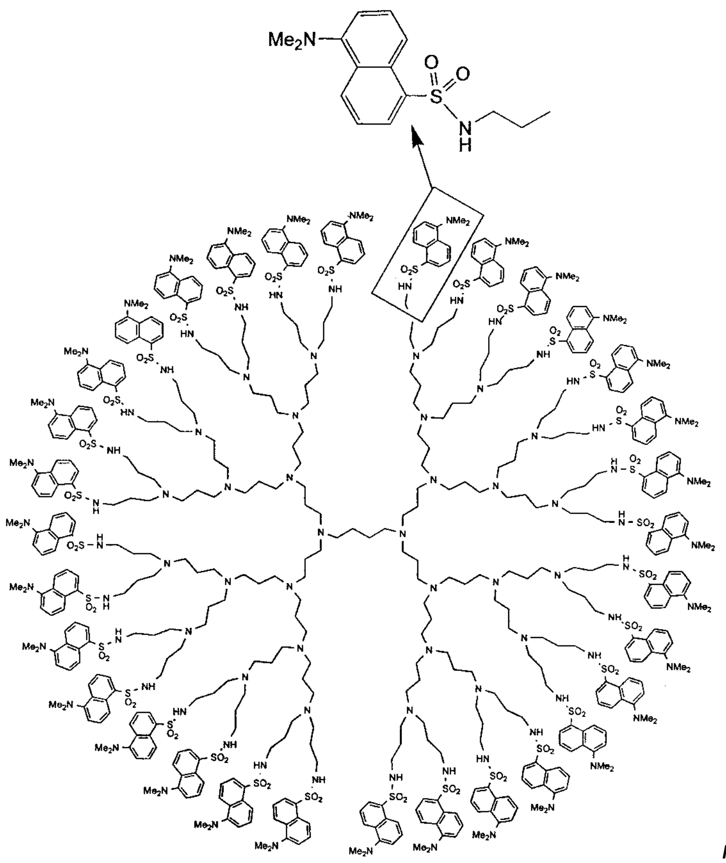

4D

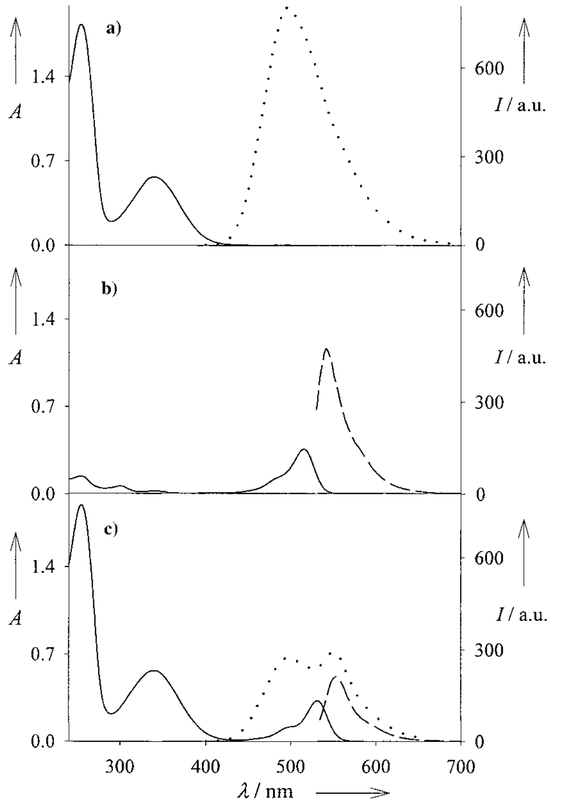

Figure 1. *Absorption (A; ——) and fluorescence intensity (I; ---- $\lambda_{ex} = 520$ nm; •••• $\lambda_{ex} = 370$ nm) spectra of a)* ***4D*** *in CH_2Cl_2 (4.7×10^{-6} M), b)* ***E*** *in H_2O (9.8×10^{-6} M), and c) the CH_2Cl_2 phase after shaking the two solutions.*

Dendrimer **4D** is soluble in CH_2Cl_2 but not in H_2O. The absorption and emission spectra of a solution of **4D** in CH_2Cl_2 are shown in Figure 1 a. Eosin **E** (as a disodium salt) is soluble in H_2O but not in CH_2Cl_2. The absorption and emission spectra of a solution of **E** in H_2O are shown in Figure 1 b. When equal volumes of the CH_2Cl_2 solution of **4D** and of the H_2O solution of **E** are shaken together, all the eosin molecules transfer from water to dichloromethane, as shown by the complete disappearance of any absorption or emission in the H_2O phase and by the appearance of the absorption and emission spectra of eosin in the CH_2Cl_2 phase (Figure 1 c). Since eosin is not transferred at all from the aqueous phase to the CH_2Cl_2 phase in the absence of the dendrimer, we can conclude that, when the CH_2Cl_2 solution of **4D** and the H_2O solution of **E** are shaken together, the eosin molecules transfer to the CH_2Cl_2 phase because they are hosted by the dendrimer. Comparison of the spectra shown in Figure 1 shows that the transfer of eosin from the H_2O phase into the dendrimer causes a small red shift in the absorption and emission spectra of **E**[6] and a substantial quenching of both the dendrimer and eosin fluorescence bands.

Extraction experiments carried out using a CH_2Cl_2 solution of **4D** (4.7×10^{-6} M) and aqueous solutions of **E** in the concentration range 1.0×10^{-6} – 8.0×10^{-5} M have shown that, on increasing the concentration of **E**, the amount of extracted eosin increases to a maximum of about six eosin molecules per dendrimer molecule.

As shown in Figure 1, the absorption spectra of the host and guest species are quite different. Fully selective excitation of the eosin guest can be performed with 520 nm light, whereas 370 nm light can be used for selective excitation (when necessary, with minor corrections) of the dansyl units of the dendrimer. This lucky circumstance allowed us to investigate

Editorial Advisory Board Member:[*]

Vincenzo Balzani *received his "laurea" in Chemistry from the University of Bologna in 1960. Since 1972, he has been Professor of Chemistry at the same University. His research interests include electron-transfer processes, photochemistry, photophysics, supramolecular chemistry, and artificial molecular machines. He is the author of more than 400 scientific papers, two edited books, and two monographs. He has presented many plenary or invited lectures at International Conferences and Research Centers all over the world and he has obtained several awards, including the Doctorate Hororis Causa from the University of Fribourg (1989), the Italgas European Prize for Research and Innovation (1994), and the Porter Medal of the European, American, and Japanese Photochemical Societies (2000).*

---

[*] *Members of the Editorial Advisory Board will be introduced to the readers with their first manuscript.*

quantitatively the effect of the guest on the fluorescence properties of the host and vice versa.

In CH_2Cl_2, the fluorescence of **4D** (namely, of its dansyl units) has a lifetime $\tau = 16$ ns and quantum yield $\phi = 0.46$. Extraction of increasing amounts of eosin causes a progressive decrease in the fluorescence intensity of the dendrimer (Figure 2) but does not affect the fluorescence decay, which remains monoexponential with a lifetime of 16 ns. Extrapolation of the initial slope of the quenching plot of Figure 2 shows that a single eosin guest is sufficient to completely quench the fluorescence of any excited dansyl unit of the host dendrimer. The curvature of the plot at higher eosin concentration is due to the fact that each dendrimer can host more than one eosin molecule, so that even at relatively high [**E**]/[**4D**] ratios there are still some "empty" dendrimers, in agreement with the unquenched fluorescence lifetime. Comparison between fluorescence intensities obtained upon excitation at 370 nm (dansyl absorption) and 520 nm (eosin absorption) showed that quenching of the dansyl fluorescence by eosin is due to energy transfer, as expected because of the very good overlap between the emission spectrum of the dansyl units and the absorption spectrum of the eosin molecules (Figure 1).

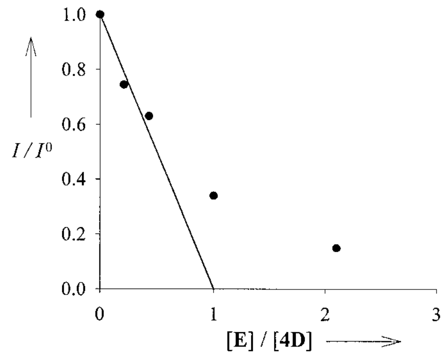

Figure 2. Effect of addition of eosin on the fluorescence intensity of the ***4D*** *dendrimer. The concentration of* ***4D*** *was* 4.7×10^{-6} *M.*

Examination of the fluorescence properties of the eosin molecules encapsulated into the dendrimers has revealed other interesting features. The fluorescence of "free" **E** in CH_2Cl_2 (solubilized by using an excess of [18]crown-6 to complex the sodium cations) has quantum yield $\phi = 0.21$ and lifetime $\tau =$ 3.8 ns. When eosin is hosted in the dendrimer dissolved in CH_2Cl_2, the fluorescence quantum yield is much lower and the fluorescence decay is no longer monoexponential. A good fit can be obtained assuming a two-exponential decay, which yields the lifetimes shown in Table 1. A two-exponential decay is observed even at a very low eosin concentration ([**E**]/[**4D**] = 0.21), that is, under conditions in which there is at most one eosin molecule per dendrimer. This means that eosin molecules can occupy two different sites (or two families of substantially different sites) in the interior of the dendrimer (Figure 3), which give rise to different radiative and/or nonradiative[7] rate constants for the decay of the fluorescent excited state of the eosin guest. The data obtained with higher eosin concentrations (Table 1) confirm that there are two substantially different sites in which eosin can be hosted, even when five eosin molecules are contained in the same dendrimer. The changes in the fluorescence quantum yield and lifetimes with the [**E**]/[**4D**] ratio show that the properties of the hosting sites (and, therefore, their influence on the decay processes of the eosin excited state) are somewhat affected by the number of hosted molecules, as expected for a flexible structure like that of the poly(propylene amine) dendrimers.

Table 1. *Photophysical data.*[a]

	4D[b]		**E**[c]	
	ϕ_{em}	τ [ns]	ϕ_{em}	τ [ns]
4D	0.46	16	–	–
E	–	–	0.45	3.8
[**E**]/[**4D**] = 0.21	0.35	16	0.10	0.76, 2.41
[**E**]/[**4D**] = 2.1	0.07	16	0.05	0.56, 2.12
[**E**]/[**4D**] = 5.3	≤ 0.05[d]	16	0.02	0.41, 2.19

[a] Air-equilibrated CH_2Cl_2 solutions at 298 K. [b] $\lambda_{ex} = 370$ nm; $\lambda_{em} = 495$ nm. [c] $\lambda_{ex} = 520$ nm; $\lambda_{em} = 540$ nm. [d] Large experimental error because of spectral overlap.

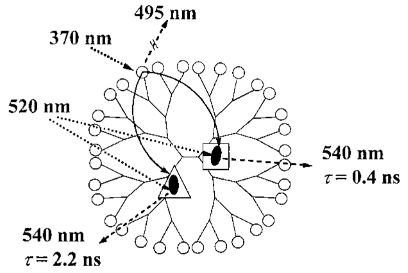

Figure 3. Schematic representation of the photophysical processes occurring in the dendrimer – eosin host – guest systems. The 32 peripheral dansyl units of the dendrimer are represented by empty circles and eosin molecules by black ovals. Excitation, emission, and energy transfer processes are represented by dotted, dashed, and full arrows, respectively. The two different sites in which the eosin molecules can be hosted are represented by a square and a triangle.

Finally, we have found that excitation of eosin (both free and hosted into the dendrimer) causes the characteristic dioxygen emission with maximum at $\lambda = 1260$ nm. Since the intensity and lifetime of eosin fluorescence are not affected by dioxygen, the sensitization of the dioxygen emission has to occur through an eosin triplet excited state. Interestingly, the intensity of the sensitized dioxygen emission is four times stronger upon excitation of free eosin compared with eosin hosted inside the dendrimer. This is consistent with previous results showing that an excited state in the dendrimer core is in some way protected by the dendrimer branches against the action of a quencher.[3a,d,e]

Experimental Section

The synthesis and characterization of dendrimer **4D** was previously reported.[8] Fluorescence lifetimes were measured with a spectrofluorometer (FLUOROLOG Spex FL3/11) equipped with a phase-shift unit (Tau 3, 10 ps time resolution). Dioxygen emission was measured by a home-modified apparatus based on an spectrofluorimeter (Edinburg CD900), equipped with an argon-ion laser (Spectra Physics model 164 – 09) for the sample excitation at $\lambda_{ex} = 514$ nm and a liquid-nitrogen cooled, hyperpure germanium-crystal detector. Other equipment and techniques have been described elsewhere.[3c,d] The estimated experimental error is ±2 nm on the band maximum, ±10% on the fluorescence quantum yields ϕ, and ±5% on the fluorescence lifetimes τ.

[1] a) D. A. Tomalia, H. D. Durst, *Topics Curr. Chem.*, **1993**, *165*, 193; b) J. M. J. Fréchet, *Science* **1994**, *263*, 1710; c) N. Ardoin, D. Astruc, *Bull. Soc. Chim. Fr.* **1995**, *132*, 875; d) G. R. Newkome, C. Moorefield, F. Vögtle, *Dendritic Molecules: Concepts, Syntheses, Perspectives,* VCH, Weinheim, **1996**; e) F. Zeng, S. C. Zimmerman, *Chem. Rev.* **1997**, *97*, 1681; f) V. Balzani, S. Campagna, G. Denti, A. Juris, S. Serroni, M. Venturi, *Acc. Chem. Res.* **1998**, *31*, 26; g) A. W. Bosman, H. M. Janssen, E. W. Meijer, *Chem. Rev.* **1999**, *99*, 1665; h) G. R. Newkome, E. He, C. Moorefield, *Chem. Rev.* **1999**, *99*, 1689; i) M. Fischer, F. Vögtle, *Angew. Chem.* **1999**, *111*, 934; *Angew. Chem. Int. Ed.* **1999**, *38*, 884.

[2] For some recent papers, see: a) D. M. Junge, D. V. McGrath, *J. Am. Chem. Soc.* **1999**, *121*, 4912; b) T. Sato, D.-L. Jiang, T. Aida, *J. Am. Chem. Soc.* **1999**, *121*, 10658; c) A. Adronov, S. L. Gilat, J. M. J. Fréchet, K. Ohta, F. V. R. Neuwahl, G. R. Fleming, *J. Am. Chem. Soc.* **2000**, *122*, 1175; d) K. Tsuda, G. C. Dol, T. Gensch, J. Hofkens, L. Latterini, J. W. Weener, E. W. Meijer, F. C. De Schryver, *J. Am. Chem. Soc.* **2000**, *122*, 3445; e) C. M. Cardona, J. Alvarez, A. E. Kaifer, T. D. McCarley, S. Pandey, G. A. Baker, N. J. Bonzagni, F. V. Bright, *J. Am. Chem. Soc.* **2000**, *122*, 6139; f) S. F. Swallen, Z. Zhu, J. S. Moore, R. Kopelman, *J. Phys. Chem. B* **2000**, *104*, 3988.

[3] a) J. Issberner, F. Vögtle, L. De Cola, V. Balzani, *Chem. Eur. J.* **1997**, *3*, 706; b) A. Archut, F. Vögtle, L. De Cola, G. C. Azzellini, V. Balzani, P. S. Ramanujam, R. H. Berg, *Chem. Eur. J.* **1998**, *4*, 699; c) A. Archut, G. C. Azzellini, V. Balzani, L. De Cola, F. Vögtle, *J. Am. Chem. Soc.* **1998**, *120*, 12187; d) M. Plevoets, F. Vögtle, L. De Cola, V. Balzani, *New J. Chem.* **1999**, 63; e) F. Vögtle, M. Plevoets, M. Nieger, G. C. Azzellini, A. Credi, L. De Cola, V. De Marchis, M. Venturi, V. Balzani, *J. Am. Chem. Soc.* **1999**, *121*, 6290; f) F. Vögtle, S. Gestermann, C. Kauffmann, P. Ceroni, V. Vicinelli, L. De Cola, V. Balzani, *J. Am. Chem. Soc.* **1999**, *121*, 12161; g) V. Balzani, P. Ceroni, S. Gestermann, C. Kauffmann, M. Gorka, F. Vögtle, *Chem. Commun.* **2000**, 853.

[4] Recent examples: a) H. Stephan, H. Spies, B. Johannsen, L. Klein, F. Vögtle, *Chem.* Commun. **1999**, 1875; b) G. Pistolis, A. Malliaris, D. Tsiourvas, C. M. Paleos, *Chem. Eur. J.* **1999**, *5*, 1440; c) V. Chechik, M. Zhao, R. M. Crooks, *J. Am. Chem. Soc.* **1999**, 121, 4910.

[5] a) J. F. G. A. Jansen, E. M. M. de Brabander-van den Berg, E. W. Meijer, *Science* **1994**, *266*, 1226; b) A. P. H. J. Schenning, E. Peeters, E. W. Meijer, *J. Am. Chem. Soc.* **2000**, *122*, 4489 and references therein.

[6] A red shift of both absorption and emission bands of eosin upon decreasing solvent polarity was reported: G. R. Fleming, A. W. E. Knight, J. M. Morris, R. J. S. Morrison, G. W. Robinson, *J. Am. Chem. Soc.* **1977**, *99*, 4306.

[7] A contribution to the nonradiative decay could also come from the electron-transfer quenching by the dendrimer amine functions. For the quenching of excited eosin by amines, see: R. F. Bartholomew, R. S. Davidson, *J. Chem. Soc. C* **1971**, 2347.

[8] A. Archut, S. Gestermann, R. Hesse, C. Kauffmann, F. Vögtle, *Synlett* **1998**, 546.

Received: July 12, 2000 [Z 65]

The 2000 Nobel Prize in Chemistry—A Personal Accolade

Joel S. Miller*[a]

The discovery and development of conductive polymers has just been awarded the 2000 Noble Prize in Chemistry in Stockholm. This stunning, paradigm-shifting discovery was made at the University of Pennsylvania by chemists Alan G. MacDiarmid and Hideki Shirakawa and physicist Alan J. Heeger in 1977. The revelation that polymeric materials could provide additional function far beyond the well established structural and mechanical properties continues to engender exciting new opportunities for future electronic, optoelectronic, as well as photonic devices. Commercial products are emerging that are based on conductive polymers.

Conductive polymers evolved from earlier studies on organic electron-transfer salts that exhibited high direct-current electrical conductivity at room temperature. Organic conductors, described as "organic amalgams", were first envisioned four decades[1] prior to the 1954 report that perylene electron-transfer salts with bromine exhibited high electrical conductivity.[2] Independently, while searching for new polymers akin to Teflon, Du Pont researchers discovered that electron-transfer salts of TCNQ (7,7,8,8-tetracyano-*p*-quinodimethane) also produced highly conducting materials.[3] Metallike conductivity, that is, an increase in conductivity with decreasing temperature, was observed a few years later in a TCNQ complex containing an electron-transfer salt.[4] These highly conducting materials spawned a flurry of activity worldwide aimed at seeking new materials with enhanced properties and, as a consequence, related electron-transfer, salt-based organic superconductors were first reported in 1980.[5]

With soluble organic-based conductors established extension to polymers were inevitable. The lustrous, highly reflecting inorganic polymer, poly(sulfur nitride) or $(SN)_x$, was reported to exhibit metallike conductivity between 2.4 and 300 K,[6] and even superconductivity at 0.26 K,[7] but it lacked the ability to be modified akin to organic polymers. Hence, enhanced electrical conductivity via chemical modification as well as improved chemical stability and processing could not be achieved for $(SN)_x$. Conjugated polymers, akin to poly(sulfur nitride) but unlike saturated polymers such as polyethylene, could be envisioned to be conductive. These polymers, however, had to be in a useful form and partially oxidizable (or reducable). The Ziegler–Natta polymerization of acetylene to form polyacetylene was well established but the polyacetylene was only available as a powder.

A fortuitous error on the part of Hideki Shirakawa in 1975, then of the Tokyo Institute of Technology, led to the formation of lustrous silver films of polyacetylene. Currently he is Professor Emeritus at the Institute for Materials Science at the University of Tsukuba, where he has been since 1979. The error was the use of the Ziegler–Natta catalyst a thousand times more concentrated than previously used. Although Shirakawa's research interests were far removed from conducting polymers, he shared his then-new discovery with MacDiarmid, who was visiting the institute. MacDiarmid shared the potential importance of this observation with Kenneth J. Wynne, of the U.S. Office of Naval Research who concurred and was the first to fund research on conducting polymers. MacDiarmid seized the opportunity to invite Shirakawa to join him in his laboratory to jointly study the electrical and optical properties of the films with him and Heeger at the University of Pennsylvania; Heeger subsequently moved to his current position at the University of California, Santa Barbara. The rest, of course, is history.

Unsurprisingly, polyacetylene was a semiconductor; however, upon reaction with iodine, among other oxidants, a greater than million-fold enhancement in the electrical conductivity was achieved. This oxidation process was termed "doping" in accord with the enhancement of the conductivity of semiconductors. This remarkable observation altered in a permanent way how organic chemists viewed the old reaction of iodination of double bonds for extended systems. This seminal work was essentially published[8] and presented simultaneously. Along with Arthur J. Epstein, Alan G. MacDiarmid, and Henry Taube, I chaired the Conference on *Synthesis and Properties*

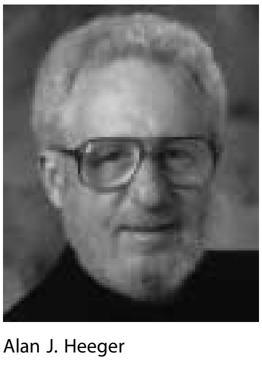

Alan J. Heeger

Alan G. MacDiarmid

Hideki Shirakawa

---

[a] Prof. J. S. Miller
Department of Chemistry
University of Utah
Salt Lake City, UT 84112 (USA)
Fax: (+1) 801-581-8433
E-mail: jsmiller@chemistry.utah.edu

of Low-Dimensional Materials sponsored by the New York Academy of Sciences.[9] This meeting had a strong chemical focus and provided the ideal forum for dissemination of the then-revolutionary discovery of their conducting organic polymer. This stunning result was highlighted in the press.[10]

The area encompassing conducting organic materials has grown exponentially through the years, as illustrated by a snapshot of the interests and number of attendees at its biennial international conferences. The interests have migrated from electron-transfer salts and linear chain metal-based soluble conductors and their associated physics and chemistry issues to the solid-state physics of polyacetylene on to the development of new classes of conducting polymers and their electrochemical p- and n-doping, polymer physics, chemical modifications, and materials processing properties. The available conducting polymers expanded to include poly(*p*-phenylene), polythiophene, polypyrrole, polyaniline, and poly(*p*-phenylenevinylene), to name a few, with several of them presently commercially used. Due to its instability, neither p- nor n-"doped" polyacetylene itself has any commercial appeal.

An early sample of highly reflecting "doped" polyacetylene, perhaps destined for a major science museum such as the Franklin Institute or even the Smithsonian, that was prepared in MacDiarmid's laboratory, was lost forever. I personally take the blame. At my request, Alan MacDiarmid kindly sent me his remaining sample, which was to be promptly returned. It vanished from my office and in-depth sleuthing led to identification that the custodial staff deemed it as garbage and promptly discarded it. Even after sifting through numerous trash repositories, we failed to recover it. My sadness over this loss continues to be exasperated as the importance of this sample increases with time. But Alan MacDiarmid was as gracious as ever and well understood my torment.

Applications and commercialization of organic conductors were never distant and today are on the research and development forefront. Amusingly, the early expectation to use them as battery materials was not sustainable, while a plethora of unexpected applications evolved.[11] These include polypyrrole-based electrolytic capacitors, polyaniline-based high capacity floppy disks, polypyrrole-based conductive coatings for textile, polypyrrole-based copper plating baths for printed circuit boards, and polyaniline-based antistatic coatings. In the waning years of the twentieth century, new conductive polymer-based organic light emitting diodes (LED) beckoned. In 1990, Richard Friend's group at Cambridge University reported light was produced upon application of an electrical potential to a conductive polymer;[12] this was similar to the light produced with application of an applied voltage to an anthracene crystal that was reported from Martin Pope's laboratory in 1962.[13] Today, numerous groups worldwide are working feverishly to commercialize a myriad of products based on thin-film organic LEDs. Likewise, organic devices such as field-effect transistors[14] and "plastic chips"[15] are being pushed towards commercialization. Clearly, conductive polymers certainly have a bright, if not illuminating, future and their discoverers, Alan G. MacDiarmid, Hideki Shirakawa, and Alan J. Heeger, certainly deserve the high accolade bestowed by the Noble Foundation for their seminal discovery.

[1] a) H. N. McCoy, W. C. Moore, *J. Am. Chem. Soc.* **1911**, *33*, 273; b) H. Kraus, *J. Am. Chem. Soc.* **1913**, *34*, 1732.

[2] H. Akamatsu, H. Inokuchi, Y. Matsunaga, *Nature* **1954**, *173*, 168.

[3] a) D. S. Acker, R. J. Harder, W. R. Hertler, W. Mahler, L. R. Melby, R. E. Benson, W. E. Mochel, *J. Am. Chem. Soc.* **1960**, *82*, 6408; b) R. G. Kepler, P. E. Bierstedt, R. E. Merrifield, *Phys. Rev. Lett.* **1960**, *5*, 503.

[4] L. R. Melby, *Can. J. Chem.* **1965**, *43*, 1448.

[5] D. Jerome, A. Mazaud, M. Ribault, K. Bechgaard, *J. Phys. Lett. (Paris)* **1980**, *41*, L45.

[6] V. V. Walatka, Jr., M. M. Labes, J. H. Perlstein, *Phys. Rev. Lett.* **1973**, *31*, 1139.

[7] R. L. Green, G. B. Street, L. J. Sutter, *Phys. Rev. Lett.* **1975**, *34*, 557.

[8] H. Shirakawa, E. J. Louis, A. G. MacDiarmid, C. K. Chiang, A. J. Heeger, *J. Chem. Soc. Chem. Comm.* **1977**, 579.

[9] "Synthesis and Properties of Low-Dimensional Materials" in *Ann. N.Y. Acad. Sci.* (Eds.: J. S. Miller, A. J. Epstein), **1978**, p. 313.

[10] J. H. Kreiger, *Chem. Eng. News* **1977**, *55*(27), 14.

[11] J. S. Miller, *Adv. Mater.* **1993**, *5*, 587, 671.

[12] J. H. Burroughes, D. D. C. Bradley, A. R. Brown, R. N. Marks, K. Mackay, R. H. Friend, P. L. Burns, A. B. Holmes, *Nature* **1990**, *347*, 539.

[13] M. Pope, H. P. Kallmann, P. Magnante, *J. Chem. Phys.* **1963**, *38*, 2042.

[14] a) G. Horowitz, *Adv. Mater.* **1990**, *2*, 287; b) G. Horowitz, X-Z. Peng, D. Fichou, F. Garnier, *J. Mole Electron.* **1991**, *7*, 85.

[15] G. H. Gelinck, T. C. T. Geuns, D. M. de Leeuw, *Appl. Phys. Lett.* **2000**, *77*, 1487.